

A review of band structure and material properties of transparent conducting and semiconducting oxides: Ga_2O_3 , Al_2O_3 , In_2O_3 , ZnO , SnO_2 , CdO , NiO , CuO , and Sc_2O_3



Cite as: Appl. Phys. Rev. **9**, 011315 (2022); doi: [10.1063/5.0078037](https://doi.org/10.1063/5.0078037)

Submitted: 9 November 2021 · Accepted: 5 January 2022 ·

Published Online: 4 March 2022



View Online



Export Citation



CrossMark

Joseph A. Spencer,^{1,2,a)} Alyssa L. Mock,^{3,4} Alan G. Jacobs,² Mathias Schubert,^{5,6} Yuhao Zhang,¹ and Marko J. Tadjer²

AFFILIATIONS

¹Center for Power Electronics Systems (CPES), Virginia Polytechnic Institute and State University, Blacksburg, Virginia 24060, USA

²U.S. Naval Research Laboratory, 4555 Overlook Ave. SW, Washington, DC 20375, USA

³National Research Council Research Associateship Programs, 500 Fifth Street, Washington, DC 20001, USA

⁴Department of Electrical and Computer Engineering, Weber State University, Ogden, Utah 84408, USA

⁵Department of Electrical and Computer Engineering, University of Nebraska Lincoln, Lincoln, Nebraska 68588-0511, USA

⁶Department of Physics, Chemistry and Biology (IFM), Linköping University, 58183 Linköping, Sweden

^{a)}Author to whom correspondence should be addressed: jspencer95@vt.edu

ABSTRACT

This Review highlights basic and transition metal conducting and semiconducting oxides. We discuss their material and electronic properties with an emphasis on the crystal, electronic, and band structures. The goal of this Review is to present a current compilation of material properties and to summarize possible uses and advantages in device applications. We discuss Ga_2O_3 , Al_2O_3 , In_2O_3 , SnO_2 , ZnO , CdO , NiO , CuO , and Sc_2O_3 . We outline the crystal structure of the oxides, and we present lattice parameters of the stable phases and a discussion of the metastable polymorphs. We highlight electrical properties such as bandgap energy, carrier mobility, effective carrier masses, dielectric constants, and electrical breakdown field. Based on literature availability, we review the temperature dependence of properties such as bandgap energy and carrier mobility among the oxides. Infrared and Raman modes are presented and discussed for each oxide providing insight into the phonon properties. The phonon properties also provide an explanation as to why some of the oxide parameters experience limitations due to phonon scattering such as carrier mobility. Thermal properties of interest include the coefficient of thermal expansion, Debye temperature, thermal diffusivity, specific heat, and thermal conductivity. Anisotropy is evident in the non-cubic oxides, and its impact on bandgap energy, carrier mobility, thermal conductivity, coefficient of thermal expansion, phonon modes, and carrier effective mass is discussed. Alloys, such as AlGaO , InGaO , $(\text{Al}_x\text{In}_y\text{Ga}_{1-x-y})_2\text{O}_3$, ZnGa_2O_4 , ITO, and ScGaO , were included where relevant as they have the potential to allow for the improvement and alteration of certain properties. This Review provides a fundamental material perspective on the application space of semiconducting oxide-based devices in a variety of electronic and optoelectronic applications.

Published under an exclusive license by AIP Publishing. <https://doi.org/10.1063/5.0078037>

TABLE OF CONTENTS

I. INTRODUCTION	2	2. Temperature dependence of bandgap energy	12
II. GALLIUM OXIDE	4	D. Material properties	12
A. Crystal structure	4	1. Thermal properties	12
B. Growth	5	2. Phonon properties	13
C. Electronic band structure	7	3. Electrical properties	17
1. Experimentally determined bandgap	8	E. Doping and defects	20
		F. Polymorphs	21

G. Alloys	24	G. Summary of SnO ₂ property values	66
1. Aluminum gallium oxide—(Al _x Ga _{1-x}) ₂ O ₃	25	VII. CADMIUM OXIDE.....	66
2. Indium gallium oxide (In _x Ga _{1-x}) ₂ O ₃	27	A. Crystal structure	66
3. Aluminum indium gallium oxide—		B. Growth	67
(Al _x In _y Ga _{1-x-y}) ₂ O ₃	28	C. Electronic band structure.....	67
4. Zinc gallium oxide—(ZnGa ₂ O ₄).....	28	1. Bandgap energy.....	69
H. Summary of β-Ga ₂ O ₃ property values	29	2. Temperature dependence of bandgap energy	70
III. ALUMINUM OXIDE	30	D. Material properties.....	70
A. Crystal structure	30	1. Thermal properties.....	70
B. Growth	33	2. Phonon properties	71
C. Electronic band structure.....	33	3. Electrical properties	71
1. Bandgap energy.....		E. Doping and defects	72
2. Temperature dependence of bandgap energy		F. Polymorphs.....	73
D. Material properties.....	36	G. Summary of CdO property values	73
1. Thermal properties.....		VIII. NICKEL OXIDE	73
2. Phonon properties		A. Crystal structure	73
3. Electrical properties		B. Growth	75
E. Doping and defects	38	C. Electronic band structure.....	75
F. Summary of Al ₂ O ₃ property values	39	1. Bandgap Energy	76
IV. INDIUM OXIDE	39	D. Material properties	76
A. Crystal structure	40	1. Thermal properties.....	77
B. Growth	41	2. Phonon properties	77
C. Electronic band structure.....	42	3. Electrical properties	77
1. Bandgap energy.....		E. Doping and defects	78
2. Temperature dependence of bandgap energy		F. Summary of NiO property values	78
D. Material properties	42	IX. COPPER OXIDE	78
1. Thermal properties.....		A. Crystal structure	78
2. Phonon properties		B. Growth	80
3. Electrical properties		C. Electronic band structure.....	81
E. Doping and defects	44	1. Bandgap energy.....	82
F. Summary of In ₂ O ₃ property values	45	D. Material properties	84
V. ZINC OXIDE.....	45	1. Thermal properties.....	84
A. Crystal structure	50	2. Phonon properties	84
B. Growth	51	3. Electrical properties	85
C. Electronic band structure.....	52	E. Doping and defects	86
1. Bandgap energy.....		F. Summary of CuO property values	86
2. Temperature dependence of the bandgap		X. SCANDIUM OXIDE.....	86
energy		A. Crystal structure	88
D. Material properties	52	B. Growth	88
1. Thermal properties.....		C. Electronic band structure and bandgap.....	89
2. Phonon properties		1. Temperature dependence of bandgap energy	90
3. Electrical properties		D. Material properties	90
E. Doping and Defects	57	1. Thermal properties.....	91
F. Polymorphs.....	57	2. Phonon properties	91
G. Alloys	58	3. Electrical properties	91
H. Summary of ZnO property values.....	59	E. Doping and defects	91
VI. TIN OXIDE	59	F. Alloys	91
A. Crystal structure	60	G. Summary of Sc ₂ O ₃ property values	92
B. Growth	61	XI. COMPARATIVE SUMMARY OF MATERIAL	
C. Electronic band structure.....	61	PROPERTIES	92
1. Bandgap energy.....		XII. CONCLUSION	100
2. Temperature dependence of bandgap energy			
D. Material properties	63		
1. Thermal properties.....			
2. Phonon properties			
3. Electrical properties			
E. Doping and defects	66		
F. Polymorphs.....	66		

I. INTRODUCTION

Transparent conducting and semiconducting oxides have become some of the most heavily researched material classes. Investigations have been driven by the desire for a better understanding of the material, electrical, electronic, and optical properties that

encompass these oxides. Understanding of these properties could lead to breakthroughs in many aspects of semiconductor device designs. Increasing research could lead to improved growth quality of bulk crystals and thin films, which could decrease material defects and improve electrical properties. This stands to help further device efficiency and implementation of these oxides into novel device designs in the power electronics field. Reviewed literature included in this work spans almost an entire century. With increased knowledge and understanding, the prospect of implementing oxides into electronic applications grows. Many improvements have been made concerning oxides over the years. Many material synthesis improvements are evident in measured parameters, such as increased carrier mobility, increased growth and crystalline quality, increased precision of bandgap engineering, and alloying advancements.

An oxide is a chemical compound that forms between at least one oxygen atom and another element. The selected elements for the nine oxides are highlighted within the periodic table in Fig. 1 and include Al, Ga, In, Sn, Zn, Cd, Ni, Cu, and Sc. Of the nine, five are transition metals (Zn, Cd, Ni, Cu, and Sc) and four are basic metals (Al, Ga, In, and Sn). These elements and their oxides were selected based on their contributions and relevance to power electronic devices. Device design has become increasingly complex, and extensive research into materials such as these oxides is needed.

Although anisotropy is a common trait among many oxides, it poses challenges for the determination of many material properties. Anisotropy is a difference within a material property dependent upon direction or orientation. Material properties, such as optical, thermal, and mechanical, are affected by anisotropy depending on the rank of their respective response tensor.¹ This can lead to a specific direction

having more advantageous properties for certain applications. Cubic structures (CdO , $\text{bcc-In}_2\text{O}_3$, NiO , Cu_2O , Sc_2O_3 , zinc-blende- CdO , and NaCl-NiO) are the least complicated and are generally considered to have isotropic properties due to the high degree of crystal symmetry present as evidenced by $a = b = c$ and $\alpha = \beta = \gamma = 90^\circ$ within the crystal structure. However, even with the high degree of crystal symmetry, cubic structures are not entirely isotropic. The fourth ranked elastic tensor of the cubic structure is anisotropic. The wurtzite, tetragonal, and rhombohedral structures have uniaxial anisotropy ($\alpha\text{-Al}_2\text{O}_3$, $\alpha\text{-Ga}_2\text{O}_3$, ZnO , and $\text{rh-In}_2\text{O}_3$, and Cu_4O_3) with $a = b \neq c$, yielding two non-equivalent high-symmetry directions. For example, a measure of the bandgap energy or dielectric constant along a and b will differ from the same measurement taken along c . Orthorhombic structures ($\kappa\text{-Ga}_2\text{O}_3$) are even more complicated as there are now three different lattice constants $a \neq b \neq c$ resulting in biaxial anisotropy. Monoclinic ($\beta\text{-Ga}_2\text{O}_3$ and CuO) and triclinic structures, where the angles between axes are no longer constrained to 90° , have even less crystal symmetry and, thus, are more complicated and challenging to characterize. For example, correct analysis to obtain the complete dielectric tensor is necessary in order to identify the directional dependencies of the optical features, which stem from dipole oriented electronic transitions or polarized infrared (IR) phonon modes. A thorough understanding of the impact of anisotropy on the material properties will allow for more intentional and novel design of complex oxide-based devices for electronic and optoelectronic applications.

This review focuses on a multitude of material properties that have strong relevance to the implementation of oxides in electronic devices. Basic material properties allow for an understanding of how a material can be implemented into device structures. Each section focuses on a different oxide: Ga_2O_3 , Al_2O_3 , In_2O_3 , ZnO , SnO_2 , CdO ,

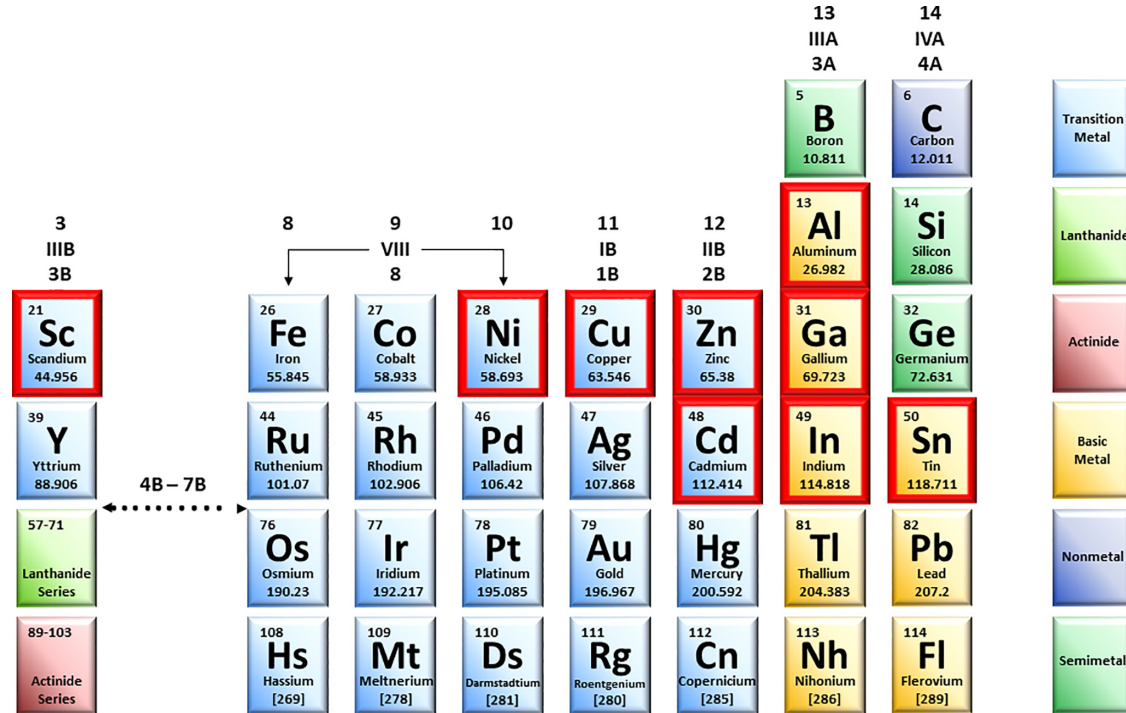


FIG. 1. A partial periodic table highlighting the elements Sc, Ni, Cu, Zn, Cd, Al, Ga, In, and Sn that comprise the oxides discussed in this review.

NiO , CuO , and Sc_2O_3 with alloys addressed in the subsections within relevant sections. For each oxide, the crystal and electronic structures are detailed. The crystallographic cell structures presented for each of the oxides were obtained and visualized using the VESTA program.² Special attention is given to electronic structure, summarizing bandgap (E_g) values reported across the literature along with methods used to determine E_g . Where it is reported, the temperature dependence of the bandgap is also highlighted. Material related parameters are grouped into four subsections: basic material properties, thermal properties, phonon properties, and electrical properties. The basic and structural material properties include crystal allotropes, material density, bulk modulus, and melting point. Within the thermal properties, parameters including Debye temperature, specific heat, thermal diffusivity, coefficient of thermal expansion (CTE), and thermal conductivity are discussed. The phonon properties section highlights the irreducible representations for the Raman and IR phonons as well as the experimental and theoretical values for the phonon mode frequencies. In addition to the bandgap, the summary of electrical properties includes electron affinity, breakdown field strength, static and high frequency dielectric constants, effective mass, and carrier mobility. Growth techniques for both the bulk crystal and thin film samples are highlighted as well as possible dopants and known material defects are seen throughout the literature. Where relevant, the properties of the polymorphs and metastable phases for the oxides are highlighted for comparison to the stable phase along with potential uses and benefits.

In addition, material properties are grouped into four tables allowing for comparison across all nine oxides. A wide range of values and literature sources have been included for each property to show where there is good agreement or the need for more research. Section XI discusses the comparisons of the basic material, thermal, electrical, and optical properties. Of note, the optical properties comparison table includes values for the bandgap, static and high frequency dielectric constants, and the Raman and IR active phonon modes. While this Review highlights many key properties and parameters, the electronic structure are the focus of this work. In-depth texts and reviews on condensed matter physics cited here provide further details on properties discussed in this work, such as electronic bandgap properties.^{3–7} This Review aims to provide wide ranging insight into material properties to further advance integration into electronic and optoelectronic devices.

II. GALLIUM OXIDE

Gallium oxide or Gallia, sometimes abbreviated as “GO,” is a transparent semiconducting oxide that has gained significant attention recently because of its ultra wide bandgap, high critical field, and anisotropic transport and optical properties. Ga_2O_3 research and technology development are driven by continuing improvement of substrate and epitaxial growth techniques and resulting material, resulting in a similar technology development road map followed in recent years by wide bandgap semiconductors such as 4H-SiC and GaN. Due to its large bandgap, applications in power electronics,⁸ solar applications, such as solar cells and solar blind UV photodetectors,^{9–11} microwave and RF applications,¹² and novel sensor technologies,¹³ have emerged with the potential to compete or eventually improve over 4H-SiC and GaN technology.

Gallium oxide was discovered in 1875 but was not considered for electronic applications until increased attention in the early 2000s

brought to the forefront the possibility of its use as an ultrawide bandgap semiconductor for power device applications. Prior to the 2000s, the material quality of Ga_2O_3 was rather poor and limited the complexity of potential devices. As inexpensive high-quality substrates have become more widely available, the field of applications and devices has expanded greatly and interest in Ga_2O_3 has grown exponentially.¹⁴

A. Crystal structure

Ga_2O_3 consists of five polymorphs/phases: α , β , γ , δ , and ε .¹⁵ A κ phase has gained attention in the recent literature as a possible sixth polymorph but is considered a subgroup of ε .^{16,17} As with most material polymorphs, each phase belongs to its own space group with its own structure and has its own unique gallium ion coordination number.¹⁸ Table I highlights the polymorphs with their respective space groups and lattice parameters while a brief discussion of their material properties is presented in Sec. II F.

The α - Ga_2O_3 phase belongs to space group $R\bar{3}c$ (#167) and has a rhombohedral lattice structure belonging to the trigonal crystal system which is the same as corundum, the primary structure of the stable phase of Al_2O_3 .^{19–21}

The γ -phase has been scarcely researched with little known about the polymorph. Zinkevich and Aldinger (Ref. 22) and Pohl (Ref. 23) report a face-centered cubic centrosymmetric structure belonging to space group $Fd\bar{3}m$ (#227). Other sources report the γ -phase to be a cubic defective spinel structure.^{22,24} This polymorph was shown to grow on cubic spinel structures.²⁵

The δ -phase is also a cubic structure belonging to space group $Ia\bar{3}$ (#206), a centrosymmetric body-centered cubic structure. This structure is considered a C-type rare earth.^{15,26} The lattice constant was predicted to be 9.52 Å and reported to be $a = 10.0$ Å.^{15,27}

The ε -phase of Ga_2O_3 is one of the more complicated and lesser understood polymorphs due in part to a lack of research. It is predicted to exhibit piezoelectric properties as the crystal structure breaks inversion symmetry.²⁸ Initially thought to be an orthorhombic structure of space group $Pna2_1$ ²⁰ (#33), it was later concluded to be a hexagonal structure belonging to space group $P6_3mc$ (#186).²⁶ The orthorhombic structure seen by Yoshioka *et al.* (Ref. 20) has been shown to belong to κ - Ga_2O_3 with space group $Pna2_1$ (#33), which was found to be a subgroup of the ε phase.^{16,17}

The β -phase of Ga_2O_3 is thermodynamically stable under ambient conditions and has become the focus of much of electronic materials research. This focus has necessitated significant work to determine the material properties and the anisotropy of this specific phase. Kohn *et al.* (Ref. 35) reported what is thought to be the first known growth of β - Ga_2O_3 crystals in 1957. These crystals were found to be anisotropic and hypothesized to be either tetragonal, hexagonal, orthorhombic, or monoclinic in symmetry. Measured interfacial angles (around 53° and 76°) were not consistent with uniaxial symmetry, thus narrowing the structure down to either being monoclinic or orthorhombic. Optical findings and diffraction patterns pointed toward an orthorhombic unit cell; however, the absence that was observed in the single-crystal pattern did not coincide with any other orthorhombic space groups. This left the monoclinic structure as the only remaining option. Using a high magnification, re-entrant angles often seen in twinning were observed. In crystallography, twinning shows that the orthorhombic structure can be derived from the

TABLE I. Ga_2O_3 polymorphs and crystal structure with associated lattice constants determined from experiment and theory.

Phase	Structure	Space group	Lattice (Å)
α	Trigonal/rhomb.	$R\bar{3}c$ (#167)	$a = 4.97^{27,29,a}$ $c = 13.437$ $a = 4.975^{30,b}$ $c = 13.457$ $a = 4.983^{31,a}$ $c = 13.433$
β	Monoclinic	$C2/m$ (#12)	$a = 12.214^{32,a}$ $b = 3.037$ $c = 5.798$ $\beta = 103.83^\circ$ $a = 12.23^{33,a}$ $b = 3.03$ $c = 5.80$ $\beta = 103.7^\circ$
γ	Cubic	$Fd\bar{3}m$ (#227)	$a = 8.35^{15,34,d}$ $a = 8.237^{26,a}$ $a = 8.22^{23,27,a}$
δ^c	Body-centered-cubic	$Ia\bar{3}$ (#206)	$a = 9.52^{15,29,d}$ $a = 10.00^{15,29,a}$
ε	Hexagonal	$P6_3mc$ (#186)	$a = 2.907^{26,a}$ $c = 9.255^{26,a}$
κ^e	Orthorhombic	$Pna2_1$ (#33)	$a = 5.0463^{16,d}$ $b = 8.7020$ $c = 9.2833$ $a = 5.066^{17,a}$ $b = 8.700$ $c = 9.261$

^aExperimental.^bTheoretical.^cNanocrystalline form of ε phase (Ref. 26).^dPredicted.^eSubgroup of ε phase.

monoclinic structure, explaining the initial orthorhombic classification. The symmetry for $\beta\text{-}\text{Ga}_2\text{O}_3$ was then concluded to be monoclinic belonging to space group $A2/m$ with lattice parameters $a = 5.80$ Å, $b = 3.04$ Å, and $c = 12.23$ Å and $\beta = 103^\circ 42'$.³⁵ However, in 1960, Geller (Ref. 36) proposed that $\beta\text{-}\text{Ga}_2\text{O}_3$ should be designated as $C2/m$ (#12), in keeping the monoclinic cell convention of $c < a$. This is supported by the fact that the material does not exhibit piezoelectric or pyroelectric properties.³⁶ A decade later in 1976, Wolten *et al.* (Ref. 37) reported that $\beta\text{-}\text{Ga}_2\text{O}_3$ possessed a lower triclinic symmetry (P1). This lower symmetry was refuted later by both Geller (Ref. 38) and Åhman *et al.* (Ref. 32). Recently, Åhman *et al.* (Ref. 32) used precise

x-ray diffraction and found that there exists a clear “C-centered monoclinic cell” that belongs to the $C2/m$ (#12) space group, further supporting Geller’s designation.³² Åhman reported values of $a = 12.214$ Å, $b = 3.037$ Å, and $c = 5.998$ Å.³²

A key feature that leads to very unique property behaviors and further elevates the complexities of the β -phase is the monoclinic angle (β) of the crystal. This angle is at around 103° .^{32,33} Schematics for the crystal structure of $\beta\text{-}\text{Ga}_2\text{O}_3$ and $\alpha\text{-}\text{Ga}_2\text{O}_3$ are shown in Fig. 2. Within these structures, there are two positions for the Ga ion labeled Ga(I), which resides with a tetrahedral geometry and Ga(II), which resides with an octahedral geometry. The oxygen ions arrange themselves around the Ga sites in a “distorted cubic” packing structure with oxygen ions occupying three distinct positions denoted O(I), O(II), and O(III).¹⁸ Anisotropy is prevalent among the material properties of $\beta\text{-}\text{Ga}_2\text{O}_3$ (and several other polymorphs to a lesser extent). Anisotropy arises from the low symmetry crystal structure leading to the variation of properties depending upon orientation of the crystal axes, which affects the optical, physical, thermal, and the electrical properties of the material. For example, there are variations in thermal conductivity values,^{39–41} effective mass,⁴² static dielectric constants,⁴³ high frequency dielectric constants,⁴⁴ bandgap energy, thermal diffusivity,⁴¹ hardness (Vicker’s),⁴¹ and coefficients of thermal expansion^{41,45} all depending on a specific crystal direction. By understanding the specific properties and the effects of anisotropy, $\beta\text{-}\text{Ga}_2\text{O}_3$ devices can continue to improve in design and efficiency.

Table I summarizes the lattice constants for the five Ga_2O_3 polymorphs as well as the κ phase subgroup. With the exception of the predicted value for the lesser known δ -phase, the reported lattice constants are in good agreement across the cited literature. Unless stated otherwise, all discussions throughout the remainder of this section refer to the stable, single crystalline, β phase.

B. Growth

The history of crystal growth for $\beta\text{-}\text{Ga}_2\text{O}_3$ dates back to the late 1950s when the first crystals were successfully grown from excess gallium.³⁵ The process involved sealing elemental phosphorus and gallium into a silica tube for 3 h at a temperature of 1100°C before cooling at a rate of 40°C/h . The primary material that resulted from this process was not $\beta\text{-}\text{Ga}_2\text{O}_3$ but rather GaP crystals. However, within the silica tube on the walls above the melt growth was very small amount of light-blue crystals that had a lath-shape to them. These minor phase crystals that formed on the tube were later shown to be the very first samples of $\beta\text{-}\text{Ga}_2\text{O}_3$ crystals grown from the vapor phase.³⁵ Six years later in 1963, Remeika (Ref. 46) was the first to successfully demonstrate $\beta\text{-}\text{Ga}_2\text{O}_3$ crystals using a flux-growth method. The Verneuil method of melt-grown $\beta\text{-}\text{Ga}_2\text{O}_3$ crystals was first shown one year later in 1964.⁴⁷ Chemical vapor transport (CVD) growth of single-crystal $\beta\text{-}\text{Ga}_2\text{O}_3$ was first reported by Lorenz *et al.*⁴⁸ in 1967 with many other groups (Refs. 49–51) following up on their success for a number of years. It was not until 1983 that the Czochralski growth method was first mentioned in the literature by Vasiltsov *et al.* (Ref. 52). Unfortunately, no context or specifics for this melt-growth process were given. In the year 2000, the first details regarding the Czochralski growth method were published by Tomm *et al.* (Ref. 53). From this study, the use of the Czochralski growth method in the literature for the growth of $\beta\text{-}\text{Ga}_2\text{O}_3$ increased greatly.^{54–57} In 1996, another method of crystal growth for $\beta\text{-}\text{Ga}_2\text{O}_3$ called the optical

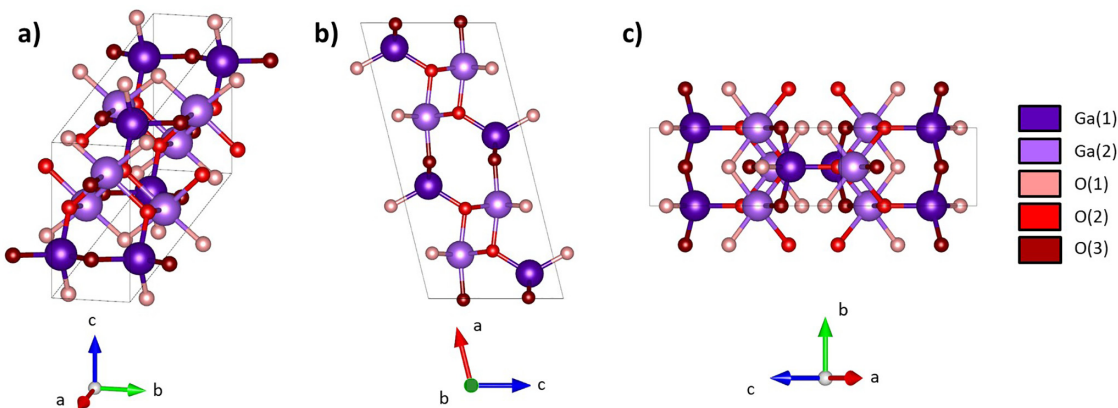


FIG. 2. Schematics for the crystal structure of (a) β -Ga₂O₃ belonging to space group C2/m shown with the c-axis orientated upward, (b) the (010) plane for β -Ga₂O₃, and (c) the (201) plane for β -Ga₂O₃. For α -Ga₂O₃, purple, Ga and red, O. The Ga(1), Ga(2), O(1), O(2), and O(3) atom colors are shown for β -Ga₂O₃.

floating zone (OFZ) was published.⁵⁸ As a result, other published works using OFZ appeared across the literature with much success.^{59–61} Another melt-growth process known as edge-defined film-fed growth (EFG) was first successfully shown for β -Ga₂O₃ single-crystals in 2008 by Aida *et al.* (Ref. 62). It should be noted that Shimamura *et al.* were the first to attempt and show proof of EFG β -Ga₂O₃; however, their attempt yielded heavily cracked crystals with many polycrystalline inclusions. From the initial success that Aida *et al.* saw in 2008, research into EFG of β -Ga₂O₃ increased greatly. Kuramata *et al.* (Ref. 63) published a now heavily cited work in 2016 where 2 in. and 4 in. diameter substrates of β -Ga₂O₃ were achieved from EFG.

When growing β -Ga₂O₃ float zone crystals, the conductivity can be controlled by changing the gas ambience. Ueda *et al.* (Ref. 64) showed that if a pure O₂ atmosphere is used, the resultant crystals will be clear and colorless and exhibit a conductivity in the range of $10^{-9} \Omega^{-1} \text{ cm}^{-1}$. When adding nitrogen partial pressures, the resultant crystals turned pale blue with increasing conductivity yielding a maximum conductivity of $38 \Omega^{-1} \text{ cm}^{-1}$.⁶⁴ Maximum conductivity was achieved with a N₂/O₂ ratio of 0.4/0.6, and it was determined that very low oxygen partial pressure yielded unstable growth.

Another study by Galazka *et al.* (Ref. 54) had contrasting results in terms of the relationship of grown crystal color, the amount of O₂ present, and the resultant conductivity. Using the Czochralski growth method, Ga₂O₃ crystals were grown in a Ar/CO₂ or pure CO₂ atmosphere. When the CO₂ partial pressure was increased, the crystal color went from blue to clear to gray. It was found that transparent crystals possessed low conductivity. The color change toward a blue crystal was a result of the free carrier absorption, while gray coloring resulted from carbon incorporation. When high amounts of oxygen partial pressure were used in the Czochralski growth, the carrier concentration was found to be high. This leads to a higher conductivity under high CO₂ partial pressure, coming from the carbon contamination.⁵⁴

Galazka *et al.* (Ref. 65) also studied dopant segregation using trivalent Cr, Ce, and Al doping in β -Ga₂O₃ Czochralski crystals. There is a strong dependence on the concentration of O₂ in the growth atmosphere for Cr and Ce dopant segregation and charge state. The segregation coefficient of the grown crystals also saw a decrease as a result

of the Cr-Si co-doping. The Si⁴⁺ and Cr³⁺ ions were observed to compete for the octahedral Ga(I) site.⁶⁵

The increased conductivity from CZ growth under oxygen led to a hypothesis that the n-type conductivity was the result of oxygen vacancies. This hypothesis was opposed by Varley *et al.* (Ref. 66) using first principles calculations. From their findings, the oxygen vacancies that are present in the crystal are deep donors with a high ionization energy (1 eV). This means that the oxygen vacancies could not be contributing to the conductivity. Varley *et al.* hypothesized that it is in fact the hydrogen that is increasing the conductivity and not the oxygen vacancies.⁶⁶

In a more recent report by Galazka *et al.* (Ref. 54), the Czochralski crystal growth method was utilized to better understand how the incorporation of dopants impacted characteristics such as the crystal appearance, growth stability, and electrical properties. The Czochralski method produced single crystals of β -Ga₂O₃ all grown along the $\langle 0\ 1\ 0 \rangle$ direction at a 1.5 mm/h growth rate and at 9 rpm. The grown crystals had a diameter of 18 mm with a length ranging from 20 to 50 mm, depending on the specific dopant and concentration. According to Galazka *et al.*, there are two important factors that were considered for doping segregation and the subsequent incorporation into the crystal growth of β -Ga₂O₃. These factors are the difference of the atomic radii of Ga³⁺ and the dopant used as well as the dopants thermal stability at elevated temperatures often experienced during crystal growth.⁶⁷ The dopants consisted of Li¹⁺, Cu¹⁺ (monovalent), Mg²⁺, Co²⁺, Ni²⁺ (divalent), Ce³⁺, Cr³⁺, Al³⁺ (trivalent), and Si⁴⁺, Sn⁴⁺, Ge⁴⁺ (tetravalent). When thermally unstable carbonates are used as dopants during crystal growth, their decomposition is not immediate but gradual. This decomposition alters the melt thermodynamic equilibrium and acts as a continuous oxygen source with little to no additional metal incorporation. This source of oxygen also differs from the atmospheric oxygen as the dopant oxygen is being produced within the melt volume as opposed to just on the melt surface. This drastically alters the resultant crystal growth resulting in a smoother crystal surface and little to no coloration. With a continuous and gradual source of oxygen from the unstable dopants, there is no longer a need for such high oxygen concentrations in the growth atmosphere.⁶⁷

Growth of thin films of Ga_2O_3 has important implications for device fabrication.^{68–70} Techniques, such as ozone assisted molecular beam epitaxy (MBE), have been used to successfully grow thin films of $\beta\text{-}\text{Ga}_2\text{O}_3$ capable of achieving device quality.^{71–73} The growth rate from the epitaxial method has drastic dependence on the growth plane with the (010) plane having a growth rate ten times higher than the (100) plane.⁷¹ Atomic layer deposition (ALD) has also been shown to be an effective method for growth of Ga_2O_3 thin films.⁷⁴ In a recent study, Wheeler *et al.* (Ref. 75) reported using plasma-enhanced ALD (PEALD) to grow crystalline films of multiple phases of Ga_2O_3 . Metal organic vapor deposition (MOCVD) is another popular method for film growth.⁷⁶ Alema *et al.* (Ref. 77) reported MOCVD growth of Ga_2O_3 thin films at speeds of up to $10 \mu\text{m/h}$.⁷⁷ Halide vapor-phase epitaxy (HVPE) and pulsed laser deposition (PLD) was also shown to produce high quality films grown homoepitaxially.^{78,79}

When fabricating thin films of $\beta\text{-}\text{Ga}_2\text{O}_3$, it was found that bandgap can be altered by varying the annealing temperature. The optical bandgap has been shown to increase with an increased annealing temperature for films deposited by PEALD. Using transmission spectra, $\beta\text{-}\text{Ga}_2\text{O}_3$ films displayed optical bandgaps of 5.00 and 5.24 eV, the larger bandgap being a result of the increased annealing temperature.⁸⁰

C. Electronic band structure

The electronic band structure of $\beta\text{-}\text{Ga}_2\text{O}_3$ is a complex topic that is still being heavily researched. Bandgap calculations are not trivial, leading to a variety of different calculation methods with varying results. Many advancements have been made over the last few decades in producing calculated electronic bandgap structures of $\beta\text{-}\text{Ga}_2\text{O}_3$. Density functional theory (DFT) calculations particularly the use of hybrid functionals have proven to be instrumental in the study of $\beta\text{-}\text{Ga}_2\text{O}_3$. The progress that has been made is evident in the anisotropic details and accurate transition energies being produced. One of the earliest works dating back to 1999 by Hajnal *et al.* (Ref. 81) used a combination of the cyclic cluster model and the PM3 semiempirical method to produce a single bandgap energy of 5.58 eV. Using local density approximation (LDA) to produce a bandgap energy was proposed but ultimately not utilized as it was said to have an overbinding effect and, thus, a less accurate value than the PM3 method. There was a brief mention on the observed polarization dependence that is present in the optical absorption and that it could be a result of anisotropy. Hajnal *et al.* made note of the wide range of experimentally determined bandgap energies that they saw reported in the literature and stated “the reason of this relative uncertainty might be the anisotropy of the monoclinic material, and/or the difference in preparation”.⁸¹ No other details or values associated with the electronic band structure or its anisotropy were given. A few years later in 2004, Yamaguchi *et al.* (Ref. 82) used LDA along with the first principles full-potential linearized augmented plane wave method (FLAPW). Calculations showed an indirect bandgap with an isotropic shape of the conduction band maximum at Γ and a flat, anisotropic valence band minimum at the E line. The effective mass of the valence band is larger than that of the conduction band effective mass.⁸² Again, very few details on the specifics of the anisotropy of the band-to-band transition energy calculations were discussed.

Often times reported ground state DFT bandgap values are skewed to lower energy levels as the potential among the excited electrons from the exchange correlation is underestimated. Even LDA

without the addition of hybrid functionals and generalized gradient approximation (GGA) with multiple hybrid functions such as PBE are shown to underestimate the bandgap energy of $\beta\text{-}\text{Ga}_2\text{O}_3$. LDA yielded a bandgap of energy of 2.19 eV while GGA-PBE and GGA-DFT yielded values of 2.356 and 4.40 eV, respectively.^{33,82,83} The upper valence bands consist of Ga 4s, 4p, and O 2p orbitals. The lower conduction bands are formed from Ga 4s and O 2p states. The middle and lower valence band orbitals are usually ignored as the electronic structure properties are dictated by the upper valence and lower conduction band. Another example of ground state DFT yielding significantly lower bandgap values is shown by Zhang *et al.* (Ref. 83) with intrinsic $\beta\text{-}\text{Ga}_2\text{O}_3$ displaying a calculated bandgap of 2.356 eV.

Many types of functionals and hybrid functionals have been used in the DFT framework to investigate the bandgap including LDA, GGA, B3LYP, HSE06, and PBE.^{19,53,66,82,84} Using a hybrid functional can result in a more accurate bandgap value when compared to the lower DFT value. Varley *et al.* (Ref. 66) used a 120-atom supercell for unintentionally n-doped single crystal $\beta\text{-}\text{Ga}_2\text{O}_3$ along with HSE06 screened hybrid functionals in order to investigate how oxygen vacancies and impurities influence the optical and electrical properties. An indirect bandgap off the M point is found to be 4.83 eV and a direct bandgap of 4.87 eV at the Γ point.⁶⁶

While many of the DFT and hybrid functional studies resulted in slightly different reported bandgap values, it was shown that the conduction band edge occurred at the Γ point and the valence bands are predominately flat. Calculations show an indirect bandgap for $\beta\text{-}\text{Ga}_2\text{O}_3$ but it is by such a small margin (often a few meV) that it is experimentally considered to be a direct bandgap. This review reports $\beta\text{-}\text{Ga}_2\text{O}_3$ as a direct bandgap material. DFT calculations coupled with linear combination of atomic orbitals (LCAO) approximation carried out by He *et al.* (Ref. 19) yielded theoretically determined bandgap values in good agreement with experimentally determined values discussed in Sec. II C 1. The use of this all-electron DFT method allows for the optical, electrical, and structural properties of the oxide to be studied. Using LCAO and treating the exchange correlation via B3LYP function form produced calculated bandgap values of 4.66 eV for the indirect bandgap and 4.69 eV for the direct band. The indirect bandgap occurs at $M\text{-}\Gamma$ point with the M point at the valence band max only 0.03 eV higher than the Γ point. The valence band maximum is almost degenerate along two points of the Brillouin zone; Γ and M .¹⁹ According to Stepanov *et al.* (Ref. 18), there is some disagreement on the location of the valence band maximum (as evidenced by Varley and He), but it is seen to not affect the bandgap value.

Another study by Peelaers *et al.* (Ref. 85) produced band structures using the HSE density functional that continue to show some disagreement with other reported results.⁸⁵ The location of the valence band maximum was found to be on the face of the Brillouin zone on the I-L line yielding an indirect bandgap of 4.84 eV. The direct gap remained at the Γ point on the Brillouin zone and was found to be 4.88 eV for a difference of 0.04 eV between the direct and indirect bandgaps. The transitions of the bandgaps were studied, and it was reported that the indirect transition was over an order of magnitude weaker than the direct vertical transition at the Γ point. Because of the already small energy difference between the direct and indirect bandgaps and the very weak transitions of the indirect gap; a direct bandgap can be assumed for the bulk single crystal unintentionally doped $\beta\text{-}\text{Ga}_2\text{O}_3$.⁸⁵

In 2017, Mock *et al.* (Ref. 86) reported on the complexities of the bandgap while accounting for the anisotropic properties of the bandgap and excitonic contributions associated with the monoclinic nature of β -Ga₂O₃. Results yielded multiple band-to-band transition energies between the valence and conduction bands and highlighted the large amount of anisotropy present in the electronic band structure. This work shows just how far the electronic band structure calculations have advanced over the years serving to propel β -Ga₂O₃ research further into experimental device integration. Brillouin zone center plots were produced using two theoretical DFT methods, Perdew–Burke–Ernzerhof (PBE), and Gau-PBE functionals. As seen in Fig. 3, the main difference between the PBE and Gau-PBE methods is the energy gap opening that occurs between the valence and conduction band, roughly 2 eV wider for the Gau-PBE band structure. Using Gau-PBE, the lowest two band-to-band transitions were calculated from the band structure. The lowest transition which is mainly parallel to c is 4.74 eV while the second transition which is mainly parallel to a is 4.969 eV.⁸⁶ Both of these values are within ± 1 eV of Peelaers *et al.* direct and indirect bandgap values. For both plots, the Γ -point (Brillouin zone) center is dominated by the lowest point of the conduction band. Both Mock *et al.* and Peelaers *et al.* utilized the same high-symmetry points; however, Peelaers *et al.* used a HSE functional with a larger amount of Hartree–Fock (HF) exchange. The shift in the

conduction band could stem from the choice of the explicit density functional as well as the HF exchange weighting (35% HSE by Peelaers *et al.* as compared to 24% Gau-PBE by Mock *et al.*). The curvature of the valence bands appeared in good agreement across both works while Peelaers *et al.* displayed steeper and slightly shifted conduction bands. Possible causes for this shifted conduction band could stem from the larger amount of HF exchange used in the study of Peelaers *et al.* (35% compared to 24% Gau-PBE by Mock *et al.*), the differing hybrid functionals between the two studies, or a combination of both the selected hybrid functional and weighting. This shows how selecting a specific hybrid functional can alter Brillouin zone and bandgap energy calculations. With less of a conduction band shift in the Gau-PBE calculations, it is possible that Mock *et al.* (Ref. 86) present a more accurate theoretical representation for the bandgap energy in Fig. 3 that better aligns with current experimental values and better accounts for the anisotropic properties of monoclinic β -Ga₂O₃.

An experimental study by Janowitz *et al.* (Ref. 87) employing angle-resolved photoemission spectroscopy (ARPES) was used to determine the band structure and compare it to theoretical findings. Bulk β -Ga₂O₃ crystals were grown using the Czochralski method, and dispersion relations along the Γ -Z direction parallel to the b^* c^* cleavage plane were observed. At the Γ point, the lower binding energy bands have high intensity but only slight dispersion while the deeper valence bands have weaker intensity and higher dispersion. The A-M direction at the M point in the Brillouin zone has the deepest valence band, which is located at -11.05 eV. At the M point, the valence bandwidth is much more narrow than at the Γ point. Just off the M point is a valence band maximum. At the indirect bandgap, the overall width of the valence band is 7.37 eV and the energy difference between the direct and indirect bandgap is found to be \sim 50 meV.⁸⁷

The anisotropy of the electronic band structure and bandgap is also of importance when studying the band offsets and alloys of β -Ga₂O₃. Using projector augmented wave potential calculations, Mu *et al.* (Ref. 88) studied the band alignments between Ga₂O₃ and Al₂O₃ and how different orientations alter the offsets as a result of the low symmetry of the crystal structure. Band alignments between Al₂O₃ and Ga₂O₃ were investigated for four different crystal orientations [(100), (010), (001), and (201)] using DFT with a hybrid functional. Mu *et al.* reported conduction band offset for both strained and unstrained Al₂O₃, with and without atomic relaxation on the Ga₂O₃ surface. It was shown that the (100) orientation results in the largest conduction band offset, suggesting that the highest two-dimensional electron gas (2DEG) density by modulation doping could form at ternary interfaces along this orientation. A better understanding of the anisotropy within β -Ga₂O₃ can lead to more accurate values of the bandgap energies for the different crystallographic orientations and directions within the material. Further details on the calculated band offsets of Ga₂O₃ and Al₂O₃ can be found in Ref. 88. Ahmadi *et al.* (Ref. 89) were first to demonstrate 2DEG formation in β -(Al_xGa_{1-x})₂O₃/Ga₂O₃ heterostructures. Low-field transport properties of 2DEGs in β -(Al_xGa_{1-x})₂O₃/Ga₂O₃ heterostructures were performed by Kumar and Singisetti.⁹⁰

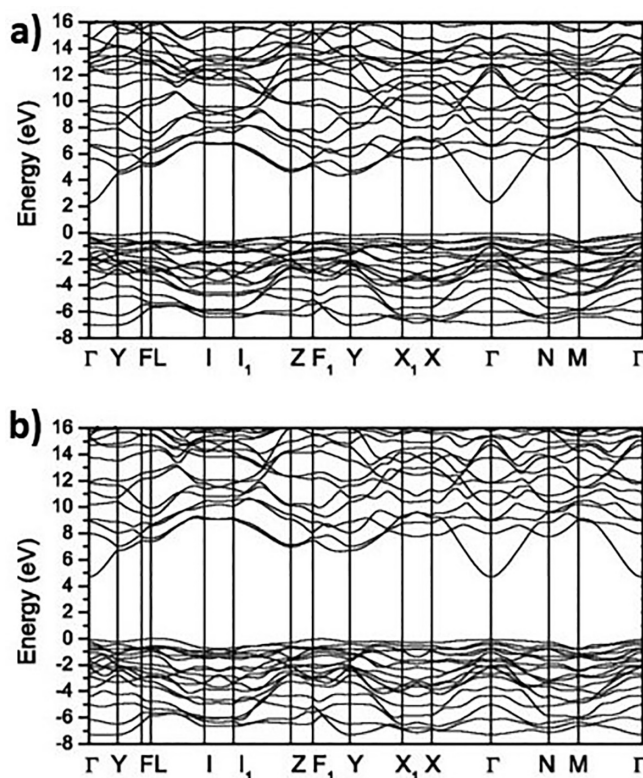


FIG. 3. Electronic band structure and high symmetry points of β -Ga₂O₃ at (a) GGA-DFT (PBE) level and (b) hybrid functional (HF) HF-DFT (Gau-PBE) level. Reproduced with permission from Mock *et al.*, Phys. Rev. B **96**, 245205 (2017). Copyright 2017 APS (Ref. 86).

1. Experimentally determined bandgap

The bandgap of β -Ga₂O₃ is a very widely researched topic and reported values vary depending on method. The binding and excitonic

peak energies for $\beta\text{-Ga}_2\text{O}_3$ are instrumental in determining an accurate value for the bandgap energy. They have recently been reported and are highlighted in Table II. Table III highlights selected values for the bandgap of $\beta\text{-Ga}_2\text{O}_3$ found in the literature from bulk and thin films using experimental and theoretical methods. The bandgap energy is often measured by optical methods, which are convenient and easily accessible. However, due to the low symmetry of $\beta\text{-Ga}_2\text{O}_3$, the direct optical transitions depend on the polarization direction of the electromagnetic wave traveling through a sample. The direct optical transition energies (band-to-band transition energies) can be tested and found by varying propagation and polarization directions in optical experiments, e.g., in polarized transmission and intensity measurements and transmission and reflection type ellipsometry. The band structure of $\beta\text{-Ga}_2\text{O}_3$ is highly complex at the Γ -point valence band maximum. The fundamental band-to-band transitions are regulated by quantum mechanic selection rules, which identify non-zero transition matrix elements between conduction and valence band states depending on valence and conduction band state and index and photon energy polarization (vector of the electric field). In $\beta\text{-Ga}_2\text{O}_3$, the first, second, and fourth top valence band participate in the lowest three transitions, and each has a different polarization direction of the photon involved in the transition. Wurtzite-structure GaN is similar but not nearly as complex as $\beta\text{-Ga}_2\text{O}_3$. In GaN, the top of the valence band is split into three bands, A, B, and C, with A and B being very similar in energy, and transitions from band C to the conduction band are blocked for polarization perpendicular to the lattice **c** axis, while strongly dominating for polarization parallel to **c** (see, for example, Feneberg *et al.* in Ref. 91). As a result, in GaN, the optical response is optically uniaxial in wide spectral regions, and dichroic (two-colored) in the near-band-gap spectral region. The two lowest transitions in GaN from bands A and B to the conduction band cause the same onset of absorption for all polarization directions perpendicular to **c**, while the onset of absorption is dominated by transition from band C to the conduction band for polarization parallel **c**. In fact, one can generally state that every material has three lowest fundamental band-to-band transitions, which may all become degenerate and isotropic for high symmetry materials, for example, in cubic zinc blende structure

TABLE II. Anisotropy of the binding energies and excitonic peak energies of $\beta\text{-Ga}_2\text{O}_3$. Transition dipole orientation within the a-c plane, α , given with respect to a-axis.

Direction	Binding energy (eV)	Excitonic peak (eV)	Reference
$\approx \parallel c$	0.4	$\approx 4.65 (\varepsilon_{zz})$	92 ^a
$\alpha = 115.1^\circ$	0.12	4.92	86
$\alpha = 110^\circ$	0.27	4.88	94
$\approx \parallel a$	0.4	$\approx 4.90 (\varepsilon_{xx})$	92 ^a
$\alpha = 25.2^\circ$	0.23	5.17	86
$\alpha = 17^\circ$	0.27	5.10	94
$\parallel b$	≈ 0.1	$\approx 5.54 (\varepsilon_{yy})$	92 ^a
$E \parallel b$	0.18	5.46	86
$E \parallel b$	0.27	5.41	94

^aCalculated.

GaAs. There, the Γ -point top valence band (point group T_d) is three-fold degenerate, and hence all associated transitions are the same in energy. In addition to the concept of the band-to-band transition, there is also exciton formation which must be considered. Once an electron has transitioned to the conduction band, it can form a complex with the positively charged hole left behind in its valence band. Depending on the curvatures (effective mass parameters) and the dimensionality of the van Hove singularity (critical point structure) in the combined band structure and density of states between the associated valence and conduction bands, this exciton can be stable, may possess three dimensional character or two dimensional character, for example, and its binding energy will depend on these scenarios. As a result, the onset of absorption for a given polarization direction and propagation direction will appear at lower photon energies, reduced by the energy of the exciton formation (effective Rydberg energy).

The experimental determination of the bandgap of $\beta\text{-Ga}_2\text{O}_3$ has progressed greatly over the past few decades. One of the greatest hurdles in understanding the bandgap of $\beta\text{-Ga}_2\text{O}_3$ is recognizing that not only the excitonic but also the monoclinic nature of the material must be accounted for. Thus, a direction must be specified for any given measurement or value. Additionally, the onset of absorption measurements, for example, underestimate the true bandgap value because they do not take into account the excitonic contribution that is present in $\beta\text{-Ga}_2\text{O}_3$. The comparison of bandgap values throughout the literature is, therefore, complicated by the differences in experimental methods. In fact, $\beta\text{-Ga}_2\text{O}_3$ has three unique fundamental bandgap values that are offset from the onset of absorption by excitonic binding energies and can be isolated depending on the direction the crystal is oriented, while many papers only report a single value.

The excitonic effects are instrumental in determining a true and accurate bandgap energy. The excitonic effects are often overlooked and not accounted for. While there has been much improvement in band structure calculations by means of hybrid functionals, excitonic effects are either left out entirely or only partially accounted for.⁹² When the excitonic effects are considered, then the onset of absorption due to electronic transition from the valence to the conduction band occurs within the bandgap. As a result, the real transition energy is larger than the apparent (i.e., visible) transition energy at the onset on photon absorption. These features are due to the bound exciton states.^{92,93} In theoretical work, Furthmüller *et al.* (Ref. 92) observed key features such as an increase in the imaginary parts around the absorption edge and within the intraband transition range. Accounting for the excitonic effects also was found to result in a larger discrepancies in the averaged dielectric functions across sources. With such low symmetry in the monoclinic structure, one might expect that there would be anisotropy within the excitonic effects. Around the onset of absorption, there are large amounts of anisotropy. The overall anisotropy of the exciton binding energy is small compared to the bandgap anisotropy. These excitonic effects and properly accounting for their anisotropy are instrumental in understanding the large difference in reported bandgap values as they will hugely effect the onset of absorption. Furthmüller *et al.* also produced calculations for the exciton ground state binding energy for varying orbital characters ($p_x/p_y/p_z$). The lowest two excitons have binding energies of 0.4 eV for $s - p_x$ and $s - p_z$, while $s - p_y$ was found to have an energy of ≈ 0.1 eV. Excitonic energies were identified experimentally using ellipsometric techniques by Mock *et al.* and Sturm *et al.* (Refs. 86 and 94).

TABLE III. Reported bandgap values of $\beta\text{-Ga}_2\text{O}_3$ determined from theory and experiment for bulk single crystals and thin films. Transition dipole orientation within the a-c plane, α , given with respect to a-axis. Films were assumed to be isotropic.

E_g (eV)	Direction	Method	Growth method	Reference
Expt. bulk				
4.48	$E \parallel c$	Polarized Ref./Trans.-Abs. edge	Float zone	95
4.52	$E \parallel c$	Polarized Ref./Trans.-Abs. edge	Float zone	59
4.57	$E \parallel a^*$	Polarized Ref./Trans.-Abs. edge	Float zone	95
4.70	$E \parallel b$	Polarized Ref./Trans.-Abs. edge	Float zone	95
4.70	Assumed $E \parallel b$	Optical absorption-Abs. edge	Verneuil	96
4.79	$E \parallel b$	Polarized Ref./Trans.-Abs. edge	Float zone	59
5.04	$\alpha = 115.1^\circ$	Ellipsometry	EFG	86
5.15	$\alpha = 110^\circ$	Ellipsometry	EFG	94
5.37	$\alpha = 17^\circ$	Ellipsometry	EFG	94
5.40	$\alpha = 25.2^\circ$	Ellipsometry	EFG	86
5.64	$E \parallel b$	Ellipsometry	EFG	86
5.68	$E \parallel b$	Ellipsometry	EFG	94
Expt. film				
4.72	...	Ellipsometry-Abs edge	RF Mag sputtering on Si	97
4.74	...	Ellipsometry-Abs edge	E-beam evap. on GaAs	97
4.79	...	Optical absorption	Pyrolysis on glass	98
4.9	...	Transmittance	PLD on glass	99
4.9	...	UV-Vis Trans.	MOCVD on sapphire	77
4.94	...	Manifacier method (Ref. 100)	Pyrolysis on Si	101
4.99	...	Manifacier method (Ref. 100)	Pyrolysis on Si	101
5.40	...	Ellipsometry	ALD on glass	102
Calc.				
4.66		B3LYP—Indirect gap	...	19
4.69		B3LYP	...	19
4.74	$\alpha = 100.504^\circ$	Gau-PBE	...	86
4.81		HSE hybrid functional	...	103
4.84		HSE06-Abs edge	...	85
4.87	Assumed $E \parallel c$	HSE06	...	66
4.88		HSE06	...	85
4.969	$\alpha = 7.498^\circ$	Gau-PBE	...	86
5.341	$\alpha = 110.8^\circ$	B3LYP	...	94
5.35	$E \parallel b$	Gau-PBE	...	86
5.581	$\alpha = 17.7^\circ$	B3LYP	...	94
5.911	$E \parallel b$	B3LYP	...	94

Notably, Mock *et al.* identified unique and anisotropic binding energies associated with the lowest three band-to-band transitions while Sturm *et al.* held these values to be equal. The excitonic peaks along with the subsequent binding energies associated with the lowest three band-to-band transitions are listed in Table II.

Anisotropy was seldom considered when studying the bandgap energy early on. This was due to a combination of lack of knowledge and the inability to properly determine the anisotropy of the bandgap. Anisotropy of the bandgap and its origins were not accurately reported until the mid- to late 2010s. Below, we discuss the progression of

understanding of the bandgap of $\beta\text{-Ga}_2\text{O}_3$ throughout the years and present the anisotropic values reported in the literature with comparisons to calculated values in Table III.

In 1965, Tippins (Ref. 96) determined the optical absorption edge of $\beta\text{-Ga}_2\text{O}_3$ and how the atomic structure influenced the observed bandgap. There was an absorption edge shift of around 100 Å when the temperature was reduced from room temperature to around 77 K. When reducing further to liquid helium temperature, there was no observable shift. The observed bandgap was 4.7 eV with a first exciton transition ΔE of 5.3 eV.⁹⁶ Kim *et al.* (Ref. 104) showed

the optical density spectrum for polycrystalline β -Ga₂O₃ recorded at 295 K which revealed a rapid increase in the spectrum at 290 nm that may line up with the materials bandgap absorption.¹⁰⁴ The optical density spectrum coupled with a direct optical energy gap formula¹⁰⁵ yielded an evaluated optical energy gap of 4.23 eV.¹⁰⁴

A few decades later in the late 1990s, reports on the observation of anisotropy within β -Ga₂O₃ began to appear in the literature gaining lots of attention. Ueda *et al.* (Ref. 59) reported findings of the absorption edge for single crystal β -Ga₂O₃. Values of 4.79 and 4.52 eV were observed for light polarized along E \parallel b and E \parallel c, respectively.⁵⁹ With values of Ueda *et al.* being reported for the bulk crystal, it is important to compare these values to thin films which may display different properties than that of bulk samples depending on the growth method. Direct absorption edge values were seen using ellipsometry and multi-sample techniques with values of 4.72 eV for thin film sputtered samples and 4.74 eV for e-beam evaporated samples⁹⁷ in agreement with Ueda *et al.* (Ref. 59). Wu *et al.* (Ref. 98) found a bandgap of 4.79 eV for spray pyrolysis fabricated thin films. A crystal direction for the transmission data was not specified.⁹⁸ Other studies using optical transmission data as a function of the photon energy along with the Manifacier method¹⁰⁰ yielded bandgap values of 4.94 and 4.99 eV for as-deposited films and annealed samples, respectively.¹⁰¹

Orita *et al.* (Ref. 99) reported a direct bandgap of 4.9 eV obtained using internal transmittance which is the energy loss due to absorption. The polycrystalline thin films were fabricated using pulsed laser deposition (PLD).⁹⁹ Extrapolation of the zero intercept in $(\alpha\hbar\omega)^2$ vs $\hbar\omega$ suggested a direct bandgap of 4.75 eV for as-grown films with a polycrystalline structure in a study by Hao *et al.* (Ref. 106), and bandgap values of 4.48 and 4.44 eV were estimated for films annealed at 600 and 800 °C, respectively.

In 2015, Onuma *et al.* (Ref. 95) also observed and reported on strong optical anisotropy. Absorption edge energies from various samples and theoretical reports were split into six ranges, and the authors provided a symmetry analysis for the Γ -point transitions. Assignments were made where the lowest transition (\approx 4.4–4.6 eV) is polarized parallel to c, the second transition (\approx 4.4–4.7 eV) is polarized parallel to a*, and the third transition (\approx 4.8–5.3 eV) is polarized parallel to b. The polarization assigned was made from experimental observation, while symmetry analysis indicated the split among the valence band structure.⁹⁵ Building further, several comprehensive band-to-band transition studies using spectroscopic ellipsometry (SE) and DFT showed how each transition of β -Ga₂O₃ is polarized along unique and identifiable directions.^{86,94} This continues to exemplify just how much more complex of a material β -Ga₂O₃ is compared to other popular wide bandgap semiconductors such as GaN and SiC.

A few years later in 2017, Mu *et al.* (Ref. 41) went into great detail describing the anisotropic properties determined using a diffractometer, refractive index prism coupler, and Van der Pauw Hall effect measurements. However, the authors only reported a bandgap value of 4.73 eV along a* neglecting the bandgap along b and c*.⁴¹ Ricci *et al.* (Ref. 107) present a comprehensive theoretical and experimental study on the bandgap anisotropy in order to verify and support past works that they claim did not provide measurement geometry or sample orientation. Measurements were completed on undoped EFG NCT Corp. (formerly Tamura) samples and cut from a boule with (010) and (201) surfaces. Room temperature polarized absorption spectra were reported. Similar experimental measurements were completed

on Sn-doped samples but the absorption edge was shown to match that of the undoped samples. To further support the experimental findings as well as other results across the literature, theoretical calculations, HSE, self-interaction corrected (VPSIC), and generalized gradient (GGA) were used. The calculated values for the bandgaps and absorption edges were in good agreement with the experimental values. Anisotropy was seen in the optical absorption as a function of light polarization and orientation of the crystal. For example, larger absorption shifts were seen for the (201) wafer than for the (010) cut. The magnitude of the shifts was 0.2 and 0.03 eV, respectively.¹⁰⁷

Due to the monoclinic structure of β -Ga₂O₃ and the associated anisotropy, determining the true and accurate bandgap has proven challenging. Most bandgap energies reported in the literature do not take into account anisotropy or the contributions of other optical directions, merely reporting a value parallel to a crystallographic direction. Mock *et al.* (Ref. 86) and Sturm *et al.* (Ref. 94) published some of the first works that considered monoclinic symmetry as well as excitonic effects when measuring the three unique fundamental bandgap values which can be isolated depending on the polarization direction and the β -Ga₂O₃ crystal orientation. Mock *et al.* and Sturm *et al.* used SE to determine the fundamental bandgap energies within the a-c plane and along the b-axis.

The optical transitions were found to be polarized at specific angles within the monoclinic plane. The first band-to-band transition (corresponding to Γ_{1-1}) and what many refer to as the “bandgap” was found oriented within the monoclinic plane at 115.1° for Mock and 110° for Sturm from the a-axis toward positive c-axis for both works. The bandgap energy or first band-to-band transition determined by Mock *et al.* was found to be 5.04 eV within the a-c plane. The excitonic peak was reported to be slightly less at 4.92 eV yielding a binding energy of 120 meV. Sturm *et al.* reported a slightly larger bandgap energy, using the excitonic peak and the binding energy to determine the band-to-band transition in the a-c plane. With an extracted binding energy of 270 meV and an excitonic peak of 4.88 eV, the bandgap was found to be 5.15 eV.^{86,94}

The second band-to-band transition (corresponding to Γ_{1-2}) also occurs within the monoclinic plane at 25.2° from the a-axis toward positive c-axis according to Mock *et al.* The bandgap energy was reported to be 5.40 eV with an excitonic peak at 5.17 eV.⁸⁶ Values of Sturm *et al.* differed slightly, using an angle of approximately 17° from the a-axis toward positive c-axis within the monoclinic plane. Again, using a binding energy of 270 meV and an excitonic peak of 5.10 eV, the bandgap energy of the second transition was found to be 5.37 eV.⁹⁴

The third fundamental band-to-band transition (corresponding to Γ_{1-4}) and excitonic peak according to Mock were 5.64 and 5.46 eV, respectively, yielding a binding energy of 180 meV.⁸⁶ Sturm’s bandgap energy was again slightly larger at 5.68 eV with an excitonic peak at 5.41 eV along the b-axis. The first fundamental band-to-band transitions can be observed in the band structure at the gamma point of the Brillouin zone shown in Fig. 6.

While both works reported similar results, a few key differences can be found throughout. Sturm *et al.* fixed all binding energies to be the same throughout (270 meV) and fit for a single value.⁹⁴ Findings of Mock *et al.* allowed for anisotropic and unique binding energies. The reported values for the first and second transitions show that the binding energy is increasing with increasing transition states. This

coupled with the difference in binding energies for the different orientations of the dipoles used in the ellipsometry analysis show that the binding energy is also anisotropic.⁸⁶ The fundamental bandgap energies as determined by ellipsometry and as shown in Table III are systematically higher than those determined by absorption. Reported values from absorption measurements fail to include excitonic effects, effectively shifting the reported bandgap down by the neglected binding energy value. Ellipsometry investigations were able to fully account for anisotropy, excitonic effects, and dipole orientations thus we conclude that to date these values best represent the true fundamental bandgap values of $\beta\text{-Ga}_2\text{O}_3$.

2. Temperature dependence of bandgap energy

The temperature dependence of the bandgap energy is often described by the so-called Bose–Einstein model¹⁰⁸

$$E_g(T) = E_g(0) - \frac{2a_B}{\exp(\theta_B/T) - 1}, \quad (1)$$

where $E_g(0)$ is the gap energy at zero temperature, a_B represents the strength of the exciton–phonon interaction, and θ_B is the average phonon temperature energy equivalent. In this approximation, the exciton, which is the quasi-particle formed in association with a band to band transition, and its interaction with the lattice is considered by an effective phonon mode. This effective mode thereby represents the much larger ensemble of phonons, which form the bath of constant lattice interaction at a given temperature. For temperatures large against the effective phonon temperature, one can approximate the shift of bandgap energy with a linear slope, $\gamma = \delta E_g / \delta T \approx -2a_B / \theta_B$ ($T \gg \theta_B$), and which is often reported in the literature. For low temperatures, one can determine $E_g(0)$, and from the curvature of $E_g(T)$, one can differentiate a_B from θ_B . Often, θ_B is found consistent with an average over all IR-active phonon modes.

$\beta\text{-Ga}_2\text{O}_3$ exhibits a bandgap dependence with temperature as seen experimentally by Rafique *et al.* (Ref. 109). Using $\beta\text{-Ga}_2\text{O}_3$ thin films grown on *c*-plane sapphire by low pressure vapor deposition, photoluminescence excitation, and absorbance spectra were used to find this dependence. This specific study looked at the direct bandgap as opposed to the indirect bandgap. For $[-201] \beta\text{-Ga}_2\text{O}_3$ in the experimental temperature range of 77 to 298 K, there was a red shift in photoluminescence excitation measurements from 257 to 266.4 nm as the temperature increased. This showed the bandgap narrowing from 4.82 to 4.65 eV with increasing temperature, hence, $\gamma = -0.769 \text{ meV/K}$.

Matsumoto *et al.* investigated vapor grown single crystal platelets using polarized absorption and reflection spectra, and provided absorption edge parameters at 77 K and room temperature for polarization parallel axes *c* (4.54 eV [300 K] and 4.76 eV [77 K]) and *b* (4.90 eV [300 K] and 4.94 eV [77 K]), hence, $\gamma = -0.98 \text{ meV/K}$ ($E||c$) and $\gamma = -0.18 \text{ meV/K}$ ($E||b$). More recently, studies on temperature dependence were conducted using ellipsometric techniques and EFG single crystals with different surface orientations by Mock *et al.* and Sturm *et al.*^{110,111} Mock *et al.* (Ref. 110) explored the high temperatures and reported critical point (CP) transition energy parameter decreases with increasing temperature. Anisotropic below-band-gap dielectric tensors and eigendielectric vectors all displayed shifts and temperature dependence ranging from room temperature to 550 °C.¹¹⁰ The authors reported linear shifts for all three fundamental

bandgap energy parameters. In their notation (the authors report parameters α and P , where $P = k_B\theta_B$ and $\alpha P = 2a_B$), $\gamma = -0.83 \text{ meV/K}$, -1.03 meV/K , and -0.60 meV/K for the lowest transition polarized nearly along axis *a*, the second lowest transition polarized nearly along *c*, and the third lowest transition polarized nearly along *b*, respectively.

Sturm *et al.* (Ref. 111) reported temperature dependent observations for temperatures ranging from 10 to 300 K. With increasing temperature, the exciton ground state energy decreases while broadening of exciton transitions increases.¹¹¹ Sturm *et al.* provide parameters which permit derivation of $\gamma = -0.90$, -0.90 , and -0.47 meV/K for the lowest transition polarized nearly along axis *a*, the second lowest transition polarized nearly along *c*, and the third lowest transition polarized nearly along *b*, respectively. Temperature shifts determined in the low and high temperature regions by Sturm *et al.* and Mock *et al.*, respectively, are in excellent agreement which indicate that the effective phonon bath temperature approximation is applicable to $\beta\text{-Ga}_2\text{O}_3$. These parameters also agree well with the earlier observations by Rafique *et al.* and Matsumoto *et al.* The isotropically averaged phonon temperature was reported as $\theta_B = 0.067 \text{ eV}$ (537.7 cm^{-1}) from all investigated transition parameter shifts. The arithmetic average of all (symmetry independent) optical phonon modes described by Schubert *et al.*⁴⁴ was found to be 507.5 cm^{-1} , in excellent agreement with the Bose–Einstein model assumptions. Because Sturm *et al.* investigated the low-temperature response at temperatures below the effective phonon temperature, the authors were able to determine the zero temperature bandgap energy parameters ($E_g(T=0)[E||a] = 5.069 \text{ eV}$; $E_g(T=0)[E||c] = 5.41 \text{ eV}$; $E_g(T=0)[E||b] = 5.7 \text{ eV}$).

D. Material properties

$\beta\text{-Ga}_2\text{O}_3$ has many unique and intriguing material properties that have spurred a surge in research interest. Such properties include the anisotropic thermal conductivity relevant to the field of power electronics and RF devices, the vast number of Raman and IR phonon modes, the charge carrier mobility, and the thought of learning and reaching the theoretical maximum charge carrier mobility. The basic understanding of the oxides properties begin with a knowledge of the bulk modulus, material density, and melting point, of which reported values are compared in Sec. XI. There is noticeable variation in the bulk modulus values that range from 174 to 255 GPa.^{19,112,113} The variation in values stems from using different theoretical equations of state, overall experimental method, and the specifics of the sample. Since bulk modulus is the change in volume vs applied pressure it is not a vector/tensor quantity and therefore cannot be anisotropic. Vicker's hardness displayed anisotropy with values ranging from 656.5 to 1029.6 kg/mm² depending on direction.⁴¹ There is a slight variation in the melting point across the cited values. Values reported throughout literature include 1725 °C,^{114,115} $1740 \pm 15 \text{ }^\circ\text{C}$,¹¹⁶ 1795 °C,¹¹⁷ and 1806 °C.¹¹⁸

1. Thermal properties

With $\beta\text{-Ga}_2\text{O}_3$ being heavily researched for power and RF device applications, thermal properties and especially thermal management are vital to improving device efficiency and capabilities. Important thermal properties to consider for semiconductor device materials include the coefficient of thermal expansion (CTE), Debye temperature, specific heat, thermal diffusivity, and thermal conductivity. The

CTE has been reported by multiple sources across multiple temperature ranges both experimentally and theoretically.^{41,45,115} Experimental values range from 4.70×10^{-6} to $8.9 \times 10^{-6} \text{ K}^{-1}$ while theoretical values range from 1.54×10^{-6} to $3.37 \times 10^{-6} \text{ K}^{-1}$. While the numerical values differ across temperature ranges and theoretical/experimental methods, the order of magnitude and pattern for the values across different crystal planes remains constant. The highest CTE value is seen along the [010] direction while the lowest CTE value is seen along the [100] direction for all three given references. All cited CTE values are listed and compared in Sec. XI.

The Debye temperature has been reported experimentally by analyzing heat capacity data to be 738 K.³⁹ First principles calculations yield a Debye temperature of 872 K.¹⁹ Specific heat values were determined experimentally to be 0.56 J/(gK) for [010] using the Czochralski method vs temperature⁵⁵ and 0.47 J/(gK) along the a^* direction using differential scanning calorimetry.⁴¹ The latter value was found on EFG samples. Both values for $\beta\text{-Ga}_2\text{O}_3$ are noticeably lower than the specific heat values for silicon [0.71 J/(gK)] and sapphire [0.76 J/(gK)]. The larger molar mass of $\beta\text{-Ga}_2\text{O}_3$ (187.4 g/mol) is suggested to be responsible for the lower specific heat.⁵⁵

Thermal diffusivity values exhibit anisotropy with reported values being $5.23 \text{ mm}^2/\text{s}$ along a^* , $9.76 \text{ mm}^2/\text{s}$ along b , and $6.26 \text{ mm}^2/\text{s}$ along c^* . The values were determined experimentally using the laser pulse method across a temperature range of 24.5 to 750 °C.⁴¹ The thermal diffusivity values decrease monotonically as the temperature increased to 750 °C.

Perhaps one of the most important thermal properties when considering high power semiconductor devices is the material's thermal conductivity/diffusivity. The thermal conductivity of Ga_2O_3 is low compared to other wide bandgap semiconductors. The low thermal conductivity leads to very localized self-heating and must be considered for high-power, high-frequency device applications.^{14,19} Different values have been reported across different crystal directions due to the monoclinic crystal symmetry. Mu *et al.* reported values obtained from the previously mentioned specific heat values. The thermal conductivity values are 15 W/(mK) along a^* , 28 W/(mK) along b , and 18 W/(mK) along c^* .⁴¹ Guo *et al.* (Ref. 39) investigated thermal conductivity in Sn-doped ($5\text{--}6 \times 10^{18} \text{ cm}^{-3}$) bulk $\beta\text{-Ga}_2\text{O}_3$ single crystals grown using the EFG technique by NCT Corp. Multiple surface cuts were investigated using time domain thermoreflectance and the highest room temperature thermal conductivity was found experimentally along [010] with a value of 27.0 W/(mK), while the lowest value of 10.9 W/(mK) was found along [100].³⁹ Other values were reported both experimentally and theoretically ranging from 10.68 to 29.21 W/(mK) across multiple directions.^{55,120–124} Across the cited values, the [010] direction consistently had the highest thermal conductivity values while the [100] had the lowest. Figure 4 shows the cited thermal conductivity values plotted against their respective direction. Calculated values for thermal conductivity are known to underestimate experimental values. This is evident in Fig. 4 with the calculated data from Li *et al.* (Ref. 124) symbolized by the orange stars. It is important to note that the thermal conductivity values (along all directions) are approximately an order of magnitude lower than that of other popular wide bandgap materials such as GaN (~130 W/(mK)) and SiC (~360 to 490 W/(mK)).^{18,40,125,126} Thus, the thermal management of devices fabricated using Ga_2O_3 has become an important topic, which is the subject of much ongoing research. All cited values

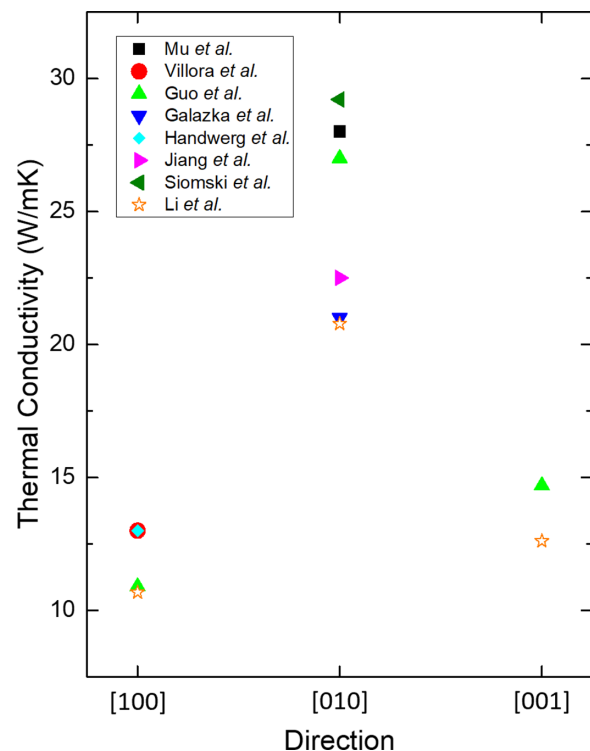


FIG. 4. Experimental (solid) and calculated (open) thermal conductivity values of $\beta\text{-Ga}_2\text{O}_3$ from literature. Data points were collected from Refs. 39, 41, 55, and 120–124. Data are plotted for anisotropic values found for each of the three crystallographic directions.

for the thermal properties of $\beta\text{-Ga}_2\text{O}_3$ are listed and compared in Sec. XI.

Chatterjee *et al.* (Ref. 127) discuss various methods for device level thermal management. Such methods include air-jet cooling, embedded micro channels, as well as known methods already used in GaN and GaAs devices such as flip chip integration.¹²⁷ Paret *et al.* (Ref. 128) discuss how double sided cooled packages are able to reduce thermal resistance more than single sided packages. It was concluded that due to the lower thermally conductive nature of Ga_2O_3 , innovation in the device cooling and packaging sector would be imperative, similar to innovations made for SiC and Si devices.¹²⁸ At the packaging level, the thermal management of Ga_2O_3 devices has become a hot topic of research. Xiao *et al.* (Ref. 129) demonstrate the first double-side-cooling packaging of large-area Ga_2O_3 devices experimentally. The transient thermal performance of the double-side-cooled Ga_2O_3 was shown to be superior to the SiC counterpart as well.¹²⁹ Other studies on Ga_2O_3 thermal management from the packaging level can be found in Refs. 130 and 131.

2. Phonon properties

Since the primitive unit cell of $\beta\text{-Ga}_2\text{O}_3$ contains ten atoms, six oxygen, and four gallium atoms, 30 normal modes of vibration are expected. The irreducible representations for these are¹³²

$$\Gamma_{aco} = A_u + 2B_u,$$

$$\Gamma_{opt} = 10A_g + 4A_u + 5B_g + 8B_u,$$

for the acoustical zone center modes and for the optical zone center modes, respectively.¹³² Of the optical modes, A_g and B_g are Raman active (15 modes) and A_u and B_u are IR active (12 modes). The IR modes are further split into transverse (TO) and longitudinal optical (LO) modes. This is vastly more complex than other binary semiconductors, such as GaN and SiC, that have a simple primitive unit cell of only two different atoms.^{32,133}

Phonon mode studies for semiconducting materials are important as they provide insight into electrical and thermal transport, and optical processes. Machon *et al.* (Ref. 112) report a high-pressure Raman study for β -to- α transitions in Ga_2O_3 . Powdered samples of Ga_2O_3 were used in a diamond anvil cell measured using unpolarized Raman up to 40 GPa. Machon *et al.* did not identify the symmetry of the reported modes. However, they were able to identify the polarization conditions under which modes become observable.¹¹² The results from Machon *et al.* in 2006 were later compared to a 2007 study by Liu *et al.* (Ref. 132) using *ab initio* calculations at ambient pressure. The two studies appeared consistent in their findings. Liu *et al.* provide theoretical phonon frequencies located at the Γ point of the Brillouin zone.

Polarized Raman spectra measurements are of interest to help improve $\beta\text{-Ga}_2\text{O}_3$ materials for device applications. One of the first published and highly cited reports by Dohy *et al.* (Ref. 135) studied the Raman and IR spectra with varying temperature. Polarized Raman spectra were reported for a single-crystalline sample. The results show ten bands belonging to parallel polarization and five bands belonging to the crossed polarization condition. Polarization considerations allowed for component separation in 111 to 114 cm^{-1} and 345 to 353 cm^{-1} accounting for the 15 modes. Temperature alters the Raman and IR modes via anharmonic lattice interaction, thermal reorientation, vibrational dephasing, and defect creation.

Onuma *et al.* (Ref. 136) reported polarized Raman spectra at room temperature in order to provide lattice vibration modes for high

quality $\beta\text{-Ga}_2\text{O}_3$ substrates and devices. Polarized Raman measurements allow for separation of A_g and B_g modes similar to Dohy's work. Phonon frequencies were determined from the positions of the spectral peaks with no need for fitting procedures. Results were compared to first principles values using VASP¹¹² and ABINIT¹³² codes with majority agreement. The few modes that appear outside the rounding error are $A_g(8)$ - $A_g(10)$ and $B_g(5)$, which were hypothesized to be a result of crystalline quality and/or lattice parameter differences. Unlike Dohy's study, separation of $A_g(7)$ and $B_g(4)$ was possible due to uniformity of the crystalline orientation and good surface flatness seen in the substrates used.¹³⁶ Kranert *et al.* (Ref. 134) used a tensor method to account for the monoclinic symmetry appropriately that resulted in the ability to determine the polarized orientation for the net vibrations of the Raman modes. The dependence of the intensity on the scattering direction for the majority of the phonon modes was modeled for monoclinic symmetry. The resultant experimental Raman tensors obtained from the model aligned well with the *ab-initio* theoretical results.¹³⁴ Raman mode frequencies are listed in Table IV. The IR and Raman irreducible representations for the active phonon modes are also summarized in Sec. XII.

IR active phonons in $\beta\text{-Ga}_2\text{O}_3$ were investigated by Dohy *et al.* (Ref. 135) in the early 1980s using transmission measurements on polycrystalline samples diluted in solution. The spectra were analyzed in conjunction with valence force field calculation results, and symmetry assignment was made tentatively from frequency order rather than polarization characteristics. IR spectra model calculations could not be performed because of the random orientation of the polycrystalline sample, and frequencies listed were suggested to be somewhat falling between actual TO and LO frequencies. It was then still thought that paradigms for interpreting IR spectra from isotropic materials were valid and could be applied to anisotropic samples. However, as shown later by Schubert *et al.* (Ref. 44), these early tentative assignments were incorrect since the IR modes reveal a much more intricate behavior due to the monoclinic symmetry. Modes are listed in Table V for providing historical account and should not be seen as actual phonon

TABLE IV. $\beta\text{-Ga}_2\text{O}_3$ polarized Raman phonon mode frequencies (cm^{-1}).

Mode	Expt. ¹³⁴	Expt. ¹³⁵	Expt. ¹¹²	Expt. ¹³⁶	Theory ¹³⁴	Theory ¹³⁵	Theory ¹¹²	Theory ¹³²
$A_g(1)$	111.0	111	110.2	112	113.5	113	104	104.7
$B_g(1)$	114.8	114	113.6	115	118.6	114	113	112.1
$B_g(2)$	144.8	147	144.7	149	145.6	152	149	141.3
$A_g(2)$	169.9	169	169.2	173	176.4	166	165	163.5
$A_g(3)$	200.2	199	200.4	205	199.1	195	205	202.3
$A_g(4)$	320.0	318	318.6	322	318.5	308	317	315.8
$A_g(5)$	346.6	346	346.4	350	342.5	353	346	339.7
$B_g(3)$	353.2	353	...	355	359.2	360	356	348.3
$A_g(6)$	416.2	415	415.7	421	432.0	406	418	420.2
$A_g(7)$	474.9	475	...	479	472.8	468	467	459.4
$B_g(4)$	474.9	475	473.5	480	486.1	474	474	472.8
$A_g(8)$	630.0	628	...	635	624.4	628	600	607.1
$B_g(5)$	652.3	651	628.7	659	653.9	644	626	627.1
$A_g(9)$	658.3	657	652.5	663	655.8	654	637	656.1
$A_g(10)$	766.7	763	763.9	772	767.0	760	732	757.7

TABLE V. $\beta\text{-Ga}_2\text{O}_3$ IR active transverse (TO) and longitudinal (LO) phonon mode frequencies and orientation angles with respect to the a axis. Frequencies reported in units of (cm^{-1}).

Label	ω_{TO} Expt. ^{44,a}	ω_{LO} Expt. ^{44,a}	ω_{TO} Expt. ⁹⁴	ω Expt. ^{135,b}	ω_{LO} Theory ¹³²	ω_{TO} Theory ¹³²	ω Theory ⁹⁴	ω Theory ^{135,b}
$A_u(1)$	154.8	156	...	155	146.5	141.6	160.7	155
$B_u(1)$	$213.7 \angle 80.9^\circ$	$271.2 \angle 30.7^\circ$...	250	190.5	187.5	224.3	216
$B_u(2)$	$262.3 \angle 158.5^\circ$	$286.5 \angle 26.1^\circ$	253.5	290	264.5	251.6	267.3	300
$B_u(3)$	$279.1 \angle 0.0^\circ$	$307.5 \angle 150^\circ$...	310	283.6	265.3	281.9	337
$A_u(2)$	296.6	344.7	295.3	...	325.5	296.2	300.5	352
$B_u(4)$	$356.8 \angle 144^\circ$	$391.8 \angle 151^\circ$	$356.7 \angle 166^\circ$	375	354.1	343.6	361.0	374
$B_u(5)$	$432.5 \angle 21.0^\circ$	$579.3 \angle 74.2^\circ$	$430.3 \angle 46^\circ$	455	484.7	410.5	434.2	500
$A_u(3)$	448.6	558.9	446.7	525	510.6	383.5	447.0	526
$B_u(6)$	$572.5 \angle 10.6^\circ$	$719.1 \angle 20.1^\circ$	$572.1 \angle 128^\circ$	640	625.3	574.3	560.8	626
$A_u(4)$	663.2	770.3	661.5	668	738.5	647.9	665.8	656
$B_u(7)$	$692.4 \angle 5.4^\circ$	$778.1 \angle 115^\circ$	$691.0 \angle 28^\circ$	692	728.2	672.6	692.5	720
$B_u(8)$	$743.5 \angle 48.7^\circ$	$817.0 \angle 7.2^\circ$	$743.0 \angle 74^\circ$	731	746.6	741.6	742.5	760

^aPolarization angles reported within the monoclinic plane with respect to the crystallographic a -axis.

^bListed to provide historical account and should not be seen as actual phonon mode frequencies.

mode frequencies. In 2002, Villora *et al.* (Ref. 137) investigated IR active phonons in single crystal $\beta\text{-Ga}_2\text{O}_3$ using polarized intensity measurements, and correctly identified the TO modes for polarization along axis **b**. However, spectra obtained with electric field oriented along the monoclinic plane were analyzed using isotropic model approaches, and the resulting frequencies were incorrectly determined. In 2016, Schubert *et al.* (Ref. 44) investigated the IR phonons in single crystalline samples using generalized SE and introduced an eigendielectric polarization model for TO and LO modes. Thereby, the authors first accounted properly for the monoclinic nature by presenting vibrational orientation within the monoclinic plane, and obtained the first accurate and complete mode description for Brillouin zone center modes in $\beta\text{-Ga}_2\text{O}_3$. Schubert *et al.* (Ref. 44) also provided DFT calculations for the phonon displacements, dispersions, and directions within the monoclinic lattice, and excellent agreement was found between experiment and theory.

Schubert *et al.* used a dielectric function tensor model approach to identify uncoupled far-IR and IR active modes using spectroscopy ellipsometry. Dielectric function tensor elements were matched to a monoclinic model to observe and determine anisotropic TO and LO optical phonon modes having A_u and B_u symmetry. Schubert *et al.* found all four A_u and eight B_u IR modes experimentally while distinguishing between TO and LO modes. Polarization orientation angles with respect to the a -axis were determined for the eight B_u modes. The IR active modes reported were found to be either orientated at unique directions within the monoclinic plane (B_u) or parallel the b -axis (A_u). The frequencies and angles with respect to the a axis in comparison with several theoretical calculations are shown in Table V. Soon after, a report by Sturm *et al.* (Ref. 94) came to the same conclusions and their findings being in excellent agreement with Schubert *et al.* A polarization angle for the five highest frequency B_u modes was reported as well.⁹⁴ The IR phonon mode frequencies are calculated using DFT by Schubert *et al.* (Ref. 44), Liu *et al.* (Ref. 132), Sturm *et al.* (Ref. 94), and Dohy *et al.* (Ref. 135). The works by Schubert (Ref. 44) and Sturm (Ref. 94) are considered state of the art findings due to the

directional orientation. Other published reports build off these findings and report on phonon ordering,¹³⁸ the generalized Lyddane–Sachs–Teller (LST) relationships,¹³⁹ and the plasmon LO mode coupling.¹⁴⁰

Mengle and Kioupakis (Ref. 141) used DFT and DFPT to calculate vibrational properties, phonon–phonon interactions, and electron–phonon coupling and obtained the phonon dispersion including effects of isotope substitution. The authors also reported electron–phonon coupling for the lowest conduction band and identified a polar-optical mode with a phonon energy of 29 meV which limits the room temperature mobility.

Another material parameter (numerical approximation) involving the phonon modes is the phonon deformation potentials (PDPs). The frequencies of the vibration modes will experience a shift based on the applied stress and strain. A recent study by Korlacki *et al.* (Ref. 142) in 2020 provided a first derivation of the strain–stress relationship in linear perturbation theory for property variations under monoclinic symmetry while maintaining the symmetry. A linear relationship for all phonon modes with all strain (ε_{ij}) parameters was concluded,

$$\Delta\omega_n = P_{n,xx}\varepsilon_{xx} + P_{n,yy}\varepsilon_{yy} + P_{n,zz}\varepsilon_{zz} + P_{n,xy}\varepsilon_{xy}, \quad (2)$$

or for the stress (σ_{ij}) parameters

$$\Delta\omega_n = \tilde{P}_{n,xx}\sigma_{xx} + \tilde{P}_{n,yy}\sigma_{yy} + \tilde{P}_{n,zz}\sigma_{zz} + \tilde{P}_{n,xy}\sigma_{xy}, \quad (3)$$

where $P_{n,ij} = \langle S_n | v^j | S_n \rangle$ ($\tilde{P}_{n,ij} = \langle S_n | v^j | S_n \rangle$) are the strain (stress) deformation potentials with $n \in \{A_g, B_g, A_u, B_u\}$ and $ij \in \{xx, xy, yy, zz\}$. Hence, four strain ($P_{n,ij}$) and four stress deformation potentials ($\tilde{P}_{n,ij}$) are required for every phonon mode to calculate its energy shift $\Delta\omega_n$ for small strain/stress parameters. Accordingly, for $\beta\text{-Ga}_2\text{O}_3$, for 10 A_g , 4 A_u , 5 B_g , and 8 B_u modes 216 potential parameters exist. It is noted that none are determined so far from experiment. The authors only provided the deformation potential parameters for Raman active and TO modes (summarized in Table VI), and 48 additional potential parameters exist for the LO modes which have not been reported yet.

LO phonons couple with free charge carriers and form so-called LO-phonon-plasmon (LPP) modes. This is a property universal to all semiconductors with polar (IR-active) phonon modes. In $\beta\text{-Ga}_2\text{O}_3$, again due to its monoclinic symmetry which is lower than any other semiconductor studied until now, the LPP mode coupling reveals yet another peculiarity of this crystal class. In 2019, Schubert *et al.* (Ref. 140) demonstrated that LPP mode frequencies depend on the free charge carrier density, which is commonly known from other semiconductors and often used to deduce carrier properties from LPP mode measurements; however, in $\beta\text{-Ga}_2\text{O}_3$, the LPP mode excitations are anisotropic and change their polarization direction with carrier concentration as well (Fig. 5). This finding is potentially consequential since scattering with LPP modes affect thermal and electrical transport and, thus, may not only be directional dependent but also dependent on the carrier density.

Due to the monoclinic symmetry of the $\beta\text{-Ga}_2\text{O}_3$ lattice, hyperbolic shear polaritons occur and which are of interest for phonon and plasmon propagation in two-dimensional layer systems.¹⁴³ Recently, these hyperbolic shear polaritons have been observed in $\beta\text{-Ga}_2\text{O}_3$ for the first time by Passler *et al.* (Ref. 143).

According to the literature, both the static and high frequency dielectric constants exhibit anisotropy.^{43,44,86,94} In a recent report by

Gopalan *et al.* (Ref. 144), the static dielectric permittivity constants were presented using two types of measurement techniques, terahertz (THz) ellipsometry, and THz polarized transmission (PT). Measurements were recorded along five axes consisting of a , a^* , b , c , and c^* and compared to previously reported values found in the literature. Values for the static dielectric constants are listed in Table VII. Values across all references and methods appear in good agreement. The THz measurements from Gopalan *et al.* also served to build upon work by Fiedler *et al.* (Ref. 43) that was published just one year prior. Fiedler obtained static dielectric constants using AC capacitance measurements taken perpendicular to the three principle planes (100), (010), and (001). As seen in Table VII, anisotropy was also present.⁴³ There was one issue; however, a full set of the intrinsic permittivity values could not be obtained since the principle lattice planes and the unit cell directions are not perpendicular in the low-symmetry crystal system.¹⁴⁴ The more recent publication from Gopalan *et al.* filled in the gaps. Fiedler *et al.* also showed that the static dielectric constants exhibit temperature dependence as the values increase with increasing temperature.⁴³ Schubert *et al.* (Ref. 44) utilized the Schubert–Lydanne–Sachs–Teller relation, which is coordinate invariant to determine the static dielectric

TABLE VI. DFPT-derived frequency (ω_0), linear strain ($P_{\eta,xx}$), and stress ($\tilde{P}_{\eta,xx}$) potentials for phonon modes in $\beta\text{-Ga}_2\text{O}_3$ in units of cm^{-1} , $\text{cm}^{-1}/(\text{unit strain})$, and $\text{cm}^{-1}/\text{kbar}$, respectively. Reproduced with permission from Korlacki *et al.*, Phys. Rev. B **102**, 180101(R) (2020). Copyright 2020 APS (Ref. 142).

Mode	ω_0	$P_{\eta,xx}$	$P_{\eta,xy}$	$P_{\eta,yy}$	$P_{\eta,zz}$	$\tilde{P}_{\eta,xx}$	$\tilde{P}_{\eta,xy}$	$\tilde{P}_{\eta,yy}$	$\tilde{P}_{\eta,zz}$
A_u -1	632.4	-589	-27	-376	-637	0.217	0.095	0.012	0.118
A_u -2	431.4	-28	137	-773	-570	-0.263	-0.121	0.297	0.208
A_u -3	293.7	-485	-5	-351	-967	0.109	0.164	0.009	0.246
A_u -4	148.6	43	62	-116	-9	-0.067	-0.073	0.059	0.017
B_u -1	708.6	-658	342	-1339	-658	0.037	-0.049	0.376	0.111
B_u -2	659.2	-886	98	-614	-983	0.311	0.109	0.033	0.182
B_u -3	536.2	-1155	422	-1270	-733	0.371	-0.085	0.244	0.046
B_u -4	410.3	-952	-58	-550	-255	0.541	0.406	-0.015	-0.115
B_u -5	343.5	-301	11	-402	-489	0.050	0.113	0.079	0.108
B_u -6	266.3	-309	236	-283	-254	0.051	-0.294	0.066	0.054
B_u -7	248.6	-402	47	-34	-306	0.211	0.003	-0.075	0.037
B_u -8	195.9	547	-163	122	301	-0.257	-0.201	0.057	-0.023
A_g -1	731.7	-773	384	-1239	-656	0.122	-0.132	0.317	0.095
A_g -2	624.6	-939	223	-871	-1006	0.335	0.049	0.129	0.068
A_g -3	596.7	-996	151	-805	-1014	0.346	0.126	0.080	0.165
A_g -4	458.3	-705	111	-770	-403	0.263	0.169	0.136	-0.002
A_g -5	396.9	-115	176	-505	-140	-0.068	-0.077	0.170	0.033
A_g -6	333.0	-619	209	-735	-822	0.098	-0.092	0.155	0.185
A_g -7	303.4	-488	95	-454	-126	0.226	0.091	0.066	-0.053
A_g -8	188.5	-189	176	-404	-285	-0.042	-0.202	0.128	0.081
A_g -9	160.7	-185	114	-149	-75	0.061	-0.106	0.026	0.010
A_g -10	106.7	20	-34	-89	-57	-0.028	0.083	0.033	0.017
B_g -1	620.8	-615	-11	-289	-694	0.245	0.131	-0.030	0.132
B_g -2	458.5	-309	178	-852	-635	-0.111	-0.081	0.267	0.181
B_g -3	344.1	-644	133	-249	676	0.268	-0.028	-0.049	0.124
B_g -4	140.1	-182	95	-287	-372	-0.012	-0.051	0.071	0.105
B_g -5	109.7	10	-67	154	156	0.067	0.0774	-0.062	-0.060

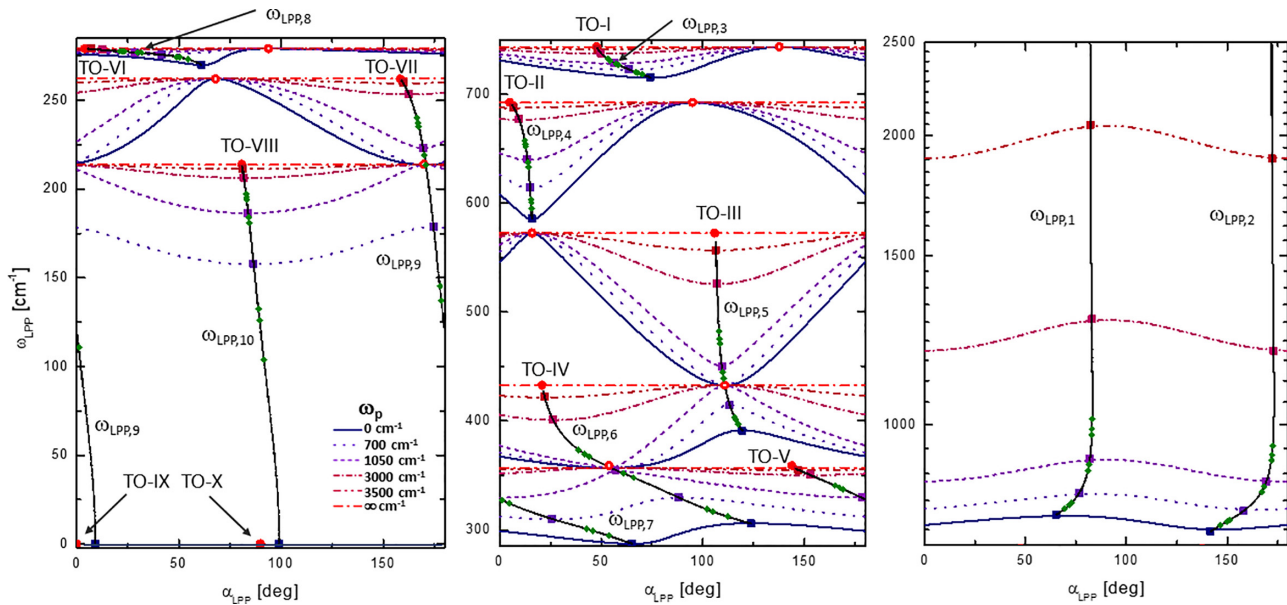


FIG. 5. Dispersion of B_u LPP modes for $\beta\text{-Ga}_2\text{O}_3$ within the monoclinic plane and vs plasma frequency parameters (see inset for labels). Black solid lines: LPP modes with increasing carrier density, which is proportional to the square of the plasma frequency ω_p . Square symbols: B_u LPP modes. Full red circles: B_u TO modes. Green symbols: experimental data. Reproduced with permission from Schubert *et al.*, Appl. Phys. Lett. **114**, 102102 (2019). Copyright 2019 AIP Publishing LLC (Ref. 140).

constants from ellipsometry measurements.¹³⁹ Passlack *et al.* (Ref. 145) also reported the static dielectric constants ranging between 9.93 and 10.2. Methods for obtaining these values as well as the direction(s) with which they occur were not detailed. It should also be noted that Passlack *et al.* did not specify the phase of the Ga_2O_3 films used in the published work.

The anisotropy among the high frequency dielectric constant does not appear to be as extreme as the reported static dielectric constants. Schubert *et al.* (Ref. 44) reports experimental values of 3.7(5),

3.7(1), and 3.2(1) for $\epsilon_{\infty,a}$, $\epsilon_{\infty,b}$, and ϵ_{∞,c^*} , respectively. Other theoretical values from Liu *et al.* (Ref. 132) and He *et al.* (Ref. 19) both show anisotropy within the calculated high frequency dielectric constants. Another study calculated a value of 3.57 (ϵ_∞) determined from a Cauchy dispersion model fit but was assumed to be isotropic.⁹⁷ Values for both the static and high frequency dielectric constants are compared in Sec. XI.

3. Electrical properties

The electrical properties of $\beta\text{-Ga}_2\text{O}_3$ are of considerable interest for power and RF device applications. These properties include the electron affinity, electrical breakdown field, effective mass, and electron

TABLE VII. $\beta\text{-Ga}_2\text{O}_3$ static dielectric constants reported in literature from experiment and theory.

Static	a	a^*	b	c	c^*	Reference
FIR-IR SE	10.9(1)	10.8(1)	11.2	12.6	12.7(1)	44
THz-SE	10.19	10.05	10.6	12.4	12.27	144
THz-PT	10.11	9.97	10.09	12.35	12.21	144
AC capacitance		10.2	10.87		12.4	43
Theory	10.84		11.49	13.89		132
High frequency	a		b		c^*	Reference
SE	3.7(5)			3.7(1)	3.2(1)	44
Theory	3.85			3.81	4.08	132
Theory	2.86			2.78	2.84	19
SE					3.57 ^a	97

^aIsotropic thin film average.

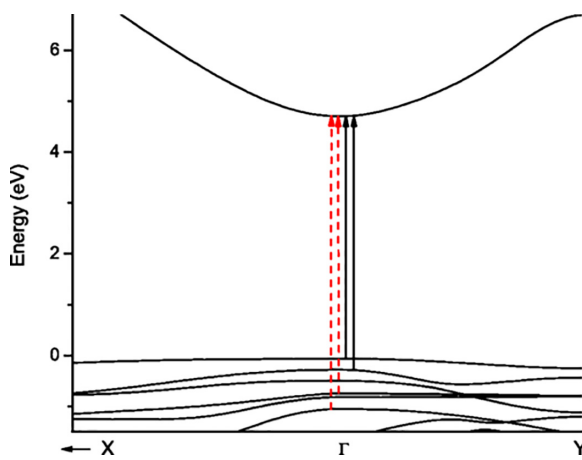


FIG. 6. Evidence of non-negligible anisotropy in the valence band curvatures at the Γ point of the Brillouin zone. The dashed red arrows represent two lowest vertical band-to-band transitions with polarization along the b axis while the black arrows represent transitions polarized within the a - c plane. Reproduced with permission from Mock *et al.*, Phys. Rev. B **96**, 245205 (2017). Copyright 2017 APS (Ref. 86).

mobility among others. Reported electron affinity determined experimentally using photoemission spectroscopy (PES) at room temperature along the (100) surface was 4.00 ± 0.05 eV.¹⁴⁶ The electrical breakdown field is one of the material parameters that propelled Ga_2O_3 into the spotlight, predominantly for high power and high voltage applications. The theoretical breakdown strength of 8 MV/cm stems from the material's ultra wide bandgap.^{40,147} The critical breakdown field strength seen experimentally has not reached the high theoretical value yet. Values include 0.54¹⁴⁸ and 3.5 MV/cm for a lower bound average and 5.3 MV/cm for a maximum field strength of a MOSFET fabricated using MOCVD.¹⁴⁹ The latter two values were determined by using the electric field gradient approximation from the given I-V data. A value of 3.5 MV/cm was also reported for vertical Ga_2O_3 Schottky barrier diodes.¹⁵⁰ Getting closer to the theoretical value, Choi *et al.* (Ref. 102) reports much higher values of 7.6 MV/cm at 250 °C. The ALD $\beta\text{-Ga}_2\text{O}_3$ samples deposited on Si exhibited very low leakage current of 1×10^{-11} A at 1 MV/cm. It is notable that the very high breakdown value was found using samples with an observed optical bandgap of 5.4 eV at 250 °C determined using spectroscopy ellipsometry.¹⁰² Other reported experimental values include 1.3 MV/cm for a silicon δ -doped $\beta\text{-Ga}_2\text{O}_3$ MESFET¹⁵¹ and 0.46 MV/cm for a top-gated MOSFET.¹⁵² Values for the electron affinity and electrical breakdown strength are listed and compared in Sec. XI.

The anisotropy of the electrical properties in bulk and thin films is an important aspect of $\beta\text{-Ga}_2\text{O}_3$. Due to the octahedral GaO_6 and tetrahedral GaO_4 lattice units as well as the low symmetry of the monoclinic structure, it can be expected that the electrical properties will exhibit anisotropy similar to what has been reported among the thermal properties.⁵⁹

The effective mass of the carriers is another important property. Of interest are extrema within the band structure. The effective mass is obtained from band structure calculations by interpolations for selected bands. Usually, a band is plotted in high resolution around a Brillouin zone point and the band energy vs reciprocal distance of wavevector coordinate k_j is then fitted using a second-order polynomial. The quadratic term coefficients then correspond to the effective mass parameters

$$(m^{*-1})_{jj} = \frac{1}{\hbar^2} \frac{\partial^2}{\partial k_j^2} E(\mathbf{k}). \quad (4)$$

The electron effective mass of $\beta\text{-Ga}_2\text{O}_3$ has been reported from experiment as well as theory. Results from theory for the electron effective mass of single crystal $\beta\text{-Ga}_2\text{O}_3$ typically fall around 0.28 m_e with some deviation depending on the direction. Peelaers *et al.* (Ref. 85) found values between 0.27 m_e and 0.28 m_e that were directionally dependent.⁸⁵ Varley *et al.* reported a value of 0.281 m_e using HSE06 calculations.⁶⁶ Mock *et al.* (Ref. 86) showed calculated anisotropy with more directional dependence than Peelaers *et al.* Calculated values of the effective mass were determined to be $m_a^* = 0.224 m_e$, $m_b^* = 0.301 m_e$, and $m_c^* = 0.291 m_e$ using DFT calculation with Gau-PBE.⁸⁶ Bechstedt *et al.* (Ref. 153) also theorized about anisotropy in the effective mass using density functional perturbation theory (DFPT) and found values of $m_x = m_y = 0.271 m_e$ and $m_z = 0.263 m_e$. Furthmüller *et al.* (Ref. 92) found very little anisotropy within the effective mass parameters from HSE calculations, only around 3.5% with values of $m_a^* = 0.272 m_e$, $m_b^* = 0.270 m_e$, and $m_c^* = 0.263 m_e$. He *et al.* (Ref. 19) used B3LYP hybrid functionals to calculate the band structure. The effective mass values were obtained by fitting the energy

dispersion of the conduction band minimum to a parabolic function along different \mathbf{k} directions in the vicinity of Γ , and the effective electron mass parameters are found practically isotropic with $0.342 m_e$.¹⁹

Knight *et al.* (Ref. 42) observed the electron effective mass experimentally investigating the optical Hall effect from two samples with different surfaces of $\beta\text{-Ga}_2\text{O}_3$, (010) and (201). For the (010) sample, the effective mass was shown to be isotropic within the error bars of the MIR-OHE method and fitting parameters. However, for the (201) sample, some anisotropy was observed, but still remained within the uncertainty limits.⁴² Values for the experimental electron effective mass produced by Knight *et al.* are shown in Table VIII in comparison with results from various theoretical methods.

The flat valence band structure of $\beta\text{-Ga}_2\text{O}_3$ results in very large effective hole mass parameters. The effective hole mass varies strongly with direction and with band. Varley *et al.* (Ref. 66) estimated 0.4 m_e for the effective hole mass from the band curvatures along the $\Gamma\text{-Z}$ direction, and 0.40 m_e along the $\Gamma\text{-A}$ direction at the top of the valence band. Yamaguchi (Ref. 82) used a first principles full-potential linearized augmented plane wave method and obtained a valence band maximum at the E line connecting the Z and M points, and curvature parameters were provided for this point, which are also heavily anisotropic ($m_{xx} = 6.14 m_e$, $m_{yy} = 2.0 m_e$, $m_{zz} = 4.19 m_e$). Mock *et al.* (Ref. 86) highlight DFT determined hole effective mass parameters involving the valence bands for the lowest band-to-band transitions with anisotropy being non-negligible as seen in Fig. 6. For $\beta\text{-Ga}_2\text{O}_3$, the effective hole mass parameters are calculated for the three of the four uppermost valence bands at the Γ point, which are involved in the three lowest-energy band-to-band transitions.⁸⁶ In agreement between theory and experiment, it was observed that each of the transition is polarized nearly parallel to one of the monoclinic lattice directions with some small deviations in the monoclinic plane. It was noted that the polarization direction for each transition is nearly identical with the direction along which the strongest curvature occurs within the valence band associated with the transition.

The lowest transition is between the top valence band (index 1) and the bottom of the conduction band, and polarized nearly along direction c . The curvature of band 1 is 0.409 m_e , the second transition is between the second top valence band (index 2) polarized nearly parallel to a , and the curvature is 0.409 m_e . The third transition is between the fourth valence band (index 4) and the bottom of the conduction band, and polarized along direction b . The curvature of band 4 along b is 0.566 m_e . For each band, the reported curvature is the lowest among all other directions.⁸⁶

TABLE VIII. Experimental and theoretical anisotropic conduction band effective mass parameters for $\beta\text{-Ga}_2\text{O}_3$. Experimental values determined using mid-IR optical Hall measurements. Effective mass in units of m_e .

Expt.	m_a^*	m_b^*	m_c^*	Reference
(010)	0.288 ± 0.044	0.283 ± 0.046	0.286 ± 0.044^a	42
(201)	0.295 ± 0.039	0.276 ± 0.037	0.311 ± 0.044^a	42
Calc.				
Gau-PBE	0.244	0.301	0.291	86
HSE	0.272	0.270	0.263	92
DFPT	0.271	0.271	0.263	153

^aParameter determined for direction c^* .

Presently, the full extent of lattice anisotropy and its influence on electrical transport properties is not fully understood.^{44,59} The carrier mobility, or electron mobility in the case of $\beta\text{-Ga}_2\text{O}_3$ is a highly researched property pertaining to improving power device performance. Jeon *et al.* (Ref. 154) highlights the vast amount of research that has been reported in the literature on the electron mobility of $\beta\text{-Ga}_2\text{O}_3$ for various deposition methods and carrier concentrations (Fig. 7). Special attention is made for the values that fall to the right of the dashed model line, representing experimental mobilities reported for highly doped samples. The work of Jeon *et al.* is represented by the solid red stars. This work is currently the highest electron mobility reported for $\beta\text{-Ga}_2\text{O}_3$ samples doped above 10^{20} cm^{-3} . Jeon *et al.* discuss how passivating or eliminating unintentional acceptors is key to increasing mobility in highly doped films. They state that while other mechanisms of scattering could be impacting the mobility, the higher mobility is driven by the decreased N_A/N_D compensation ratio. Other data points in Fig. 7 that fall to the right of the dashed model line likely have lower N_A/N_D ratios improving their mobility relative to the model. As highlighted by Ma *et al.* (Ref. 155), ionized acceptor impurities greatly reduces the carrier mobility at high doping, wherein clean material enables superior mobilities exceeding the model shown as a dashed line in Fig. 7, which assumes significant compensation. While this model captures many essential qualities for carrier density dependent doping, it does not incorporate the still nascent understanding of the crystal anisotropy effects in transport.

Anisotropy of the carrier mobility and its origin have disagreements in the literature.^{14,167} Phonon interactions within $\beta\text{-Ga}_2\text{O}_3$ are important to consider when discussing mobility as there are so many modes compared to GaN.^{44,134} Gosh and Singisetti (Ref. 168) first demonstrated the role of polar optical phonon scattering in limiting the low-field mobility to estimated $115\text{ cm}^2/(\text{V s})$ in $\beta\text{-Ga}_2\text{O}_3$, and studies of field-velocity and electron mobility as a function of phonon–plasmon coupling, considering anisotropy and confinement were reported. Ma *et al.* (Ref. 155) observed that polar optical phonon scattering is the main factor limiting the electron mobility below $200\text{ cm}^2/(\text{V s})$.¹⁵⁵ Estimating electron mobility using experimental data from Sn-doped samples produced a value of $300\text{ cm}^2/(\text{V s})$.¹⁴⁷ Unintentionally doped samples at room temperature and 54 K yielded experimental Hall mobility values of 176 and $3481\text{ cm}^2/\text{V s}$, respectively.⁷⁶ One of the

highest low temperature mobility values currently seen in the literature was reported by Seryogin *et al.* and Agnitron Technology (Ref. 172) with a mobility value of $23\,400\text{ cm}^2/(\text{V s})$ at 32 K. At room temperature, Hall mobility measurements using a Van der Paul configuration resulted in a value of $130\text{ cm}^2/(\text{V s})$,⁵⁷ while Si doped EFG samples had a Hall mobility of $93\text{ cm}^2/(\text{V s})$.¹³⁶

Single crystal room temperature electron mobility in $\beta\text{-Ga}_2\text{O}_3$ presently are 10–20-fold smaller than electron mobility in GaN.^{155,173} Ueda *et al.* report anisotropic electron mobility along b and c axes on (100) oriented UID ($N_e = 5.2 \times 10^{18}\text{ cm}^{-3}$) floating zone single crystal with larger room temperature mobility parallel b [$46\text{ cm}^2/(\text{V s})$] than c [$2.6\text{ cm}^2/(\text{V s})$]. The authors hypothesized that a heavy anisotropic electron effective mass is the reason for the observed anisotropy; however, it is now known to require different reasons since the effective electron mass was found nearly isotropic at room temperature and for similar carrier densities.^{42,59} There have been reports of carrier mobility variations across different directions in the crystal as well as different crystallographic orientations. The carrier mobility measurements reported by Ueda *et al.* (Ref. 59) show strong anisotropy that was stated to be a result of conduction band anisotropy. Villora *et al.* (Ref. 61) investigated floating zone single crystals grown along different directions using different ceramic seeds, and determined room temperature mobility values of 83, 78, and $98\text{ cm}^2/(\text{V s})$ along directions a, b, and c, respectively.⁶¹ Similar values were reported from room temperature IR ellipsometry investigations for a large set of single crystals with no systematic order with respect to crystal directions.¹⁴⁰ On the other hand, many experimental works report no observation of significant anisotropy in carrier mobility.^{57,174}

Kang *et al.* (Ref. 103) published first principles calculations of the fundamental electron mobility limit within $\beta\text{-Ga}_2\text{O}_3$. The findings aim to address the contradictions seen among previous experimental and theoretical works regarding carrier mobility anisotropy and to identify possible origins. Experimental measurements show that there is a large decrease in the room temperature electron mobility as the electron density is increased from 10^{17} to 10^{20} cm^{-3} .^{57,71} The theoretical findings from Kang *et al.* do not agree with this, in fact, the calculated mobility increases with increasing carrier density from 10^{17} to 10^{20} cm^{-3} . Compensation was not accounted for in the theoretical results, and Kang *et al.* concluded that compensation centers present

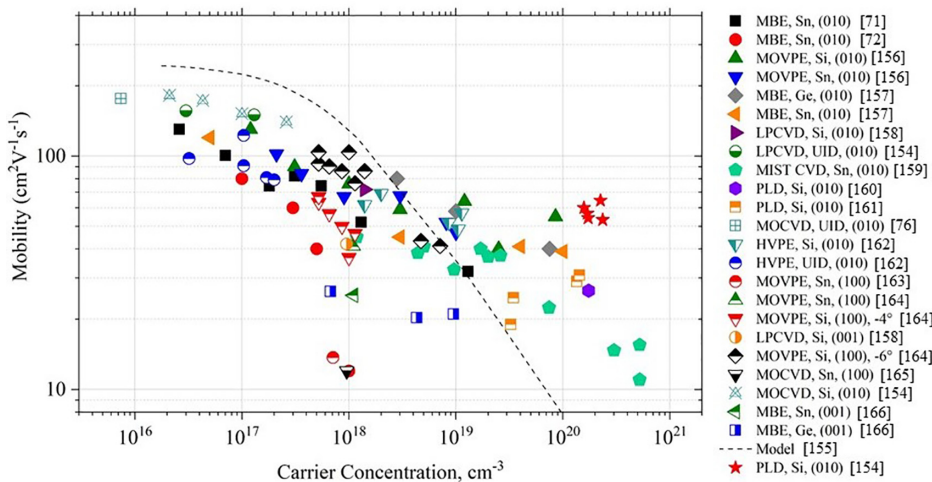


FIG. 7. Dependence of electron mobility vs carrier concentration for homoepitaxial $\beta\text{-Ga}_2\text{O}_3$ deposited on $\beta\text{-Ga}_2\text{O}_3$ substrates. Figure reproduced with permission from Jeon *et al.*, Appl. Phys. Lett. **9**, 101105 (2021). Copyright 2021 AIP Publishing LLC (Ref. 154). References for data points within the figure are as follows: Refs. 71, 72, 76, and 154–166.

in the material were the cause of the experimentally observed decrease in mobility. As electron carrier concentration increases, the suppression of mobility from the compensation centers is increasingly apparent. Similar to Peelaers *et al.* (Ref. 85), Kang *et al.* also computed a nearly isotropic conduction band using a HSE hybrid functional. The calculated mobility results show little anisotropy, less than 30% difference between different directions. This is significantly less anisotropy than what was shown experimentally by Ueda *et al.* (Ref. 59). There is even a weak anisotropy among the electron–phonon scattering, which could be seen as surprising given the nature of the monoclinic lattice. Kang *et al.* conclude that the large anisotropy that is seen experimentally is not an intrinsic property of $\beta\text{-Ga}_2\text{O}_3$ but rather a result of extended defects within the material such as twin boundaries. These boundaries may play a large role in scattering electrons.^{57,103,167} Zhang *et al.* (Ref. 175) used a refined ensemble Monte Carlo method to investigate the low-field electron transport considering acoustic deformation scattering, ionized impurity scattering, and polar optical phonon scattering. A room-temperature low-field mobility of $110 \text{ cm}^2/(\text{V s})$ was obtained, while anisotropy was not considered.

Using non-contact optical Hall-effect measurements on two different surfaces, Knight *et al.* (Ref. 42) experimentally found nearly isotropic mobility values around $44 \text{ cm}^2/(\text{V s})$ across all three axes with a carrier concentration of $6 \times 10^{18} \text{ cm}^{-3}$ on the (201) surface. The values are considered nearly isotropic. Measurements on a (010) surface found the mobility that was also nearly isotropic around 42 to $45 \text{ cm}^2/(\text{V s})$ with a carrier concentration of $4.1 \times 10^{18} \text{ cm}^{-3}$.⁴² Oishi *et al.* measured room temperature mobility of $153 \text{ cm}^2/(\text{V s})$ using a Schottky barrier on a (201) surface and reported a maximum mobility of $886 \text{ cm}^2/(\text{V s})$ at 85 K . Optical phonon scattering and ionized impurity scattering were suggested as dominant mechanisms impeding transport for temperatures >200 and $<100 \text{ K}$, respectively.¹⁷⁶ Villora *et al.* (Ref. 120) used van der Pauw geometry and Hall effect measurement on a-cut float zone single crystal and measured room temperature mobility of approximately $110 \text{ cm}^2/(\text{V s})$.¹²⁰ Galazka *et al.* (Ref. 54) reported van der Pauw and Hall effect measurement mobility parameters on (100) cleavage planes on numerous Czochralski grown single crystals under different atmospheres (CO_2 , Ar , O_2) and list values from 110 to $150 \text{ cm}^2/(\text{V s})$.⁵⁴

E. Doping and defects

$\beta\text{-Ga}_2\text{O}_3$ is a unique ultra wide bandgap material because it can be doped n-type with substitutional shallow donors (10^{13} to 10^{20} cm^{-3}) and achieve a very wide range of conductivity. A carrier concentration of 10^{20} cm^{-3} is considered to be the upper limit and was shown by Ahmadi *et al.* (Ref. 157) in Sn doped thin films. In this section, we briefly summarize literature on the effects of doping (donors and acceptors) on conductivity, bandgap, and thermal properties of $\beta\text{-Ga}_2\text{O}_3$. For more detailed reviews, the reader is highly encouraged to consult existing literature.^{14,177}

The most researched group IV dopants include silicon, germanium, and tin, where silicon and germanium substitute on the tetrahedral Ga(I) site and tin does so onto the octahedral Ga(II) site. Group VII dopants include chlorine and fluorine that will both go to the three-fold O(I) site.⁶⁶ Silicon has a -40% atomic radius difference with gallium, whereas the atomic radii difference between germanium and tin with gallium is only -16% and $+14\%$, respectively.¹²⁰ Thus, germanium and tin offer good spatial fits for the gallium cationic site. With

regard to oxygen vacancies, as mentioned earlier, Varley *et al.* (Ref. 66) have shown that even though such vacancies should act as donors, the levels are energetically too deep to induce electrical conductivity in otherwise undoped $\beta\text{-Ga}_2\text{O}_3$ crystals. Thus, any unintentional doping in $\beta\text{-Ga}_2\text{O}_3$ is caused by impurities introduced during growth, most notably silicon.⁶⁶ Gallium vacancies, on the other hand, create three dangling oxygen bonds (thus, a triple acceptor), leading to effective donor compensation and reduced free-electron concentration.¹⁷⁸

One of the first reports of controlled silicon doping of $\beta\text{-Ga}_2\text{O}_3$ crystals used a float zone method with feed rods forming a controlled mixture of SiO_2 and Ga_2O_3 .¹²⁰ This yielded $\beta\text{-Ga}_2\text{O}_3$ crystals with a silicon concentration that ranged from 10^{16} – 10^{18} cm^{-3} and showed that at lower doping concentrations, most of the silicon was incorporated into the crystal. If the doping concentration was higher, the amount of silicon incorporation was lower, usually 5% of what was in the feed rod. With increasing silicon in the feed rod, the crystal's conductivity continued to increase with a value of up to $50 \Omega^{-1} \text{ cm}^{-1}$ for the highest doped crystal. This supports the findings that electron conductivity is related to doping (silicon specifically in this case) and not oxygen vacancies.

It has also been shown that if $\beta\text{-Ga}_2\text{O}_3$ is annealed in oxygen, the free electron density will be decreased, but if annealed in the presence of nitrogen or hydrogen, there will be an increase in the conductivity (n-type).¹⁴ Tadjer *et al.* (Ref. 179) studied the effects of annealing Ga_2O_3 in nitrogen and oxygen. Annealing in the presence of nitrogen showed a free carrier concentration increase seen using electrochemical C-V and electron paramagnetic resonance. Annealing in the presence of oxygen resulted in a suppression of the electron conductivity which significantly reduced diode forward bias current.¹⁷⁹

Rafique *et al.* (Ref. 109) have studied the effect of doping on the bandgap of heteroepitaxial Ga_2O_3 on sapphire. An increase in bandgap from 4.69 to 4.716 eV for n-type doping concentrations of 1×10^{16} to $2.52 \times 10^{18} \text{ cm}^{-3}$ was reported. Burstein–Moss band filling was found to be the reasoning behind this increase. At even higher doping level, when electron concentration increased from 6.23×10^{18} to $3.05 \times 10^{19} \text{ cm}^{-3}$, there was a narrowing of the bandgap from 4.7 eV to 4.68 eV . The decrease is due to Mott semiconductor–metal transition, which is found to theoretically occur around $4 \times 10^{18} \text{ cm}^{-3}$ for $\beta\text{-Ga}_2\text{O}_3$.¹⁸⁰ A distribution of impurities in highly doped semiconductors can also lead to band narrowing from electrostatic potential fluctuations. When doping concentration is increased beyond $7.23 \times 10^{19} \text{ cm}^{-3}$, the bandgap widens again due to the Burstein–Moss effect and the bandgap renormalization effect taking over.¹⁰⁹

Theoretical investigations on the possibility of p-type conductivity in $\beta\text{-Ga}_2\text{O}_3$ have shown that, due to the strong localization of the holes in the material, substitutional p-type doping of this material will most likely not be possible. Any holes localized around oxygen sites will be practically unable to drift within the crystal lattice regardless of a present electrical field. This results in a very low or even negligible hole mobility for $\beta\text{-Ga}_2\text{O}_3$.^{181,182} Several approaches to overcoming this significant technological hurdle have been proposed, of which the metal–nitrogen co-doping approach proposed by Yan *et al.* (Ref. 183) and the Bismuth alloying approach proposed by Cai *et al.* (Ref. 184) could be most promising. In the former, Yan shows via density functional theory calculations that when $\beta\text{-Ga}_2\text{O}_3$ is co-doped with magnesium or zinc as donor and nitrogen as acceptor species, the energy levels for nitrogen are significantly reduced to 0.16 and 0.01 eV , respectively.¹⁸³ Furthermore,

using electron-poor metals for co-doping also hinders the formation of compensating vacancy defects. In the bismuth alloying approach, Cai *et al.* show that adding even a few percent of bismuth to form a dilute $(\text{Bi}_x\text{Ga}_{1-x})_2\text{O}_3$ alloy facilitates the formation of an intermediate valence band which lowers the acceptor energy.¹⁸⁴

Deep acceptor levels also play a role in the conductivity and the extremely low hole mobility and should be considered as well.^{185,186} Neal *et al.* showed that iron doping resulted in a deep acceptor behavior that still resulted in the crystal being weakly n-type and the iron acceptor energy was reported to be 860 meV relative to the conduction band.¹⁸⁶ Deep acceptors were considered by Peelaers *et al.* (Ref. 185) in a first principles study. Their findings concluded that dopants in $\beta\text{-Ga}_2\text{O}_3$ often result in deep acceptor levels that occur more than 1.3 eV above the valence band maximum. These defects further hinder the possibility of any p-type conductivity within $\beta\text{-Ga}_2\text{O}_3$. However, deep acceptors are beneficial for creating highly insulating layers within devices.¹⁸⁵

Schubert *et al.* (Ref. 140) have reported that the presence of free charge carriers as a result of doping Ga_2O_3 causes both the frequency and polarization direction of the LO-phonon plasmon coupled modes to shift (see also Fig. 5).¹⁴⁰ Doping has also shown to play a role in affecting the thermal conductivity. When doping with tin or iron, it was shown that the thermal conductivity was lower than an undoped sample. These dopants increase the phonon scattering, which causes a decrease in thermal conductivity.^{14,187}

Vibrational spectroscopy is a viable method to identify polarization dependencies with principal dielectric axes of lattice defect-related IR absorptions in $\beta\text{-Ga}_2\text{O}_3$, as shown by Portoff *et al.* (Ref. 188) who identified the dominant O-H center as a Ga(1) vacancy-2H[V_{Ga(1)}]-2D center.

It is further noted that Kumar and Singisetti used first principles and calculated the thermoelectric transport coefficients, Seebeck coefficient, Peltier coefficient, and electronic thermal conductivity in $\beta\text{-Ga}_2\text{O}_3$ for a wide range of temperatures and doping densities.¹⁸⁹ The room temperature Seebeck coefficient was found to be $-341 \mu\text{V/K}$, which is high compared to that of the other commonly studied semiconductors. Kumar and Singisetti suggest the larger Seebeck coefficient is due to the higher density of states arising from comparatively high electron effective mass. $\beta\text{-Ga}_2\text{O}_3$ thin films also exhibit a bandgap dependence on the dopant concentration of 1×10^{16} – $2.52 \times 10^{18} \text{ cm}^{-3}$ showing an increase in the bandgap from 4.69 to 4.716 eV.¹⁰⁹

F. Polymorphs

The other polymorphs of Ga_2O_3 are metastable; however, they are still of interest for device applications. The phases α , ϵ , and κ possess slightly larger bandgaps and potential bandgap engineering that could offer advantages for power applications. Investigations into thin films of α and ϵ -phase have gained considerable traction in the literature.^{190–192} The remaining phases, δ and γ , are currently less known and scarcely researched due to lack of high quality samples and difficulty in synthesis. Figure 8 highlights the various crystal structures of the five Ga_2O_3 polymorphs.

There are conflicting reports of the crystal structure and lattice parameters of $\alpha\text{-Ga}_2\text{O}_3$ as referenced by Roy and Hill,¹⁵ and Zachariasen.¹⁹³ Published 17 years before Prewitt's findings,²⁹ Roy and Zachariasen state the crystal structure of the α -phase polymorph is hexagonal with only one lattice parameter reported; $a = 5.31 \text{ \AA}$.^{15,193} This hexagonal structure is in disagreement with the now widely

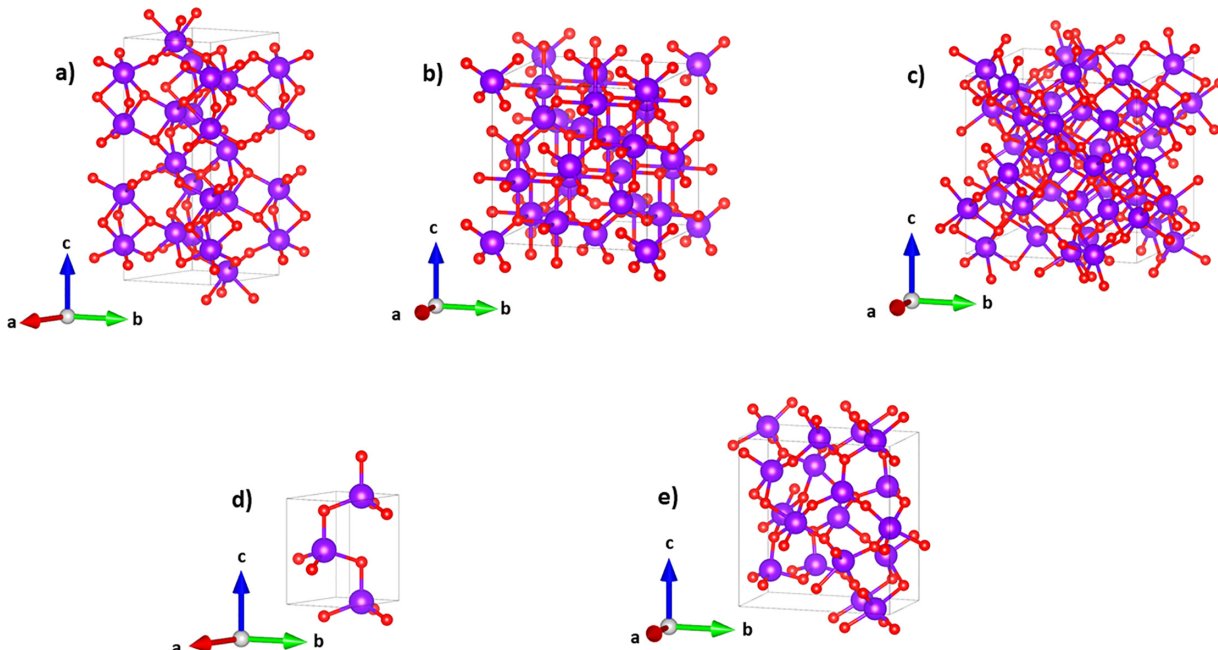


FIG. 8. Schematics for the crystal structure of the metastable Ga_2O_3 consisting of (a) trigonal/rhombohedral $\alpha\text{-Ga}_2\text{O}_3$ belonging to space group $R\bar{3}C$ (#167) with the c -axis orientated upwards, (b) cubic $\gamma\text{-Ga}_2\text{O}_3$ belonging to space group $Fd\bar{3}m$ (#227) with the c -axis orientated upward, (c) body centered cubic $\delta\text{-Ga}_2\text{O}_3$ belonging to space group $Ia\bar{3}$ (#206) with the c -axis orientated upward, (d) hexagonal $\epsilon\text{-Ga}_2\text{O}_3$ belonging to space group $P6_3mc$ (#186) with the c -axis orientated upward, and (e) orthorhombic $\kappa\text{-Ga}_2\text{O}_3$ belonging to space group $Pna2_1$ (#33) with the c -axis orientated upward. Purple, Ga; red, O.

accepted rhombohedral crystal structure.^{29,30} Recent studies discuss the thermal stability of the α -phase as well as the limitations on growth. The α -phase has been a cost-effective alternative polymorph to β -Ga₂O₃ that is considered thermodynamically semistable. The corundum structure allows for growth on sapphire as well as for alloying with other corundum oxides, including Al₂O₃, *rh*-In₂O₃, and α -Fe₂O₃.¹⁹⁴ Opportunities for future device design also can arise from integration with isostructural p-type oxides, such as Rh₂O₃ or Ir₂O₃, and ferromagnetic or ferroelectric oxides, such as α -Fe₂O₃, α -Cr₂O₃, α -V₂O₃, or ScFeO₃.¹⁹⁵ Of note, the bulk modulus of α -Ga₂O₃ is noticeably higher than of β -Ga₂O₃.^{19,113}

The limitations of α -Ga₂O₃ come from the polymorph's thermodynamically semistable nature and the difficulties to obtain isomorphic material depending on growth and annealing conditions. Higher growth temperatures and higher annealing temperatures result in the formation of β -phase within the α -phase. The inclusions of β -phase structures begin to appear when temperatures reach around 550 °C.^{194,196,197} Below this temperature, the optical bandgap of α -Ga₂O₃ is around 5.25 eV. At higher annealing temperatures with the inclusions of β -phase, the bandgap is decreased to around 4.75 eV.¹⁹⁷ State-of-the-art growth methods such as MBE or MOCVD are still beginning to be explored. No isomorphic growth using MOCVD is reported yet.¹⁹⁸ It appears that only limited film thickness can be obtained for isomorphic α -Ga₂O₃ on sapphire using MBE (\approx 0.3 nm on *c*-plane, 14 nm on *a*-plane, 200 nm on *m*-plane). Jinno *et al.* (Ref. 199) reported growth of isomorphic high-quality corundum-structure Ga₂O₃ on *m*-plane sapphire by plasma assisted molecular beam epitaxy (PAMBE). The film thicknesses and the growth rates were in the range of 52–84 nm and 0.43–0.7 nm/min, respectively. The large lattice mismatch between α -Ga₂O₃ and sapphire may be overcome by the growth of thick films and using techniques such as grading the composition from Al₂O₃ to Ga₂O₃, thereby reducing the dislocation density. Very low growth rates make this a challenging task. Jinno *et al.* (Ref. 200) obtained reduced edge dislocation density α -Ga₂O₃ thin films on sapphire substrates by depositing first quasi-graded α -(Al_xGa_{1-x})₂O₃ buffer layers, and structural studies revealed that most strains remained in the graded buffer layers. High-purity material has

been reported using HVPE at high growth rates. Oshima *et al.* (Ref. 201) obtained rates over 100 μ m/h on *c*-plane sapphire. Epitaxial lateral overgrowth (ELO) was reported to reduce the dislocation density to less than 5×10^6 cm⁻².²⁰² Using double ELO, no detectable dislocations were found in TEM investigations.²⁰³ The addition of Al to the precursor chemistry was shown to increase thermal stability and suppress the formation of the β -phase, leading to the formation of α -phase (Al_xGa_{1-x})₂O₃ up to 20% alloy composition with the measured bandgap of 5.95 eV. Specifically, the formation of β -phase was observed after annealing at 800 °C for α -(Al_xGa_{1-x})₂O₃ grown at 650 °C with 2.5% Al. Increasing the growth temperature to 800 °C and the Al ratio to 20% enabled the films to be annealed up to 850 °C without β -phase presence detected via X-ray diffraction. The addition of Al was shown to increase thermal stability and to decrease the presence of β -phase all while increasing the operation and growth temperature of the α -phase before the onset of β formation. With the Al alloying, the growth temperature without beta phase presence was shown to increase up to 150 °C while widening the bandgap up to 6.0 eV.¹⁹⁴

Sharma and Singisetti (Ref. 204) calculate the band structure of α -Ga₂O₃ from first principles calculations in agreement with He *et al.*¹⁹ The electronic structure using a HSE hybrid functional is compared with the LDA electronic structure in Fig. 9. The indirect bandgap at the Γ -F symmetry line is narrowly (0.05 eV) lower than the direct Γ -point transition. As is typical, the LDA level electronic structure calculation results underestimate the bandgap energy.

α -Ga₂O₃ has been shown to have a large exciton binding energy of 110 meV using a fitting of the first derivative of the absorption curve on the bandgap.²⁰⁵ Segura *et al.* (Ref. 205) determined bandgap energies for the two lowest-energy allowed transitions accounting for the excitonic binding energy using fitting parameters, optical transmission, and ellipsometry data. At room temperature, the bandgap energies across four samples ranged from 5.60 to 5.62 eV for the lowest transition. The second lowest transition ranged from 6.28 to 6.44 eV for two samples at room temperature. Bandgap energies were also reported at 6 K. Energies ranged from 5.718 to 5.722 eV for the lowest transition and a single value of 6.39 eV for the second lowest transition. This

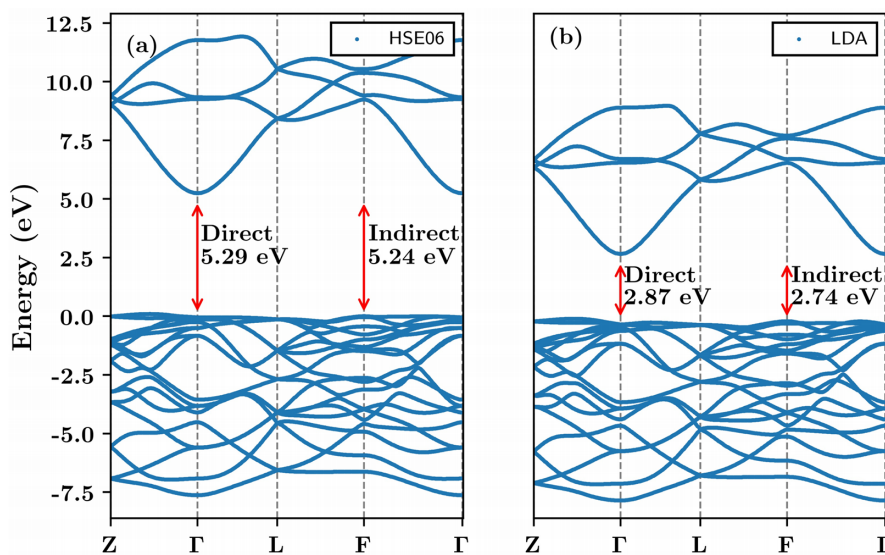


FIG. 9. Electronic band structure of α -Ga₂O₃ in comparison between HSE hybrid functional and LDA level DFT calculations. The indirect gap is narrowly smaller than the direct gap. Reproduced with permission from Sharma and Singisetti, Appl. Phys. Lett. **114**, 032101 (2021). Copyright 2021 AIP Publishing LLC (Ref. 204).

temperature dependence of the bandgap is thought to be due to the electron–phonon interactions.²⁰⁵

In a 2021 report by Hilfiker *et al.* (Ref. 206), the band structure, excitonic contributions, band-to-band transitions, and the anisotropy of α -Ga₂O₃ were determined. The band structure was produced using hybrid-level-DFT and highlights the uppermost valence bands that are involved in the lowest band-to-band transitions. Calculated bandgap energies determined using hybrid-level-DFT for the ordinary and extraordinary directions are found to be 5.25 and 5.266 eV, respectively. The lowest band-to-band transitions were reported experimentally using ellipsometry for $E_{0,\perp}$ (ordinary direction) and $E_{0,\parallel}$ (extraordinary direction) with values of 5.46 and 5.62 eV, respectively. This reveals clear anisotropy that has been mostly neglected prior to Hilfiker *et al.* (Ref. 206). A calculated quasiparticle gap value for the extraordinary direction of 5.625 eV was reported by Furthmüller *et al.* (Ref. 92), in good agreement with the experimental value for the same direction from Hilfiker *et al.* Excitonic contributions are also present as a result of the anisotropic band structure of α -Ga₂O₃. The first is the excitonic contribution containing a small binding energy of 7 meV belonging to the M_0 -type (\perp) transition. The second excitonic contribution contains a larger binding energy of 178 meV associated with the M_1 -type (\parallel) transition.²⁰⁶ With respect to the calculated excitonic effects, the absorption edge of β -Ga₂O₃ resides much lower in energy when compared to the rhombohedral Ga₂O₃ polymorph.^{92,93} Hilfiker *et al.* present data containing a wider spectral range and more accurate assignments of the critical points within the band structure when compared to previous reports. The effective mass parameters also experience anisotropy as a result of the anisotropic valence bands and rather isotropic conduction band structure. The reduced effective mass parameters for the lowest three transitions are 0.18 m_e for the ordinary transition and 0.14 m_e for the extraordinary transition.²⁰⁶

The phonon modes for α -Ga₂O₃ have also been reported.^{30,207} In 2015, Cusco *et al.* studied the lattice dynamics and phonon modes stating that the irreducible representation for the α -phase,

$$\Gamma_{aco} = 2A_{1g} + 2A_{1u} + 3A_{2g} + 2A_{2u} + 5E_g + 4E_u.$$

The Raman active modes consist of 2A_{1g} and 5E_g while the IR active modes are 2A_{2u} and 4E_u. The silent modes consist of 2A_{1u} and 3A_{2g}. Measured phonon mode frequencies for the Raman active modes were reported by both Cusco *et al.* (Ref. 207) and Feneberg *et al.* (Ref. 30) and showed good agreement. Feneberg *et al.* has also produced detailed works on the IR active modes.^{30,208} In the earlier of the two works (Ref. 208), calculated IR active modes were reported for ω_{TO} of both A_{2u} and E_u. Calculations show that there should be two A_{2u} modes and four E_u modes. The E_u modes appear to pose an issue as only three of the four modes are observed experimentally. The mode with the lowest calculated frequency (220 cm⁻¹) does not appear experimentally in either of Feneberg's works as it was outside the spectral range of the experimental capabilities. Reported values are listed in Table IX.

In a recent work, Stokey *et al.* report on a combined far infrared and IR ellipsometry study and DFT calculations at the LDA and GGA levels and obtain all optical phonon modes, including longitudinal frequencies from experiment and all Brillouin zone center modes from calculation. The authors compare all results for gallium oxide with the isostructural compound sapphire. Overlap calculations are provided for all phonon mode eigenvectors, and the authors discuss the predicted evolution of all Raman, silent, and IR-active modes into the ternary alloy system and whether modes may form single mode or more

TABLE IX. α -Ga₂O₃ Raman, silent, and IR-active phonon mode frequencies (cm⁻¹) from experiment.

Mode	$l=1$	$l=2$	$l=3$	$l=4$	$l=5$	Reference
Raman						
A _{1g}	218.0	574.3				30 ^a
	218.2	569.7				207 ^b
E _g	241.9	286.8	328.0	431.3	688.4	30 ^a
	240.7	285.3	328.8	430.7	686.7	207 ^b
IR						
A _{2u} (TO)	271.3	546.6				30 ^a
A _{2u} (TO)	270.8	547.1				209 ^a
A _{2u} (LO)	461.8	702.3				209 ^a
E _u (TO)		333.2	474.1	571.7		30 ^a
E _u (TO)		333.4	469.9	562.7		208 ^a
E _u (TO)	221.7	334.0	469.5	568.5		209 ^a
E _u (LO)	221.9	390.0	564.3	718.3		209 ^a

^aExp—Spectroscopic ellipsometry.

^bExp—Polarized Raman scattering.

complex mode behaviors. Stokey *et al.* also provide the first experimental assessment of the static dielectric constant for rhombohedral structure gallium oxide ($\epsilon_{DC,\parallel} = 18.01 \pm 0.16$ and $\epsilon_{DC,\perp} = 12.14 \pm 0.11$).²⁰⁹ Reported values are also listed in Table IX. Sharma and Singisetti (Ref. 204) recently also provide anisotropic static and high frequency dielectric constants and zone center phonon modes from first principles.

Sharma and Singisetti (Ref. 204) report an isotropic effective electron mass of 0.25 m_e from first-principles studies. Anisotropy was evident in the electron effective mass of the α -Ga₂O₃ samples studied by Feneberg *et al.* (Ref. 30) using ellipsometry and the plasma frequency derived from the anisotropic dielectric functions. Perpendicular to [0001] the effective mass was 0.297 m_e \perp while parallel to [0001] had an effective mass of 0.316 m_e \parallel . These values were determined from the highest doped sample containing an electron concentration of $n = 1.1 \times 10^{19}$ cm⁻³.

The effective mass values for α -Ga₂O₃ are higher than those typically seen in moderately doped β -Ga₂O₃ samples.^{30,42} Feneberg *et al.* (Ref. 30) expect nonparabolicity in the conduction band of α -Ga₂O₃, and hence, the conduction band bottom effective mass parameters should be smaller, and also anisotropic similar to rutile SnO₂.²¹⁰

Sharma and Singisetti (Ref. 204) estimate the low field electron mobility in α -Ga₂O₃ from first principles calculations considering full phonon energy dispersions. Evaluation of the electron mobility is performed including effects of the polar, nonpolar, and ionized impurity scattering mechanisms. The authors find a room temperature limit of approximately 220 cm²/(V s) mostly limited by the polar optical phonon scattering at an electron density of 1.0×10^{15} cm⁻³.

The cubic γ -phase was originally thought to be analogous to γ -Al₂O₃ but attempts at preparing the polymorph and testing via XRD yielded no such relationship,¹⁹³ more than likely due to very poor crystalline quality of the samples. In more recent studies, Oshima *et al.* (Ref. 25) reported epitaxial growth for γ -phase films of the cubic spinel-defect structure. Undoped samples not only resulted in poor crystalline quality, but also exhibited a transition to the beta phase.

Doping with Mn was shown to be an effective way of increasing crystalline quality and overall stability. Conclusions were made that along with doping, the crystalline quality was heavily influenced by growth substrate and substrate temperature.^{25,211} Cubic γ -Ga₂O₃ was shown to have a lattice parameter of $a = 8.237 \text{ \AA}$ calculated from the Rietveld refinement²⁶ and the ability to be grown on cubic spinel structures.²⁵ The bandgap of γ -Ga₂O₃ was estimated to be 5.0 eV for a direct transition and 4.4 eV for an indirect transition.²⁵

The C-type rare earth structure of δ -phase is also a cubic structure and is similar to *bcc*-In₂O₃ and Mn₂O₃ meaning it must have octahedral metal sites.^{15,26} Later studies dispute the initial findings of a δ -phase polymorph from Roy *et al.*, (Ref. 15), stating that the very poor crystalline δ -phase is not a distinct polymorph but is a mixture of β and ε phase. By having similarities with the β -phase, the metal sites cannot be solely octahedral but must be shared across the tetrahedral and octahedral sites. Neutron diffraction data support that the δ -phase is merely a nanocrystalline ε -phase.²⁶ δ -phase Ga₂O₃ is also considered an isomorph of Ti₂O₃.¹⁵ The specific phase of Ti₂O₃ was not specified.

In the early 1950s, Roy *et al.* (Ref. 15) used powder x-ray diffraction to determine that ε phase was distinctly different from the characteristics of γ and δ phase with a symmetry that is predicted to be lower than hexagonal or tetragonal; however, the structure was unable to be determined and no lattice parameters were reported. Roy *et al.* describe this phase as being a definite structure, supported by the observations they made on GaAlO₃. They concluded that at 100° (no unit given) above the equilibrium transformation temperature, there exists the formation of solid ε -phase solutions.¹⁵ In the work by Bosi *et al.* (Ref. 212), much attention has been brought to possible methods of stabilizing and promoting the nucleation of the ε polymorph in 2020. Multiple growth methods such as HVPE, MOCVD, MBE, and PLD were examined as well how the addition of Cl, H, Sn, and In during the growth process played a role in polymorph stabilization. The detailed work by Bosi *et al.* is driven by (i) ε possessing higher symmetry than β -Ga₂O₃, (ii) the piezoelectric properties of ε -Ga₂O₃, and (iii) growth on widely available and cheap sapphire substrates.²¹²

Recently, more work has been published on the ε -phase, bringing a better understanding to this phase and the relation to κ -phase. It was believed that κ -phase was simply another name for ε -phase as they were so similar. It was initially reported that ε -phase was orthorhombic (space group *Pna*2₁) with lattice constants $a = 5.120 \text{ \AA}$, $b = 8.792 \text{ \AA}$, and $c = 9.410 \text{ \AA}$.²⁰ In contradiction to the orthorhombic ε -phase, Rietveld calculations showed a hexagonal structure with lattice parameters $a = 2.904 \text{ \AA}$ and $c = 9.255 \text{ \AA}$.²⁶ In 2017, Cora *et al.* (Ref. 16) published a report specifying their findings on the relationship between ε -phase and κ -phase, again partly contradicting Yoshioka *et al.* (Ref. 20) who found ε and κ -phase were the same. The ε -phase is considered to be the second most stable phase behind β and classifies the ε -phase as hexagonal with 4H close-packed oxygen stacking and κ -phase as orthorhombic. The ordering scheme for the Ga atoms within the hexagonal ε -phase is the cause of the κ -phase. This stems from edge sharing of the octahedral Ga atoms, corner sharing of the tetrahedral Ga atoms, and the formation of octahedra zig-zag ribbons as highlighted in Fig. 8(e). Reported lattice constants for the orthorhombic κ -phase are $a = 5.0463 \text{ \AA}$, $b = 8.7020 \text{ \AA}$, and $c = 9.2833 \text{ \AA}$.¹⁶

The conclusions drawn from this study show that the orthorhombic κ -phase is not just another name for ε -phase, but is instead an ordered subgroup of the hexagonal phase. The difference being the

Ga atomic arrangement between the oxygen planes of the structure. Success in growing κ -phase thin films via heteroepitaxial PLD growth with high crystalline quality that has the potential to be an alternative for β -phase layers among devices has been shown in the literature recently.¹⁷ Increasing the substrate temperature during growth showed an increase in crystalline quality as well. The lattice constants were in better agreement with the values by Cora *et al.* than Yoshioka *et al.* and were shown to be $a = 5.066 \text{ \AA}$, $b = 8.700 \text{ \AA}$, and $c = 9.261 \text{ \AA}$. Along with comparable crystalline quality to the β -phase, the κ -phase was shown to have a bandgap of around 4.9 eV.¹⁷ In one of the more recent works on κ -Ga₂O₃, Cora *et al.* (Ref. 213) followed up their 2017 work by detailing the phase transitions of the κ -phase toward both the γ -phase and thermodynamically stable β -phase. A detailed TEM study involving both *in situ* and *ex situ* conditions were carried out. With an increase in temperature up to 950 °C under vacuum, κ -Ga₂O₃ quickly transitions to β -Ga₂O₃ via an exothermic transition. The heating rate was the driving factor behind the speed of the transition. When samples were annealed *ex situ* in air, κ -Ga₂O₃ transitions to γ -Ga₂O₃ where the oxygen partial pressure and heating rate were the driving factors. It should be noted that this transition was considered to be an intermediate step occurring before the final exothermic transition to β -Ga₂O₃, only seen under *ex situ* conditions.²¹³

Similar to the AlGaN system,^{214,215} the hexagonal epsilon phase of Ga₂O₃, and its alloys with In and Al are anticipated to possess piezoelectric and spontaneous interface charges. This also means that Ga, Al, or O terminated surfaces should reveal different surface charge accumulations, also depending on the state of strain across a given heterointerface. Thus, also the surface polarity will most likely matter in epitaxial growth of the epsilon phase [Fig. 8(d)], and affect device performance. Similar piezoelectric and spontaneous interface charge properties are known for the wurtzite-structure Zn(Mg)O system.²¹⁶ It is noted in passing that combinations with ferroelectric oxides offer many fascinating device architectures.^{217–219}

Figure 10 highlights the variation of the bandgap energies across five of the six polymorphs. The bandgap energies for the β phase grouped into three approximate directions to describe the drastic anisotropy within that phase for the first three fundamental transitions. The experimental β -phase values labeled * denote measurements of the onset of absorption. The remaining β -phase experimental values were determined from SE and are noticeably higher in energy than the values for the onset of absorption because of the inclusion of excitonic effects, which the absorption measurements neglect. There is also a clear trend among the sets of experimental β -phase values. For both the onset of absorption and SE measurements, the trend of $b > a > c$ is present. The variation of roughly 0.5 eV can be considered a large dispersion even for such a widely researched phase. The dispersion in values is even larger for the α -phase as it begins to gain popularity across literature. As seen from the plot, there are very limited values for the lesser known γ , ε , and κ polymorphs with none available for the δ polymorph. Considering the similarities that ε and κ share, it comes as no surprise that the plotted values vary by less than 0.1 eV. The lack of values for certain polymorphs is also due to the unavailability and difficulty of obtaining high quality material growths amenable to performing bandgap studies on.

G. Alloys

As research continues to accelerate and improve for β -Ga₂O₃, new investigations are arising for the complex alloys between Ga₂O₃

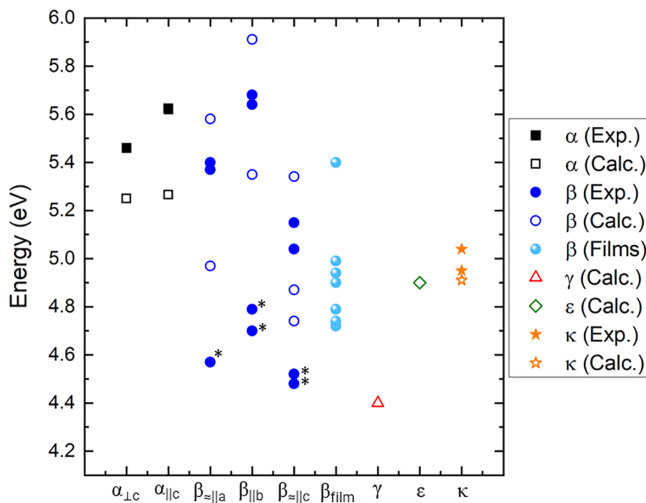


FIG. 10. Experimental (solid) and calculated (open) bandgaps of the Ga_2O_3 polymorphs from literature. Data points collected from Refs. 17, 25, 59, 66, 86, 92, 94–99, 101, 102, 206, and 220. We note that to date, there are no reported values of the bandgap of $\delta\text{-}\text{Ga}_2\text{O}_3$ as well as no experimental reports on the bandgap of the γ -phase. Values marked with * are reported from the onset of absorption.

and Al_2O_3 and/or In_2O_3 . These alloys offer a unique solution to some of the issues and problems currently plaguing Ga_2O_3 power devices. Of note is the possibility of controlled bandgap engineering. More research and progress is needed to increase growth capabilities and availability of bulk and thin film samples of these alloys.

Gallium oxide alloys have gained considerable traction in research due to increased considerations and implementation into power, RF, and optoelectronic device applications. Each alloy will likely warrant their own reviews; however, a brief discussion of some pertinent alloys follows. Alloying allows for alterations to the electronic and material properties of Ga_2O_3 such as bandgap and crystal structure. Choosing a specific alloy to incorporate into Ga_2O_3 thin films and bulk crystals is important, and there are a number of candidates that offer many advantages. Alloys with aluminum oxide, indium oxide, and zinc oxide are highlighted below with potential significant applications in electronic devices.

1. Aluminum gallium oxide— $(\text{Al}_x\text{Ga}_{1-x})_2\text{O}_3$

The alloy of alumina and gallia ($\text{Al}_x\text{Ga}_{1-x})_2\text{O}_3$, sometimes abbreviated as “AlGO” or “AGO” in the literature, is of particular interest for power electronics due to the potential of a widening and tunable bandgap yielding higher breakdown fields and potential for devices analogous to the $\text{GaN}-\text{AlGaN}$ system. Work has accelerated concomitantly with the increased availability of films via various growth methods. The $\text{Al}_2\text{O}_3-\text{Ga}_2\text{O}_3$ phase behavior was mapped out by Hill, Roy and Osborn (Ref. 114) and reproduced in Fig. 11 showing significant aluminum solubility in the β phase at elevated temperature, up to 70%. However, upon quenching to low temperatures, a line compound of AlGaO_3 precipitated out from the $\beta\text{-}\text{Ga}_2\text{O}_3$ resulting in the limited low temperature solubility of <10%. This line compound is formed in 2-phase stability with either $\beta\text{-}\text{Ga}_2\text{O}_3$ and $\alpha\text{-Al}_2\text{O}_3$ based on the total aluminum content. While this suggests high aluminum content $\beta\text{-}\text{Ga}_2\text{O}_3$ is thermodynamically unstable at low temperatures, significant aluminum content has been

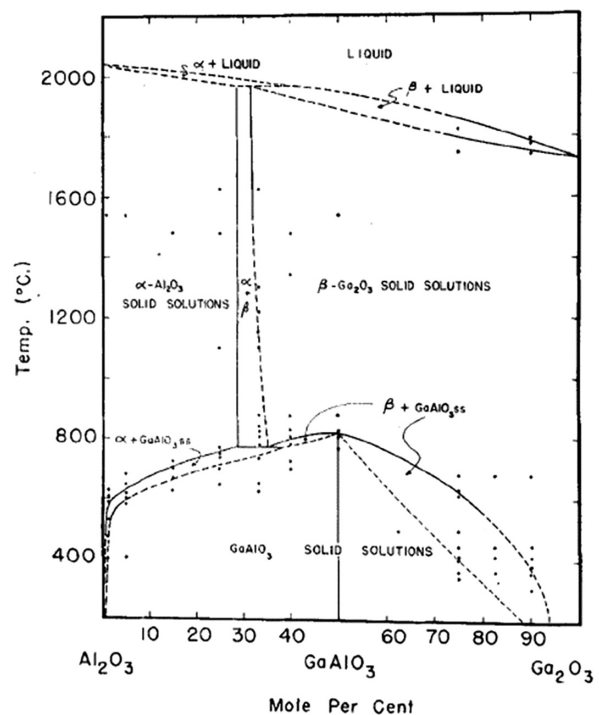


FIG. 11. Measured $(\text{Al}_x\text{Ga}_{1-x})_2\text{O}_3$ equilibrium diagram. Reproduced with permission from Hill *et al.*, J. Am. Ceram. Soc. 35, 135 (1952). Copyright 1952 Wiley Online Library (Ref. 114).

demonstrated by various growth methods.^{221,222} Both $\beta\text{-}\text{Ga}_2\text{O}_3$ and $\alpha\text{-Al}_2\text{O}_3$ possess differing ground-state crystal structures, which can be expected to limit Al_2O_3 solubility within $\beta\text{-}\text{Ga}_2\text{O}_3$.²²³ First principles DFT calculations conclude that the monoclinic β -phase of AlGaO is the preferred phase up until 71% Al concentration. Beyond this concentration, it is predicted that the α -phase will be preferred.^{223,224}

Experimentally, Bhuiyan *et al.* (Ref. 225) produced β -phase (100) $(\text{Al}_x\text{Ga}_{1-x})_2\text{O}_3$ thin films grown epitaxially via MOCVD. Samples were grown atop $\beta\text{-}\text{Ga}_2\text{O}_3$ (100) orientated substrates. Pure β -phase (100) $(\text{Al}_x\text{Ga}_{1-x})_2\text{O}_3$ thin films were grown with an Al composition of up to 52%. Adequate tuning of growth conditions, temperature, and VI/III molar ratio led to such high quality samples on native substrates that were characterized using XRD and high-resolution scanning transmission electron microscope (STEM). When the Al composition was high, step flow growth with a smooth surface morphology was shown. The Al adatoms were considered to be incorporation sites that influenced the nucleation and growth of AlGaO . XRD was used to estimate the Al content of three samples. An Al content of 17%, 34%, and 47% corresponded to XPS bandgap energy estimations of 5.1, 5.4, and 5.7 eV, respectively, across the three samples.²²⁵

The bandgaps of the two oxides, Al_2O_3 and Ga_2O_3 , are around 8.8 and 4.8–4.9 eV, respectively. This results in an alloyed bandgap that ranges from 5 to \sim 7.9 eV for $\beta\text{-}(\text{Al}_x\text{Ga}_{1-x})_2\text{O}_3$ based on the high temperature solubility limit. When comparing the atomic properties of Al and Ga, both elements possess similar electron configurations besides their respective oxides having almost a 4 eV bandgap difference.²²¹ Recent studies show the solubility of Al^{3+} ions within a Ga_2O_3 crystal

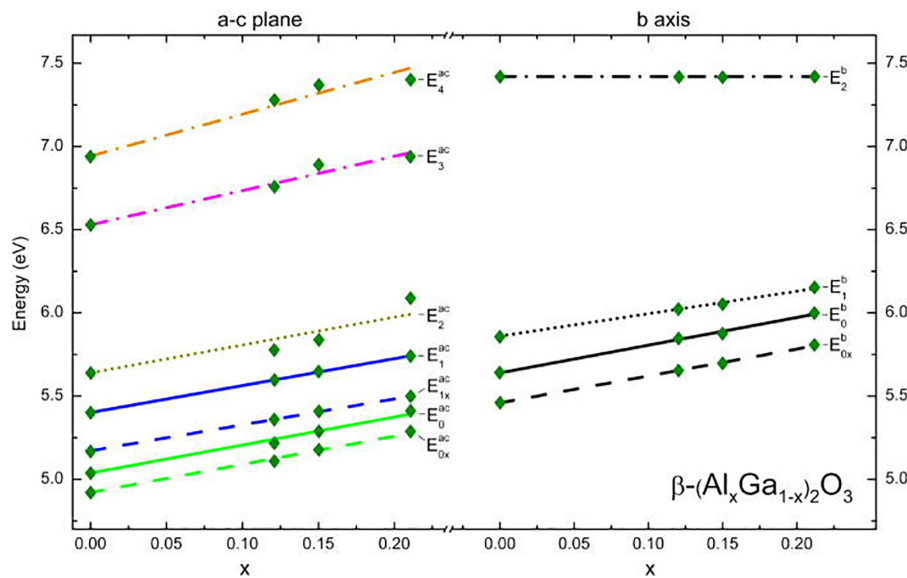


FIG. 12. Transition energies (symbols) vs Al content x of $\beta\text{-}(\text{Al}_x\text{Ga}_{1-x})_2\text{O}_3$ films determined from ellipsometry investigations on (010)-oriented PAMBE-grown thin films on (010) FEG gallium oxide substrates. Reproduced with permission from Hilfiker *et al.*, Appl. Phys. Lett. 114, 231901 (2019). Copyright 2019 AIP Publishing LLC (Ref. 227).

can be as high as 78%.²²⁶ Hilfiker *et al.* (Ref. 227) reported on the evolution of the three fundamental band-to-band transition energies and their excitonic contributions for $\beta\text{-}(\text{Al}_x\text{Ga}_{1-x})_2\text{O}_3$ ($x < 0.21$) thin films deposited by PAMBE onto (010)-oriented $\beta\text{-}\text{Ga}_2\text{O}_3$ substrates. The observed shift in transition energies are reported in perfect agreement with theoretical predictions (Fig. 12). Jinno *et al.* (Ref. 199) reported lowest bandgap energies for $\alpha\text{-}(\text{AlGa})_2\text{O}_3$ thin films over the entire composition range. Figure 13 reproduces their results also in comparison with the bandgap evolution in the related systems AlGaAs and AlGaN. Hilfiker *et al.* (Ref. 228) report the evolution of the anisotropic high frequency dielectric constants and frequency diversions over the entire composition range for $\alpha\text{-}(\text{Al}_x\text{Ga}_{1-x})_2\text{O}_3$ ($0 \leq x \leq 1$) thin films. The high frequency values decrease by approximately 25% between $x = 0$ and $x = 1$. The difference between ordinary and extraordinary values also decreases.

Calculated lattice parameters, specific heat, and thermal conductivity for ordered AlGaO_3 (50% Al) were obtained by Mu *et al.* (Ref. 229) and shown to be $a = 12.16$ Å, $b = 2.99$ Å, and $c = 5.78$ Å with a monoclinic structure. The thermal conductivity was calculated to be anisotropic with calculated values being 19.8 [100], 25.0 [010], and 30.4 W/(mK) [001].²²⁹

Krueger *et al.* (Ref. 230) report on lattice parameter and bandgap variation within $\beta\text{-}(\text{Al}_x\text{Ga}_{1-x})_2\text{O}_3$ powder samples produced by solution combustion synthesis. With an increasing Al fraction all three lattice parameters are shown to decrease linearly. The decrease of the slopes depends on whether x is below or above 0.5. According to DFT calculations, Al fills the octahedral sites first due to preference over the tetrahedral sites. The rate with which the lattice parameters change is also directionally dependent along with Al content. The lattice parameters a and b change in unison at a faster rate than c when x is low, but upon the increasing aluminum content, a and b begin to diverge. The b lattice parameter, which is the shortest, is shown to be the edge of both the octahedron and tetrahedron features of the crystal. The a parameter consists of several different bond lengths while the c parameter is the sum of cation octahedral and tetrahedral edges. Krueger *et al.* conclude that experimental and theoretical findings for the lattice constants are in general agreement concerning the change with the

overall Al content. The theoretical data are shown to be an overestimation of the lattice contractions when the Al content is low.²³⁰ Krueger *et al.* (Ref. 230) summarize how the Al content alters the DFT calculated bandgap as well, allowing for a tunable bandgap within the deep ultraviolet spectrum that ranges between 4.8 and 6.6 eV. This also makes $\beta\text{-}(\text{Al}_x\text{Ga}_{1-x})_2\text{O}_3$ an attractive material for optical devices.²³⁰

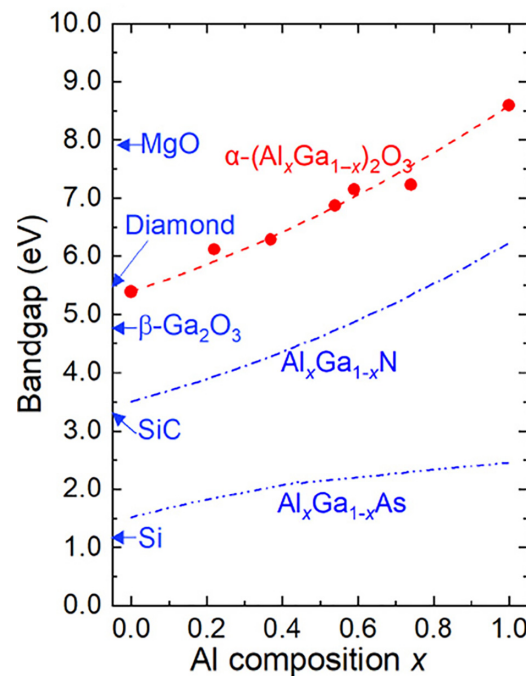


FIG. 13. Evolution of the lowest bandgap energy in $\alpha\text{-}(\text{AlGa})_2\text{O}_3$ thin films in comparison with AlGaAs and AlGaN. Reproduced with permission from Jinno *et al.*, Sci. Adv. 7, eabd5891 (2021). Copyright 2021 AAAS; licensed under a Creative Commons Attribution (CC BY) license. (Ref. 199).

Kranert *et al.*²³¹ report similar findings for the lattice parameters with the changing Al content in polycrystalline samples of β -(Al_xGa_{1-x})₂O₃ thin films grown by PLD as well as their Raman active phonon modes. The composition dependent lattice constants were reported to be $a = (12.21 - 0.42x)$ Å, $b = (3.04 - 0.13x)$ Å, and $c = (2.81 - 0.17x)$ Å using a composition gradient method.²³¹ All three parameters followed similar trends to those reported by Krueger *et al.*²³⁰ While Raman modes have been observed, it should be noted that there has been no thorough study on the phonon modes of AlGaO or any reports on the IR phonon modes of β or α AlGaO. Kranert observed 7 A_g and 4 B_g Raman modes experimentally. The modes observed appear to be small and not very strong. This is partly due to the lack of high quality materials needed to accurately study the Raman modes. Also, the assignment of modes was done *ad hoc* as no polarization rules were investigated. The Raman shifts with changing Al content allow for the determination of the Al composition from the Raman spectrum.²³¹ Wang *et al.* (Ref. 232) report Raman peaks in (AlGa)₂O₃ thin films as well as the effect of growth temperature onto specific Raman peaks.²³²

Like other semiconductor materials, (AlGa)₂O₃ thin film properties are altered with substrate growth temperature. Epitaxial samples of (AlGa)₂O₃ grown with a substrate temperature of 500–550 °C are shown to have their crystal structure altered to differ from the β -Ga₂O₃ structure. If the substrate temperature was increased above 600 °C, the Ga atoms were shown to evaporate, resulting in no film growth.²³³ This implies that understanding the effects of substrate temperature with the Al concentration is important to (AlGa)₂O₃ film growth. The growth process for the (AlGa)₂O₃ films involved using a KrF laser source PLD. Films were grown onto (0001) sapphire substrates. A frequency of 2 Hz was used for the pulsed laser with a 30 mm distance between the substrate and target. The target was a 0.17 Al content target. High purity oxygen gas was present in the growth chamber due to the low chamber pressure (1×10^{-1} Pa). The sapphire substrate underwent various temperature changes ranging from 300 to 600 °C.²³² Wang *et al.* (Ref. 232) report that increasing substrate temperature in PLD reduces the growth rate for (AlGa)₂O₃ as well as changes the surface morphology. A temperature increase from 300 to 400 °C results in a small growth rate decrease while surpassing 500 °C substrate temperature drastically reduces growth rate. For substrate temperatures above 350 °C, grain structures are observed on the surface with larger grain features being observed as temperatures reach 400–450 °C. Samples grown at 300 °C substrate temperature show a smooth surface morphology. Bandgap is also altered by substrate temperature. (AlGa)₂O₃ films grown on substrates with a temperature of 400 °C have a larger optical bandgap compared to samples with substrate temperature of 300 °C due to an increase in the Al content at higher temperatures. At 450 °C substrate temperature, the optical gap decreases with decreasing the transition tail. With any temperature increase beyond this point, the bandgap is shown to increase with increasing temperature. Again, this stems from the increased Al content that arises from a difference in vapor pressure of the Al and Ga species as the substrate temperature is increased.²³⁴ This behavior is analogous to other systems such as MgZnO, which has been shown to have the same behavior with increased substrate temperature.²³⁴

A study published by Jinno *et al.* (Ref. 199) in 2020 described how the substrate orientation used for α -(Al_xGa_{1-x})₂O₃ growth improved the MBE growth of the alloy. The orientation of the substrate crystal plays a role in determining the crystal phases of the

UWBG material being epitaxially grown. Reports of (Al_xGa_{1-x})₂O₃ being grown on *c*-plane sapphire have shown the formation of the β -phase in the epitaxial layers. The *c*-plane acts as a catalyst for this formation as the epitaxial layers transition from the α -phase to the β -phase.¹⁹⁹ STEM revealed that when grown on *c*-plane sapphire, a three monolayer thick α -Ga₂O₃ formed followed by the transition to the beta phase.²³⁵ Kracht *et al.* (Ref. 236) observed epitaxial growth on *r*-plane sapphire. The initial epitaxial growth was shown to be α -Ga₂O₃. *c*-plane facets were observed following the initial α -phase growth that resulted in the growth of β -phase similar to the *c*-plane sapphire growth.²³⁶ By switching to the *m*-plane of sapphire, perpendicular to the *c*-plane, the transition to the β -phase is restricted. This allows for epitaxial growth of higher bandgap AlGO ranging from 5.4 to 8.6 eV, making α -(Al_xGa_{1-x})₂O₃ a better UWBG material than nitride alloys.¹⁹⁹ Epitaxial growth on *m*-plane sapphire was shown to allow for phase stabilization across the full alloy composition range. This allows for changing the bandgap as high as 8.6 eV.¹⁹⁹

In one of the most recent literature works on α -(Al_xGa_{1-x})₂O₃, Hilfiker *et al.* (Ref. 228) reported on the anisotropy of the high-frequency dielectric constants with changing Al compositions. Using the best match Cauchy model, Fig. 14 shows $\varepsilon_{\infty,\perp}$ and $\varepsilon_{\infty,\parallel}$ as the Al composition is changing. A bowing parameter b_j is defined from the following equation:

$$\varepsilon_{\infty,j}[x] = (1 - x)\varepsilon_{\infty,j}[0] + x\varepsilon_{\infty,j}[1] - b_j x(1 - x). \quad (5)$$

The perpendicular/ordinary direction has a larger bowing parameter than the parallel/extraordinary direction, 0.386 and 0.307, respectively. The bowing parameters and anisotropic high-frequency dielectric constants reported here will further research into how the Al composition affects bandgap shifting in α -(Al_xGa_{1-x})₂O₃.

2. Indium gallium oxide (In_xGa_{1-x})₂O₃

Indium gallium oxide (In_xGa_{1-x})₂O₃ sometimes labeled InGO is another alloy that has gained attention in the literature for gallium

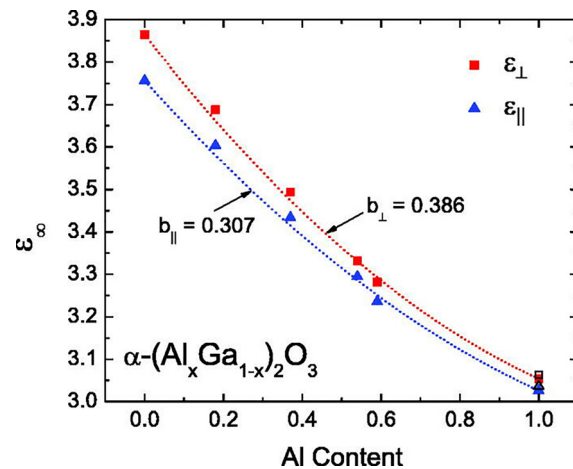


FIG. 14. $\varepsilon_{\infty,\perp}$ (red squares) and $\varepsilon_{\infty,\parallel}$ (blue triangles) for α -(Al_xGa_{1-x})₂O₃ as determined from the Cauchy dispersion extrapolation. Short dashed lines indicate the best fit to Eq. (5) with associated bowing parameter b . Black square and triangle indicate $\varepsilon_{\infty,\perp}$ and $\varepsilon_{\infty,\parallel}$ for the *m*-plane sapphire substrate, respectively. Reproduced with permission from Hilfiker *et al.*, Appl. Phys. Lett. 119, 092103 (2021). Copyright 2021 AIP Publishing LLC (Ref. 228).

oxide alloys. Contrary to AlGO, gallium oxide is here alloyed with a parent material whose bandgap is smaller than its own. Indium oxide has a bandgap of around 3.6 eV.²³⁷ Using indium lowers the bandgap for $(In_xGa_{1-x})_2O_3$ to be used in deep-ultraviolet phototransistors²³⁸ and UV photodetectors,²³⁹ for example. This is not possible with AlGaO as there is a large gap between the solar spectrum edge and detector cutoff energy.²⁴⁰ InGaO films have been grown and fabricated using different methods across the literature, including PLD,²⁴¹ co-sputtering of amorphous thin films,²³⁸ and ALD.²⁴²

Kraner *et al.* (Ref. 240) studied lattice constants and Raman peaks in β -phase $(In_xGa_{1-x})_2O_3$ thin films grown by PLD using the composition spread method. They reported the lattice constants using Vegard's law as $a = 12.295 + 1.43x$, $b = 3.035 + 0.35x$, $c = 5.795 + 0.39x$ with x being the indium content. These parameters are shown to increase by 1%–2% as the indium content is increased. Once a critical point in the indium content was reached in their process, a high-pressure InGaO₃ phase was detected. The slopes with composition x for eight Raman modes were identified. The eight Raman modes were reported consisting of six with A_g symmetry, one with B_g symmetry, and one with A_g/B_g symmetry.²⁴⁰ Their finding also show that the increasing indium content causes a significant change in the lattice parameters. The strain that the β -($In_xGa_{1-x})_2O_3$ films experience, which to first order approximation is proportional to the changes seen in the lattice parameters, is large and shows there must be a substantial amount of strain from epitaxial growth of $(In_xGa_{1-x})_2O_3$. This large amount of strain seen in the growth of $(In_xGa_{1-x})_2O_3$ is similar to both the β and α -phases of AlGO.

Liu *et al.* (Ref. 243) used first principles calculations to derive the bandgap for β -($In_xGa_{1-x})_2O_3$ from DFT studies with a scissor operator.²⁴³ The band structure of β -($In_xGa_{1-x})_2O_3$ is similar to β -Ga₂O₃. The conduction band minimum is located at the Γ point in both materials. The valence band maximum is shown to be off the Γ point for both materials in the Γ -Y direction. When the indium content was altered in the β -($In_xGa_{1-x})_2O_3$ alloy, the location of the indirect band does not change its location in the Brillouin zone. With 3.125% indium content, the alloy contains a band dispersion similar to β -Ga₂O₃, further confirming the indirect bandgap calculations. The bandgap was 4.769 eV, compared to the accepted value of around 4.8 to 4.9 eV for β -Ga₂O₃. Increasing the indium content up to 18.75% shows the valence band maximum still occurring off the Γ point in the Y direction. Along with the consistent location of the valence band maximum, both the indirect and direct bandgaps show linear decrease with an increase in the indium content.²⁴³ The bandgap decrease also allows for β -($In_xGa_{1-x})_2O_3$ to be considered for deep UV photodetector devices as the wavelength increases from around 256 to 280 nm.²⁴³ When the indium content is raised above 20%, the undesirable possibility of phase separation arises.^{244,245}

3. Aluminum indium gallium oxide—($Al_xIn_yGa_{1-x-y})_2O_3$

Aluminum indium gallium oxide ($Al_xIn_yGa_{1-x-y})_2O_3$) is another complex alloy that has begun appearing across literature. By incorporating combinations of both Indium and Aluminum atoms into β -Ga₂O₃ compounds, quaternary alloys can be achieved.²⁴⁶ This process has been shown in the III-nitride alloys InGaAlN.²⁴⁷ Due to the large number of atoms in the unit cell for the oxides compared, for example, with the nitrides, very large supercells must be constructed for computation of quaternary alloy band structures. For example, β -Ga₂O₃ has 32 Ga atoms and 48 O atoms when a $1 \times 2 \times 2$ supercell is

constructed, where then one Ga atom can be replaced by one Al or In atom. Due to multiple possible lattice sites, different type of atomic ordering can be conceived and larger supercells are then required. Then also effects of uniformly cation distribution vs cation clustering can be investigated, for example.²⁴⁷ As of date of writing, no such investigations have been reported for β -($Al_xIn_yGa_{1-x-y})_2O_3$.

Liu and Tan (Ref. 246) used first principles DFT calculations with GGA-PBE exchange correlation functionals to investigate the electronic properties of quaternary β -($Al_xIn_yGa_{1-x-y})_2O_3$ alloys. Lie and Tan's calculations predict the quaternary alloys to possess indirect bandgap energies for both Al-content x and In-content y from 0% to 18.75% with bandgap energy ranging from 5.171 to 4.432 eV. The authors also report isotropic electron effective masses parameters, which reduce with increasing In-content and increase with increasing Al-content. In addition, the authors discuss the lattice parameters of the quaternary alloys and lattice-matching conditions for β -($Al_xIn_yGa_{1-x-y})_2O_3/\beta$ -Ga₂O₃ growth. The authors point out the possibility to tune bandgap energy, effective mass, and lattice parameters upon alloying with Al and In, but also caution to presume parallel behaviors with the wurtzite structure quaternary system (Al,Ga,In)N because the thermodynamically stable binary phases Al₂O₃ (rhombohedral corundum structure) and In₂O₃ (cubic bixbyite structure) each have phases differing from Ga₂O₃ (monoclinic).

4. Zinc gallium oxide—(ZnGa₂O₄)

Zinc gallium oxide or zinc gallate (ZnGa₂O₄) appeared in the literature in the early 1990s and has since been used in optoelectronic applications such as vacuum fluorescence displays, ultraviolet photodetectors, and low-voltage field-emission devices.^{248–250} Omata *et al.* (Ref. 251) were studying and looking for a new ultraviolet electroconductive oxide. The basis for the study revolved around materials having a spinel structure with a $M^{2+}M_2^{3+}O_4$ composition alongside a cation with the electronic configuration $d^{10}s^0$. Other materials of this composition such as MgIn₂O₄ and CdGa₂O₄ have been reported previously.^{252,253} However, these materials possessed bandgap energies of around 3.5 eV and were not transparent in the ultraviolet region. A wider bandgap energy along with transparency in the ultraviolet region was desired. The ZnO-Ga₂O₃ system provided an electronic conductor that meets those requirements. The structure of ZnGa₂O₄ contains a double oxide along with a spinel structure. Samples of ZnGa₂O₄ were synthesized from ZnO and Ga₂O₃. The samples were polycrystalline in nature with x-ray powder diffraction confirming the spinel structure. Diffusion reflectance spectra yielded a bandgap energy of almost 5 eV noting that this energy gap is larger than ZnO even though both materials exhibit the Zn²⁺ cation.²⁵¹

As technology progressed from the early 1990s, the growth capabilities and the research conducted on ultraviolet semiconductors increased. In 2017, Horng *et al.* (Ref. 255) published work on the epitaxial growth of ZnGa₂O₄. According to Horng *et al.*, previous literature showed mainly polycrystalline growth of ZnGa₂O₄ similar to that found by Omata *et al.* (Ref. 251). This shows that the growth of single-crystalline films is difficult given the high congruent melting temperature and immiscibility of the ZnO-Ga₂O₃ system. Samples where grown on *c*-plane sapphire using MOCVD. The MOCVD process utilized varying flow rates of diethylzinc (DEZn) during growth which heavily altered the crystal formation. It was shown that films grown with a DEZn flow rate of 10 sccm formed a single-crystalline β -Ga₂O₃

phase orientated along $(\bar{2}01)$. When the flow rate was increased to 30–60 sccm the resultant growth was (111)-orientated single-crystalline films of the ZnGa_2O_4 phase. Samples grown with the low DEZn flow rate and resultant $\beta\text{-Ga}_2\text{O}_3$ phase had poor electrical properties when compared to the samples grown with a higher DEZn flow rate. ZnGa_2O_4 films prepared with a flow rate of 30 sccm exhibited the highest electron mobility of $5.6 \text{ cm}^2/(\text{V s})$. Increasing the flow rate up to 60 sccm, the mobility decreased to $1.4 \text{ cm}^2/(\text{V s})$. This decrease in mobility can be explained as a result of larger lattice distortions that occur at the higher flow rates. A luminescence peak occurring at 236 nm is a possible result of the electrons transitioning up to the conduction band yielding a bandgap energy of 5.25 eV.²⁵⁵ This value is close to the theoretical value of 5.2 eV.²⁵⁵ CL spectra also showed a weak luminescence peak at 499 nm in all sampled films yielding an energy transition of 2.48 eV. However when ZnGa_2O_4 forms after the incorporation of Zn into Ga_2O_3 , it creates a donor–acceptor pair transition that causes the green emission band seen at 499 nm to be suppressed.²⁵⁵ In all epilayers there also exists a peak at 332 nm corresponding to a transition energy of 3.73 eV. This peak is a result of the radiative carrier transition that occurs between the donor level and the valence band. The two peaks that occur at 236 and 332 nm suggest ZnGa_2O_4 films may have a large potential in short-wavelength applications.²⁵⁵

A few years later in 2019, Galazka *et al.* (Ref. 254) successfully grew high quality bulk single crystals of ZnGa_2O_4 from the melt. Two methods, including the vertical gradient freeze (VGF) and CZ growth method, were utilized to achieve the bulk single crystals. XRD measurements showed a cubic crystal structure for ZnGa_2O_4 belonging to space group $Fd\bar{3}m$ (#227). The Zn^{2+} cations occupy the tetrahedral lattice sites while the Ga_3^+ cations occupy the octahedral sites. A cubic lattice constant of 8.3342 \AA was reported.²⁵⁶ The lattice constant and cubic symmetry make ZnGa_2O_4 a possible substrate for iron based magnetic spinel films due to the high lattice matching.²⁵⁴ High quality crystals of Galazka *et al.* were conductive and possessed a high Hall mobility of $107 \text{ cm}^2/(\text{V s})$. The growth conditions and material starting composition dictated whether the single crystal ZnGa_2O_4 were electrically insulating or an n-type semiconductor. Annealing the semiconducting crystals in the presence of oxygen at temperatures above 700° for multiple hours resulted in the switch to an electrically insulating crystal. Absorption coefficient measurements allowed for the estimation of the direct and indirect bandgap energies, 4.59 and 4.33 eV , respectively.²⁵⁴ Comparisons of ZnGa_2O_4 to $\beta\text{-Ga}_2\text{O}_3$ were also a focal point of the work of Galazka *et al.* and are highlighted in Table X.

Phonon modes for ZnGa_2O_4 have recently been reported by Stokey *et al.* (Ref. 257) for high-quality melt grown single bulk crystals. The primitive cell of ZnGa_2O_4 contains 14 atoms resulting in 42 phonon modes shown by the irreducible representation:

$$\Gamma_{opt} = \text{A}_{1g} + 2\text{A}_{2u} + 2\text{E}_u + \text{E}_g + 4\text{T}_{1u} + 2\text{T}_{2u} + \text{T}_{1g} + 3\text{T}_{2g}.$$

The static and high frequency dielectric constants have also been determined. The LST relationship was utilized to produce a value of 10.5 ± 0.06 for the static dielectric constant (ϵ_{DC}). The high frequency constant (ϵ_∞) was determined to be 3.78 ± 0.02 using fitting parameters from ellipsometric analysis. RF capacitance measurements resulted in a extracted experimental static dielectric value of 11.3 ± 0.7 , in decent agreement with the calculated LST value. It was shown that the ratio of ϵ_{DC} to ϵ_∞ for spinel ZnGa_2O_4 was similar to the ratio in $\beta\text{-Ga}_2\text{O}_3$.²⁵⁷ With ϵ_{DC} being similar between ZnGa_2O_4 and

TABLE X. Comparisons of ZnGa_2O_4 to $\beta\text{-Ga}_2\text{O}_3$ bulk single crystals grown from the melt. Table of values reproduced from Galazka *et al.* (Ref. 254).

	ZnGa_2O_4	$\beta\text{-Ga}_2\text{O}_3$
Growth method	VGF, CZ	CZ
Growth status	Beginnings of expt. development	Advanced development
Max volume (cm^3)	8	160
Melting point ($^\circ\text{C}$)	1900	1800
Symmetry	Cubic	Monoclinic
Polishing, slicing	Easy	Difficult
Best cleavage plane(s)	N/A	{100} and {001}
	4.570 dir.	4.56 [001] dir.
Bandgap energy (eV)	4.325 ind.	4.59 [100] dir. 4.85 [010] dir.
	$n = 3 \times 10^{18}$ $-9 \times 10^{19} \text{ cm}^{-3}$	$n = 5 \times 10^{16}$ $-2 \times 10^{18} \text{ cm}^{-3}$
UID elect. properties	$\mu = 40\text{--}100 \text{ cm}^2/(\text{V s})$ $\rho = 1\text{--}0.002 \Omega \text{ cm}$	$\mu = 100\text{--}150 \text{ cm}^2/(\text{V s})$ $\rho = 1\text{--}0.04 \Omega \text{ cm}$
Max carrier conc. (cm^{-3})	10^{20} UID	10^{19} Si or Sn doped ^a
RT thermal cond. [$\text{W}/(\text{mK})$]	22.1	Along [100] ¹¹ Along [010] ²⁹ Along [001] ²¹

^aMax carrier conc. considered to be 10^{20} (Ref. 157), see Subsection II E.

$\beta\text{-Ga}_2\text{O}_3$, it can be hypothesized that the phonon scattering limitations of the intrinsic free charge mobility are also similar between the two materials.¹⁵⁵ With dielectric constants so similar to $\beta\text{-Ga}_2\text{O}_3$ as well as the isotropic lattice structure of spinel ZnGa_2O_4 , there is potential for ZnGa_2O_4 to be applicable as material in high power devices.²⁵⁷ Hilfiker *et al.* (Ref. 258) determined the band-to-band transition energy, the exciton properties, and the dielectric constants of zinc gallate in a combined ellipsometry and DFT study. The material is predicted to be indirect. The authors find an isotropic effective mass parameter ($0.24 m_e$) at the bottom of the Γ -point conduction band, which equals the lowest valence band effective mass parameter at the top of the highly anisotropic and degenerate valence band ($0.24 m_e$). A Wannier–Mott type exciton with an effective Rydberg energy of 14.8 meV was obtained with bandgap energy of $5.27(3) \text{ eV}$. Similar to monoclinic gallium oxide, the valence band top is mostly composed of oxygen $2p$ orbitals and low hole mobility is anticipated (Fig. 15).

H. Summary of $\beta\text{-Ga}_2\text{O}_3$ property values

Tables XI and XII highlight a summary of the properties reviewed for $\beta\text{-Ga}_2\text{O}_3$. Values for each of the properties are presented along with references and notation of whether they are experimental or calculated findings, where relevant anisotropy is denoted. Currently $\beta\text{-Ga}_2\text{O}_3$ is one of the most widely researched materials in the

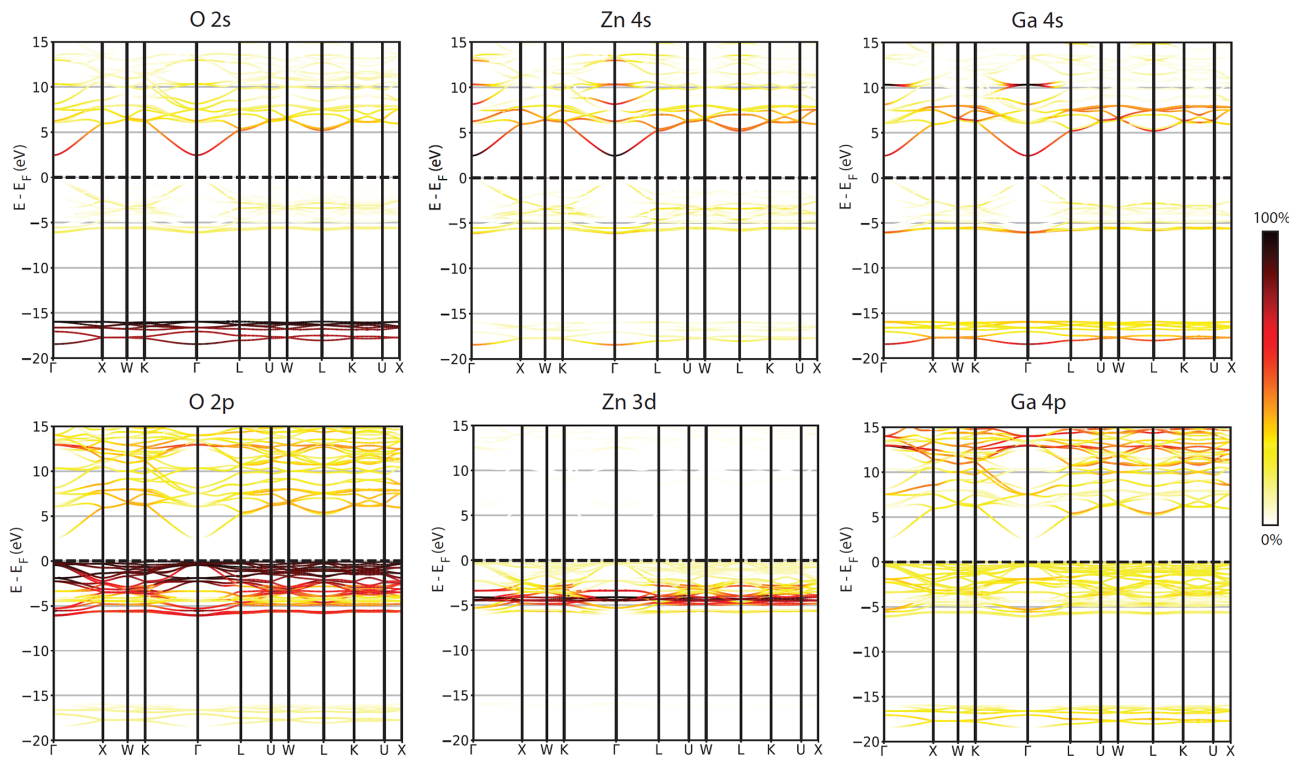


FIG. 15. Color-plot density distributions of 2s-O and 2p-O, 4s-Zn and 3d-Zn, and 4s-Ga and 4p-Ga admixture to DFT/GGA computed valence and conduction bands in zinc gallate. Reproduced with permission from Hilfiker *et al.*, Appl. Phys. Lett. **118**, 132102 (2021). Copyright 2021 AIP Publishing LLC (Ref. 264).

literature. While this review focuses on material properties, it is also important to recognize the rapid advancements in the field of β -Ga₂O₃ power electronic devices^{259–262} due in part to the exceptional material research highlighted throughout Sec. II as well as the active research in device packaging and thermal management to overcome the low thermal conductivity of β -Ga₂O₃.^{263,264}

III. ALUMINUM OXIDE

Aluminum oxide or alumina (Al₂O₃) is an ultrawide bandgap material often used in ceramic applications.^{268–270} With a bulk crystal bandgap of around 9 eV,²⁷¹ and very good thermal properties such as a relatively high thermal conductivity,²⁷² relative to other oxides highlighted in this review. Al₂O₃ has gained interest in device applications as an insulating substrate in its crystalline form or a gate oxide where it is typically amorphous. While single crystals can be grown using a variety of methods,²⁷³ ALD has been heavily researched for thin film growth.²⁷⁴ Even though Al₂O₃ differs from the other oxides reviewed in the sense that is not regarded as a semiconducting oxide, an understanding of its crystal structure as well as its electronic band structure and subsequent properties are useful for device engineering and as a baseline comparison with the rest of the materials presented here, particularly where other oxides such as Ga₂O₃ can readily form alloys with Al₂O₃. Al₂O₃ has been studied and reviewed heavily from a commercial and manufacturing standpoint as evidenced by Abyzov (Ref. 275). However, this section differs from a manufacturing review as it focuses on the properties of Al₂O₃ bulk crystals and thin films relevant for electronic device applications.

A. Crystal structure

Aluminum oxide has many phases, all of which are metastable with the exception of the stable corundum phase α -Al₂O₃.²⁶⁵ The metastable phases include γ , η , θ , δ , κ , and χ . Of the six metastable polymorphs, four of them (γ , η , θ , δ) have a face-centered cubic oxygen anion arrangement while κ , χ , and the stable α phases have a hexagonal oxygen anion arrangement. With the polymorphs being divided as such, it is the distribution of the cations that distinguish each phase. There is additional evidence to support the existence of three other phases consisting of θ' , θ'' , and λ .²⁶⁵ Table XIII shows reported lattice constants and crystal structures for the metastable and stable Al₂O₃ polymorphs.

There is some disparity of the nomenclature within the literature about the precise crystal structure of α -Al₂O₃. However, the lattice parameters do not appear to be affected by this disparity as they are in relatively good agreement throughout the literature. Levin *et al.* (Ref. 265) report that α -Al₂O₃ contains trigonal symmetry along with rhombohedral Bravais centering. This reported structure belongs to space group $R\bar{3}c$ (#167) with 10 atoms within the unit cell.^{265,285} The reported lattice constants are considered to be hexagonal parameters with $a = 4.75 \text{ \AA}$ and $c = 12.97 \text{ \AA}$.²⁷⁶ The oxygen anions reside in Wyckoff spots within the hexagonal description.²⁶⁵ Ching *et al.* (Ref. 284) report a corundum structure for α -phase which has a rhombohedral or trigonal unit cell. The unit cell contains two Al₂O₃ molecules and belongs to the space group $R\bar{3}c$ (#167). At the same time, the corundum structure can also be considered a hexagonal cell with six Al₂O₃ molecules.

The lattice parameters for the hexagonal cell at room temperature are $a = 4.762 \text{ \AA}$ and $c = 12.896 \text{ \AA}$. Figure 16 shows a schematic of the

TABLE XI. Summary of theoretical and experimental structural and thermal properties of $\beta\text{-Ga}_2\text{O}_3$. Common names of gallium oxide, gallium sesquioxide, and gallia.

Stable phase	$\beta\text{-Ga}_2\text{O}_3$	Ref. 265
Stable structure	Monoclinic	$C2/m$ (#12)
	$a = 12.214$	Ref. 32
	$b = 3.037$	
	$c = 5.998$	
	$\beta = 103.83^\circ$	
	$a = 12.27$	Ref. 33
	$b = 3.04$	
	$c = 5.80$	
	$\beta = 103.7^\circ$	
Metastable phases	$\alpha, \gamma, \varepsilon, \delta^{\text{a}}, \kappa^{\text{b}}$	
Density (g/cm ³)	5.88–5.95	Expt. ^{115,266}
Bulk modulus (GPa)	174	Calc. ¹⁹
	184–255	Expt. ^{112,113}
T _m (°C)	1725–1795	Expt. ^{115,117}
Debye temp. (K)	738	Expt. ⁵⁵
	872	Calc. ³³
Specific heat (J/(gK))	0.47–0.56	Expt. ^{41,55,115,117}
Thermal cond. (W/(mK))	15 (a^*)	Expt. ⁴¹
	28 (b)	Expt. ⁴¹
	18 (c^*)	Expt. ⁴¹
	10.9–13.6 [100]	Expt. ^{39,115}
	22.8 [010]	Expt. ¹¹⁵
	14.7 [001]	Expt. ³⁹
	13.3 [-201]	Expt. ³⁹
	27.0 [110]	Expt. ³⁹
Thermal diff. (mm ² /s)	5.23 (a^*)	Expt. ⁴¹
	9.76 (b)	Expt. ⁴¹
	6.26 (c^*)	Ref. 41
CTE ($\times 10^{-6}/\text{K}$)	4.7–5.3 [100]	Expt. ^{41,115}
	5.45–8.9 [010]	Expt. ^{41,115}
	5.35–8.2 [001]	Expt. ^{41,115}
	1.54 [100]	Calc. ⁴⁵
	3.37 [010]	Calc. ⁴⁵
	3.15 [100]	Calc. ⁴⁵

^aNanocrystalline form of ε phase.^bSubgroup of ε phase.

crystal structure for $\alpha\text{-Al}_2\text{O}_3$. When the temperature is increased to 2000 °C the lattice parameters increase by 1.83% and 1.86% for a and c respectively.^{284,286} The trigonal unit cell has a parameter $a = 5.128 \text{ \AA}$ at room temperature that increases by 1.35% at 2000 °C.^{277,284,286} Shirai *et al.* (Ref. 287) also detail the corundum structure of $\alpha\text{-Al}_2\text{O}_3$ that contains alternating A and B planes of packed oxygen atoms.²⁸⁷ Stoichiometrically, there must be two Al³⁺ ions for every three O²⁻ ions due to the +3 valence of aluminum and the -2 valence of oxygen resulting in 2/3 occupancy of the octahedral sites by aluminum cations. Because of the 2/3 occupancy, the aluminum cation layers form an A-B-C stacking pattern that exists between the A-B-A-B stacked oxygen planes.²⁸⁷

TABLE XII. Summary of theoretical and experimental electrical and optical properties of $\beta\text{-Ga}_2\text{O}_3$.

Electron affinity (eV)	4.00 ± 0.05	Expt. ¹⁴⁶
Breakdown field (MV/cm)	8.0	Pred. ¹⁴⁷
m_e^*	$m_a^* 0.288$	Expt. ⁴²
	$m_b^* 0.283$	Expt. ⁴²
	$m_c^* 0.286$	Expt. ⁴²
	$m_d^* 0.224–0.41$	Calc. ^{42,86}
	$m_b^* 0.301–0.41$	Calc. ^{42,86}
	$m_c^* 0.291–0.37$	Calc. ^{42,86}
m_h^*	$m_a^* 1.769$	Calc. ⁸⁶
	$m_c^* 0.409$	Calc. ⁸⁶
μ_e [cm ² /(V s)]	220–300	Calc. ^{147,155}
	112–176	Expt. ^{57,76,95,267}
Gap type	Direct	Ref. 66
E_g (eV)	2.19–2.36	Bulk calc. ^{82,83}
	4.37–5.04 ^a	Bulk calc. ^{19,33,66,85,86}
	5.04–5.15 E _c	Bulk expt. ^{86,94}
	5.37–5.40 E _a	Bulk expt. ^{86,94}
	5.64–5.68 E _b	Bulk expt. ^{86,94}
	5.341 E _c	Bulk calc. ⁹⁴
	4.969–5.581 E _a	Bulk calc. ^{86,94}
	5.35–5.911 E _b	Bulk calc. ^{86,94}
	4.72–5.40	Film expt. ^{77,97–99,101,102}
ϵ_0	10.9 ϵ_a	Expt. ⁴⁴
	10.8 ϵ_{a*}	Expt. ⁴⁴
	11.2 ϵ_b	Expt. ⁴⁴
	12.6 ϵ_c	Expt. ⁴⁴
	12.7 ϵ_{c*}	Expt. ⁴⁴
	10.19 ϵ_a	Expt. ¹⁴⁴
	10.05 ϵ_{a*}	Expt. ¹⁴⁴
	10.6 ϵ_b	Expt. ¹⁴⁴
	12.4 ϵ_c	Expt. ¹⁴⁴
	12.27 ϵ_{c*}	Expt. ¹⁴⁴
ϵ_∞	3.89 ϵ_a	Expt. ⁴⁴
	3.87 ϵ_b	Expt. ⁴⁴
	2.9 ϵ_{c*}	Expt. ⁴⁴
	3.85 ϵ_a	Calc. ¹³²
	3.81 ϵ_b	Calc. ¹³²
	4.08 ϵ_{c*}	Calc. ¹³²
Phonon modes		
IR active	4A _u , 8B _u	Ref. 44
Raman active	10A _g , 5B _g	Refs. 112 and 135

^aIncludes both indirect and direct gap.

The metastable phase of $\delta\text{-Al}_2\text{O}_3$ has been described as a tetragonal structure cell consisting of lattice parameters $a_0 = 7.96 \text{ \AA}$ and $c_0 = 11.70 \text{ \AA}$ according to XRD data.²⁸⁸ Levin *et al.* (Ref. 265) further complicate matters by referencing works that support either a

TABLE XIII. Al_2O_3 polymorphs and crystal structure with associated lattice constants. All reported values below were determined using experimental methods.

Phase	Structure	Space group	Lattice (\AA)
α	Trigonal ^a	$R\bar{3}c$ (#167)	$a = 4.75$ ^{265,276} $c = 12.97$
	Hexagonal	$R\bar{3}c$ (#167)	$a = 4.762$ ²⁷⁷ $c = 12.896$ $a^b = 5.128$ ²⁷⁷
δ	Tetragonal	$P\bar{4}m2$ (#115)	$a = 5.599$ ²⁷⁸ $c = 23.657$
	Orthorhombic	$P2_12_12_1$ (#19)	$a = 16.4$ ²⁷⁹ $b = 12.2$ $c = 8.2$ $a \approx a_\gamma$ ^{265,c} $b \approx 2a_\gamma$ $c \approx 1.5a_\gamma$
η	Cubic	$Fd\bar{3}m$ (#227)	$a_\gamma \approx 7.9$ ²⁶⁵ $a = 7.94$ ²⁸⁰
γ	Cubic	$Fd\bar{3}m$ (#227)	$a_\gamma \approx 7.9$ ²⁶⁵
κ	Orthorhombic	$Pna2_1$ (#33)	$a = 4.6$ ^{265,281} $b = 8.18$ $c = 8.87$
χ	Hexagonal	$P6_3/mcm$ (#193)	$a = 5.56$ ²⁶⁵ $c = 13.44$ $a = 5.57$ ²⁸² $c = 8.64$
	Cubic ^d		$a = 7.94$ ²⁸⁰
θ	Monoclinic	$C2/m$ (#12)	$a = 11.813$ ²⁸³ $b = 2.906$ $c = 5.625$ $\beta = 104.1^\circ$ $a = 11.795$ ²⁷⁸ $b = 2.91$ $c = 5.6212$ $\beta = 103.79^\circ$

^aTrigonal symmetry with hexagonal parameters.^{265,276}

^bTrigonal unit cell parameter within the hexagonal lattice.^{277,284}

^c $a_\gamma \approx 7.9 \text{ \AA}$.²⁶⁵

^dNon-spinel cubic.²⁸⁰

tetragonal or orthorhombic structure with conflicting lattice parameters. Jayaram *et al.* (Ref. 279) conclude that the δ -phase is an orthorhombic structure belonging to space group $P2_12_12_1$ (#19). $P2_12_12$ (#18) has also been considered as a possible space group; both proposals were based on convergent beam electron diffraction.²⁷⁹ Both the tetragonal and orthorhombic structures are included in Table XIII as there appears to be no concrete resolution on the crystal structure. Levin *et al.* (Ref. 289) state that when the tetragonal δ phase was observed, it originated from the mineral boehmite (AlOOH). The

orthorhombic δ phase was seen when a precursor phase was thermally oxidized or the melt was quenched.²⁸⁹

Both γ and η - Al_2O_3 are considered to be a cubic spinel crystal structure with practically identical parameters.^{265,289} They both share the space group $Fd\bar{3}m$ (#227) and Levin *et al.* (Ref. 265) state the lattice parameter $a = a_\gamma \approx 7.9 \text{ \AA}$.²⁶⁵ There are also reports that γ - Al_2O_3 can have a tetragonal structure when derived from boehmite.^{290,291} Stumpf *et al.* (Ref. 280) report that the lattice constant for cubic η -phase is $a = 7.94 \text{ \AA}$,²⁸⁰ consistent with Levin *et al.* (Ref. 265). Even though these two metastable phases share identical crystal structure, space grouping, and a lattice parameter, they are still considered two distinct phases. This is a result of the chemical ordering within the cations of the fcc anion structure.²⁶⁵

Values for the bandgap energy of the metastable γ -phase have also been reported in the literature. The bandgap energy of bulk γ - Al_2O_3 was found to be 8.7 eV.^{292,293} Ealet (Ref. 294) reports the same value for bulk γ samples while the bandgap decreases to 2.5 eV for thin films. The explanation behind such a large bandgap decrease is reported to be similar to the α - Al_2O_3 decrease: defect levels located amongst the bandgap.²⁹⁴

κ - Al_2O_3 is an orthorhombic phase of alumina belonging to the space group $Pna2_1$ (#33).²⁸⁹ Originally thought to have hexagonal structure,^{282,295} it was confirmed to be orthorhombic by Liu *et al.* (Ref. 281). Within the unit cell there are 16 cations that are ordered both octahedrally and tetrahedrally.²⁶⁵ The space group was determined using convergent-beam electron diffraction.²⁸¹ Lattice constants for κ - Al_2O_3 are reported in Table XIII. Figure 17 shows a schematic of the crystal structure of κ - Al_2O_3 . The crystal structure of κ - Al_2O_3 was included as it is one of the most widely researched alumina polymorphs.

χ - Al_2O_3 is another phase with multiple possible crystal structures and parameters reported. The first suggested structure is a non-spinel cubic structure determined by XRD patterns. The lattice constant is approximated to be the same as the η -phase parameter of 7.94 \AA , reported by Stumpf (Ref. 280). No space group is reported for this suggested cubic structure. There are two reported possible hexagonal unit cells. The first belongs to space group $P6/m$ or $P6_3/mcm$ (#193) with

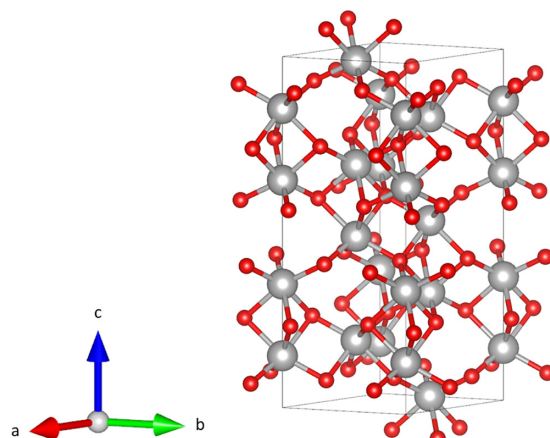


FIG. 16. α - Al_2O_3 crystal structure belonging to space group $R\bar{3}c$ (#167) with the c -axis oriented upward (gray = Al, red = O).

lattice constants $a = 5.56 \text{ \AA}$ and $c = 13.44 \text{ \AA}$.²⁶⁵ The second reported hexagonal structure has lattice constants $a = 5.57 \text{ \AA}$ and $c = 8.64 \text{ \AA}$ (Ref. 282) without a space group to be determined.

$\theta\text{-Al}_2\text{O}_3$ possess a monoclinic crystal structure belonging to the space group $C2/m$ (#12).^{278,283} Reported lattice constants and monoclinic angles for both calculated and experimental methods are listed in Table XIII. The lattice constants are in good agreement between calculated and experimental values.^{278,283,296}

There currently does not appear to be a large amount of interest in the metastable phases, unlike $\alpha\text{-Al}_2\text{O}_3$ (sapphire), which has been widely used as a substrate for devices. Possible explanations for a lack of research and interest into the metastable phases include difficulty of growing the metastable phases, scarcity and lack of sample availability, and poor growth quality. Unless stated otherwise, all discussion throughout this section refers to the stable, bulk single crystalline, α phase.

B. Growth

Bulk crystals and thin film samples of Al_2O_3 vary in their growth and fabrication process. The desired application for the grown oxide also influences the specific method of growth. The sapphire crystal, or $\alpha\text{-Al}_2\text{O}_3$, can be grown by many methods utilizing high temperature melt growth. The Verneuil process is a process from the 19th century²⁹⁷ that allows for growth and fabrication of small diameter sapphire crystals. These crystals are not ideal for electronic applications as they often have high dislocation densities. However, Verneuil sapphire can be utilized by other melt growth methods as the starting material.²⁷³ The Czochralski (CZ) method can be used for a very large number of oxide crystals. Once a common technique for sapphire growth from melt, it was pushed aside as it became difficult to grow large samples along the c -axis as well as larger diameter. Akselrod *et al.* (Ref. 273) states that as of 2012, the CZ method could re-emerge as a viable method of sapphire growth along the c -axis as a result of the promising findings seen using proprietary growth methods and improvements. At the time of publishing their work, Akselrod *et al.* said their results and improvements were being “closely held.” The

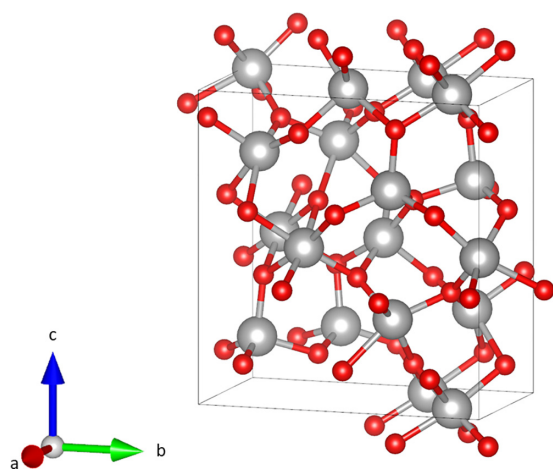


FIG. 17. $k\text{-Al}_2\text{O}_3$ crystal structure belonging to space group Pna_2_1 (#33) with the c -axis oriented upward (gray = Al, red = O).

heat exchange method (HEM) is another method that can be used for Al_2O_3 crystal growth. The reduction of the heating power can be used to control crystallization. The overall process can take multiple weeks if the desired crystal size is large. ARC Energy Corp. developed a modification called the Combined Heat Exchanger Solidification (CHES) that increases the wafer volume yield by allowing for c -axis crystal growth.²⁷³ EFG was originally designed for sapphire fiber growth that displayed high tensile strength for uses such as missile warheads and IR transmitting domes.²⁷³ The Stepanov EFG method has the ability to reduce sapphire machine and production costs by 50%. Common advantages of EFG sapphire growth are high linear pulling rates and small profile shapes. Disadvantages include layers of bubbles that must be removed using a grinding method as well as commonly having high dislocation densities.²⁷³

Thin film growth of Al_2O_3 has been utilized to produce dielectric films for a wide variety of device applications including Si and III-V semiconductors.^{298,299} Chemical vapor deposition (CVD) is commonly used for Al_2O_3 film growth. Maruyama *et al.* (Ref. 300) used atmospheric pressure CVD with aluminum acetylacetone pyrolysis, an inexpensive organometallic compound.³⁰⁰ Using the same organometallic compound, Kim *et al.* (Ref. 301) fabricated amorphous thin films. ALD is another common Al_2O_3 thin film growth method that is immensely researched,^{302–305} often used for depositing amorphous gate dielectrics. Examples of ALD growth are seen on GaAs,³⁰⁶ $\beta\text{-Ga}_2\text{O}_3$,^{307,308} 4H-SiC,³⁰⁹ as well as high field surface passivation in GaN and other materials.³¹⁰ ALD is a good choice for Al_2O_3 film growth due to the ability to use a wide range of precursors and efficient cycle times, as well as homogeneous coverage and precise control over film thickness. An optimal growth temperature of around 350 °C was observed for electronics applications desiring low impurities and high dielectric constants.³⁰⁴ Temperatures as low as 33 °C have also been shown to produce ALD grown Al_2O_3 with properties that are in comparison to those grown at higher temperatures, regarded as optimal.³¹¹ Of note, thin films grown at low temperatures exhibited low leakage currents, low surface roughness, and contained high dielectric constants. This is all contradictory to the presence of increased hydrogen concentrations and decreased densities found in films grown at low temperatures.³¹¹

C. Electronic band structure

As interest in $\alpha\text{-Al}_2\text{O}_3$ began to expand beyond ceramics and into electronic applications,^{312–315} the electronic band structure gained considerable attention. First principles calculations such as Orthogonalized Linear Combination of the Atomic Orbitals (OLCAO)²⁸⁴ as well as experimental methods have been utilized to better understand the electronic band structure of $\alpha\text{-Al}_2\text{O}_3$. Theoretically, the valence band maximum and conduction band minimum both occur at the Γ point of the Brillouin zone.²⁸⁵ The DFT and OLCAO method result in a lower than expected bandgap energy due to the local exchange potential being unable to negate the self-interaction within the Coulomb potential. The larger exchange parameters could be accounting for a greater cancellation of the self-interaction of the Coulomb potential, resulting in a more accurate bandgap energy.²⁸⁵ Electronic band structures determined from GGA-PBE Kohn-Sham³¹⁶ and tight-binding parameterization³¹⁷ can be seen in Fig. 18. From Figs. 18(a) and 18(b), Santos *et al.* (Ref. 316) describe the electronic structure of $\alpha\text{-Al}_2\text{O}_3$. The maximum of the

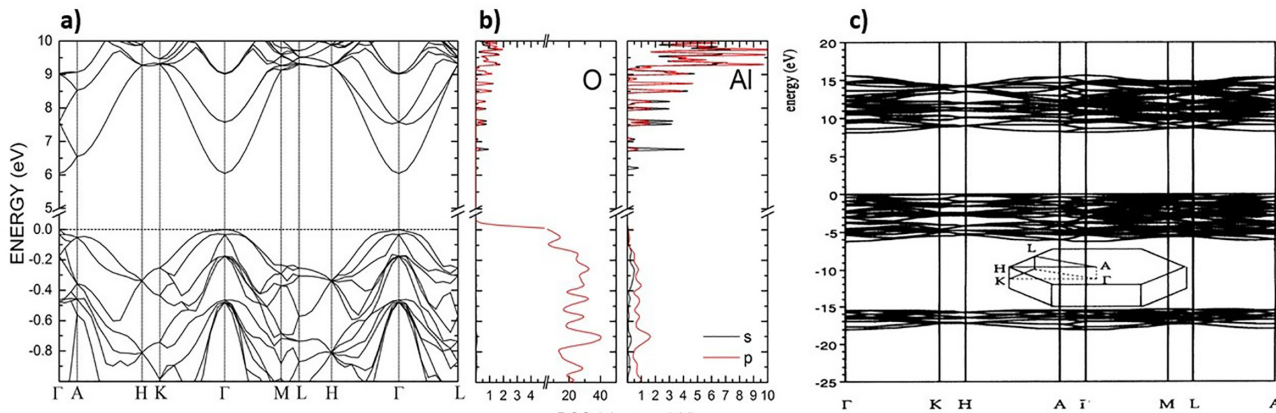


FIG. 18. (a) The GGA-PBE Kohn–Sham electronic band structure of α -Al₂O₃ (Ref. 316), (b) partial density of states located around the main bandgap (Ref. 316), and (c) electronic band structure determined using tight-binding parametrization. The high symmetry points are labeled for the Brillouin zone inset (Ref. 317). Reproduced with permission from Santos *et al.*, Chem. Phys. Lett. **637**, 172 (2015). Copyright 2015 Elsevier and Godin and LaFemina, Phys. Rev. B **49**, 7691 (1994). Copyright 1994 APS. Note the resolution of (c) is identical to that of the source.

valence band occurs at Γ with only a minor amount of band dispersion occurring everywhere except along Γ -A. This leads to large amounts of anisotropy of the effective hole mass. The large curvature and parabolic nature seen in the conduction band at Γ results in an isotropic electron effective mass. The density of states of the conduction band minimum is also quite small at around 1 electron/eV where the Al 3s states dominate, followed by O 2s states, and very small contributions from Al 3p. The secondary conduction band has a significantly larger DOS at around 6 electron/eV. Figure 18(c) shows a much older interpretation of the bandgap from Godin *et al.* produced from tight-binding parameterization. The curvature within the valence band is not as pronounced as in Fig. 18(a), but it is included to show the high-symmetry points.

One of the distinct features of the electronic band structure alongside the ultrawide bandgap is the grouping of bands shown in Fig. 18. The band structure of α -Al₂O₃ is shown to be separated into three groupings with the Al and O atomic orbitals contributing differently to each group throughout the structure. The lowest lying bands within the valence band are comprised mainly of s-type orbitals from oxygen atoms with some Al contribution. Going up in energy of the lowest band grouping, the amount of Al contribution will decrease. The next grouping of bands in the valence structure are comprised of both Al(3s) and O(2p) orbitals. Again, the Al contribution decreases with increasing energy of this band grouping. The uppermost grouping closest to the valence band maximum are almost entirely comprised of O(2p_x), O(2p_y), and O(2p_z) orbitals. Crossing the bandgap into the lower most conduction band consists of Al(3s) orbitals. The valence bands are also seen to be grouped into three distinct groupings in α -quartz with O and Si orbitals comprising the bands in a similar way to O and Al within α -Al₂O₃. The atomic bonding within α -Al₂O₃ is found to be heavily ionic, meaning the valence bands are not pulled as deep into the valence structure, unlike α -quartz which exhibits covalent bonding and very deep valence bands.²⁸⁵ It should be noted the comparison made by Batra (Ref. 285) between α -quartz and α -Al₂O₃ is not ideal. Although they are related to similar structures, there are differences in the stoichiometry and space grouping of α -quartz and α -Al₂O₃.

Ching *et al.* (Ref. 284) performed first principles calculations using OLCAO on corundum structure α -Al₂O₃. The uppermost valence bands appear flat resulting in a large effective hole mass. With a single band comprising the conduction band minimum, the effective mass of the electron was found to be around 0.4 m_e .²⁸⁴ More information and further studies on the effective mass of Al₂O₃ can be found in Sec. IIID3. The specifics of the electron band structure in regard to the O and Al orbitals is reported to be in good agreement with those previously determined by Batra (Ref. 285). The bonding of O and Al within the electronic structure is also found to be highly ionic from the calculated valence charge density. While both Batra (Ref. 285) and Ching *et al.* (Ref. 284) agree on the nature of the bonding within α -Al₂O₃, Xu *et al.* (Ref. 318) proposes potential covalent bonding.³¹⁸

French (Ref. 271) reported on the electronic structure of Al₂O₃ using pseudofunction band structure calculations. The orbital composition of the bands were found in good agreement with those mentioned previously in this subsection. The higher conduction bands are derived from Al(3p) anti-bonding orbitals and tend to have flatter bands compared to the lower most conduction band. The ionic nature of Al₂O₃ causes the upper valence band to be derived from the O 2p states, and the conduction band minimum derived from the Al 3s and 3p states.²⁷¹ The nature of the atomic bonding is found to be ionic and is supported by comparing the rather ionic α -Al₂O₃ to other covalent materials such as AlN and GaAs. An explanation for the previously proposed covalent bonding was hypothesized to be due to the hybridized Al-O bonding. The large area between the valence band groupings detailed by Batra (Ref. 285) is often called an ionicity gap that is lacking electronic states, providing further support of ionic bonding.²⁷¹

1. Bandgap energy

The bandgap values for Al₂O₃ and have been reported from theoretical and experimental investigations. The bandgap energies vary widely depending on the level of theory involved, experimental approach, and sample investigated. Many reports ignore anisotropy and polarization dependence of the bandgap energy. Overall, a precise assessment of exciton properties, accurate band to band transition

energies, and their polarization dependence, e.g., as previously reported for $\alpha\text{-Ga}_2\text{O}_3$ (Ref. 206) remain unknown as of yet. There appears a wide range of results spanning several eV depending on whether the sample is bulk or thin film. Historic conclusions on bulk and single crystal samples tend to have larger bandgaps in the range 8–9 eV (Refs. 271 and 319) compared to that of amorphous thin films with an experimentally determined bandgap ranging from 6.2 to 6.8 eV.^{307,320–323} Single crystal high quality $\alpha\text{-Al}_2\text{O}_3$ samples have become available only recently, for interest due to bandgap engineering via alloying with Al and Ga. We note here that preliminary investigations by some of the current authors have revealed that bandgap energy parameters and their anisotropy of MBE grown $\alpha\text{-Al}_2\text{O}_3$ thin films are in excellent agreement with results obtained from high quality single crystalline bulk samples (see Table XIV).

Batra calculated a bandgap energy of around 8 eV.²⁸⁵ Increasing the exchange parameter within the calculations drastically alters both the bandgap and bandwidth. When Batra (Ref. 285) increased the exchange parameter, the bandgap for $\alpha\text{-Al}_2\text{O}_3$ increased and became more comparable to larger experimental values seen by Arakawa *et al.* (Ref. 319) of 9.5 eV. The bandwidth of $\alpha\text{-Al}_2\text{O}_3$ is decreased with an increasing exchange parameter as well.²⁸⁵ Ching *et al.* (Ref. 284) used OLCAO and obtained a direct bandgap of 6.31 eV but the true minimum bandgap was shown to be indirect with a gap of 6.29 eV. Due to such a small difference that could be considered undetectable, Ching *et al.* refer to the bandgap as direct with the gap occurring at the Γ point of the Brillouin zone. Schmid *et al.* (Ref. 324) reported bandgap values using GGA-DFT and HF-DFT (HSE03 level) calculations and obtained 6.3 and 8.0 eV for GGA-DFT and HF-DFT (HSE03 level), respectively.

Experimentally determined bandgap energies have been reported throughout the literature. French (Ref. 271) also reported on the electronic structure of Al_2O_3 using optical spectroscopy and vacuum ultraviolet (VUV) techniques. The electronic transition and exciton formation associated with the bandgap energy can be seen in VUV

reflectance and absorbance spectra. The distinct excitonic peak feature was determined in reflectance at approximately 9 eV. French also observes a transmission cutoff at approximately 8.8 eV; however, the cutoff energy where transmitted intensity drops below measurement sensitivity also depends on the sample thickness, defect densities, and instrument capabilities and does not serve as good reference for the bandgap energy. The observed transition was identified with the direct bandgap located at the Γ point of the Brillouin zone with no mention of any possible indirect gap. Tomiki *et al.* (Ref. 325) performed VUV reflectance in the range from 6 to 120 eV on single crystal sapphire for both polarization parallel and perpendicular to the lattice c axis, and thereby permitting for identifying the two potentially different bandgap energy parameters. Kramers–Kronig analysis was performed to obtain the real and imaginary parts of both ordinary and extraordinary dielectric functions. The authors identify peaks in the imaginary parts at approximately 9 eV in both spectra, but did not perform a line shape analysis. The authors conclude, given that exciton properties are not yet known, that the direct bandgap energy of sapphire is somewhere around 10 eV. Harman *et al.* (Ref. 326) performed a model line shape analysis using Lorentzian oscillators, and identified the lowest resonance features in both spectra at 9.2 eV (electric field $E||c$) and 9.25 eV ($E\perp c$). It is anticipated that sapphire will behave similar optically than $\alpha\text{-Ga}_2\text{O}_3$, hence, excitonic absorption and ground state features will be superimposed onto the reflectance spectra. Therefore, the values obtained by Harman *et al.* may identify the excitonic transition, while the true bandgap energy parameters remain hidden yet. A full line shape analysis using physical model functions, e.g., as performed by Hilfiker *et al.*²⁰⁶ will be necessary. Regardless, data in Table XIV reflect recent findings and are summarized here as bandgap energy parameters.

Miyazaki *et al.* (Ref. 327) report a bulk sample bandgap of around 8.8 eV for $\alpha\text{-Al}_2\text{O}_3$ determined by photoemission signals.³²⁷ Kamimura *et al.* (Ref. 307) reported a bandgap of 6.8 ± 0.2 eV for Al_2O_3 thin films grown via plasma-enhanced ALD formed at 250 °C. The bandgap was extracted from the core-level XPS peak and energy loss structure. The reported value for the ALD-deposited amorphous films was consistent with prior literature which reported bandgap values ranging from 6.4 to 6.9 eV for ALD Al_2O_3 thin films.^{306,309,321,328} Nohira *et al.* produced ALD Al_2O_3 thin films with a bandgap of 6.7 ± 0.2 eV with a negligible dependence of bandgap on film thickness.³²² All cited bandgap values are listed in Table XIV as well as values compared in Sec. XI. Of the nine oxides reviewed, Al_2O_3 has the highest bandgap; this could be a possible advantage to incorporation of Al_2O_3 in alloys. The large bandgap allows for tailoring through a wide range. Alloys involving Al_2O_3 such as aluminum gallium oxide (AlGaO) and aluminum indium gallium oxide ($(\text{Al}_{x}\text{In}_{y}\text{Ga}_{1-x-y})_2\text{O}_3$) are highlighted in Sec. II G.

We note here in passing that the ternary system $\alpha\text{-}(\text{Al},\text{Ga})\text{O}_3$ should reveal a transition from indirect ($\alpha\text{-Ga}_2\text{O}_3$) to direct ($\alpha\text{-Al}_2\text{O}_3$) bandgap behavior since, as discussed above, computational results suggest $\alpha\text{-Ga}_2\text{O}_3$ is indirect and $\alpha\text{-Al}_2\text{O}_3$ is direct. This resembles to some extent the inverse of the behavior in the system (AlGaAs) which is lattice matched to GaAs , where the bandgap behavior expands from direct (GaAs) to indirect (AlAs).

2. Temperature dependence of bandgap energy

Due to the historic usage as a ceramic insulator and in high temperature environments, Al_2O_3 is often subject to very high

TABLE XIV. Selected bandgap energy parameters of Al_2O_3 determined from theory and experiment.

E_g (eV)	Method	Bulk/film	Reference
Experimental			
8.8	VUV Trans; $\parallel c$	Bulk	271
9	Ref; $\parallel c$	Bulk	271
9.2 ^a	VUV-Ref.; $\parallel c$	Bulk	326
9.25 ^a	VUV-Ref.; $\perp c$	Bulk	326
9.9	Polarized Ref/Trans	Bulk	319
6.2	Photoconductivity	Film	320
6.52	Energy loss spectra	Film	321
6.7	XPS	Film	322
6.7	X-ray absorption	Film	323
6.8	XPS	Film	307
Calc.			
6.29	OLCAO	Bulk	318
6.3	HSE03	Bulk	324
8.0	HSE03	Bulk	324

^aModel analysis of Kramers–Kronig reflectance spectra.

temperatures whether it be during material processing or structural and device applications. The temperature dependence of the bandgap is an important parameter to understand, specifically in Al_2O_3 due to the mixture of electronic-ionic character within the defect chemistry.²⁷¹ Typically, the linear bandgap expansion coefficient of the temperature dependence, $\gamma = \delta E_g / \delta T \approx -2a_B/\theta_B$ ($T \gg \theta_B$), is reported [See also introduction to Eq. (1)]. French (Ref. 271) observed this temperature dependence when reporting electronic structure and optical properties. As stated previously, the room temperature bandgap of the single crystals were reported to be 8.8 eV. $\alpha\text{-Al}_2\text{O}_3$ exhibited a linear decrease in the bandgap when the sample was heated from 300 to 1573 K. The shift that appears in the absorption edge also shows a linear decrease in the bandgap of $\gamma = -1.1 \text{ meV/K}$.²⁷¹ The magnitude of this decrease is substantial when compared to other covalent semiconductors like Si or Ge that exhibit decreases of $\gamma = -0.22 \text{ meV/K}$ and $\gamma = -0.44 \text{ meV/K}$.³²⁹ The first exciton peak located around 9 eV at room temperature displays a shift of $\gamma = -1.0 \text{ meV/K}$ as well as a decrease in magnitude and peak broadening with increasing temperature. This broadening and decrease in magnitude is a result of the phonon scattering seen amongst the electron-hole pairs. A second peak located around 12–13 eV decreases at a smaller rate of $\gamma = -0.7 \text{ meV/K}$. Overall, the temperature dependence causes an optical bandgap decrease of 1.6 eV (8.8 to 7.2 eV) from room temperature to 1763 K.²⁷¹ The temperature dependence within the electronic structure can be attributed to two aspects, the lattice thermal expansion and electron-phonon interaction.^{330,331} Thermal expansion accounts for $\gamma = -0.31 \text{ meV/K}$ of the overall temperature dependence of the bandgap while phonon mode interactions are calculated to account for $\gamma = -0.62 \text{ meV/K}$. This adds to a calculated temperature dependence from thermal expansion and phonon modes of $\gamma = -0.93 \text{ meV/K}$ compared to the experimental value of $\gamma = -1.1 \text{ meV/K}$.²⁷¹

D. Material properties

Basic material properties reviewed throughout literature include the material density, bulk modulus, Vicker's hardness, and the melting point. The density of the stable $\alpha\text{-Al}_2\text{O}_3$ is roughly 3.95 g/cm³. When the Al percentage in ceramic Al_2O_3 is varied, the density changes accordingly. Going from 80% to 86% Al content in Al_2O_3 results in a density ranging from 3.30 to 3.60 g/cm³ while 99.8% Al_2O_3 has a density of 3.97 to 3.99 g/cm³.^{332,333} The Al percentage is often a factor of the ceramic grade, sintering aids, impurities, or alloys.³³² With increasing temperature the density is also shown to decrease in sintered $\alpha\text{-Al}_2\text{O}_3$.³³⁴ Bulk modulus values exhibit both temperature and porosity dependence. With increasing temperature from 20 to 1500 °C, the bulk modulus drops from 257 to 227 GPa.³³⁴ Vicker's hardness is shown to decrease drastically with increasing temperature, having a value of 2.5 GPa at 1500 °C. At room temperature, the Vicker's hardness increases to around 15 GPa.³³⁴ Melting point values are in good agreement across literature, ranging from 2323 to 2344 K.^{334,335} All cited basic parameter values are compared in Sec. XI.

1. Thermal properties

With applications ranging from high temperature insulators and structural components to device oxides such as gate oxides and insulators, the thermal properties are of particular importance. The phonon-phonon interactions dominate the heat transport mechanisms similar to other dielectric solids.³³⁶ Thermal properties highlighted here

include CTE, specific heat, Debye temperature, thermal conductivity, and thermal diffusivity. Engberg *et al.* (Ref. 337) report on the average coefficient of linear thermal expansion across a temperature range of 1000 to 1600 °C to be $7.5 \pm 0.4 \times 10^{-6} \text{ 1/K}$. Data were taken across multiple samples including cold pressed, extruded, and single crystals. The percentage of change from the room temperature length was shown to increase for all samples.³³⁷ Throughout experiments the orientation of the samples was not considered as any anisotropy was believed to be negligible. Comparing Engberg's findings to other data presented in the literature,³³⁸ it was stated that the CTE is isotropic. Of note, Wachtman *et al.* (Ref. 339) considers the thermal expansion to be nearly isotropic but did consider the small amount of anisotropy.³³⁹ That small amount of anisotropy was enough for Munro (Ref. 334) to cite Wachtman *et al.* (Ref. 339) as well as Amatuni *et al.* (Ref. 340) as proof of anisotropy amongst the thermal expansion. Munro only reports values of thermal expansion for sintered samples that exhibit an increase with increasing temperatures. Since sintered samples are polycrystalline, there is no anisotropy (unless the sample is textured). Munro does, however, present plots of thermal expansion along the *a* and *c* axes for single crystals with plotted data being derived from calculations.³³⁴ Other CTE values were reported across Al_2O_3 samples with varying Al_2O_3 percentages (80.0% to 99.6%). Values ranged from 4.5×10^{-6} to $5.4 \times 10^{-6} \text{ 1/K}$ at room temperature. The lower values of CTE are primarily for samples with lower Al_2O_3 percentages.^{332,333} Samples with lower Al percentages were reported to have higher porosity. All cited CTE values are listed and compared in Sec. XI.

The specific heat parameter for Al_2O_3 offers insight into how quantities of heat are added to the oxide with increasing temperature. Values reported near or at room temperature show good agreement between high-purity high-density sintered samples and samples with greater porosity that utilized cheaper growth methods. Values ranged from 0.750 to 0.785 J/(gK).^{332–334} Specific heat values for sintered samples increased from 0.755 to 1.33 J/(gK) with increasing temperature from 20 to 1500 °C.³³⁴

The Debye temperature has been reported by Chung *et al.* (Ref. 341) for polycrystalline samples with an emphasis on the elastic modulus, temperature, and pressure. Across a temperature range of 4.2 to 1300 K, the (elastic) Debye temperature decreased from 1044 ± 3 to 965 K. At a constant temperature of 298 K and increasing pressure from 1 bar to 10 kbar, the (elastic) Debye temperature increased slightly from 1034.9 to 1039.9 K.³⁴¹ The low temperature elastic Debye value is found to be in agreement with the thermal Debye temperature reported by Wachtman *et al.* (Ref. 339). With the 0.5% increase in Debye temperature with increasing pressure, the Gruneisen theory of solids provides understanding by stating that the frequency of lattice vibrations is only a function of volume.³⁴¹ Slack (Ref. 335) offers a different take on the Debye temperature by considering the acoustic Debye temperature. θ_0 and θ_∞ are considered the acoustic mode Debye temperature at absolute zero and the high temperature limit of the acoustic modes, respectively. Reported values are $\theta_0 = 478 \text{ K}$ and $\theta_\infty = 390 \text{ K}$ for $\alpha\text{-Al}_2\text{O}_3$ samples.³³⁵ While these values are outliers compared to previously reported values they do follow the trend of decreasing Debye value with increasing temperature.

The thermal conductivity is one of the most wide ranging and differing material properties for Al_2O_3 . A key factor in the varying thermal conductivity values comes from the deposition and growth method of the sample and whether it is a single crystal

or amorphous. Reported thin film thermal conductivities range from 0.25 to 0.8 W/(mK)³⁴² with the exception of a value reported by Ristau *et al.* (Ref. 343) and Akhtar *et al.* (Ref. 344) deposited via electron beam evaporation that had a thermal conductivity of 33 W/(mK). Single crystal samples generally have much higher thermal conductivity values than amorphous samples and range from 35 to 54 W/(mK).²⁷² Zeller *et al.* (Ref. 345) state that dielectric solids that are non-crystalline will exhibit a nearly identical thermal conductivity for temperatures higher than 100 K. That statement is found to be true based on Stark's findings.³⁴² Munro (Ref. 334) evaluated high-purity and high-density sintered α -Al₂O₃ samples. Thermal conductivity was found to decrease from 33 to 6.23 W/(mK) as temperature was increased from 20 to 1500 °C. The minimum thermal conductivity is a topic studied by Slack (Ref. 335) for reasons of understanding the minimum mean free path of phonons within crystals and how the temperature dependence of the thermal conductivity is affected by frequently scattered phonons with a minimum mean free path. Calculated minimum thermal conductivities yield a value of 2.93 W/(mK) for the high temperature limit around the melting point of 2345 K.³³⁵ Experimental data for the minimum thermal conductivity for temperatures above 700 K were presented by Schatz *et al.* (Ref. 346) where the measured data had a slope of around $\varepsilon = 2.6$, far different from the calculated minimum thermal conductivity value. If this slope value were in fact correct, it would point to a large number of optical modes in the crystal.³³⁵ However, Slack (Ref. 335) considered the data to be inaccurate due to uncertainty at the higher temperature values, even though the measured data did begin to approach the calculated values at temperatures of 1500 K.

Thermal diffusivity values were reported and shown to exhibit strong temperature dependence. At room temperature, the thermal diffusivity was around 1.0 to 1.1×10^{-5} m²/s and decreased to around 0.2×10^{-5} m²/s at 1000 K.³⁴⁷ Munro's (Ref. 334) thermal diffusivity values for sintered samples exhibited the same temperature dependence.³³⁴ There was also great homogeneity of the thermal diffusivity among multiple specimens cut from alumina plates. Ten different cuts from a single alumina plate displayed a negligible difference in value with a standard of 0.86%. Across 20 different alumina plates, the standard deviation of the thermal diffusivity was 1.36%. Heat treatment did not change the thermal diffusivity of alumina specimens either.³⁴⁷ All cited values of thermal diffusivity are compared in Sec. XI.

2. Phonon properties

The unit cell of α -Al₂O₃ contains ten atoms (4 Al and 6 O). From a unit cell of the corundum structure of α -Al₂O₃, group theory predicts that 30 Γ -point vibrational modes should exist. These 30 modes are separated into three acoustic branches and 27 optical branches.³⁴⁸ The irreducible representation of the optical modes was reported as^{349,350}

$$\Gamma = 2A_{1g} + 2A_{1u} + 3A_{2g} + 2A_{2u} + 5E_g + 4A_{Eu}.$$

Of the irreducible representation, the acoustical modes consist of $2A_{2u} + E_u$. Due to the center-of-inversion that is present within the corundum structure, any mode that is IR allowed is Raman forbidden, and any mode that is Raman allowed is IR forbidden. This results in $2A_{1g}$ and $5E_g$ Raman active modes and $2A_{2u}$ and $4E_u$ for the IR modes. $2A_{1u}$ and $3A_{2g}$ are neither Raman nor IR active vibrational modes (silent modes).³⁴⁹ Watson *et al.* (Ref. 350) report that the Raman

modes of sapphire crystals exhibit pressure dependence, increasing in frequency slightly with an increase in applied pressure and uniaxial stress.³⁵⁰

Schubert *et al.* (Ref. 351) report findings for the specific frequencies of the IR modes for both LO and TO modes. IR-ellipsometry was performed to determine the frequencies of the modes.³⁵¹ The results were also compared to other reported findings that used IR-reflectivity.^{352–354} Across the multiple methods reported, IR frequencies were in good agreement with each other. Raman and IR mode frequencies can be found listed in Table XV while a list of the Raman active modes can be found in Sec. XI. Stoekey *et al.* (Ref. 209) report the DFT calculation of the Brillouin zone center phonon mode eigenvector overlaps with the zone center modes in α -Ga₂O₃. From these overlaps, similarities and differences arise between the phonon modes of the same index and symmetry between the two binary isostructural parent compounds in the α -(Al,Ga)₂O₃ system. For example, Raman modes with A_{1g} symmetry should reveal a one mode behavior and maintain their displacement character almost 100%, while IR-active modes E_g – 3 and E_g – 5 in α -Al₂O₃ almost merge in displacement character with that of mode E_g – 3 in α -Ga₂O₃. It is predicted that these modes may show a complex behavior upon alloying.

PDPs help to present the stress and strain relationship of a material. Zhu *et al.* (Ref. 355) provide what is reported to be the first comprehensive study of the PDP stress analysis for α -Al₂O₃. The frequencies of the vibration modes will experience a shift based on the applied stress and strain. How rapid and significant of a shift is determined by the PDPs. Zhu *et al.* present how the strain anisotropy alters the A_{1g} and E_g Raman modes spectral shifts. The present Raman active modes (2A_{1g} and 5E_g) and the Raman scattering aids in the observation of the optical phonons for both the transverse and longitudinal directions. Zhu *et al.* were able to experimentally determine the PDP values for both single-crystal and polycrystalline samples of α -Al₂O₃, presented in Table XVI. The PDPs were calculated using calibration data from single-crystal samples that were uniaxially loaded across varying crystallographic directions. A data set from a polycrystalline

TABLE XV. Al₂O₃ Raman and IR active TO and LO phonon mode frequencies.

Raman ³⁵⁰	ω (cm ⁻¹)	
A _{1g} (1)	417.4	
A _{1g} (2)	644.6	
E _g (1)	378.7	
E _g (2)	430.2	
E _g (3)	448.7	
E _g (4)	576.7	
E _g (5)	750.0	
Infrared ³⁵¹		
	ω_{TO} (cm ⁻¹)	
	ω_{LO} (cm ⁻¹)	
A _{2u} (1)	397.52	510.87
A _{2u} (2)	582.41	881.10
E _u (1)	384.99	387.60
E _u (2)	439.10	481.68
E _u (3)	569.00	629.50
E _u (4)	633.63	906.60

TABLE XVI. Phonon deformation potential values for single-crystal and polycrystalline α -Al₂O₃ determined using bending calibrations. Values from Zhu *et al.* (Ref. 355).

	K_1 ($\times 10^3$ cm $^{-2}$)	K_2 ($\times 10^3$ cm $^{-2}$)	K_3 ($\times 10^3$ cm $^{-2}$)	K_4 ($\times 10^3$ cm $^{-2}$)
A _{1g}	-396 ± 19	-406 ± 6	-777 ± 18	...
E _g	-293 ± 22	-227 ± 24	-3.2 ± 0.5	-8.5 ± 1

sample was also used. Calculated Raman band shifts were in good agreement with those seen experimentally, yielding only small errors in the A_{1g} and E_g bands of <5% and <10%, respectively.

Along with IR phonon modes, Schubert *et al.* (Ref. 351) were able to obtain values for the static dielectric and the high-frequency dielectric constants. To calculate values for high-frequency dielectric constants, the Lyddane–Sachs–Teller (LST) relation was utilized with data from IR experiments.³⁵⁶ Perpendicular to the *c*-axis, values of 9.385 and 3.077 were reported for the static and high frequency dielectric constants, respectively. Parallel to the *c*-axis, values of 11.614 and 3.072 for static and high frequency dielectric constants were reported, respectively. There is clear anisotropy for the static dielectric constants due to the uniaxial nature of the material; however, anisotropy does not appear as strongly for the high-frequency constants.³⁵¹ Several other reports in literature also report on this strong anisotropy in the static dielectric constant and weak anisotropy in the high frequency dielectric constant.^{326,352,357} All cited values for both the static and high-frequency dielectric constants are listed and compared in Sec. XI.

3. Electrical properties

Al₂O₃ has often been used as a ceramic in non-electrical applications. With the oxide being used in more electrical applications such as gate oxides, the electrical properties are of importance. These properties include electron affinity, electrical breakdown field, effective mass, and electron mobility. The reported values for the electron affinity of Al₂O₃ range from around 1 to 2.58 eV.^{328,358–360} Using thermally grown Al₂O₃ thin films, Pollack *et al.* (Ref. 358) determined the electron affinity to be 1.58 eV, extracting the parameter from current density vs voltage data. α -Al₂O₃ has a bandgap of almost double β -Ga₂O₃, but that value does not correlate to a superior electrical breakdown field. Reported values for the electrical breakdown field of Al₂O₃ range from 5.2 to 8 MV/cm.^{304,361,362} Groner *et al.* (Ref. 304) finds catastrophic breakdown at 5.2 MV/cm using 12 nm thick ALD grown amorphous thin films.³⁰⁴ Higashiwaki *et al.* (Ref. 147) plotted the breakdown field (MV/cm) vs the bandgap to produce the well-known breakdown field of 8 MV/cm for β -Ga₂O₃. If that plot were to be followed in order to predict the breakdown field of single crystal α -Al₂O₃, it would result in a value of well over 20 MV/cm or possibly as high as 25 MV/cm for a bandgap of around 9.5 eV (exceeding the range calculated by Higashiwaki *et al.*) and a value of 15 MV/cm for the bandgap of around 6.2 eV observed of amorphous films. Al₂O₃ thin films with bandgaps of around 6.7 eV would have a predicted breakdown field of around 17 MV/cm. All reported values of the electron affinity and electrical breakdown field are listed and compared in Sec. XI.

Due to the flat valence band maximum seen in Fig. 18, the effective mass of the holes are expected to be large.³¹⁸ Perevalov *et al.*

(Ref. 363) report that there is a strong anisotropy of the effective hole mass that is not seen for the effective mass of the electrons. Along the Γ -M and Γ -K directions, the heavy hole effective mass was found to be 6.2 m_h and 6.4 m_h, respectively. What can be considered the light holes have an effective mass of 0.36 m_h along the Γ -A direction.³⁶³ Calculated electron effective mass values are around 0.4 m_e along all directions³⁶³ and compare well with experimental tunneling effective mass values ranging from 0.05 m_e to 0.42 m_e. While Perevalov *et al.* (Ref. 363) found no anisotropy for the effective mass of the electrons, Xu *et al.* (Ref. 318) found strong anisotropy for α -Al₂O₃ calculated along four varying directions of the Brillouin zone, for an average electron effective mass of 0.35 m_e.³¹⁸

The mobility of Al₂O₃ is not a widely researched topic, with very little available in the literature. This lack of interest stems from the oxide predominately being used as a gate dielectric. If interest in using Al₂O₃ as an alloy for device applications continues to gain ground, more information regarding the carrier mobility should become available. The predominant charge carrier within Al₂O₃ was reported to be electrons.^{284,367} Reported Hall effect mobility values range from 0.8 to 100 cm²/(V s) across a wide temperature range.^{368–370} Using these reported Hall values, Will *et al.* (Ref. 367) calculated mobility values along two directions based on the previously cited values. Parallel to the *c*-axis, mobility was predicted to be 24 cm²/(V s) at 900 °C, and perpendicular to the *c*-axis, mobility was predicted to be 7.3 cm²/(V s) at 900 °C.³⁶⁷ The anisotropy seen for the calculated mobility values within Al₂O₃ stems from the structure of sapphire. Along the *c*-axis there is substantially less atomic packing than the direction perpendicular to the *c*-axis, resulting in fewer scattering centers and a higher mobility along the *c*-axis.³⁶⁷ The reported room temperature values for both the carrier effective mass and mobility are listed and compared in Sec. XI.

E. Doping and defects

Al₂O₃ has many possible doping candidates that have been discussed across the literature. Some of the dopants are researched in regard to the electrical properties of Al₂O₃ while others are considered for density changes among single crystals. Dopants used include Ti, Co, Fe, Mg, Y, Cr, Ca, Mg, Si, and V. Mohapatra *et al.* (Ref. 371) observes how Ti affects the defect structure of α -Al₂O₃. Titanium acts as a donor when used as a dopant and is found occupying the aluminum site in both trivalent and quadrivalent states.³⁷¹ Within Al₂O₃ Ti solubility is greater for polycrystalline samples and smaller for single crystals.³⁷² Ti³⁺ incorporates without native defects and Ti⁴⁺ exhibits native defect formation to account for charge compensation.^{373,374} With Ti⁴⁺ incorporated into Al₂O₃ the conductivity was shown to increase due to an increase in self-diffusion that occurs as a result of the increase in native ionic defects.³⁷¹ Ti³⁺ brings about three optical absorption band systems; one in the visible range, one in the far IR range and one occurring at 6.9 eV. Ti⁴⁺ did not have any observable absorption bands related to the dopant.³⁷¹

Cobalt doping of Al₂O₃ causes the conductivity to increase within oxygen and air.³⁷⁵ The divalent dopant has been shown to increase positively charged native defect concentrations and is thought to be present at Al sites.³⁷⁶ For iron doped Al₂O₃ Dutt *et al.* (Ref. 377) proposes similarities to their previous work involving cobalt doping. Similar models can be used that show how the ionic defects are the main source of charged species and yield an explanation for the

conduction of cobalt doped Al_2O_3 . Carrying that model over to iron doped Al_2O_3 , a model was proposed that accounted for creep, sintering, and conductivity.³⁷⁷ Heiba *et al.* (Ref. 378) examined how iron doping altered the structural, optical, and electronic properties of Al_2O_3 nanoparticles. The addition of iron doping allowed for bandgap narrowing and changes to the emission peaks.³⁷⁸ When single crystal Al_2O_3 is doped with magnesium then magnesium acts as an acceptor that is substituted for aluminum. With the addition of magnesium the native ionic defect concentration is increased as well as the hole concentration with the holes still remaining a minority species within the crystal. Ionic conductivity was found to be anisotropic while electronic conductivity was isotropic.³⁷⁹ Rare-earth elements such as yttrium were also a studied dopant of Al_2O_3 .³⁸⁰ In regard to the ceramic properties of Al_2O_3 , there are many structural applications involving high temperatures. High-temperature creep deformation is a known issue that stems from grain boundary diffusion. When doping with yttrium it is possible to retard and control the high-temperature creep in fine-grained Al_2O_3 . The grain boundary diffusivity of yttrium doped Al_2O_3 was reduced by ten times when compared to pristine crystals.³⁸⁰ Rasmussen *et al.* (Ref. 381) examined the role that dopants had on the defect structure for single crystal Al_2O_3 . Dopants included Cr_2O_3 , CaO , MgO , SiO_2 , V_2O_5 , and TiO_2 . Densities of the crystals as well as X-ray peak locations were measured and compared to undoped pure Al_2O_3 crystals.³⁸¹ With Cr_2O_3 doping, the molecular weight change can be calculated with the Cr^{3+} substituting for Al^{3+} . For CaO doping, measurements of density and transmission electron micrographs reveal the presence of a second phases forming within the doped crystal. MgO doping results in a deviation of the measured and calculated densities that appear to increase at a fast rate with an increase in the Mg concentration. Within the SiO_2 doped samples Si^{4+} solutions forms with Al^{3+} vacancies to account for charge neutrality. With V_2O_5 , V^{5+} was added but the resultant change of density reveals V^{3+} substituting for Al^{3+} ions.³⁸¹ TiO_2 shows similar findings as Mohapatra *et al.* (Ref. 371) in that the titanium forms a mixed valence state with Ti^{3+} and Ti^{4+} being present.^{381,382}

As is common with most oxides, there is the occurrence of oxygen vacancies. These vacancies act as defects within the crystal structure and are prevalent within $\alpha\text{-Al}_2\text{O}_3$. These oxygen vacancies occur as a result of oxygen loss or incorporation into the material.³⁸³ As a result of the vacancies, charge trapping occurs and fixed charge centers arise.³⁸⁴ The oxygen vacancies are also considered nanoscale absorption centers that attract metallic clusters or molecules. These types of structural defects are believed to be key in enhancing catalytic reactions.^{385,386} Aluminum ions within $\alpha\text{-Al}_2\text{O}_3$ have five valence states that are supported by the oxygen vacancies ranging from $2+$ to $2-$. With these vacancy states $\alpha\text{-Al}_2\text{O}_3$ exhibits a form of electron transport known as Poole-Frenkel hopping. This form of transport is a method of electron conduction that allows an insulator to conduct a current and explains how an oxide with such a large bandgap as that of $\alpha\text{-Al}_2\text{O}_3$ can be considered a semiconducting oxide at times. The vacancy states of $\alpha\text{-Al}_2\text{O}_3$ allow charge carriers to “slowly” make their way up through the energy bandgap by stopping in the localized traps of the vacancies. The carriers are excited to the next vacancy or trap by a stimulus as simple as a slight thermal increase or fluctuation.³⁸⁷

A comparison of the band alignment of $\alpha\text{-Al}_2\text{O}_3$ and $\theta\text{-Al}_2\text{O}_3$ was made alongside the band edge of silicon.³⁸⁸ The two Al_2O_3 phases are also shown against HfO_2 at the silicon band edge. The comparison

shows the possibility of the Al_2O_3 dielectric being a possible replacement for HfO_2 , an oxide that has received much attention as a possible gate dielectric for MOSFETs and other electronic devices.^{321,389–392} For both phases of Al_2O_3 , the $+0$ vacancy level resides lower in the energy gap than HfO_2 . The vacancy states for Al_2O_3 also remain in stable form as the Fermi energy is increased; that is not the case for the HfO_2 vacancy states.³⁸⁸ Other defects that occur with Al_2O_3 are aluminum vacancies as well as oxygen and aluminum interstitial sites. The aluminum vacancies and the oxygen interstitial sites are deep acceptors within the band while aluminum interstitial sites are deep donors and the oxygen vacancies are both donors and acceptors as seen from the $2+$ to $2-$ charge states.³⁸⁴

Jones *et al.* (Ref. 393) highlight defect diffusion within titanium doped single crystal Al_2O_3 samples. Titanium doped Al_2O_3 exhibits a shift in color boundary with a change in the oxidation state. This means that diffusion transport within the crystal controls the oxidation. The point defects in the crystal lattice have a diffusion coefficient that controls the color boundary migration. Lattice diffusion can be attributed to either the concentration of i th defects per concentration of lattice sites or the correlation coefficient of the i th type of defect. The defect that has the most overall contribution to the transport can be considered the means of lattice diffusion.³⁹³

Shifting from single crystal to Al_2O_3 thin films, Schmid *et al.* (Ref. 324) reports a first of its kind study involving oxygen-deficient line defects. It is demonstrated how anti-phase domain boundaries within thin film Al_2O_3 grown on NiAl(110) substrates are oxygen deficient and act as adsorption sites for electronegative species.³²⁴ The energies of the empty conduction band states were previously reported to be $+2.5$, $+3.0$, and $+4.5$ eV using scanning tunneling spectroscopy experiments by Nilius *et al.* (Ref. 394) and are in good agreement with the defect state energies found by Schmid *et al.* (Ref. 324). The findings suggest that while O atoms exhibit defect behavior they are not localized structure defects. Stoichiometry of the model and electronic properties show an O deficient structure. Oxygen deficient domain boundaries act as native electron donors.³²⁴ This donor like behavior is very much debated for oxygen-deficient defects that occur within transition metals oxides like ZnO , for example.^{395,396} Of note, there still exists electronic defects within the thin film even though the films building principles are maintained perfectly. This negates the one-to-one correlation between electronic and structural defects.³²⁴

F. Summary of Al_2O_3 property values

Table XVII highlights a summary of the properties reviewed for Al_2O_3 . Values for each of the properties are presented along with references and notation of whether they are experimental or calculated findings. Where relevant anisotropy is denoted.

IV. INDIUM OXIDE

Indium oxide is a widely researched oxide commonly grown in the form of single crystal or thin film. With a combination of dopants such as Sn, and material coatings, In_2O_3 has many electronic and optoelectronic applications such as solar cells,^{403–405} energy efficient windows,^{406,407} thin film transistors,^{408–410} and Schottky contacts and diodes.^{411–413} There are also numerous ceramics applications for In_2O_3 ,^{414–416} similar to Al_2O_3 . Over the past few decades, the availability of high crystalline quality bulk samples and thin films have furthered the interest in integration of In_2O_3 into device applications.

TABLE XVII. Summary of theoretical and experimental basic properties of Al_2O_3 . Common names of aluminum oxide, aluminum sesquioxide, alumina, and corundum.

Stable phase	α - Al_2O_3	Ref. 265
Stable structure	Trigonal ^a $R\bar{3}c$ $a = 4.75$ $c = 12.97$	Refs. 265 and 276
	Hexagonal $R\bar{3}c$ $a = 4.762$ $c = 12.896$ $a^b = 5.128$	Refs. 277 and 284
Metastable phases	$\gamma, \eta, \theta, \delta, \kappa, \chi$	
Density (g/cm ³)	3.92–3.984	Expt. ^{334,347}
Bulk modulus (GPa)	257 (20 °C) 225–252	Expt. ³³⁴ Calc. ^{397–399}
T_m (°C)	2050–2071.85	Expt. ^{334,335,400}
Debye temp. (K)	1045 965–1044 ^c	Calc. ³³⁹ Expt. ³⁴¹
Specific heat (J/(gK))	0.750–0.785	Expt. ^{332–334}
Th. Cond.(W/(mK))	30, 33, 30–40	Expt. ^{332–334,347}
CTE ($\times 10^{-6}/\text{K}$)	4.5–5.5	Expt. ^{332–334}
Electron affinity (eV)	1.58	Ref. 358
Breakdown field (MV/cm)	>20 5.2–7	Pred. ¹⁴⁷ Expt. ^{304,362}
m_e^*	0.38–0.40	Calc. ^{284,318,328}
	0.40 ($\perp c$) 0.40 ($\parallel c$)	Est. ³⁶³
m_h^*	6.3 ($\perp c$) 0.36 ($\parallel c$)	Est. ³⁶³ Est. ³⁶³
μ_e [cm ² /(Vs)]	0.8	Expt. ³⁶⁸
Gap type	Direct	Ref. 271
E_g (eV)	6.3–8.8 8.8–9.9 4.0–6.8	Bulk calc. ^{324,401} Bulk expt. ^{271,319,324,402} Film calc. ^{307,321,322,324}
ϵ_0	8.9–9.385 ($\perp c$) 11.614 ($\parallel c$) 9.395 ($\perp c$) 11.589 ($\parallel c$)	Calc. ^{326,351} Calc. ^{326,351} Expt. ³⁵⁷ Expt. ³⁵⁷
ϵ_∞	3.038–3.077 ($\perp c$) 3.065–3.072 ($\parallel c$)	Calc. ^{326,351,357,d} Calc. ^{351,357}
Phonon modes		
IR active	2A _{2u} , 4E _u	Expt. ³⁵⁰
Raman active	2A _{1g} , 5E _g	Expt. ³⁵⁰

^aTrigonal symmetry with hexagonal parameters.^{265,276}

^bTrigonal unit cell parameter within the hexagonal lattice.^{277,284}

^cPolycrystalline sample.

^dDerived from IR experiment using LST relation.

For the purpose of the present review, we note that a thorough summary of the properties of Sn-doped In_2O_3 (also known as ITO) is beyond the scope of this work. However, where relevant, ITO comparisons are made to In_2O_3 throughout this section. The reader is referred

to existing literature specific to this material.^{417–419} Material properties including crystal and electronic structure, as well as thermal, phonon, and electrical properties are reviewed to provide further insight into In_2O_3 .

A. Crystal structure

In_2O_3 contains multiple widely accepted crystal structures, a body-centered cubic and a rhombohedral structure according to Wang *et al.* (Ref. 420). Hagleitner *et al.* (Ref. 421) state there are three possible alternative structures for In_2O_3 to exist in, but do not specify any of them besides the body-centered cubic structure. This structure and phase has thermodynamic stability in ambient conditions.⁴²² The body-centered cubic structure of In_2O_3 belongs to the space group $Ia\bar{3}$ (#206) with a lattice constant of 10.118 Å^{420,423} regarded as having a C rare-earth sesquioxide⁴²⁴ or a bixbyite structure.⁴²¹ Figure 19 shows a schematic for the In_2O_3 crystal structure. Within a unit cell there are 80 atoms.⁴²⁵ Of the 80 atoms, 32 are metallic indium atoms with 24 located in the *d* position and 8 located in the *b* position. The remaining 48 atoms are oxygen with no special position or location.⁴²⁴ The *b* atoms are coordinated with axial symmetry while the *d* atoms have a high asymmetry within their coordination.⁴²¹ When looking down the (001) direction of the crystal, there are 3 alternating layers that makeup the crystal. There is a mixed layer that contains both *b* and *d* atoms which referred to as the M layer, a layer of *d* atoms known as the D layer, and a layer containing O atoms known as the O layer. There exists a net dipole that is perpendicular to the surface due to the indium and oxygen layers alternating.⁴²¹ The In atoms have a coordination to six oxygen atoms thus forming an octahedron. The bond lengths between the In and O range from 2.12 to 2.21 Å and the In to In bond lengths range from 3.35 to 3.36 Å.⁴²⁶

Karazhanov *et al.* (Ref. 427) report that there is an additional body-centered cubic In_2O_3 structure, called In_2O_3 -I. The structure of In_2O_3 -I belongs to the space group $I2\bar{1}3$ (#199) and possess a lattice constant of 10.120 Å.⁴²⁷ In_2O_3 -I contains three types of indium atoms and two types of oxygen atoms. The indium atoms, In(1), In(2) and In(3), reside at 8*a*, 12*b*, and 12*b*, respectively. The oxygen atoms O(1) and O(2), both reside at 24*c* Wyckoff locations.⁴²⁷ First principles studies on the quasiparticle electronic states by Fuchs *et al.* (Ref. 428) report that this specific cubic polymorph is unstable.⁴²⁸

The second accepted phase of In_2O_3 is the rhombohedral structure. This phase belongs to the $R\bar{3}c$ (#167) space group with lattice constants $a = 5.478$ Å and $c = 14.51$ Å.⁴²⁰ Zhang *et al.* (Ref. 422) state that the *rh*-phase of In_2O_3 is stabilized under high pressure conditions. The rhombohedral cell, sometimes called a hexagonal cell, contains six formula units within each hexagonal cell and contains a slightly smaller volume per formula unit than the *bcc*-phase; 62.85 Å³ and 64.72 Å³, respectively.⁴²² Karazhanov *et al.* (Ref. 427) state there are 12 indium atoms and 18 oxygen atoms within the unit cell occupying the *c* and *e* Wyckoff positions, respectively.⁴²⁷ Very little is known about the rhombohedral phase compared to the *bcc* phase due to lack of overall research interest and suitable synthesis methods.^{420,429} Notably, there are known property and parameter differences between the *bcc*-phase and the rhombohedral phase that will be highlighted throughout.

The third accepted phase of In_2O_3 is the orthorhombic phase, or o' - In_2O_3 belonging to space group $Pbcn$ (#60). The orthorhombic phase is similar to the rhombohedral phase in that they are connected

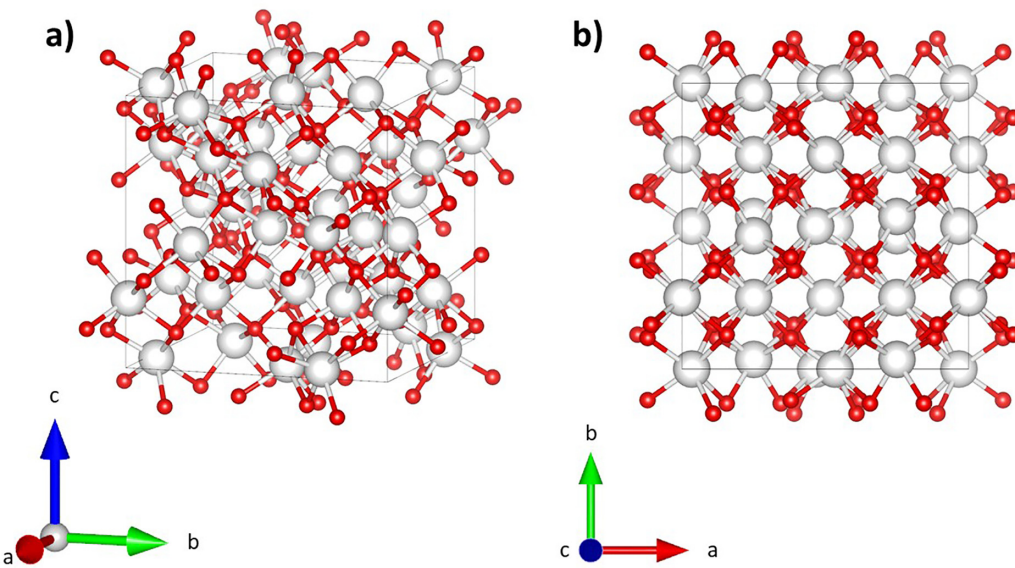


FIG. 19. Schematic for the crystal structure of In_2O_3 with space group $I\bar{a}3$ (#206) (a) with the c -axis orientated upward and (b) along the c -axis (white = In, red = O).

via a diffusionless pathway of the $P2/c$ monoclinic subgroup.⁴³⁰ Bekheet *et al.* report lattice constants of $a = 7.929 \text{ \AA}$, $b = 5.482 \text{ \AA}$, and $c = 5.589 \text{ \AA}$ for samples recovered from 9 GPa and 600°C . Lattice constants did not vary more than 0.001 \AA with 8 GPa recovery at 1100°C while bringing the oxide back to ambient pressure and temperature and while still maintaining the orthorhombic phase and not transforming to the rhombohedral phase. There was much disagreement about the conditions for obtaining the orthorhombic phase. Yusa *et al.* (Ref. 431) states that orthorhombic In_2O_3 is only stable between a pressure range of 8.1 to 19.9 GPa and will transform into the rhombohedral phase upon decompression. Bekheet was able to recover orthorhombic samples from 30 GPa to ambient pressure and temperature, but yielded very few and small samples. In further studies, Bekheet *et al.* (Ref. 430) were able to synthesize orthorhombic samples from the rhombohedral phase, successfully recovering the orthorhombic phase from moderate high pressure (8–9 GPa) and moderate high temperatures (600 – 1100°C) back to ambient pressure and characterizing the crystal structure. It was concluded that σ' - In_2O_3 was an orthorhombic distortion of the rhombohedral phase. While σ' - In_2O_3 contains octahedrally coordinated indium and tetrahedrally coordinated oxygen similar to the cubic and rhombohedral phases, it differs in the stacking of the InO_6 octahedra. σ' - In_2O_3 does not vary much in the interatomic distancing compared to bcc and rh , but does possess the smallest volume of 60.74 \AA^3 .⁴³⁰

Yusa *et al.* (Ref. 431) states that there is a fourth phase obtainable at pressures above 19.9 GPa. The phase is an orthorhombic α - Gd_2S_3 -type σ' - In_2O_3 , belonging to possible space groups $Pnma$ (#62) and $Pn2_1a$ ^{430,431} with lattice constants reported to be $a = 5.473 \text{ \AA}$, $b = 3.003 \text{ \AA}$, $c = 11.618 \text{ \AA}$ using XRD data.⁴³¹ This phase is a transformation from the $\text{Rh}_2\text{O}_3(\text{II})$ structure with very little known about the stability of the structure or possible recovery similar to σ' - In_2O_3 .⁴³¹ The lattice parameters, space grouping, and structure for the reviewed phases of In_2O_3 are highlighted in Table XVIII. An additional

reference detailing the high pressure Gd_2S_3 structure can be found in Yusa *et al.* (Ref. 432).

B. Growth

There are many growth and fabrication methods that have been explored since the dawn of the In_2O_3 crystal and thin film research. As seen from the parameters obtained from older works such as Weiher *et al.* (Ref. 434), the purity and growth quality plays a large role. As growth and fabrication methods have improved, so have the resultant material properties, as evidenced by the reported electron mobility values below. Concerning bulk crystal growth there are a wide range of methods spanning back as far as the 1950s. Using a hydrothermal method, the first bulk crystal samples of In_2O_3 were obtained by Roy *et al.* (Ref. 435) with few details regarding the overall quality and dimensions.^{435,436} Flux methods for bulk crystal samples have been explored by a multitude of groups as well.^{421,437,438} Contamination is a common consequence of using a flux method, thus altering the electrical properties as well as the overall crystalline quality.⁴³⁸ Physical and chemical vapor transport (PVT and CVT) as well vapor phase methods are other well-known methods for bulk growth.^{434,436,439} Galazka *et al.* (Ref. 439) grew samples using PVT as well as melt-grown methods to compare the resultant crystals. With PVT samples having a higher carrier concentration, the overall mobility was lower than melt-grown samples.⁴³⁹

Galazka *et al.* (Ref. 440) reported on a novel growth method from melt called Levitation-Assisted Self-Seeding Crystal Growth Method (LASSCGM). Melt growth is a difficult growth method for metal oxides like those discussed in this review. The decomposition of the melt must be suppressed and oxygen partial pressure must be managed. As the oxygen partial pressure requirements are increased, the difficulty of growth increases as well. Compared to other oxides, In_2O_3 has been shown to be far less stable.⁴⁴⁰ LASSCGM allows for the oxide melt to be levitated using electromagnetics. This allows for

TABLE XVIII. In_2O_3 polymorphs and crystal structure with associated lattice constants determined from experiment and theory.

Phase	Structure	Space group	Lattice (Å)
<i>bcc</i> - In_2O_3	Cubic	$Ia\bar{3}$ (#206)	$a = 10.118^{420,\text{a}}$ $a = 10.117^{421,423,\text{a}}$
<i>bcc</i> - In_2O_3 -I	Cubic	$I2_13$ (#199)	$a = 10.120^{427,\text{b}}$
<i>rh</i> - In_2O_3	Rhombohedral	$R\bar{3}c$ (#167)	$a = 5.478^{420,433,\text{a}}$ $c = 14.51$
<i>o'</i> - In_2O_3	Orthorhombic	$Pbcn$ (#60)	$a = 7.929^{430,\text{a,d}}$ $b = 5.482$ $c = 5.589$ $a = 7.92^{430,\text{a,e}}$ $b = 5.488$ $c = 5.597$ $a = 8.072^{430,\text{b}}$ $b = 5.588$ $c = 5.678$
α - Gd_2S_3 type	Orthorhombic	$Pnma$ (#62) $Pn2_1a$ (#33)	$a = 5.473^{431,\text{c}}$ $b = 3.003$ $c = 11.618$

^aExperimental.^bTheoretical.^cModeled.^d9 GPa recovery, 600 °C.^e8 GPa recovery, 1100 °C.

the melt to be pulled away from areas of highest temperature during growth in the iridium crucible apparatus which proves advantageous as it decreases the eutectic formation probability. While the conditions of the LASSCGM are extreme, the resultant crystals were shown to have good quality.⁴⁴⁰

As with many other thin film materials, the methods of fabrication are numerous. In_2O_3 thin films have been fabricated using ALD,^{441–443} spin coating,⁴⁴⁴ PLD,^{445,446} MBE,⁴⁴⁷ MOCVD,^{448,449} spray pyrolysis,⁴⁵⁰ and dc magnetron sputtering.⁴⁵¹ Ramachandran *et al.* (Ref. 443) reported on the versatility of ALD temperatures. The growth rate was shown to remain mostly constant across a temperature range of 100–400 °C. The evident possibility of wide ranging deposition temperatures is key for insuring compatibility with various dopants that require various deposition temperatures. Ramachandran's work was the first to publish crystalline In_2O_3 thin films grown using ALD at a temperature of 100 °C.⁴⁴³ MOCVD is a well-known method due to the ability to control the film composition as well as achieve high uniformity at a high growth rate.⁴⁴⁹

C. Electronic band structure

The electronic structure of In_2O_3 , derived from the atomic composition of the oxide, provides insight and understanding into the electronic properties that make In_2O_3 a candidate for device applications.

The stable body-centered cubic phase will be the focal point here with comparisons to the other metastable phases highlighted where relevant. Karazhanov *et al.* (Ref. 427) reported a conduction band minimum located at the Γ point, shown to be very dispersive and uneven. The conduction bands that reside just above the conduction minimum share the same dispersive feature. The valence bands are predominately flat, similar to Al_2O_3 and a common trait of many transparent conducting oxides (TCO).⁴²⁷ Peelaers *et al.* (Ref. 452) found that within the valence bands there is low dispersion of O(p) orbital character. The lower level conduction bands are primarily s orbitals that have a very large dispersion.⁴⁵² There are three groupings of bands within the valence band structure. The lowest in energy reside around –15 eV below the flat uppermost valence band. Between –10 and –14 eV lies the middle grouping of valence bands. The third grouping resides just below the valence band maximum and is the broadest section of bands. The stable body-centered cubic phase has a valence band maximum located at the Γ point, resulting in a direct bandgap. The rhombohedral In_2O_3 has a conduction band minimum at the Γ point and a valence band maximum located at the L point, resulting in an indirect bandgap.⁴²⁷ This direct bandgap is the topic of much discussion and disagreement, as presented below. The band structure for cubic In_2O_3 is shown in Fig. 20 as well as the comparison to the electronic structure for rhombohedral In_2O_3 .

Fuchs *et al.* (Ref. 428) present a first principles study providing further insight into the electronic structure of In_2O_3 . The Γ position for the resultant direct bandgap is considered to be widely accepted with some disagreement about the indirect bandgap energy. Quasiparticle calculations show that the overall electronic structure and density of states for both the stable cubic phase and high pressure rhombohedral phase are similar. There is large k space dispersion seen in the lowest conduction bands near the Γ point. This is commonly seen among other In materials and compounds like InN.⁴⁵³ The highest valence bands are derived from predominately O(2p) orbitals with a bandwidth of around 6 eV. Between the energy range of –11 to –13 eV, bands are derived from In(4d) orbitals and the lowest bands are a result of mainly O(2s) valence bands. Fuchs *et al.* (Ref. 428) explain the complexity of the electronic band structure as a result of atomic orbital hybridization. Beginning with the lower conduction bands, In(5s) is dominant but will begin to combine with In(5p) character with increasing k vector. The top of the valence band contains hybridization of In(4d) states.⁴²⁸ The binding energies of In(4d) as well as the coupling of the In(4d) and O(2p) states are often reasons for an under estimation of bandgap value seen for LDA and other DFT theoretical methods. According to angular resolved photoemission studies (ARPES) by Janowitz *et al.* (Ref. 87) the beginning of the allowed transitions start in the band states located 0.8 eV below the valence band maximum. This transition is reported to be 3.7 eV. XAS data find that the conduction band minimum is made of oxygen atoms with indium contributions. At low binding energy there exists mainly O(2p) character, and In(5P) at the higher binding energies. This is derived from the symmetry selection rules.⁸⁷ Methods for determining the value of the In_2O_3 bandgap are discussed below.

1. Bandgap energy

The bandgap energy for In_2O_3 has been reported often for both theoretical and experimental methods. Theoretical methods include

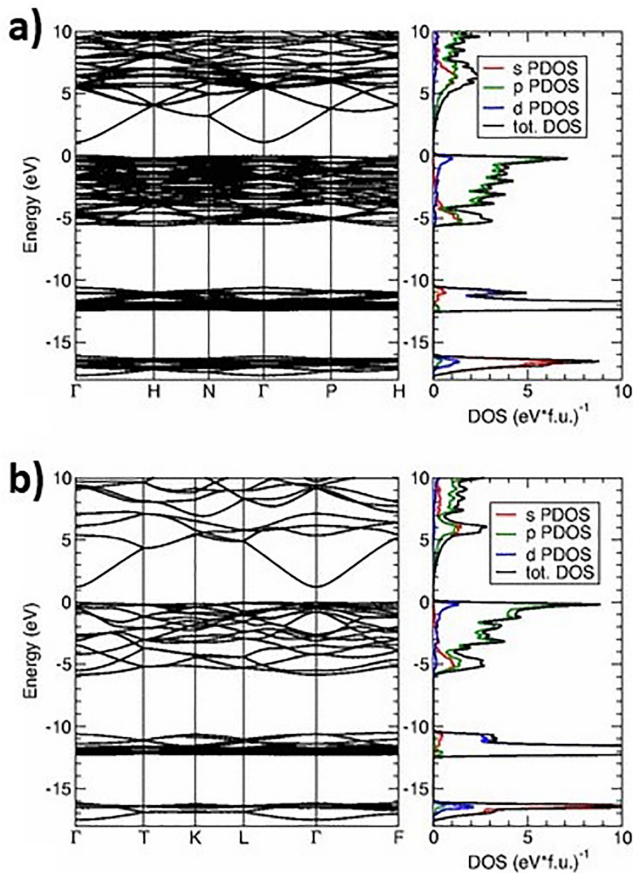


FIG. 20. The band structure, density of states (DOS), and partial DOS for (a) cubic In_2O_3 and (b) rhombohedral In_2O_3 . Calculations were performed within DFT-LDA. Note that the resolution of the figure is identical to that of the source. Reproduced with permission from Fuchs and Bechstedt, Phys. Rev. B **77**, 155107 (2008). Copyright 2008 APS (Ref. 428).

LDA, LDA+ U , HSE03, HSE03+ G_0W_0/Δ , and GGA.^{427,428} Fuchs *et al.* (Ref. 428) reported calculated bandgaps for both the direct and indirect transitions for both the cubic and rhombohedral polymorphs using LDA, HSE03, and HSE03+ G_0W_0/Δ . For cubic In_2O_3 , LDA calculations produced the lowest values; 1.12 eV and 1.11 eV for direct and indirect gaps, respectively. As seen from the values, the difference between the direct and indirect values are small. HSE03+ G_0W_0/Δ provided the highest theoretical value of 3.10 eV for the direct bandgap. Across all calculated methods used by Fuchs, the bandgaps of the rhombohedral polymorph were larger than the cubic polymorph. The difference between the direct and indirect bandgaps were also more pronounced; 1.27 and 1.23 eV, respectively.⁴²⁸ While there is a difference in value across the LDA and HSE03 methods, the positioning of the upper valence bands are unchanged across the two varying methods. That was the case when switching to LDA+ U calculations that resulted in a lower valence band located at the Γ point, thus increasing the difference between the direct and indirect bandgap.^{428,454}

King *et al.* (Ref. 455) provide a comparison of the theoretically and experimentally determined bandgaps for both the fundamental and optical gaps for single-crystalline epitaxial thin films. The theoretical gaps were higher in value than the experimental gaps for both the cubic and rhombohedral polymorphs. This is due to the theoretical method using a zero temperature limit for calculations and being consistent with a bandgap reduction as temperature increases. The theoretical fundamental and optical gaps for cubic In_2O_3 were 3.10 and 3.72 eV, respectively. Experimentally, the fundamental and optical gaps were 2.93 and 3.55 eV, respectively. Rhombohedral In_2O_3 has larger fundamental gaps than the cubic polymorph but a small optical gap for both theoretical and experimental values. For the cubic (bixbyite) structure, optical transitions between the valence band maximum and conduction band minimum are dipole forbidden. Transitions from the lower valence bands up to the conduction band minimum are forbidden or have optical transition matrix elements that are small. These forbidden transitions are seen among the optical absorption spectrum calculations in that the absorption coefficient has a significant increase that is only seen for energies 0.5 to 1.0 eV above the fundamental bandgap.⁴⁵⁵ Weiher *et al.* (Ref. 237) observed that at around 2.6 eV there was the onset of optical absorption that continued up to 2.94 eV; reported to be the indirect forbidden transitions. This led to the proposal that In_2O_3 contained a conduction band maximum at the Γ point of the Brillouin zone with a valence band maximum away from the Γ point making for an indirect bandgap. This valence band maximum is around 1 eV higher in the gap than the valence band at the Γ point. The model concluded that there is an absorption edge with a direct energy gap of around 3.7 eV at the Γ point for direct allowed transitions, and that there are indirect forbidden transitions between the conduction band maximum and the valence band maximum with an energy gap of 2.6 eV,²³⁷ in good agreement with ARPES studies by Janowitz *et al.* (Ref. 87). All reported bandgap values for the *bcc* and *rh* structure are listed in Table XIX.

Wang *et al.* (Ref. 429) determined the bandgap of both the cubic and rhombohedral polymorphs by plotting the square of the optical absorption coefficient against photon energy. Interestingly, the reported values show that the cubic polymorph has a larger bandgap than the rhombohedral polymorph; 3.7 and 3.0 eV, respectively.⁴²⁹ The cubic bandgap of 3.7 eV is noted to be in good agreement with a value of around 3.6 eV reported by Bender *et al.* (Ref. 456) using photoconductivity measurements.

The bandgap energies have a dependence on the thickness of In_2O_3 films as well. There is a decrease in the optical bandgap from 3.57 to 3.49 eV in a 420 to 35 nm In_2O_3 film. Note that there is an inequivalence between electronic and optical bandgaps in relation to the optically forbidden transitions within the valence and conduction band. This comes from the dipole in the spatial inversion symmetry. When the material is strained, the optical and electronic bandgap trends are equivalent. The observed bandgap changes come from the energy difference of the conduction and valence band. Calculations show that compressing/straining the crystal will increase the bandgap. The calculation results show that the bandgap is altered due to lattice strain and comes from a change in the materials electron affinity. In_2O_3 has deformation potential values greater than ZnO but less than GaAs and GaN. Calculated deformation potential values for In_2O_3 range from -4.2 to -3.66 eV. The valence band deformation potential 4α tends to be positive and has a large role in the overall deformation

TABLE XIX. Bandgaps of the *bcc* and *rh* In_2O_3 structures determined from theory and experiment.

E_g (eV)	Method	Bulk/film	Reference
<i>bcc</i> —Expt.			
2.72	Transmission spect.	Bulk	458
2.93	Optical absorption	Bulk	455
3.10	Optical measurements	Bulk	434
3.55	Optical absorption	Bulk	455
2.61 ^a	Absorption data	Film	237
2.63 ^a	ARPES	Film	87
3.71	ARPES	Film	87
3.75	Absorption data	Film	237
<i>bcc</i> —Calc.			
1.11 ^a	LDA	...	428
1.12	LDA	...	428
1.16 ^a	LDA	...	454
1.21	LDA	...	454
1.82	GGA+U	...	454
2.18 ^a	LDA+U	...	454
2.20 ^a	HSE03	...	459
2.21	LDA+U	...	454
2.44 ^a	HSE03	...	428
2.45	HSE03	...	428
3.10	Calc.	...	455
3.10	HSE03+ G_0W_0/Δ	...	428
3.7	Est.	Bulk	459
3.72	Calc.	...	455
<i>rh</i> —Expt.			
3.02	Optical absorption	Bulk	455
3.16	Optical absorption	Bulk	455
<i>rh</i> —Calc.			
1.23 ^a	LDA	...	428
1.27	LDA	...	428
2.57 ^a	HSE03	...	428
2.61	HSE03	...	428
3.26	HSE03+ G_0W_0/Δ	...	428
3.26	Calc.	Bulk	455
3.40	Calc.	Bulk	455

^aIndirect gap.

potential of the unit cell volume. This positive valence deformation sets In_2O_3 apart from typical III-V and II-VI semiconductors. The primarily flat valence band of In_2O_3 is insensitive to any changes in volume that may arise from strain.⁴⁵⁷

2. Temperature dependence of bandgap energy

Building off the optical properties study by Weiher *et al.* (Ref. 237), Irmscher *et al.* (Ref. 458) observed the nature of the bandgap

and its temperature dependence. The absorption onset of 2.7 eV was found to be intrinsic of In_2O_3 .⁴⁵⁸ To study the transition process of the material, four transition mechanisms were considered. These mechanisms include direct allowed, direct forbidden, indirect allowed, and indirect forbidden. There is a proportionality between the photon energy and the absorption coefficient for each transition mechanism. For direct allowed $\propto (h\nu - E_{g,\text{dir}})^{1/2}$, for direct forbidden $\propto (h\nu - E_{g,\text{dir}})^{3/2}$, for indirect allowed $\propto (h\nu \pm E_{\text{phonon}} - E_{g,\text{indir}})^2$, and for indirect forbidden $\propto (h\nu \pm E_{\text{phonon}} - E_{g,\text{indir}})^3$. It should be noted that the wide ranging and contradicting bandgap values presented in Table XIX are often a result of incorrect use and simplification of these equations. By taking the absorption coefficient from each mechanism and plotting it against the photon energy, the transition will be linearized. At room temperature (300 K) the indirect transition had a value of 2.76 eV. At a low temperature of 9 K the value was 2.94 eV. Both indirect transition values included the phonon energy. This concluded that within In_2O_3 the optical absorption begins at the indirect allowed transitions and are followed by the direct transitions at higher photon energies. This is in agreement with Weiher *et al.* (Ref. 237) findings of an indirect bandgap with the valence band maximum and the N point of the Brillouin zone. There is a temperature dependence of the indirect bandgap that can be determined by using the fitting of a single oscillator model with the measure of electron-phonon coupling strength. Further details on this are discussed in Sec. II. Starting at low temperatures and increasing to room temperature there exists an indirect bandgap of 2.887 eV and an electron-phonon coupling strength of 6.73. At higher temperatures up to 1200 K a drastic decrease of the indirect bandgap was observed, and was strong compared to other semiconductors. At 1200 K the indirect bandgap is reduced by half when compared to the indirect bandgap at lower temperatures. This was predominately caused by the strength of the electron-phonon coupling parameter, which is shown to increase to 8.24 at these higher temperatures. The zero temperature bandgap was calculated to be 2.884 eV, and at 1200 K the bandgap was roughly 1.5 eV.⁴⁵⁸

Schmidt-Grund *et al.* (Ref. 460) investigate the temperature dependence of the dielectric function from 0.5 eV to 8.5 eV of a cubic In_2O_3 thin film deposited onto yttrium stabilized zirconium oxide substrate (YSZ). The authors observed a redshift of the onset of absorption with decrease in temperature from 300 K to 10 K. A model dielectric function approach was employed to differentiate between indirect and direct electronic transitions and to quantify transition energy parameter temperature dependencies. The Bose-Einstein model [Eq. (1)] was used, and a phonon coupling strength of $\alpha_B = 16$ meV, phonon temperature of $\theta = 30.1$ meV, and bandgap shift $\gamma = -0.001$ eV/K were reported for the indirect transition. The reduction in energy toward low temperatures was only half of what was observed previously by Irmscher *et al.* (Ref. 458) who studied bulk samples, and Schmidt-Grund *et al.* suggested the cause being differing crystal quality between film and bulk. However, Schmidt-Grund *et al.* did not consider the possibility that the epitaxial film undergoes thermally induced strain due to differing lattice expansion coefficients between YZO and In_2O_3 , and such strain could strongly affect the band structure property of the In_2O_3 film. For a quantitative value for the temperature dependence of the bandgap, both De Wit *et al.* and Weiher *et al.* (Refs. 438 and 237) report values of $\gamma = -1.1 \times 10^{-3}$ and $\gamma = -1.0 \times 10^{-3}$ eV/K, respectively. Compared to $\beta\text{-Ga}_2\text{O}_3$, γ

values for In_2O_3 are very similar. All reported values for the bandgap of In_2O_3 are compared in Sec. XI.

D. Material properties

Many properties are utilized and studied to further research into materials and their applications. The thermal, phonon, and electrical properties are key to the understanding and implementation of In_2O_3 into technological and device applications. The basic material properties such as the density, bulk modulus, and melting point are some of the most basic parameters that begin to open the door for possible uses on In_2O_2 . The density is regarded as being around 7.1 to 7.2 g/cm³^{406,424,436}. As noted in Sec. IV D 1, Wheeler (Ref. 461) states the density is much lower at 6.3 g/cm³. This value is used to determine theoretical values for certain thermal properties causing some deviation from results using the more widely regarded density of 7.1 to 7.2 g/cm³. The bulk modulus has been reported both theoretically and experimentally. An experimental value of 194.24 GPa⁴⁶² was found to be much higher than a DFT calculated value of 174 GPa.⁴²⁸ With increasing pressure, the bulk modulus is shown to increase. The rhombohedral polymorph has a higher bulk modulus at all pressures than the stable cubic polymorph.⁴⁶³ The melting point of In_2O_3 is in good agreement, averaging a temperature of 1950 °C.^{458,464,465} All reported basic material properties are compared in Sec. XI.

1. Thermal properties

Thermal properties reported for In_2O_3 include CTE, Debye temperature specific heat, thermal diffusivity, and thermal conductivity.

CTE has been studied by multiple groups for multiple varieties of In_2O_3 including powders, bulk crystal, and thin films. Kundra *et al.* (Ref. 466) explored the CTE for powder samples across an increasing temperature range. A CTE was reported to be $7.20 \pm 0.06 \times 10^{-6}/^\circ\text{C}$, similar to the value of $6.15 \pm 0.11 \times 10^{-6}/^\circ\text{C}$ from Weiher *et al.* (Ref. 467 for a crystal sample). Both were considered to be linear with temperature.⁴⁶⁶ Of the cited values, tin doped In_2O_3 (ITO) films used as a substrate have the highest CTE, a value of $10.2 \times 10^{-6}/^\circ\text{C}$, similar to the CTE of glass.⁴⁶⁸ The Debye temperature for In_2O_3 has wide ranging values of 420 to 811 K.^{469,470} Bachmann *et al.* (Ref. 469) extracted a Debye temperature of 420 ± 20 K from the heat capacity but did not specify if the value was for pure In_2O_3 or tin doped samples. Preissler *et al.* (Ref. 470) published a study detailing the electrothermal transport within In_2O_3 single-crystalline films. An effective Debye temperature of 700 K was calculated using the temperature-dependent mobility. Error analysis yields a Debye temperature ranging from 650 to 811 K.⁴⁷⁰ Specific heat (heat capacity) for In_2O_3 has been reported across a wide range of temperatures as well. From 1 to 40 K the heat capacity increases from 1.0×10^{-5} to 2.91 cal/(mol K).⁴⁶⁹ Bachmann's values are contested by Cordfunke *et al.* (Ref. 471). Heat capacity measurements show disagreement with Bachmann's low temperature values. Below 20 K, Bachmann's values are much lower; above 20 K they are higher with much deviation.⁴⁷¹ At a room temperature of 298.15 K, Cordfunke reported a molar heat capacity of 99.08 J/(mol K). Other values reported by Cordfunke include molar heat capacity for temperatures ranging from 6.94 to 346.51 K resulting in 0.069 to 105.592 J/(mol. K).⁴⁷¹ Heat capacity per unit volume was also cited by Yagi *et al.* (Ref. 472) to be 2.58×10^6 J/(m³ K).

At room temperature, thermodynamic calculations were reported for In_2O_3 thin films in the ground state. The specific heat ranged from 18.98 to 19.199 cal/(mol K).⁴⁷³ Wheeler (Ref. 461) offers a different take on the specific heat value. The density of a material along with the known specific heat can be used to calculate a thermal conductivity value. Wheeler lists the material density of In_2O_3 to be 6.3 g/cm³, much lower than the reported density values listed above. The specific heat was also stated to be assumed constant at a value of 0.2 cal/(g K). In_2O_3 was the only material within that study to use an assumed value for specific heat instead of a cited value.⁴⁶¹ This is further evidence that the specific heat of In_2O_3 is one of the lesser researched thermal properties, and what is available is in much disagreement. Converting Wheeler's specific heat in cal/(gK) to units of J/(gK) yields a specific heat 0.837 J/(gK). Finally, Cordfunke *et al.* (Ref. 471) present the molar heat capacity in units of J/(mol K) across a wide temperature range. At room temperature (299.99 K), the molar heat capacity was reported to 99.040 J/(mol K). Using the known molecular weight of In_2O_3 , 277.64 g/mol, the molar heat capacity converts to 0.356 J/(gK). The specific heat values are listed and compared in Sec. XI.

Thermal diffusivity values are in better agreement than the specific heat values, especially for tin doped In_2O_3 thin films. The reported thermal diffusivity for thin film samples ranges from 1.2×10^{-6} to 2.27×10^{-6} (Refs. 472 and 474) with some dependence on O₂ flow rate during thin film fabrication. Using 100% Ar gas during deposition, thermal diffusivity was 2.24×10^{-6} m²/s. Values peaked at 2.27×10^{-6} m²/s with an increase in the O₂ flow rate before falling to 1.53×10^{-6} m²/s as the flow ratio of O₂ increased.⁴⁷⁴ Of note, these values are almost double the thermal diffusivity of amorphous ITO and Indium Zinc Oxide (IZO) films.^{472,475} With the values of thin films being similar, bulk single crystal thermal diffusivity appears to deviate. At 7.0×10^{-6} m²/s the bulk crystal thermal diffusivity is significantly higher than the reported thin film values.⁴⁶⁵ However, compared to Si, In_2O_3 has a thermal diffusivity of more than one order of magnitude less.⁴⁷⁶

The thermal conductivity of bulk crystal In_2O_3 has only recently been reported due to the availability of high quality bulk crystal samples. In a recent study by Xu *et al.* (Ref. 465) the thermal conductivity was studied across multiple crystal samples and orientations, utilizing various annealing conditions. Peak thermal conductivity ranged from 100 to 5000 W/(mK) with the lowest value coming from an as-grown sample with no specified annealing conditions. Across six samples, each subsequent peak thermal conductivity occurred at lower temperatures, possibly pointing to disorder evolution in the samples. Along the (111) orientation, the peak thermal conductivity of 5000 W/(mK) was achieved at 20 K following multiple annealing conditions.⁴⁶⁵ This peak thermal conductivity value is comparable to diamond⁴⁷⁷ and silicon,⁴⁷⁸ and only slightly lower than Al₂O₃⁴⁷⁹ at 20 K. Room temperature thermal conductivity was reported to be around 15 W/(mK), which is three times larger than the room temperature thermal conductivity of Indium Tin Oxide (ITO) thin films.⁴⁷⁴ Bulk crystal temperature dependence of the thermal conductivity shows a room temperature value of 13.09 W/(mK) that falls to 2.89 W/(mK) at 800 °C.⁴³⁶ Another temperature dependence study shows a quadratic behavior as the thermal conductivity decreased from 7 to 10 W/(mK) at room temperature to around 2 to 3 W/(mK) at 1200 K.⁴⁸⁰ Thin film samples of In_2O_3 are usually tin doped and referred to ITO, which has received considerable attention in research for device

applications.^{481,482} Fermi gas models estimate the electronic thermal conductivity of ITO thin films to range from 1.0 to 1.4 W/(mK) for thin films increasing in thickness from 27 to 62 nm.⁴⁷² Other ITO thermal conductivity values derived from the thermal diffusivity range from 4.00 to 5.86 W/(mK) and show dependence on the O₂ flow rate.⁴⁷⁴

In₂O₃ has been considered as a thermoelectric oxide for applications that can generate electrical power from heat. Thermoelectric devices are measured by a dimensionless figure of merit, ZT. Thermal conductivity resides in the denominator of the figure of merit, $ZT = S^2 T \sigma / \lambda$, where S is the thermopower or Seebeck coefficient, T is temperature, σ is electrical conductivity, and λ is the thermal conductivity. While most power electronics applications such as transistors and diodes strive for higher thermal conductivity values, thermoelectric devices rely on lower values of thermal conductivity. Bérardan *et al.* (Ref. 483) report how Ge doping in In₂O₃ resulted in a decreased thermal conductivity and a ZT FOM almost 4× higher than undoped In₂O₃. Thermal conductivity has two components due to charge carriers and phonons. At 1273 K, the thermal conductivity of undoped In₂O₃ is mainly comprised of thermal transporting phonons. When Ge doping is added, the charge carrier component of thermal conductivity increases, strongly decreasing the electrical resistivity as well. Past the solubility limit, Ge doping will decrease the charge carrier thermal conductivity contribution and increase the electrical resistivity. Undoped In₂O₃ has a reported thermal conductivity of around 3 W/(mK) while the addition of Ge doping lowers the thermal conductivity to 0.6 W/(mK) in In_{1.8}Ge_{0.2}O₃, enhancing the thermoelectric FOM from 0.1 to 0.45.⁴⁸³ All reported thermal property values are compared in Sec. XI.

2. Phonon properties

The phonon properties of In₂O₃ are important for understanding of electrical and thermal transport, charge carrier mobility, Debye temperature, as well as Raman, IR, and vibrational modes. The cubic crystal structure of In₂O₃ has a primitive unit cell containing 40 atoms for a total of 117 optical phonon modes. The irreducible representation for the optical modes is⁴⁸⁴

$$\Gamma_{opt} = 4A_g + 5A_u + 4E_g + 5E_u + 14T_g + 16T_u.$$

The A_g, E_g, and T_g are Raman-active while T_u are the IR-active modes. The remaining A_u and E_u modes are silent. It should be noted that previous works list the T_g Raman-active modes as F_g or F_{2g} and the T_u IR-active modes as F_u.^{485,486} The IR and far-IR active modes have been determined using DFT calculations and are listed in Table XX. Group theory predicts that all 16 modes should be present but only 11 modes had been detected experimentally until recently by Stokey *et al.* (Ref. 484). TO and LO modes for T_u 12–16 contain low intensities, which offers a possible explanation for why they remained undetected experimentally for so long. Stokey *et al.* were able to observe and determine the far-IR phonons. Since this is the first experimental recording of these modes there were no such values to compare to within the literature except for their own DFT analysis. There was an overall good agreement between the calculated and experimental phonon modes.⁴⁸⁴ Experimental IR and far-IR TO and LO modes are also included in Table XX. The set of TO and LO modes reported by Sobotta *et al.* (Ref. 486) are within decent agreement with the full set of DFT calculated modes except for the absence of the far-IR

TABLE XX. In₂O₃ TO and LO IR and far-IR active phonon mode frequencies determined by theory and experiment. All frequencies are in units of cm⁻¹.

Mode	ω_{TO} Calc. ^a	ω_{TO} Expt. ^b	ω_{TO} Expt. ^c	ω_{TO} Expt. ^d	ω_{LO} Calc. ^a	ω_{LO} Expt. ^b	ω_{LO} Expt. ^c
T _u (1)	588.61	594.9 ± 0.7	612	595.5	611.35	624 ± 0.3	625
T _u (2)	553.45	561.0 ± 0.9	570	560.5	569.28	579.1 ± 0.3	578
T _u (3)	527.83	534.0 ± 1.3	542	534.1	540.15	549.1 ± 5.9	548
T _u (4)	460.07	470.0 ± 0.1	489	...	503.84	518.0 ± 0.6	513
T _u (5)	409.12	408.2 ± 0.2	409	408.0	460.01	470.1 ± 0.2	...
T _u (6)	386.87	384.7 ± 0.1	380	386.2	394.19	394.0 ± 0.1	391
T _u (7)	363.37	362.2 ± 0.2	362	361.7	383.47	383.2 ± 0.1	381
T _u (8)	330.41	327.3 ± 0.1	322	327.3	339.21	337.4 ± 0.1	352
T _u (9)	310.89	309.7 ± 1.2	301	307.3	312.26	310.4 ± 1.1	318
T _u (10)	260.02	260.2 ± 5.3	245		260.09	260.9 ± 4.7	245
T _u (11)	214.71	216.3 ± 0.4	205		216.00	217.6 ± 0.2	224
T _u (12)	171.00	172 ± 0.9			171.29	172.4 ± 0.1	
T _u (13)	152.81	154.2 ± 1.1			152.85	154.4 ± 1.1	
T _u (14)	148.44	150.5 ± 1.2			148.48	150.6 ± 2.1	
T _u (15)	123.27	126.4 ± 1.7			123.32	126.7 ± 0.3	
T _u (16)	100.86	99.0 ± 0.2			100.86	99.1 ± 0.2	

^aDFT calculations from Ref. 484.

^bBest-match model dielectric function analysis from Ref. 484.

^cReflectance from Ref. 486.

^dIR ellipsometry from Ref. 487.

modes. Sobotta *et al.* used low quality samples from a pellet source material which could provide reasoning for some of the slight deviation from DFT values. Feneberg *et al.* (Ref. 487) only reported TO modes with the absence of T_u (4) and no modes below 300 cm^{-1} .

The Raman-active modes have been extensively studied by Kranert *et al.* (Ref. 485) and Garcia-Domene *et al.* (Ref. 488). *Ab initio calculations* were reported showing the frequencies for all 22 Raman modes expected from group theory. Experimental Raman modes were also reported using Raman spectroscopy. All values are listed in Table XXI. The calculated work from Garcia *et al.* and symmetry assignments that were used show good agreement with Raman selection rules of Kranert *et al.* Kranert *et al.* performed two experimental tests with the first at a spectra excitation of $\lambda = 532\text{ nm}$ at room temperature. This sample was a (111)-oriented film. The second experiment used a spectra excitation of $\lambda = 325\text{ nm}$ at 10 K. The values for this “sample” consist of averages across multiple samples. Therefore, only rough comparisons can be made between the two experimental sets of values found by Kranert *et al.*⁴⁸⁵ Across the experimental values reported by both groups, each of the 22 predicted and calculated Raman modes for In_2O_3 are seen.

In_2O_3 has a polar nature due to the bonding between the In and O atoms. This means that the carrier mobility within In_2O_3 is limited

TABLE XXI. In_2O_3 Raman phonon mode frequencies determined from theory and experiment (cm^{-1}). Note that the F_g Raman modes are equivalent to the T_g Raman modes listed in the irreducible representation above.

Mode	Calc. ^a	Expt. ^b	Expt. ^c	Expt. ^d
$F_{2g}(1)$	106	108	109	112
$F_{2g}(2)$	114	118	119	...
$A_g(1)$	128	131	133	135
$F_{2g}(3)$	148	152	154	...
$E_g(1)$	165	169	...	172
$F_{2g}(4)$	199	205	...	209
$F_{2g}(5)$	204	211	...	215
$F_{2g}(6)$	302	306	306	307
$A_g(2)$	302	306	309	310
$E_g(2)$	308	317
$F_{2g}(7)$	312	321
$F_{2g}(8)$	356	365	369	369
$F_{2g}(9)$	379	392
$E_g(3)$	385	396	...	400
$F_{2g}(10)$	438	454
$F_{2g}(11)$	447	467	...	469
$A_g(3)$	476	495	499	499
$F_{2g}(12)$	499	513	...	520
$F_{2g}(13)$	520	547
$E_g(4)$	565	590	...	589
$A_g(4)$	576	...	634	629
$F_{2g}(14)$	600	628	636	633

^aReference 488.

^bReference 488— $\lambda = 633\text{ nm}$ and $T = 300\text{ K}$.

^cReference 485— $\lambda = 532\text{ nm}$ and $T = 300\text{ K}$.

^dReference 485— $\lambda = 325\text{ nm}$ and $T = 10\text{ K}$.

by acoustic and optical phonon scattering. Since the stable polymorph of In_2O_3 is cubic and centrosymmetric, piezoelectric scattering does not need to be accounted for. Instead, acoustic deformation potential (ADP) makes up the acoustic phonon scattering,⁴⁷⁰ with an ADP value reported to be -4.31 eV .⁴⁵⁷ As stated in the electronic structure section, the conduction band is mainly comprised of $\text{In}(5s)$ orbitals.⁴²⁸ This s-orbital symmetry and character causes the scattering from optical deformation potential to disappear, similar to what has been observed in GaAs.⁴⁸⁹ The LO phonons are the cause of the optical phonon scattering.⁴⁷⁰ Preissler *et al.* (Ref. 470) modeled how the mobility is altered due to polar optical phonon scattering with changing carrier concentration, and predicted a maximum room temperature mobility, which is further discussed in Sec. IV D 3. Polar optical phonon scattering is dominant for low carrier concentrations and the acoustic deformation potential scattering can be considered negligible with increasing carrier concentrations.⁴⁷⁰ This statement refutes previous findings from Weiher *et al.* (Ref. 434) stating that acoustic phonon scattering and impurity scattering are not negligible, but are the main forms of scattering in the crystal. When looking at polar optical phonon scattering with respect to the electron carrier concentration, the mobility is shown to decrease for carrier densities from 2.0×10^{18} to $2.0 \times 10^{19}\text{ cm}^{-3}$. This means that optical phonon emission in the form of kinetic electron energy is nearing the energy of the LO phonons. Once carrier concentration increases past this point, mobility increases due to LO-phonon plasmon coupling.^{470,490} The Debye temperature, as discussed in Sec. IV D 1, along with the number of LO phonon modes, helps to characterize the polar optical phonon scattering.

Due to the indirect nature of absorption, the phonons provide momentum to allow for unoccupied conduction band states off the Brillouin Zone center to be reached. First principles calculations show LO phonons dominating indirect absorption. When considering phonon modes for the intraband transitions, it can be assumed that the main factor for any phonon assisted absorption comes from LO phonon modes. Fröhlich models for electron phonon coupling give insight into this process. Modeling shows that when comparing In_2O_3 to another TCO like SnO_2 , In_2O_3 has 50% less phonon assisted indirect absorption. SnO_2 has stronger electron-phonon coupling. The difference in the static and high frequency dielectric constants is larger for SnO_2 , stemming from its more ionic nature compared to In_2O_3 . When comparing LO phonon frequencies of SnO_2 and In_2O_3 , the largest frequency of SnO_2 is greater than the largest frequency of In_2O_3 . The smaller electron phonon coupling and smaller LO phonon frequency attribute to In_2O_3 having a weak indirect absorption compared to SnO_2 .⁴⁵²

In regard to the rhombohedral In_2O_3 phase, Wang *et al.* (Ref. 420) reported the irreducible representations for the optical modes in a single crystal to be

$$2A_{1g} + 2A_{1u} + 3A_{2g} + 2A_{2u} + 5E_g + 4E_u.$$

Due to the primitive cell and its two In_2O_3 molecular units, there are 30 Γ point vibrational modes. Due to the center of symmetry, the allowed Raman modes are IR forbidden, and the allowed IR modes are Raman forbidden. The A_{1u} and A_{2g} modes are inactive for both Raman and IR modes. A_{1g} and E_g are considered Raman active while A_{2u} and E_u are considered IR active. The acoustical modes are $1A_{2u} + 1A_u$.^{420,491} The difference in the space groups and crystal symmetry

of the cubic and rhombohedral polymorphs causes the difference in the vibrational modes.⁴²⁰

3. Electrical properties

The electrical properties reported help to show the material characterization and device potential of In_2O_3 and include electron affinity, electrical breakdown field, static and high frequency dielectric constants, effective mass, and electron mobility. The electron affinity, often an important parameter for band alignment and heterojunctions, is somewhat contested. An early value of around 3.3 eV was determined using theory.⁴⁹² This value is the lowest electron affinity that is cited within this review. Most reported values range from 4.3 to 4.5 eV.^{493–495} Lang *et al.* determined the electron affinity to be around 3.7 eV from the experimental values of work function (4.3 eV), bandgap, and Fermi level of highly conductive In_2O_3 films.⁴⁹⁶ In studying tunneling solar cells, the theoretical electron affinity of 3.3 eV was considered. It was found that an electron affinity below that value increased the solar cell efficiency while a higher affinity caused the efficiency to deteriorate.⁴⁹⁷ The electrical breakdown field of In_2O_3 crystals or thin films is not a parameter of great interest, making it hard to find throughout literature. Following Higashiwaki *et al.* (Ref. 147) and their hypothesized breakdown field values based on a materials bandgap, In_2O_3 would have a breakdown field of around 3 to 4 MV/cm. Solely based off of the bandgap, this would make the breakdown field comparable to GaN and 4H-SiC.¹⁴⁷ Values for the electron affinity and electrical breakdown field are compared in Sec. XI.

The static and high frequency dielectric constants of In_2O_3 are reported to be in good agreement. In regard to the static dielectric constant, both theoretical and experimental values are around 9.0,^{406,457,463} with Hamberg *et al.* (Ref. 406) stating that a value of 9.5 has been used in calculations previously with no reason as to why.^{498,499} The high frequency dielectric constant have very little deviation and are reported to be around 3.82 to 4.0, with LDA-DFT calculations yielding the lowest value.^{406,457,463} According to Walsh *et al.* (Ref. 463), there is no evidence of anisotropy within the cubic bixbyite structure, and very little anisotropy within the rhombohedral structure for both the static and high frequency dielectric constants.⁴⁶³ Alongside producing the current state of the art work for the phonon modes of In_2O_3 , Stokey *et al.* (Ref. 484) also reported on the static and high frequency dielectric constants. The high frequency dielectric constant ϵ_{∞} was approximated from wavelength-by-wavelength analysis to be 4.05 ± 0.05 , in good agreement with the DFT predicted ϵ_{∞} of 4.128⁴⁸⁴ and 4.08 from Feneberg *et al.* (Ref. 487). The static dielectric constant ϵ_{DC} was then determined from the LST relationship to be 10.55 ± 0.07 , again, in good agreement with the DFT predicted value of 10.74 from the same work.⁴⁸⁴ Values for the static and high-frequency dielectric constants are compared in Sec. XI.

The electron effective mass is another heavily researched electrical parameter of In_2O_3 . This parameter has been reported both experimentally and theoretically using methods such as Hall and Seebeck coefficients, ARPES, and LDA. The possibility of anisotropy has also been examined for both the cubic and rhombohedral polymorphs. There is a wide range of reported effective mass values found throughout the literature and summarized in Table XXII. An early report dating back to 1962 by Weiher (Ref. 434) stated that the effective mass was as high as 0.55 m_e from single crystal samples. The crystal quality

TABLE XXII. Effective mass values determined from theory and experiment for bcc In_2O_3 .

Effective mass (m_e)	Method	Reference
Expt.		
0.14	Hall–Seebeck	500
0.18	Plasma frequency	487
0.208	Optical Hall effect	484
0.30	Hall–Seebeck	470
0.40	Plasma frequency	487
0.55	Hall-thermoelectric power	434
Calc.		
0.16	LDA	452
0.18	LDA	428
0.22	HSE03	428

of the sample used must be considered as a possible reason for such a larger value. At the time, quality and purity of single crystal In_2O_3 was lacking. A few decades later, a much smaller value of 0.14 m_e was determined using Hall and Seebeck coefficients.⁵⁰⁰ The very same method also produced an effective mass of $0.30 \pm 0.03 m_e$.⁴⁷⁰ Finally, using a combination of a Drude model and Hall-effect measurements, Feneberg *et al.* (Ref. 487) reported a zero-density effective mass of 0.18 m_e . This value is in very good agreement with the calculated effective mass of 0.16 m_e found by Peelaers *et al.* (Ref. 452) using LDA. Once the carrier concentration surpassed $n = 5 \times 10^{19} \text{ cm}^{-3}$, the effective mass increased reaching a value of 0.40 m_e at $n = 10^{21} \text{ cm}^{-3}$.⁴⁸⁷ The wide range of values could be a result of the pronounced nonparabolic nature of the conduction band near the Γ point of In_2O_3 . This causes the effective mass to increase with increasing carrier concentration. In a recent study by Stokey *et al.* (Ref. 484) optical Hall effect measurements were used to determine the near zero-density effective mass, found to be $0.208 \pm 0.006 m_e$. This near zero-density effective mass is in good agreement with the other zero-density value of 0.18 m_e found by Feneberg.⁴⁸⁷ Fuchs *et al.* (Ref. 428) reported calculations that support an increasing effective mass with an increased electron carrier density. The effective mass was found to increase up to 0.30 m_e for carrier densities that eclipse 10^{20} cm^{-3} . This value is still well below the outlying large effective mass of 0.55 m_e .⁴³⁴ As expected for a bcc structure no anisotropy has been reported for the effective mass.

Fuchs *et al.* (Ref. 428) observes the difference in effective mass values for cubic and rhombohedral polymorphs of In_2O_3 . From a theoretical approach Fuchs *et al.* calculated an effective mass for cubic In_2O_3 found to be nearly isotropic with values of 0.18 m_e and 0.22 m_e for LDA and HSE03 methods, respectively. The rhombohedral polymorph took into account two independent directions that makeup the effective mass tensor. The anisotropy was considered to be almost negligible with values of $m_x = m_y = 0.22 m_e$ and $m_z = 0.23 m_e$ from HSE03 calculations. LDA calculations showed an effective mass of 0.16 m_e for all directions.⁴²⁸

The electron mobility for In_2O_3 single crystals and thin films appears to be as wide ranging as the bandgap values. The electron mobility is effected by many aspects and variables including crystalline quality, carrier concentration, and temperature. The theoretical limits

of the electron mobility are stated to be $270 \text{ cm}^2/(\text{V s})$ ⁴⁷⁰ and $274 \text{ cm}^2/(\text{V s})$,⁵⁰¹ with the latter being determined using Matthiessen's rule. Experimental values are wide ranging, spanning from as low as $7.81 \text{ cm}^2/(\text{V s})$ for undoped In_2O_3 films⁵⁰² to as high as $180 \text{ cm}^2/(\text{V s})$ to $190 \text{ cm}^2/\text{V s}$ and even $226 \text{ cm}^2/(\text{V s})$ for bulk crystals.^{440,464,501} Of the cited values, thin films tend to have lower values than those of single crystal samples. There is also some orientation dependence on the electron mobility of both UID In_2O_3 thin films and ITO thin films. Along the (111) orientation, UID thin films are reported to have a mobility of $110 \text{ cm}^2/(\text{V s})$,⁵⁰³ while UID samples along the (001) orientation have a mobility of only $55 \text{ cm}^2/(\text{V s})$.⁵⁰⁴ In ITO thin films, the (222) and (400) directions result in mobilities of $22.30 \text{ cm}^2/(\text{V s})$ to $30.00 \text{ cm}^2/(\text{V s})$ and $43.97 \text{ cm}^2/(\text{V s})$ to $80.54 \text{ cm}^2/(\text{V s})$, respectively.⁵⁰⁵ King *et al.* (Ref. 455) reported on the mobility of the differing cubic and rhombohedral polymorphs. While the cubic was grown using molecular beam epitaxy (MBE) and the rhombohedral was grown using MOCVD, the single rhombohedral sample possessed a higher mobility.⁴⁵⁵ Weiher *et al.* (Ref. 434) analyzed the experimental Hall mobility with temperatures from around 300 to 90 K, comparing theoretical equations to experimental results. Bierwagen *et al.* (Ref. 501) also reported on the mobility's temperature dependence. Room temperature measurements showed a maximum mobility of $226 \text{ cm}^2/(\text{V s})$,⁵⁰¹ surpassing the previously reported maximum mobility value of $160 \text{ cm}^2/(\text{V s})$ for bulk samples at room temperature by Weiher (Ref. 434). The mobility was shown to increase as the temperature decreased from 300 to 100 K, peaking at $1290 \text{ cm}^2/(\text{V s})$. Polar optical phonon scattering hinders the mobility at room temperatures. Below 100 K, dislocation and impurity scattering take over. Comparing works by Bierwagen *et al.* and Weiher (Refs. 501 and 434), it is evident from the room temperature and peak mobility values that high crystalline quality and purity plays a large role in increasing mobility.^{434,501} A few years after the work by Bierwagen *et al.*, Galazka *et al.* (Refs. 440 and 464) produced mobility values for bulk In_2O_3 of $180 \text{ cm}^2/(\text{V s})$ and $190 \text{ cm}^2/(\text{V s})$, respectively. All cited electron mobility values are listed and compared in Sec. XI.

E. Doping and defects

In_2O_3 in its undoped form can be considered a transparent semiconducting oxide. In this form, with near perfect stoichiometry, In_2O_3 and other wide bandgap oxides exhibit insulating behavior. When large amounts of dopants are implanted, In_2O_3 and other oxides are considered TCOs with n-type conductivity being seen most commonly. When dopants are added, the conductivity will be increased beyond the level of the unintentionally doped sample.⁵⁰⁶ There are many possible dopants that have been implanted into In_2O_3 with tin being the most widely used dopant. An entirely separate review could be compiled just on tin doped In_2O_3 (ITO) as it is such a widely studied oxide with a wide range of device applications.^{481,507,508} Bel Hadj Tahar *et al.* (Ref. 509) reported on the electrical properties of tin doped In_2O_3 with a few comparisons to undoped In_2O_3 . With a multitude of preparation methods, the properties of ITO are heavily dependent on the specific method used. When doping with tin, it takes the role of the cationic dopant, replacing the indium and yielding n-type conductivity while still preserving the oxide's charge neutrality. According to Bel Hadj Tahar *et al.*, there is a theoretical maximum carrier density from the tin doping that is dependent on the tin concentration. But it was stated that the carrier concentration does not reach the levels that

are theoretically expected.⁵⁰⁹ The overall carrier mobility of tin doped In_2O_3 is lower than that of UID samples. At the time of reporting, the highest room-temperature mobility of undoped In_2O_3 was around 160 to $170 \text{ cm}^2/(\text{V s})$,⁴⁵⁴ later improved upon as seen from the above In_2O_3 Electronic Properties section, Sec. IV D 3. Tin doping increases the free carrier scattering and yields a mobility lower than that of undoped samples. With increasing carrier concentration the mobility has been shown to decrease. Ionized centers appear to be a large cause of lower mobility within ITO thin films.⁵⁰⁹ Shigesato *et al.* (Ref. 510) published a study on how tin doping altered the electronic transport of In_2O_3 thin films. With increasing tin wt. % up to 5%, Hall mobility and resistivity dropped sharply with around 1% of tin. The carrier density was shown to increase up to $5 \times 10^{20} \text{ cm}^{-3}$ at 1% tin. The mean free path also decreased with added tin.⁵¹⁰ With increasing tin, some amount of tin remain electrically inactive.^{509,510} If it is possible to decrease the amount of inactive tin, the resistivity of ITO will improve by means of fewer scattering centers and increasing free carrier concentrations. Tin was reported to be the origin of donor centers as well as scattering centers.⁵¹⁰

Titanium is another commonly used dopant in In_2O_3 .^{511–515} Gupta *et al.* (Ref. 511) reported that using titanium doping in PLD grown samples had some advantages over tin doping. The surface roughness of was found to be 2 nm,⁵¹¹ half of the surface roughness of tin doped In_2O_3 .⁵¹⁶ Mobility values increased with substrate temperature, peaking at $154 \text{ cm}^2/(\text{V s})$ all while the resistivity decreased. Gupta *et al.* (Ref. 511) state that these mobility values are substantially better than other TCOs that are commercially available, making titanium doped In_2O_3 a viable candidate in the commercial application space.⁵¹¹

One uncommon dopant used in In_2O_3 seen in literature was molybdenum.^{517,518} Addition of Mo into the In_2O_3 thin films resulted in a reduction of the ionized impurity scattering and an increase in the electron mobility. Mo(4d) states do not experience much hybridization with the In(5s) states. The lack of hybridization between the Mo(4d) and In(5s) states causes a separation of the conduction from the donors and reduces the scattering from ionized impurities. DFT calculations show the molybdenum doping residing high in the conduction band despite the low hybridization.⁵¹⁸ If an undoped sample was shown to contain both cubic and rhombohedral features, the addition of molybdenum suppressed the rhombohedral phase. Compared to equal concentrations of tin doping, molybdenum resulted in much lower ionized impurity scattering and a larger carrier mobility.⁵¹⁸ Using molybdenum doping, some reported carrier mobility values are 65.3, and 80 to $130 \text{ cm}^2/(\text{V s})$.^{407,517,519} Other In_2O_3 dopants across literature are hydrogen,⁵²⁰ tungsten,⁵²¹ iron,^{522,523} zinc,^{434,524,525} and tantalum.⁵¹⁵

Defects and impurities play a large role in shaping the overall quality of the oxide as well as the electrical properties. Oxygen vacancies are seen as the most probable donor other than the indium interstitial according to theory, while there is no clear consensus on the prominent acceptor.^{506,526,527} Reunchan *et al.* (Ref. 528) used first principles DFT studies to explore the vacancy defects within In_2O_3 .⁵²⁸ It was concluded that oxygen vacancies are double donors while indium vacancies are triple acceptors. The indium vacancies also act as compensation centers that occur within n-type In_2O_3 ; thus reducing n-type carriers. While this seems like it could lead to possible p-type In_2O_3 , the high formation energy makes it unlikely. The first principles

calculations were inconclusive in regard to whether oxygen vacancies were deep or shallow donors. Regardless of the donors being shallow or deep, it would not help in achieving p-type In_2O_3 as the oxygen vacancies would negate the doping.

With a lack of experimental work into the vacancies and defects of In_2O_3 , Korhonen *et al.* (Ref. 506) utilized positron annihilation spectroscopy to further study the vacancy defects in bulk and doped thin film samples. Doppler broadening shows that the UID bulk sample had one of the lowest vacancy concentrations of all the studied samples. Thin films exhibit growth kinetics that make vacancy formation favorable while bulk samples reveal little to no vacancy detection compared to thin films.⁵⁰⁶ The doping used for the thin film samples were tin and magnesium. A single type of vacancy was seen in the tin doped thin films after annealing in oxygen. Vacuum annealed samples exhibit a different type of defect compared to the oxygen annealed samples. The vacuum annealing caused an increase in the oxygen vacancies that resulted in an increased conductivity when compared to the oxygen annealed samples.⁵⁰⁶ Analysis of the Mg doped samples resulted in similar trends just with smaller changes. Intrinsic defects overcompensated Mg,⁵²⁹ resulting in n-type conductivity.⁵⁰⁶ It was concluded that in highly tin doped thin films (ITO), the interstitial oxygen was the compensating acceptor and not the indium vacancies.

Building off of Korhonen's work, Makkonen *et al.* (Ref. 530) identified the vacancy defect complexes of In_2O_3 and other transparent semiconducting oxides. Within the cubic structure of In_2O_3 there are two In sites as discussed in Sec. IV A. Each site has a different makeup of the oxygen atoms around it. There are two missing oxygen sites surrounding each indium vacancy. Makkonen *et al.* reported an overall agreement with Korhonen *et al.* (Ref. 506) for the open-volume defects that were observed in oxygen annealed samples.

F. Summary of In_2O_3 property values

Tables XXIII and XXIV highlight a summary of the properties reviewed for In_2O_3 . Values for each of the properties are presented along with references and notation of whether they are experimental or calculated findings. Where relevant, anisotropy is denoted.

V. ZINC OXIDE

The stable phase of zinc oxide or zincite (ZnO) is a widely researched, semiconducting oxide with a well-established high quality material base, with similar properties to GaN.⁵³³ However, ZnO cannot be made readily p-type conductive as a result of the O(2p) orbitals that reside at the top of the valence band. The direct bandgap and doping of ZnO make it a viable candidate for device applications such as optoelectronics,⁵³⁴ gas sensors,⁵³⁵ thin film transistors,⁵³⁶ and solar cells.^{537,538} The crystal and electronic structures for ZnO are highlighted throughout this section, as well as the thermal, phonon and electrical properties. A number of excellent reviews of ZnO properties have been published already and can be further referenced beyond this review.^{539–541}

A. Crystal structure

The stable hexagonal wurtzite phase of ZnO gives rise to each individual anion being surrounded by cations at each of the four anion corners. This creates a tetrahedral coordination that is common in covalent sp^3 bonding. It is possible for the material to be ionic even

TABLE XXIII. Summary of theoretical and experimental structural and thermal properties of In_2O_3 . Common names of indium oxide, indium sesquioxide, and india.

Stable phase	<i>bcc</i> - In_2O_3	Ref. 422
Stable structure	Cubic (BCC)	<i>Ia</i> ³ (#206)
	$a = 10.118 \text{ \AA}$	Ref. 420
	$a = 10.117 \text{ \AA}$	Refs. 421 and 423
Metastable phases	<i>bcc</i> - In_2O_3 -I <i>rh</i> - In_2O_3 <i>o'</i> - In_2O_3 α - Gd_2S_3 type	
Density (g/cm ³)	7.12 7.2	Expt. ⁴⁰⁶ Calc. ⁴²⁴
Bulk modulus (GPa)	194.24 174–192.66	Expt. ⁴⁶² Calc. ^{428,459}
T_m (°C)	1949–1950	Expt. ^{458,464,465}
Debye temp. (K)	700–811 420	Calc. ^{469,470} Expt. ⁴⁶⁹
Specific heat (J/(gK))	0.356 ^a 0.837 ^b	Calc. ⁴⁷¹ Calc. ⁴⁶¹
Thermal cond. (W/(mK))	10–15.0	Expt. ^{436,480,495}
Thermal diff. (mm ² /s)	1.2 7.0	ITO film Expt. ⁴⁷² Calc. ⁴⁶⁵
CTE ($\times 10^{-6}/\text{K}$)	6.15–10.2	Expt. ^{436,466–468}

^aCalculated from molar heat capacity.

^bConverted from cal/(g °C).

with this covalent bonding and in this sense ZnO can be seen as an exception among II-VI compound semiconductors. The ionicity of wurtzite structure is considered borderline straddling between a covalent semiconductor and an ionic semiconductor. Along with the thermodynamically stable wurtzite structure, there are two other polymorphs: cubic zinc blende and rocksalt structures. Rocksalt structure is formed at very high pressures while zinc blende is formed when grown on another cubic substrate. Figure 21 shows the crystal structures of the three ZnO phases.

Hexagonal wurtzite contains four atoms per unit cell,⁵⁴² one of the fewest atoms per unit cell of any oxide discussed in this review. Hexagonal wurtzite ZnO belongs to the space groups $P6_3mc$ (#186).⁵⁴² The lattice parameters have been extensively reported, both theoretically from first principles and experimentally via x-ray diffraction (XRD).^{543,544} Gerward *et al.* (Ref. 544) used XRD to find constants of $a = 3.2475 \text{ \AA}$ and $c = 5.2075 \text{ \AA}$. The calculated lattice constants were slightly larger than those reported experimentally. Catti *et al.* (Ref. 545) used Hartree-Fock *ab initio* calculations to find constants of $a = 3.286 \text{ \AA}$ and $c = 5.241 \text{ \AA}$.

The zinc blende polymorph has cubic structure belonging to space group $F\bar{4}3m$ (#216).⁵⁴² Lattice constants were determined experimentally using XRD and TEM,⁵⁴⁶ and theoretically using Hartree-Fock.⁵⁴⁵ Similar to the wurtzite structure, the calculated lattice constants were slightly larger than those determined experimentally. The lattice constant a was reported to range from 4.463 to 4.619 \AA .^{545–547}

The cubic rocksalt polymorph belongs to space group $Fm\bar{3}m$ (#225).⁵⁴² The lattice constant was determined both experimentally

TABLE XXIV. Summary of theoretical and experimental electrical and optical properties of In_2O_3 .

Electron affinity (eV)	3.3 3.7 4.3 4.45	Calc. ⁴⁹² Expt. ⁴⁹⁶ Ref. ⁴⁹⁴ Expt. ⁴⁹⁵
Breakdown field (MV/cm)	3–4	Pred. ¹⁴⁷
m_e^*	0.16–0.23 0.14–0.55 $0.18\text{--}0.24\text{m}^{CB}$ $0.27\text{--}0.28\text{m}^{VB}$	Calc. ^{427,428,452} Expt. ^{434,500} Calc. ⁵³¹ Calc. ⁵³¹ Calc. ^{470,501}
μ_e [cm ² /(V s)]	270–274 7.81–190	Expt. ^{434,440,455,500,502}
Gap type	Debated	Ref. ⁴⁵⁴
E_g (eV)	1.11–3.72 ^a 2.72–3.55 2.619–2.63	Bulk calc. ^{428,454,455,459} Bulk expt. ^{434,455,458} Film indirect expt. ^{87,237}
ϵ_0	3.71–3.75 9.0–10.74 8.9	Film direct expt. ^{87,237} Calc. ^{457,463,484} Expt. ⁴⁰⁶
ϵ_∞	3.82–4.128 4.0–4.05	Calc. ^{428,457,463,484,487} Expt. ^{406,484}
Phonon modes		
IR active	16F_u	Refs. ^{484, 486} , and ⁵³²
Raman active	4A_g , 4E_g , 14F_g	Refs. ^{484, 485} , and ⁵³²

^aIncludes direct and indirect gap.

and theoretically.⁵⁴⁷ a was found to range from 4.271 Å to 4.30 Å, a smaller difference between the experimental and theoretical constants than the other structures. All cited lattice constants for the three ZnO structures are listed in Table XXV. Unless stated otherwise, all discussion throughout this refers to the stable, single crystalline, wurtzite phase.

The c/a parameter of ZnO offers insight into the lattice structure. The ideal hexagonal wurtzite structure has a value of 1.633. The c/a ratio for the cited lattice constants range from 1.595 to 1.604, slightly lower than the ideal structure. The difference could be attributed to the ionicity of the ZnO crystal and the stability of the lattice. Causes of lattice constant deviations include defects caused by oxygen vacancies and zinc antisites. Extended defects which include threading dislocations are often times responsible for lattice constant increases. Free charge has been shown to be the factor that causes greater lattice expansion in relation to the deformation potential of the conduction band minimum.⁵⁴² Further details on the defects of ZnO are discussed in Subsection V E.

B. Growth

ZnO bulk crystal and thin films have been grown using multiple methods. Bulk crystals have been grown using hydrothermal,^{550–552} vapor phase transport,⁵⁴² and melt growth.⁵⁵³ The growth of bulk crystal was first reported by Fritsch (Ref. 553) in 1935. Almost 20 years later in 1953, growth using the hydrothermal method was first reported by Walker (Ref. 554). Hydrothermal growth has been studied extensively since this method has the ability to produce large crystal samples. Growth rate for the hydrothermal method was shown to be anisotropic⁵⁵² with metallic impurities such as potassium and lithium being seen throughout.⁵⁴² In 2006, Ehrentraut *et al.* (Ref. 555) was able to grow three inch diameter crystals hydrothermally. CVT growth of ZnO crystals was first reported in literature by Kubo (Ref. 556) in 1965 around a decade following the first hydrothermal growth. Vapor transport has been shown to grow ZnO wafers at very high quality.⁵⁴²

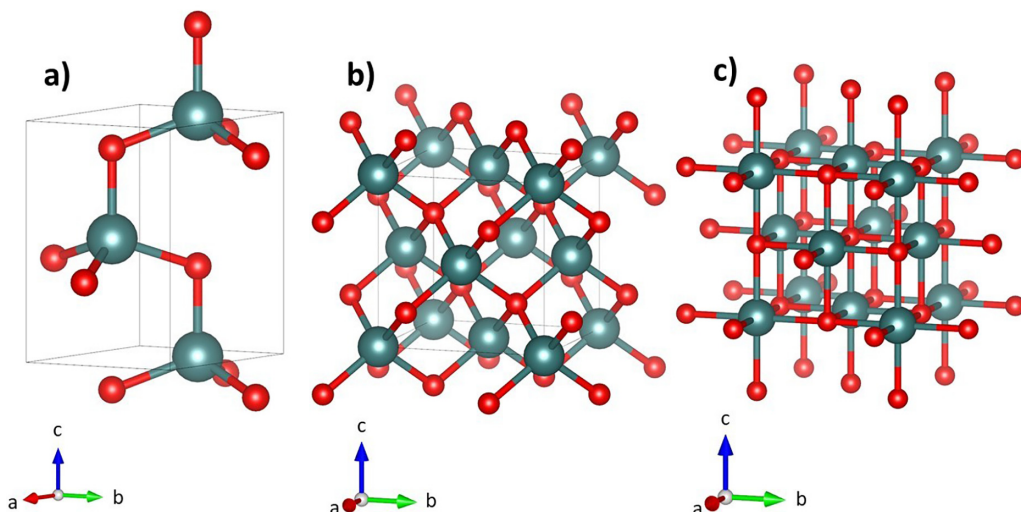


FIG. 21. Unit cells for (a) wurtzite ZnO belonging to space group $P6_3mc$ (#186), (b) zinc blende ZnO belonging to space group $\bar{F}\bar{4}3m$ (#216), and (c) rocksalt ZnO belonging to space group $Fm\bar{3}m$ (#225). All three unit cells are shown with the c -axis orientated upwards (olive = Zn, red = O).

TABLE XXV. Crystal structure, space group, and lattice constants of the ZnO phases determined from experiment and theory.

Phase	Structure	Space group (Ref. 542)	Lattice (Å)
Wurtzite	Hexagonal	$P6_3mc$ (#186)	$a = 3.2459^{549,a}$ $c = 5.2069$ $a = 3.2501^{543,a}$ $c = 5.2071$ $a = 3.286^{545,b}$ $c = 5.241$ $a = 3.2475^{544,a}$ $c = 5.2075$
Zinc blende	Cubic	$F\bar{4}3m$ (#216)	$a = 4.619^{545,b}$ $a = 4.60^{547,b}$ $a = 4.463^{546,a}$
Rocksalt	Cubic	$Fm\bar{3}m$ (#225)	$a = 4.271^{548,a}$ $a = 4.30^{547,b}$

^aExperimental.

^bTheoretical.

One of the higher reported electron mobility values of $205 \text{ cm}^2/(\text{V s})$ was obtained using vapor-phase transport to grow large-diameter ZnO crystals. The same vapor-phase samples exhibited peak mobility of around $2000 \text{ cm}^2/(\text{V s})$ at 50 K .⁵⁵⁷ Galazka (Ref. 436) provides extensive detail as well as a historical timeline into the growth of bulk crystal ZnO across multiple methods.

The growth methods for ZnO thin films have been shown to be similar to other oxide thin films. Magnetron sputtering⁵⁵⁸ and CVD^{559,560} produced low quality and polycrystalline samples. When using methods such as MBE,^{561,562} PLD,⁵⁶³ and MOCVD,⁵⁶⁴ the crystalline quality was greatly improved due to better control over the deposition.⁵⁴² PLD offers advantages for ZnO film growth compared to other growth techniques. The pulsed laser allows for the energy of the emitted photons to be condensed quickly, resulting in a high peak energy. This proves to be an advantage for fabricating complex oxides as evaporation of ablated materials will not alter the composition.⁵⁶³ Further details on the specific ZnO thin film growth methods and are highlighted by Ozgur *et al.* (Ref. 542).

There are many potential substrates for the growth of ZnO films, most of which have a hexagonal structure to match that of wurtzite ZnO. GaN has one of the smallest lattice mismatches at 1.8% due to the similar lattice parameters and the same stacking order. AlN is another hexagonal candidate that has a lattice mismatch of only 4.5%. Even though the lattice mismatches of ZnO on GaN and AlN are quite small, nitrides are not a widely used substrate for the growth of ZnO. This is due in part to single crystal ZnO possessing higher quality properties than nitrides. 6H-SiC has a lattice mismatch of 3.5% with a c lattice parameter that is almost 8 Å longer than ZnO. α -Al₂O₃ has the largest lattice mismatch of the common hexagonal substrates at 18.4%. This value only arises after a 30° in plane rotation.⁵⁴² The need for this 30° rotation can be eliminated with improved and proper growth conditions such as adding an MgO buffer layer for example.⁵⁶⁵

The final hexagonal substrate is ScAlMgO₄ with the lowest lattice mismatch of only 0.09%.^{542,563} ScAlMgO₄ provides the advantage of eliminating in-plane domain rotation when grown via laser-assisted MBE. Si and GaAs are two cubic substrate candidates that have larger lattice mismatches of 40.1% and 42.4%, respectively.⁵⁴² Si and GaAs are uncommon substrates for ZnO epitaxial growth as evidenced by the larger lattice mismatch values. The lattice mismatch can often be reduced with the addition of a buffer layer.⁵⁶⁶

C. Electronic band structure

The calculations for the electronic band structure of ZnO have been widely studied and reported on in great detail, particularly by Vogel *et al.* (Ref. 567) who details some of the shortcomings of certain calculation methods such as LDA. The Brillouin zone shows a valence band maximum and a conduction band minimum that both occur at the Γ point making ZnO a direct bandgap semiconductor.⁵⁶⁸ Figure 22 shows the direct nature of the calculated bandgap of ZnO determined using LDA-PP and SIC-PP.⁵⁶⁷ Vogel *et al.* (Ref. 567) detailed the difference between the LDA and SIC-PP calculations. LDA calculations on the left-hand side show drastic underestimations, a common short-coming within ZnO that is detailed later in Subsection V C 1. The right-hand side of Fig. 22 shows how SIC-PP calculations raise the bandgap energy to a more reasonable value. The increase in the energy gap of the SIC-PP calculations is a result of the d bands being lowered in energy, thus widening the bandgap energy to be more in line with experimental values. The O 2p valence bands also exhibit more dispersion than the LDA calculations.⁵⁶⁷ Examining the theoretical nature of the bandgap, Chelikowsky *et al.* (Ref. 568) used pseudo-charge density analysis to better understand the orbitals that makeup the energy bands. The lowest energy bands of ZnO occur deep within the valence band around -20 eV , comprised of O(2s) states with analysis showing there is no hybridization of the O(2s) with the O(2p) states. Moving up the valence bands, the next group of

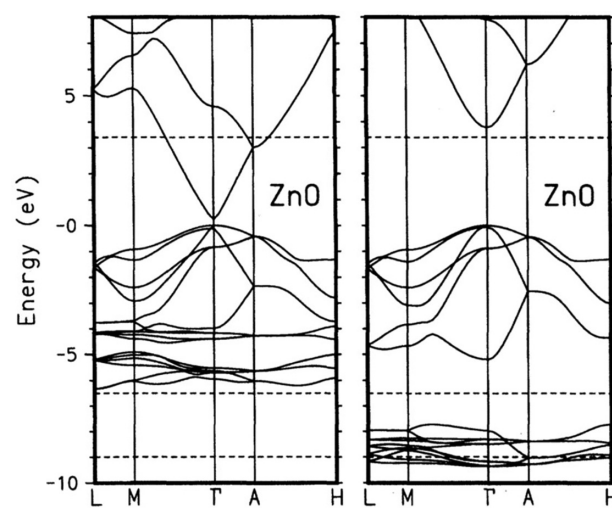


FIG. 22. The calculated bandgap of ZnO. LDA was first used to determine a bandgap of 0.23 eV . Using SIC-PP, the bandgap was determined to be 3.77 eV . Reproduced with permission from Vogel *et al.*, Phys. Rev. B **52**, R14316 (1995). Copyright 1995 APS (Ref. 567).

bands consist of six energy bands that range in energy level from -6 eV to 0 eV. These bands are comprised of the O(2p) states.⁵⁶⁸ In between the groups of valence bands is another grouping that occurs around -9 eV consisting of ten bands. These valence bands are comprised of the Zn(3d) levels.⁵⁶⁷ Moving to the conduction band, the lowest two energy bands localize with Zn and are a result of the 3s energy level which is unoccupied. Going farther up the conduction band, these bands behave like free electrons but exhibit some anti-bonding because of the O(p) states. From this theoretical electronic structure and bandgap analysis, it was determined that the direct bandgap was 3.5 eV.⁵⁶⁸

Experimentally determined bandgap energy values and band locations have shown some level of disagreement with the theoretically determined bandgap energy values, especially the theoretical values and Zn(3d) band locations found using Green's function from Rossler.⁵⁶⁹ Langer *et al.* (Ref. 570) experimentally looked at the core electron energy levels using an x-ray induced photoemission spectroscopy (XPS). By analyzing the core electron energy levels, they arrived at two findings; that the Zn(3d) orbital location inside of the oxide could be determined "unambiguously" and that any of the bandgap energy differences between experimental and theoretical findings were arising due to angular momentum dependence.⁵⁷⁰ Powell *et al.* (Ref. 571) also reported studies attempting to clarify the differences in theoretical and experimental values.⁵⁷¹ Powell states that Green's function used by Rossler (Ref. 569) is suitable for determining the *d* band location in most II-VI semiconductors including ZnS and ZnSe. This is because it uses an *ad hoc* potential with one adjustable parameter to determine the bandgap value and does not need experimental data to arrive at a calculated value. The issue is that many of the initial calculated ZnO bandgap values were determined before any optical data values were available to compare.

Electron-energy loss measurements concluded that the low value for the free-electron density means that the Zn(3d) electrons reside deeper in energy, around 7.5 eV.⁵⁷¹ Langer *et al.* (Ref. 570) showed results from x-ray induced photoemission spectroscopy that yielded a value of 7.6 eV below the valence band max for the Zn(3d) levels.⁵⁷⁰ Both findings from the electron-energy loss measurement⁵⁷¹ and the x-ray induced photoemission spectroscopy⁵⁷⁰ disagree with the Zn(3d) location that was calculated from Green's function. Photoemission measurements carried out in a later study by Powell *et al.* (Ref. 572) again produced a Zn(3d) value that was in agreement with prior experimental studies and at odds with Rossler's 3d level location. The experimental photoemission values were around 3 eV lower in value. This photoemission study also showed the width of the 3d band to be about 5 eV wide which gives it a width of around 2 eV greater than in ZnS, CdS, and CdSe; other comparable II-VI materials.⁵⁷² Later photoemission studies arrived at values of 8.5 (Ref. 573) and 8.81 eV (Ref. 574) which could be considered to be in disagreement with both Powell's photoemission⁵⁷² value and Langer's x-ray induced photoemission⁵⁷⁰ value at around 1.0 eV higher than the latter two.

With these discrepancies in mind, further theoretical methods including LDA and tight-binding methods were carried out that took into account Zn(3d) states and considered them to be core levels.^{568,575} Ivanov *et al.* (Ref. 575) discussed how the theoretical and experimental values arrived at an agreeable value for the Zn(3d) location. It was found that the 3d band resides 3 eV beneath the valence *s-p* bands.

The 3d bands have a density of states peak around -7.8 eV below the valence band max. It was also concluded that this Zn(3d) band provided no influence on the bonding of ZnO. Interestingly, it was shown that ZnO, ZnSe, ZnS, and ZnTe have a Zn(3d) density of states peak that has the same energy separation from vacuum level and half width value. This concludes that the Zn(3d) level can be a core level even though it is 3 eV away from the other valence bands.⁵⁷⁵ With this conclusion, theoretical models for the band calculations of ZnO have improved. By considering Zn(3d) to be a valence band state, the estimation of band locations has become easier and allowed for the observation of a non-negligible influence of the Zn(3d) bands on the *s* and *p* valence bands.⁵⁴²

Bundesmann *et al.* (Ref. 576) provided details into the valence band ordering at the Γ -point. In ZnO the lowest conduction band contains Γ_7 symmetry while the highest valence band splits into two bands (Γ_7 and Γ_9) as a result of crystal field interaction and spin-orbit. There is a debate regarding the highest valence band ordering within unstrained ZnO. The two debated possibilities are Γ_{797} and Γ_{977} .^{577,578} Experiment has shown that ZnO thin films deposited on sapphire have properties at RT that support Γ_{797} . This is due to transitions between the valence and conduction band containing Γ_9 symmetry being forbidden from coupling with photons that are polarized \perp to the *c*-axis.⁵⁷⁶

1. Bandgap energy

The bandgap of wurtzite ZnO has been reported throughout the literature both theoretically and experimentally. ZnO is an excitonic material which plays a role in determining the bandgap energy. Numerous theoretical methods have been applied to produce bandgap values. Such methods include LDA,^{579,580} HSE03,⁵⁸⁰ FALPW,⁵⁸¹ PBE,⁵⁸² Hartree-Fock,⁵⁸⁰ and multiple variations of G_0W_0 .⁵⁸² The reported calculated values range from 0.23 to 3.77 eV. The Hartree-Fock calculations reported by Fuchs *et al.* (Ref. 580) is an outlying value, drastically overestimating the bandgap energy at 11.07 eV. LDA calculations experience short comings due to how the *d* electrons within the structure are accounted for. If the *d* electrons are considered core electrons, the resultant calculated lattice constants cause the experimental values to be underestimated. If the *d* electrons are included in the valence shell, lattice constants are shown to be more accurate.^{567,579} However, LDA still shows underestimations for other parameters such as the bandgap.

Using LDA, the cationic *d* bands have been shown to reside at locations too high in energy. This leads to the cationic bands having enlarged interactions with the anionic valence *p* bands. This causes LDA calculations of II-VI semiconductors to be even more skewed and underestimated than those of III-V semiconductors. A specific example for ZnO involves LDA failing to model the middle valence bands comprised of the Zn(3d) electrons.⁵⁶⁷ These are the same Zn(3d) discussed heavily in Sec. V C. Using LDA without any hybrid functional, Schroer *et al.* (Ref. 579) reported the theoretically determined bandgap to only be 0.23 eV. LDA-PP calculations from Vogel *et al.* (Ref. 567) also reported a bandgap of 0.23 eV. Fuchs *et al.* (Ref. 580) had similar results using LDA, producing a bandgap of only 0.6 eV. Other calculated methods besides LDA also drastically underestimate the bandgap energy of ZnO. PBE, HSE03, G_0W_0 , all-electron GW, and GW_0 yield values of 0.67 , 2.11 , 2.12 , 2.44 , and 2.54 eV,

respectively.^{580,582,583} These values are not included in Table XXVI as they are not a good representation of the bandgap of ZnO.

There are modified hybrid functionals that yield higher bandgap energies (listed in Table XXVI) that are comparable to experimental values. These hybrid functions help compensate for the issues that are encountered when calculating the bandgap energy of II-VI semiconductors such as ZnO. Modified versions of LDA (GW and U+GW), produced calculated values of 3.4 and 3.6 eV, respectively.⁵⁸⁰ The modified LDA calculations were in better agreement with experimental findings. Vogel *et al.* (Ref. 567) proposes a theoretical approach called self-interaction-corrected pseudopotential (SIC-PP) to calculate the bandgap of ZnO and to avoid the short falls of LDA. From the SIC-PP measurement a theoretically determined bandgap of 3.77 eV was determined.

Experimental methods for determining the bandgap energy of ZnO show just how well known the bandgap is. Values for bulk single crystal ZnO presented in Table XXVI show very little difference, no more than a few meV. SE is a common method used to determine the bandgap energy. With wurtzite ZnO being a hexagonal structure,

TABLE XXVI. Bandgaps energy parameters (eV) and excitonic binding energy parameters (E_{xb}^1) (meV) of wurtzite ZnO determined from experiment and theory. Anisotropy labeled where relevant.

$E_g(\varepsilon_\perp)$	$E_g(\varepsilon_\parallel)$	$E_{xb}^1(\varepsilon_\perp)$	$E_{xb}^1(\varepsilon_\parallel)$	Method	Reference
Expt. bulk					
3.372	3.405	56	50	SE	584
3.373	3.407	55.3	51.3	SE	585
3.406	3.445	72	73	SE	586
3.407	3.4889	90	78	SE	586
3.448	3.492	66	66	Trans.	587
3.45	3.45	59	59	SE	588
Expt. film					
3.366	3.366	60	60	SE	590
3.08–3.37 ^a	Trans/Abs.	591
3.27–3.31 ^a	Abs.	592
3.28 ^a	Abs.	594
3.29 ^a	Abs.	594
3.3 ^a	Trans/Abs.	595
Calc.					
2.97	xS-Approx. ^b	580
2.99	FLAPW	581
3.03	PBE0	580
3.20	GW	582
3.39	Pseudopotential calc.	569
3.4	LDA+GW	596
3.5	Calc.	568
3.6	LDA+U+GW	596
3.77	SIC-PP	567

^aAnisotropy not measured or accounted for.

^bScreened-exchange approximation.

anisotropy should be present. Multiple literature sources observed anisotropy by determining the lowest band-to-band transition for ε_\perp and ε_\parallel .^{584–588} The differences in the bandgap energies for the two directions is reported to be small often differing by less than 100 meV. Yoshikawa *et al.* (Ref. 588) carried out SE experiments to account for anisotropy but ultimately found the same bandgap energy (3.54 eV) for both directions. Other reported values showing anisotropy of the ZnO bandgap energy include 3.372 eV (ε_\perp) and 3.405 eV (ε_\parallel) (Ref. 584), 3.373 eV (ε_\perp) and 3.407 eV (ε_\parallel) (Ref. 585), and 3.406 eV (ε_\perp) and 3.445 eV (ε_\parallel) (Ref. 586). It can also be observed that with the reported values of anisotropy, although quite small, the bandgap energy for the ε_\parallel direction is always equal or larger than ε_\perp . From the reported values for the two directions the average experimental bulk bandgap energy is 3.409 and 3.447 eV for ε_\perp and ε_\parallel , respectively. The excitonic binding energy is also reported alongside the bandgap energies. Small anisotropy is present with the largest difference between the binding energies of the two directions among the reported values being 12 meV.⁵⁸⁶ Srikant *et al.* (Ref. 589) report a single bandgap value of 3.3 eV without taking into account anisotropy. The excitonic levels are not identified which could be contributing to the a lower value compared to the other experimental bulk values.

The experimentally determined bandgaps of ZnO thin film samples were shown to have slightly smaller bandgap energies than the experimentally determined bulk values. A value of 3.366 eV was found using SE by Schmidt *et al.* (Ref. 590) which determined the band-to-band transition as opposed to the onset of absorption and as a result is much more in line with the bulk single crystal bandgap energy values. Benramache *et al.* (Ref. 591) observed how the electrical and optical properties of thin films changed with growth precursor molarities. The bandgap was shown to increase from 3.08 to 3.37 eV as the precursor molarity increased from 0.05 to 0.1 M.⁵⁹¹ Zhu *et al.* studied the bandgaps of thin films with differing substrate temperatures. The bandgaps ranged from 3.27 to 3.31 eV. The largest bandgap of 3.31 eV was found at 200 °C.⁵⁹² It was concluded that the bandgap energy relied on the carrier concentration and grain size of the thin films.^{592,593} Zhu *et al.* (Ref. 592) hypothesized that the maximum observed bandgap at 200 °C correlated to the smallest grain size. With increasing temperature, the oxygen vacancies could cause an increase in carrier concentration which should raise the bandgap. However, the increasing bandgap is stopped by the increasing film grain size at higher temperatures.⁵⁹² Finally, Ilican *et al.* (Ref. 594) determined bandgap energies of 3.28 and 3.29 eV from absorption measurements of thin films. All cited values for the bandgap of ZnO are listed in Table XXVI. Values are also compared in Sec. XI.

2. Temperature dependence of the bandgap energy

Photoluminescence excitation and Photoluminescence measurements performed on bulk ZnO crystals can be used to determine the temperature dependence of the A exciton energy (E_{XA}). From this exciton temperature dependence, the energy bandgap temperature dependence can be extracted. The free-exciton binding energy of ZnO is almost three times larger than GaN. At room temperature, the exciton emissions are significant due to this large binding energy. In undoped bulk ZnO there is often an ultraviolet edge emission that occurs near 3.26 eV which is around 0.11 eV below the energy bandgap. There is some disagreement as to the cause of the ultraviolet

room temperature emission exhibited in the undoped bulk ZnO. It has been reasoned that the emission is due to the free-exciton recombination⁵⁹⁷ but Ohashi *et al.* (Ref. 598) experimentally concluded that the emission was due to an unspecified localized state.⁵⁹⁸

The temperature dependence of the bandgap energy of ZnO was analyzed in a study by Wang *et al.* (Ref. 597). In order to determine and report on the bandgap energy temperature dependence, Wang *et al.* used the Varshni equation

$$E_g(T) = E_g(0) - \alpha T^2 / (T + \beta), \quad (6)$$

for curve-fitting analysis. Due to the consideration that the free exciton binding energy in ZnO is nearly independent of temperature for the range of 4.8 to 300 K, E_{XA} can replace E_g inside of Varshni's formula,

$$E_{XA}(T) = E_g(0) - \alpha T^2 / (T + \beta). \quad (7)$$

For temperatures above 200 K, the value of the temperature dependence of E_{XA} (and thus E_g) is found to be $dE_{XA}/dT = -0.35 \text{ meV/K}$.⁵⁹⁷ This slightly modified Varshni formula [Eq. (7)] allows for the prediction of the temperature dependence of the bandgap energy of ZnO up to room temperature. The Varshni formula presented above [Eq. (6)] is an often used approximation to the Bose-Einstein equation. It should be noted that the equation $\gamma = \delta E_g / \delta T$, first introduced in Sec. II has the same meaning, resulting in $\gamma = -0.35 \text{ meV/K}$ for ZnO.

D. Material properties

Across the literature, the material properties for ZnO have been reported. Important properties for the study of ZnO include the basic material properties as well as the thermal, phonon, and electrical properties. The basic material properties consist of the material density, melting point, and bulk modulus. ZnO has a reported density of 5.605 g/cm³.⁵⁴⁹ The melting point of ZnO was reported to be around 1975 °C.¹¹⁸ The reported bulk modulus values were wide-ranging across literature. Calculated values ranged from 154 to 173 GPa.^{547,548,599,600} Experimentally, Karzel *et al.* (Ref. 548) reported the bulk modulus to be 183 GPa. That value differed from another reported experimental value of 140 GPa.⁵⁴⁷ XRD was used to report a bulk modulus of 142.4 GPa for polycrystalline ZnO.⁶⁰¹ All cited basic material properties are listed and compared in Sec. XI.

1. Thermal properties

The thermal properties reviewed for ZnO included the Debye temperature, CTE, specific heat, and thermal conductivity. Debye temperature values reported throughout the literature are wide ranging and lacking in consistency. Multiple authors using varying methods have reported different Debye temperatures values. Abrahams *et al.* (Ref. 602) reported the Debye temperature to range from 355 to 416 K. Boemare *et al.* (Ref. 603) found an estimative Debye temperature of 305 K by using a semi-empirical expression with equivalence to the Bose-Einstein model. The semi-empirical Bose-Einstein expression was proposed by Pässler *et al.* (Ref. 604). In one of the earliest reported Debye temperature values, Ehrhardt *et al.* (Ref. 605) found a value of 355 K from electron diffraction measurements. Lawless *et al.* (Ref. 606) reported the calorimetric Debye temperature of pure ZnO to be 399.5 K. While the four values reported above are in decent agreement,

other literature works have reported significantly higher Debye temperature values. Using extended x-ray absorption fine structure spectroscopy, Troger *et al.* (Ref. 607) found a Debye temperature of over 800 K while Wang *et al.* (Ref. 597) reported a value of 700 K. It is interesting to note that a Debye temperature of 700 K value gives a Debye/Einstein temperature ratio of 0.34 which is very similar to the Debye/Einstein temperature ratio for GaN of 0.3, another material with a wurtzite crystal structure and similar lattice parameters.⁵⁹⁷

The CTE has been reported to be in good agreement by multiple sources. There is significant anisotropy observed in the CTE as well. α_a ranges from $4.31 \times 10^{-6} \text{ /K}$ to $4.75 \times 10^{-6} \text{ /K}$ and α_c ranges from $2.49 \times 10^{-6} \text{ /K}$ to $2.9 \times 10^{-6} \text{ /K}$.^{542,608} Reeber (Ref. 609) studied changing of the lattice parameters from 4.2 to 296 K, the results are shown in Fig. 23. The reported specific heat capacity at constant pressure was 40.3 J/(mol K).⁵⁴⁹ Using the known molar mass of ZnO, 81.38 g/mol, the specific heat capacity can be converted to 0.495 J/(gK). Klimm *et al.* (Ref. 610) reported the specific heat capacity to be 41.05 to 61.58 J/(mol K) across a temperature range of 23 to 1975 K.⁶¹⁰ That specific heat capacity converts to 0.504 to 0.756 J/(gK). The room temperature value from Klimm was in good agreement with the constant pressure value of 0.495 J/(mol K).

The thermal conductivity has been reported throughout literature for ZnO. Ozgur *et al.* (Ref. 611) studied the thermal conductivity of bulk ZnO crystals after different surface treatments. The highest reported thermal conductivity was 147 W/(mK). That specific sample was treated with N-plasma at a temperature of 750 °C. Other treated samples had thermal conductivity values ranging from 45 to 144 W/(mK). The lowest thermal conductivity values were seen for the two samples that received forming gas annealing. It was thought that the surface defects from the post treatments were the cause of the varied thermal conductivity values. However, no conclusion could be made as there was no correlation between the optical quality, surface defects, and thermal conductivity. The forming gas annealing could have caused an increase in surface roughness, which would lower the thermal conductivity according to modeling.⁶¹¹ The thermal conductivity of the Zn and O surfaces of bulk ZnO crystals was also measured.⁶¹² The first sample had thermal conductivity values of 116 and 110 W/(mK) for the Zn and O face, respectively. The second sample

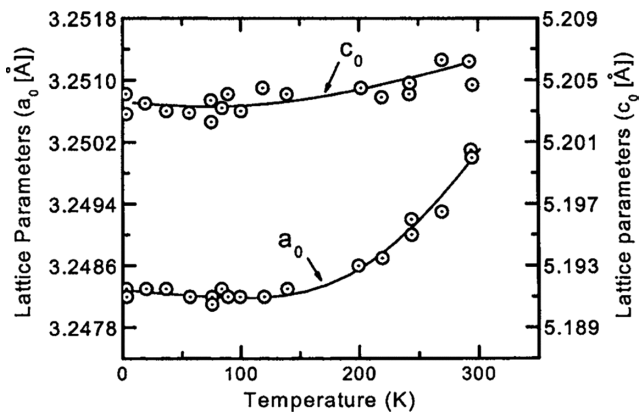


FIG. 23. Temperature dependence of the ZnO lattice parameters from 4.2 to 296 K. Reproduced with permission from Reeber, J. Appl. Phys. 41, 5063–5066 (1970). Copyright 1970 AIP Publishing LLC (Ref. 609).

had thermal conductivity values of 102 and 98 W/(mK) for the Zn and O face, respectively. While beyond the scope of this review, it was discussed how surface roughness altered the effective thermal conductivity.⁶¹² No values for the thermal diffusivity of ZnO were reported across literature. The cited thermal property values for ZnO are listed and compared in Sec. XI.

2. Phonon properties

Wurtzite ZnO contains four atoms in each unit cell, leading to 12 phonon modes. The 12 modes consist of a single longitudinal acoustic, two transverse acoustic, three LO, and six TO branches.⁵⁴¹ The irreducible representation for the phonon modes is⁶¹³

$$\Gamma = 2A_1 + 2B_1 + 2E_1 + 2E_2.$$

The A₁ and E₁ branches are both Raman and IR active. Both of the non-polar E₂ branches are Raman active. The B₁ branches are silent. The vibration of the Zn sub-lattice correlates to the low frequency E₂ mode while the high frequency E₂ mode mostly involves oxygen atoms.⁵⁴¹ The A₁ and E₁ branches are also shown to split into LO and TO modes. The splitting, or removal of degeneracy at or near the center of the Brillouin zone, is larger for TO-LO than A₁-E₁ because the anisotropy is dominated by the electrostatic forces. In the A₁ mode, the lattice vibration is parallel to the *c*-axis while the E₁ mode is perpendicular. The reported Raman and IR phonon mode frequencies determined both experimentally and theoretically are highlighted in Table XXVII. The silent B₁ and B₂ modes are only reported theoretically.

TABLE XXVII. Phonon mode frequencies (cm⁻¹) of wurtzite ZnO determined from experiment and theory.

Symmetry	Raman ^{a,b}	IR	Calculated ^e
A ₁ -TO	380, 378	380 ^c	382, 386 ^g
E ₁ -TO	413, 409.5	412 ^c , 408.2 ^d	316, 407 ^g
A ₁ -LO	574, 576	570 ^c , 577.1 ^d	548
E ₁ -LO	591, 588	591 ^c , 592.1 ^d	628
E ₂ -low	101, 98		126, 98 ^g
E ₂ -high	444, 437.5		335, 433 ^g
B ₁ -low			240 ^f
B ₂ -high			540 ^f

^aArguello *et al.* (Ref. 614).

^bBairamov *et al.* (Ref. 615).

^cVenger *et al.* (Ref. 616).

^dAshkenov *et al.* (Ref. 617).

^eZaoui and Sekkal (Ref. 618).

^fOzgur *et al.* (Ref. 542).

^gTsuboi and Wada (Ref. 619).

The phonon frequencies of bulk and thin film samples show little to no differences for the E₁(TO), A₁(TO), and E₂ modes. Thin films were reported to have a slight redshift of LO-phonon mode frequencies. The redshift was attributed to vacancy point defects of the thin films. Further studies on the phonon modes of ZnO were reported by Ashkenov *et al.* (Ref. 617), Damen *et al.* (Ref. 620), Koyano *et al.* (Ref. 621), and Tsuboi *et al.* (Ref. 619).

3. Electrical properties

The electrical properties of ZnO include the electron affinity, electrical breakdown field, static and high frequency dielectric constants, effective mass, and electron mobility. The electron affinity has been reported to range from 4.1 to 4.5 eV. Ultraviolet photoelectron spectroscopy found the electron affinity of ZnO on the (000-1) surface to be 4.1 eV.⁵⁴¹ ZnO thin films used in ZnO/Si heterojunctions had an electron affinity of 4.5 eV.⁶²² The electrical breakdown strength can be predicted using the bandgap vs breakdown field strength plot from Higashiwaki *et al.* (Ref. 147). Using the experimentally determined bandgap energies that range from around 3.2 to 3.6 eV, the breakdown field strength for ZnO is predicted to be 2–3 MV/cm. Values for the electron affinity and electrical breakdown strength are compared in Sec. XI.

The static and high-frequency dielectric constants have been reported for both bulk and thin film samples. Anisotropy was evident in the reported results. Experimentally, ZnO bulk samples studied by Ashkenov *et al.* (Ref. 617) had static dielectric constants of 7.77 and 8.91 measured perpendicular and parallel to *c*, respectively.⁶¹⁷ In the same study, thin film samples exhibited similar anisotropy but had slightly lower values of 7.46 and 8.59 measured perpendicular and parallel to *c*, respectively.⁶¹⁷ Other reported calculated values were in good agreement ranging from 7.44 to 7.65 for perpendicular measurements and 8.36 to 8.57 for parallel measurements.^{588,623,624}

High-frequency dielectric constants were reported by the same authors, highlighting anisotropy across bulk and thin film samples. Bulk samples had values ranging from 3.68 to 3.70 for calculations perpendicular to *c* while parallel calculations ranged from 3.72 to 3.78. Thin films were again similar but slightly lower. Perpendicular calculations ranged from 3.60 to 3.61 while parallel calculations ranged from 3.66 to 3.76.^{588,617,623,624} Values for the static and high-frequency dielectric constants are listed and compared in Sec. XI.

The conduction band minimum effective mass parameter was reported to range from 0.23 m_e to 0.34 m_e.^{625–628} The effective mass of holes and heavy holes was reported to be 0.59 m_h and 0.79 m_{hh}, respectively.^{629,630} Both the electron and hole mobility have also been reported. One of the highest calculated electron mobility values was around 300 cm²/(V s), determined using a Monte Carlo method.⁶³¹ Look *et al.* measured the low-field electron mobility in bulk crystal samples to be 205 cm²/(V s). *c* and *a* plane sapphire was a common substrate used for thin film growth. Electron mobility values were reported to be 120 cm²/(V s),⁵⁶² for *a* plane while growth on the *c* plane had electron mobility values ranging from 130 to 155 cm²/(V s).^{632–634} According to Galazka (Ref. 436), the highest experimental electron mobility of bulk crystal ZnO was around 230 cm²/(V s) determined by Allen *et al.* (Ref. 635). Maeda *et al.* (Ref. 636) studied the carrier mobility distribution across two inch ZnO bulk single crystals showing similar results to findings of Allen *et al.*⁶³⁶ Hole mobility

values were also seen throughout literature ranging from $0.5 \text{ cm}^2/(\text{V s})$ to $1.3 \text{ cm}^2/(\text{V s})$.^{637,638} Values of the effective mass and carrier mobility are compared in Sec. XI.

Due to its crystal structure symmetry, wurtzite ZnO reveals piezoelectric as well as spontaneous interface charges. The piezoelectric charges occur upon strain parallel to the lattice *c*-axis, and can change signature depending on the strain signature (tensile or compressive). The spontaneous charge is a result of the lattice distortion from the ideal crystal structure at room temperature. These properties are analogous to the wurtzite structure in the GaN/AlGaN system.^{214,215} Theoretical results for the spontaneous polarization were reported throughout the literature to be $P(\text{ZnO}) = -0.032 \text{ C/m}^2$,⁶³⁹ $P(\text{ZnO}) = -0.05 \text{ C/m}^2$,⁶⁴⁰ and $P(\text{ZnO}) = -0.057 \text{ C/m}^2$.⁶⁴¹ Experimental studies using second harmonic generation reported $P(\text{ZnO}) = -0.07 \pm 0.015 \text{ C/m}^2$.⁶⁴² A capacitance evaluation approach using double and triple wurtzite-structure piezoelectric n-type ZnO and perovskite-structure ferroelectric highly insulating BaTiO₃ thin film diode structures observed spontaneous interface polarization coupling, and determined $P(\text{ZnO})$ ranging from -0.041 C/m^2 to -0.004 C/m^2 .²¹⁶

E. Doping and Defects

Donor dopants for ZnO include aluminum, indium, gallium, and zirconium.⁵⁶³ The conductivity of n-type doped ZnO is comparable to ITO, making ZnO a possible replacement among TCO applications such as solar cells and displays. The possibility of p-type ZnO was also reported using dopants such as nitrogen,⁶⁴³ arsenic,⁶⁴⁴ phosphorus,⁶⁴⁵ and Ga-N⁶⁴⁶ complexes. Galazka (Ref. 436) provides a detailed list of shallow donors contributing to n-type conductivity and shallow acceptors for p-type conductivity. Shallow donors include gallium, aluminum, indium, and scandium that will substitute for the Zn²⁺ ions.^{647,648} Other shallow donors consist of zinc interstitials,⁶⁴⁹ hydrogen interstitials,⁶⁵⁰ and phosphorous substituting for zinc.⁶⁵¹ Shallow acceptors for p-type conductivity include lithium and sodium doping on the zinc site. The p-type dopants mentioned above including nitrogen, phosphorus, and arsenic are doped on the oxygen site.⁶⁵²

Intrinsic and extrinsic defects within undoped ZnO are the cause of the natural n-type conductivity. These defects include zinc-on-oxygen antisites, oxygen vacancies, and zinc interstitials.^{557,649} Additionally, unintentional hydrogen incorporation is common and directly affects carrier concentrations. In many materials, hydrogen acts as an amphoteric dopant, acting both as donors or acceptors depending on conditions. Upon incorporation, it is common to act as an acceptor (H⁻) in n-type material, and a donor (H⁺) in p-type material, precluding hydrogen as a source for conductivity, and acting as a compensating species.⁶⁵⁰ Hydrogen incorporated in ZnO may instead not behave as amphoteric, but as a shallow donor, according to DFT calculations by Van de Walle (Ref. 650), producing the typical n-type conductivity in unintentionally doped ZnO. Van de Walle goes on to conclude that hydrogen dopants are likely introduced during growth of ZnO since hydrogen is present in many commonly used growth methods such as hydrothermal, MOCVD, and VPT. Hydrogen could also stem from H₂O that is often present in high vacuum systems as a residual gas. In order to better control and predict the conductivity of ZnO, the exposure to hydrogen both during and after growth must be carefully accounted for.⁶⁵⁰

Erhart *et al.* (Ref. 653) used first principles calculations to study to oxygen vacancy stability within ZnO. When under zinc-rich

conditions, oxygen vacancies are unstable. Under oxygen-rich conditions the zinc vacancies are shown to be favorable and the dominant defect when the Fermi level resides in the upper half of the bandgap. If the Fermi level resides in the lower half of the bandgap, calculations show a dumbbell split interstitial configuration for the oxygen interstitials that act as the dominating defect.⁶⁵³ In a follow up study, Erhart *et al.* (Ref. 654) reported on the diffusion of the vacancies and interstitials within ZnO.

DFT calculations showed that the most mobile defects were the zinc interstitials followed by oxygen interstitials, zinc vacancies, and oxygen vacancies in order of decreasing mobility. Intrinsic self-diffusion happens by way of a vacancy mediated mechanism for n-type ZnO.⁶⁵⁴

F. Polymorphs

Wurtzite is the stable phase of ZnO, but the metastable phase of zinc blende and the high-pressure rocksalt phase also possess interesting properties and electronic band structures. The bulk modulus of zinc blende ZnO was reported theoretically using LDA, GGA,⁵⁹⁹ and Hartree-Fock⁵⁴⁷ methods. Values ranged from 135.3 to 161.7 GPa, differing little from the bulk modulus of wurtzite ZnO. According to Hartree-Fock LCAO⁵⁴⁷ and LAPW calculations,⁵⁴⁸ rocksalt ZnO has a bulk modulus value of 203.3 and 205 GPa, respectively. From experiment the bulk modulus of rocksalt ZnO is reported to be 228 GPa.⁵⁴⁸ This results in a bulk modulus for rocksalt ZnO that is substantially higher than the wurtzite and zinc blende structures of ZnO.

Zinc blende ZnO is a direct bandgap material. LDA calculations drastically underestimate the value to be 0.79–1.36 eV.^{655,656} LDA-PP raised the calculated bandgap energy slightly to 1.77 eV.⁵⁶⁷ The experimental value was measured at 3.27 eV according to photoluminescence measurements,⁵⁴⁶ a value that is only slightly smaller than the energy gap of wurtzite ZnO.^{655,656} This experimental value for zinc blende ZnO was the only reported value found in the literature as of publication. Vogel *et al.* (Ref. 567) used SIC-PP to calculate a bandgap energy of 3.27 eV, matching the experimental value reported by Ashrafi *et al.* (Ref. 546).

Investigations into the theoretical bandgap energy of rocksalt ZnO shows that values are wide ranging across various methods. Theoretical methods seen throughout the literature for determining the bad gap energy of rocksalt ZnO include LDA,^{655,657} GW,^{655,657} and Hartree-Fock calculations.⁶⁵⁸ LDA calculations underestimate the bandgap energy when compared to other theoretical methods. Reported values range from 2.54 to 3.08 eV for the direct gap and 1.16 eV for the indirect bandgap.^{655,657} The GW approximation increases the theoretical bandgap energy to 4.51 eV for the indirect gap and 4.74 eV for the direct gap.⁶⁵⁷ Hartree-Fock results reported by Jaffe *et al.* (Ref. 658) overestimate the bandgap energy at 5.54 and 6.54 eV for the indirect and direct gaps, respectively. Only one experimental bandgap energy was found throughout the literature for the direct bandgap by Sans *et al.* (Ref. 659) via an absorption edge of 4.5 eV. Values for the experimental and theoretical bandgap energies for the polymorphs of ZnO are listed in Table XXVIII.

The transition from zinc blende ZnO to rocksalt ZnO occurs as a result of the interactions between the cation *d* states and the anion *p* states. The interaction between the cation and anion states has a dependence on symmetry and whether the ZnO polymorph contains an inversion center. Zinc blende ZnO (point group T_d) does not contain an inversion center which allows for the cation and anion states to

TABLE XXVIII. Bandgaps of ZnO polymorphs determined from experiment and theory.

E _g (eV)	Method	Bulk/film	Reference
Zinc blende			
Calc.			
0.79	LDA	...	655
1.00	LDA+GW	...	655
1.36	LDA+GW (semicore)	...	656
1.77	LDA-PP	...	567
3.27	SIC-PP	...	567
Expt.			
3.27	Photoluminescence	Bulk	546
Rocksalt			
Calc.			
1.16 ^a	LDA	...	655
2.54	LDA	...	655
3.08	LDA	...	657
3.72	LDA+GW	...	655
4.51 ^a	GW approximately	...	657
4.74	GW approximately	...	657
5.54 ^a	Hartree-Fock	...	658
6.54	Hartree-Fock	...	658
Expt.			
2.45 ^a	Avg. absorption edge	Film	660
4.5	Absorption edge	Film	659

^aIndirect gap.

mix within the Brillouin zone. As a result of the mixing of the states the valence band will experience a uniform shift. Rocksalt ZnO belongs to point O_h and has an inversion center. The presence of an inversion center means the p anions and d cations cannot mix and leads to a dispersion within the valence band, shifting the valence band maximum away from the Γ -point of the Brillouin zone and forms the origin of the indirect bandgap in rocksalt ZnO.⁶⁵⁵

Upon compression of wurtzite ZnO, the upper valence band peak shifts down in energy and height. The resultant DOS peaks for O(2s) and Zn(3d) are broadened and contain a shift in energy. The Zn(3d) state also experiences splitting. As pressure increases on the crystal, wurtzite ZnO begins shifting toward the rocksalt structure. During the process the valence band maximum is decreased. Once the rocksalt phase of ZnO is achieved under high compression/pressure, the upper valence band is widened, and Zn(3d) band splitting is increased. This results in an increase in the bandgap energy with increasing pressure.⁵⁴² Values for the bandgap of zinc blende and rocksalt ZnO are listed in Table XXVIII along with the wurtzite phase.

G. Alloys

Ohtomo *et al.* (Ref. 563) has presented multiple compounds that have the potential to be alloyed with ZnO. The alloying material

generally comes from cubic II-V compounds which are not isostructural with ZnO. Such compounds include ZnS, ZnSe, CdO, and MgO. The ZnO-MgO system is the most heavily studied due to the possibility of a wider bandgap while still maintaining lattice constants similar to ZnO. MgO is the only compound from those listed above that resulted in a bandgap widening when alloyed with ZnO.⁶⁶¹ The composition dependence of the bandgap shows that with increasing Mg, the bandgap will increase above 4 eV. Possible band offsets of up to 1 eV have been seen for ZnO/Mg_xZn_{1-x}O heterostructures as a result.⁵⁶³

Schmidt *et al.* (Ref. 590) reported on the magnesium mole fraction x dependence of the band-to-band transitions and the A, B and C exciton bandgap properties for Mg_xZn_{1-x}. There is evidence of a bowing effect in the exciton binding energy as the magnesium mole fraction x is increased. With x = 0 the exciton binding energy is 61 meV. Increasing x to 0.17 results in a minimum exciton binding energy of 50 meV before increasing to 58 meV at x = 0.29. The bandgap energy E₀^A increased from 3.369 eV to 4.101 eV for a magnesium mole fraction of 0.0 to 0.29, respectively.⁵⁹⁰ In a later report Schmidt *et al.* (Ref. 662) observed the transition energy dependence on the magnesium mole fraction x. The higher energy transitions E₁ and E₂ display no dependence on the Mg mole fraction as shown in Fig. 24. E₀ does, however, have a large dependence on the magnesium mole fraction taken from the early published work (Ref. 590). This points to the observation that any band structure modification from ZnO and magnesium alloying primarily alters the Γ -point conduction and valence bands.⁶⁶²

When the magnesium mole fraction x of Mg_xZn_{1-x}O is increased beyond 0.53 the crystal structure changes from hexagonal wurtzite to cubic rocksalt. Schmidt *et al.* (Ref. 663) also studied the bandgap properties of rocksalt Mg_xZn_{1-x}O. The fundamental bandgap E₀ at x = 0.70 was roughly 6.0 eV. E₀ increased to 7.674 eV at x = 1 determined by ellipsometry data analysis. At x = 0.70 the exciton binding energy E_{xb} was roughly 60 meV and increased to 85.3 meV for x = 1. When x decreases the fundamental bandgap decreases while the spin-orbit split parameter experiences an increase. E_{xb} decreases linearly with decreasing x, in line with the bandgap reduction. E₀ and E_{xb} values reported by Schmidt *et al.* for x = 1.0 are found to be in good agreement with others summarized in this work. Other values found throughout literature included E₀ = 7.77 eV, E_{xb} = 80 meV (Ref. 664) and E₀ - E_{xb} = 7.6 eV (Ref. 665) using reflectivity analysis and SE.

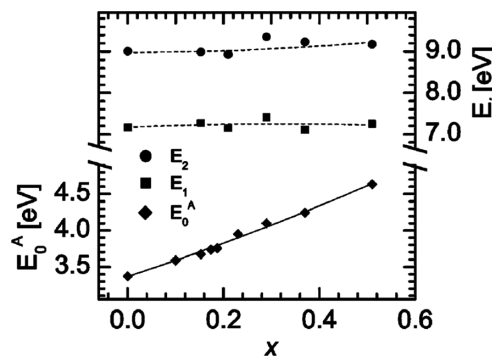


FIG. 24. The fundamental bandgap energies (E₀^A) and UV-VUV band-to-band transitions (E₁, E₂) for Mg_xZn_{1-x}O. Reproduced with permission from Schmidt-Grund *et al.*, Thin Solid Films **455**, 500 (2004). Copyright 2004 Elsevier (Ref. 662).

Finally, when observing the differences between wurtzite and rocksalt $Mg_xZn_{1-x}O$ there is a discontinuity in the bandgap parameter E_0 of ≈ 1 eV.⁵⁹⁰ This discontinuity is a result of the differing zinc and magnesium coordination between the wurtzite (fourfold) and rocksalt (sixfold) structure.⁶⁶³

Other studies detailing the bandgap of $Mg_xZn_{1-x}O$ include Takeuchi *et al.* (Ref. 666), Chen *et al.* (Ref. 667), and Takagi *et al.* (Ref. 668). The Raman active phonon mode frequencies for $Mg_xZn_{1-x}O$ have also been reported for x ranging from 0.10 to 0.52. Values are listed in Table XXIX. Note that as x increases the $A_1(TO)$ mode frequency increases. The multiphonon structure and E_2^2 mode do not increase in frequency with increasing x . For the three highest values of $x = 0.23, 0.37$, and 0.52 the existence of an addition mode was considered to be a mixed mode (MM) of Mg_xZn_{1-x} .⁶⁶⁹

Alloying with CdO has been investigated recently for applications such as optical switches⁶⁷⁰ and solar cells.⁶⁷¹ Zaoui *et al.* (Ref. 672) report on the electronic structure and stability of $Zn_xCd_{1-x}O$. The DOS of the ternary alloy was also detailed. The DOS contains three main regions with the first residing around 15 eV. This region is mainly comprised of O-s states. The second region contains hybridization of zinc (or cadmium) d states with other states making up a smaller portion. Finally, the third region is a full mixture of states. No specific bandgap was reported.⁶⁷² Optical transmission measurements were performed by Caglar *et al.* (Ref. 673) on CdZnO thin films with increasing cadmium concentration. Beginning with ZnO thin films and increasing the cadmium concentration until 100%, the bandgap energy decreased from 3.26 to 2.31 eV. XRD measurements concluded the thin film samples were polycrystalline in nature. The addition of Cd also result in an increase in film grain size. Ma *et al.* (Ref. 674) observed a bandgap energy decrease from 3.3 to 1.8 eV as the cadmium content was increased in $Cd_xZn_{1-x}O$ thin films grown using DC magnetron sputtering. The ability to tune the bandgap almost 2 eV offers great potential for wavelength tunable LEDs.⁶⁷⁴

H. Summary of ZnO property values

Table XXX highlights a summary of the properties reviewed for ZnO. Values for each of the properties are presented along with references and notation of whether they are experimental or calculated findings. Where relevant anisotropy is denoted.

VI. TIN OXIDE

Tin oxide (SnO_2), or stannic oxide, is considered a direct bandgap transparent semiconducting oxide. Tin oxide has many

TABLE XXIX. Phonon mode frequencies (cm^{-1}) of thin film $Mg_xZn_{1-x}O$ wurtzite ZnO determined from Raman scattering. Data reproduced from Ref. 669.

x	MP	$A_1(TP)$	$E_1(TO)$	E_2^2	MM
0.52	333	392	≈ 428	440	527
0.37	331	385	≈ 430	438	526
0.23	332	387	418	438	517
0.20	332	388	...	439	...
0.17	331	385	416	437	...
0.15	330	386	417	438	...
0.10	...	385	...	438	...

TABLE XXX. Summary of theoretical and experimental properties of ZnO. Common names of zinc oxide and zincite.

Stable phase	Wurtzite	Ref. 542
Stable structure	Hexagonal $a = 3.2459\text{--}3.2501 \text{ \AA}$ $c = 5.2069\text{--}5.2075 \text{ \AA}$ $a = 3.286 \text{ \AA}$ $c = 5.241 \text{ \AA}$	Refs. 543, 544, and 549 Refs. 543, 544, and 549 Ref. 545 Ref. 545
Metastable phases	Zinc blende Cubic	$F\bar{4}3m$ (#216) $Fm\bar{3}m$ (#225)
Density (g/cm ³)	5.605	Expt. ⁵⁴⁹
Bulk modulus (GPa)	154.4–173 140–183	Calc. ^{547,548,599,600} Expt. ^{547,548,601}
T_m (°C)	1975	Expt. ¹¹⁸
Debye temp. (K)	305–416 370–700	Calc. ^{602,603} Expt. ^{597,602,606}
Specific heat (J/(gK))	0.495 0.504	Expt. ⁵⁴⁹ Expt. ⁶¹⁰
Thermal cond. (W/(mK))	102–116 (Zn face) 98–110 (O face) 46–147	Expt. ⁶¹² Expt. ⁶¹² Expt. ⁶¹¹
CTE ($\times 10^{-6}/\text{K}$)	4.31–4.75 (a) 2.49–4.9 (c)	Expt. ^{542,608} Expt. ^{542,608}
Electron affinity (eV)	4.1 4.5	Expt. ⁵⁴¹ Expt. ⁶²²
Breakdown field (MV/cm)	2–3	Pred. ¹⁴⁷
m_e^*	0.23–0.34	Calc. ^{625–628}
m_h^*	0.79	Calc. ⁶³⁰
μ_e [cm ² /(V s)]	260–300 120–440	Calc. ⁶³¹ Expt. ^{557,562,563,633,636}
Gap type	Direct	Ref. 591
E_g	2.97–3.77	Bulk calc. ^{567,569,580,582} Bulk expt. ^{584,585}
ϵ_0	3.372–3.45 \perp 3.405–3.45 \parallel 3.08–3.37 ^a	Ref. 586 and 588 Film expt. ^{591,592,595}
ϵ_∞	7.61 (\perp_c) 8.50 (\parallel_c) 8.59–8.91 (\parallel_c) 7.46–7.77 (\perp_c)	Calc. ⁵⁸⁸ Calc. ⁵⁸⁸ Expt. ⁶¹⁷ Expt. ⁶¹⁷
	3.61–3.70 (\perp_c) 3.76–3.78 (\parallel_c)	Calc. ⁶¹⁷ Calc. ⁶¹⁷
Phonon modes		
IR active	$A_1, E_1,$	Ref. 618
Raman active	$A_1, E_1, 2E_2$	Ref. 618

^aAnisotropy not accounted for.

possible applications that include gas sensors,⁶⁷⁵ solar cells,⁶⁷⁶ and glass coatings.⁶⁷⁷ SnO_2 has also been shown to be a viable oxide for transistor applications as well.^{678,679} In its stable form, SnO_2 has a tetragonal rutile structure. There are also six metastable phases detailed throughout this section. Some interesting material properties highlighted throughout this section include a wide ranging electron mobility, good thermal conductivity, and a debated melting point with one source stating it is so high that the melting point is yet to be determined.⁴³⁶

A. Crystal structure

SnO_2 is a TCO with a tetragonal crystal structure at ambient pressure and room temperature and belongs to the space group $P4_2/mnm$ (#136). The tetragonal structure of SnO_2 is also known as the rutile structure. Rutile SnO_2 has a unit cell that consists of two formula units for a total of six atoms.⁶⁸⁰ Each tin atom is encompassed by six oxygen atoms in an octahedral coordination.⁶⁸¹ Figure 25 shows the stable crystal structure unit cell for SnO_2 . The metallic tin atoms occupy the Wyckoff 2(a) site while the oxygen atoms occupy the Wyckoff 4(f) sites.⁶⁸² In a bulk tin oxide crystal, the tin atoms have a sixfold coordination to the threefold oxygen atom coordination. The rutile structure of tin oxide is similar to other popular metal oxides that are known to have a rutile structure in the stable form such as TiO_2 , MnO_2 , RuO_2 , GeO_2 , VO_2 , IrO_2 , and CrO_2 .⁶⁸³ The lattice constants reported in the literature are uniform across theoretical^{684–687} and experimental⁶⁸⁸ methods, centered around $a = 4.7 \text{ \AA}$ and $c = 3.2 \text{ \AA}$. While the rutile structure is the prominent and stable phase at room temperature and normal ambient pressure, tin oxide has many polymorphs that can be achieved with added mechanical pressure to the stable phase. These polymorphs include CaCl_2 -type, $\alpha\text{-PbO}_2$ -type, pyrite-type, orthorhombic phase I ZrO_2 -type, fluorite-type, and orthorhombic phase II cotunnite-type.⁶⁸⁹ For each polymorph, the theoretical and experimental results for the lattice constants do not agree as closely as for the rutile phase as can be seen in Table XXXI.

The CaCl_2 -type phase belongs to space group $Pnnm$ (#58) with orthorhombic symmetry and considered a subgroup of the rutile phase due to the similarities in symmetry.⁶⁸⁶ The $\alpha\text{-PbO}_2$ -type phase has orthorhombic structure and belongs to the $Pbcn$ (#60) space group.⁶⁸⁶ The pyrite-type phase possesses cubic symmetry belonging to the $Pa\bar{3}$

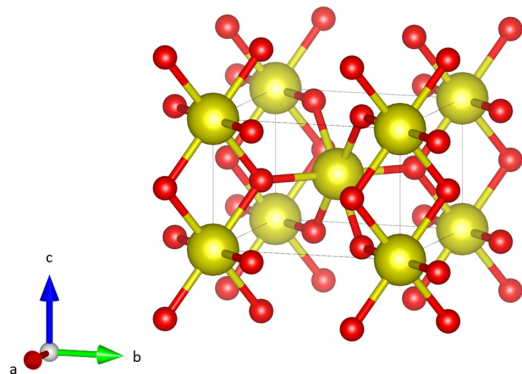


FIG. 25. SnO_2 unit cell with space group $P4_2/mnm$ (#136) with the c -axis pointed upward. Note that for tetragonal structure $a = b$ (yellow = Sn, red = O).

TABLE XXXI. Tin oxide polymorphs and crystal structure with associated lattice constants determined from experiment and theory.

Phase	Structure	Space group	Lattice (\AA)
Rutile	Tetragonal	$P4_2/mnm$ (#136)	$a = 4.74$ ^{684,a} $c = 3.19$ $a = 4.737$ ^{688,a} $c = 3.186$ $a = 4.715$ ^{686,b} $c = 3.194$ $a = 4.673$ ^{685,b} $c = 3.149$ $a = 4.776$ ^{687,b} $c = 3.212$
CaCl_2 -type	Orthorhombic	$Pnnm$ (#58)	$a = 4.653$ ^{688,a} $b = 4.631$ $c = 3.155$ $a = 4.678$ ^{690,a} $b = 4.536$ $c = 3.144$ $a = 4.708$ ^{686,b} $b = 4.720$ $c = 3.195$
$\alpha\text{-PbO}_2$ -type	Orthorhombic	$Pbcn$ (#60)	$a = 4.707$ ^{686,b} $b = 5.710$ $c = 5.246$
Pyrite-type	Cubic	$Pa\bar{3}$ (#205)	$a = 4.888$ ^{688,a} $a = 5.066$ ^{686,b}
ZrO_2 -type	Orthorhombic	$Pbca$ (#61)	$a = 9.304$ ^{690,a} $b = 4.893$ $c = 4.731$ $a = 9.970$ ^{686,b} $b = 5.113$ $c = 5.022$
Fluorite-type	Cubic	$Fm\bar{3}m$ (#225)	$a = 5.088$ ^{687,b} $a = 4.993$ ^{686,b}
Cotunnite-type	Orthorhombic	$Pnma$ (#62)	$a = 5.016$ ^{690,a} $b = 5.904$ $c = 3.028$ $a = 5.326$ ^{686,b} $b = 3.379$ $c = 6.668$

^aExperimental.

^bTheoretical.

(#205) space group.⁶⁸⁸ The ZrO_2 -type phase has orthorhombic symmetry from the $Pbca$ (#61) space group.^{686,690} A second cubic phase was seen in the Fluorite-type with $Fm\bar{3}m$ space group.⁶⁸⁷ Another observed phase is the cotunnite-type with orthorhombic symmetry belonging to the $Pnma$ (#62) space group.⁶⁹⁰

The transitions through the phases from the stable rutile structure have also been reported both theoretically and experimentally. These findings are important as they show pressures with which the transitions occur. Gracia *et al.* (Ref. 686) detail the calculated pressures with which the stable rutile phase transition to each of the six polymorphs should occur. The calculated findings are in good agreement with experimental transition pressures for the CaCl₂ and α -PbO₂-type, at 12 and 17 GPa, respectively.⁶⁸⁶ The remaining phases have large deviations between the calculated and experimental transition pressures, with no reported experimental transition pressure for the fluorite-type. The pyrite-type transition was shown to occur at 21 and 28.8 GPa (Refs. 688 and 690) by experiment and at 17 GPa by theory.⁶⁸⁶

The occurrence of the ZrO₂-type transition has been observed experimentally between 50 to 74 GPa.⁶⁹⁰ This contradicts the theoretical data stating that the transition to ZrO₂-type should occur at 18 GPa. Theory states that the transition to the Fluorite-type should occur at 24 GPa.⁶⁸⁶ The transition to cotunnite-type was found to occur experimentally at 54 to 117 GPa and by theory at 33 GPa.^{686,690}

B. Growth

Bulk crystal and thin film samples of SnO₂ have been grown in a variety of ways. For bulk crystal growth, the extremely high melting point causes limitations for certain methods and melt growth of SnO₂ is simply not a viable option. Physical vapor transport (PVT) is a common growth method for bulk crystal. Marley *et al.* (Ref. 691) produced the first known bulk crystals using PVT. Growth was observed from SnO₂ powder for both oxidizing and natural conditions. The carrier gas used in PVT process either produced or inhibited defects. Other than helium, most neutral carrier gases caused inclusions and voids while the use of helium-oxygen reduced defects. Growth temperature affected the crystalline features, causing the formation of either needles, twinned plates, or rods.⁶⁹¹ A similar vapor-transport technique was used by Marley *et al.* (Ref. 692) a few years later to grow SnO₂ crystals.⁶⁹² While less common than PVT, CVT is another possible vapor phase growth technique. Nagasawa *et al.* (Ref. 693) produced the first reported bulk crystal grown using CVT in 1965. H₂O and SnCl₄ were used for the vapor reaction at temperatures ranging from 1100 °C to 1300 °C. The crystal quality was stated to be good, backed up by a reported mobility value of 200 cm²/(V s).⁶⁹³ Other known methods for bulk crystal growth include hydrothermal^{694,695} and flux growth.^{696,697}

Methods for the growth of SnO₂ thin films are listed throughout the literature. The methods are wide ranging and similar to those used to grow thin films of other oxides reported in this review. Reported methods include PLD,^{698,699} RF sputtering,^{700–702} molecular beam epitaxy (MBE),^{703–705} MOCVD,^{706,707} ALD,⁷⁰⁸ spin coating,^{709,710} and spray-pyrolysis.^{711,712}

C. Electronic band structure

Rutile SnO₂ exhibits a direct bandgap of 3.6 eV at the Γ point of the Brillouin zone.^{681,684,713} SnO₂ has a complex band structure due to the large number of valence electrons that occupy each unit cell. There arises four narrow but deep bands within the valence bands due to the O(s) states. These deep and narrow bands are not considered core states as they are very dispersive.⁷¹³ Above the dispersive O(s) bands

reside 12 valence bands. These bands are about 10 eV higher in energy than the O(s) bands. For the lower portion of the 12 valence bands O(p) states mixed with Sn(s) states dominate. For the upper portion of the 12 valence bands, Sn(p) and Sn(d) states combine with the O(s).⁷¹³ Calculated band structures of SnO₂ show very high symmetry in the Brillouin zone. The conduction band is calculated to be very flat with a minimum that occurs at the Γ point. The width of the valence bands is about 4.5 eV. The theoretical band structure shows an indirect band edge feature. This means the lowest optical transition is a phonon aided indirect transition. This indirect transition occurs at the R_1^+ point of the valence band to the Γ_1^+ point of the conduction band for an energy gap of 2.62 eV. A second indirect transition occurs from the X_1^+ point of the valence band to the Γ_1^+ point of the conduction band for an energy gap of around 2.90 eV.⁷¹⁴

There also exist two direct transitions that are dipole forbidden with energy gaps of 3.03 and 3.50 eV. The first allowed transition is direct and occurs with a bandgap of 3.68 eV for light polarized perpendicular to the *c*-axis and a direct gap of 4.07 eV for light polarized parallel to the *c*-axis.⁷¹⁴ While the previous statements are theoretically determined bandgap energies from Arlinghaus *et al.* (Ref. 714), these are generally supported with experimental data that conclude SnO₂ is a direct bandgap material with an energy gap of around 3.6 eV.⁷¹⁴ Reimann *et al.* (Ref. 716) report similar findings in the symmetry of the conduction band minimum and the valence band maximum as well as the direct bandgap of 3.6 eV. Few studies on the deep valence bands were found in the literature. This is due in part to the limiting capabilities and poor resolution of the photoemission studies that were only able to measure and detail the valence bandwidth. One and two photon measurements performed by Reimann *et al.* provide insight into the exciton states and the upper valence bands. The three uppermost valence bands below the valence band maximum possessed bandgaps of 3.59, 3.64, and 3.71 eV according to two photon measurements. The exciton binding energies of those three transitions, respectively, are 32.76, 36.8, and 39.7 meV.⁷¹⁶ The quasiparticle band structure and density of states (DOS) are presented for SnO₂ in Fig. 26. The figure

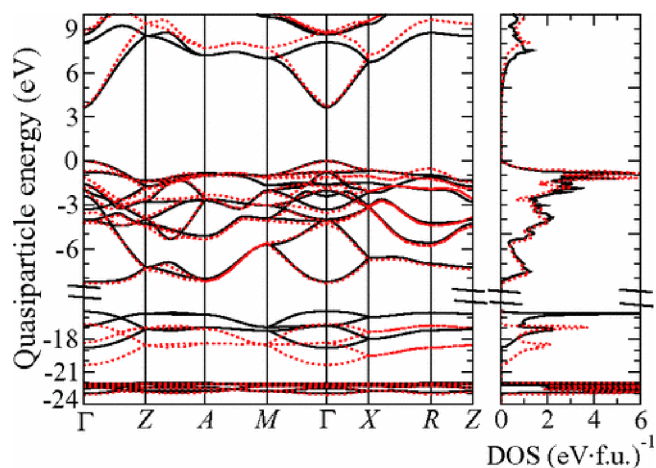


FIG. 26. Electronic structure of rutile SnO₂. The dotted red lines were determined using HSE03+G₀W₀, while the solid black lines were determined using LDA+U+ Δ . Reproduced with permission from Schleife *et al.*, Phys. Rev. B 83, 035116 (2011). Copyright 2011 APS (Ref. 715).

reproduced from Schleife *et al.* (Ref. 715) depicts the calculated electronic structure and density of states of SnO_2 determined by HSE03+ $G_0\text{W}_0$ (red line) and LDA+U+ Δ (black line). The Hubbard parameter U within the LDA calculations was set to 4.6 eV in order to accurately describe the *d*-band complex, and the results of the LDA calculations show agreement with the HSE03 calculations. The scissor shift Δ was set equal to 2.46 eV in order to move the conduction bands in relation to the valence bands, increasing the agreement between the two theoretical methods. Some deviations between the two methods was evident in the O 2s bands located at -18 eV and along the upper valence bands at Γ . The bands near the R point of the Brillouin zone also show variations between the two methods with HSE03+ $G_0\text{W}_0$, LDA+U+ Δ resulting in a smaller indirect gap along the Z and X points than at the R point, respectively. Without the addition of Δ the R point was shown to reside even lower. The differences highlighted in Fig. 26 between these two methods provides an explanation for the numerous inconsistencies found in the literature for calculated electronic band structure results.

1. Bandgap energy

There have been many reported values of the bandgap for SnO_2 . A wide range of theoretical methods for determining the bandgap energy have been used including GGA,⁶⁸⁷ LDA,^{685,717} FP-LAPW, modified Becke-Johnson (mBJ),⁶⁸⁷ $G^0\text{W}^0$ variations,^{715,717} B3LYP,⁶⁸⁶ HSE03- $G_0\text{W}_0$,⁷¹⁵ and cluster calculations.⁷¹⁸ Note that Schleife *et al.* (Ref. 715) denote their calculated method as $G_0\text{W}_0$ instead of $G^0\text{W}^0$ like Berger *et al.* (Ref. 717) does. Almost all of the reported calculation methods drastically underestimate the bandgap energy of SnO_2 . It appears that GGA and LDA calculations result in bandgap energies that are farthest from experimental comparisons with values of 0.832 eV (GGA),⁶⁸⁷ 0.94 eV (LDA),⁷¹⁷ and 1.38 eV (LDA).⁶⁸⁵ Berger *et al.* (Ref. 717) reported results using variations of $G^0\text{W}^0$, specifically EET and SOS+EET. While these values, 2.86 and 2.89 eV, respectively, still underestimate the bandgap energy these were significantly better than results from GGA and LDA calculations. It is interesting to note that Berger *et al.* also used the same $G^0\text{W}^0$ variations for calculations of the ZnO bandgap energy, a very well known and often reported value (see Subsection VIC 1). These methods also underestimated the bandgap of ZnO by almost 1 eV.

Calculated bandgap energies do not begin to show agreement with experimental values until hybrid methods such as B3LYP, HSE03- $G_0\text{W}_0$, and cluster calculations are used. Even so, these methods only begin to provide bandgap energies in agreement with some of the lower absorption edge measurements. B3LYP and HSE03- $G_0\text{W}_0$ methods resulted in bandgap energies of 3.50 and 3.65 eV, respectively.^{686,717} Cluster calculations appear to be one of the more reliable theoretical methods in determining the bandgap of pure SnO_2 , producing values as high as 3.7 eV.⁷¹⁸

The experimentally determined bandgap energies reported for rutile SnO_2 also have a large amount of spread within the reported values, similar to the theoretically determined methods. However, there does appear to be a trend related to the time period of publication. Bandgap energies cited from works dating back to the 1960s and 1970s rarely reported energies above 4.0 eV while literature works published after the 2000s often saw bandgap energies well into the 4.0 eV and sometimes 5.0 eV. Breaking down the methods of the older

literature works, the majority were absorption edge measurements.^{719–722} These bandgap energies ranged in value from 3.54 to 4.0 eV. The lowest reported value from these older works comes from a 1971 publication by Nagasawa *et al.* (Ref. 723) where photoconductivity measurements suggested a bandgap energy of 3.37 eV. In 1964, a report by Summit *et al.* (Ref. 724) detailed some of the earliest works on anisotropy of the bandgap energies in bulk SnO_2 . Pure single crystals were measured via ultraviolet absorption using light polarized parallel and perpendicular to the *c*-axis. The results showed a direct bandgap with energies of 3.93 eV for polarization parallel and 3.57 eV for polarization perpendicular to the *c*-axis. Summit *et al.* hypothesize that each of these absorption edge bands could represent a band-to-band transition belonging to two separate and distinct bandgap energies. This hypothesis of two separate bands is supported by the selection rules of dipole transitions for rutile structures.⁷²⁴

For the literature works published after the 2000s, the experimental methods included optical transmittance,⁷²⁵ absorption edge measurements,^{709,711} and SE. Abdelkrim *et al.* (Ref. 725) studied five polycrystalline thin film samples of SnO_2 with bandgap energies ranging from 3.643 to 3.949 eV according to the optical transmittance measurements. The sample with the largest refractive index of 2.175 resulted in the lowest bandgap energy of 3.643 eV. The sample with the highest bandgap energy of 3.949 eV had a refractive index of 2.105. Bandgap energy and the Urbach tail were also observed as functions of film thickness. As film thickness increased from 550 to 760 nm, the bandgap decreased before eventually increasing again beyond a thickness of 760 nm. It was thought that the bandgap decrease with thickness could be a result of the crystalline quality improving as well as changes in the grain size and atomic distance. Another explanation for the reducing bandgap with increasing film thickness could be a result of increased impurities along the conduction band. This would cause allowed states to form along or near the conduction band within the bandgap region, resulting in a decreased bandgap energy. The amount of allowed states increases with increasing film thickness.⁷²⁵

Absorption edge measurements were reported by Gu *et al.* (Ref. 709) and Serin *et al.* (Ref. 711) in 2004 and 2006, respectively. Gu *et al.* reported the highest bandgap of any of the cited literature within this review for an absorption edge measurement at 4.38 eV. The authors stated that this bandgap energy for their thin film samples was significantly higher than the bulk SnO_2 bandgap energy of 3.62 eV as a result of quantum size effects within the SnO_2 thin film.⁷²⁷ Note, the value of 3.62 eV for bulk SnO_2 was not explicitly detailed by either Gu *et al.* (Ref. 709) or Frohlich *et al.* (Ref. 727). Interestingly though, in 1978, Frohlich *et al.* produced a value of 3.56 eV for what is considered the lowest exciton transition within SnO_2 by way of a two-photon absorption method.⁷²⁷ In 2011, Schleife *et al.* (Ref. 715) stated that this value of 3.56 eV was widely considered as the accepted bandgap energy of SnO_2 .^{715,727} Furthermore, it was stated a binding energy of around 30 meV (Refs. 716, 728, and 729) being added to the lowest transition of 3.56 eV would yield the fundamental energy gap at 3.59 eV. The accuracy of that statement is refuted by more recent ellipsometry measurements from Feneberg *et al.* (Ref. 726) detailed just below.

The absorption measurements from Serin *et al.* (Ref. 711) were reported to range from 3.94 to 3.96 eV. The cause for the slight increase in the bandgap energy was the deposition temperature of the two samples, 300 and 400 °C, respectively. The carrier concentration also increased with increasing deposition temperature. The bandgap

shift by 0.02 eV was said to be a result of the Moss–Burnstein shift occurring as the low lying energy band levels of the conduction band are filled with electrons from the increased carrier concentration.^{711,730}

In 2014, Feneberg *et al.* (Ref. 726) provided perhaps the most accurate depiction of the dielectric function and bandgap properties of rutile SnO₂ films to date using SE. Details regarding the bandgap and excitonic binding energy were reported for the ordinary (perpendicular) and extraordinary (parallel) directions with respect to the *c*-axis. The results of Feneberg *et al.* produced key bandgap parameters such as the onset of excitonic absorption, the excitonic binding energy, the fundamental lowest bandgap energy, as well as evidence of anisotropy within the optical properties. Starting with the ordinary direction the onset of excitonic absorption was found to be 4.35 eV. Adding on the excitonic binding energy of 0.17 eV for that direction, the fundamental lowest bandgap energy was reported to be 4.52 eV for E ⊥ *c*. The extraordinary direction had differing results and showed clear anisotropy within the optical properties of SnO₂. The onset of excitonic absorption was slightly larger in energy at 5.59 eV. The excitonic binding energy was significantly smaller in this direction at 0.08 eV. This resulted in a fundamental lowest bandgap energy of 5.67 eV for E ∥ *c*, over 1 eV higher than the ordinary direction. Feneberg's values for the bandgap energies of SnO₂ are distinctly larger than those previously reported. Note, there is no explanation given for the large difference in the reported bandgap energies.

Feneberg *et al.* (Ref. 726) is one of the few studies to investigate anisotropy of the bandgap energy along different crystal directions. The anisotropic nature of the optical responses occurring above the bandgap had not been reported prior to the work of Feneberg *et al.* in 2014, even with a seemingly large interest in the topic from numerous theoretical works.^{685,731–734} SE was used to investigate the optical properties of SnO₂ including the extraordinary and ordinary dielectric functions. Absorption onsets occurred at 4.28 eV (E ⊥ *c*) and 5.42 eV (E ∥ *c*) revealing strong optical anisotropy. Feneberg *et al.* state that these values point toward a “fundamental but dipole forbidden” bandgap occurring at 3.59 eV.⁷²⁶ Dipole forbidden bandgap energies were also reported using model fits of the imaginary parts of the dielectric function (ε_2) occurring at 3.77 (E ⊥ *c*) and 3.41 (E ∥ *c*).

The reported experimentally and theoretically determined bandgap values for bulk and thin film samples of SnO₂ are listed in Table XXXII.

2. Temperature dependence of bandgap energy

SnO₂ exhibits temperature dependence of its bandgap. Kohnke *et al.* (Ref. 719) studied the optical properties and examined the rapid absorption coefficient increase in temperature for bulk rutile crystal samples. This allowed for the extraction of a value for the forbidden optical bandgap of 3.54 eV. By examining the cutoff shift of several samples over a temperature range of 8 to 415 K, an average bandgap change with temperature was found to be -6.0×10^{-4} eV/K. The absolute zero optical energy gap was determined to be 3.7 eV from linear extrapolation to 0 K.⁷¹⁹ Arai *et al.* (Ref. 721) reported temperature change of the absorption edge to be $-2.0 \times 10^{-4} \pm 4 \times 10^{-5}$ eV/K for thin film samples.

Sanon *et al.* (Ref. 736) report on the bandgap narrowing of SnO₂ films and the relevance that it has to the electronic properties and structure. Bandgap narrowing is a result of the electron–electron

TABLE XXXII. Bandgap energy parameters of rutile SnO₂ determined from theory and experiment. Values labeled (*) were reported disregarding anisotropy.

E _g (eV)	Method	Bulk/film	Reference
Experiment			
3.37*	Photoconductivity	Bulk	723
3.54*	Absorption edge	Bulk	719
3.56*	Two-photon absorption	Bulk	727
4.00*	Absorption edge	Bulk	720
3.57	Absorption edge (E ⊥ <i>c</i>)	Bulk	724
3.93	Absorption edge (E ∥ <i>c</i>)	Bulk	724
3.7*	Absorption edge	Film	722
3.71*	Absorption edge	Film	721
3.64–3.94*	Optical transmittance	Film	725
3.94–3.96*	Absorption edge	Film	711
4.38*	Absorption edge	Film	709
4.35 ^a	SE (E ⊥ <i>c</i>)	Film	726
4.52 ^b	SE (E ⊥ <i>c</i>)	Film	726
5.59 ^a	SE (E ∥ <i>c</i>)	Film	726
5.67 ^b	SE (E ∥ <i>c</i>)	Film	726
Calc.			
1.70	FP-LAPW	...	735
2.76	mBJ	...	687
2.86	G ^o W ^o EET	...	717
2.89	G ^o W ^o SOS+EET	...	717
3.50	B3LYP	...	686
3.65	HSE03+G _o W _o	...	715
3.7	Cluster calc. ^c	...	718

^aOnset of excitonic absorption.

^bFundamental lowest band-to-band transition, accounts for excitons.

^cCombination of scattered-wave molecular-orbit and augmented-spherical-wave band structure method.

scattering as well as the electron–impurity scattering and cannot be ignored in SnO₂ thin films. These findings concluded that with increasing carrier concentration, the bandgap will also increase as a result of a Burstein–Moss shift.⁷³⁶

D. Material properties

SnO₂ is a versatile oxide with many uses. The basic material properties included here are the oxide's density, bulk modulus, hardness, and melting point.

The material density is in good agreement across literature ranging from 6.975 to 7.02 g/cm³.^{684,737,738} Experimentally, the density was determined using the pycnometric method, the water immersion technique, and using x-ray density measurements.⁷³⁷ The bulk modulus of SnO₂ has been researched extensively considering the high pressure phase transitions. Gracia *et al.* (Ref. 686) determined the theoretical bulk modulus for the rutile phase as well as each subsequent transitional phase. The rutile phase bulk modulus was calculated to be between 221 and 228 GPa.⁶⁸⁶ Other calculations show the bulk

modulus to be 244–245 GPa.^{685,739} Experimentally, the bulk modulus was reported to be 205 GPa.⁶⁸⁸ Fluorite-type contained the highest theoretical value at 322 GPa while cotunnite had the lowest theoretical value at 180 GPa.⁶⁸⁶ However, experimentally, cotunnite-type had the highest observed bulk modulus of any of the phases at 417 GPa.⁶⁹⁰ The Mohs hardness of SnO₂ was reported to be 6.5,⁷⁴⁰ which yields a value of around 982 kg/mm² when converted to Vicker's hardness. SnO₂ is often utilized as a coating to increase scratch resistance^{741–743} of glass surfaces and ceramics. Li *et al.* (Ref. 744) reported on Knoop microhardness of single-crystal SnO₂, or cassiterite. It was concluded that there was significant anisotropy of the microhardness within the material.⁷⁴⁴

Galazka (Ref. 436) made mention of the melting point of SnO₂ and possible complications that are exhibited. It was stated that a true melting point had not been observed or recorded for SnO₂ yet.⁴³⁶ Near-stoichiometric SnO₂ would require an extremely high oxygen partial pressure for melting without decomposition; a pressure that was calculated to be around 500 times larger than the oxygen partial pressure needed for ZnO stabilization.⁷⁴⁵ The relative oxygen partial pressure was normalized to β -Ga₂O₃, a value of 1. The relative oxygen partial pressure calculated for ZnO and SnO₂ were 100 and 50 000, respectively. In absolute terms, no melting of SnO₂ was observed at 1950 °C and an oxygen pressure of 140 bars; however, sublimation/decomposition was observed indicating higher oxygen partial pressures would be needed. Furthermore, SnO₂ was also heated to 2100 °C with no melting observed under a CO₂ atmosphere producing 0.3 bar partial pressure of O₂, only sublimation/decomposition. Since pure SnO₂ can withstand temperatures well above 2000 °C, it was not possible to grow bulk crystal samples from melt-growth techniques.⁷⁴⁵ Ellmer *et al.* (Ref. 684) state the melting point above 1900 °C where decomposition into SnO and O₂ was observed once 1500 °C was reached.⁶⁸⁴ The CRC Handbook of Physics and Chemistry lists the SnO₂ melting point as 1630 °C.¹¹⁸ All reported values for the basic material properties are listed and compared in Sec. XI.

1. Thermal properties

The scope of the thermal properties reviewed for SnO₂ included CTE, specific heat, thermal diffusivity, and thermal conductivity.

The CTE of SnO₂ exhibits a slight anisotropy along the *a* and *c* axes. Along the *a*-axis the CTE was shown to be 4.0×10^{-6} K⁻¹ while along the *c*-axis a value of 3.7×10^{-6} K⁻¹ was reported.⁷⁴⁶ The volume expansion coefficient was found experimentally to be 11.7×10^{-6} K⁻¹. Another CTE value of 3.8×10^{-5} K⁻¹ was reported theoretically by Hassan *et al.* (Ref. 687). Hassan *et al.* state that their value of 3.8×10^{-5} K⁻¹ is significantly smaller than the overall volume CTE of 11.7×10^{-6} K⁻¹ previously reported by Percy *et al.* (Ref. 746). Note, we believe this to be an error by Hassan *et al.* as their value of 3.8×10^{-5} K⁻¹ is significantly *larger* (not smaller) than the value of Percy *et al.* of 11.7×10^{-6} K⁻¹. No explanation was given for the significant difference in values.

Experimental and theoretical room temperature values for the heat capacity are in good agreement being 55.3 and 60 J/(mol K), respectively.^{687,747} Using the known molar mass of SnO₂, 150.71 g/mol, the heat capacities were converted to units of specific heat yielding values of 0.366 and 0.398 J/(g K). Thermal diffusivity values are in good agreement as well, ranging from 1.45×10^{-2} to 1.7×10^{-2} cm²/s.

All reported values for specific heat and thermal diffusivity are listed and compared in Sec. XI.

With potential device level applications,^{748–750} the thermal conductivity of SnO₂ is an important thermal property. Turkes *et al.* (Ref. 737) measured the thermal conductivity and its anisotropy in single crystals of rutile SnO₂, while also producing theoretical values far exceeding those seen experimentally. For the experimental measurements, the temperature gradient was aligned both perpendicular and parallel to the *c*-axis. The parallel measurements at room temperature resulted in a thermal conductivity of 98 W/(mK) while the perpendicular recorded a value of 55 W/(mK), leading to an anisotropy ratio of 1.78. A maximum experimental thermal conductivity of 1750 W/(mK) was observed at 26 K with the temperature gradient parallel to the *c*-axis.⁷³⁷ The increase in thermal conductivity at low temperatures is thought to be due to an increase in the isotope scattering as the Umklapp scattering is frozen out.⁷³⁷ With the difference in values with respect to the temperature gradient, it is considered evident that there exists anisotropy within the scattering mechanisms as well; perpendicular thermal conductivity measurements did not reveal the same exponential behavior as the parallel measurements.⁷³⁷ Turkes *et al.* also reported a theoretical thermal conductivity of 234 W/(mK) at room temperature, drastically higher than the experimental results. When accounting for scattering, the calculated room temperature thermal conductivity was corrected to 107 W/(mK) with anisotropy value of 1.70. It was concluded that phonon-phonon scattering was the most likely source of the thermal conductivity anisotropy.⁷³⁷ Galazka (Ref. 436) reports room temperature thermal conductivity measured using the laser flash method, at 51.4 W/(mK), comparable to Turkes *et al.* (Ref. 737) room temperature values.

The thermal conductivity properties of SnO₂ ceramics was also studied. Fayette *et al.* (Ref. 751) observed how the grain size within the ceramic influenced the thermal conductivity. With increasing theoretical density percentage, the thermal conductivity was shown to reach values around 30 W/(mK) at approximately 96% density. Notable relationships between the ceramic grain size and the thermal conductivity, as well as temperature and thermal conductivity were reported.⁷⁵¹ With grain sizes observed from around 2 to 8 μm , thermal conductivity increased with grain size from around 25 to 40 W/(mK), respectively. The temperature dependence on the thermal conductivity showed an interesting observation with sample sintering time. At lower temperatures (0–100 °C) the sintering time played a large role in the deviation of the thermal conductivity values. A thermal conductivity value of 42 W/(mK) was reported at 20 °C for samples that were sintered for 48 h at 1150 °C. Samples that received 12 min of 1150 °C sintered had a thermal conductivity at 20 °C of only 24 W/(mK). As temperature increased up to 900 °C, the difference in thermal conductivity with sintering time slowly decreased, with nearly no difference in values at higher temperatures.⁷⁵¹ All reported values of the thermal conductivity are listed and compared in Sec. XI.

2. Phonon properties

The phonon properties of rutile SnO₂ have been detailed by Batzill *et al.* (Ref. 683). Within SnO₂, there are six atoms in the unit cell, leading to 18 vibrational modes. The irreducible representations combining both the optical and acoustic modes are

$$\Gamma = A_{1g} + A_{2g} + B_{1g} + B_{2g} + E_g + 2A_{2u} + 2B_{1u} + 4E_u.$$

There are two IR active modes consisting of a single A_{2u} and triply degenerate E_u . There are four Raman active modes consisting of doubly degenerate E_g and the three non-degenerate modes of A_{1g} , B_{1g} and B_{2g} . There are also two silent modes consisting of A_{2g} and B_{1u} . The remaining A_{2u} and two E_u modes are acoustic.^{683,752} The three non-degenerate Raman modes have a vibration direction perpendicular to the c -axis. The remaining doubly degenerate E_g mode vibrates along the c -axis. All six oxygen atoms rotate around the c -axis with the vibration of B_{1g} mode. For the IR active modes, both tin and oxygen atoms vibrate in the direction of the c -axis for the A_{2g} mode. For the E_u mode, both tin and oxygen atoms have vibration perpendicular to the c -axis. The silent mode B_{1u} has vibration of tin and oxygen atoms along the c -axis. The remaining silent mode A_{2g} has vibration perpendicular the c -axis.⁷⁵² Frequencies for the Raman and IR modes were determined experimentally by Katiyar *et al.* (Ref. 753) and are presented in Table XXXIII. Frequencies for the modes B_{1g} and A_{2g} were determined experimentally.⁷⁵³ The Raman and IR active modes are listed and compared in Sec. XI.

3. Electrical properties

The electrical properties of SnO_2 reviewed below include the electron affinity, electrical breakdown field, static and high frequency dielectric constants, effective mass, and electron mobility. The electron affinity is in good agreement among the reported values summarized in Sec. XI. Determined both theoretically and experimentally, the electron affinity ranges from 4.3 to 4.85 eV.^{754,755} Ghosh *et al.* (Ref. 754) found that the electron affinity increased with added oxygen monolayers. Ghosh *et al.* also references unpublished works claiming the electron affinity was around 4.55 eV according to photoemission studies.⁷⁵⁴ The electrical breakdown field was not a parameter that was readily found in the literature.

The reported static dielectric constants for SnO_2 were in good agreement across the literature. Anisotropy was also evident, with the direction perpendicular to the tetragonal c -axis reported with the largest value. Values for the static dielectric constant perpendicular to the c -axis ranged from 13.5 to 14,^{683,756} while values parallel to the c -axis

TABLE XXXIII. SnO_2 Raman and IR active transverse and longitudinal phonon mode frequencies. All values taken from Katiyar *et al.* (Ref. 753).

Raman mode	ω (cm^{-1})
A_{1g}	638
B_{2g}	782
B_{1g}	100 ^a
A_{2g}	398 ^a
E_g	476
IR Mode	ω_{TO} (cm^{-1})
A_{2u}	477
$E_{u,1}$	244
$E_{u,2}$	293
$E_{u,3}$	618
	ω_{LO} (cm^{-1})
	705
	276
	366
	710

^aCalculated.

ranged from 9.0 to 9.6.^{683,756,757} The high frequency dielectric constant was reported to have smaller anisotropy with values being 3.70 and 3.90 for directions perpendicular and parallel to the c -axis respectively.²¹⁰

The electrical breakdown field was not a parameter that was readily found in the literature. Using predictions of Higashiwaki *et al.* for breakdown field in relation to bandgap,¹⁴⁷ the estimated breakdown field for SnO_2 is around 3.5 MV/cm, similar to GaN. The average bulk experimentally determined bandgap of 3.614 eV found in Sec. XI was used to predict the breakdown field strength.

There are numerous Γ -point calculated effective electron mass parameters for SnO_2 that range from 0.10 m_e to 0.18 m_e .^{692,757,758} Morgan *et al.* (Ref. 758) determined that the effective mass decreased with increasing temperatures for their lead doped samples. Experimentally, the reported values appeared to be slightly larger than calculated values, ranging from 0.22 m_e to 0.299 m_e .^{692,759} The effective mass values reported by Button *et al.* (Ref. 759) using cyclotron resonance data also showed anisotropy with values of 0.299 m_e for m^*_{\perp} and 0.234 m_e for m^*_{\parallel} . The values found by Button *et al.* have been used for comparison by Feneberg *et al.* (Ref. 210). In the study Feneberg *et al.* used IR ellipsometry in combination with Hall Effect measurements to derive m^*_{\parallel} and m^*_{\perp} as a function of carrier concentration from the plasma frequency parameters. This method was first proposed and used in 2000 by Kasic *et al.* (Ref. 760) to determine m^*_{\parallel} and m^*_{\perp} of wurtzite GaN. Findings showed that at lower carrier concentrations (around 10^{19} cm^{-3}) there was significantly less anisotropy than what Button *et al.* had previously reported. Values of effective mass for both directions were nearly identical at around 0.22 m_e to 0.23 m_e . However, at higher carrier concentration the anisotropy is more pronounced. At a carrier concentration of around $2 \times 10^{20} \text{ cm}^{-3}$ values were about 4.0 m_e for m^*_{\perp} and 0.26 m_e for m^*_{\parallel} , a significant increase in anisotropy. These results are also strongly indicative of a non-parabolic nature within the conduction band for both polarization directions.²¹⁰

From lead doped SnO_2 crystal samples, Morgan *et al.* concluded that the electron effective mass is decreasing above room temperature in their study across a temperature range of 100 to 1100 K. For both samples used in this study the effective mass was found to be higher at lower temperature (100 K). The Seebeck coefficient, optical mode scattering, and Hall coefficient also played a role in determining the effective mass with an average value of 0.13 m_e being reported across four samples.⁷⁵⁸ Marley *et al.* (Ref. 692) obtained an effective mass of 0.22 m_e from analyzing Hall effect data along with the thermoelectric power of SnO_2 single crystals.⁶⁹²

The mobility of charge carriers in SnO_2 has been studied by multiple groups. According to Galazka (Ref. 436), the highest experimental electron mobility seen at room temperature ranges from 240 to 260 $\text{cm}^2/(\text{V s})$.⁷⁶¹ The high experimental values were obtained on high quality SnO_2 crystal samples. The same sample that produced a value of 260 $\text{cm}^2/(\text{V s})$ also had a peak mobility of 8800 $\text{cm}^2/(\text{V s})$ at 77 K. The electron carrier concentration of the sample was $8.5 \times 10^{15} \text{ cm}^{-3}$. The crystal purity played a large role in the mobility values. A sample grown by Fonstad and Rediker (Ref. 761) had a carrier concentration of $8.6 \times 10^{16} \text{ cm}^{-3}$. The increase in carrier concentration resulted lower mobility at 240 and 2200 $\text{cm}^2/(\text{V s})$, at room temperature and 77 K, respectively. Above room temperature polar optical phonon mode scattering is dominant.⁷⁶¹

Crabtree *et al.* (Ref. 757) report on efforts to reduce the various impurities within the crystal. Reported room temperature mobilities ranged from 172 to 250 cm²/(V s). An outlying value had a mobility of 50 cm²/(V s). That sample had the lowest conductivity and the lowest carrier concentration.⁷⁵⁷ These results were compared to a previous study by Morgan *et al.* (Ref. 758) where mobility parameters of Sb doped SnO₂ were reported. Mobility values at room temperature ranged from 70 to 87 cm²/(V s).⁷⁵⁸ Crabtree *et al.* conclude that the addition of Sb doping at room temperature caused the lowering of mobility when compared to undoped SnO₂, and not due to trace impurities such as silica.⁷⁵⁷ All cited values of electron mobility are listed and compared in Sec. XI.

E. Doping and defects

Bandgap engineering and narrowing of SnO₂ have gathered attention recently. Possible n-type dopants for SnO₂ seen in the literature include palladium, antimony, platinum, and indium.⁷⁶² At low doping concentrations, those dopants did not alter the grain size of SnO₂ thin films. The Fermi level was altered with the addition of all of the dopants except platinum.⁷⁶² Other dopants include cobalt, zinc,^{763–765} cupric oxide,⁷⁶⁶ nickel,⁷⁶⁷ niobium, and tantalum.⁷⁶⁸ Lead has been shown to be an effective additive/dopant for modification of the bandgap of SnO₂. The ability to modulate the bandgap from 3.17 to 3.67 eV has been shown by Ganose *et al.* (Ref. 769) using DFT calculations. This modulation is key for increasing the relevance of SnO₂ in the field of photovoltaics. The bandgap modulation happens through the lowering of the conduction band maximum from the vacuum level. This lowering increases the electron affinity, which enables changing the work function and achieving improved alignment of the work function to cathodes and formation of Ohmic contacts.⁷⁶⁹

SnO₂ is an n-type material,⁷³⁷ but Morgan *et al.* (Ref. 758) offered some insight to the possibility of p-type SnO₂. Attempts at doping SnO₂ with gallium or indium to achieve p-type conductivity have proven unsuccessful. Investigation of the Seebeck coefficient revealed that gallium doped crystals were p-type with very high resistivity and the crystals were not well formed at all.⁷⁵⁸

Intrinsic defects within SnO₂ have been studied using first principles DFT calculations. The defect energies have been presented for stoichiometric, oxygen-deficient, and oxygen-excess scenarios. According to the DFT results, nonstoichiometric defects are more probable than stoichiometric ones, thus leading to the nonstoichiometry of SnO₂. The n-type conductivity was said to be a result of the oxygen vacancies. When the oxygen partial pressure was altered, the defect becomes unstable, resulting in oxygen excess when oxygen-rich conditions are met. Along with the oxygen vacancies, the structure of the tin and oxygen interstitials are presented. Further details are provided in Ref. 770.

F. Polymorphs

Bandgap energies and electronic structures for SnO₂ polymorphs have been reported throughout the literature. Gracia *et al.* (Ref. 686) calculated bulk band structures for each of the three (tetragonal, orthorhombic, and cubic) Bravais lattices as well as zero pressure bandgap values for each of the polymorphs. The bandgaps for the polymorphs are: CaCl₂-type, 3.58 eV; α -PbO₂-type, 3.80 eV; pyrite-type, 3.55 eV; ZrO₂-type, 3.44 eV; fluorite-type, 3.01 eV; and cotunnite-type,

2.84 eV.⁶⁸⁶ With the exception of the fluorite and cotunnite-type polymorphs, the zero pressure bandgaps are in good agreement with the bandgap of the stable rutile phase at 3.50 eV. SnO₂ bandgap energy values increase as the oxide transitions toward the α -PbO₂ phase where it reaches a peak energy. The bandgap energy decreases as SnO₂ transitions away from α -PbO₂ toward the cotunnite phase. Other theoretical and experimental rutile phase energy bandgaps are discussed in Secs. IV A and IV C 1, as well as in Sec. XI. Density of states analysis shows that each polymorph has a direct bandgap with the exception of cotunnite-type, exhibiting an indirect bandgap according to the electronic structure make-up. Similar to other oxides that have been discussed, the conduction bands are a result of the Sn *s* and *p* states while the upper valence bands results from the Sn(*p*) and O(*p*) states. The direct bandgap polymorphs have a valence band maximum and conduction band minimum located at the Γ -point of the Brillouin zone. The single indirect bandgap polymorph, the cotunnite-phase, has a valence band maximum located somewhere between the *U* and *X* symmetry points of the Brillouin zone.⁶⁸⁶ Other theoretical values for the polymorph bandgaps were reported by Li *et al.* and Hassan *et al.* (Refs. 685 and 687). As is often the case, the DFT bandgap values are underestimated compared to reported experimental values. Both Li *et al.* and Hassan *et al.* state that all polymorphs have a direct bandgap except fluorite-type, with an indirect gap located at the *W*- Γ points.^{685,687,689} This contradicts the findings of Gracia *et al.* (Ref. 686), who states that the cotunnite-type was the only indirect bandgap according to their calculations. Very little experimental data on the polymorph bandgaps has been reported across literature. The calculated methods for determining the bandgaps include GGA, mBJ,⁶⁸⁷ DFT-LDA,⁶⁸⁵ and DFT-B3LYP.⁶⁸⁶

G. Summary of SnO₂ property values

Tables XXXIV and XXXV highlight a summary of the properties reviewed for SnO₂. Values for each of the properties are presented along with references and notation of origin. Where relevant anisotropy is noted.

VII. CADMIUM OXIDE

Cadmium oxide (CdO) is another TCO material. CdO has a thermodynamically stable cubic rocksalt crystal structure with a very high electrical conductivity as well as very high carrier concentrations that can reach 10²¹ cm⁻³.⁷⁷⁵ CdO is transparent within the visible spectrum and has the potential for device applications including thermoelectrics,^{776,777} thin-film conductors,⁷⁷⁸ plasmonics,⁷⁷⁹ transparent electrodes, and photovoltaic cells.⁷⁸⁰

A. Crystal structure

CdO has a cubic crystal structure under ambient conditions with the Rocksalt or NaCl-type lattice.⁷⁸¹ The rocksalt structure is considered to be the ground-state phase.⁷⁸² This sets CdO apart from other II-VI semiconductors that usually possess a ground-state structure of either wurtzite or zinc-blende.⁵⁵⁸ The single lattice constant for rock-salt CdO is reported around $a = 4.6$ to 4.7 Å^{781,783,784} with broad agreement between the calculated and experimental lattice constants in the literature. A schematic of the crystal structure for rocksalt CdO is shown in Fig. 27. Schleife *et al.* (Ref. 782) report on additional polymorphs of CdO including a wurtzite and a zinc blende structure.

TABLE XXXIV. Summary of theoretical and experimental structural and thermal properties of rutile SnO_2 . Common names of tin oxide and stannic oxide.

Stable phase	Rutile	Ref. 680
Stable structure	Tetragonal $a = 4.673\text{--}4.776 \text{ \AA}$ $c = 3.149\text{--}3.212 \text{ \AA}$	$P4_2/mnm$ (#136) Refs. 684–688
Metastable phases	CaCl ₂ -type $\alpha\text{-PbO}_2$ -type Pyrite-type ZrO ₂ -type Fluorite-type Cotunnite-type	$Pnmm$ (#58) $Pbcn$ (#60) $Pa\bar{3}$ (#205) $Pbca$ (#61) $Fm\bar{3}m$ (#225) $Pnma$ (#62)
Density (g/cm ³)	6.975–7.02	Expt. 684,737,738
Bulk modulus (GPa)	221–245 205 270 ^a	Calc. 685,686,739 Expt. 688 Expt. 771 Calc. 684
T_m (° C)	>1900 >2100	Expt. 745 Calc. 687,737
Debye temp. (K)	550–570	Calc. 687,737
Specific heat (J/(gK))	0.398 ^b 0.366	Calc. 687 Expt. 747
Thermal cond. (W/(mK))	51.4 55.0 \perp_c 98.0 \parallel_c 107.0	Expt. 436 Expt. 737 Expt. 737 Calc. 737
Thermal diff. (mm ² /s)	1.45–1.7	Expt. 772,773

^aNanocrystalline sample.^bCalculated from molar heat capacity.

Guerrero *et al.* (Ref. 785) discuss two other phases of CdO in a study of high pressure phases; a cesium chloride and a nickel arsenide structure. The lattice parameters for all of the CdO polymorphs are listed in Table XXXVI. Further details on the high pressure phases can be found in Subsection VII F. When comparing CdO thin films to bulk crystals, the lattice constants appear smaller in the thin films due to possible lattice contractions.⁷⁸⁶ Unless stated otherwise, all discussion throughout this section refers to the stable, single crystalline, rocksalt phase.

B. Growth

CdO bulk crystal and thin film samples can be grown using numerous methods. Due to the difficulties of CdO growth and less advanced growth methods, it was common for CdO samples to be of polycrystalline quality.^{787–789} MOCVD was utilized by Yang *et al.* (Ref. 780) to grow yttrium-doped CdO thin films to study the effects of how ionic radius and electronic structure alter charge transport and band structure. It was reported that both phase pure and polycrystalline samples were achieved.⁷⁸⁰ Jefferson *et al.* (Ref. 790) grew single crystal CdO using metal-organic vapor-phase epitaxy (MOVPE) on *r*-plane sapphire. Further details on MOVPE growth of CdO layers atop sapphire can be found in Ref. 791. Multiple variations of sputtering including DC reactive and RF sputtering have also been utilized in the

TABLE XXXV. Summary of theoretical and experimental electrical and optical properties of rutile SnO_2 .

Electron affinity (eV)	4.3–4.7 4.5–4.85	Expt. 754 Calc. 754,755
Breakdown field (MV/cm)	3.5	Pred. 147
m_e^*	0.23 (\parallel_c) 0.3 (\perp_c) 0.26 ($\Gamma\text{-}X$) 0.21 ($\Gamma\text{-}Z$) 0.12–0.18 0.22 0.234 (\parallel_c) 0.299 (\perp_c) 0.17	Calc. 684 Calc. 684 Calc. 715 Calc. 715 Calc. 692,758 Expt. 692 Expt. 759 Expt. 759 Est. 757 Calc. 715 Calc. 715
m_h^*	1.21 ($\Gamma\text{-}X$) 1.47 ($\Gamma\text{-}Z$) μ_e [cm ² /(V s)] Gap type E_g (eV)	35–260 Direct 1.7–3.7 3.3.7–4.00 4.35–4.52 \perp 5.59–5.67 \parallel 3.64–4.38 14 ± 2 (\perp_c) 9 ± 0.5 (\parallel_c) 3.70 (\perp_c) 3.90 (\parallel_c)
ϵ_0		Bulk expt. 210,693,737,757,758,761 Bulk expt. 719,720,723,727 Bulk expt. 726 Bulk expt. 726 Film expt. 709,711,725 Expt. 756 Expt. 756 Expt. 210 Expt. 210
ϵ_∞		
Phonon modes		
IR active	A_{2u} , $3E_u$	Refs. 774 and 753
Raman active	A_{1g} , B_{1g} , B_{2g} , E_g	Refs. 774, 746, and 753

growth of CdO thin films.^{775,792} PLD is a common method for growing CdO thin films. Growth of both tin doped and stoichiometric CdO was possible using PLD.⁷⁹³ Unlike MOVPE growth on *r*-plane sapphire, growth of CdO films using PLD was achieved on the *c*-plane of sapphire.^{794,795} Glass was also shown to be a suitable substrate for the growth of CdO thin films.^{793,796} Spray pyrolysis is another common method for thin film growth, but often times results in polycrystalline quality.^{788,789} Varkey and Fort (Ref. 797) detail CdO thin film growth using a chemical bath method where films were deposited on glass substrates exhibiting a bandgap of 2.3 eV, in good agreement with other reported values.⁷⁹⁷

C. Electronic band structure

The electronic structure of CdO is generally considered to have a direct bandgap⁷⁹⁸ despite the fact there is a smaller indirect gap.

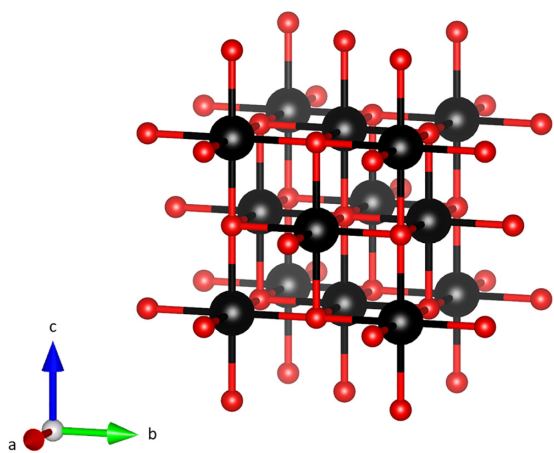


FIG. 27. Cubic CdO crystal structure belonging to space group $Fm\bar{3}m$ (#225) (black = Cd, red = O).

Considering CdO a direct bandgap material as opposed to an indirect material could be a result of the difficulties in determining and singling out the specific indirect bandgaps as there are many that lie close in energy. No sound explanation for considering CdO a direct bandgap material was presented in the reviewed literature. Figure 28 shows the calculated electronic band structure. The location of the direct

TABLE XXXVI. CdO polymorphs and crystal structure with associated lattice constants determined from experiment and theory.

Phase	Structure	Space group	Lattice (\AA)
Rocksalt-CdO	Cubic	$Fm\bar{3}m$ (#225) ⁷⁸²	$a = 4.621^{783,\text{b}}$ $a = 4.639$ $a = 4.78$ $a = 4.76$ $a = 4.6957^{784,\text{a}}$ $a = 4.674^{781,\text{b}}$
Zinc-blende-CdO	Cubic	$F\bar{4}3m$ (#216) ⁷⁸²	$a = 5.148^{782,\text{b}}$ $5.15^{785,\text{b}}$
Wurtzite-CdO	Hexagonal	$P6_3mc$ (#186) ⁷⁸²	$a = 3.678^{782,\text{b}}$ $c = 5.825$ $u = 0.3849$ $a = 3.66^{785,\text{b}}$ $c = 5.856$ $u = 0.35$
CsCl-CdO	Cubic	$Pm\bar{3}m$ (#221)	$a = 2.94^{785,\text{b}}$
NiAs-CdO	Hexagonal	$P6_3/mmc$ (#194)	$a = 3.34^{785,\text{b}}$ $c = 5.678$

^aExperimental.

^bTheoretical.

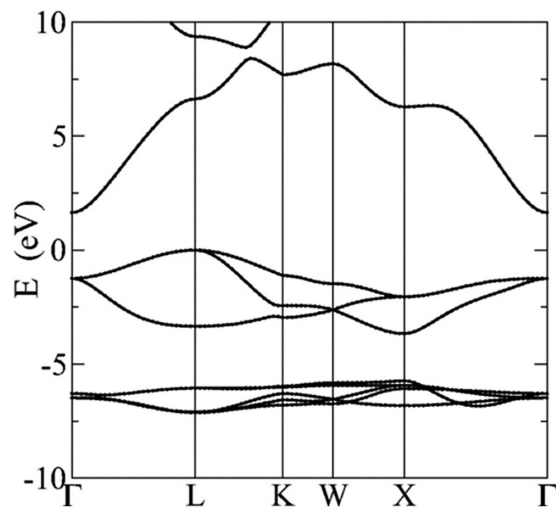


FIG. 28. Calculated band structure for CdO. The indirect gap was determined to be 1.65 eV, and the direct gap was calculated to be 2.91 eV. Reproduced with permission from Lindsay and Parker, Phys. Rev. B **92**, 144301 (2015). Copyright 2015 APS (Ref. 802).

bandgap resides at the Γ -point of the Brillouin zone, with the specific symmetry being from the Γ_1 to Γ_{15} point between the conduction and valence bands, respectively.⁷⁹⁹ The direct bandgap has been studied using methods such as reflection and absorption spectra.^{799,800} Within the electronic states of CdO, the ion site point symmetry plays a role in the intra-band hybridization. As long as the symmetry rules allow it, the Cd(4d) levels will hybridize with the O(2p) states. The hybridization results at the top of the valence band in a repulsion that occurs between the Cd(4d) and O(2p) states, raising the energy of the top of the valence band. When considering a zinc-blende structure, the increase in energy is allowed at all points of the Brillouin zone, but in the rocksalt CdO structure it is disallowed at the Γ point. The higher point symmetry of the rocksalt structure prevents the mixing of the states at that specific location while allowing the hybridization to occur at other points of the Brillouin zone.⁶⁵⁸ According to calculations by Jaffe *et al.* (Ref. 658), this causes the valence band maximum to move away from the Γ point as other points along the valence band are raised in energy.

While most literature appears to agree on a direct bandgap when reporting its value, the existence of an indirect bandgap that resides lower in energy has been mentioned as well. Boettger *et al.* (Ref. 783) produced GGA and LDA band structure calculations that contradict the reported direct bandgap. The top of the valence band occurs at the L-point of the Brillouin zone and not at the Γ -point. The bottom of the conduction band still resides at the Γ -point. This appears to show the fundamental bandgap of CdO to be indirect. Indirect bandgaps for CdO have been predicted and observed throughout the literature.^{781,799,801}

Other studies on the theoretical band structure of CdO have been reported dating back to the late 1960s through the 2000s.^{801,803,804} In 1973, Breeze *et al.* (Ref. 781) also reported on the calculated electronic structure for CdO. Atomic orbitals of Cd(4d), Cd(5s), O(2s), and O(2p) were represented by atomic parameters. CdO was predicted to be highly polar. LCAO calculations show a small overlap of the p and

d bands. The atomic makeup of the conduction band was calculated to be mainly comprised of Cd(5s) orbitals with a small amount of O(2s) mixed in. The valence band was calculated to be the opposite, containing an atomic makeup of primarily O(2s) orbitals.⁷⁸¹ The calculated findings by Tewari (Ref. 805) reported in the same year alongside Breeze *et al.*, show how the ionicity of CdO is important for determining the electronic structure. The positions of the orbitals have a dependence upon the ionicity used in the calculation. Neutral CdO shows hybridization between 4d and 5s orbitals, while ionic CdO contains a gap between the same orbitals. When ionicity was selected to be zero, CdO exhibited metallic behavior. Changing the ionicity by ± 1 resulted in semiconducting behavior. Tewari predicted that an ionicity greater than ± 1 would result in insulating characteristics.⁸⁰⁵ This only serves to highlight the importance of experimental works to help determine an accurate ionicity needed for band structure calculations.

1. Bandgap energy

Values of both the indirect and direct bandgap energies have been reported throughout the literature. Starting with the indirect bandgap, the majority of references cited in this review for CdO date back to the mid-1960s to the early 1970s. There are two indirect energy transitions that are predicted to be present throughout most of the cited literature.^{781,799} The difference in energies of the two reported transitions is small, usually a few tenths of an eV. The two indirect transitions are Σ - Γ and L- Γ . Table XXXVII shows a clear trend within the indirect transitions. The Σ - Γ tends to be the lowest indirect transition with values ranging from 0.55 to 0.95 eV.^{801,805,806} What is generally considered to be the second lowest indirect transition occurs between L- Γ . Reported values for this indirect bandgap range from 1.09 to 1.47 eV.^{781,799,801,806–808} There is one outlying value of interest reported in Table XXXVII. Breeze *et al.* (Ref. 781) used LCAO calculations to produce an indirect Σ - Γ bandgap energy of 1.12 eV, the highest value of the reported Σ - Γ transition we were able to find. This value of 1.12 eV is only 0.06 eV below their calculated L- Γ value of 1.18 eV.⁷⁸¹ A few conclusions can be made based off of these findings. First, it could be stated that LCAO calculations were unable to distinguish the two indirect energy transitions, resulting in such similar values for the two transitions. The issue could be specific to the LCAO method since augmented plane wave (APW) calculations by Maschke *et al.* (Ref. 801) were clearly able to distinguish the two indirect transitions. Secondly, Breeze *et al.* state that the similarities between the indirect gap values aligns with a single experimentally observed indirect bandgap, as opposed to two bandgaps.⁷⁸¹ However, this consensus was not shared throughout other literature sources. Based on the findings throughout literature, we conclude that CdO has two indirect transitions (Σ - Γ and L- Γ) that occur below the direct bandgap energy level. As seen with other oxides reported in this Review, most theoretical methods for determining the bandgap drastically underestimate the value when compared to experimental results. Not included within Table XXXVII are some underestimated theoretically determined bandgap values for the indirect transitions. Some calculated indirect bandgaps yielded a negative value meaning CdO should theoretically exhibit metallic behavior.⁷⁸³ Underestimated values of the calculated indirect bandgap include 0.39,⁸⁰³ 0.13,⁷⁸³ and 0.27 eV.⁷⁸³ There were a few instances of an experimental indirect bandgap reported in literature as well. Thermoreflectance measurements from Koffyberg *et al.*

TABLE XXXVII. Bandgaps of CdO determined from experiment and theory. Direct bandgap Γ - Γ was assumed unless specified otherwise.

E _g (eV)	Method	Bulk/film	Direction	Reference
Indirect gap				
0.8	APW method	Bulk	Σ_3 - Γ_1	801
0.95	APW method	Bulk	Σ_4 - Γ_1	805
1.09	Thermoreflectance	Bulk	L ₃ - Γ_1	799
1.11	Abs. spectra	Bulk	L ₃ - Γ_1	807
1.12	LCAO	Bulk	Σ_4 - Γ_1	781
1.18	LCAO	Bulk	L ₃ - Γ_1	781
1.2	Abs. edge	Film	L- Γ	808
1.2	APW method	Film	L ₃ - Γ_1	801
1.45	Abs. spectra	Film	L ₃ - Γ_1	806
1.47	Thermoreflectance	Film	L ₃ - Γ_1	799
Direct gap				
2.07	Ellipsometry	Film	Γ - Γ	812
2.13	Ellipsometry	Film	Γ - Γ	812
2.16	Ellipsometry	Film	Γ - Γ	812
2.16	Abs. edge	Bulk	Γ - Γ	790
2.18	HSE06	Bulk	Γ - Γ	809
2.20	Abs. edge	Film	Γ - Γ	811
2.22	Transmission spectra	Film	Γ_1 - Γ_{15}	792
2.22	Ellipsometry	Film	Γ - Γ	812
2.25	Abs. spectra	Film	Γ - Γ	787
2.28	Thermoreflectance	Bulk	Γ_1 - Γ_{15}	799
2.28	UV-Vis	Film	Γ - Γ	813
2.3	Abs. edge	Film	Γ - Γ	797
2.31	Ellipsometry	Film	Γ - Γ	812
2.36	Optical transmission	Film	Γ - Γ	814
2.4	Optical absorption	Film	Γ - Γ	795
2.42	Ellipsometry	Film	Γ - Γ	812
2.51	UV-Vis	Film	Γ - Γ	813
2.59	Ellipsometry	Film	Γ - Γ	812
2.73	UV-Vis	Film	Γ - Γ	813
2.81	UV-Vis	Film	Γ - Γ	813
2.86	UV-Vis	Film	Γ - Γ	813

(Ref. 799) found bandgap energies of 1.09 and 1.47 eV for bulk and thin film samples, respectively. Note, the thermoreflectance method for measuring bandgap energy is perhaps the least commonly used method we have observed in literature for the nine oxides reviewed in this manuscript. Absorption edge/spectra measurements we performed on both bulk and thin film samples as well. Three values were reported, all of which are along the L₃- Γ_1 direction of the Brillouin zone. There is noticeable disagreement with values of 1.11 eV for a bulk sample,⁸⁰⁷ and 1.2 (Ref. 808) to 1.45 eV (Ref. 806) for thin films, and which may be due to sample quality.

The direct bandgap of CdO has also received considerable attention in the literature for both theoretical and experimental investigations. Theoretical studies involving HSE06, LDA, GGA, and AWP

methods have been utilized to determine the direct bandgap of CdO. Experimental methods usually centered around absorption edge measurements as well as transmission spectra.

According to Koffyberg *et al.* (Ref. 799), the direct (and indirect) bandgap are said to be difficult to analyze using absorption spectra due to the free carrier absorption presence. LDA and GGA theoretical results from Boettger *et al.* (Ref. 783) yielded direct bandgap values ranging from 0.71 to 1.48 eV. GGA-PBE produced a direct bandgap of 0.61 eV.⁸⁰⁹ Other direct bandgap values included 1.61,⁸⁰³ 1.04,⁸¹⁰ and 0.7 eV.⁷⁸⁵ These theoretically determined bandgap energies are drastically underestimated when compared to experimentally determined values. HSE06 calculations from Burbano *et al.* (Ref. 809) had a bandgap energy of 2.16 eV, one of the closest theoretical values compared to experimental values. Experimentally, the direct bandgap was determined to be 2.28 eV at 100 K.⁷⁹⁹ This value for the direct bandgap of CdO has been considered to be the most accepted and frequently cited experimental direct bandgap despite being measured at 100 K, according to Jefferson *et al.* (Ref. 790). Other experimental direct bandgap energies are not far off. Absorption edge measurements produced direct bandgap energies of 2.16,⁷⁹⁰ 2.20,⁸¹¹ 2.25,⁷⁸⁷ 2.3,⁷⁹⁷ and 2.4 eV.⁷⁹⁵ The lowest absorption edge value of 2.16 eV was for a bulk sample while the remaining values spanning 2.2 to 2.4 eV are from thin films. According to the experimental direct bandgap values listed in Table XXXVII, the bandgap energy of CdO thin films is generally higher than bulk samples. The poor crystal quality of the CdO samples coming from some of the older literature works could be a possible cause for the inconsistencies between bulk crystal and thin film bandgap energies. Further discussion on the difference in determining the bandgap of CdO between thin film and bulk crystal samples was reported by Koffyberg *et al.* (Ref. 799). Bandgap values obtained from literature are listed and compared in Table XXXVII as well as in Sec. XI.

Ueda *et al.* (Ref. 792) report on the band widening that occurs within CdO thin films as a function of $n_e^{2/3}$ (two-thirds power of the carrier concentration). It was concluded that Burstein–Moss shifting as well as electron–electron and electron impurity scattering were responsible for the bandgap widening. Thin film thickness also appears to affect the bandgap with thicker films having larger bandgaps by a few hundredths of an eV, possibly due to a combination of increased strain effects of altered crystal quality. Ueda *et al.* also describe how the orbital makeup of CdO plays a role in the effective masses of both the conduction and valence band also in comparison to ITO.⁷⁹²

A recent 2020 report by Nolen *et al.* (Ref. 812) was one of the few literature works using SE to study indium doped CdO. Nolen *et al.* used the Tauc-Lorentz oscillator on ellipsometry data to report a direct bandgap energy ranging from 2.07 to 2.59 eV. The lowest bandgap energy of 2.07 eV was found for a carrier concentration of $1.1 \times 10^{19} \text{ cm}^{-3}$. The bandgap energy continued to increase with increasing carrier concentration up to the maximum value of 2.59 eV at a carrier concentration of $3.5 \times 10^{20} \text{ cm}^{-3}$, before decreasing to 2.42 eV at $4.1 \times 10^{20} \text{ cm}^{-3}$. The specific details of the study of Nolen *et al.* on the ultraviolet and far-IR dielectrics of CdO are beyond the scope of this section, but can be found within Ref. 812. Some of the authors published a follow up work studying the mid-to-near IR optoelectronic properties of indium doped CdO.⁸¹³ The reported band values from UV-VIS absorption data were slightly larger than the previous work of

Nolen *et al.*, ranging from 2.28 to 2.86 eV. Again, the bandgap energies increased with increasing carrier concentration. This shows a Burnstein–Moss shift of 0.58 eV as the carrier concentration is increased from 2.2×10^{19} to $5.0 \times 10^{19} \text{ cm}^{-3}$. These two recent works by Nolen *et al.* (Ref. 812) and Cleri *et al.* (Ref. 813) are perhaps the most current and state of the art findings on the bandgap energies of CdO and its dependence on doping concentration.

2. Temperature dependence of bandgap energy

There are very few reports throughout the literature on the temperature dependence of the CdO bandgap. Koffyberg *et al.* (Ref. 799) list bandgap temperature dependence for both the direct and indirect bandgaps. For the direct gap, dE_g/dT was stated to be $-4 \times 10^{-4} \text{ eV/K}$ while the indirect bandgap was $-5 \times 10^{-4} \text{ eV/K}$.⁷⁹⁹ Kohler *et al.* (Ref. 806) report an average temperature dependence of $-4.2 \times 10^{-4} \text{ eV/K}$, in good agreement with findings of Koffyberg *et al.* An indirect bandgap temperature dependence was not reported by Kohler *et al.* Slightly smaller in value, Finkenrath *et al.* (Ref. 815) report a temperature dependence of $-3.3 \times 10^{-4} \text{ eV/K}$.

D. Material properties

Basic material properties for CdO reported throughout the literature include the material density, bulk modulus, and the melting point. The density of CdO has been determined theoretically and experimentally. Values range from 7.0 to 8.218 g/cm^3 .^{777,816,817} The bulk modulus was in good agreement across multiple methods. Experimentally, the bulk modulus was determined using XRD and ranged from 108 to 150 GPa.^{818,819} Using multiple variations of LDA and GGA, including non-relativistic, scalar relativistic, and fully relativistic, the calculated bulk modulus ranged from 128 to 164 GPa.⁷⁸³ The melting point of CdO is not widely reported and was roughly stated to be greater than 1400 to 1500 °C.^{400,820} The basic material properties for CdO are compared in Sec. XI.

1. Thermal properties

The thermal properties reported for CdO include the Debye temperature, CTE, specific heat, and thermal conductivity. The Debye temperature for CdO was reported to be 255 K.⁴⁰⁰ The relatively small Debye temperature is reported to be a cause of the lower thermal conductivity, detailed later in the section.^{802,821} Singh *et al.* (Ref. 784) studied the change in lattice parameters across elevated temperatures ranging from 305 to 1005 K. The results showed a small increase of the lattice constant of around 0.05 Å across that temperature range.⁷⁸⁴ This resulted in an average value for the CTE across those temperatures of $14.33 \times 10^{-6}/\text{K}$. The values of Singh *et al.* are also in agreement with another widely cited value of $14 \times 10^{-6}/\text{K}$ from Martienssen *et al.* (Ref. 400). The specific heat of CdO was not readily found in the literature. However, the molar heat capacity was reported as 43.639 J/(mol K).⁴⁰⁰ Using the known molecular weight of CdO, 128.4 g/mol, we calculated the specific heat to be 0.339 J/(g K).

The thermal conductivity has been reported both theoretically and experimentally and is one of the more researched thermal properties of CdO. Lindsey *et al.* (Ref. 802) used *ab initio* calculation and dispute the commonly accepted value of 0.7 W/(mK) for the lattice thermal conductivity from the CRC Handbook,⁸²² compared to their

own calculated findings that range from 5.6 to 9.3 W/(mK). This value of 0.7 W/(mK) is believed to be rather low for a binary oxide, a group of materials that often exhibit higher thermal conductivities such as 54 W/(mK) as in ZnO.⁸⁰² CdO is similar to other binary equiatomic semiconductors that crystallize in the rocksalt crystal structure. Another unique feature of these binary oxides is that heat in the lattice is carried by phonons. All of these features lead to the hypothesis that a thermal conductivity of 0.7 W/(mK) is too low for CdO. While CdO does possess a low Debye temperature, which should result in a low thermal conductivity, 0.7 W/(mK) is an order of magnitude lower than the calculated results. The low Debye temperature can result in a lower phonon thermal conductivity, thus lowering the overall thermal conductivity.⁸²¹ For a CdO ceramic sample, Lu *et al.* (Ref. 777) report a calculated thermal conductivity value of 8.1 W/(mK). Experimentally, Sachet *et al.* (Ref. 779) reported total thermal conductivity with increased dysprosium doping.⁷⁷⁹ Results range from around 7 to 14 W/(mK). The maximum experimental thermal conductivity of 14 W/(mK) was reported at a dysprosium doping concentration of around $8 \times 10^{19} \text{ cm}^{-3}$ before falling to around 10 W/(mK) as the doping concentration increased to around $5 \times 10^{21} \text{ cm}^{-3}$. Reported thermal property values are listed and compared in Sec. XI. Of note, there were no reported values for the thermal diffusivity of CdO. Lu *et al.* (Ref. 777) state that the thermal diffusivity was measured using a differential scanning calorimeter in order to obtain a calculated thermal conductivity, but gave no value.⁷⁷⁷

2. Phonon properties

The long-wavelength vibrational properties, including the acoustic and optical phonon modes of CdO are not widely reported throughout the literature. The irreducible representations are also not readily available. One explanation as to the lack of literature could stem from the rocksalt structure of CdO, resulting in the first-order Raman modes being forbidden as a result of symmetry.⁸²³ Finkenrath *et al.* (Ref. 824) report IR measurements showing TO and LO phonon modes at frequencies of 262 and 523 cm⁻¹, respectively. One of the early Raman studies on (polycrystalline) CdO was published by Schaack *et al.* (Ref. 825). A pure CdO sample was expected to yield only the second order Raman spectra. Within oxygen deficient CdO, translational lattice symmetry is broken due to the oxygen deficiencies. This resulted in a prediction that the second order Raman can be superimposed upon the first order. Similar to III-V semiconductors, CdO contains plasmon, plasmon-LO-phonon, or polaron-mode excitations.⁸²⁵ IR absorption shows observable bands at 345 and 404 cm⁻¹. These bands line up well in the experimental uncertainty of the Raman spectra with higher carrier concentrations.⁸²⁵ While it is beyond the scope of this review, Oliva *et al.* (Ref. 823) report on the high-pressure Raman scattering within CdO thin films.

3. Electrical properties

The electrical properties of CdO reviewed below include the electron affinity, electrical breakdown field, static and high frequency dielectric constants, effective mass, and electron mobility. The electron affinity of CdO was determined using the known locations of the Fermi stabilization energy. Speaks *et al.* (Ref. 794) state that the electron affinity is 5.94 eV. This value is higher than the calculated value of 4.51 eV for CdO thin films used in CdO/CdTe thin films

determined by Ferro *et al.* (Ref. 826). To our knowledge there are no reported values for the electrical breakdown field strength for CdO. Similar to other oxides without an explicitly reported electrical breakdown field, an estimation can be made based on the bandgap for CdO using Higashiwaki's plot.¹⁴⁷ Using the direct bandgap with values ranging from around 2 to 2.4 eV, the predicted breakdown field strength is 0.5 to 0.8 MV/cm.

The static dielectric constant was scarcely reported throughout the literature. Finkenrath *et al.* (Refs. 827 and 824) state that the static dielectric constant is roughly 18.1 ± 2.5 at room temperature. The static dielectric constant decreases to 16.5 ± 2.5 at 85 K. Based on those values at room temperature, CdO has the highest static dielectric constant of any of the oxides reviewed. The high frequency dielectric constant is uniform across multiple sources ranging from 5.3 to 5.4.⁸²⁷⁻⁸²⁹ The effective mass of the electrons has been reported both theoretically and experimentally. Jefferson *et al.* (Ref. 790) found calculated values of 0.19 m_e, 0.21 m_e, and 0.23 m_e. Those values are in good agreement with the experimental value of 0.21 m_e determined using a combination of IR reflectivity, optical absorption, and electrical Hall effect measurements.⁷⁹⁰ Other experimental values of 0.23 m_e⁷⁷⁵ and 0.24 m_e⁸¹¹ were reported in good agreement with Jefferson's findings. In 1971, Koffyberg *et al.* (Ref. 830) highlight the (electron) effective mass at low temperatures (81 K). The (electron) effective mass was calculated to increase from 0.15 m_e to 0.45 m_e as carrier concentration increased.⁸³⁰ More details on the specifics of those findings are discussed in Sec. VII E.

In perhaps the most recent reporting of the electron effective mass of CdO, Nolen *et al.* (Ref. 812) found a strong dependence on the doping concentration. Unintentionally doped samples ($1 \times 10^{19} \text{ cm}^{-3}$) had an effective mass of 0.11 m_e. The electron effective masses from the study of Nolen *et al.* study peaked at 0.26 m_e for a doping concentration of $4 \times 10^{20} \text{ cm}^{-3}$, confirming the nonparabolic nature of the conduction band model.⁸¹² The lowest value of 0.11 m_e is in good agreement with an effective electron mass of 0.09 m_e calculated by Rodl *et al.* (Ref. 831) who hypothesize that unintentional free electrons could be the cause of the low calculated effective masses compared to experimental values. Instances of effective masses $>0.24 \text{ m}_e$ for doping concentrations well below 10^{20} cm^{-3} dispute this claim though.⁸³² This hypothesis, however, could not be fully supported as Rodl *et al.* argued that more accurate data were needed to observe the effective mass dependence on carrier concentration.⁸³¹

Koffyberg *et al.* (Ref. 799) also briefly discuss the effective mass of holes within CdO. A calculated effective hole mass of 0.05 m_h at Γ_{15} was reported. According to band structure calculations the effective hole mass at (Γ_{15}) should be significantly larger than the effective electron mass at the conduction band minimum (Γ_1).

Electron mobility values are wide ranging with values in the single digits up to 609 cm²/(V s) for tin doped thin films deposited on MgO (111). The MgO plane plays a large role in the electron mobility as well as the crystal structure. Another sample grown on MgO (100) had almost half the mobility at 330 cm²/(V s) showing that substrate cut also had a large impact on the mobility as well.⁷⁹³

More recent indium doped CdO samples from Nolen *et al.* (Ref. 812) had carrier mobilities of 285 cm²/(V s) determined from Hall measurements. A follow up in 2021 by a group of the same authors reported mobility values ranging from 298 to 365 cm²/(V s).⁸¹³ It was shown that indium doped CdO could retain a high carrier

mobility even as the doping concentration reached values well into 10^{20} cm^{-3} .⁸¹³

Dysprosium doped CdO also yielded a high mobility reaching values up to $500 \text{ cm}^2/(\text{V s})$.⁷⁷⁹ The effects of the dysprosium doping are detailed in Subsection VII E. A mobility value solely from lattice scattering was calculated to be $200 \text{ cm}^2/(\text{V s})$ derived from the temperature dependence of mobility.⁷⁷⁵ Tanaka *et al.* (Ref. 775) observed mobility values for sputtered samples and found there to be a mobility increase for samples as sputtering voltage was increased up to 500 V, corresponding with the reduction of resistivity. Lu *et al.* (Ref. 777) reported an electron mobility of $148 \text{ cm}^2/(\text{V s})$ for CdO ceramics using the Van der Pauw method. Vasheghani *et al.* (Ref. 811) report the optical mobility and the transport mobility values for degenerate samples of CdO. The optical mobility ranges from 209 to $1116 \text{ cm}^2/(\text{V s})$. The carrier lifetime was shown to decrease with increasing carrier concentration. Along with the decrease in the carrier lifetime comes a decrease in the optical mobility. The transport mobility is drastically lower than the optical mobility, reported to in the range of 20 to $124 \text{ cm}^2/(\text{V s})$.⁸¹¹

Figure 29 highlights the transport mobility as a function of carrier concentration. The stark difference in the optical and transport mobility of CdO is believed to be a result of the grain boundary and/or surface scattering. Grain boundaries can act as trap states and bring about depletion layers in the boundaries. Due to surface accumulation layers in cadmium oxide,⁸³³ Vasheghani *et al.* hypothesize that there should be accumulation of electrons at the dislocation lines and along the grain boundaries. The mean free path for CdO thin films was estimated to be around 35 nm, determined from the bulk relaxation time and the density of states averaged electron velocity. Predicted models show the overall variation in transport mobility as a function of multiple carrier concentrations. As grain size increases, the transport mobility approaches the bulk mobility in the grain. As grain sizes continues to increase, the increase in transport mobility is sharper. This shows that even small improvements in CdO growth will yield large improvement in mobility values.^{811,833} In another study by Koffyberg *et al.* (Ref. 830), the electron mobility was calculated as a function of carrier concentration and temperature. At 81 K, the calculated mobility

ranged from 700 to $1150 \text{ cm}^2/(\text{V s})$. Measured Hall mobility was also plotted and at room temperature the mobility ranges in value from 100 to $300 \text{ cm}^2/(\text{V s})$. Other topics such as the high temperature mobility, low temperature mobility, calculated optical mobility, and lattice scattering were detailed as well. At low temperatures the mobility is primarily dominated by ionized defect scattering while lattice scattering controls the mobility at higher temperatures.⁸³⁰

For comparison to the other reviewed oxides, values for the static and high frequency dielectric constants along with the electrical properties of CdO including electron affinity, electrical breakdown field, effective mass, and carrier mobility of CdO are summarized in Sec. XI.

E. Doping and defects

Doping and defects within CdO have been discussed throughout the literature.^{833–838} Possible dopants used in CdO include indium, gallium,⁸³⁹ silver, sodium,⁸³⁴ and yttrium.⁷⁸⁰ CdO is an *n*-type semiconductor with much uncertainty about the possibility of *p*-type CdO. Burbano *et al.* (Ref. 809) used hybrid DFT to report the doping limits as well as explain the shallow donors that are found within CdO. The doping limit was found to be greater than 1.2 eV above the conduction band minimum, the point where compensation by *p*-type defects begins to occur. According to Burbano *et al.*, *p*-type CdO is not possible since the *p*-type defect formation energy is too high. Oxygen vacancies were found to be the main intrinsic defect, and was considered a doubly ionized shallow donor.⁸⁰⁹

Koffyberg *et al.* (Ref. 830) discussed the implications of defects within the oxide. It was reported that the carrier concentrations were not dependent on temperature, meaning that the defect donors were completely ionized. With increasing defect concentrations the effective mass increased at low temperatures indicative of a non-parabolic conduction band shape.⁸³⁰

Dysprosium was another dopant seen in literature. Details pertaining to the effects of Dy doping on CdO are highlighted in Refs. 779 and 787. As mentioned in the Electronic Properties section (Sec. VII D 3) above, one of the higher reported mobility values comes from Sachet *et al.* (Ref. 779) in a study where CdO was doped with dysprosium. The mobility reached a value of around $500 \text{ cm}^2/(\text{V s})$.⁷⁷⁹ When dysprosium was introduced into CdO, the substitutional lattice strain was found to decrease to very small values, thus allowing for such a high mobility. Sachet *et al.* explain that the large mobility achieved by Dy doping was possible due to defect equilibrium engineering. The extrinsic doping allowed for the Fermi level to be pinned above the conduction band minimum. This Fermi level pinning caused an increase in the oxygen vacancy formation energy that is a native occurrence in CdO. This resulted in a decrease in the oxygen vacancy population by multiple orders of magnitude. CdO mobility also exhibits a decrease with increasing doping up to the solubility limit that was achieved at $5 \times 10^{21} \text{ cm}^{-3}$.⁷⁷⁹ The trend of decreasing mobility with increasing carrier concentration was seen for most of the referenced mobility values.^{775,811,825} Findings of Sachet *et al.* show that with dysprosium doping, defect engineering is possible and that CdO will behave like a metal with an inverse mobility dependence on temperature. When impurity cations are added to the material, electron scattering is decreased due to a decrease in the lattice defects.⁷⁷⁹ Dakhel (Ref. 787) reported mobility values for CdO:Dy. It should be noted that the samples used were of polycrystalline quality. The highest mobility achieved was only $23.36 \text{ cm}^2/(\text{V s})$, but showed a 3.5 times

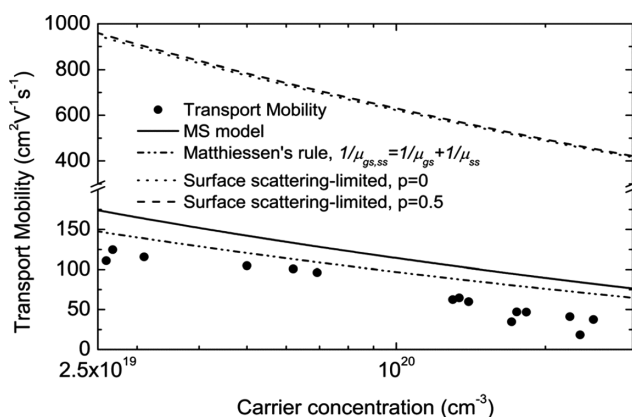


FIG. 29. Transport mobility of CdO thin films plotted as a function of carrier concentrations. Simulations using the MS model and Matthiessen's rule are included. Reproduced with permission from Vasheghani Farahani *et al.*, J. Appl. Phys. **109**, 073712 (2011). Copyright 2011 AIP Publishing LLC (Ref. 811).

increase over the mobility of undoped CdO.⁷⁸⁷ According to other references pertaining to the bandgap of CdO thin films, the bandgap does not differ drastically when compared to bulk samples. However, the bandgap of Dy doped thin films was shown to range from 1.72 to 1.81 eV.⁷⁸⁷ Dakhel *et al.* discussed the effects of Dy doping onto bandgap reduction and Burstein–Moss shift (widening). An undoped film showed a bandgap of 2.25 eV, more in line with other reported CdO thin film bandgaps. There was a 20% shrinkage in the bandgap with Dy doping. This was suggested as a result of Dy affecting the crystal potential and intermixing with 4f states. However, many body interactions may also be present.

F. Polymorphs

There are a number of CdO polymorphs and high pressure transitions phases that are less extensively reported on. Guerrero *et al.* (Ref. 785) carried out first principles calculations on the transition phases. There are four polymorphs including a zinc-blende, wurtzite, CsCl, and NiAs phase as well two additional phases, cinnabar and orthorhombic *Cmcm*. The fact that CdO contains a metastable wurtzite phase is key for the fabrication of cadmium, oxygen, and sulfur ternary compounds containing CdO and CdS multilayers. Guerrero *et al.* produced energy vs volume data for all of the phases except the orthorhombic *Cmcm* phase. Wurtzite and NiAs contain two formula units per cell while there are three formula units in the cinnabar cell. Rock salt, CsCl, and zinc-blende structures all contain a single formula unit per cell. Across the polymorphs the bulk modulus ranges from 82 GPa to 130 GPa. The calculated bulk modulus for the wurtzite and zinc-blende structures are similar at 86 GPa and 82 GPa, respectively. These two phases share many structural features including equilibrium volume and tetrahedral coordination.⁷⁸⁵

The total density of states presented by Guerrero *et al.* shows that the rocksalt-CdO phase undergoes a high pressure phase transition to the CsCl phase. The CsCl-CdO phase contains atoms with eightfold coordination but a reduction of the neighboring atom distance. The bulk modulus was calculated to be 114 GPa. The cinnabar (*P3₁21* or *P3₂21*) phase has a hexagonal lattice, but is considered to be a distortion of the cubic rock salt structure. The cinnabar phase is not energetically favorable for CdO. Orthorhombic *Cmcm* is considered a deformation of rock salt-CdO as well. The *Cmcm* phase is not stable and the transition from rock salt to the CsCl-CdO structures will have already occurred before reaching the pressure needed to achieve the *Cmcm* phase.⁷⁸⁵

Guerrero-Moreno and Takeuchi studied structural properties of CdO polymorphs under pressure (rock salt, cinnabar, orthorhombic *cmc*, cesium chloride, nickel arsenide, zinc blende, and wurtzite) using first principles total energy calculations.⁷⁸⁵ The ground state structure is rock salt with $a = 4.77 \text{ \AA}$, and $B_0 = 130 \text{ GPa}$, in agreement with the experimental lattice constant of $a = 4.704 \text{ \AA}$. The wurtzite structure was found to be potentially stable as well. A phase transformation was predicted from rock salt to CsCl at around 89 GPa. Band structure calculations predict an indirect gap NaCl structure with metallic property at zero pressure, with the valence band maximum at the L point. However, the conduction band is too small by an estimated energy of 1.5 eV and hence the structure is still an indirect semiconductor. At pressure less than 89 GPa, the NaCl structure widens in bandgap but maintains most of its character. For pressure above 89 GPa, the predicted stable CsCl phase is indirect with the

valence band maximum at X and the conduction band minimum at G. The calculated gap is zero, however, with the conduction band correction it would be 1.5 eV. The zero pressure wurtzite phase is direct, with both band extrema at the G point, and the gap again with band correction is predicted at 1.5 eV.⁷⁸⁵

G. Summary of CdO property values

Table XXXVIII highlights a summary of the properties reviewed for CdO. Values for each of the properties are presented along with references and notation of whether they are experimental or calculated findings.

VIII. NICKEL OXIDE

Nickel oxide (NiO), or bunsenite, is another cubic NaCl-type material that has many favorable properties with a wide bandgap and p-type doping⁸⁴⁰ which are attractive for device applications, prompting considerable research interest. Such devices include antiferromagnetics,⁸⁴¹ electrochromic displays,⁸⁴² transparent p-type conducting films,⁸⁴⁰ and biosensors.⁸⁴³ NiO has also been seen in power device applications, used alongside materials such as GaN.^{844,845} The stoichiometry of NiO is also a critical component to the material properties of NiO. Stoichiometry is heavily dependent upon growth process and conditions which allows for wide ranging alterations to the properties of NiO. The details of the deposition methods and resulting film properties for NiO result in wide ranging parameters that make NiO difficult to characterize and compare within the literature. Indeed NiO appears particularly sensitive to deposition parameters yielding significant variation film properties. In particular, the carrier concentration of NiO is known to be widely affected by deposition parameters as well as annealing.^{846–851} The specifics of the varying stoichiometry within NiO is beyond the scope of this review but further details and examples can be found in the listed references.^{852–854}

A. Crystal structure

The consensus throughout literature is that the stable crystal structure of NiO is effectively cubic NaCl-type.⁸⁵⁵ The crystal structure for cubic NiO is shown in Fig. 30. NiO has antiferromagnetic properties that are present below the Neel temperature of NiO, which is around 520 K.^{856–858} At lower temperatures, the crystal structure of NiO becomes distorted into a rhombohedral structure. Toussaint (Ref. 858) reports that at room temperature (22 °C), NiO exhibits rhombohedral symmetry with a lattice constant of 2.952 Å. These findings were also supported by Rooksby (Ref. 859) who detailed the change in structure from rhombohedral to cubic. Rooksby states that with the improved measurement devices used during his time of study, it was possible to examine extra reflections in powder photographs. Rooksby cites a previous study by Cairns *et al.* (Ref. 860) that found NiO to be face centered cubic with a lattice constant of 4.168 Å and having NaCl type structure. With the improved imaging devices, it was found that the distorted reflections were doubled and, in some cases, tripled. This showed a possible deviation from the cubic structure toward a rhombohedral structure. The reflection distortion was so small that it proved difficult to determine the angle of the lattice. At a temperature of 20 °C, it was stated that it was likely that the unit cell was of rhombohedral structure with a lattice constant of 2.9459 Å and an angle of 60° and 4.2'. That reported lattice constant is almost half of the

TABLE XXXVIII. Summary of theoretical and experimental properties of CdO. Common name of cadmium oxide.

Stable phase	Rocksalt-CdO	Ref. 782
Stable structure	Cubic $a = 4.66\text{--}4.78 \text{ \AA}$	$Fm\bar{3}m$ (#225) Refs. 781, 783, and 784
Metastable phases	Zinc blende-CdO	$F\bar{4}3m$ (#216)
	Wurtzite-CdO	$P6_3mc$ (#186)
	CsCl-CdO	$Pm\bar{3}m$ (#221)
	NiAs-CdO	$P6_3/mmc$ (#194)
Density (g/cm ³)	8.00–8.15 7.0 8.218	Expt. 118,777 Expt. 816 Calc. 817 Calc. 783
Bulk modulus (GPa)	128–164 108–150	Expt. 818,819 Ref. 400
T _m (°C)	>1500 1559	Sublimation ¹¹⁸ Calc. 400 Calc. 400 Calc. 777,802 Expt. 779
Debye temp. (K)	255	
Specific heat (J/(gK))	0.339 ^a	
Thermal cond. (W/(mK))	5.6–9.3 5.6	Calc. 777,802 Expt. 779
CTE ($\times 10^{-6}/\text{K}$)	13.31–14.33	Refs. 784 and 400
Electron affinity (eV)	5.94 4.51	Expt. 794 Calc. 826
Breakdown field (MV/cm)	0.5–0.8	Pred. 147
m_e^*	0.09 0.19–0.23 0.21–0.24	Calc. 831 Calc. 790 Expt. 775,790,811
m_h^*	0.05 >0.14	Pred. 799 Calc. 799
μ_e (cm ² /V s)	2–609 209–1116 ^b	Expt. 775,777,779,793,811,825 Expt. 811 Ref. 798
Gap type	Direct	
E _g (eV)	2.18 0.8–1.18 ^c 2.16–2.28 1.09–1.11 ^c 1.2 ^c 2.07–2.86	Bulk calc. ⁸⁰⁹ Bulk calc. ^{801,805} Bulk expt. ^{790,799} Bulk expt. ^{799,807} Film calc. ⁸⁰¹ Film expt. ^{787,792,795,797,798,812–814}
ϵ_0	18.1 ± 2.5	Film expt. ^{799,806,808} Expt. 824,827
ϵ_∞	5.4 5.4	Calc. 827 Expt. 829

^aCalculated from molar heat capacity.

^bOptical mobility.

^cIndirect gap.

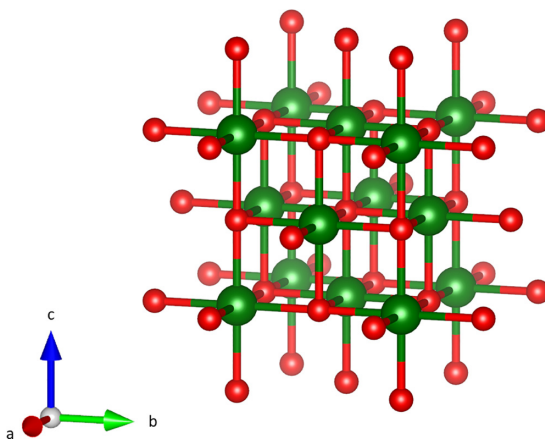


FIG. 30. Cubic NiO unit cell with space group $Fm\bar{3}m$ (#225). The c-axis is oriented upward (green = Ni, red = O).

cubic lattice constant of 4.168 Å.⁸⁶⁰ Most of the reported values for the lattice parameter of NiO that were published before Rooksby's study state that the structure was face-centered-cubic with lattice constants around 4.17 Å.⁸⁶⁰ The lattice constants for the cubic and distorted rhombohedral structures are listed in Table XXXIX.

Building on Rooksby's (Ref. 859) work, Toussaint (Ref. 858) studied the x-ray diffraction for NiO with some incorporated lithium. Initial x-ray measurements at 22 °C found that at room temperature NiO possess rhombohedral symmetry with a lattice constant of 2.95 Å and revealed the same angle as Rooksby's measurements. It was explained that the rhombohedral structure derives from the face-centered-cubic structure and a small lattice contraction that occurs on the threefold axis. When lithium was added to NiO, the lattice distortion was decreased with increasing lithium content and eventually returns to the cubic structure when the lithium content reaches 0.12 composition (x). Toussaint also looked at the structure of NiO at higher temperatures. It is reported that with increasing temperature the rhombohedral distortion within the lattice would be reduced. Toussaint states that the temperature with which the rhombohedral cell distortion is effectively removed is around 210 °C.⁸⁵⁸

To clarify the differences presented in the literature whether NiO should be considered rhombohedral or cubic, Du Plessis *et al.* (Ref. 864) concluded that the slight rhombohedral lattice distortion is small enough to be ignored. Their study of the elastic constants shows that the overall distortion of the lattice is extremely small in terms of angle, only 4.2 arc minutes to be exact; and does not vary from the cubic orthogonal axis significantly. The explanation for the slight distortion is similar to Toussaint's explanation in that the lattice contraction is of the ⟨111⟩ axis, which is normal to the lattice planes that have spin.^{858,864} Unless stated otherwise, all discussion throughout this section refers to the stable, single crystalline, cubic structure.

Along with the decrease in rhombohedral distortion, NiO changes from antiferromagnetic to paramagnetic with increased temperature. The reasoning behind this property change is thought to be either the reduction in the nickel ion effective radius or the interaction of the electron spin.⁸⁵⁸ Of note, the Neel temperature is supposed to be the temperature with which most iron oxides change from paramagnetic to antiferromagnetic. It was previously stated that the Neel

TABLE XXXIX. NiO crystal structure with associated lattice constants determined from experiment and theory.

Structure	Space group	Lattice (\AA)
Cubic	$F\bar{m}\bar{3}m$ (#225)	4.176 ^{855,a}
		4.17 ^{861,a}
		4.08 ^{861,b}
		4.19 ^{861,b}
		4.26 ^{861,b}
		4.177 ^{862,a}
		4.168 ^{860,a}
		4.177 ^{856,a}
		4.1788 ^{863,a}
Distorted rhomb.	$R\bar{3}m$ (#166)	2.95 ^{859,a}
		2.95 ^{858,a}
		2.95 ^{856,a}

^aExperimental.

^bTheoretical.

temperature for NiO was around 520 K, but the observed transition temperature was 210 °C (483 K). Three other iron group oxides, MnO, FeO, and CoO, all undergo the transition at their respective Neel temperature, but NiO does not. The NiO transition occurs almost 40 K below the reported Neel temperature. One possible explanation for this difference is that the reported Neel temperature value of 520 K for NiO could be incorrect. Nesbet *et al.* (Ref. 865) calculated a Neel temperature value of 476 K for NiO which is more in line with the observed transition temperature, but this value appears to be an outlier compared to the other calculated Neel temperature values.^{856–858} Kunz (Ref. 866) reports a Neel temperature of 525 K but does not specify if the transition from antiferromagnetic to paramagnetic occurs at that temperature or at a lower temperature. The description of the lattice is that of an fcc structure with some trigonal distortion at lower temperatures.⁸⁶⁶

B. Growth

Reports on the growth of bulk NiO do not appear widely across the literature and few methods are reported. O'Keefe *et al.* (Ref. 867) reported on the diffusion coefficients of a bulk NiO sample grown using the Verneuil method. No further detail was provided for the growth method.⁸⁶⁷ Choi *et al.* (Ref. 868) used the Verneuil method to grow crystals for the study of the electrical conduction and the effective hole mass.⁸⁶⁸ Hill *et al.* (Ref. 869) reported a flux-melt growth of NiO bulk crystals. Other methods include a halide decomposition and flame-fusion technique.^{870,871} The growth of NiO thin films utilizes a wide variety of methods including RF sputtering,⁸⁴³ thermal evaporation,⁸⁷² spray pyrolysis,⁸⁷³ PLD,⁸⁷⁴ electron beam evaporation,⁸⁷⁵ anodic oxidation,⁸⁷⁶ and chemical bath deposition.⁸⁷⁷ Manjuntha *et al.* (Ref. 872) highlight the advantages of the thermal evaporation process for NiO thin film deposition, which tends to be cheaper while still allowing for large area deposition at low temperatures. PLD and sputtering prove useful as both allow for the stoichiometry to be maintained with the introduction of oxygen.⁸⁷⁴

C. Electronic band structure

NiO contains broad *s* and *p* bands that are separated due to the electrostatic Madelung energy. This energy causes a stabilization of the filled O(2p) bands related to the empty Ni(4s) bands.⁸⁷⁸ Band splitting within the electronic structure is quite large despite the covalent nickel and oxygen mixing that reduces the ion effective charges. The covalent mixing also brings about anionic behavior to the Ni(4s) bands and cationic behavior to the O(2p) bands.⁸⁷⁹ The photoelectron spectra can be used to estimate the positions of the Ni 3d⁸ and O(2p) bands. This is important as it can be difficult to calculate the 3d⁸ band position in relation to the band edge and the splitting of the 3d⁸ and 3d⁹ energies.⁸⁷⁹ NiO shows an absorption edge in the optical spectrum at 3.6 eV (Refs. 855 and 880) and can be explained by two interpretations. The interpretations include a Ni 3d⁸ to Ni 3d⁷(4s) transition⁸⁸¹ and a charge transform transition from the O(2p)⁶ to the Ni 3d⁹.⁸⁵⁵ The Ni 3d⁸ to 4s transition is considered to be indirect by Mattheiss (Ref. 882) but that finding is contradicted by the sharp absorption edge in the observed spectrum indicating a direct transfer.⁸⁸⁰ The second interpretation involves the energy gap of the correlation splitting within the Ni 3d⁸ and 3d⁹ bands.⁸⁷⁹ Dare *et al.* (Ref. 879) summarize their findings by stating that the valence and conduction bands are Ni²⁺d⁸ and Ni⁺d⁹ bands, respectively. The valence O(2p) bands reside around 1.4 eV below the valence maximum. Evidence suggests there also exists states that go below the conduction band and correspond to surface-donor states that arise from d⁸ and d⁹ bands. A band is also shown to extend up past the valence maximum to contribute to acceptor states.⁸⁷⁹ Agapito *et al.* (Ref. 883) published one of the few NiO band structures found in the literature, shown in Fig. 31. The gray lines represent the PBE calculated band structure while the black lines represent ACBN0 calculations. The calculated values are discussed below.

Choisnet *et al.* (Ref. 884) state that the forbidden bandgap ranges from 4 to 6 eV. The top of the valence band is composed of O(2p) and Ni(3d) hybrid states. A sub band consisting of occupied Ni(3d) states resides 2 eV below the Fermi level. The numerical value of the Hubbard parameter, the *d*-*d* peak splitting, was reported to be 6.6 eV. The experimental forbidden bandgap value was found to be 4.3 eV, a result of the hybrid O(2p)-Ni(3d) transition to the vacant Ni(3d) band.⁸⁸⁴

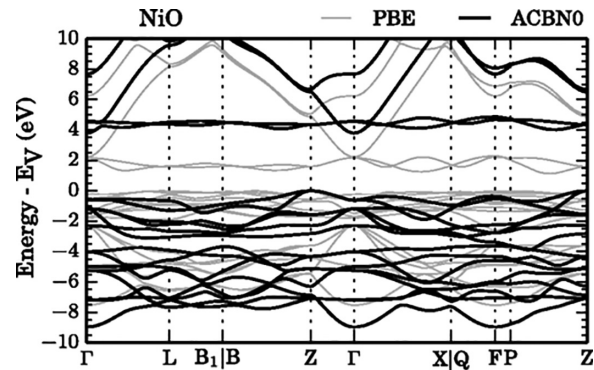


FIG. 31. Band structure of NiO with all energies relative to the valence band maximum. The gray lines represent PBE calculations, while the black lines represent ACBN0 calculations. Reproduced with permission from Agapito *et al.*, Phys. Rev. X 5, 011006 (2015). Copyright 2015 APS, licensed under a Creative Commons Attribution (CC BY) license (Ref. 883).

1. Bandgap Energy

Methods for calculating the indirect⁸⁸⁵ bandgap include LSDA,⁸⁶¹ LSDA+U,^{861,886} SIC-LDA,⁸⁸⁷ PBE,⁸⁸³ ACBN0,⁸⁸³ and Hartree-Fock.⁸⁶¹ LSD and LSDA produced underestimations of 0.2 and 0.6 eV, respectively.^{861,887} Hartree-Fock provided an overestimated indirect bandgap of 14.2 eV.⁸⁶¹ The addition of the Hubbard U parameter to the LSD and LSDA calculations was needed in order to raise the bandgap energy. Using LSD+U raised the indirect bandgap to 3.10 eV while LSDA+U resulted in a value of 3.00 eV.^{861,886} Other calculated values of 2.54 and 4.80 eV were reported from SIC-LDA and optical calculations, respectively.^{866,887} Calculated values from Agapito *et al.* (Ref. 883) were reported using PBE and ACBN0 methods. PBE underestimated the indirect gap with a bandgap energy of 1.13 eV while ACBN0 yielded a value of 4.04 eV.⁸⁸³

Experimentally, the bandgap of NiO was determined primarily using optical data such as the absorption coefficient with values ranging from 3.25 to 4.5 eV.^{872,888} The experimentally determined bandgap for bulk samples ranged from 3.6 to 4.3 eV determined from thermal deduction and XPS-BIS measurements, respectively.^{866,889} The experimental values for thin film samples are wide ranging compared to bulk samples. This is likely a result of the various growth techniques as well as differences in thin film quality and thickness skewing the bandgap energies. Optical data from Patil *et al.* (Ref. 873) produced experimental values for the bandgap energies and found that the gap decreased with increasing film thickness. The film thickness ranged from 28 to 230 nm with a bandgap ranging from 3.58 to 3.40 eV, respectively. The activation energy was also shown to increase with increasing film thickness. NiO contains an absorption edge within the UV region while there exists no absorption in the visible region.⁸⁷³ The Ni³⁺ ions that attribute to the p-type conductivity contain charge transfer transitions and absorption in the visible region.⁸⁹⁰ Patil *et al.* (Ref. 873) suggested that the variation in optical bandgap with film thickness could be a result of the differences in the crystallinity and homogeneity that arise during the growth. It was suggested that the NiO optical transition occurs through direct intra-band transitions.⁸⁷³ Koffyberg *et al.* (Ref. 891) produced experimental results stating that the optical transition for the bandgap from the valence to the conduction band was indirectly allowed. Koffyberg *et al.* stated there is a range for the bandgap of NiO (3.4–3.7 eV) and their results were on the lower end of that range at 3.47 eV. The NiO bandgap absorption causes a very strong UV region absorption according to results from Boschloo *et al.* (Ref. 892) who determined that the bandgap for their thin film study was 3.55 eV. Irwin *et al.* (Ref. 893) report an optical bandgap of 3.6 eV and describe the differences in reported bandgap values being a consequence to how the band edge location was defined.⁸⁹³

A study by Valyukh *et al.* (Ref. 894) on the optical properties of NiO thin films utilized SE to produce three bandgap values that contained direct optical transitions. The model consisted of two layers, one uniaxial layer atop of an isotropic film. The first bandgap was reported to be 3.95 eV parallel to the optical axis. The second reported bandgap energy was recorded perpendicular to the optical axis with an energy of 3.97 eV. The third reported bandgap energy was slightly lower in energy at 3.63 eV and said to be the isotropic bottom portion of the film samples. The authors did not provide a reasoning for why the NiO film was considered anisotropic. No further data analysis of the bandgap energies was provided. All reported values for the

bandgap of NiO are listed in Table XL. NiO bandgap values are also compared in Sec. XI.

D. Material properties

Basic material properties reviewed throughout the literature for NiO include the material density, bulk modulus, and the melting point. The density of NiO appears in good agreement across multiple sources, ranging from 6.67 to 6.8279 g/cm³.^{897–899} The bulk modulus was reported by Clendenen *et al.* (Ref. 900) and Jifang *et al.* (Ref. 899) to be 199 and 205 GPa, respectively. Clendenen *et al.* arrived at the bulk modulus using a static compression method. An outlying bulk modulus value of 137.3 GPa was reported by Du Plessis *et al.* (Ref. 864). Note, the bulk modulus reported by Du Plessis *et al.* was converted to GPa from 1.37×10^{12} dyn/cm². For comparison, polycrystalline samples had a reported bulk modulus of 190 and 220 GPa.⁹⁰¹ The melting point of NiO ranged from 1949 to 1983 °C across multiple sources.^{897,902,903} Oliver *et al.* (Ref. 903) studied the molecular-dynamics of NiO surfaces. Their reported calculated melting points from the molecular-dynamics study were drastically higher than those

TABLE XL. Bandgap energy parameters of NiO determined from theory and experiment.

E _g (eV)	Method	Bulk/film	Reference
Experiment			
3.60	Thermally deduced	Bulk	866
4.30	XPS-BIS	Bulk	889
3.25	Optical absorption	Film	888
3.40	Optical absorption	Film	873
3.47	Optical absorption	Film	895
3.47	Absorption coefficient	Film	891
3.49	Optical absorption	Film	873
3.50	Absorption coefficient	Film	872
3.55	Absorption spectrum	Film	892
3.55	Optical absorption	Film	873
3.58	Optical absorption	Film	873
3.60	Optical absorption	Film	895
3.60	Optical absorption	Film	893
3.63	Ellipsometry	Film	894
3.69	Optical absorption	Film	895
3.86	Optical absorption	Film	895
3.95	Ellipsometry	Film	894
3.97	Ellipsometry	Film	894
4.00	Photoemission measurements	Film	896
4.20	Absorption coefficient	Film	872
4.50	Absorption coefficient	Film	872
Calc.			
2.54	SIC-LDA	...	887
3.00	LSDA+U	...	861
3.10	LSD+U	...	886
4.80	Optical calc.	...	866

listed previously, reaching as high as 3173 °C. Details on the specific study and the calculated differences in the melting point of NiO can be found in Ref. 903. Reported values for the basic material properties of NiO are compared in Sec. XI.

1. Thermal properties

Thermal properties reported for NiO include the Debye temperature, CTE, specific heat, thermal diffusivity, and thermal conductivity. The Debye characteristic temperature was reported to be 495 K.⁹⁰⁴ Other values for the Debye temperature range from 580 to 595 K.^{905,906} It should be noted that the Debye temperature of 595 K reported by White (Ref. 906) was determined using specific heat data at low temperatures. White states that the Debye temperature from the specific heat was not in agreement with the Debye temperature (elastic) calculated using the elastic constants data recorded at higher temperatures. Srivastava *et al.* (Ref. 863) studied the CTE of NiO for temperatures ranging from 105 to 813 K. The CTE increased from $11.23 \times 10^{-6}/\text{K}$ to $14.93 \times 10^{-6}/\text{K}$. Around room temperature (305 K), the CTE was $12.28 \times 10^{-6}/\text{K}$. Keem *et al.* (Ref. 905) listed a room temperature mean CTE of $10.00 \times 10^{-6}/\text{K}$. The instantaneous CTE was $10.04 \times 10^{-6}/\text{K}$. Keem also reported the specific heat [in units of cal/(g K)] across a temperature range from 0 to 1000 K. At room temperature the specific heat, converted to J/(g K), was found to be 0.5903.⁹⁰⁵ DuBose *et al.* (Ref. 907) reported a specific heat of 43.378 J/(mol K) at 280 K. Using the known molar mass of NiO, 74.6928 g/mol, the specific heat converts to 0.5807 J/(g K). A room temperature (294.8 K) thermal diffusivity was reported to be $8.80 \times 10^{-6} \text{ m}^2/\text{s}$. Thermal diffusivity was around $32 \times 10^{-6} \text{ m}^2/\text{s}$ at 135 K and decreased with increasing temperature.⁸⁹⁸ The thermal conductivity of NiO was studied again by Keem *et al.* (Ref. 905) across temperatures from 2.8 to 700 K. The room temperature thermal conductivity was reported to be 20.2 W/(m K). The thermal conductivity peaked at a value of 401 W/(m K) at a temperature of 45 K before decreasing with increasing temperature.⁹⁰⁵ Sahoo *et al.* (Ref. 908) stated that the room temperature thermal conductivity of bulk NiO was around 50 W/(m K). In the same study, NiO samples with nanoscale grain sizes had a thermal conductivity of around 20 W/(m K). The decreases in thermal conductivity with decreasing grain size to the nanoscale is attributed to the increase in phonon scattering.⁹⁰⁸ Further studies on the thermal conductivity of NiO with discussion of the Neel temperature are reported by Lewis *et al.* (Ref. 909). The cited thermal property values are compared below in Sec. XI.

2. Phonon properties

The phonon properties of NiO are not as widely researched or as well known as for other oxides. The irreducible representations were not readily found in the literature. For cubic rock salt structure the first-order TO and LO phonons are not Raman active.^{910,911} However, when a weak rhombohedral distortion exists below the Neel temperature, it can allow for the activation of the Raman modes. The first-order Raman processes are still very weak with low intensity, but the second-order modes are visible. Two-magnon (2M) bands often make it difficult to observe the second-order Raman as well. UV Raman spectroscopy can suppress the 2M bands and allow for extraction of the LO and TO phonons and spin coupling. Weak peaks were shown from 350 to 410 cm⁻¹ for TO phonon modes and from 520 to

580 cm⁻¹ for LO phonon modes. Second-order Raman showed peaks of 2TO at 738 cm⁻¹, 2LO at 1142 cm⁻¹, and TO + LO at 913 cm⁻¹.

Two-photon absorption studies were carried out by Willet-Gies *et al.* (Ref. 912) using IR ellipsometry. A strong TO absorption peak was shown at 393 cm⁻¹ along with a weak TA+TO absorption peak occurring at 548 cm⁻¹. A strong LO peak was shown with a loss function at 549 cm⁻¹. NiO also experiences a weak ionic TO/LO mode splitting. Willett-Gies *et al.* summarize their findings by stating that reststrahlen bands dominate as a result of the zone-center TO/LO pairs. These bands are modified by the weaker TA+TO phonon absorption. They also concluded that the antiferromagnetic coupling or the magnetic unit cell doubling do not alter the zone-center phonons.⁹¹² The phonon parameters are listed in Table XLI along with the various models used in the study.

Other studies on the phonon modes of NiO include Dietz *et al.* (Ref. 913), Mironova-Ulmane *et al.* (Ref. 856), and Lacerda *et al.* (Ref. 914). Of note, the study by Lacerda *et al.* involves Raman spectroscopy above the Neel temperature of NiO.

3. Electrical properties

The electrical properties of NiO reviewed below include the electron affinity, electrical breakdown field, static and high frequency dielectric constants, effective mass, and carrier mobility. The electron affinity of NiO was reported in good agreement across literature. The values ranged from 1.40 to 1.47 eV.^{891,915,916} The electrical breakdown field can be estimated using Higashiwaki's (Ref. 147) bandgap vs breakdown field plot. Using the experimentally determined bandgap values ranging from 3.25 to around 4.50 eV, the predicted electrical breakdown field strength ranges from 2 to 5 MV/cm.

The static dielectric constants were reported by multiple sources. Newman *et al.* (Ref. 855) and Rao *et al.* (Ref. 917) reported what is considered a low frequency dielectric constant with values of 12.0 and 11.9, respectively. Gielisse *et al.* (Ref. 871) reported the high frequency dielectric constant to be 5.4 and 5.7 for a calculated and experimental value, respectively.^{855,871} Values for the static and high frequency dielectric constants are compared in Sec. XI. Rodl *et al.* (Ref. 831) calculated the effective hole mass along two directions. For the T-Γ direction the effective hole mass was 0.86 m_h for both the upper and lower valence band. For the T-K direction the upper valence band had an effective hole mass of 0.55 m_h while the lower valence band had an effective hole mass of 1.66 m_h.⁸³¹ Choi *et al.* (Ref. 868) reported an effective hole mass with a range of 0.8 m_h to 1.0 m_h. That range of values was calculated using a band conduction scheme. The effective

TABLE XLI. Phonon parameters of NiO from various models. Data reproduced from Willet-Gies *et al.* (Ref. 912).

Model	ε_{∞}	$\omega(\text{TO})$	$A(\text{TO})$	$\gamma(\text{TO})$	$\omega(\text{TO})$	$\gamma(\text{TO})$	MSE
One Lorentz	4.96	390.5	6.26	28.8			4.78
Two Lorentz	4.96	393.9	5.86	17.6			3.81
		565	0.081	81			
One Lowndes	4.93	391.1		18.2	585.9	35.1	4.28
Two Lowndes	4.97	392.9		17.2	593.9	42	3.55
		548		55	542	38	

hole mass was also shown to decrease slightly with an increase in temperature.⁸⁶⁸

The carrier mobility for both electrons and holes has been reported. The electron mobility was shown to be low while the drift mobility of the holes was found to be twice that of the electrons from a photoionization study.⁹¹⁸ The hole drift mobility was around $0.3 \text{ cm}^2/(\text{V s})$ while the electron drift mobility was around $0.14 \text{ cm}^2/(\text{V s})$. A reasoning for the low electron drift mobility was given by Goodenough (Ref. 919). Cationic orbitals compose most of the electron bands. This results in cation vacancies and localized spins causing scattering.⁹¹⁹ A higher electron mobility of $3.3 \text{ cm}^2/(\text{V s})$ was reported using Hall and Van der Pauw measurements.⁸⁹²

The hole mobility ranged from 0.3 to $2.8 \text{ cm}^2/(\text{V s})$.^{881,920,921} Osburn *et al.* (Ref. 922) calculated a hole mobility of $0.53 \text{ cm}^2/(\text{V s})$ that appeared independent of temperature. According to Tyagi *et al.* (Ref. 843), a hole mobility of $2.8 \text{ cm}^2/(\text{V s})$ was reported for p-type NiO thin films, considered a high hole mobility value. The substrate temperature was also altered and resulted in a hole mobility ranging from 0.3 to $3.5 \text{ cm}^2/(\text{V s})$ as the temperature increased from 200 to 500 °C. It was found that when the temperature of the substrate increases, the crystallinity was improved, and scattering centers are reduced because of the increased crystallite size.⁸⁴³ From the same study, the electron mobility of n-type NiO thin films was found to be $3.3 \text{ cm}^2/(\text{V s})$. Cited values for the electrical properties including the electron affinity, electrical breakdown field, effective mass, and carrier mobility of NiO are compared in Sec. XI.

When considering device applications for NiO, the hole concentration is crucial. The hole concentration helps determine the heterogeneous p-n junction designs for devices. At times, the hole concentration is even more important than the hole mobility in instances where NiO is used as a gate region to lift the threshold voltage. The hole concentration and the subsequent hole mobility have been reported throughout literature. A hole concentration of $1.16 \times 10^{18} \text{ cm}^{-3}$ and hole mobility of $0.85 \text{ cm}^2/(\text{V s})$ was reported by Li *et al.* (Ref. 923). Ohta *et al.* (Ref. 924) reported a hole concentration of $6.0 \times 10^{18} \text{ cm}^{-3}$ and hole mobility of $0.1 \text{ cm}^2/(\text{V s})$. Finally, Ma *et al.* (Ref. 845) reported a hole concentration of $5.0 \times 10^{19} \text{ cm}^{-3}$ and hole mobility of $0.7 \text{ cm}^2/(\text{V s})$.

E. Doping and defects

Pure stoichiometric crystals of NiO make excellent insulators and contain a high room temperature resistivity of around 10^{13} Ohm cm .⁸⁸¹ Koffyberg *et al.* (Ref. 891) also reaffirm that NiO is an insulator in pure stoichiometric form. The presences of defects within the lattice and other impurities cause variations within the conductivity of the material. Lithium is a very common dopant of NiO and acts as a substitute for the nickel ions. The p-type conductivity occurs in undoped samples as well as in lithium doped samples. Often the lithium doped samples will exhibit higher conductivity values.⁸⁹¹ Lithium is Li^+ within the NiO lattice due to the second ionization potential of lithium being higher than the third ionization potential of nickel. With every Li^+ , a Ni^{3+} should be present for charge neutrality, but often times an O^{2-} vacancy will compensate for two of the Li^+ ions. The Li^+ impurities are acceptors since Ni^{3+} is just Ni^{2+} with an extra positively charged hole. Within undoped samples the p-type conductivity arises from monovalent impurities or nickel vacancies within the lattice.⁸⁸¹ It is possible to achieve n-type conductivity of NiO with oxygen

vacancies or metallic impurities dominating the defects.⁹²⁵ While lithium appears across literature as the most common dopant used within NiO, other dopants include copper,⁹²⁶ oxygen,⁹²⁷ iron,⁹²⁸ and cobalt.⁹²⁹ With the addition of copper doping, the grain size and transmission of the thin film was altered. The bandgap of copper doped NiO films was 3.69 eV compared to a bandgap of 3.73 eV measured of pure films.⁹²⁶ With the addition of oxygen doping, there was evidence that oxygen vacancy formation was reduced and the Fermi level was not lifted. The addition of iron dopants into NiO was shown to reduce the required potential for oxygen evolution. Further details can be found in the electrochemical study of iron doped NiO by Miller *et al.* (Ref. 928). Cobalt doping was studied in (polycrystalline) NiO thin film samples.⁹²⁹ The bandgap decreased from 3.44 to 3.26 eV with increased cobalt content. The amount of cobalt present controls the cation vacancies within the film, thus altering the optical bandgap.⁹²⁹

F. Summary of NiO property values

Table XLII highlights a summary of the properties reviewed for NiO. Values for each of the properties are presented along with references and notation of whether they are experimental or calculated findings. Where relevant anisotropy is denoted.

IX. COPPER OXIDE

Copper oxide is a semiconducting oxide with many unique material properties that make it a candidate for device applications. Three specific phases of copper oxide have been studied extensively in literature: CuO (cupric oxide), Cu_2O (cuprous oxide), and Cu_4O_3 (paramelaconite). Of these three phases, Cu_2O is a direct bandgap material while CuO and Cu_4O_3 are indirect bandgap materials.⁹³⁰ Across the three phases there are differing copper morphologies and oxidation states.⁹³¹ Copper oxide is another p-type conductive semiconductor similar to NiO. Copper oxide has been of interest for device applications due to the possibility of its use in solar cell technology,^{932–935} high temperature superconductivity,⁹³⁶ photo-thermal and photoconductive applications,⁹³⁷ solid state catalysis,⁹³⁸ and magnetic materials due to its antiferromagnetic behavior below the Neel temperature.⁹³⁹ Predictions using the Shockley-Queisser limit (SQL) show that copper oxide solar cells have the potential to achieve an efficiency upwards of 20%,⁹³² thus the reasoning behind the renewed interest in copper oxide. Heterojunction copper oxide solar cells have been a large focus since heterojunction diodes are not feasible due to little or no n-type conductivity.⁹³⁰ Copper oxide also has potential for use in composites with ZnO and SnO_2 .^{940,941} Similar to NiO, the properties of CuO and its polymorphs are heavily influenced by the stoichiometry. Many of these stoichiometric changes are often a result of the growth and fabrication method and play a large role in altering properties such as the optical and electrical properties. This topic is beyond the scope of this review but references for further reading and examples on the stoichiometric effects of CuO are given.^{942–944} This section will be centered around cupric oxide (CuO) with parameters for the other phases discussed alongside for comparison where applicable.

A. Crystal structure

The three stable copper oxide phases have their own unique crystal structures. Cupric oxide (CuO) maintains a monoclinic structure belonging to space group C2/c (#12).^{930,945} The copper and oxygen

TABLE XLII. Summary of theoretical and experimental properties of NiO. Common names of nickel oxide and bunsenite.

Stable phase	Distorted rhomb.	Ref. 858
Stable structure	Trigonal	$R\bar{3}m$ (#166)
	$a = 2.95 \text{ \AA}$	Refs. 856, 858, and 859
Metastable phase	Cubic	$Fm\bar{3}m$ (#225)
	$a = 4.08\text{--}4.26 \text{ \AA}$	Refs. 855, 856, 860–863
Density (g/cm ³)	6.8	Expt. ⁸⁹⁸
	6.8279	Ref. 899
Bulk modulus (GPa)	199–205	Expt. ^{899,900}
	137.3	Calc. ⁸⁶⁴
T_m (°C)	1955–1983	Refs. 118, 897, and 903
	3127 (bulk)	Calc. ⁹⁰³
Debye temp. (K)	495–595	Expt. ^{904–906}
Specific heat (J/(gK))	0.5903 ^a	Expt. ⁹⁰⁵
	0.5807	Expt. ⁹⁰⁷
Thermal cond. (W/(mK))	50	Expt. ⁹⁰⁸
	20.2	Expt. ⁹⁰⁵
Thermal diff. (mm ² /s)	8.8	Expt. ⁸⁹⁸
CTE ($\times 10^{-6}/\text{K}$)	12.28	Expt. ⁸⁶³
Electron affinity (eV)	1.4	Calc. ⁸⁹¹
	1.46–1.47	Expt. ^{915,916}
Breakdown field (MV/cm)	2–5	Pred. ¹⁴⁷
m_h^*	0.8–1.0	Calc. ⁸⁶⁸
	0.86 T-Γbc	Calc. ⁸³¹
	0.55 T-K ^b	Calc. ⁸³¹
	1.66 T-K ^c	Calc. ⁸³¹
μ_e [cm ² /(V s)]	0.14–3.3	Expt. ^{843,918,919}
	0.64	Calc. ⁹²¹
μ_h [cm ² /(V s)]	0.43–0.53	Calc. ^{920,922}
	0.3–2.8	Expt. ^{843,881,918,919,921}
Gap Type	Indirect	Ref. 892
E_g (eV)	2.54–4.8	Bulk Calc. ^{861,866,886,887}
	3.60–4.30	Bulk Expt. ^{866,889}
	3.25–4.5	Film Expt. ^{872,873,888,892,895}
ϵ_0	11.9–12	Expt. ^{855,871,917}
	11.75	Calc. ⁸⁷¹
ϵ_∞	5.4	Expt. ⁸⁵⁵
	5.7	Calc. ⁸⁷¹

^aConverted from cal/(g °C).^bUpper valence.^cLower valence.

atoms within the lattice exhibit a square planar coordination.⁹⁴⁶ The primitive cell contains two CuO units while the unit cell contains four CuO units.⁹³⁰ Individual atoms within the unit cell consist of four oxygen atoms in the 4e position and four copper atoms in the 4c position. Cupric oxide has a Neel temperature of around 230 K, below which CuO is antiferromagnetic.⁹⁴⁶ The lattice constants for CuO found in

literature are in decent agreement across experimental and calculated methods. Experimental values range from $a = 4.662$ to 4.683 \AA , $b = 3.417$ to 3.422 \AA , and $c = 5.118$ to 5.128 \AA .^{930,945,947} Calculated values range from $a = 4.513$ to 4.588 \AA , $b = 3.35$ to 3.61 \AA , and $c = 5.035$ to 5.14 \AA .⁹³¹ The lattice constants for CuO as well as comparisons to Cu₂O and Cu₄O₃ are listed in Table XLIII. Crystal structures for CuO, Cu₂O, and Cu₄O₃ are shown in Fig. 32.

Cu₂O forms a cubic structure belonging to space group $Pn\bar{3}m$ (#224). Each unit cell contains a total of six atoms consisting of four copper atoms and two oxygen atoms. The copper takes a face-centered

TABLE XLIII. CuO, Cu₂O, and Cu₃O₄ crystal structures with associated lattice constants determined from experiment and theory.

Structure	Space group	Lattice (Å)
CuO		
Monoclinic	$C2/c$ (#15)	$a = 4.6837^{930,945,a}$ $b = 3.4226$ $c = 5.1288$ $\beta = 99.54^\circ$
		$a = 4.5882^{931,b}$ $b = 3.3544$ $c = 5.0354$ $\beta = 99.39^\circ$
		$a = 4.5130^{931,b}$ $b = 3.6121$ $c = 5.1408$ $\beta = 97.06^\circ$
		$a = 4.66^{947,a}$ $b = 3.40$ $c = 5.09$ $\beta = 99^\circ 30'$
Cu ₂ O		
		$a = 4.1656^{931,b}$ $a = 4.2675^{931,b}$ $a = 4.2685^{948,a}$ $a = 4.2696^{930,a}$, $a = 4.27^{956,a}$
		$a = 5.837^{951,a}$ $c = 9.832$ $a = 5.83^{952,a}$ $c = 9.88$ $a = 5.817^{957,a}$ $c = 9.893$ $a = 5.6544^{931,b}$ $c = 9.7728$ $a = 5.8392^{931,b}$ $c = 9.8966$
Cu ₄ O ₃	$I4_1/amd$ (#141)	

^aExperimental.^bTheoretical.

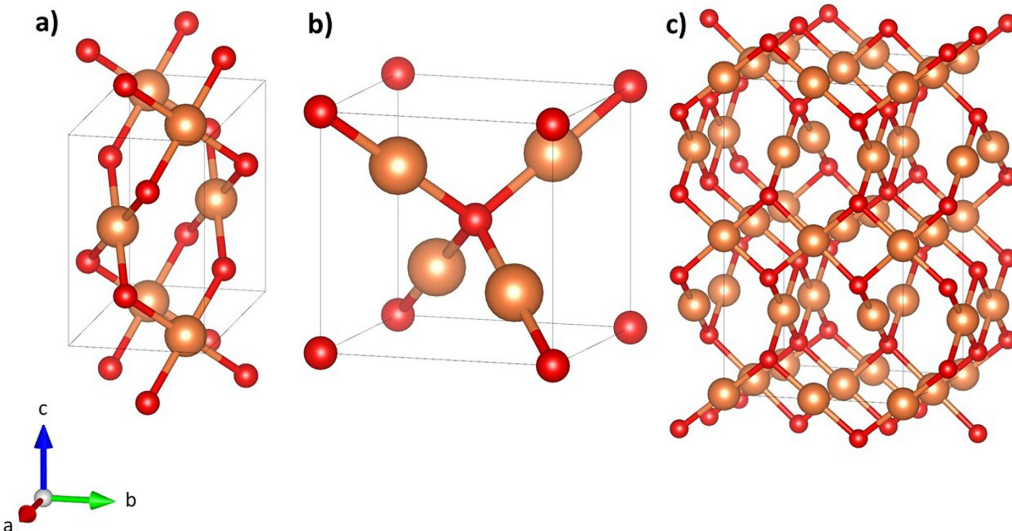


FIG. 32. Crystals structures for (a) CuO, cupric oxide with space group C2/c (#12); (b) Cu₂O, cuprous oxide with space group Pn $\bar{3}$ m (#224); and (c) Cu₄O₃, paramelaconite with space group I4/*amd* (#141). All unit cells are shown with the c-axis pointing upward (orange = Cu, red = O).

position in the simple cubic structure while the two oxygen atoms take the tetrahedral sites to form a body-centered structure.⁹³⁰ The lattice constant for the cubic cuprite across literature is constant with only small variations ranging from $a = 4.1656$ to 4.269 Å.^{930,931,948} The oxygen atoms have fourfold coordination with the neighboring copper atoms. The copper atoms have linear coordination with the oxygen atoms.⁹³⁰ The bonds between the Cu–O and the Cu–Cu have been a topic of study and were examined using x-ray diffraction and electron diffraction,⁹⁴⁹ as well as electron density mapping.⁹⁵⁰

Cu₄O₃ is the third stable phase of copper oxide found across the literature. Of the three stable copper oxide phases, Cu₄O₃ is the least studied. The crystal structure of Cu₄O₃ is tetragonal belonging to space group I4/*amd* (#141).⁹⁵¹ The atomic structure consists of twofold coordinated copper atoms stacked on top of fourfold coordinated copper atoms. This stacking structure shares features with both CuO (fourfold coordinated copper) and Cu₂O (twofold coordinated copper).⁹³⁰ Cu₄O₃ contains a stoichiometry that resides between the other two copper oxides, CuO and Cu₂O.^{951,952} There are unique interpenetrating atomic chains consisting of Cu⁺–O and Cu²⁺–O as well as planar coordination between the Cu²⁺ and O²⁻ ions.⁹⁵³ This specific configuration exists in CuO and other superconductors at high temperatures.⁹³⁶ The Neel temperature of Cu₄O₃ is low at 42 K (Refs. 954 and 955) with the source of magnetism being the Cu²⁺ ions, similar to CuO.⁹⁵³

The phase stability of CuO, Cu₂O, and Cu₄O₃ is another important aspect of the copper oxide system. Heinemann *et al.* (Ref. 931) investigated the structural stability using a hybrid functional approach and a Debye model. The phase diagram for the three copper oxides polymorphs is highlighted in Fig. 33. The calculated results have an accuracy of ± 30 K for the phase transition temperatures. It should be noted that Cu₄O₃ is absent from the phase diagram since the calculations show that this phase is not thermodynamically stable. However, the grand potential of Cu₄O₃ is shown to reside in close relation to that of Cu₂O and CuO according to the inset in Fig. 33. The

temperature dependence and location of the phase transformations from Heinemann *et al.* are also in line with phase transformations seen experimentally.⁹⁵⁸

B. Growth

Growth of bulk single crystal CuO has been achieved using a variety of methods. One possible process is the floating zone melting method.^{959,960} Ito *et al.* (Ref. 959) were able to produce bulk samples with a 5 mm radius and 50 mm length. A flux growth method was reported by Wanklyn *et al.* (Ref. 961). With the loss of oxygen, CuO tended to dissociate into Cu₂O. Using acidic oxides with a CuO starting composition mainly resulted in powders. Adding PbF₂ to the melt

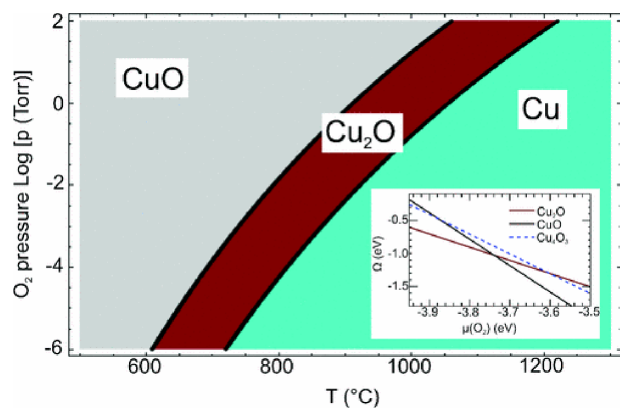


FIG. 33. Phase diagram for the copper oxide polymorphs calculated using DFT hybrid functionals. The inset displays the copper oxide polymorphs grand potential as a function of oxygen chemical potential. Reproduced with permission from Heinemann *et al.*, Phys. Rev. B **87**, 115111 (2013). Copyright 2013 APS (Ref. 931).

resulted in very small samples. The addition of K₂O to the starting composition yielded larger crystals and extended the crystallization field for successful flux growth.⁹⁶¹ Pieters *et al.* (Ref. 962) used a sublimation method to achieve single crystal growth. Growth was achieved inside of a closed quartz ampoule with a temperature of 900 °C. The addition of small percentages of In₂O₃ doping was shown to be necessary for crystal growth. CVT was another method reported across literature.^{963,964} Zheng *et al.* (Ref. 965) presented a novel CVT growth method capable of yielding crystals with dimensions as large as 14 × 3 × 0.3 mm³. The novel method utilized CVT of CuI and BaO₂ to produce very high quality single crystals reported to be free of impurities. CuI evaporates quickly which allows for the oxidation-to-crystal-growth process to occur simultaneously. Thin film growth of CuO has also been achieved throughout literature using a variety of growth methods. These methods include PLD,⁹⁶⁶ reactive magnetron sputtering,^{967,968} molecular beam epitaxy (MBE),⁹⁶⁹ and successive ionic layer adsorption.⁹⁷⁰

C. Electronic band structure

CuO is widely considered to be an indirect bandgap material. The direct bandgap is often times reported alongside the indirect gap from calculations. LDA+U and HSE calculations show a direct bandgap at the B point of the Brillouin zone, but the indirect values found from the same theoretical methods show a smaller indirect bandgap energy.⁹³¹ CuO has been shown to have an open shell for 3d.⁹³⁷ XPS data show how the valence band spectra differs from Cu₂O. The d band spectral weight within Cu₂O ranges from 1.0 to 4.0 eV while the spectral weight for CuO is spread, ranging from 1.0 to 12.0 eV. The large distribution of CuO compared to Cu₂O can be explained by the strong electron-electron interactions found within CuO. Along with the more compact d spectral weight for Cu₂O, the O(2p) character ranges from 6.0 eV to 7.0 eV while the CuO O(2P) character ranges from 1.0 to 6.0 eV.⁹⁷¹ The conduction band of CuO has a leading peak at 1.8 eV, due to the complexities brought about by the 3d shell. Other conduction band peaks are seen at 6.8 and 10.6 eV

due to empty *sp* states of copper or oxygen being filled.⁹⁷¹ Koffyberg *et al.* (Ref. 937) reported an experimental indirect bandgap of 1.35 eV. Their findings show a valence band that resides higher than most oxides, approximately 5.42 eV below the vacuum level.⁹³⁷ This is similar to NiO, another p-type oxide whose valence band is only 4.9 eV below vacuum level.⁸⁹¹ Most oxides are over 7.0 eV below the vacuum level.⁹⁷² An explanation to a valence band that resides so close to the vacuum level could be the valence band consisting of metal ions and 3d atomic wave functions. This varies from other oxides as the valence band is usually comprised of O(2p) orbitals and characteristics.⁹¹⁹ The uppermost valence band is shown by XPS to be made of 3d metal orbitals and is separated from O(2p) valence bands by only a few eV.⁹⁷³ Estimation of the bandgaps showed anisotropy but the values are not accurate as an orthorhombic system was used as opposed to a monoclinic system.⁹⁷⁴ The anisotropy along the different directions can be expected given the monoclinic crystal structure of CuO. While CuO has monoclinic structure and should exhibit anisotropy, the literature primarily neglects this aspect and assumes isotropic behavior. Of the reviewed materials, no such works detailed anisotropy of the electronic structure or bandgap energies. Since CuO is a monoclinic system we would expect transitions to be polarized either parallel to the *b*-axis or within the monoclinic plane similar to β-Ga₂O₃. To date such a study of this nature on CuO does not exist. Figure 34 shows the calculated electronic band structures for all three copper oxide structures determined using DFT.⁹³¹

The electronic structure of Cu₂O has been well studied throughout literature. The conduction band minimum and the valence band maximum both occur at the Γ point of the Brillouin zone resulting in a direct bandgap material.⁹³⁰ The upper most valence band is comprised of mainly 3d¹⁰ states from the copper atoms. The lower section of the conduction band is comprised of Cu(4s) states. The valence band splits into two bands as a result of the spin interaction. The Γ_7^+ band corresponds to the light holes and the Γ_8^+ band corresponds to the heavy holes.⁹³⁰ The calculated values for the bandgap are in far less agreement with values as low as 0.70 eV for LDA calculations⁹³¹ and

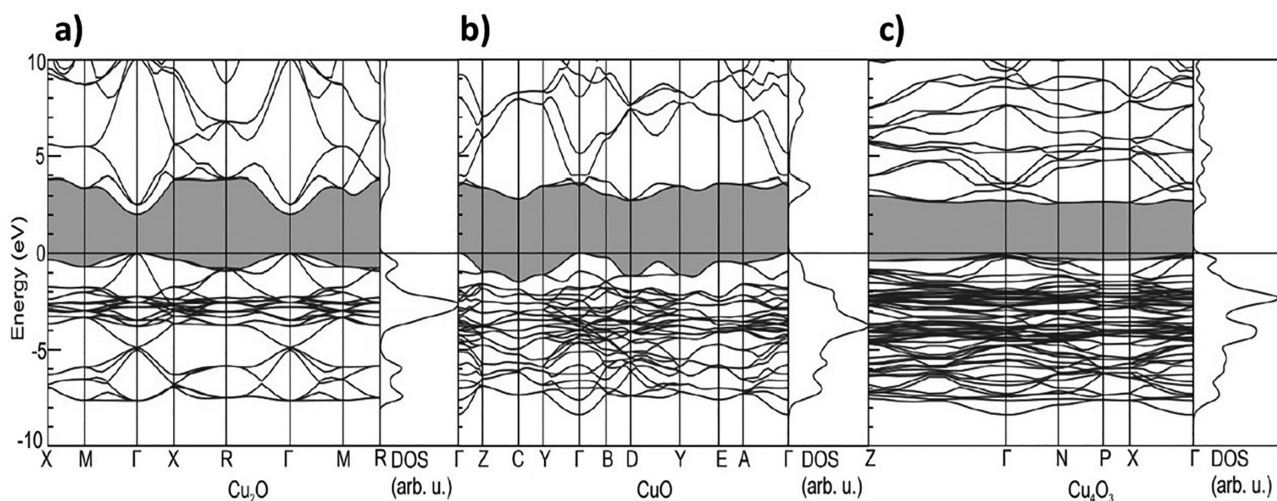


FIG. 34. Electronic band structure and density of states for (a) Cu₂O, (b) CuO, and (c) Cu₄O₃ determined using hybrid functional DFT calculations. Reproduced with permission from Heinemann *et al.*, Phys. Rev. B **87**, 115111 (2013). Copyright 2013 APS (Ref. 931).

0.63 for LDA+U calculations.⁹⁷⁵ LDA calculations find Cu₂O to be semiconducting while CuO and Cu₄O₃ are not shown to be semiconducting from LDA. Like other oxide materials seen previously, LDA results in low calculated bandgap values in comparison to the experimental values. Hartree-Fock calculations yield a theoretically determined bandgap that is far too high at 9.70 eV.⁹⁷⁶ Using an LDA+U calculation does not improve the theoretically determined bandgap values much either. The reason for this little to no change is found to be a result of the Cu²⁺ ion d shell being completely occupied. This lowers the effectiveness of the LDA+U theoretical measurements because the on-site correlation is reduced.⁹³⁰

This ineffective LDA+U that is seen in Cu₂O calculations is a more effective theoretical method in the other copper oxides of CuO and Cu₄O₃. By using LDA+U to theoretically determine the bandgap, the two compounds (CuO and Cu₄O₃) that were found to be metals under LDA calculations are now shown to be semiconducting with an indirect bandgap. The calculated LDA+U values for CuO and Cu₄O₃ are also shown to be in better agreement with the experimental values for each respective material. It was shown that this good agreement between theoretical and experimental values relies heavily on the U parameter of the LDA+U calculations.⁹³⁰

Ching *et al.* (Ref. 977) used OLCAO to theoretically determine the band structure of Cu₂O as well. Calculations show Cu₂O to be a direct bandgap semiconductor with the bandgap being around 0.78 eV along the Γ point. The valence band is found to be split into two components; an upper section with a width of 4 eV comprised of Cu(3d) states, and a lower section of width 3.5 eV comprised of mainly O(2p) states. The two sections are separated at the Γ point by a direct gap of 0.8 eV.⁹⁷⁷ Ching *et al.* discredits previous bandgap theoretical studies⁹⁷⁸ on copper oxide due to the underdeveloped methods of calculation. A study completed almost a decade prior to Ching *et al.* by Kleinman *et al.* (Ref. 979) uses spin-orbit splitting to observe the electronic bands and finds a theoretical direct bandgap of 1.07 eV. This value is slightly larger than Ching *et al.*'s findings but still much lower than the 2.0 to 2.2 eV experimental values that are often used in literature.⁹⁷⁷ Optical studies show that any absorption is negligible until 2.6 eV. This provides evidence that the wave functions along the band edge lead to the direct transition being forbidden at the Γ point. Eigenvalues for the top of the valence band show that the wave functions are comprised of O(p), Cu(s), and Cu(d) orbitals. O(s) orbitals makeup most of the conduction band bottom with some mixing of Cu(s) and Cu(d) orbitals. Note, that from the eigenvalue inspection there is the absence of Cu(p) orbital components in both the conduction minimum and valence maximum.⁹⁷⁷

Cu₄O₃ is an indirect bandgap material similar to CuO. Of the three copper oxides, Cu₄O₃ has the smallest bandgap according to experimental values.^{930,967} Both the calculated and the experimental direct bandgaps occur at the Γ point of the Brillouin zone.⁹⁵³ Pierson *et al.* (Ref. 967) detail how the bandgaps were determined experimentally using Cu₄O₃ thin films and assuming an indirect bandgap.⁹⁶⁷ The ratio found between the direct and indirect bandgap energies is 1.53 for calculated values and 1.84 for experimental values.⁹⁵³ Across all three copper oxide compounds, it was shown that the majority of the calculated results undervalued the bandgap by anywhere from 10% to 50% and has been hypothesized to be a result of the shortcomings of the LDA and LDA+U methods, and/or missing electron correlations.⁹⁵³ Heinemann *et al.* (Ref. 931) observed through the calculated

methods that HSE hybrid functional was a more fitting theoretical method for Cu₂O but less reliable for CuO and Cu₄O₃.⁹³¹ In examining the electronic structure of Cu₄O₃, there is 3d¹⁰ configuration that stems from the Cu⁺ ions filling the d-band. Cu²⁺ forms an unfilled 3d shell and yields a smaller DOS peak compared to Cu⁺. Cu²⁺ ions have hole states that are almost fully spin-polarized. Cu²⁺ is also hybridized with the O-p states. The hole states are shown to be Cu²⁺.⁹⁵³

1. Bandgap energy

The values for the indirect bandgap of CuO are widely reported across the literature. The bandgap has been determined theoretically using methods such as HSE,⁹³¹ OLCAO,⁹⁷⁷ LDA+U,^{886,931,953} SIC-LSD,^{887,980} and DFT.⁹⁸¹ CuO has a bandgap that ranges in theoretical value from 0.91 to 2.74 eV depending on the theoretical method used. Table XLIV shows that GGA calculations provide a wide range of calculated values for CuO spanning 0.91 to 2.11 eV for that single method alone. With the addition of the Hubbard parameter U to the

TABLE XLIV. Bandgaps of CuO determined from experiment and theory. Substrates for the experimental thin film samples have also been listed.

E _g (eV)	Method	Bulk/film	Substrate	Reference
Experiment				
1.35	Optical absorption	Bulk		937
1.60	Ellipsometry	Bulk		974
1.70	Optical absorption	Bulk		983
1.40	Optical absorption	Film	SnO ₂ :F glass	984
1.55	Optical absorption	Film	Glass	968
1.56	Optical absorption	Film	Glass	968
1.65	Optical absorption	Film	Glass	968
1.67	Optical absorption	Film	Glass	968
1.68	Optical absorption	Film	Glass	968
1.70	Photocurrent vs λ	Film	Pt foil	982
1.79	Optical absorption	Film	Glass	970
1.87	Optical absorption	Film	Glass	970
1.97	Optical absorption	Film	Glass	970
2.03	Optical absorption	Film	Glass	970
Calc.				
0.91	GGA+U (U = 5)	...		981
1.00	LSDA+U	...		985
1.00	SIC-LSD	...		980
1.10	LDA+U	...		953
1.24	GW	...		986
1.39	LDA+U	...		931
1.43	SIC-LSD	...		887
1.48	GGA+U (U = 7)	...		981
1.60	OLCAO	...		977
1.90	LDA+U	...		886
2.11	GGA+U (U = 9)	...		981
2.20	Pseudo-SIC	...		987
2.74	HSE	...		931

GGA calculations the bandgap energy was shown to increase as U increased from $U=5$ up to $U=9$.⁹⁸¹ As U is increased there is an improvement in the electronic structure description used for the calculations, resulting in a theoretical value that is more comparable to experimental values.⁹⁸¹ The direct bandgap has also been reported using LDA+U and HSE with values ranging from 1.91 to 2.74 eV.⁹³¹ HSE calculations appear to overestimate the bandgap by almost 1 eV when compared to the highest cited experimental values.

The experimental indirect bandgap of CuO is found to range from 1.35 to 1.7 eV in bulk samples with a few values that go up to 2.03 eV in thin film samples. One of the earliest experimentally determined bandgap energies comes from Hardee *et al.* (Ref. 982) in 1977 where the photoelectrochemical properties of certain metal oxides were investigated. Measuring the photocurrent vs wavelength resulted in a bandgap energy of 1.7 eV for a polycrystalline thin film sample of CuO. Hardee *et al.* state that there was no other value for the bandgap energy of CuO found in previous literature to compare to. Jumping forward a few decades to 1995, a similar bandgap energy of 1.7 eV was produced by Sukhorukov *et al.* (Ref. 983) using optical absorption measurements on single crystal samples of CuO. Sukhorukov *et al.* noticed that the absorption of CuO experienced a rise that corresponded to $E=1.43$ eV, marking the fundamental absorption edge. This absorption edge is 0.27 eV lower than the bandgap energy of 1.7 eV represented by the first spectral band peak. An absorption edge value of 1.43 eV is more in line with the experimentally determined bandgap energy of 1.35 eV reported by Koffyberg *et al.* (Ref. 937) using lithium doped CuO. This means that Koffyburg's value could very well be the onset of absorption as opposed to the first indirect band-to-band transition, or it could be a result of the lithium doping possibly lowering the indirect bandgap. While optical absorption is the primary experimental method used in the cited literature for determining the bandgap energy of CuO, there is reported work on using ellipsometry to determine the bandgap energy as well.⁹⁷⁴ Ito *et al.* (Ref. 974) studied polycrystalline CuO samples at room temperature and found four distinct energies $E_1=1.6$ eV, $E_2=2.0$ eV, $E_3=2.6$ eV, and $E_4=3.4$ eV. The value of 1.6 eV is considered to be the first band-to-band transition and the indirect bandgap energy. It should be noted that while CuO contains a monoclinic structure and should exhibit anisotropy of the optical properties, Ito *et al.* state the polycrystalline nature of the samples dissuaded them from measuring optical anisotropy.⁹⁷⁴

Akaltun *et al.* (Ref. 970) observed by optical absorption how the bandgap increased with decreasing thin film thickness. As the thickness decreased from 310 to 125 nm, the bandgap increased from 1.79 to 2.03 eV.⁹⁷⁰ In another thin film study, Cho *et al.* (Ref. 968) observed how the optical bandgap varied with growth temperature. A peak bandgap of 1.68 eV was observed at a growth temperature of 300 °C. All cited bandgaps for CuO including the method used to determine the bandgap are listed in Table XLIV. Values of the bandgap are also listed and compared in Sec. XI.

The bandgap of Cu₂O has been reported across literature with a wide variety of theoretical methods with only a few experimental reports. Such theoretical methods include LDA,⁹⁸⁸ LDA+U,⁹³¹ HSE,⁹⁸⁹ OLCAO,⁹⁷⁷ LAPW-LDA,⁹⁹⁰ PBE0,⁹⁷⁵ and scGW.⁹⁹¹ The calculated values for the direct bandgap range from 0.53 eV to 2.77 eV, with the vast majority of those being underestimated values compared to the cited experimental results. It appears that LDA, PBE, and

TABLE XLV. Bandgap energy values of Cu₂O determined from experiment and theory.

E _g (eV)	Method	Bulk/film	Reference
Calc.			
1.77	APW	...	978
1.97	scGW	...	988
2.02	HSE	...	931
2.03	GW ^{LF} +V _d	...	992
2.04	GW	...	986
2.12	HSE	...	989
2.36	scGW	...	991
2.50 ^a	HSE	...	931
2.77	PBE0	...	975
Experiment			
2.17	Expt. ^b	Bulk	978
2.20	Expt. ^b	Bulk	992
2.38–2.51	Absorption coefficient	Film	994

^aOptical absorption threshold.

^bExperimental method not detailed.

OLCAO⁹⁷⁷ calculation methods are not best suited for achieving an accurate value of bandgap energy. LDA calculations produced values as low as 0.53,⁹⁷⁵ 0.54,⁹⁸⁸ and 0.70 eV.⁹³¹ Even with the addition of the Hubbard parameter U to the LDA calculations, a maximum value of only 1.88 eV was reported.⁹³¹ PBE calculations appeared to improve from 0.53 to 2.77 eV with the addition of PBE0.⁹⁷⁵ A value of 9.70 eV was reported as a clear outlier obtained using the periodic Hartree-Fock method. Similar to other reported values found using Hartree-Fock, the bandgap is drastically overestimated.⁹⁷⁶ Calculation methods such as HSE and GW variations provided more accurate bandgap energies when compared to reported experimental results. HSE calculations yielded bandgap energies of 2.02,⁹³¹ 2.12 eV,⁹⁸⁹ and an optical absorption threshold of 2.50 eV.⁹³¹

The experimentally determined bandgap of Cu₂O proved to be a difficult property to observe and report on, much more complex than most of the other oxides throughout this review. There are few experimentally determined bandgap energies present that are in much better agreement than the calculated values with far less spread. Starting with bulk crystal samples, a value of 2.17 eV is commonly seen throughout the literature and widely accepted as the direct bandgap energy of Cu₂O. This direct bandgap has been commonly cited over the past few decades but appears to neglect the details the experimental method used to determine it. The bandgap energy of 2.17 eV was tracked back to a 1966 report on the energy bands of Cu₂O by Dahl *et al.* (Ref. 978). In the study Dahl *et al.* write that Cu₂O is a semiconductor containing a bandgap of 2.17 eV. There is no mention of an experimental method or means of determining this value. Dahl *et al.* list four subsequent references following a statement about band structure proposals being put forth. We were unable to obtain or locate three of the four references and the last of the four references provided no explicit explanation detailing a bandgap of 2.17 eV. We are making the assumption this bandgap energy of 2.17 eV is for bulk samples of Cu₂O determined experimentally. Another similar value of 2.20 eV appears to have the same short comings regarding its origin. Lany (Ref. 992) included an

experimentally determined bandgap energy of 2.20 eV in a review of band structure calculations of 3d transition metal oxides. Again, no explanation is provided for the value of 2.20 eV. Lany explains that experimental data, especially bandgap data, for the transition metal oxides is not as accurately reported or comprehensive as “main-group compounds” such as GaAs, Si, and ZnO.⁹⁹² This could be an explanation for the lack of values as well as the ambiguity of the origin sources. Lany also states that the experimental data used in their 3d transition metal review came from two sources, Refs. 930 and 993. The first source did not cite a value of 2.20 eV for a bandgap energy but did list seven transition energies with the lowest being 2.59 eV. We could not locate the second source. We are again assuming this value is representative of bulk samples of Cu₂O.

Experimentally determined bandgap energies for thin films of Cu₂O range from 2.38 to 2.51 eV determined using the absorption coefficients and optical transmittance spectra.⁹⁹⁴ Wang *et al.* (Ref. 994) used reactive magnetron sputtering to fabricate the thin film samples. As deposited samples exhibited a bandgap energy of 2.38 eV. The bandgap energy increased to 2.51 eV as the air annealing temperature was increased to 280 °C. Other transitions that occur close to the fundamental bandgap are detailed by Daunois *et al.* (Ref. 995). These inter-band transitions occur between Γ_8^+ to Γ_6^+ , Γ_7^+ to Γ_8^- , and Γ_8^+ to Γ_8^- . They correspond to the limits of the green, blue, and indigo exciton series, respectively. Cited values for the bandgap of Cu₂O are listed in Table XLV.

For Cu₄O₃, the calculated values of the indirect bandgap range from 0.78 to 2.54 eV determined using LDA+U,^{931,953} GW calculations,⁹⁸⁶ and HSE.⁹³¹ Similar to the calculated values for CuO and Cu₂O, the HSE theoretical method yields one of the highest value at 2.54 eV. This value is over 1.0 eV higher than the experimental value of 1.34 eV.⁹⁶⁷ Direct bandgap values are also calculated for Cu₄O₃ and range from 1.19 to 2.71 eV.^{931,953} Experimental data show the direct bandgap to be 2.47 eV,⁹⁶⁷ much larger than the experimental indirect gap. Cited values for the indirect and direct bandgap energies of Cu₄O₃ are listed in Table XLVI.

D. Material properties

Basic material properties reviewed throughout the literature include the material density, bulk modulus, and the melting point.

TABLE XLVI. Bandgap energy values of Cu₄O₃ determined from experiment and theory.

E _g (eV)	Method	Bulk/film	Reference
Calc.			
0.78	LDA+U	...	953
0.84	GW	...	986
1.27	LDA+U	...	931
1.47 ^a	LDA+U	...	931
2.54	HSE	...	931
2.71 ^a	HSE	...	931
Experiment			
1.34	UV–Vis transmission	Film	967
2.47 ^a	UV–Vis transmission	Film	967

^aDirect gap.

CuO is the densest of the three copper oxides with a value of 6.545 g/cm³.^{930,945} For comparison, the density of Cu₂O and Cu₄O₃ was reported to be 5.749 to 6.140 g/cm³, and 6.04 g/cm³, respectively.^{930,951,952} The bulk modulus of CuO was reported by Zivkovic *et al.* (Ref. 996) using various calculated methods. The Voigt–Reuss–Hill approximation utilized DFT and DFT+U to determine values of 144.25 and 99.16 GPa, respectively. The third method used Birch–Murnaghan equations of state to arrive at 95.58 GPa.⁹⁹⁶ For comparison, the bulk modulus of Cu₂O was determined experimentally to range from 112 to 114 GPa.^{956,997} Theoretical methods using pseudopotentials found Cu₂O bulk modulus values ranging from 106 to 141 GPa.⁹⁹⁸ The melting point of CuO was reported to be 1201 °C, one of the lowest values cited for all of the reviewed oxides.^{930,945} Similarly, Cu₂O had a melting point of 1235 °C.⁹³⁰ The basic material properties of CuO are compared in Sec. XI.

1. Thermal properties

The thermal properties reviewed for CuO included the Debye temperature, CTE, specific heat, and thermal conductivity. The Debye temperature has received much attention across the literature. At 0 K, a value of 390 ± 10 K was estimated by Junod *et al.* (Ref. 939). A room temperature value was not specifically stated but plots of the calculated Debye temperature vs temperature have been presented by both Junod *et al.* (Ref. 939) and Loram *et al.* (Ref. 999). At room temperature the values appear to range anywhere from 560 to 670 K (Refs. 939 and 999) depending on how the Debye temperature was calculated. The CTE was reported for CuO across a temperature range of 50 to 200 K. The resultant CTE was found to be $1.6 \times 10^{-6}/\text{K}$.¹⁰⁰⁰ For comparison, Cu₂O showed a CTE of $2.3 \times 10^{-7}/\text{K}$ at 283 K.⁹³⁰

The specific heat (or specific heat capacity) is a widely reported value, especially since it is an instrumental parameter for certain Debye temperature calculations from the sources cited above. At room temperature, a specific heat capacity of 41.88 J/(mol K) was reported by Junod *et al.* (Ref. 939). Using the known CuO molar mass of 79.545 g/mol, the specific heat was determined to be 0.526 J/(g K). Junod *et al.* also reported values for temperatures ranging from 100 K to 200 K. The specific heat increased from 0.207 to 0.433 J/(g K) across that temperature range. Hu *et al.* (Ref. 1001) reported a heat capacity of 39.11 J/mol at 250 K. This converts to 0.4916 J/(g K) and fits well with the other values for temperatures above and below 250 K. The thermal conductivity of CuO appears frequently in literature for topics involving nanofluids.^{1002–1005} The topic of nanofluids/nanoparticles is well beyond the scope of this Review, but these references are included as they were the main source for CuO thermal conductivity values. Hwang *et al.* (Ref. 1005) reports that CuO nanoparticles have a thermal conductivity of 76.5 W/(m K). Liu *et al.* (Ref. 1006) states that the typical thermal conductivity of CuO is 33 W/(m K) with very little details provided beyond the value. It is not specified if that value was from nanoparticles or bulk. The value of 33 W/(m K) is half of the thermal conductivity reported by Hwang *et al.* Values for the thermal properties of CuO are compared in Sec. XI.

2. Phonon properties

As discussed in Sec. IX A, CuO has monoclinic structure in the space group C2/c (#15). Derived from the two CuO units within the cell, there are four atoms in the primitive cell. This results in three

acoustic and nine optical phonon branches. The irreducible representations are reported to be^{1007,1008}

$$\Gamma = A_g + 4A_u + 2B_g + 5B_u.$$

A_g and $2B_g$ modes are Raman active for a total of three Raman modes. There are six IR active modes consisting of three A_u modes and three B_u modes. The remaining A_u and two B_u modes are the acoustic modes. The three Raman modes involve solely oxygen atom movement. A_g moves along the b -direction while the B_g modes move perpendicular to the b -axis. IR modes have movement of both the copper and oxygen atoms. A_u modes have an induced dipole moment along the direction of the b -axis while B_u modes are perpendicular.¹⁰⁰⁹ Similar to $\beta\text{-Ga}_2\text{O}_3$, B_u modes are polarized at specific angles within the monoclinic plane. This was shown experimentally for TO modes by Kuz'menko *et al.* (Ref. 1010). The IR LO mode orientations have yet to be shown experimentally. The reported phonon frequencies for both the Raman and IR modes are listed in Table XLVII.

The phonon properties for Cu_2O are also detailed in the literature. Within the Cu_2O structure, there are six atoms in the primitive unit cell. 15 optical and three acoustic modes arise from that structure.⁹³⁰ The irreducible representations are shown to be^{930,1014}

$$\Gamma = A_{2u} + E_u + T_{2u} + 3T_{1u}.$$

Debbichi *et al.* (Ref. 1009) report on the vibrational properties of Cu_4O_3 . Due to the crystal structure there are predicted to be 42 modes. The irreducible representations for Cu_4O_3 are¹⁰⁰⁹

$$\Gamma = 3E_g + A_{1g} + 2B_{1g} + 9E_u + 6A_{2u} + 5B_{2u} + 2B_{1u} + 2A_{1u}.$$

Calculated zone center Raman frequencies show six modes consisting of A_{1g} , $3E_g$, and $2B_{1g}$. Experimentally only four of these modes

TABLE XLVII. Phonon mode frequencies (cm^{-1}) of CuO determined from theory (ω_c) and experiment (ω_e). No experimental LO frequencies and modes have been reported yet.

Modes	ω_c^{a}	ω_e^{b}	ω_e^{a}	ω_e^{c}	ω_e^{b}
Raman					
A_g	319	308	296	303	301
B_g	382	355	346	350	348
B_g	639	633	631	636	633
Modes	ω_c^{a}	ω_e^{d}	$\omega_e^{\text{e TO}}$	$\omega_c^{\text{e LO}}$	θ^{e}
IR					
B_u	141	142	144.9	149.6	53.0°
A_u	164	160	160.5	168.3	
A_u	327	326	321.5	324.2	
A_u	457	423	408.7	535.6	
B_u	503	480	469.6	620.7	30.5°
B_u	568	520	522.8	585.5	-57.6°

^aReference 1009.

^bReference 1011.

^cReference 1012.

^dTaken from neutron data (Ref. 1013).

^eReference 1010.

were reported. Calculated zone center IR modes consist of $8E_u$ and $5E_u$ modes. Experimentally only six of these modes were reported. The specific calculated and experimental phonon frequencies of Cu_4O_3 are detailed by Debbichi *et al.* (Ref. 1009) as well as similarities between the CuO and Cu_4O_3 vibrational properties.

3. Electrical properties

The electrical properties of CuO reviewed below include the electron affinity, electrical breakdown field, static and high frequency dielectric constants, effective mass, and carrier mobility. The electron affinity was reported to be 1.77 eV by Polak *et al.* (Ref. 1015). Analysis of CuO photoelectron spectrum was used to determine the electron affinity. The electrical field breakdown for CuO is not readily available in literature. Using Higashikawa's (Ref. 147) bandgap vs breakdown field strength plot, the breakdown field for CuO can be estimated. Using the experimentally determined bandgap values that range from around 1.3 to 2 eV, the breakdown field strength is predicted to be in the range of 0.2–0.5 MV/cm.

The static dielectric constants for CuO have been reported by both Akaltun *et al.* (Ref. 970) and Ching *et al.* (Ref. 977). Akaltun *et al.* showed that the static dielectric constant decreased with decreasing film thickness. Values ranged from 13.00 to 12.26 as film thickness decreased from 310 to 125 nm. The same thickness dependence on the bandgap was detailed in Sec. IX C 1.⁹⁷⁰ Ching *et al.* reported a calculated value of 12.3. Of note, the calculated static dielectric constant of Cu_2O was reported to be 3.7,⁹⁷⁷ half of the experimental value reported to be 7.5.¹⁰¹⁶ Akaltun *et al.* (Ref. 970) also calculated the optical high frequency dielectric constant of CuO using a relation to the refractive index. The optical high frequency dielectric constant decreased from 7.84 to 7.29 as film thickness and refractive index decreased.⁹⁷⁰ Knight *et al.* (Ref. 1017) measured the low-frequency response (approximately 350 to 1300 GHz) on single crystal CuO and noted no dispersion in the dielectric constants. The optical response was approximated by orthorhombic properties because of no detectable monoclinic shear element. Knight *et al.* report $\epsilon_{xx} = 10.59 \pm 0.09$ approximately parallel to \vec{a} , hence, equal to $\epsilon_{DC,a}$, $\epsilon_{yy} = 9.64 \pm 0.08$ ($\epsilon_{DC,c}$), and $\epsilon_{zz} = 11.94$ ($\epsilon_{DC,b}$), with a small imaginary parts reported due to scattering.

CuO has an electron effective mass that is shown to be anisotropic. This anisotropic property stems from the conduction band minimum not residing at the Γ point and means the effective masses must be examined from the longitudinal and transverse directions. The transverse direction is perpendicular to the $D\Gamma$ direction while the longitudinal direction is along $D\Gamma$.⁹³⁰ The transverse effective mass is 3.52 m_e and the longitudinal effective mass is 0.78 m_e . The hole effective mass was averaged and found to be 1.87 m_h .⁹⁸⁵ Findings from Ching *et al.* (Ref. 977) also show there is anisotropy among the electron effective mass and hole effective mass along different directions stemming from the monoclinic crystal structure. The electron effective mass in the conduction band is found to be the smallest along the z -direction. For the hole effective mass in the valence band, the y -direction is drastically larger than the other directions. The uppermost valence band has hole effective masses of $+1.75 m_h$, $+3.01 m_h$, $+0.60 m_h$, and $+0.54 m_h$ along the directions X, Y, B, and A, respectively.⁹⁷⁷ Going from the uppermost valence band to the band residing just below, the hole effective masses change to $+0.72 m_h$, $+3.72 m_h$,

$+0.58 m_h$, and $+1.33 m_h$, respectively. The hole effective mass is concluded to be larger than the electron effective mass.^{977,985}

Cu_2O differs from CuO in that the electron and light hole effective mass was found to be isotropic across three directions; Γ -X, Γ -M, and Γ -R.^{930,1018,1019} This can be expected just on the basis that CuO is monoclinic while Cu_2O is cubic. The light hole effective mass is found to be around half of the electron effective mass due to the split of the valence band from coupling of the $\Gamma 7^+$ (light hole) and $\Gamma 8^+$ (heavy hole) states.⁹³⁰ The heavy hole effective mass does exhibit anisotropy across the directions. $\Gamma - X$ has a heavy hole of $2.83 m_h$, $\Gamma - M$ has a mass of $0.91 m_h$, and $\Gamma - R$ has a mass of $0.72 m_h$.^{930,1018} Ching *et al.* (Ref. 977) concluded an isotropic value $0.66 m_e$ for the electron effective mass. The hole effective mass is anisotropic at the Γ point of the valence band and the states are triply degenerate. The directions for the hole effective mass anisotropy in Cu_2O are [100, 110], and [111]. The uppermost valence band has a hole effective mass of $+3.16 m_h$, $+3.14 m_h$, and $+2.74 m_h$ along [100, 110], and [111], respectively. The hole effective mass changes drastically looking just below the uppermost valence band. In the [100] direction, the lowest valence band that Ching studied had a hole effective mass of $+0.34 m_h$ while the uppermost valence band in the same direction had an effective hole mass of $+3.16 m_h$.⁹⁷⁷

The mobility for all three copper oxides has been reported in the literature. Koffyberg *et al.* (Ref. 937) found a hole Hall mobility in CuO of $0.1 \text{ cm}^2/(\text{V s})$ and hypothesized that the low mobility value could provide evidence of a hopping method of conduction. The hole-effective mass, mentioned above, also leads to evidence that there is a large phonon coupling and/or a narrowing valence band that explains the low mobility. CuO shares some properties with another p-type oxide, NiO . The heavy holes with very low mobility move within the narrow valence 3d band for both materials.⁹³⁷ For Cu_2O , Lee *et al.* (Ref. 1020) report mobilities that range from 10 to $100 \text{ cm}^2/(\text{V s})$. Lee found that by changing the growth temperature of sputtered polycrystalline samples, the Hall mobility changed. A growth temperature of 1070 K yielded a hole Hall mobility value of $62 \text{ cm}^2/(\text{V s})$ measured at room temperature (293 K) and $43 \text{ cm}^2/(\text{V s})$ measured at 333 K.¹⁰²⁰ Lee found that the polycrystalline samples had Hall mobilities that were comparable to monocrystalline samples of Cu_2O . It was concluded that the mobility was hindered by different factors than monocrystalline samples at temperatures lower than 250 K. Polycrystalline samples had larger carrier concentrations and more native defects and ionized centers.¹⁰²⁰ Li *et al.* (Ref. 1021) produced Cu_2O thin films that achieved a hole mobility upwards of $256 \text{ cm}^2/(\text{V s})$, stated to be the highest mobility achieved at the time. Murali *et al.* (Ref. 1022) reports a mobility value for Cu_4O_3 , the least studied of the three copper oxide phases. Van der Pauw measurements were completed at room temperature on Cu_4O_3 thin films with a hole Hall mobility of $0.04 \text{ cm}^2/(\text{V s})$.

E. Doping and defects

Possible dopants for CuO have been explored using DFT analysis.¹⁰²⁴ Group IA acceptor dopants include lithium and sodium. Extrinsic doping with lithium and sodium could increase the p-type conduction. Group IIIA donor dopants include aluminum, gallium, and indium. Group IVB donor dopants include titanium, hafnium, and zirconium. The maximum solubility of IVB dopants within CuO can be achieved under oxygen-poor conditions. Titanium has a lower formation energy within CuO than zirconium and hafnium. Three

charge states of 0, +1, and +2 exist for group IVB dopants in the bandgap of CuO . N-type CuO could be achieved with zirconium and hafnium since they are predicted to have shallow donor levels. The formation energy is high for IVB dopants which could lead to a reduction of the carrier concentrations, similar to IIIA donors. Further details on the potential dopants of CuO are reported by Peng *et al.* (Ref. 1024).

The formation of defects within CuO has been studied and reported by Zivkovic *et al.* (Ref. 1025). The specific type of intrinsic defects that arise are influenced by the growth conditions. Under copper-rich growth conditions, oxygen vacancies (V_O) and copper interstitials (Cu_i) are the most dominant neutral defects. When oxygen-rich growth conditions are met, p-type defects such as V_{Cu} , O_{Cu} (antisites), and O_i are dominant compared to the n-type defects. There exists a very large energy difference between the two growth conditions, allowing for the growth of undoped CuO that contains a particular conductivity. For copper-rich growth, the formation energy for the V_O and Cu_i is around 1.0 eV. V_O exhibits deep donor behavior that possibly contributes to the low mobility values seen in n-type CuO . Cu_i are considered a neutral defect that should not provide any effective charge compensation. V_{Cu} are also shown to exist under copper-rich conditions and is considered to be the lowest energy acceptor defect. The V_{Cu} reside high in energy and are unable to compensate for the other defects such as the donor impurities. Acceptors are dominant under oxygen-rich conditions. Oxygen interstitials are the acceptors with the lowest formation energy. V_{Cu} are considered to be shallow acceptors while O_{Cu} produce two deep acceptor levels. These defects are not compensated across the bandgap and thus lead to the p-type nature of CuO .¹⁰²⁵ This study supports the basis of the n-type conductivity due to oxygen vacancies and copper interstitial atoms, and the p-type conductivity due to copper vacancies that has been presented across literature.^{1026–1028}

F. Summary of CuO property values

Table XLVIII highlights a summary of the properties reviewed for CuO as well the crystal structure and lattice parameters for Cu_2O and Cu_4O_3 . Values for each of the properties are presented along with references and notation of whether they are experimental or calculated findings. Where relevant anisotropy is denoted.

X. SCANDIUM OXIDE

Sc_2O_3 (scandia or scandium sesquioxide) is not as widely studied of a material as the other oxides highlighted in this review. Being a rare-earth oxide, some of the known properties such as crystal structure, bandgap, melting point, and refractive index have been shown within the literature to have merit in device and research applications. For example, the high refractive index makes Sc_2O_3 useful for anti-reflective coatings,¹⁰²⁹ optical devices,¹⁰³⁰ superluminescent LED coatings,¹⁰³¹ and gate dielectrics in multiple types of MOSFETs.^{1032–1034} Thin films of Sc_2O_3 are grown using methods such as ion beam sputtering,¹⁰³⁵ molecular beam epitaxy (MBE),¹⁰³⁶ CVD,¹⁰³⁷ ALD,¹⁰³⁸ and electron beam evaporation.^{1029,1030} Sc_2O_3 has similar property behaviors with other oxides, such as tantalum oxide,¹⁰³⁹ zirconium oxide,¹⁰⁴⁰ and hafnium oxide¹⁰⁴¹ which have been studied extensively as possible MOSFET gate dielectric materials. While Sc_2O_3 has a larger bandgap than HfO_2 , they share a key property where the refractive index increases when the material is metal rich.^{1042,1043}

TABLE XLVIII. Summary of theoretical and experimental properties of copper oxide. Common names of CuO are copper(II) oxide, cupric oxide, and tenorite. Common names of Cu₂O are copper(I) oxide, cuprous oxide, and cuprite. Common name of Cu₄O₃ is paramelaconite. All values listed for CuO unless otherwise noted.

CuO stable phase	Monoclinic	C2/c (#15)
	$a = 4.5130\text{--}4.6837$	Refs. 930, 931, 945, and 947
	$b = 3.3544\text{--}3.6121$	
	$c = 5.0354\text{--}5.1408$	
	$\beta = 97.06\text{--}99.54^\circ$	
Cu ₂ O stable phase	Cubic	<i>Pn</i> $\bar{3}$ <i>m</i> (#224)
	$a = 4.1656\text{--}4.27$	Refs. 930, 931, 948, and 956
Cu ₄ O ₃ stable phase	Tetragonal	I4 ₁ /amd (#141)
	$a = 5.6544\text{--}5.8392$	Refs. 931, 951, 952, and 957
	$c = 9.7728\text{--}9.8966$	
Density (g/cm ³)	6.545	Expt. 930, 945
Bulk modulus (GPa)	99.16–114.25	Calc. 996
T _m (°C)	1201	Expt. 930, 945
	1446	Ref. 118
Debye temp. (K)	640	Calc. 939
	575	Calc. 939
Specific heat (J/(gK))	0.526 ^a	Expt. 939
Thermal cond. (W/(mK))	33	Ref. 1006
	76.5	Expt. 1005
Thermal diff. (mm ² /s)	Not reported	
CTE ($\times 10^{-6}$ /K)	1.6	Expt. 1000
Electron affinity (eV)	1.77	Expt. 1015
Breakdown field (MV/cm)	0.2–0.5	Pred. 147
m_e^*	0.78 ^b	Calc. 985
	3.52 ^c	Calc. 985
	0.16–0.46	Calc. 977
m_h^*	1.87	Calc. 985
	0.54–3.01	Calc. 977
μ_h [cm ² /(V s)]	0.1	Expt. 891
Gap type	Indirect	Ref. 937
E _g (eV)	0.9–2.74	Bulk calc. 886, 887, 931, 953, 977, 980, 981, 985–987, 1023
	1.35–1.7	Bulk expt. 937, 987
	1.4–2.03	Film expt. 968, 970, 984
ϵ_0	12.26–13.0	Calc. 970, 977
ϵ_{DC}	10.59 ϵ_{xx}	Expt. 1017
	9.64 ϵ_{yy}	Expt. 1017
	11.94 ϵ_{zz}	Expt. 1017
ϵ_∞	7.29–7.84	Calc. 970
Phonon modes		
IR active	3A _u , 3B _u	Ref. 1009
Raman active	A _g , 2B _g	Ref. 1009

^aCalculated from molar heat capacity.

^bLongitudinal.

^cTransverse.

A. Crystal structure

Scandium oxide has a cubic crystal structure in the bixbyite phase.^{1044,1045} Other elements that form sesquioxides similar to Sc_2O_3 are iron, manganese, indium, and yttrium. In these sesquioxides there is often polymorphism that is dependent upon temperature and cation radius. The known sesquioxide polymorph structures found across the listed elements are a monoclinic B-type, a cubic phase C-type, and a hexagonal A-type. At higher temperatures, hexagonal H-type and cubic X-type have been seen.¹⁰⁴⁴ For Sc_2O_3 , the agreement within the literature is that the stable phase is the cubic structure^{1030,1044–1046} with scarce mention of the monoclinic transition occurring after calcination.¹⁰⁴⁷ Lattice constants for both the cubic and monoclinic Sc_2O_3 structures are listed in Table XLIX. Bixbyite is the mineral name for Fe_2O_3 and Mn_2O_3 . In a bixbyite structure, an almost face centered cubic lattice is formed by the cations. Within the cation face centered structure, there are eight tetrahedral sites with six being occupied by oxygen. The structure is classified by two sites, C and D, formed by the nonequivalent cation sites. Both the C and D sites have O(6) coordination. The C site is a distorted cube of C2 symmetry with two free corners on the face diagonal. The D site has axial symmetry with a single cation being surrounded by six oxygen atoms. There are two free corners on one diagonal.¹⁰⁴⁴ Richard *et al.* (Ref. 1044) provides specifics for the internal parameters u, x, y, z in relation to the scandium atom location. Ubaldini *et al.* (Ref. 1048) states that Sc_2O_3 is a body centered cubic structure consistent with the bixbyite structure. Figure 35 shows the crystal structure of Sc_2O_3 . The body centered cubic structure plays an important role in the phonon properties of Sc_2O_3 and is detailed in Subsection XD2. Unless stated otherwise, all discussion throughout this section refers to the stable, single crystalline, cubic structure.

Calculated values for the cubic lattice constant range from 9.7 to 9.9 Å (Ref. 1044) while experimental lattice constants found from XRD measurements show a lattice constant of around 9.84 Å.^{1030,1045} Along with the bixbyite structure, Sc_2O_3 is said to have C-type structure belonging to space group $Ia\bar{3}$ (#206).^{1044,1049} Belosludtsev *et al.* (Ref. 1043) grew Sc_2O_3 thin films and concluded that the lattice

parameter increased with the amount of oxygen that was present in the lattice. Literature does mention other crystal structures for Sc_2O_3 . Horovitz (Ref. 1047) reports that the structure of Sc_2O_3 shifts to monoclinic once calcination of the material occurs at 1273 K and 13 GPa.^{1047,1050} Reid *et al.* (Ref. 1051) reports more on the transition from cubic C-type to the monoclinic B-type and how it relates to other rare-earth oxides.¹⁰⁵¹ Their findings show that at 1000 °C and a pressure of 13 GPa, the cubic Sc_2O_3 transitions to a monoclinic structure with lattice constants $a = 13.173$ Å, $b = 3.194$ Å, $c = 7.976$ Å and $\beta = 100.40^\circ$. The reported density of 3.838 g/cm³ for the cubic structure was found to increase to 4.16 g/cm³ for the monoclinic structure. Pressure levels ranging from 3 GPa to 8 GPa did not result in a change in the structure but pressure levels of 11 GPa resulted in a very poor B-type crystallization. The monoclinic structure sees a coordination number increase as well. Two-thirds of the Sc atoms increase from six-fold coordination to sevenfold coordination.¹⁰⁵¹ Overall, the general consensus regarding the crystal structure of Sc_2O_3 is that the oxide contains cubic structure with lattice constant a being reported in relatively good agreement across literature. There is mention of a transition to a monoclinic phase that Sc_2O_3 undergoes, but this was only found in the literature among a few sources. It was not stated if this monoclinic phase was stable or metastable; however, the density change and pressures required to form it suggest it is metastable at ambient conditions.

B. Growth

While research into certain material parameters of Sc_2O_3 are lacking in the literature, methods of Sc_2O_3 growth and fabrication are not. Almost every source cited throughout this section utilized a different method of growth and fabrication. With bulk single crystal growth, only one method was found across literature. Masui *et al.* (Ref. 1049) grew single crystals using an electrochemical method. It was reported that a low temperature of 1223 K was achieved with a simple electrolysis method. Conventional methods would require temperatures above 2800 K to achieve the same results. The crystal size was also shown to be adjustable by altering the electrolysis period.¹⁰⁴⁹

Thin films of Sc_2O_3 have been grown by numerous methods. Such methods include MOCVD,¹⁰³⁷ ion beam sputtering,¹⁰³⁵ solution process growth,¹⁰⁵⁴ MBE,¹⁰³⁴ ALD,¹⁰⁵⁵ and electron beam evaporation.^{1030,1056} Reactive magnetron sputtering and reactive evaporation have also been utilized.^{1029,1043} Finally, Liu *et al.* (Ref. 1033) published a growth process involving a novel water-inducement method. This method was utilized in producing IZO/ Sc_2O_3 thin film transistors (TFTs).¹⁰³³

The crystalline form was also shown to change with film deposition temperature. Films deposited by electron beam evaporation with substrate temperatures above 150 °C were shown to be polycrystalline with higher refractive indexes and larger film densities. Lower substrate temperature (50 °C) produced amorphous films.¹⁰³⁰ The deposition and growth method used to produce Sc_2O_3 samples and films alters the electrical and crystallographic properties. Using pulsed DC magnetron sputtering,¹⁰⁴³ films of Sc_2O_3 were prepared. They possessed a similar or higher refractive index and bandgap compared to films prepared via ion beam sputtering¹⁰³⁵ and electron beam evaporation. The DC magnetron sputtered samples had a refractive index of 2.07 to 2.08 at 355 nm, an indirect bandgap of 5.7 eV, and a direct bandgap of 6.1 eV.¹⁰⁴³ The ion beam sputtered samples had a

TABLE XLIX. Sc_2O_3 crystal structure with associated space group and lattice constants determined from experiment and theory.

Structure	Space group	Lattice (Å)
Cubic	$Ia\bar{3}$ (No. 206) ¹⁰⁵²	$a = 9.8459$ ^{1045,a} $a = 9.810$ ^{1046,a} $a = 9.845$ ^{1030,a} $a = 9.708$ ^{1044,b} $a = 9.798$ ^b $a = 9.90$ ^b $a = 9.848$ ^{1053,a}
Monoclinic	$C2/m$ (No. 12) (assumed) ¹⁰⁵¹	$a = 13.173$ ^{1051,a} $b = 3.194$ $c = 7.976$ $\beta = 100.40^\circ$

^aExperimental.

^bTheoretical.

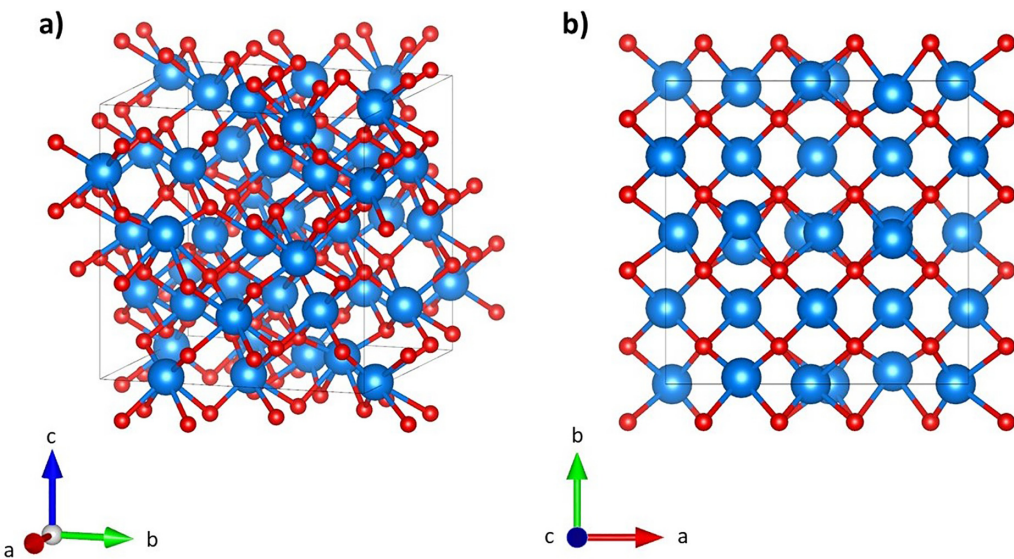


FIG. 35. The crystal structure of Sc_2O_3 belonging to space group $I\bar{a}3$ with (a) the c -axis shown pointing upward and (b) shown along the c -axis. Sc_2O_3 was symmetric around the a , b , and c axes (blue = Sc, red = O).

refractive index of 2.07 and an indirect bandgap of 5.8 eV.¹⁰³⁵ Electron beam evaporation samples had a refractive index of 1.82 to 1.92, an indirect gap of 5.84 eV, and a direct bandgap of 6.04 eV.^{1030,1056} The varying results across multiple deposition methods highlight how the stoichiometry and deposition characteristics play a significant role in the parameters and properties of Sc_2O_3 films.¹⁰⁴³

C. Electronic band structure and bandgap

The bandgap of single crystal scandium oxide has been studied to show similarities with other 3d transition metal oxides and their optical properties.^{1052,1057} Dating back to the 1960s, it was concluded that a bandgap value of 5.4 eV fit the trend of the neighboring transition metal oxides which include TiO_2 (3.23, 3.26, and 3.00 eV),¹⁰⁵⁸ V_2O_5 (2.1 eV) and CrO_3 (1.4 eV).¹⁰⁵⁷ In 3d transition metals, there is a likelihood of 3d wave functions overlapping to form a band as the ionic radius is decreased with increasing atomic number.¹⁰⁵² With Sc^{3+} being categorized as the first of this grouping and having a large atomic radius, the 3d wave function overlap and 3d bandwidth is expected to be larger than titanium and vanadium oxides. Companion *et al.* (Ref. 1057) predicted bandgap energy of 5.4 eV while two years later in 1966 Tippins (Ref. 1052) found values of 6.0 eV and 6.2 eV for room temperature and 80 K, respectively.

In the early 2000s, the bandgap of Sc_2O_3 was reported to be an indirect bandgap with a value around 5.7 to 6 eV.^{1030,1050,1056} Herrero *et al.* (Ref. 1032) state that Sc_2O_3 has a bandgap of 6.3 eV (no method given) and a dielectric constant of 14.¹⁰³² It was not specified if this was the static or high frequency dielectric constant. Similar to trends seen among previously reported oxides in this review, calculation methods such as DFT along with specific hybrid functionals can skew the bandgap energy. This applies to Sc_2O_3 as well with DFT calculations underestimating the bandgap, producing a direct bandgap of 4.0 eV located at the Γ point¹⁰⁴⁴ compared to the experimental value of 5.7 eV.^{1044,1047} The DFT functionals used by Richard *et al.*

(Ref. 1044) were LDA and GGA, which underestimated the bandgap. The calculated band structure from Richard can be seen in Fig. 36. From the DFT band structure calculations, the density of states (DOS) was produced. There are three valence bands that makeup the DOS. The total and partial DOS are presented in Fig. 37. At -26 eV in the DOS, there is a narrow band made up of $\text{Sc}(3p)$ states. At -26 eV there is a very faint contribution of the $\text{O}(2s)$ states, but the majority

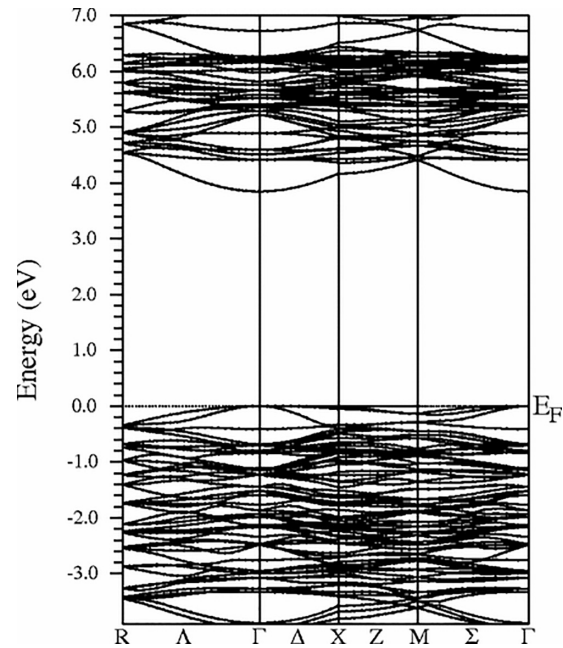


FIG. 36. Calculated band structure of Sc_2O_3 . Reproduced with permission from Richard *et al.*, Phys. Rev. B **82**, 035206 (2010). Copyright 2010 APS (Ref. 1044).

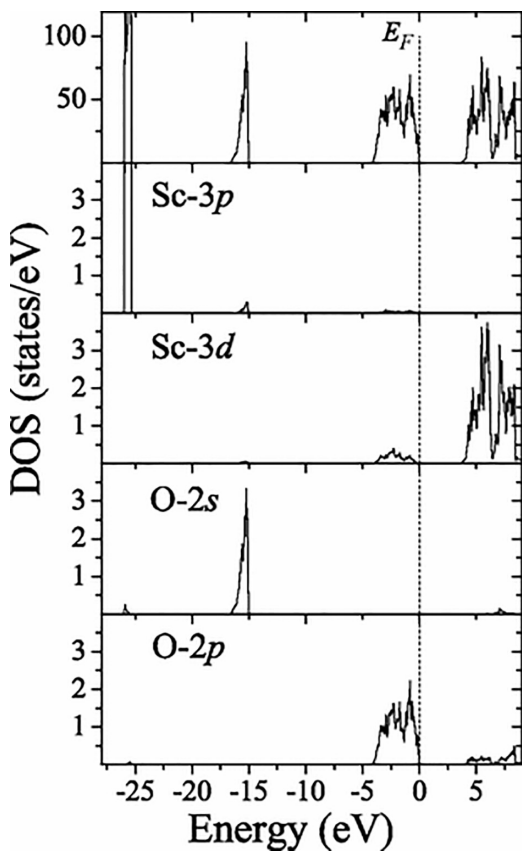


FIG. 37. Sc_2O_3 total and partial density of states (DOS). The vertical dashed line denotes the Fermi level at 0 eV. Reproduced with permission from Richard *et al.*, Phys. Rev. B **82**, 035206 (2010). Copyright 2010 APS (Ref. 1044).

of O(2s) states are located at -15 eV with a narrow band as well. The third band is located between -4.5 eV and the Fermi level of the DOS. It is mainly comprised of O(2p) states with a very small amount of Sc(3d) orbitals.¹⁰⁴⁴ The mixing of the states provides evidence of Sc_2O_3 having ionic characteristics between the Sc and O bonds as well as some covalent bonding.^{1044,1059,1060} Sc_2O_3 has an electron configuration of $\text{Sc}^{3+} 3\text{d}^0$. From this configuration, it can be concluded that if the absorption edge occurs due to the transition from the O(2p) band to the empty $\text{Sc}^{2+} 3\text{d}^1$, there would exist a conduction band of specific width that arises from 3d wave function overlap. The 3d band experiences a splitting into sub-bands from the crystal field as well. Due to the cubic bixbyite nature of Sc_2O_3 , the splitting sub-bands will vary among the two sites.¹⁰⁵²

1. Temperature dependence of bandgap energy

There is evidence in the literature of bandgap dependence on substrate temperature. Liu *et al.* (Ref. 1030) examined the bandgap and the absorption coefficient of Sc_2O_3 films deposited via electron beam evaporation with varying substrate temperatures. They found that the indirect energy gap ranged from 5.75 to 5.84 eV and the direct energy gap ranged from 6.02 to 6.05 eV. The bandgap was shown to decrease with increasing substrate temperature. An increase in

refractive index was also shown with increasing substrate temperature, highlighted in Fig. 38.¹⁰³⁰ Herve *et al.* (Ref. 1061) also showed that the refractive index increased with a decreasing bandgap.¹⁰⁶¹ The absorption edge was shown to redshift with temperature for both the direct and indirect bandgap. The absorption edge of the indirect bandgap redshifts from 212 to 215 nm as the substrate temperature increased from 50 to 350 °C. The direct bandgap absorption edge increased from 205 to 206 nm across the same substrate temperature range.¹⁰³⁰ Liu *et al.* highlight the theory of the optical bandgap decrease and states that it can be associated with volume change that arises from the temperature change and electron phonon interaction.^{1062,1063} The temperature coefficient for Sc_2O_3 was found to be 3×10^{-4} eV/K.¹⁰³⁰ This temperature coefficient as well as the theory used to arrive at this value, aligned well with other common semiconductors. Liu states that $E_0(T)$ is equal $5.9369 - 3 \times 10^{-4}T(\text{K})$, and that there is evidence of a linear bandgap change with temperature for higher temperatures. A multi-slope phenomenon was observed in the direct absorption spectra and was concluded to arise from the indirect transitions.¹⁰³⁰ Tippins (Ref. 1052) also reported a bandgap temperature coefficient, for single crystal Sc_2O_3 . The temperature coefficient for the bandgap was found to be 9.6×10^{-4} eV/K, which was a much larger coefficient than the one reported previously for thin films. The question of the overall crystal quality could be a possible reason for the difference.

D. Material properties

Sc_2O_3 has the fewest reported material properties throughout literature. The basic material properties highlighted below include the material density, melting point, and Young's modulus. The density of cubic Sc_2O_3 ranges from 3.791060 to 4.1 g/cm³.^{1038,1043} Experimentally, the density of thin film samples was slightly higher than bulk, 3.9 and 4.1 g/cm³, respectively.¹⁰³⁸ In looking at the difference between the density of the cubic and monoclinic density, a reported density of 3.838 g/cm³ for the cubic structure was found to increase to 4.16 g/cm³ for the monoclinic structure.¹⁰⁵¹ The melting point was reported to range from 2753 to 2823 K, the highest melting

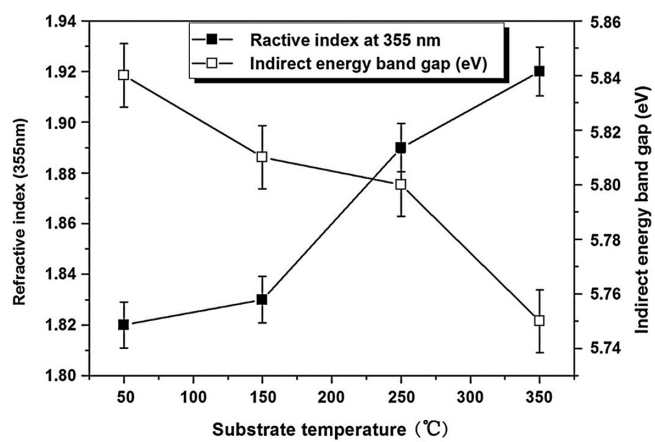


FIG. 38. The substrate temperature dependence of the indirect bandgap and the refractive index of Sc_2O_3 . (Note typo in legend.) Reproduced with permission from Liu *et al.*, Thin Solid Films **518**, 2920–2923 (2010). Copyright 2010 Elsevier (Ref. 1030).

point of the reviewed oxides.^{1049,1050,1065} The bulk modulus was not found in the literature, but Young's modulus for Sc_2O_3 was reported by Gogotsi (Ref. 1064) who calculated values of 218 and 251 GPa. Specifics were not given for the difference in values. Outside the scope of this review, Gogotsi also reported other properties pertaining to thermal stress behavior including, the brittleness measure, modulus of rupture, bending strength, static modulus of elasticity, and ultimate strain for Sc_2O_3 ceramics.¹⁰⁶⁴ In good agreement, Dole *et al.* (Ref. 1066) found Young's modulus to range from 214.3 to 227.6 GPa experimentally. One of the only values for the bulk modulus of Sc_2O_3 found in the literature was reported by the Materials Project in conjunction with the Lawrence Berkeley National Lab, a value of 168 GPa.¹⁰⁶⁷ Poisson's ratio was also reported alongside the bulk modulus to be 0.30. Assuming the Young's modulus from Dole *et al.* (Ref. 1066) and the Poisson ratio above, the expected bulk modulus would be from 178.6 to 189.7 GPa in relatively good agreement with the Materials Project. The basic material properties for Sc_2O_3 are compared in Sec. XI.

1. Thermal properties

Throughout literature discussion of the thermal properties of Sc_2O_3 was scarce and seldom reported. The thermal properties included in this review such as the thermal conductivity, Debye temperature, thermal diffusivity, CTE were not readily found highlighting the need for additional basic research. A specific heat value of 94.2 J/(mol K) was reported.¹¹⁸ Using the known Sc_2O_3 molar mass of 137.91 g/mol, the specific heat can be converted to 0.683 J/(g K).

2. Phonon properties

The IR and Raman active modes for Sc_2O_3 have been calculated by Ubaldini *et al.* (Ref. 1048). Due to the body-centered cubic structure, the primitive cell structure appears twice within the unit cell. This allows for the need of eight theoretical unit formulas to determine the vibration modes. The irreducible representations for both the optical and acoustical phonon modes are reported to be

$$\Gamma_{op} = 4A_g + 4E_g + 14F_g + 5A_{2u} + 5E_u + 16F_u,$$

$$\Gamma_{ac} = F_u.$$

There are predicted to be 22 Raman lines consisting of $4A_g$, $4E_g$ and $14F_g$; 16 infrared modes consisting of $16F_u$ and 10 silent modes consisting of $5A_{2u}$ and $5E_u$.¹⁰⁴⁸ Sc_2O_3 has similar structure to Y_2O_3 , both are considered C-type sesquioxides. Repelin *et al.* (Ref. 1068) highlights the vibrational spectroscopy for Y_2O_3 , which was taken into account by Ubaldini in producing the Sc_2O_3 vibrational mode calculations. The individual phonon mode frequencies are not detailed for Sc_2O_3 , but the most intense Raman peak was discussed. It was shown to be located around 420 cm^{-1} and was a combination of the A_g and F_g mode.¹⁰⁴⁸ The active Raman and IR modes are listed and compared in Sec. XI.

3. Electrical properties

The electrical properties of Sc_2O_3 are also scarcely found throughout literature. Of the electrical parameters highlighted in this review, only the electron affinity and electrical breakdown field strength of Sc_2O_3 were found. The electron affinity is hypothesized to

likely be 0.85 eV based on the work function of 4 eV.¹⁰⁶⁹ The electrical breakdown field was reported for ALD thick films of Sc_2O_3 . Rouffignac *et al.* (Ref. 1055) produced samples that had an average electrical breakdown field strength of 3.5 MV/cm.¹⁰⁵⁵ That value for electrical breakdown field strength can be compared to the predicted value determined from the plot of bandgap vs breakdown field from Higashiwaki *et al.* (Ref. 147). Using the bandgap of 5.7 eV (determined using the average bandgap from the cited sources),^{1030,1050} the breakdown field strength is predicted to be around 11 MV/cm,¹⁰⁵⁵ a stark difference from the experimental value of 3.5 MV/cm.¹⁰⁵⁵ Values for mobility were not readily found in the literature for both bulk crystal and thin film Sc_2O_3 . The static and high-frequency dielectric constants for Sc_2O_3 as well as the effective carrier mass were also not found in the literature. Pachecka *et al.* (Ref. 1070) studied the metal diffusion in high- k Sc_2O_3 where they also stated there were no known values of effective mass reported.¹⁰⁷⁰ The cited electrical properties are listed and compared in Sec. XI.

E. Doping and defects

Dopants for Sc_2O_3 are not readily seen throughout literature. However, Sc was seen as the dopant for many materials. Details regarding Sc doping within other materials is beyond the scope of the review, and can be found in the cited references.^{1071–1075}

Descriptions of defects within Sc_2O_3 are also scarce in the literature, but the topic of oxygen defects has been reported recently by Langston *et al.* as well as by Kong *et al.*^{1035,1076} In both cases, ion beam sputtering was used for preparation of the studied thin films. Langston *et al.* (Ref. 1035) observed oxygen interstitials within amorphous Sc_2O_3 thin films. The deposition conditions also played a role in the density of the defects. With an increase of oxygen interstitials, there was an increase in the films absorption. Absorption was seen as a result of trap states being present in the bandgap of the oxide.¹⁰³⁵ Kong *et al.* (Ref. 1076) reported on the oxygen defects within Sc_2O_3 thin films using different oxygen flow rates. It was shown that when the oxygen flow rate was 0 sccm, the large amount of oxygen defects caused large amounts of strain on the films. It was concluded that the oxygen flow rate needed to be controlled and limited in order to decrease the oxygen defects.¹⁰⁷⁶ Much more research is needed on the defects of Sc_2O_3 and their origins, as well as how other deposition methods beside ion beam sputtering play a role.

F. Alloys

Alloys for Sc_2O_3 are even rarer than Sc_2O_3 itself. Kuz'micheva *et al.* (Ref. 1077) were able to grow scandium gallium oxide samples using Czochralski process. Ga³⁺ and Sc³⁺ have differing ionic radii of 0.62 Å and 0.745 Å, respectively. This difference makes some of the possible solid solutions unlikely. Gallium oxide and scandium oxide alloy systems should contain certain phases with four possibilities listed: (a) Ga_2O_3 based substitutional solid solution, (b) Ga_2O_3 based solid solution with partial ordering, (c) an ordered solution in which the gallium and scandium ions contain differing site orders, (d) or a completely new compound with a structure that varies from Ga_2O_3 . The phases listed are in order with increasing scandium oxide content.¹⁰⁷⁸ The transparent scandium gallium oxide crystals had a melting temperature of around 1770 °C. The lattice parameters were reported for three samples of varying cuts and did not differ greatly.

The three cuts of scandium gallium oxide boule included a seed-end, central, and tail-end cut. One significant difference amongst the three scandium gallium oxide cuts was the increase in Sc content from the tail-end toward to the seed end of the sample crystal. Lattice constants were reported to be $a = 12.496 \text{ \AA}$, $b = 3.101 \text{ \AA}$, $c = 5.873 \text{ \AA}$, and $\beta = 103.26^\circ$.¹⁰⁷⁸

A recent 2022 report by Zhu *et al.* (Ref. 1078) details the structural and electronic properties of the Sc_2O_3 and Ga_2O_3 alloy. In their report Zhu *et al.* identify a method of altering the conduction band and valence offsets by incorporating more Sc into the alloy. More details on their DFT study can be found in Ref. 1078 below.

Kakehi *et al.* (Ref. 1079) produced thin film samples of copper scandium oxide (CSO). The samples were fabricated using PLD on $\alpha\text{-Al}_2\text{O}_3$ substrates. Two crystal structures were observed among CSO, rhombohedral and hexagonal. They contain threefold and sixfold symmetry for the (0001) planes and share a -axis lattice constants that are similar to ZnO. CSO is a p-type material that has a good interface with ZnO, an n-type material. This leads to the possibility of p-n heterojunctions of CSO/ZnO thin films. CSO has the ability to induce holes as a result of the substitution of divalent cations for Sc. Optical transmission measurements were produced for CSO oriented along the c -axis. Optical transmission data showed a bandgap of 3.7 eV from direct allowed transitions.¹⁰⁷⁹ Yttrium scandium oxide ($\text{Y}_{x}\text{Sc}_{1-x}\text{O}_3$) thin films, a ternary alloy was also grown by Hu *et al.* (Ref. 1054) Studies were reported on various amounts of yttrium added to the alloy. Of note, the breakdown field was increased to a range of 4.0 to 4.8 MV/cm.¹⁰⁵⁴

$\text{Sr}_2\text{ScCaO}_5$ is another alloy of the few found in the literature with decent properties and parameters being reported.¹⁰⁸⁰ Considered to be a long lasting phosphorescence (LLP) material, this compound was prepared to compare to the likes of other LLP oxides such as ZnGa_2O_4 , LiGa_5O_8 , and $\text{Zn}_3\text{Ga}_2\text{Ge}_2\text{O}_{10}$. Host samples of the compound are found to be of the orthorhombic crystal structure with lattice constants $a = 5.908 \text{ \AA}$, $b = 15.180 \text{ \AA}$, and $c = 5.709 \text{ \AA}$. DFT calculations revealed an indirect bandgap of around 4.24 eV. The valence band maximum occurs at the X point of the Brillouin zone while the conduction band minimum occurs at the G point. The optical bandgap was determined to be 4.75 eV using an extrapolation and UV diffuse reflectance spectra measurements. The larger optical bandgap was concluded to arise from an underestimation of the non-optical bandgap at 4.24 eV calculated using LDA. The key findings of the study by Li *et al.* (Ref. 1080) involved the addition of samarium (Sm^{3+}) ions at the expense of the strontium percentage. Chernov *et al.* (Ref. 1081) described similar compounds that exist as perovskite phases within $\text{SrGa}_{1-x}\text{Sc}_x\text{O}_{2.5}$ that include $\text{Sr}_2\text{GaScO}_5$, $\text{Sr}_{10}\text{Ga}_6\text{Sc}_4\text{O}_{25}$, and $\text{SrGa}_{0.75}\text{Sc}_{0.25}\text{O}_{2.5}$. Each compound contains its own unique crystal structure; a Brownmillerite structure, a novel oxygen-deficient perovskite structure, and a cubic perovskite, respectively. The findings report how the variation between the compounds highlights the Sc^{3+} and Ga^{3+} cation crystal chemistry difference. Varying the Sc to Ga ratio will result in a changing of the perovskite phase and structure with the fixed oxygen content.¹⁰⁸¹ While this report deviates from the scope of the oxide review, it was included to highlight the rarity and complexity of alloys containing Sc_2O_3 in the literature. Currently, scandium aluminum nitride is understood much better as it is under intensive development as a barrier layer for nitride heterostructure devices, owing to its much higher piezoelectricity than the other ternary GaN alloys (AlGaN and InAlN) developed for electronic device applications.^{1082–1085}

G. Summary of Sc_2O_3 property values

Table L highlights a summary of the properties reviewed for Sc_2O_3 . Values for each of the properties are presented along with references and notation of whether they are experimental or calculated findings. Where relevant anisotropy is denoted.

XI. COMPARATIVE SUMMARY OF MATERIAL PROPERTIES

By observing the reported values listed in Tables LI-LV, comparisons across the oxides can be made, as well as noting outliers. Starting with basic material properties, CdO has the highest reported density both experimentally and theoretically. The lowest value of density was reported for Sc_2O_3 . In_2O_3 , SnO_2 , NiO, and CuO all have similar density values. The highest bulk modulus values were experimentally and theoretically reported for SnO_2 . The bulk modulus was a very wide ranging parameter with some differences being up to 65 GPa for reported values of a single material. CuO had the smallest range across the reported bulk modulus values, only differing by around 19 GPa. The oxide with the highest reported melting point was Sc_2O_3 . SnO_2 was a special case having a melting point that was stated to be undetermined in the literature due to decomposition. The lowest melting point was found for CuO.

The highest Debye temperature was reported for Al_2O_3 while CdO had the lowest value. Debye temperature was another parameter with wide ranging results for certain oxides. The reported Debye temperatures for ZnO spanned almost 500 K. NiO and SnO_2 had similar

TABLE L. Summary of theoretical and experimental properties of Sc_2O_3 . Common names are scandium oxide, scandium sesquioxide, and scandia.

Stable phase	Bixbyite (C-type)	Ref. 1052
Stable structure	Cubic $a = 9.708\text{--}9.90$	$Ia\bar{3}$ (No. 206) Refs. 36,1030, 1044, and 1053
Metastable phase	Monoclinic (B-type)	Ref. 1051
Potential phases	Hexagonal (A-type)	Ref. 1044
	Hexagonal (H-type)	Ref. 1044
	Cubic (X-type)	Ref. 1044
Density (g/cm ³)	3.79–4.1	Expt. 1038,1043,1051,1064
	4.16	Calc. 1047
Bulk mod. (GPa)	168	Ref. 1067
T_m (° C)	2479.85 2485 2549.85	Ref. 1050 Ref. 118 Refs. 1049 and 1065
Specific heat (J/(gK))	0.683	Ref. 118
Electron affinity (eV)	0.85	Pred. 1069
Breakdown field (MV/cm)	11 3.5	Pred. 147 Expt. 1055
Gap type	Indirect	Ref. 1030
E_g (eV)	5.7–5.84	Film expt. 1030,1050
Phonon modes		
IR active	$16F_u$	Pred. 1048
Raman active	$4A_g$, $4E_g$, $14F_g$	Pred. 1048

TABLE LI. Comparison of basic properties.

	Al ₂ O ₃		Ga ₂ O ₃		In ₂ O ₃		ZnO		CdO		SnO ₂		NiO		CuO		Sc ₂ O ₃	
Property	Value	Met./Ref.	Value	Met./Ref.	Value	Met./Ref.	Value	Met./Ref.	Value	Met./Ref.	Value	Met./Ref.	Value	Met./Ref.	Value	Met./Ref.	Value	Met./Ref.
Stable structure (Space group #)	<i>R</i> ̄3 <i>c</i>	Ref. 265	<i>C</i> 2/ <i>m</i>	Ref. 32	<i>Ia</i> ̄3	Ref. 420	<i>P</i> 6 ₃ <i>mc</i>	Ref. 549	<i>Fm</i> ̄3 <i>m</i>	Ref. 782	<i>P</i> 4 ₂ / <i>mnm</i>	Ref. 684	<i>Fm</i> ̄3 <i>m</i>	Ref. 855	<i>C</i> 2/ <i>c</i>	Ref. 930	<i>Ia</i> ̄3	Ref. 1052
(#167)	(#12)	(#206)	(#186)	(#225)	(#136)	(#225)	(#15)	(No. 206)										
Density (g/cm ³)	3.984 3.92	Expt. ³³⁴ Expt. ³⁴⁷	5.95 5.88	Ref. 115	7.12 7.2 6.3	Expt. ⁴⁰⁶ Calc. ⁴²⁴ Ref. 461	5.605 8.218 7.0	Expt. ⁵⁴⁹ Calc. ⁸¹⁷ Expt. ⁸¹⁶ 8.15 Ref. 118	8.00 8.218 6.975	Expt. ⁷⁷⁷ Calc. ⁸¹⁷ Expt. ⁷³⁸	6.99 7.02 6.975	Expt. ⁶⁸⁴ Expt. ⁷³⁷ Expt. ⁸⁹⁹	6.8 6.8279 6.8279	Expt. ⁸⁹⁸ Ref. 899	6.545	Expt. ^{930,945}	4.1	Expt. ^{1038,1043}
Bulk modulus (GPa)	257 239 225.9 252	Expt. ³³⁴ Calc. ³⁹⁷ Calc. ³⁹⁷ Refs. 398 and 399	174 184 199 255 202	Calc. ¹⁹ Expt. ¹¹³ Expt. ¹¹³ Expt. ¹¹³ Expt. ¹¹²	194.24 174 192.66 154.4 162.3	Expt. ⁴⁶² Calc. ⁴²⁸ Calc. ⁴⁵⁹ Calc. ⁵⁴⁷ Calc. ⁵⁹⁹	183 140 160 131 164	Expt. ⁵⁴⁸ Expt. ⁵⁴⁷ Expt. ⁵⁴⁷ Expt. ⁷⁸³ Expt. ⁷⁸³	148 150 108 120 142.4 ^a	Expt. ⁸¹⁸ Expt. ⁸¹⁸ Expt. ⁸¹⁹ Expt. ⁷⁸³ Expt. ⁶⁰¹	244.7 245 221 205 128	Calc. ⁷³⁹ Calc. ⁸⁵ Calc. ⁶⁸⁶ Expt. ⁹⁰⁰ Calc. ⁶⁰⁰	205 137.3 199 114.25 173	Expt. ⁸⁹⁹ Calc. ⁸⁶⁴ Expt. ⁹⁰⁰ Calc. ⁹⁹⁶ Calc. ⁶⁰⁰	99.16	Calc. ⁹⁹⁶	168	Ref. 1067
Melting point (°C)	2054 2050 2071.85	Expt. ⁴⁰⁰ Expt. ³³⁴ Ref. 335	1725 1740 1795	[114, 115] Ref. 116 Ref. 118	1950 1949 1912	Expt. ⁴⁵⁸ Ref. 464 Ref. 118	1975 1974 1912	Expt. ¹¹⁸ Ref. 118 Ref. 118	>1500 1559 ^b	Ref. 400 Ref. 118 Ref. 118	>1900 >2100 1630	Calc. ⁶⁸⁴ Expt. ⁷⁴⁵ Ref. 118	1955 1983 3127	Refs. 118 Expt. ⁹⁰³ Calc. ⁹⁰³	1201 1446 (bulk)	Expt. ^{930,945} Ref. 118 2485	2479.85 2549.85 Ref. 118	

^aNanocrystalline sample.^bSublimation point.

TABLE LII. Comparison of thermal properties.

	Al ₂ O ₃		Ga ₂ O ₃		In ₂ O ₃		ZnO		CdO		SnO ₂		NiO		CuO		Sc ₂ O ₃	
Property	Value	Met./Ref.	Value	Met./Ref.	Value	Met./Ref.	Value	Met./Ref.	Value	Met./Ref.	Value	Met./Ref.	Value	Met./Ref.	Value	Met./Ref.	Value	Met./Ref.
Debye temp. (K)	1045 965–1044 ^a	Calc. ³³⁹ Expt. ³⁴¹	738 872	Expt. ⁵⁵ Calc. ³³	700 811 420	Calc. ⁴⁷⁰ Calc. ⁴⁶⁹ Expt. ⁴⁶⁹	305 355–416 370	Ref. ⁶⁰³ Calc. ⁶⁰² Expt. ⁶⁰²	255	Calc. ⁴⁰⁰	570 550 580	Calc. ⁷³⁷ Ref. ⁶⁸⁷	495 595	Expt. ⁹⁰⁴ Expt. ⁹⁰⁶	640 575	Calc. ⁹³⁹ Calc. ⁹³⁹ Ref. ⁹⁰⁵	Not reported	
Specific heat (J/(gK))	0.755 0.775 0.780 0.750–0.785	Expt. ³³⁴	0.49 0.56 0.47 Expt. ^{332,333}	Expt. ^{115,117}	0.356 ^c	Ref. ⁴⁷¹	0.495 ^c	Expt. ⁵⁴⁹	0.339 ^c	Calc. ⁴⁰⁰	0.398 ^c	Calc. ⁶⁸⁷	0.5903 ^d	Expt. ⁹⁰⁵	0.526 ^c	Expt. ⁹³⁹	0.683 ^c	Ref. ¹¹⁸
Thermal conductivity (W/(mK))	33 (20 °C) 30 30–40	Expt. ³³⁴	15 (<i>a</i>) 28 (<i>b</i>) Expt. ^{332,333}	Expt. ⁴¹	15.0 13.09 18 (<i>c</i>)	Expt. ⁴⁶⁵ Expt. ⁴³⁶ Expt. ⁴¹	116 (Zn face) 102 (Zn face) 110 (O face) 98 (O face) 22.8 [010] 10.9 [100] 13.3 [-201] 14.7 [001] 27.0 [110]	Expt. ⁶¹² Expt. ⁶¹² Expt. ⁶¹² Expt. ⁶¹² Ref. ¹¹⁵	8.1 5.6–9.3 5.76 5.6 147 144 135 125 100 95 67 46	Calc. ⁷⁷⁷ Calc. ⁸⁰² Calc. ⁸⁰² Expt. ⁷³⁷ Expt. ⁷³⁷ Expt. ⁶¹¹ Expt. ⁶¹¹ Expt. ⁶¹¹ Expt. ⁶¹¹ Expt. ⁶¹¹ Expt. ⁶¹¹ Expt. ⁶¹¹	51.4 55.0 \perp_c 98.0 \parallel_c 107.0 Expt. ⁶¹¹	Ref. ⁴³⁶	50 20.2 Expt. ⁹⁰⁵	Expt. ⁹⁰⁸ Expt. ⁹⁰⁷ 76.5 Expt. ¹⁰⁰⁵	33 Ref. ¹⁰⁰⁶	Not reported		
Thermal diffusivity (mm ² /s)	Not reported	5.23 (<i>a</i>)	Expt. ⁴¹	1.2 (ITO film)	Expt. ⁴⁷²	Not reported	Not reported	Not reported	1.45	Ref. ⁷⁷²	8.8	Expt. ⁸⁹⁸	Not reported	Not reported	Not reported	Not reported		
Coefficient of thermal expansion	9.76 (<i>b</i>) 6.26 (<i>c</i>)	Expt. ⁴¹	7.0	Calc. ⁴⁶⁵					1.6	Ref. ⁷⁷³								
	5.4	Expt. ^{332,333}	5.3 [100]	Expt. ¹¹⁵	10.2 ^b	Expt. ⁴⁶⁸	4.31 (<i>a</i>)	Expt. ⁶⁰⁸	14.33 (avg)	Expt. ⁷⁸⁴	4.0(\parallel_a)	Expt. ⁷⁴⁶	12.28	Expt. ⁸⁶³	1.6	Expt. ¹⁰⁰⁰	Not reported	
	4.5–5.5	Expt. ^{332,333}	8.9 [010]	Expt. ¹¹⁵	6.15 ^b	Expt. ⁴⁶⁷	2.49 (<i>c</i>)	Expt. ⁶⁰⁸	13.31	Expt. ⁷⁸⁴	3.7(\parallel_c)	Expt. ⁷⁴⁶						

TABLE LII. (Continued.)

	Al ₂ O ₃		Ga ₂ O ₃		In ₂ O ₃		ZnO		CdO		SnO ₂		NiO		CuO		Sc ₂ O ₃	
Property	Value	Met./Ref.	Value	Met./Ref.	Value	Met./Ref.	Value	Met./Ref.	Value	Met./Ref.	Value	Met./Ref.	Value	Met./Ref.	Value	Met./Ref.	Value	Met./Ref.
($\times 10^{-6}/\text{K}$)	4.6	Expt. ³³⁴	8.2 [001]	Expt. ¹¹⁵	8.66	Ref. ⁴³⁶	4.75 (a)	Ref. ⁵⁴²	14.0	Expt. ⁴⁰⁰								
(20 °C)			4.7 [100]	Expt. ⁴¹	7.2 ^b	Expt. ⁴⁶⁶	2.9 (c)	Ref. ⁵⁴²										
			5.45 [010]	Expt. ⁴¹														
			5.35 [100]	Expt. ⁴¹														
			1.54 [100]	Calc. ⁴⁵														
			3.37 [010]	Calc. ⁴⁵														
			3.15 [100]	Calc. ⁴⁵														

^aPoly-crystalline.^b($\times 10^{-6}/\text{C}$)^cCalculated from molar heat cap J/(mol K).^dConverted from cal/(g °C).

TABLE LIII. Comparison of electrical properties.

	Al ₂ O ₃		Ga ₂ O ₃		In ₂ O ₃		ZnO		CdO		SnO ₂		NiO		CuO		Sc ₂ O ₃		
Property	Value	Met./Ref.	Value	Met./Ref.	Value	Met./Ref.	Value	Met./Ref.	Value	Met./Ref.	Value	Met./Ref.	Value	Met./Ref.	Value	Met./Ref.	Value	Met./Ref.	
Electron Affinity (eV)	1.58	³⁵⁸	4.00±0.05	Exp. ¹⁴⁶	3.3	Calc. ⁴⁹²	4.1	Exp. ⁵⁴¹	5.94	Exp. ⁷⁹⁴	4.3-4.7	Exp. ⁷⁵⁴	1.4	Calc. ⁸⁹¹	1.77	Exp. ¹⁰¹⁵	0.85	Pred. ¹⁰⁶⁹	
					3.7	Exp. ⁴⁹⁶	4.5	Exp. ⁶²²	4.51	Calc. ⁸²⁶	4.85	Calc. ⁷⁵⁴	1.46	Exp. ⁹¹⁵					
						4.3						4.5	Calc. ⁷⁵⁵	1.47	Exp. ⁹¹⁶				
						4.45	Exp. ⁴⁹⁵												
Electrical breakdown field [MV/cm]	>20 ^f	Pred. ¹⁴⁷	8 ^f	Pred. ¹⁴⁷	3-4 ^f	Pred. ¹⁴⁷	2-3 ^f	Pred. ¹⁴⁷	0.5-0.8 ^f	Pred. ¹⁴⁷	3.5 ^f	Pred. ¹⁴⁷	2-5 ^f	Pred. ¹⁴⁷	0.2-0.5 ^f	Pred. ¹⁴⁷	11 ^f	Pred. ¹⁴⁷	
	5.2	Exp. ³⁰⁴																3.5	Exp. ¹⁰⁵⁵
	6-7	Exp. ³⁶²																	
Effective mass (m_e^*)	0.16	Calc. ³¹⁸	m_a^* 0.288	Exp. ⁴²	0.16	Calc. ⁴⁵²	0.24	Calc. ⁶²⁶	0.19	Calc. ⁷⁹⁰	0.23 (_c)	⁶⁸⁴	Not	Applicable	0.78 ^c	Calc. ⁹⁸⁵	Not Reported		
	0.45	Calc. ³¹⁸	m_b^* 0.283	Exp. ⁴²	0.18	Calc. ⁴²⁸	0.3	Calc. ⁶²⁸	0.21	Calc. ⁷⁹⁰	0.3 (⊥ _c)	⁶⁸⁴			3.52 ^d	Calc. ⁹⁸⁵			
	0.40	Calc. ³¹⁸	m_c^* 0.286	Exp. ⁴²	0.14	Exp. ⁵⁰⁰	0.34	Calc. ⁶²⁸	0.23	Calc. ⁷⁹⁰	0.12-0.18	Calc. ⁶⁹²			0.37	Calc. ⁹⁷⁷			
	0.38	Calc. ³¹⁸	m_a^* 0.41	Calc. ⁴²	0.18	Exp. ⁴⁸⁷	0.23	Calc. ⁶²⁵	0.21	Exp. ⁷⁹⁰	0.17	Calc. ⁷⁵⁸			0.42	Calc. ⁹⁷⁷			
	0.40	Calc. ²⁸⁴	m_b^* 0.41	Calc. ⁴²	0.208	Exp. ⁴⁸⁴	0.265	Calc. ⁶²⁷	0.23	Exp. ⁷⁷⁵	0.22	Exp. ⁶⁹²			0.46	Calc. ⁹⁷⁷			
	0.28	Calc. ³²⁸	m_c^* 0.37	Calc. ⁴²	0.30	Exp. ⁴⁷⁰					0.09	Calc. ⁸³¹	0.234 ()	Exp. ⁷⁵⁹		0.16	Calc. ⁹⁷⁷		
	0.40 (⊥)	Est. ³⁶³	m_a^* 0.224	Calc. ⁸⁶	0.40	Exp. ⁴⁸⁷					0.24	Exp. ⁸¹¹	0.299 (⊥)	Exp. ⁷⁵⁹					
	0.40 ()	Est. ³⁶³	m_b^* 0.301	Calc. ⁸⁶	0.55	Exp. ⁴³⁴							0.17	Est. ⁷⁵⁷					
			m_c^* 0.291	Calc. ⁸⁶									0.26 (Γ-X)	Calc. ⁷¹⁵					
													0.21 (Γ-Z)	Calc. ⁷¹⁵					

TABLE LIII. (Continued.)

	Al ₂ O ₃		Ga ₂ O ₃		In ₂ O ₃		ZnO		CdO		SnO ₂		NiO		CuO		Sc ₂ O ₃	
Property	Value	Met./Ref.	Value	Met./Ref.	Value	Met./Ref.	Value	Met./Ref.	Value	Met./Ref.	Value	Met./Ref.	Value	Met./Ref.	Value	Met./Ref.	Value	Met./Ref.
Effective mass (m_h^*)	6.3 (\perp) 0.36 (\parallel)	Est. ³⁶³ Est. ³⁶³	Not Applicable		0.28m ^{V,B} 0.27m ^{V,B}	Calc. ⁵³¹ Calc. ⁵³¹	0.79 Calc. ⁶³⁰	Calc. ⁶³⁰	0.05 >0.14	Pred. ⁷⁹⁹ Calc. ⁷⁹⁹	1.21 (Γ -X) 1.47 (Γ -Z)	Calc. ⁷¹⁵ Calc. ⁷¹⁵	0.8-1.0m _h 0.86m _h T- Γ ^a 0.86m _h T-I ^b 0.55m _h T-K ^a 1.66m _h T-K ^b	Calc. ⁸⁶⁸ Calc. ⁸³¹ Calc. ⁸³¹ Calc. ⁸³¹ Calc. ⁸³¹	1.87 1.75 3.01 0.60 0.54	Calc. ⁹⁸⁵ Calc. ⁹⁷⁷ Calc. ⁹⁷⁷ Calc. ⁹⁷⁷ Calc. ⁹⁷⁷	Not Reported	
Mobility of electrons (cm ² /(Vs))	0.8	Exp. ³⁶⁸	300 220-230 130 176 172 112	Calc. ¹⁴⁷ Calc. ¹⁵⁵ Calc. ⁵⁷ Exp. ⁷⁶ Exp. ⁹⁵ Exp. ²⁶⁷	270 274 7.81 11 32 37	Calc. ⁴⁷⁰ Calc. ⁵⁰¹ Exp. ⁵⁰² Exp. ⁴⁵⁵ Exp. ⁴⁵⁵ Exp. ⁴⁴⁰	300 260 205 200 120 130	Calc. ⁶³¹ Calc. ⁶³¹ Exp. ⁵⁵⁷ Exp. ⁶³⁶ Exp. ⁵⁶² Exp. ⁶³³	2-120 609 330 20-124 209-1116 ^e 80	Exp. ⁷⁷⁵ Exp. ⁷⁹³ Exp. ⁷⁹³ Exp. ⁸¹¹ Exp. ⁸¹¹ Exp. ⁸²⁵	35 61 95 172 200 222	Exp. ²¹⁰ Exp. ²¹⁰ Exp. ²¹⁰ Exp. ⁷⁵⁷ Exp. ⁷⁵⁷ Exp. ⁸²⁵	0.14 0.64 3.3 Exp. ⁸⁴³	Exp. ^{918,919}	Not Applicable	Not Reported		
Mobility of holes	Not Applicable		Not Applicable		Not Applicable		Not Applicable		Not Applicable		Not Applicable		0.43 0.53 0.3 0.5 2.8 0.3	Calc. ⁹²⁰ Calc. ⁹²² Exp. ^{918,919} Exp. ⁸⁸¹ Exp. ⁸⁴³ Exp. ⁹²¹	0.1 0.53 Exp. ⁸⁹¹	Not Reported		
^a Upper valence. ^b Lower valence. ^c Longitudinal. ^d Transverse. ^e Optical mobility. ^f Predicted using Ref. 147.																		

^aUpper valence.^bLower valence.^cLongitudinal.^dTransverse.^eOptical mobility.^fPredicted using Ref. 147.

TABLE LIV. Comparison of optical properties.

	Al ₂ O ₃		Ga ₂ O ₃		In ₂ O ₃		ZnO		CdO		SnO ₂		NiO		CuO		Sc ₂ O ₃			
Property	Value	Met./Ref.	Value	Met./Ref.	Value	Met./Ref.	Value	Met./Ref.	Value	Met./Ref.	Value	Met./Ref.	Value	Met./Ref.	Value	et./Ref.	Value	Met./Ref.		
Gap Type	Direct	Ref. 271	Direct	Ref. 66	Debated	Ref. 454	Direct	Ref. 591	Direct	Ref. 798	Direct	Ref. 714	Indirect	Ref. 892	Indirect	Ref. 937	Indirect	Ref. 1030		
Bandgap	Bulk		Bulk		Bulk		Bulk		Bulk		Bulk		Bulk		Bulk		Film			
(Selected values from sections	6.3	Calc. 324	4.66	Calc. 19	1.70	Calc. 735	2.97	Calc. 580	0.8 ^a	Calc. 801	1.70	Calc. 735	2.54	Calc. 887	0.91	Calc. 981	5.7	Expt. 1050		
V C 1, IV C 1,	6.3	Calc. 324	4.74 \parallel_c	Calc. 86	2.76	Calc. 687	2.99	Calc. 581	0.95 ^a	Calc. 805	2.76	Calc. 687	3.0	Calc. 861	1.0	Calc. 985	5.75–5.84	Expt. 1030		
VIC 1, VIII C 1,	8.0	Calc. 324	4.81	Calc. 103	2.86	Calc. 717	3.20	Calc. 582	1.09 ^a	Expt. 799	2.86	Calc. 717	3.1	Calc. 886	1.0	Calc. 980				
VII C 1, IX C 1,	8.8	Expt. 271	4.969 \parallel_a	Calc. 86	2.89	Calc. 717	3.40	Calc. 596	1.11 ^a	Expt. 807	2.89	Calc. 781	4.8	Calc. 866	1.1	Calc. 953				
XC1, XI C 1,	9.5	Expt. 324	5.341 \parallel_c	Calc. 94	3.50	Calc. 686	3.6	Calc. 596	1.12 ^a	Calc. 781	3.50	Calc. 686	14.2	Calc. 861	1.24	Calc. 986				
XII C	9.9	Expt. 319	5.35 \parallel_b	Calc. 86	3.65	Calc. 715	3.372 ε_{\perp}	Expt. 584	1.18 ^a	Calc. 781	3.65	Calc. 715	3.6	Expt. 866	1.39	Calc. 931				
			5.581 \parallel_a	Calc. 94	3.7	Calc. 718	3.373 ε_{\perp}	Expt. 585	2.16	Expt. 790	3.70	Calc. 718	4.30	Expt. 889						
			Film		5.911 \parallel_b	Calc. 94	3.37	Expt. 723	3.406 ε_{\perp}	Expt. 586	2.18	Calc. 809	3.37	Expt. 723		1.43	Calc. 887			
			4.0	Calc. 324	4.52 \parallel_c	Expt. 59	3.54	Expt. 719	3.405 ε_{\parallel}	Expt. 584	2.28	Expt. 799	3.54	Expt. 719	Film	1.48	Calc. 981			
			6.29	Calc. 318	4.57 \parallel_a	Expt. 95	3.56	Expt. 727	3.407 ε_{\parallel}	Expt. 585			3.56	Expt. 727	3.25	Expt. 888	1.6	Calc. 977		
			6.52	Expt. 321	4.79 \parallel_b	Expt. 59	4.0	Expt. 720	3.445 ε_{\parallel}	Expt. 586	Film		4.0	Expt. 720	3.55	Expt. 892	1.9	Calc. 886		
			6.7	Expt. 322	5.04 \parallel_c	Expt. 86	3.57 \perp_c	Expt. 724			1.2 ^a	Expt. 808	3.57 \perp_c	Expt. 724	3.4–3.58	Expt. 873	2.11	Calc. 981		
			6.8	Expt. 307	5.15 \parallel_c	Expt. 94	3.93 \parallel_c	Expt. 724	Film		1.2 ^a	Calc. 801	3.93 \parallel_c	Expt. 724	3.5–4.5	Expt. 872	2.2	Calc. 987		
					5.37 \parallel_a	Expt. 94		3.08–3.37	Expt. 591	1.45 ^a	Expt. 806			3.47–3.86	Expt. 895	1.35	Expt. 937			
					5.40 \parallel_a	Expt. 86	Film	3.27–3.31	Expt. 592	1.47 ^a	Expt. 799	Film		3.8	Est. 840	1.7	Expt. 987			
					5.64 \parallel_b	Expt. 86	3.7	Expt. 722	3.29	Expt. 594	2.20	Expt. 811	3.7	Expt. 722						
					5.68 \parallel_b	Expt. 94	3.71	Expt. 721	3.3	Expt. 595	2.22	Expt. 792	3.71	Expt. 721	Film					
							3.64–3.94	Expt. 725	3.366 ε_{\perp}	Expt. 590	2.25	Expt. 787	3.64–3.94	Expt. 725		1.4	Expt. 984			
							4.72	Expt. 97	3.94–3.96	Expt. 711	3.366 ε_{\parallel}	Expt. 590	2.3	Expt. 797	3.94–3.96	Expt. 711	1.55	Expt. 968		
							4.74	Expt. 97	4.38	Expt. 709		2.36	Expt. 814	4.38	Expt. 709		1.56	Expt. 968		
							4.94	Calc. 101	4.35 \perp_c	Expt. 726		2.4	Expt. 795	4.35 \perp_c	Expt. 726		1.65	Expt. 968		
							4.99	Calc. 101	4.52 \perp_c	Expt. 726			4.52 \perp_c	Expt. 726			1.67	Expt. 968		
							4.9	Expt. 99	5.59 \parallel_c	Expt. 726			5.59 \parallel_c	Expt. 726			1.79	Expt. 970		
							4.9	Expt. 77	5.67 \parallel_c	Expt. 726			5.67 \parallel_c	Expt. 726			1.87	Expt. 970		
															1.97	Expt. 970				
															2.03	Expt. 970				
Static dielectric constant ϵ_0	9.385 (\perp_c)	Calc. 351	10.84 (a)	Calc. 132	9.0	Calc. 463	7.61 (\perp_c)	Calc. 588	18.1 ± 2.5	Expt. 824, 827	14 ± 2 (\perp_c)	Expt. 756	12	Expt. 855	12.3	Calc. 977	Not Reported			
	11.614 (\parallel_c)	Calc. 351	13.89 (c)	Calc. 132	9.05	Calc. 457	8.50 (\parallel_c)	Calc. 588			9 ± 0.5 (\parallel_c)	Expt. 756	11.9	Expt. 917	12.26	Calc. 970				
	8.9 (\perp_c)	Calc. 326	11.49 (b)	Calc. 132	8.9	Expt. 406	8.12	Calc. 557					11.9	Expt. 871	12.45	Calc. 970				
	11.614 (\parallel_c)	Calc. 326	12.4 (c^*)	Expt. 43			8.91 (\parallel_c)	Expt. 617					11.75	Calc. 871	12.76	Calc. 970				
	9.395 (\perp_c)	Expt. 357	10.2 (a^*)	Expt. 43			7.77 (\perp_c)	Expt. 617						13.0	Calc. 970					
	11.589 (\parallel_c)	Expt. 357	10.87 (b)	Expt. 43			8.59 (\parallel_c)	Expt. 617												
			10.19 (a)	Expt. 144			7.46 (\perp_c)	Expt. 617												
			12.27 (c^*)	Expt. 144																
			10.05 (a^*)	Expt. 144																
			12.4 (c)	Expt. 144																

TABLE LIV. (*Continued.*)

^aIndirect gap.

TABLE LV. The average experimentally determined bandgaps (eV) of bulk β -Ga₂O₃ along three directions. Differentiation is made for bandgap energies determined using SE and values considered to be the onset of absorption (Abs.).

Method	Direction	Avg. expt. E _g
SE	E \parallel c	5.095
	E \parallel a	5.385
	E \parallel b	5.66
Abs.	E \parallel c	4.50
	E \parallel a	4.57
	E \parallel b	4.73

Debye temperatures while certain values for In₂O₃ were comparable to Ga₂O₃. Al₂O₃ had the largest specific heat values while CdO saw the lowest reported value. This follows the same trend seen in the Debye temperature; Al₂O₃ being the highest and CdO being the lowest. Of note, Ga₂O₃, ZnO, NiO, and CuO all reported similar specific heat values. The highest values of thermal conductivity were shown in ZnO. The reported ZnO thermal conductivity values were also very wide ranging across multiple samples, differing up to 101 W/(mK). Continuing with the trend seen throughout the thermal property comparisons, CdO has the lowest thermal conductivity. Anisotropy was seen in the thermal conductivity of Ga₂O₃ and SnO₂. The thermal diffusivity was the least reported parameter throughout the review with no value being reported for five of the nine oxides, though calculated values can be derived from the thermal conductivity and specific heat capacity. Values of thermal diffusivity were specifically reported for Ga₂O₃, In₂O₃, SnO₂, and NiO. NiO had the highest reported thermal diffusivity while SnO₂ had the lowest average thermal diffusivity. The single lowest thermal diffusivity value was found experimentally in an In₂O₃ (ITO) thin film. CdO has the highest average CTE of the nine reviewed oxides. The single highest reported value for CTE was seen along the [100] direction of Ga₂O₃. This could be considered an outlier as other sources report a much lower CTE along the [100] both experimentally and theoretically. The lowest CTE value was seen for CuO. By observing the reported thermal property values, it can be concluded that CdO may experience the greatest thermal effects due to low conductivity and high CTE. Al₂O₃, NiO, and CuO are often the three oxides with the most advantageous thermal properties that we reported on. Ga₂O₃ had thermal property values that appeared “middle of the pack” in comparison to the other oxides. The reported values were generally neither the highest nor the lowest. For an ultra-wide bandgap material, these thermal property values show why there has been a strong increase in interest of Ga₂O₃ in high voltage and high temperature applications.

The electron affinity was reported for all of the reviewed oxides. The lowest electron affinity was reported theoretically for Sc₂O₃. The lowest experimental electron affinity was found for CuO. Al₂O₃ and NiO appeared to have similar electron affinities varying by around 0.1 eV. The highest electron affinity was reported experimentally for CdO. The electrical breakdown field was a parameter that could be predicted based on the bandgap. Predictions were made for each of the oxides; CuO had the smallest electrical breakdown field while Al₂O₃ had the largest predicted value. For Al₂O₃ and Sc₂O₃, there were experimental values reported. For both instances, the experimental value were

drastically lower than the predicted value. The electron effective mass was widely reported throughout literature for most of the oxides. P-type NiO had no applicable values, and Sc₂O₃ had no reported values. A large portion of the reported values were calculated and often wide ranging. Anisotropy was seen in the effective masses of Ga₂O₃ and SnO₂. The heaviest effective electron mass was a calculated transverse effective mass for CuO and could be considered an outlying value as it is almost 3.0 m_e higher than the other values. The lowest electron effective was a calculated value for CdO. CdO and In₂O₃ appear to have the lowest average effective masses for the reported values. The effective hole mass was not as widely reported. Ga₂O₃ had no applicable values while Sc₂O₃ had no reported values. The effective hole mass was drastically larger than the effective electron mass with the exception of CdO. While no anisotropy was seen in the electron effective mass of Al₂O₃, there is estimated anisotropy for the hole effective mass. Anisotropy was also calculated to be present in SnO₂ and NiO. The largest effective hole mass was predicted for Al₂O₃ while CdO had the smallest predicted value. According to the reported values, there were no experimentally determined effective hole mass values. Electron mobility was another wide ranging parameter that had heavy dependence on the crystal and film quality as well as the dopants used. The largest experimental mobility value was seen in CdO thin films. The second largest experimental mobility was seen in dysprosium doped CdO. The smallest electron mobility was seen experimentally in NiO with Al₂O₃ having only a slightly larger mobility. Oxides such as In₂O₃, ZnO, CdO, and SnO₂ had wide ranging reported values. It can be concluded that much of the lower mobility values seen in the literature were a result of immature growth techniques and poor quality. With time and expanded research, quality increased greatly, resulting in increased mobility values. Both Ga₂O₃ and In₂O₃ have a calculated theoretical maximum mobility. Experimental mobility values show there is still much room for improvement in the mobility of these oxides, as they are well below the theoretical limit. Hole mobility was only reported for NiO and CuO. NiO had the larger hole mobility both experimentally and theoretically.

The bandgap values were wide ranging across each of the oxides due to the multiple experimental and theoretical methods used to determine the bandgap. CuO contains some of the smallest experimentally determined bandgap energies while Al₂O₃ has the largest experimentally determined bandgap energy. The second largest bandgap energy was found in Sc₂O₃; however, only three values were reported for thin films and none for bulk. Table LI highlights the anisotropic bandgap energies of β -Ga₂O for the three unique crystallographic directions from ellipsometry measurements and absorption edge measurements. The ellipsometry measurements are notoriously higher than the absorption edge measurements as they account for the excitonic nature of the monoclinic β -Ga₂O₃ and offer what we believe to be representations of the true bandgap energies. The trend of $b > a > c$ hold true regardless of the experimental method used to determine the bandgap energy. Values for the average ellipsometry measurements are from Refs. 86 and 94, while the values for the average absorption edge measurements are from Refs. 59, 95, and 96. Calculated and first principles methods were not considered in this comparison because they span large values and can be easily altered by changing the functionals used in the calculation. The static dielectric constant was reported for each of the oxides with the exception of Sc₂O₃. Anisotropy of the static dielectric constant was reported in

Al_2O_3 , Ga_2O_3 , ZnO , and SnO_2 . In Ga_2O_3 , the anisotropy seen theoretically was much smaller than the experimental anisotropy. The highest value for the static dielectric constant was reported for CdO , while the lowest value was seen in ZnO . The high frequency dielectric constant was reported for all the oxides except Sc_2O_3 and was lower than the static dielectric constants for all oxides. Anisotropy was seen in the same oxides that had anisotropy within the static dielectric constant; Al_2O_3 , Ga_2O_3 , ZnO , and SnO_2 . In Ga_2O_3 the magnitude of the anisotropy was noticeably smaller.

XII. CONCLUSION

We have provided a comprehensive review of transparent conducting and semiconducting oxides that include Ga_2O_3 , Al_2O_3 , In_2O_3 , ZnO , SnO_2 , CdO , NiO , CuO , and Sc_2O_3 . We have highlighted basic material properties, including the density, bulk modulus, and melting point. Thermal properties include the CTE, specific heat, Debye temperature, thermal conductivity, and thermal diffusivity. The phonon properties of the oxides were highlighted and included the irreducible representations as well experimental and calculated phonon frequencies. The electrical properties included throughout the review consisted of the electron affinity, electrical breakdown field, effective mass, carrier mobility, and the static and high frequency dielectric constants. Special attention has been given to the electronic structure and bandgap values for each oxide. Where applicable, the makeup of the electronic structure was detailed. A wide range of bandgap values were cited to provide a broad outlook on what has been reported across literature. Comparisons were made between the multitude of theoretical and experimental methods that are used to determine the bandgap; often resulting in differing values.

Illustrations have been provided for applicable crystal structures and unit cells as well as electronic band structures and Brillouin zones where applicable. The numerous bandgap values cited from the literature are presented in tables within each oxide section. Tables LI-LV highlighted the basic material, thermal, electrical, and optical properties as well as presented those values for comparison across the nine oxides. By comparing these oxides with each other, trends can be identified such as the relatively good thermal conductivity of Al_2O_3 in comparison with that of CdO , for instance. A lack of reported values, as was the case of Sc_2O_3 where thermal data are essentially nonexistent in the literature, highlights the possibility for future research. A wide range in experimentally determined bandgaps, as was the case of the monoclinic Ga_2O_3 phase, highlighting an ongoing debate in the literature regarding basic material properties whose determination may be complicated by a number of factors. We also have highlighted the continued need for research into metastable phases where sample availability could hinder basic research, as was the case for many of the Ga_2O_3 and Al_2O_3 metastable phases as well as the many theorized and expected phases of Sc_2O_3 .

Oxide materials have progressed much over the past decades as is evident from the cited sources used in this review that span 92 years. Oxides have provided many key elements in a wide range of electrical devices and applications that have been highlighted throughout this review. As the limits of technology continue to be pushed further, the understanding of how oxides integrate into applicable fields as well as the research methods behind them is expected to progress. This review has intended to facilitate future research into oxide semiconductors by

comprehensively providing as much information as it is practical to compile into a single document.

ACKNOWLEDGMENTS

J.A.S. was grateful for financial support from the Naval Research Enterprise Internship Program (NREIP), Office of Naval Research. J.A.S and Y.Z. thank the support from the Jeffress Trust Awards Program in Interdisciplinary Research by Thomas F. and Kate Miller Jeffress Memorial Trust, Bank of America, Trustee. J.A.S and Y.Z. also thank the partial support by the Center for Power Electronics Systems High Density Integration (HDI) Industry Consortium at Virginia Tech. A.L.M. was sincerely grateful for postdoctoral fellowship from the National Research Council. Discussions with Dr. John Lyons (NRL) are gratefully acknowledged. Research at the Naval Research Laboratory was supported by the Office of Naval Research. This work was supported in part by the National Science Foundation (NSF) under Award Nos. NSF DMR 1808715 and OIA-2044049; by Air Force Office of Scientific Research under Award Nos. FA9550-18-1-0360, FA9550-19-S-0003, and FA9550-21-1-0259; and by the Knut and Alice Wallenbergs Foundation supported grant “Wide-bandgap semiconductors for next generation quantum components.” Mathias Schubert acknowledges the University of Nebraska Foundation and the J. A. Woollam Foundation for support.

AUTHOR DECLARATIONS

Conflict of Interest

The authors have no conflicts of interest to report.

DATA AVAILABILITY

Data sharing is not applicable to this article as no new data were created or analyzed in this study.

APPENDIX A: PROPERTY DEFINITIONS

The parameters covered in this Review encompass a wide range of material properties such as electrical, optical, and thermal properties. The parameters that are included throughout the review are listed and defined below. Specific growth methods for single-crystal and thin film samples of each oxide are also highlighted throughout the review. Process details and a brief historical context to the development of the growth method are also listed below.

Bandgap—The difference between the valence band maximum and conduction band minimum of a material. When the valence band maximum and conduction band minimum occur at the same point in reciprocal (k) space, the material is said to have a direct bandgap and no momentum transfer is needed for electronic transition. If the valence band maximum and the conduction band minimum do not occur at the same point in reciprocal space, the material is said to have an indirect bandgap and momentum transfer is required for electronic transitions, units of eV.

Bulk modulus—Measure of materials' resistance to uniform compression, units of GPa.

Debye temperature—The temperature with which the highest normal mode of vibration occurs for a crystal, units of K.

Density—The mass per unit volume of a material or substance, units of g/cm³.

Effective mass—The effective mass is a quasi-particle's inertial mass that it appears to have when it is interacting with other similar particles or responding to applied forces. The effective mass is also considered a characteristic property of a material since particles move and interact differently within different materials, units of m_e^* (free electron mass). The effective mass is a tensor by definition and depends on momentum, energy, and band index of the quasi-particle, and individual tensor elements are real-valued and can be positive or negative.

Electrical breakdown field—A measure of how high of an electric field a given material can withstand before conducting charge. This corresponds to the peak electric field of a material, units of MV/cm.

Electron affinity—The amount of energy an electron needs in order to be excited from the conduction band minimum up to the vacuum level. It can also be considered as the amount of energy released when an electron is moved from the vacuum level to the bottom of the conduction band, units of eV.

Fundamental bandgap—Often referred to as the lowest direct band-to-band transition. The fundamental bandgap usually requires a variety of methods and techniques in order to determine since the excitonic contributions alter the results, units of eV.

High frequency dielectric constant—The dielectric constant of a material under high frequency conditions, unit-less parameter. This parameter is usually understood to be measured at frequencies far above the phonon mode bands and far below the onset of absorption at the fundamental band to band transition such that dispersion from both processes—phonon mode absorption and band-to-band transitions—can be ignored. Typically, for most oxides, this range is in the near IR spectral region, below 1 and above 0.2 eV.

Melting point—The temperature with which a material, element, or substance will transition from solid to liquid. Multicomponent systems may undergo solidification across a temperature range determined by the phase diagram solidus and liquidus (e.g., alloys of AlGaO). At this temperature, the solid and liquid phases exist in equilibrium, units of °C or K.

Mobility—The measure of a charged carrier saturation velocity for a given applied electric field. Determined by charge carrier scattering due to multiple mechanisms such as impurity scattering and phonon scattering. High quality material with few defects produces charge carrier mobilities limited by intrinsic factors. Units of cm²/(V s).

Optical bandgap—Photons of a selected frequency are used to help excite electrons from the valence band to the conduction band. The energy of the exciton determines the onset of the transition between vertical intrabands, units of eV.

Phonon mode—An elementary vibrational motion of atoms in a crystal lattice uniformly oscillating at a single frequency.

Specific heat—How much heat is required in order to raise the temperature of a unit mass or quantity for a material or substance by one degree. This amount is usually one degree. Specific heat is found across literature in units of J/(mol K), cal/(mol K), cal/(g °C). Where possible, this review uses J/(gK) to represent units of specific heat.

Static dielectric constant—The dielectric constant of a material when under conditions such as low frequency or a constant electric field, unit-less parameter.

Thermal conductivity—The ability for a material or substance to conduct heat including electronic and phononic contributions, units of W/(m K).

Thermal diffusivity—Measure of the rate of heat transfer in a material from a cold point to a hot point. Related to the thermal conductivity by material constants of heat capacity and density. A high thermal diffusivity means that heat will transfer quickly. It can also be described as a material ability to conduct thermal energy relative to the ability to store thermal energy, units of mm²/s.

Coefficient of thermal expansion (CTE)—The amount of change in the length, area, or volume of a material when the temperature is changed. May be of unspecified dimension in the literature typically meaning the linear coefficient of thermal expansion, units of $\times 10^{-6}$ K⁻¹ (e.g., ppm K⁻¹).

APPENDIX B: GROWTH METHODS

Atomic layer deposition (ALD)—Atomic layer deposition is reported to have been discovered and developed twice over the course of the 1960s and 1970s. In the 1960s, Stanislav Koltsov and Valentin Aleksovsky of the Leningrad Technological Institute developed ALD by using the metal chloride reaction alongside water with silica to fabricate thin films. This process was named molecular layering.¹⁰⁸⁷ The second discovery, said to be independent of the first, was made by Tuomo Suntola in the mid-1970s. He developed this method as a way to produce and fabricate high quality thin films for electroluminescent displays. Suntola named his process atomic layer epitaxy (ALE).¹⁰⁸⁸ The first experiment that Suntola attempted with this process was the growth of ZnS using elemental Zn and S. Further advancements were made to the process when Suntola and his fellow researchers decided to switch from a high vacuum reactor to an inert gas reactor. The inert gas reactor allowed for the use of reactants such as hydrogen sulfide, water vapor, and metal chlorides.¹⁰⁸⁸ The name “atomic layer deposition” was suggested by Markku Leskelä at the ALE-1 conference in 1990. It took around 10 years for the name ALD to gain traction and acceptance.¹⁰⁸⁹

The process of ALD involves growing thin films by exposing a surface to gaseous precursors. These precursors flow within the reaction chamber as separate pulses, where no two precursors are ever present at the same time. During the pulse of each single precursor, the gaseous molecules begin to interact with the target surface. Once all of the reactive sites that are exposed on the surface have been consumed by the precursor, the reaction self-terminates. Typically, the chamber is then flushed and the alternate precursor pulse begins. A single ALD cycle occurs after the substrate has been exposed each precursor typically once. The number, duration, pressure, fill rate, and flush rates of ALD cycles and the precursor-surface interaction determine the thickness, uniformity, and precision of deposited material.¹⁰⁹⁰

Chemical vapor transport (CVT)—Chemical vapor transport was first seen in the literature around the early 1960s by Harold Schäfer after publishing his text on chemical transport reactions.¹⁰⁹¹ The process involves taking compounds and elements that are nonvolatile and converting them into volatile derivatives. The reactions and transport occur within a sealed reactor tube where there is a temperature gradient between the two ends of the reactor.

This temperature gradient is essential for the CVT process. The volatile derivative travels through the reactor from the heated starting point by way of a transport agent and moves freely toward the other side. Once reaching the other side of the reactor, the gaseous agent will undergo a reaction and form a solid that is deposited at that end of the reactor tube. CVT differs from chemical vapor deposition (see MOCVD) in that there is no need for the decomposition of a gaseous precursor.

Czochralski method (CZ)—The Czochralski method was invented by Jan Czochralski in 1916 in what could be called an accident. Instead of dipping his ink pen into an inkwell, he placed it into a crucible of molten tin that was left on a table to crystallize. Upon rapidly withdrawing the pen, he observed thin threads of tin that had solidified at the pen tip. This showed that crystallization could occur by pulling from a melt surface.¹⁰⁹² The now well researched growth method often utilizes an iridium or suitably inert crucible containing the desired melt typically heated via induction. A seed crystal is dipped into the melt, withdrawn and rotated at a specific rate unique to a given material. These rates also control the desired crystal diameter.¹⁰⁹³

Edge-defined film-fed growth (EFG)—EFG is a process that was developed in the mid-1960s by Harold LaBelle and Ed Mlavsky. The process involves using a die or shaper to control the crystal dimensions. A crucible holds the melt for the desired crystal and resides below the shaper. By utilizing capillary action, the melt material is driven upward through a small slit within the shaper. A seed crystal is placed in contact with the liquid melt that has risen through the slit. A crystal begins to form where the solid seed crystal touches the liquid melt. As the seed is pulled upward, the crystal begins to grow in size with more liquid melt being added.^{62,1093}

Float zone growth (FZ)—The float zone growth technique, sometimes referred to as vertical zone melting, was originally developed by William Gardner Pfann in the early 1950s at Bell Labs. His zone melting helped to control impurities within semiconductors such as germanium.¹⁰⁹⁴ The process was further improved a few years later in 1955 by Henry Theurer, another Bell Labs scientist. His modified method allowed for the purification of silicon, which required a higher melt temperature than germanium, which could not be obtained from Pfann's original method. Theurer called his method float-zone refining and involved clamping a rod of silicon at both ends and passing it through a vertical heating coil. Surface tension holds the molten segment in place between the solid portions of the rod.^{1095,1096} This method does not require the use of a crucible, which is often the source of many contaminants.

Flux growth method—The flux method for growing single crystals uses high temperature solutions. The flux in the process is often an oxide or molten salt that is used as a solvent. A substance that is used as a “flux” is commonly used in order to dissolve an oxide similar to soldering or to reduce the melting temperature.¹⁰⁹⁷ Due to the broad applications and long history of the flux growth method, it was not possible to track down a citable source on the origins or the inventors of this growth method.

Magnetron sputtering—Sputter deposition is often used to produce large quantities of thin films. Sputtering is also a form of physical vapor transport/deposition (PVT/PVD). Sputtering utilizes simple equipment that allows for large area coatings that have a strong adhesion. In the magnetron sputtering process, a sputtering

gas at low pressure, typically argon, is inserted into the chamber and energized into a plasma, wherein it is directed electromagnetically to impinge upon a target material producing spall and erosion of the target. The liberated atoms or small clusters are directed away from the target surface they originated from and travel toward and deposit onto the substrate. Common modifications include the use of an applied sample bias to increase the impingement energy of the atoms and clusters, thereby increasing density or adhesion as well as reactive gasses (e.g., oxygen or nitrogen) to control deposited material stoichiometry.¹⁰⁹⁸

Metalorganic chemical vapor deposition (MOCVD)—Metalorganic chemical vapor deposition (MOCVD) or metalorganic vapor-phase epitaxy (MOVPE) was first reported in the literature by H. M. Manasevit in the late 1960s. First in 1968, Manasevit reports on the use of chemical vapor deposition for the successful growth of GaAs single-crystals on other single-crystal insulating oxides. No mention of metalorganics was made in this publication.¹⁰⁹⁹ A year later in 1969, Manasevit *et al.* (Ref. 1100) used MOCVD to successfully grow single crystal films of GaAs, GaP, $\text{GaAs}_{1-x}\text{P}_x$, and $\text{GaAs}_{1-x}\text{Sb}_x$ onto GaAs. Decompositions of alkyl-gallium placed in the presence of phosphine, arsine, arsine-phosphine, and arsine-stibine were used. These findings showed the possibility of growing compound semiconductor films using MOCVD.¹¹⁰⁰ The MOCVD process uses ultra-pure precursor gases that are inserted into a reactor with a carrier gas. As the precursor gas approaches the wafer held inside the reaction chamber, pyrolysis occurs and the subspecies present in the gaseous precursor are adsorbed onto the substrate.

Molecular beam epitaxy (MBE)—Molecular beam epitaxy is another method for thin film deposition that was first invented in the 1960s by Bell Lab scientists Alfred Cho and J. R. Arthur. Prior to their credited invention, K. G. Günther was said to have had the original idea behind the MBE process after he deposited non epitaxial films onto glass substrates.¹¹⁰¹ Günther's method did yield successful epitaxial growth when John Davey and Titus Pankey grew GaAs films onto a GaAs single crystal. According to Davey *et al.* (Ref. 1102), the process was named vacuum evaporation. However, it was the advancements made by Cho and Arthur that propelled the MBE into the spotlight and earned them credits for inventing the process.¹¹⁰³

The MBE process occurs at high or ultra-high vacuum. Under these vacuum conditions, atoms will have a large mean free path and will be able to travel toward the substrate without being impeded. The substrate for the deposition is held on a heated holder and rotated for high uniformity. Effusion cells or chambers aimed at the substrate contain the materials for deposition. Heating coils around the effusion cells allow for precise temperature control. Each effusion cell has a shutter that prevents any excess material from being deposited. MBE is a slow but very precise deposition process. Accurate measures of layer thickness is obtained by electrons that are shot incident to the substrate using reflection high-energy electron diffraction (RHEED).

Optical float zone—Optical float zone growth of single crystals is similar to the float zone growth mentioned above. The only major difference is the heating method. An optical heating method is applied since other methods such as RF or electron beam heating require close coupling to the material of either an RF coil, also

requiring absorbing material or an electron gun source requiring vacuum. The process of using a carbon arc along with elliptical mirrors made crystal growth of magnesium ferrite and sapphire more feasible.¹¹⁰⁴

Physical vapor transport (PVT)—Physical vapor transport or physical vapor deposition (PVD) can be used for both single-crystal and thin film growth. PVT can be considered a broad classification for a variety of deposition methods that occur under vacuum conditions. Examples include pulsed laser deposition, sputter deposition, evaporative deposition, and cathodic arc deposition. The basic process involves taking a starting solid material and transforming it into a vapor or gas phase before eventually returning it to a solid phase. The resultant solid phase will have a change in physical morphology. The starting material is turned into the gas phase by various methods of evaporation. One major disadvantage of PVT/PVD is that once the source material is vaporized and transported it will be deposited on many surfaces within the vacuum chamber, not just the target substrate. However, this disadvantage is often outweighed by the plethora of advantages that PVT/PVD offers such as a wide range of possible coating materials, a wide range of specific methods of application, lack of potentially toxic chemicals or solvents, and coatings that are often durable and resistant to high temperatures.

Pulsed laser deposition (PLD)—Pulsed laser deposition is a specific form of physical vapor transport/deposition (PVT/PVD). According to Mihaleescu *et al.* (Ref. 1105), the first intentional attempt at deposition via a laser-ablated substance was not until the mid-1960s when Smith *et al.* (Ref. 1106) used a ruby laser to deposit CdTe, ZnTe, PbTe, and other various films. The attempt was met with disappointment as the samples were of poor quality and uniformity. It was not until the development of high quality lasers in the 1970s and 1980s that PLD began to gain traction. Newer lasers had the ability to deliver high intensity, shorter pulses on the nano-to femtosecond range. UV lasers also provided great improvement for ablation, and thus allowed for congruent vaporization. From these advancements, it was now possible to transfer a stoichiometric substance from the target or to control the chemical reactions to improve deposition uniformity.¹¹⁰⁵ The process involves focusing a laser onto a target containing the substance desired for deposition. In vacuum, the laser vaporizes the target where a plasma plume carries the vaporized material to the substrate for deposition. A high vacuum or background gas, such as oxygen, is required for this deposition process. Many complications beyond the scope of this review occur from the laser interaction with the target and the ejected species.

Spray pyrolysis—According to Mooney *et al.* (Ref. 1107), spray pyrolysis was first reported in 1966 by Chamberlin *et al.* (Ref. 1108). In the same year, they proceeded to use their new technique called chemical spray deposition in order to fabricate CdS solar cells.¹¹⁰⁹ The process of spray pyrolysis involves spraying a solution from an atomizer onto a heated surface. A chemical compound is then formed. Any component of the solution that is not desired for the thin film growth is chosen so that it is volatile under the temperature conditions for the given deposition. The deposition temperature is important as it plays a role in numerous processes, including the aerosol generation, transport, solvent evaporation, precursor decomposition, and droplet impact. Film morphology is usually determined by the substrate temperature.¹¹¹⁰

Verneuil method—The Verneuil method for crystal growth (often called flame fusion) is considered to be the first commercially successful method for growing gemstones. The process is named after A. V. L. Verneuil himself who published his flame fusion technique in 1902 after synthesizing ruby.²⁹⁷ The Verneuil method was created to solve the issue of achieving the high melting point of alumina at over 2000 °C. Verneuil solved this issue by only heating and melting a small portion or volume of the material. The technique involves an inverted oxy-hydrogen burner that heats the top of a pile of alumina powder. The flame causes the powder to fuse and begin a seed crystal. More powder is inserted into the gas stream often containing oxygen. The powder travels down a tube toward the flame which causes it to melt into droplets fusing onto the seed crystal. As the amount of droplets continues to build up on the seed crystal, the rod is lowered. This allows for existing drops to crystallize upon the seed while the droplets nearest the flame remain liquid. The liquid–solid phase boundary can be kept at a steady and continuous height within the flame if the crystal retraction rates and powder flow are balanced.^{1093,1111}

REFERENCES

- ¹R. E. Newnham, *Properties of Materials: Anisotropy, Symmetry, Structure* (Oxford University Press, 2005).
- ²K. Momma and F. Izumi, “Vesta 3 for three-dimensional visualization of crystal, volumetric and morphology data,” *J. Appl. Crystallogr.* **44**, 1272–1276 (2011).
- ³H. Jones and N. Chako, “The theory of Brillouin zones and electronic states in crystals,” *Phys. Today* **15**(1), 66 (1962).
- ⁴F. Bassani, G. P. Parravicini, R. A. Ballinger, and J. L. Birman, “Electronic states and optical transitions in solids,” *Phys. Today* **29**(3), 58 (1976).
- ⁵M. Cardona and Y. Y. Peter, *Fundamentals of Semiconductors* (Springer, 2005).
- ⁶D. Smith and C. Mailhiot, “Theory of semiconductor superlattice electronic structure,” *Rev. Mod. Phys.* **62**, 173 (1990).
- ⁷M. Burt, “An exact formulation of the envelope function method for the determination of electronic states in semiconductor microstructures,” *Semicond. Sci. Technol.* **3**, 739 (1988).
- ⁸H. Dong, S. Long, H. Sun, X. Zhao, Q. He, Y. Qin, G. Jian, X. Zhou, Y. Yu, W. Guo, W. Xiong, W. Hao, Y. Zhang, H. Xue, X. Xiang, Z. Yu, H. Lv, Q. Liu, and M. Liu, “Fast switching β -Ga₂O₃ power MOSFET with a trench-gate structure,” *IEEE Electron Device Lett.* **40**, 1385–1388 (2019).
- ⁹P. Mukhopadhyay and W. V. Schoenfeld, “High responsivity tin gallium oxide schottky ultraviolet photodetectors,” *J. Vac. Sci. Technol. A* **38**, 013403 (2020).
- ¹⁰X. Chen, F. Ren, S. Gu, and J. Ye, “Review of gallium-oxide-based solar-blind ultraviolet photodetectors,” *Photonics Res.* **7**, 381–415 (2019).
- ¹¹D. Zhang, Z. Du, M. Ma, W. Zheng, S. Liu, and F. Huang, “Enhanced performance of solar-blind ultraviolet photodetector based on Mg-doped amorphous gallium oxide film,” *Vacuum* **159**, 204–208 (2019).
- ¹²A. J. Green, K. D. Chabak, M. Baldini, N. Moser, R. Gilbert, R. C. Fitch, G. Wagner, Z. Galazka, J. McCandless, A. Crespo, K. Leedy, and G. H. Jessen, “ β -Ga₂O₃ MOSFETs for radio frequency operation,” *IEEE Electron Device Lett.* **38**, 790–793 (2017).
- ¹³A. V. Almaev, E. V. Chernikov, N. A. Davletkildeev, and D. V. Sokolov, “Oxygen sensors based on gallium oxide thin films with addition of chromium,” *Superlattices Microstruct.* **139**, 106392 (2020).
- ¹⁴S. Pearton, J. Yang, P. H. Cary, I. V. F. Ren, J. Kim, M. J. Tadjer, and M. A. Mastro, “A review of Ga₂O₃ materials, processing, and devices,” *Appl. Phys. Rev.* **5**, 011301 (2018).
- ¹⁵R. Roy, V. Hill, and E. Osborn, “Polymorphism of Ga₂O₃ and the system Ga₂O₃–H₂O,” *J. Am. Chem. Soc.* **74**, 719–722 (1952).
- ¹⁶I. Cora, F. Mezzadri, F. Boschi, M. Bosi, M. Čaplovicová, G. Calestani, I. Dódony, B. Pécz, and R. Fornari, “The real structure of ε -Ga₂O₃ and its relation to κ -phase,” *CrystEngComm* **19**, 1509–1516 (2017).

- ¹⁷M. Kneiß, A. Hassa, D. Splith, C. Sturm, H. Von Wenckstern, T. Schultz, N. Koch, M. Lorenz, and M. Grundmann, "Tin-assisted heteroepitaxial PLD-growth of $\kappa\text{-Ga}_2\text{O}_3$ thin films with high crystalline quality," *APL Mater.* **7**, 022516 (2019).
- ¹⁸S. Stepanov, V. Nikolaev, V. Bougov, and A. Romanov, "Gallium oxide: Properties and applications—A review," *Rev. Adv. Mater. Sci.* **44**, 63–86 (2016).
- ¹⁹H. He, R. Orlando, M. A. Blanco, R. Pandey, E. Amzallag, I. Baraille, and M. Rérat, "First-principles study of the structural, electronic, and optical properties of Ga_2O_3 in its monoclinic and hexagonal phases," *Phys. Rev. B* **74**, 195123 (2006).
- ²⁰S. Yoshioka, H. Hayashi, A. Kuwabara, F. Oba, K. Matsunaga, and I. Tanaka, "Structures and energetics of Ga_2O_3 polymorphs," *J. Phys.: Condens. Matter* **19**, 346211 (2007).
- ²¹M. Marezio and J. Remeika, "Bond lengths in the $\alpha\text{-Ga}_2\text{O}_3$ structure and the high-pressure phase of $\text{Ga}_{2-x}\text{Fe}_x\text{O}_3$," *J. Chem. Phys.* **46**, 1862–1865 (1967).
- ²²M. Zinkevich, F. M. Morales, H. Nitsche, M. Ahrens, M. Rühle, and F. Aldinger, "Microstructural and thermodynamic study of $\gamma\text{-Ga}_2\text{O}_3$," *Z. Metallkunde* **95**, 756–762 (2004).
- ²³K. Pohl, "Hydrothermale bildung von $\gamma\text{-Ga}_2\text{O}_3$," *Naturwissenschaften* **55**, 82–82 (1968).
- ²⁴C. O. Areán, A. L. Bellan, M. P. Mentruit, M. R. Delgado, and G. T. Palomino, "Preparation and characterization of mesoporous $\gamma\text{-Ga}_2\text{O}_3$," *Microporous Mesoporous Mater.* **40**, 35–42 (2000).
- ²⁵T. Oshima, T. Nakazono, A. Mukai, and A. Ohtomo, "Epitaxial growth of $\gamma\text{-Ga}_2\text{O}_3$ films by MIST chemical vapor deposition," *J. Cryst. Growth* **359**, 60–63 (2012).
- ²⁶H. Y. Playford, A. C. Hannon, E. R. Barney, and R. I. Walton, "Structures of uncharacterised polymorphs of gallium oxide from total neutron diffraction," *Chemistry* **19**, 2803–2813 (2013).
- ²⁷M. Zinkevich and F. Aldinger, "Thermodynamic assessment of the gallium-oxygen system," *J. Am. Ceram. Soc.* **87**, 683–691 (2004).
- ²⁸S.-D. Guo and H.-M. Du, "Piezoelectric properties of Ga_2O_3 : A first-principle study," *Eur. Phys. J. B* **93**, 7 (2020).
- ²⁹C. T. Prewitt, R. D. Shannon, D. B. Rogers, and A. W. Sleight, "C rare earth oxide-corundum transition and crystal chemistry of oxides having the corundum structure," *Inorg. Chem.* **8**, 1985–1993 (1969).
- ³⁰M. Feneberg, J. Bläsing, T. Sekiyama, K. Ota, K. Akaiwa, K. Ichino, and R. Goldhahn, "Anisotropic phonon properties and effective electron mass in $\alpha\text{-Ga}_2\text{O}_3$," *Appl. Phys. Lett.* **114**, 142102 (2019).
- ³¹Z. Cheng, M. Hanke, P. Vogt, O. Bierwagen, and A. Trampert, "Phase formation and strain relaxation of Ga_2O_3 on c-plane and a-plane sapphire substrates as studied by synchrotron-based x-ray diffraction," *Appl. Phys. Lett.* **111**, 162104 (2017).
- ³²J. Åhman, G. Svensson, and J. Albertsson, "A reinvestigation of β -gallium oxide," *Acta Crystallogr. Sect. C* **52**, 1336–1338 (1996).
- ³³H. He, M. A. Blanco, and R. Pandey, "Electronic and thermodynamic properties of $\beta\text{-Ga}_2\text{O}_3$," *Appl. Phys. Lett.* **88**, 261904 (2006).
- ³⁴J. Böhm, "Über galliumoxyd und-hydroxyd," *Angew. Chem.* **53**, 131 (1940).
- ³⁵J. Kohn, G. Katz, and J. Broder, "Characterization of $\beta\text{-Ga}_2\text{O}_3$ and its alumina isomorph, $\theta\text{-Al}_2\text{O}_3$," *Am. Miner.* **42**, 398–407 (1957).
- ³⁶S. Geller, "Crystal structure of $\beta\text{-Ga}_2\text{O}_3$," *J. Chem. Phys.* **33**, 676–684 (1960).
- ³⁷G. Wolten and A. Chase, "Determination of the point group of $\beta\text{-Ga}_2\text{O}_3$ from morphology and physical properties," *J. Solid State Chem.* **16**, 377–383 (1976).
- ³⁸S. Geller, "On the structure of $\beta\text{-Ga}_2\text{O}_3$," *J. Solid State Chem.* **20**, 209–210 (1977).
- ³⁹Z. Guo, A. Verma, X. Wu, F. Sun, A. Hickman, T. Masui, A. Kuramata, M. Higashiwaki, D. Jena, and T. Luo, "Anisotropic thermal conductivity in single crystal β -gallium oxide," *Appl. Phys. Lett.* **106**, 111909 (2015).
- ⁴⁰S. Pearton, F. Ren, M. Tadjer, and J. Kim, "Perspective: Ga_2O_3 for ultra-high power rectifiers and MOSFETs," *J. Appl. Phys.* **124**, 220901 (2018).
- ⁴¹W. Mu, Z. Jia, Y. Yin, Q. Hu, Y. Li, B. Wu, J. Zhang, and X. Tao, "High quality crystal growth and anisotropic physical characterization of $\beta\text{-Ga}_2\text{O}_3$ single crystals grown by EFG method," *J. Alloys Compd.* **714**, 453–458 (2017).
- ⁴²S. Knight, A. Mock, R. Korlacki, V. Darakchieva, B. Monemar, Y. Kumagai, K. Goto, M. Higashiwaki, and M. Schubert, "Electron effective mass in Sn-doped monoclinic single crystal β -gallium oxide determined by mid-infrared optical hall effect," *Appl. Phys. Lett.* **112**, 012103 (2018).
- ⁴³A. Fiedler, R. Schewski, Z. Galazka, and K. Irmscher, "Static dielectric constant of $\beta\text{-Ga}_2\text{O}_3$ perpendicular to the principal planes (100), (010), and (001)," *ECS J. Solid State Sci. Technol.* **8**, Q3083 (2019).
- ⁴⁴M. Schubert, R. Korlacki, S. Knight, T. Hofmann, S. Schöche, V. Darakchieva, E. Janzén, B. Monemar, D. Gogova, Q.-T. Thieu, R. Togashi, H. Murakami, Y. Kumagai, K. Goto, A. Kuramata, S. Yamakoshi, and M. Higashiwaki, "Anisotropy, phonon modes, and free charge carrier parameters in monoclinic β -gallium oxide single crystals," *Phys. Rev. B* **93**, 125209 (2016).
- ⁴⁵F. Orlando, F. Mezzadri, G. Calestani, F. Boschi, and R. Fornari, "Thermal expansion coefficients of $\beta\text{-Ga}_2\text{O}_3$ single crystals," *Appl. Phys. Express* **8**, 111101 (2015).
- ⁴⁶J. Remeika, U.S. patent 3075831 (January 29, 1963).
- ⁴⁷A. Chase, "Growth of $\beta\text{-Ga}_2\text{O}_3$ by the Verneuil technique," *J. Am. Ceram. Soc.* **47**, 470 (1964).
- ⁴⁸M. Lorenz, J. Woods, and R. Gambino, "Some electrical properties of the semiconductor $\beta\text{-Ga}_2\text{O}_3$," *J. Phys. Chem. Solids* **28**, 403–404 (1967).
- ⁴⁹T. Matsumoto, M. Aoki, A. Kinoshita, and T. Aono, "Absorption and reflection of vapor grown single crystal platelets of $\beta\text{-Ga}_2\text{O}_3$," *Jpn. J. Appl. Phys., Part 1* **13**, 1578 (1974).
- ⁵⁰H. Juskowiak and A. Pajaczkowska, "Chemical transport of $\beta\text{-Ga}_2\text{O}_3$ using chlorine as a transporting agent," *J. Mater. Sci.* **21**, 3430–3434 (1986).
- ⁵¹A. Pajaczkowska and H. Juskowiak, "On the chemical transport of gallium oxide in the $\text{Ga}_2\text{O}_3/\text{H}-\text{Cl}$ system," *J. Mater. Sci.* **21**, 3435–3439 (1986).
- ⁵²V. Vasiltsov and Y. Zakarko, *Zh. Prikl. Spektrosk.* **39**, 423–428 (1983).
- ⁵³Y. Tomm, P. Reiche, D. Klimm, and T. Fukuda, "Czochralski grown Ga_2O_3 crystals," *J. Cryst. Growth* **220**, 510–514 (2000).
- ⁵⁴Z. Galazka, R. Uecker, K. Irmscher, M. Albrecht, D. Klimm, M. Pietsch, M. Brützam, R. Bertram, S. Ganschow, and R. Fornari, "Czochralski growth and characterization of $\beta\text{-Ga}_2\text{O}_3$ single crystals," *Cryst. Res. Technol.* **45**, 1229–1236 (2010).
- ⁵⁵Z. Galazka, K. Irmscher, R. Uecker, R. Bertram, M. Pietsch, A. Kwasniewski, M. Naumann, T. Schulz, R. Schewski, D. Klimm, and M. Bickermann, "On the bulk $\beta\text{-Ga}_2\text{O}_3$ single crystals grown by the Czochralski method," *J. Cryst. Growth* **404**, 184–191 (2014).
- ⁵⁶Z. Galazka, R. Uecker, D. Klimm, K. Irmscher, M. Naumann, M. Pietsch, A. Kwasniewski, R. Bertram, S. Ganschow, and M. Bickermann, "Scaling-up of bulk $\beta\text{-Ga}_2\text{O}_3$ single crystals by the Czochralski method," *ECS J. Solid State Sci. Technol.* **6**, Q3007 (2016).
- ⁵⁷K. Irmscher, Z. Galazka, M. Pietsch, R. Uecker, and R. Fornari, "Electrical properties of $\beta\text{-Ga}_2\text{O}_3$ single crystals grown by the Czochralski method," *J. Appl. Phys.* **110**, 063720 (2011).
- ⁵⁸V. Vasiltsov, Y. I. Rym, and Y. M. Zakharko, "Optical absorption and photoconductivity at the band edge of $\beta\text{-Ga}_{2-x}\text{In}_x\text{O}_3$," *Phys. Status Solidi (b)* **195**, 653–658 (1996).
- ⁵⁹N. Ueda, H. Hosono, R. Waseda, and H. Kawazoe, "Anisotropy of electrical and optical properties in $\beta\text{-Ga}_2\text{O}_3$ single crystals," *Appl. Phys. Lett.* **71**, 933–935 (1997).
- ⁶⁰Y. Tomm, J. Ko, A. Yoshikawa, and T. Fukuda, "Floating zone growth of $\beta\text{-Ga}_2\text{O}_3$: A new window material for optoelectronic device applications," *Sol. Energy Mater. Solar cells* **66**, 369–374 (2001).
- ⁶¹E. G. Villora, K. Shimamura, Y. Yoshikawa, K. Aoki, and N. Ichinose, "Large-size $\beta\text{-Ga}_2\text{O}_3$ single crystals and wafers," *J. Cryst. Growth* **270**, 420–426 (2004).
- ⁶²H. Aida, K. Nishiguchi, H. Takeda, N. Aota, K. Sunakawa, and Y. Yaguchi, "Growth of $\beta\text{-Ga}_2\text{O}_3$ single crystals by the edge-defined, film fed growth method," *Jpn. J. Appl. Phys.* **47**, 8506 (2008).
- ⁶³A. Kuramata, K. Koshi, S. Watanabe, Y. Yamaoka, T. Masui, and S. Yamakoshi, "High-quality $\beta\text{-Ga}_2\text{O}_3$ single crystals grown by edge-defined film-fed growth," *Jpn. J. Appl. Phys.* **55**, 1202A2 (2016).
- ⁶⁴N. Ueda, H. Hosono, R. Waseda, and H. Kawazoe, "Synthesis and control of conductivity of ultraviolet transmitting $\beta\text{-Ga}_2\text{O}_3$ single crystals," *Appl. Phys. Lett.* **70**, 3561–3563 (1997).
- ⁶⁵Z. Galazka, S. Ganschow, A. Fiedler, R. Bertram, D. Klimm, K. Irmscher, R. Schewski, M. Pietsch, M. Albrecht, and M. Bickermann, "Doping of

- Czochralski-grown bulk β -Ga₂O₃ single crystals with Cr, Ce and Al," *J. Cryst. Growth* **486**, 82–90 (2018).
- ⁶⁶J. B. Varley, J. R. Weber, A. Janotti, and C. G. Van de Walle, "Oxygen vacancies and donor impurities in β -Ga₂O₃," *Appl. Phys. Lett.* **97**, 142106 (2010).
- ⁶⁷Z. Galazka, K. Irmscher, R. Schewski, I. M. Hanke, M. Pietsch, S. Ganschow, D. Klimm, A. Dittmar, A. Fiedler, T. Schroeder, and M. Bickermann, "Czochralski-grown bulk β -Ga₂O₃ single crystals doped with mono-, di-, tri-, and tetravalent ions," *J. Cryst. Growth* **529**, 125297 (2020).
- ⁶⁸T. Oshima, T. Okuno, and S. Fujita, "Ga₂O₃ thin film growth on c-plane sapphire substrates by molecular beam epitaxy for deep-ultraviolet photodetectors," *Jpn. J. Appl. Phys., Part 1* **46**, 7217 (2007).
- ⁶⁹T. Kawaharamura, G. T. Dang, and M. Furuta, "Successful growth of conductive highly crystalline Sn-doped α -Ga₂O₃ thin films by fine-channel MIST chemical vapor deposition," *Jpn. J. Appl. Phys., Part 1* **51**, 040207 (2012).
- ⁷⁰M. Razeghi, J.-H. Park, R. McClintock, D. Pavlidis, F. H. Teherani, D. J. Rogers, B. A. Magill, G. A. Khodaparast, Y. Xu, J. Wu, and V. P. Dravid, "A review of the growth, doping, and applications of beta-Ga₂O₃ thin films," *Proc. SPIE* **10533**, 105330R (2018).
- ⁷¹K. Sasaki, A. Kuramata, T. Masui, E. G. Villora, K. Shimamura, and S. Yamakoshi, "Device-quality β -Ga₂O₃ epitaxial films fabricated by ozone molecular beam epitaxy," *Appl. Phys. Express* **5**, 035502 (2012).
- ⁷²H. Okumura, M. Kita, K. Sasaki, A. Kuramata, M. Higashiwaki, and J. S. Speck, "Systematic investigation of the growth rate of β -Ga₂O₃ (010) by plasma-assisted molecular beam epitaxy," *Appl. Phys. Express* **7**, 095501 (2014).
- ⁷³N. Moser, J. McCandless, A. Crespo, K. Leedy, A. Green, A. Neal, S. Mou, E. Ahmadi, J. Speck, K. Chabak, N. Peixoto, and G. Jessen, "Ge-doped β -Ga₂O₃ MOSFETs," *IEEE Electron Device Lett.* **38**, 775–778 (2017).
- ⁷⁴R. K. Ramachandran, J. Dendooven, J. Botterman, S. P. Sree, D. Poelman, J. A. Martens, H. Poelman, and C. Detavernier, "Plasma enhanced atomic layer deposition of Ga₂O₃ thin films," *J. Mater. Chem. A* **2**, 19232–19238 (2014).
- ⁷⁵V. D. Wheeler, N. Nepal, D. R. Boris, S. B. Qadri, L. O. Nyakiti, A. Lang, A. Koehler, G. Foster, S. G. Walton, C. R. Eddy, Jr., and D. J. Meyer, "Phase control of crystalline Ga₂O₃ films by plasma-enhanced atomic layer deposition," *Chem. Mater.* **32**, 1140–1152 (2020).
- ⁷⁶Y. Zhang, F. Alema, A. Mauze, O. S. Koksaldi, R. Miller, A. Osinsky, and J. S. Speck, "MOCVD grown epitaxial β -Ga₂O₃ thin film with an electron mobility of 176 cm²/V s at room temperature," *APL Mater.* **7**, 022506 (2019b).
- ⁷⁷F. Alema, B. Hertog, A. Osinsky, P. Mukhopadhyay, M. Toporkov, and W. V. Schoenfeld, "Fast growth rate of epitaxial β -Ga₂O₃ by close coupled shower-head MOCVD," *J. Cryst. Growth* **475**, 77–82 (2017).
- ⁷⁸H. Murakami, K. Nomura, K. Goto, K. Sasaki, K. Kawara, Q. T. Thieu, R. Togashi, Y. Kumagai, M. Higashiwaki, A. Kuramata, S. Yamakoshi, B. Monemar, and A. Koukitu, "Homoepitaxial growth of β -Ga₂O₃ layers by halide vapor phase epitaxy," *Appl. Phys. Express* **8**, 015503 (2014).
- ⁷⁹N. Blumenschein, T. Paskova, and J. F. Muth, "Effect of growth pressure on PLD-deposited gallium oxide thin films for deep-UV photodetectors," *Phys. Status Solidi (a)* **216**, 1900098 (2019).
- ⁸⁰F. Shan, G. Liu, W. Lee, G. Lee, I. Kim, and B. Shin, "Structural, electrical, and optical properties of transparent gallium oxide thin films grown by plasma-enhanced atomic layer deposition," *J. Appl. Phys.* **98**, 023504 (2005).
- ⁸¹Z. Hajnal, J. Miró, G. Kiss, F. Réti, P. Déák, R. C. Herndon, and J. M. Kuperberg, "Role of oxygen vacancy defect states in the n-type conduction of β -Ga₂O₃," *J. Appl. Phys.* **86**, 3792–3796 (1999).
- ⁸²K. Yamaguchi, "First principles study on electronic structure of β -Ga₂O₃," *Solid state Commun.* **131**, 739–744 (2004).
- ⁸³L. Zhang, J. Yan, Y. Zhang, T. Li, and X. Ding, "First-principles study on electronic structure and optical properties of n-doped p-type β -Ga₂O₃," *Sci. China Phys.* **55**, 19–24 (2012).
- ⁸⁴J. B. Varley and A. Schleife, "Bethe-Salpeter calculation of optical-absorption spectra of In₂O₃ and Ga₂O₃," *Semicond. Sci. Technol.* **30**, 024010 (2015).
- ⁸⁵H. Peelaers and C. G. Van de Walle, "Brillouin zone and band structure of β -Ga₂O₃," *Phys. Status Solidi (b)* **252**, 828–832 (2015).
- ⁸⁶A. Mock, R. Korlacki, C. Briley, V. Darakchieva, B. Monemar, Y. Kumagai, K. Goto, M. Higashiwaki, and M. Schubert, "Band-to-band transitions, selection rules, effective mass, and excitonic contributions in monoclinic β -Ga₂O₃," *Phys. Rev. B* **96**, 245205 (2017).
- ⁸⁷C. Janowitz, V. Scherer, M. Mohamed, A. Krapf, H. Dwelk, R. Manzke, Z. Galazka, R. Uecker, K. Irmscher, R. Fornari, M. Michling, D. Schmeißer, J. R. Weber, J. B. Varley, and C. G. Van de Walle, "Experimental electronic structure of In₂O₃ and Ga₂O₃," *New J. Phys.* **13**, 085014 (2011).
- ⁸⁸S. Mu, H. Peelaers, Y. Zhang, M. Wang, and C. G. Van de Walle, "Orientation-dependent band offsets between (Al_xGa_{1-x})₂O₃ and Ga₂O₃," *Appl. Phys. Lett.* **117**, 252104 (2020).
- ⁸⁹E. Ahmadi, Y. Oshima, F. Wu, and J. S. Speck, "Schottky barrier height of Ni to β -(Al_xGa_{1-x})₂O₃ with different compositions grown by plasma-assisted molecular beam epitaxy," *Semicond. Sci. Technol.* **32**, 035004 (2017).
- ⁹⁰A. Kumar, K. Ghosh, and U. Singisetty, "Low field transport calculation of 2-dimensional electron gas in β -(Al_xGa_{1-x})₂O₃/Ga₂O₃ heterostructures," *J. Appl. Phys.* **128**, 105703 (2020).
- ⁹¹M. Feneberg, M. Winkler, K. Lange, M. Wieneke, H. Witte, A. Dadgar, and R. Goldhahn, "Valence band tomography of wurtzite GaN by spectroscopic ellipsometry," *Appl. Phys. Express* **11**, 101001 (2018).
- ⁹²J. Furthmüller and F. Bechstedt, "Quasiparticle bands and spectra of Ga₂O₃ polymorphs," *Phys. Rev. B* **93**, 115204 (2016).
- ⁹³F. Bechstedt, *Many-Body Approach to Electronic Excitations* (Springer, 2016).
- ⁹⁴C. Sturm, R. Schmidt-Grund, C. Kranert, J. Furthmüller, F. Bechstedt, and M. Grundmann, "Dipole analysis of the dielectric function of color dispersive materials: Application to monoclinic Ga₂O₃," *Phys. Rev. B* **94**, 035148 (2016).
- ⁹⁵T. Onuma, S. Saito, K. Sasaki, T. Masui, T. Yamaguchi, T. Honda, and M. Higashiwaki, "Valence band ordering in β -Ga₂O₃ studied by polarized transmittance and reflectance spectroscopy," *Jpn. J. Appl. Phys., Part 1* **54**, 112601 (2015).
- ⁹⁶H. Tippins, "Optical absorption and photoconductivity in the band edge of β -Ga₂O₃," *Phys. Rev.* **140**, A316 (1965).
- ⁹⁷M. Rebien, W. Henrion, M. Hong, J. Mannaerts, and M. Fleischer, "Optical properties of gallium oxide thin films," *Appl. Phys. Lett.* **81**, 250–252 (2002).
- ⁹⁸P. Wu, Y. Gao, R. Kershaw, K. Dwight, and A. Wold, "Growth and characterization of gallium (iii) oxide films," *Mater. Res. Bull.* **25**, 357–363 (1990).
- ⁹⁹M. Orita, H. Ohta, M. Hirano, and H. Hosono, "Deep-ultraviolet transparent conductive β -Ga₂O₃ thin films," *Appl. Phys. Lett.* **77**, 4166–4168 (2000).
- ¹⁰⁰J. Manifacier, J. Gasiot, and J. Fillard, "A simple method for the determination of the optical constants n, k and the thickness of a weakly absorbing thin film," *J. Phys. E* **9**, 1002 (1976).
- ¹⁰¹A. Ortiz, J. Alonso, E. Andrade, and C. Urbiola, "Structural and optical characteristics of gallium oxide thin films deposited by ultrasonic spray pyrolysis," *J. Electrochem. Soc.* **148**, F26 (2001).
- ¹⁰²D.-W. Choi, K.-B. Chung, and J.-S. Park, "Low temperature Ga₂O₃ atomic layer deposition using gallium tri-isopropoxide and water," *Thin Solid Films* **546**, 31–34 (2013).
- ¹⁰³Y. Kang, K. Krishnaswamy, H. Peelaers, and C. G. Van de Walle, "Fundamental limits on the electron mobility of β -Ga₂O₃," *J. Phys.: Condens. Matter* **29**, 234001 (2017).
- ¹⁰⁴H.-G. Kim and W.-T. Kim, "Optical properties of β -Ga₂O₃ and α -Ga₂O₃: Co thin films grown by spray pyrolysis," *J. Appl. Phys.* **62**, 2000–2002 (1987).
- ¹⁰⁵J. Pankove, *Optical Processes on Semiconductors* (Dover Publication, New York, 1971).
- ¹⁰⁶J. Hao and M. Cocivera, "Optical and luminescent properties of undoped and rare-earth-doped Ga₂O₃ thin films deposited by spray pyrolysis," *J. Phys. D: Appl. Phys.* **35**, 433 (2002).
- ¹⁰⁷F. Ricci, F. Boschi, A. Baraldi, A. Filippetti, M. Higashiwaki, A. Kuramata, V. Fiorentini, and R. Fornari, "Theoretical and experimental investigation of optical absorption anisotropy in β -Ga₂O₃," *J. Phys.: Condens. Matter* **28**, 224005 (2016).
- ¹⁰⁸P. Lautenschlager, M. Garriga, S. Logothetidis, and M. Cardona, "Interband critical points of GaAs and their temperature dependence," *Phys. Rev. B* **35**, 9174–9189 (1987).
- ¹⁰⁹S. Rafique, L. Han, S. Mou, and H. Zhao, "Temperature and doping concentration dependence of the energy band gap in β -Ga₂O₃ thin films grown on sapphire," *Opt. Mater. Express* **7**, 3561–3570 (2017).
- ¹¹⁰A. Mock, J. VanDerslice, R. Korlacki, J. A. Woollam, and M. Schubert, "Elevated temperature dependence of the anisotropic visible-to-ultraviolet

- dielectric function of monoclinic β -Ga₂O₃,” *Appl. Phys. Lett.* **112**, 041905 (2018).
- ¹¹¹C. Sturm, R. Schmidt-Grund, V. Zviagin, and M. Grundmann, “Temperature dependence of the dielectric tensor of monoclinic Ga₂O₃ single crystals in the spectral range 1.0–8.5 eV,” *Appl. Phys. Lett.* **111**, 082102 (2017).
- ¹¹²D. Machon, P. F. McMillan, B. Xu, and J. Dong, “High-pressure study of the β -to- α transition in Ga₂O₃,” *Phys. Rev. B* **73**, 094125 (2006).
- ¹¹³K. E. Lipinska-Kalita, P. E. Kalita, O. A. Hemmers, and T. Hartmann, “Equation of state of gallium oxide to 70 GPa: Comparison of quasihydrostatic and nonhydrostatic compression,” *Phys. Rev. B* **77**, 094123 (2008).
- ¹¹⁴V. Hill, R. Roy, and E. Osborn, “The system alumina-gallia-water,” *J. Am. Ceram. Soc.* **35**, 135–142 (1952).
- ¹¹⁵See <http://www.tamura-ss.co.jp/en/release/20131122/pdf/150210.pdf> for Tamura Corporation.
- ¹¹⁶H. V. Wartenberg and H. Reusch, “Schmelzdiagramme höchstfeuerfester oxyde. IV. (aluminiumoxyd),” *Z. Anorg. Allg. Chem.* **207**, 1–20 (1932).
- ¹¹⁷E. G. Villora, S. Arjoca, K. Shimamura, D. Inomata, and K. Aoki, “ β -Ga₂O₃ and single-crystal phosphors for high-brightness white LEDs and LDS, and β -Ga₂O₃ potential for next generation of power devices,” *Proc. SPIE* **8987**, 89871U (2014).
- ¹¹⁸D. R. Lide, *Handbook of Chemistry and Physics*, 84th ed. (CRC, 2003), Vol. 84.
- ¹¹⁹M. A. Mastro, A. Kuramata, J. Calkins, J. Kim, F. Ren, and S. Pearton, “Perspective-opportunities and future directions for Ga₂O₃,” *ECS J. Solid State Sci. Technol.* **6**, P356 (2017).
- ¹²⁰E. G. Villora, K. Shimamura, T. Ujiie, and K. Aoki, “Electrical conductivity and lattice expansion of β -Ga₂O₃ below room temperature,” *Appl. Phys. Lett.* **92**, 202118 (2008).
- ¹²¹M. Handwerg, R. Mitdank, Z. Galazka, and S. Fischer, “Temperature-dependent thermal conductivity in Mg-doped and undoped β -Ga₂O₃ bulk-crystals,” *Semicond. Sci. Technol.* **30**, 024006 (2015).
- ¹²²P. Jiang, X. Qian, X. Li, and R. Yang, “Three-dimensional anisotropic thermal conductivity tensor of single crystalline β -Ga₂O₃,” *Appl. Phys. Lett.* **113**, 232105 (2018).
- ¹²³M. Slomski, N. Blumenschein, P. Paskov, J. Muth, and T. Paskova, “Anisotropic thermal conductivity of β -Ga₂O₃ at elevated temperatures: Effect of Sn and Fe dopants,” *J. Appl. Phys.* **121**, 235104 (2017).
- ¹²⁴R. Li, Z. Liu, A. Rohskopf, K. Gordiz, A. Henry, E. Lee, and T. Luo, “A deep neural network interatomic potential for studying thermal conductivity of β -Ga₂O₃,” *Appl. Phys. Lett.* **117**, 152102 (2020).
- ¹²⁵M. E. Levinshtein, S. L. Rumyantsev, and M. S. Shur, *Properties of Advanced Semiconductor Materials: GaN, AlN, InN, BN, SiC, SiGe* (John Wiley & Sons, 2001).
- ¹²⁶M. Kamatagi, N. Sankeshwar, and B. Mulimani, “Thermal conductivity of GaN,” *Diamond Related Mater.* **16**, 98–106 (2007).
- ¹²⁷B. Chatterjee, K. Zeng, C. D. Nordquist, U. Singisetti, and S. Choi, “Device-level thermal management of gallium oxide field-effect transistors,” *IEEE Trans. Compon., Packaging Manuf. Technol.* **9**, 2352–2365 (2019).
- ¹²⁸P. Paret, G. Moreno, B. Kekelia, R. Kotecha, X. Feng, K. Bennion, B. Mather, A. Zakutayev, S. Narumanchi, S. Graham, and S. Kim, “Thermal and thermo-mechanical modeling to design a gallium oxide power electronics package,” in *2018 IEEE 6th Workshop on Wide Bandgap Power Devices and Applications (WiPDA)* (IEEE, 2019), pp. 287–294.
- ¹²⁹M. Xiao, B. Wang, J. Liu, R. Zhang, Z. Zhang, C. Ding, S. Lu, K. Sasaki, G.-Q. Lu, C. Buttay, and Y. Zhang, “Packaged Ga₂O₃ schottky rectifiers with over 60–A surge current capability,” *IEEE Trans. Power Electron.* **36**, 8565–8569 (2021).
- ¹³⁰C. Buttay, H.-Y. Wong, B. Wang, M. Xiao, C. Dimarino, and Y. Zhang, “Surge current capability of ultra-wide-bandgap Ga₂O₃ schottky diodes,” *Microelectron. Reliab.* **114**, 113743 (2020).
- ¹³¹W. Xu, Y. Wang, T. You, X. Ou, G. Han, H. Hu, S. Zhang, F. Mu, T. Suga, Y. Zhang, Y. Hao, and X. Wang, “First demonstration of waferscale heterogeneous integration of Ga₂O₃ MOSFETs on SiC and Si substrates by ion-cutting process,” in *2019 IEEE International Electron Devices Meeting (IEDM)* (IEEE, 2019), pp. 12–15.
- ¹³²B. Liu, M. Gu, and X. Liu, “Lattice dynamical, dielectric, and thermodynamic properties of β -Ga₂O₃ from first principles,” *Appl. Phys. Lett.* **91**, 172102 (2007).
- ¹³³D. C. Look and K. D. Leedy, “Classical and quantum conductivity in β -Ga₂O₃,” *Sci. Rep.* **9**, 1290 (2019).
- ¹³⁴C. Kranert, C. Sturm, R. Schmidt-Grund, and M. Grundmann, “Raman tensor elements of β -Ga₂O₃,” *Sci. Rep.* **6**, 35964 (2016).
- ¹³⁵D. Dohy, G. Lucazeau, and A. Revcolevschi, “Raman spectra and valence force field of single-crystalline β -Ga₂O₃,” *J. Solid State Chem.* **45**, 180–192 (1982).
- ¹³⁶T. Onuma, S. Fujioka, T. Yamaguchi, Y. Itoh, M. Higashiwaki, K. Sasaki, T. Masui, and T. Honda, “Polarized Raman spectra in β -Ga₂O₃ single crystals,” *J. Cryst. Growth* **401**, 330–333 (2014).
- ¹³⁷E. Villora, Y. Morioka, T. Atou, T. Sugawara, M. Kikuchi, and T. Fukuda, “Infrared reflectance and electrical conductivity of β -Ga₂O₃,” *Phys. Status Solidi (a)* **193**, 187–195 (2002).
- ¹³⁸M. Schubert, A. Mock, R. Korlacki, and V. Darakchieva, “Phonon order and reststrahlen bands of polar vibrations in crystals with monoclinic symmetry,” *Phys. Rev. B* **99**, 041201 (2019).
- ¹³⁹M. Schubert, “Coordinate-invariant Lyddane-Sachs-Teller relationship for polar vibrations in materials with monoclinic and triclinic crystal systems,” *Phys. Rev. Lett.* **117**, 215502 (2016).
- ¹⁴⁰M. Schubert, A. Mock, R. Korlacki, S. Knight, Z. Galazka, G. Wagner, V. Wheeler, M. Tadjer, K. Goto, and V. Darakchieva, “Longitudinal phonon plasmon mode coupling in β -Ga₂O₃,” *Appl. Phys. Lett.* **114**, 102102 (2019).
- ¹⁴¹K. A. Mengle and E. Kioupakis, “Vibrational and electron-phonon coupling properties of β -Ga₂O₃ from first-principles calculations: Impact on the mobility and breakdown field,” *AIP Adv.* **9**, 015313 (2019).
- ¹⁴²R. Korlacki, M. Stokey, A. Mock, S. Knight, A. Papamichail, V. Darakchieva, and M. Schubert, “Strain and stress relationships for optical phonon modes in monoclinic crystals with β -Ga₂O₃ as an example,” *Phys. Rev. B* **102**, 180101 (2020).
- ¹⁴³N. Passler, X. Ni, G. Hu, J. Matson, M. Wolf, M. Schubert, A. Alu, J. Caldwell, T. Folland, and A. Paarmann, “Hyperbolic shear polaritons in low-symmetry crystals,” *Nature* **602**, 595–600 (2022).
- ¹⁴⁴P. Gopalan, S. Knight, A. Chanana, M. Stokey, P. Ranga, M. A. Scarpulla, S. Krishnamoorthy, V. Darakchieva, Z. Galazka, K. Irmischer, A. Fiedler, S. Blair, M. Schubert, and B. Sensale-Rodriguez, “The anisotropic quasi-static permittivity of single-crystal β -Ga₂O₃ measured by terahertz spectroscopy,” *Appl. Phys. Lett.* **117**, 252103 (2020).
- ¹⁴⁵M. Passlack, N. Hunt, E. Schubert, G. Zydzik, M. Hong, J. Mannaerts, R. Opila, and R. Fischer, “Dielectric properties of electron-beam deposited Ga₂O₃ films,” *Appl. Phys. Lett.* **64**, 2715–2717 (1994).
- ¹⁴⁶M. Mohamed, K. Irmischer, C. Janowitz, Z. Galazka, R. Manzke, and R. Fornari, “Schottky barrier height of Au on the transparent semiconducting oxide β -Ga₂O₃,” *Appl. Phys. Lett.* **101**, 132106 (2012).
- ¹⁴⁷M. Higashiwaki, K. Sasaki, A. Kuramata, T. Masui, and S. Yamakoshi, “Gallium oxide (Ga₂O₃) metal-semiconductor field-effect transistors on single-crystal β -Ga₂O₃ (010) substrates,” *Appl. Phys. Lett.* **100**, 013504 (2012).
- ¹⁴⁸M. H. Wong, K. Sasaki, A. Kuramata, S. Yamakoshi, and M. Higashiwaki, “Field-plated Ga₂O₃ MOSFETs with a breakdown voltage of over 750 V,” *IEEE Electron Device Lett.* **37**, 212–215 (2015).
- ¹⁴⁹A. J. Green, K. D. Chabak, E. R. Heller, R. C. Fitch, M. Baldini, A. Fiedler, K. Irmischer, G. Wagner, Z. Galazka, S. E. Tetlak, A. Crespo, K. Leedy, and G. H. Jessen, “3.8-mV/cm breakdown strength of MOVPE-grown Sn-doped β -Ga₂O₃ MOSFETs,” *IEEE Electron Device Lett.* **37**, 902–905 (2016).
- ¹⁵⁰N. Allen, M. Xiao, X. Yan, K. Sasaki, M. J. Tadjer, J. Ma, R. Zhang, H. Wang, and Y. Zhang, “Vertical Ga₂O₃ schottky barrier diodes with small-angle beveled field plates: A baliga’s figure-of-merit of 0.6 gW/cm²,” *IEEE Electron Device Lett.* **40**, 1399–1402 (2019).
- ¹⁵¹Z. Xia, C. Joishi, S. Krishnamoorthy, S. Bajaj, Y. Zhang, M. Brenner, S. Lodha, and S. Rajan, “Delta doped β -Ga₂O₃ field effect transistors with regrown ohmic contacts,” *IEEE Electron Device Lett.* **39**, 568–571 (2018).
- ¹⁵²M. Higashiwaki, K. Sasaki, T. Kamimura, M. Hoi Wong, D. Krishnamurthy, A. Kuramata, T. Masui, and S. Yamakoshi, “Depletion-mode Ga₂O₃ metal-oxide-semiconductor field-effect transistors on β -Ga₂O₃ (010) substrates and temperature dependence of their device characteristics,” *Appl. Phys. Lett.* **103**, 123511 (2013).
- ¹⁵³F. Bechstedt and J. Furthmüller, “Influence of screening dynamics on excitons in Ga₂O₃ polymorphs,” *Appl. Phys. Lett.* **114**, 122101 (2019).

- ¹⁵⁴H. M. Jeon, K. D. Leedy, D. C. Look, C. S. Chang, D. A. Muller, S. C. Badescu, V. Vasilyev, J. L. Brown, A. J. Green, and K. D. Chabak, "Homoepitaxial β -Ga₂O₃ transparent conducting oxide with conductivity $\sigma = 2323 \text{ s cm}^{-1}$," *APL Mater.* **9**, 101105 (2021).
- ¹⁵⁵N. Ma, N. Tanen, A. Verma, Z. Guo, T. Luo, H. Xing, and D. Jena, "Intrinsic electron mobility limits in β -Ga₂O₃," *Appl. Phys. Lett.* **109**, 212101 (2016).
- ¹⁵⁶K. Sasaki, M. Higashiwaki, A. Kuramata, T. Masui, and S. Yamakoshi, "MBE grown Ga₂O₃ and its power device applications," *J. Cryst. Growth* **378**, 591–595 (2013).
- ¹⁵⁷E. Ahmadi, O. S. Koksalidi, S. W. Kaun, Y. Oshima, D. B. Short, U. K. Mishra, and J. S. Speck, "Ge doping of β -Ga₂O₃ films grown by plasma-assisted molecular beam epitaxy," *Appl. Phys. Express* **10**, 041102 (2017).
- ¹⁵⁸S. Rafique, M. R. Karim, J. M. Johnson, J. Hwang, and H. Zhao, "LPCVD homoepitaxy of Si doped β -Ga₂O₃ thin films on (010) and (001) substrates," *Appl. Phys. Lett.* **112**, 052104 (2018).
- ¹⁵⁹S.-D. Lee, K. Kaneko, and S. Fujita, "Homoepitaxial growth of beta gallium oxide films by MIST chemical vapor deposition," *Jpn. J. Appl. Phys.* **55**, 1202B8 (2016).
- ¹⁶⁰K. D. Leedy, K. D. Chabak, V. Vasilyev, D. C. Look, J. J. Boeckl, J. L. Brown, S. E. Tetlak, A. J. Green, N. A. Moser, A. Crespo *et al.*, "Highly conductive homoepitaxial Si-doped Ga₂O₃ films on (010) β -Ga₂O₃ by pulsed laser deposition," *Appl. Phys. Lett.* **111**, 012103 (2017).
- ¹⁶¹K. D. Leedy, K. D. Chabak, V. Vasilyev, D. C. Look, K. Mahalingam, J. L. Brown, A. J. Green, C. T. Bowers, A. Crespo, D. B. Thomson *et al.*, "Si content variation and influence of deposition atmosphere in homoepitaxial Si-doped β -Ga₂O₃ films by pulsed laser deposition," *APL Mater.* **6**, 101102 (2018).
- ¹⁶²J. Leach, K. Udwary, J. Rumsey, G. Dodson, H. Splawn, and K. Evans, "Halide vapor phase epitaxial growth of β -Ga₂O₃ and α -Ga₂O₃ films," *APL Mater.* **7**, 022504 (2019).
- ¹⁶³D. Gogova, M. Schmidbauer, and A. Kwasniewski, "Homo- and heteroepitaxial growth of Sn-doped β -Ga₂O₃ layers by MOVPE," *CrystEngComm* **17**, 6744–6752 (2015).
- ¹⁶⁴M. Baldini, Z. Galazka, and G. Wagner, "Recent progress in the growth of β -Ga₂O₃ for power electronics applications," *Mater. Sci. Semicond. Process.* **78**, 132–146 (2018).
- ¹⁶⁵X. Du, Z. Li, C. Luan, W. Wang, M. Wang, X. Feng, H. Xiao, and J. Ma, "Preparation and characterization of Sn-doped β -Ga₂O₃ homoepitaxial films by MOCVD," *J. Mater. Sci.* **50**, 3252–3257 (2015).
- ¹⁶⁶S.-H. Han, A. Mauze, E. Ahmadi, T. Mates, Y. Oshima, and J. S. Speck, "n-type dopants in (001) β -Ga₂O₃ grown on (001) β -Ga₂O₃ substrates by plasma-assisted molecular beam epitaxy," *Semicond. Sci. Technol.* **33**, 045001 (2018).
- ¹⁶⁷J. L. Lyons, D. Steiauf, A. Janotti, and C. G. Van de Walle, "Carbon as a shallow donor in transparent conducting oxides," *Phys. Rev. Appl.* **2**, 064005 (2014).
- ¹⁶⁸K. Ghosh and U. Singisetti, "Ab initio calculation of electron-phonon coupling in monoclinic β -Ga₂O₃ crystal," *Appl. Phys. Lett.* **109**, 072102 (2016).
- ¹⁶⁹K. Ghosh and U. Singisetti, "Ab initio velocity-field curves in monoclinic β -Ga₂O₃," *J. Appl. Phys.* **122**, 035702 (2017).
- ¹⁷⁰K. Ghosh and U. Singisetti, "Electron mobility in monoclinic-Ga₂O₃-effect of plasmon-phonon coupling, anisotropy, and confinement," *J. Mater. Res.* **32**, 4142–4152 (2017).
- ¹⁷¹A. Parisini, K. Ghosh, U. Singisetti, and R. Fornari, "Assessment of phonon scattering-related mobility in β -Ga₂O₃," *Semicond. Sci. Technol.* **33**, 105008 (2018).
- ¹⁷²G. Seryogin, F. Alema, N. Valente, H. Fu, E. Steinbrunner, A. T. Neal, S. Mou, A. Fine, and A. Osinsky, "MOCVD growth of high purity Ga₂O₃ epitaxial films using trimethylgallium precursor," *Appl. Phys. Lett.* **117**, 262101 (2020).
- ¹⁷³R. S. Pengelly, S. M. Wood, J. W. Milligan, S. T. Sheppard, and W. L. Pribble, "A review of GaN on SiC high electron-mobility power transistors and mmics," *IEEE Trans. Microwave Theory Tech.* **60**, 1764–1783 (2012).
- ¹⁷⁴M. H. Wong, K. Sasaki, A. Kuramata, S. Yamakoshi, and I. M. Higashiwaki, "Electron channel mobility in silicon-doped Ga₂O₃ MOSFETs with a resistive buffer layer," *Jpn. J. Appl. Phys.* **55**, 1202B9 (2016).
- ¹⁷⁵Z.-S. Zhang, Y. Wu, C. Lu, and S. Ahmed, "Electron mobility in β -Ga₂O₃: An ensemble Monte Carlo study," *Appl. Phys. A* **124**, 637 (2018a).
- ¹⁷⁶T. Oishi, Y. Koga, K. Harada, and M. Kasu, "High-mobility β -Ga₂O₃ (201) single crystals grown by edge-defined film-fed growth method and their schottky barrier diodes with Ni contact," *Appl. Phys. Express* **8**, 031101 (2015).
- ¹⁷⁷M. J. Tadjer, J. L. Lyons, N. Nepal, J. A. Freitas, Jr., A. D. Koehler, and G. M. Foster, "Review-theory and characterization of doping and defects in β -Ga₂O₃," *ECS J. Solid State Sci. Technol.* **8**, Q3187 (2019).
- ¹⁷⁸M. D. McCluskey, "Point defects in Ga₂O₃," *J. Appl. Phys.* **127**, 101101 (2020).
- ¹⁷⁹M. J. Tadjer, J. Freitas, J. Culbertson, M. Weber, E. R. Glaser, A. Mock, N. Mahadik, K. J. Schmieder, E. Jackson, J. Gallagher, B. N. Feigelson, and A. Kuramata, "Structural and electronic properties of Si-and Sn-doped (-201) β -Ga₂O₃ annealed in nitrogen and oxygen atmospheres," *J. Phys. D: Appl. Phys.* **53**, 504002 (2020).
- ¹⁸⁰E. Chikoidze, H. Von Bardeleben, K. Akaiwa, E. Shigematsu, K. Kaneko, S. Fujita, and Y. Dumont, "Electrical, optical, and magnetic properties of Sn doped α -Ga₂O₃ thin films," *J. Appl. Phys.* **120**, 025109 (2016).
- ¹⁸¹J. Varley, A. Janotti, C. Franchini, and C. G. Van de Walle, "Role of self-trapping in luminescence and p-type conductivity of wide-band-gap oxides," *Phys. Rev. B* **85**, 081109 (2012).
- ¹⁸²H. Kawazoe, H. Yanagi, K. Ueda, and H. Hosono, "Transparent p-type conducting oxides: Design and fabrication of pn heterojunctions," *MRS Bull.* **25**, 28–36 (2000).
- ¹⁸³C. Yan, J. Su, Y. Wang, Z. Lin, J. Zhang, J. Chang, and Y. Hao, "Reducing the acceptor levels of p-type β -Ga₂O₃ by (metal, N) co-doping approach," *J. Alloys Compd.* **854**, 157247 (2021).
- ¹⁸⁴X. Cai, F. P. Sabino, A. Janotti, and S.-H. Wei, "Approach to achieving a p-type transparent conducting oxide: Doping of bismuth-alloyed Ga₂O₃ with a strongly correlated band edge state," *Phys. Rev. B* **103**, 115205 (2021).
- ¹⁸⁵H. Peelaers, J. L. Lyons, J. B. Varley, and C. G. Van de Walle, "Deep acceptors and their diffusion in Ga₂O₃," *APL Mater.* **7**, 022519 (2019).
- ¹⁸⁶A. T. Neal, S. Mou, S. Rafique, H. Zhao, E. Ahmadi, J. S. Speck, K. T. Stevens, J. D. Blevins, D. B. Thomson, N. Moser, K. D. Chabak, and G. H. Jessen, "Donors and deep acceptors in β -Ga₂O₃," *Appl. Phys. Lett.* **113**, 062101 (2018).
- ¹⁸⁷P. Paskov, M. Slomski, J. Leach, J. Muth, and T. Paskova, "Effect of Si doping on the thermal conductivity of bulk GaN at elevated temperatures—Theory and experiment," *AIP Adv.* **7**, 095302 (2017).
- ¹⁸⁸A. Portoff, A. Venzie, M. Stavola, W. B. Fowler, and S. J. Pearson, "Determination of dielectric axes and transition moment directions in β -Ga₂O₃ from the polarization dependence of vibrational spectra," *J. Appl. Phys.* **127**, 055702 (2020).
- ¹⁸⁹A. Kumar and U. Singisetti, "First principles study of thermoelectric properties of β -gallium oxide," *Appl. Phys. Lett.* **117**, 262104 (2020).
- ¹⁹⁰Y. Zhuo, Z. Chen, W. Tu, X. Ma, Y. Pei, and G. Wang, " β -Ga₂O₃ versus ϵ -Ga₂O₃: Control of the crystal phase composition of gallium oxide thin film prepared by metal-organic chemical vapor deposition," *Appl. Surf. Sci.* **420**, 802–807 (2017).
- ¹⁹¹T. Ma, X. Chen, F. Ren, S. Zhu, S. Gu, R. Zhang, Y. Zheng, and J. Ye, "Heteroepitaxial growth of thick α -Ga₂O₃ film on sapphire (0001) by MIST-CVD technique," *J. Semicond.* **40**, 012804 (2019).
- ¹⁹²Y. Chen, X. Xia, H. Liang, Q. Abbas, Y. Liu, and G. Du, "Growth pressure controlled nucleation epitaxy of pure phase ϵ -and β -Ga₂O₃ films on Al₂O₃ via metal-organic chemical vapor deposition," *Cryst. Growth Des.* **18**, 1147–1154 (2018).
- ¹⁹³W. Zachariasen, "The crystal structure of sesquioxides and compounds of the type ABO₃," *Skr. Nor. Vidensk. Akad.* **4**, 7–165 (1928).
- ¹⁹⁴S.-D. Lee, Y. Ito, K. Kaneko, and S. Fujita, "Enhanced thermal stability of alpha gallium oxide films supported by aluminum doping," *Jpn. J. Appl. Phys., Part 1* **54**, 030301 (2015).
- ¹⁹⁵M.-R. Li, U. Adem, S. R. C. Mitchell, Z. Xu, C. I. Thomas, J. E. Warren, D. V. Giap, H. Niu, X. Wan, R. G. Palgrave, F. Schiffmann, F. Cora, B. Slater, T. L. Burnett, M. G. Cain, A. M. Abakumov, G. van Tendeloo, M. F. Thomas, M. J. Rosseinsky, and J. B. Claridge, "A polar corundum oxide displaying weak ferromagnetism at room temperature," *J. Am. Chem. Soc.* **134**, 3737–3747 (2012).

- ¹⁹⁶D. Shinohara and S. Fujita, "Heteroepitaxy of corundum-structured α -Ga₂O₃ thin films on α -Al₂O₃ substrates by ultrasonic MIST chemical vapor deposition," *Jpn. J. Appl. Phys., Part 1* **47**, 7311 (2008).
- ¹⁹⁷S.-D. Lee, K. Akaiwa, and S. Fujita, "Thermal stability of single crystalline alpha gallium oxide films on sapphire substrates," *Phys. Status Solidi (c)* **10**, 1592–1595 (2013).
- ¹⁹⁸H. Sun, K.-H. Li, C. G. T. Castanedo, S. Okur, G. S. Tompa, T. Salagaj, S. Lopatin, A. Genovese, and X. Li, "HCl flow-induced phase change of α -, β -, and ϵ -Ga₂O₃ films grown by MOCVD," *Cryst. Growth Des.* **18**, 2370–2376 (2018).
- ¹⁹⁹R. Jinno, C. S. Chang, T. Onuma, Y. Cho, S.-T. Ho, D. Rowe, M. C. Cao, K. Lee, V. Protasenko, D. G. Schlom, D. A. Muller, H. G. Xing, and D. Jena, "Crystal orientation dictated epitaxy of ultralow-bandgap 5.4-to 8.6-eV α -(AlGa)₂O₃ on m-plane sapphire," *Sci. Adv.* **7**, eabd5891 (2021).
- ²⁰⁰R. Jinno, T. Uchida, K. Kaneko, and S. Fujita, "Reduction in edge dislocation density in corundum-structured α -Ga₂O₃ layers on sapphire substrates with quasi-graded α -(AlGa)₂O₃ buffer layers," *Appl. Phys. Express* **9**, 071101 (2016).
- ²⁰¹Y. Oshima, E. G. Villora, and K. Shimamura, "Halide vapor phase epitaxy of twin-free α -Ga₂O₃ on sapphire (0001) substrates," *Appl. Phys. Express* **8**, 055501 (2015).
- ²⁰²Y. Oshima, K. Kawara, T. Shinohe, T. Hitora, M. Kasu, and S. Fujita, "Epitaxial lateral overgrowth of α -Ga₂O₃ by halide vapor phase epitaxy," *APL Mater.* **7**, 022503 (2019).
- ²⁰³K. Kawara, Y. Oshima, M. Okigawa, and T. Shinohe, "Elimination of threading dislocations in α -Ga₂O₃ by double-layered epitaxial lateral overgrowth," *Appl. Phys. Express* **13**, 075507 (2020).
- ²⁰⁴A. Sharma and U. Singisetti, "Low field electron transport in α Ga₂O₃: An *ab initio* approach," *Appl. Phys. Lett.* **118**, 032101 (2021).
- ²⁰⁵A. Segura, L. Artús, R. Cuscó, R. Goldhahn, and M. Feneberg, "Band gap of corundumlike α -Ga₂O₃ determined by absorption and ellipsometry," *Phys. Rev. Mater.* **1**, 024604 (2017).
- ²⁰⁶M. Hilfiker, R. Korlacki, R. Jinno, Y. Cho, H. G. Xing, D. Jena, U. Kilic, M. Stokey, and M. Schubert, "Anisotropic dielectric functions, band-to-band transitions, and critical points in α -Ga₂O₃," *Appl. Phys. Lett.* **118**, 062103 (2021).
- ²⁰⁷R. Cuscó, N. Domènech-Amador, T. Hatakeyama, T. Yamaguchi, T. Honda, and L. Artús, "Lattice dynamics of a MIST-chemical vapor deposition-grown corundum-like Ga₂O₃ single crystal," *J. Appl. Phys.* **117**, 185706 (2015).
- ²⁰⁸M. Feneberg, J. Nixdorf, M. D. Neumann, N. Esser, L. Artús, R. Cuscó, T. Yamaguchi, and R. Goldhahn, "Ordinary dielectric function of corundumlike α -Ga₂O₃ from 40 meV to 20 eV," *Phys. Rev. Mater.* **2**, 044601 (2018).
- ²⁰⁹M. Stokey, R. Korlacki, M. Hilfiker, S. Knight, S. Richter, V. Darakchieva, R. Jinno, Y. Cho, G. H. Xing, D. Jena, Y. Oshima, K. Khan, E. Ahmadi, and M. Schubert, "Infrared dielectric functions and brillouin zone center phonons of α -Ga₂O₃ compared to α -Al₂O₃," *Phys. Rev. Mater.* **6**, 014601 (2021).
- ²¹⁰M. Feneberg, C. Lidig, K. Lange, M. E. White, M. Y. Tsai, J. S. Speck, O. Bierwagen, and R. Goldhahn, "Anisotropy of the electron effective mass in rutile SnO₂ determined by infrared ellipsometry," *Phys. Status Solidi (a)* **211**, 82–86 (2014).
- ²¹¹H. Hayashi, R. Huang, F. Oba, T. Hirayama, and I. Tanaka, "Epitaxial growth of mn-doped γ -Ga₂O₃ on spinel substrate," *J. Mater. Res.* **26**, 578–583 (2011).
- ²¹²M. Bosi, P. Mazzolini, L. Seravalli, and R. Fornari, "Ga₂O₃ polymorphs: Tailoring the epitaxial growth conditions," *J. Mater. Chem. C* **8**, 10975–10992 (2020).
- ²¹³I. Cora, Z. Fogarassy, R. Fornari, M. Bosi, A. Rečnik, and B. Pécz, "In situ TEM study of κ β and κ γ phase transformations in Ga₂O₃," *Acta Mater.* **183**, 216–227 (2020).
- ²¹⁴O. Ambacher, J. Smart, J. R. Shealy, N. G. Weimann, K. Chu, M. Murphy, W. J. Schaff, L. F. Eastman, R. Dimitrov, L. Wittmer, M. Stutzmann, W. Rieger, and J. Hilsenbeck, "Two-dimensional electron gases induced by spontaneous and piezoelectric polarization charges in n- and Ga-face AlGaN/GaN heterostructures," *J. Appl. Phys.* **85**, 3222–3233 (1999).
- ²¹⁵O. Ambacher, B. Foutz, J. Smart, J. R. Shealy, N. G. Weimann, K. Chu, M. Murphy, A. J. Sierakowski, W. J. Schaff, L. F. Eastman, R. Dimitrov, A. Mitchell, and M. Stutzmann, "Two dimensional electron gases induced by spontaneous and piezoelectric polarization in undoped and doped AlGaN/GaN heterostructures," *J. Appl. Phys.* **87**, 334–344 (2000).
- ²¹⁶V. M. Voora, T. Hofmann, M. Brandt, M. Lorenz, M. Grundmann, N. Ashkenov, H. Schmidt, N. Ianno, and M. Schubert, "Interface polarization coupling in piezoelectric-semiconductor ferroelectric heterostructures," *Phys. Rev. B* **81**, 195307 (2010).
- ²¹⁷V. Voora, T. Hofmann, M. Brandt, M. Lorenz, N. Ashkenov, M. Grundmann, and M. Schubert, "Electrical properties of ZnO-BaTiO₃-ZnO heterostructures with asymmetric interface charge distribution," *Appl. Phys. Lett.* **95**, 082902 (2009).
- ²¹⁸M. Brandt, H. Frenzel, H. Hochmuth, M. Lorenz, M. Grundmann, and J. Schubert, "Ferroelectric thin film field-effect transistors based on ZnO/BaTiO₃ heterostructures," *J. Vac. Sci. Technol. B* **27**, 1789–1793 (2009).
- ²¹⁹C. Liu, H. Sun, C. Ma, Z. Chen, Z. Luo, T. Su, Y. Yin, and X. Li, "Nonvolatile ZnO-based ferroelectric field effect transistors for active-matrix organic light-emitting diode display," *IEEE Electron Device Lett.* **41**, 42–45 (2019).
- ²²⁰X. Xia, Y. Chen, Q. Feng, H. Liang, P. Tao, M. Xu, and G. Du, "Hexagonal phase-pure wide band gap ε -Ga₂O₃ films grown on 6H-SiC substrates by metal organic chemical vapor deposition," *Appl. Phys. Lett.* **108**, 202103 (2016).
- ²²¹S.-H. Yuan, S.-L. Ou, C.-M. Chen, S.-Y. Huang, B.-W. Hsiao, and D.-S. Wuu, "Characterization of aluminum gallium oxide films grown by pulsed laser deposition," *Ceram. Int.* **45**, 702–707 (2019).
- ²²²C.-C. Wang, S.-H. Yuan, S.-L. Ou, S.-Y. Huang, K.-Y. Lin, Y.-A. Chen, P.-W. Hsiao, and D.-S. Wuu, "Growth and characterization of co-sputtered aluminum-gallium oxide thin films on sapphire substrates," *J. Alloys Compd.* **765**, 894–900 (2018).
- ²²³H. Peelaers, J. B. Varley, J. S. Speck, and C. G. Van de Walle, "Structural and electronic properties of Ga₂O₃-Al₂O₃ alloys," *Appl. Phys. Lett.* **112**, 242101 (2018).
- ²²⁴A. A. Bhuiyan, Z. Feng, J. M. Johnson, H.-L. Huang, J. Sarker, M. Zhu, M. R. Karim, B. Mazumder, J. Hwang, and H. Zhao, "Phase transformation in MOCVD growth of (Al_xGa_{1-x})₂O₃ thin films," *APL Mater.* **8**, 031104 (2020).
- ²²⁵A. Anhar Uddin Bhuiyan, Z. Feng, J. M. Johnson, H.-L. Huang, J. Hwang, and H. Zhao, "MOCVD epitaxy of ultrawide bandgap β -(Al_xGa_{1-x})₂O₃ with high-Al composition on (100) β -Ga₂O₃ substrates," *Cryst. Growth Des.* **20**, 6722–6730 (2020).
- ²²⁶A. L. Jaromin and D. D. Edwards, "Subsolidus phase relationships in the Ga₂O₃-Al₂O₃-TiO₂ system," *J. Am. Ceram. Soc.* **88**, 2573–2577 (2005).
- ²²⁷M. Hilfiker, U. Kilic, A. Mock, V. Darakchieva, S. Knight, R. Korlacki, A. Mauze, Y. Zhang, J. Speck, and M. Schubert, "Dielectric function tensor (1.5 eV to 9.0 eV), anisotropy, and band to band transitions of monoclinic β -(Al_xGa_{1-x})₂O₃ ($x \leq 0.21$) films," *Appl. Phys. Lett.* **114**, 231901 (2019).
- ²²⁸M. Hilfiker, U. Kilic, M. Stokey, R. Jinno, Y. Cho, H. G. Xing, D. Jena, R. Korlacki, and M. Schubert, "High-frequency and below bandgap anisotropic dielectric constants in α -(Al_xGa_{1-x})₂O₃ ($0 \leq x \leq 1$)," *Appl. Phys. Lett.* **119**, 092103 (2021).
- ²²⁹S. Mu, H. Peelaers, and C. G. Van de Walle, "Ab initio study of enhanced thermal conductivity in ordered AlGaO₃ alloys," *Appl. Phys. Lett.* **115**, 242103 (2019).
- ²³⁰B. W. Krueger, C. S. Dandeneau, E. M. Nelson, S. T. Dunham, F. S. Ohuchi, and M. A. Olmstead, "Variation of band gap and lattice parameters of β -(Al_xGa_{1-x})₂O₃ powder produced by solution combustion synthesis," *J. Am. Ceram. Soc.* **99**, 2467–2473 (2016).
- ²³¹C. Kranert, M. Jenderka, J. Lenzner, M. Lorenz, H. von Wenckstern, R. Schmidt-Grund, and M. Grundmann, "Lattice parameters and Raman-active phonon modes of β -(Al_xGa_{1-x})₂O₃," *J. Appl. Phys.* **117**, 125703 (2015).
- ²³²X. Wang, Z. Chen, F. Zhang, K. Saito, T. Tanaka, M. Nishio, and Q. Guo, "Influence of substrate temperature on the properties of (AlGa)₂O₃ thin films prepared by pulsed laser deposition," *Ceram. Int.* **42**, 12783–12788 (2016).
- ²³³K. Matsuzaki, H. Hiramatsu, K. Nomura, H. Yanagi, T. Kamiya, M. Hirano, and H. Hosono, "Growth, structure and carrier transport properties of Ga₂O₃ epitaxial film examined for transparent field-effect transistor," *Thin solid films* **496**, 37–41 (2006).

- ²³⁴X. Wang, K. Saito, T. Tanaka, M. Nishio, T. Nagaoka, M. Arita, and Q. Guo, "Energy band bowing parameter in MgZnO alloys," *Appl. Phys. Lett.* **107**, 022111 (2015a).
- ²³⁵R. Schewski, G. Wagner, M. Baldini, D. Gogova, Z. Galazka, T. Schulz, T. Remmeli, T. Markurt, H. von Wenckstern, M. Grundmann, O. Bierwagen, P. Vogt, and M. Albrecht, "Epitaxial stabilization of pseudomorphic α -Ga₂O₃ on sapphire (0001)," *Appl. Phys. Express* **8**, 011101 (2014).
- ²³⁶M. Kracht, A. Karg, M. Feneberg, J. Bläsing, J. Schörmann, R. Goldhahn, and M. Eickhoff, "Anisotropic optical properties of metastable (0112) α -Ga₂O₃ grown by plasma-assisted molecular beam epitaxy," *Phys. Rev. Appl.* **10**, 024047 (2018).
- ²³⁷R. Weiher and R. Ley, "Optical properties of indium oxide," *J. Appl. Phys.* **37**, 299–302 (1966).
- ²³⁸T.-H. Chang, S.-J. Chang, C. Chiu, C.-Y. Wei, Y.-M. Juan, and W.-Y. Weng, "Bandgap-engineered in indium-gallium-oxide ultraviolet phototransistors," *IEEE Photonics Technol. Lett.* **27**, 915–918 (2015).
- ²³⁹T.-H. Chang, S.-J. Chang, W.-Y. Weng, C.-J. Chiu, and C.-Y. Wei, "Amorphous indium-gallium-oxide UV photodetectors," *IEEE Photonics Technol. Lett.* **27**, 2083–2086 (2015).
- ²⁴⁰C. Kranert, J. Lenzner, M. Jenderka, M. Lorenz, H. von Wenckstern, R. Schmidt-Grund, and M. Grundmann, "Lattice parameters and Raman-active phonon modes of (In_xGa_{1-x})₂O₃ for $x < 0.4$," *J. Appl. Phys.* **116**, 013505 (2014).
- ²⁴¹F. Zhang, K. Saito, T. Tanaka, M. Nishio, M. Arita, and Q. Guo, "Wide bandgap engineering of (AlGa)₂O₃ films," *Appl. Phys. Lett.* **105**, 162107 (2014).
- ²⁴²J. Sheng, E. J. Park, B. Shong, and J.-S. Park, "Atomic layer deposition of an indium gallium oxide thin film for thin-film transistor applications," *ACS Appl. Mater. Interfaces* **9**, 23934–23940 (2017).
- ²⁴³X. Liu and C.-K. Tan, "Electronic properties of monoclinic (In_xGa_{1-x})₂O₃ alloys by first-principle," *AIP Adv.* **9**, 035318 (2019).
- ²⁴⁴M. B. Maccioni and V. Fiorentini, "Phase diagram and polarization of stable phases of (Ga_{1-x}In_x)₂O₃," *Appl. Phys. Express* **9**, 041102 (2016).
- ²⁴⁵M. B. Maccioni, F. Ricci, and V. Fiorentini, "Low in solubility and band offsets in the small- x β -Ga₂O₃/(Ga_{1-x}In_x)₂O₃ system," *Appl. Phys. Express* **8**, 021102 (2015).
- ²⁴⁶X. Liu and C.-K. Tan, "First-principle investigation of monoclinic (Al_xIn_yGa_{1-x-y})₂O₃ quaternary alloys," *Semicond. Sci. Technol.* **35**, 025023 (2020).
- ²⁴⁷I. Gorczyca, T. Suski, N. E. Christensen, and A. Svane, "Band gap bowing in quaternary nitride semiconducting alloys," *Appl. Phys. Lett.* **98**, 241905 (2011).
- ²⁴⁸J. Kim, H. Kang, W. Kim, J. Kim, J. Choi, H. Park, G. Kim, T. Kim, Y. Hwang, S. Mho, M. Jung, and M. Han, "Color variation of ZnGa₂O₄ phosphor by reduction-oxidation processes," *Appl. Phys. Lett.* **82**, 2029–2031 (2003).
- ²⁴⁹Z. Lou, L. Li, and G. Shen, "High-performance rigid and flexible ultraviolet photodetectors with single-crystalline ZnGa₂O₄ nanowires," *Nano Res.* **8**, 2162–2169 (2015).
- ²⁵⁰Y. Li, M. Lu, C. Wang, K. Li, and L. Chen, "ZnGa₂O₄ nanotubes with sharp cathodoluminescence peak," *Appl. Phys. Lett.* **88**, 143102 (2006).
- ²⁵¹T. Omata, N. Ueda, K. Ueda, and H. Kawazoe, "New ultraviolet-transport electroconductive oxide, ZnGa₂O₄ spinel," *Appl. Phys. Lett.* **64**, 1077–1078 (1994).
- ²⁵²N. Ueda, T. Omata, N. Hikuma, K. Ueda, H. Mizoguchi, T. Hashimoto, and H. Kawazoe, "New oxide phase with wide band gap high electroconductivity MgIn₂O₄," *Appl. Phys. Lett.* **61**, 1954–1955 (1992).
- ²⁵³T. Omata, N. Ueda, N. Hikuma, K. Ueda, H. Mizoguchi, T. Hashimoto, and H. Kawazoe, "New oxide phase with wide band gap and high electroconductivity CdGa₂O₄ spinel," *Appl. Phys. Lett.* **62**, 499–500 (1993).
- ²⁵⁴Z. Galazka, S. Ganschow, R. Schewski, K. Irmscher, D. Klimm, A. Kwasniewski, M. Pietsch, A. Fiedler, I. Schulze-Jonack, M. Albrecht *et al.*, "Ultra-wide bandgap, conductive, high mobility, and high quality melt-grown bulk ZnGa₂O₄ single crystals," *APL Mater.* **7**, 022512 (2019).
- ²⁵⁵R.-H. Horng, C.-Y. Huang, S.-L. Ou, T.-K. Juang, and P.-L. Liu, "Epitaxial growth of ZnGa₂O₄: A new, deep ultraviolet semiconductor candidate," *Cryst. Growth Des.* **17**, 6071–6078 (2017).
- ²⁵⁶M. G. Brik, A. Suchocki, and A. Kaminska, "Lattice parameters and stability of the spinel compounds in relation to the ionic radii and electronegativities of constituting chemical elements," *Inorg. Chem.* **53**, 5088–5099 (2014).
- ²⁵⁷M. Stokey, R. Korlacki, S. Knight, M. Hilfiker, Z. Galazka, K. Irmscher, V. Darakchieva, and M. Schubert, "Brillouin zone center phonon modes in ZnGa₂O₄," *Appl. Phys. Lett.* **117**, 052104 (2020).
- ²⁵⁸M. Hilfiker, M. Stokey, R. Korlacki, U. Kilic, Z. Galazka, K. Irmscher, S. Zollner, and M. Schubert, "Zinc gallate spinel dielectric function, band-to-band transitions, and γ -point effective mass parameters," *Appl. Phys. Lett.* **118**, 132102 (2021).
- ²⁵⁹W. Li, K. Nomoto, Z. Hu, T. Nakamura, D. Jena, and H. G. Xing, "Single and multi-fin normally-off Ga₂O₃ vertical transistors with a breakdown voltage over 2.6 kV," in *2019 IEEE International Electron Devices Meeting (IEDM) (IEEE, 2019)*, pp. 12.4.1–12.4.4.
- ²⁶⁰N. Allen, M. Xiao, X. Yan, K. Sasaki, M. J. Tadje, J. Ma, R. Zhang, H. Wang, and Y. Zhang, "Vertical Ga₂O₃ Schottky barrier diodes with small-angle beveled field plates: A Baliga's figure-of-merit of 0.6 GW/cm²," *IEEE Electron Device Lett.* **40**(9), 1399–1402 (2019).
- ²⁶¹B. Wang, M. Xiao, X. Yan, H. Y. Wong, J. Ma, K. Sasaki, H. Wang, and Y. Zhang, "High-voltage vertical Ga₂O₃ power rectifiers operational at high temperatures up to 600 K," *Appl. Phys. Lett.* **115**, 263503 (2019).
- ²⁶²S. Sharma, K. Zeng, S. Saha, and U. Singisetty, "Field-plated lateral Ga₂O₃ MOSFETs with polymer passivation and 8.03 kV breakdown voltage," *IEEE Electron Device Lett.* **41**(6), 836–839 (2020).
- ²⁶³M. Xiao, B. Wang, J. Liu, R. Zhang, Z. Zhang, C. Ding, S. Lu, K. Sasaki, G. Q. Lu, C. Buttay, and Y. Zhang, "Packaged Ga₂O₃ Schottky rectifiers with over 60-A surge current capability," *IEEE Trans. Power Electron.* **36**(8), 8565–8569 (2021).
- ²⁶⁴B. Wang, M. Xiao, J. Knoll, C. Buttay, K. Sasaki, G. Q. Lu, C. Dimarino, and Y. Zhang, "Low thermal resistance (0.5 K/W) Ga₂O₃ Schottky rectifiers with double-side packaging," *IEEE Electron Device Lett.* **42**(8), 1132–1135 (2021).
- ²⁶⁵I. Levin and D. Brandon, "Metastable alumina polymorphs: Crystal structures and transition sequences," *J. Am. Ceram. Soc.* **81**, 1995–2012 (1998).
- ²⁶⁶A. Parisini and R. Fornari, "Analysis of the scattering mechanisms controlling electron mobility in β -Ga₂O₃ crystals," *Semicond. Sci. Technol.* **31**, 035023 (2016).
- ²⁶⁷W. S. Hwang, A. Verma, H. Peelaers, V. Protasenko, S. Rouvimov, H. Xing, A. Seabaugh, W. Haensch, C. V. d. Walle, Z. Galazka, M. Albrecht, R. Fornari, and D. Jena, "Publisher's Note: 'High-voltage field effect transistors with wide-bandgap β -Ga₂O₃ nanomembranes' [Appl. Phys. Lett. **104**, 203111 (2014)]," *Appl. Phys. Lett.* **104**, 249902 (2014).
- ²⁶⁸F. Komine, M. Tomic, T. Gerds, and J. R. Strub, "Influence of different adhesive resin cements on the fracture strength of aluminum oxide ceramic posterior crowns," *J. Prosthetic Dentistry* **92**, 359–364 (2004).
- ²⁶⁹C.-W. Chang and C.-P. Kuo, "Evaluation of surface roughness in laser-assisted machining of aluminum oxide ceramics with Taguchi method," *Int. J. Mach. Tools Manuf.* **47**, 141–147 (2007).
- ²⁷⁰G. Vekinis, M. F. Ashby, and P. Beaumont, "R-curve behaviour of Al₂O₃ ceramics," *Acta Metall. Mater.* **38**, 1151–1162 (1990).
- ²⁷¹R. H. French, "Electronic band structure of Al₂O₃, with comparison to Alon and AlN," *J. Am. Ceram. Soc.* **73**, 477–489 (1990).
- ²⁷²R. Dinwiddie, A. Whittaker, and D. G. Onn, "Effect of processing conditions on thermal conduction in alumina," in *Thermal Conductivity* (Springer, 1989), Vol. 20, pp. 129–139.
- ²⁷³M. S. Akselrod and F. J. Bruni, "Modern trends in crystal growth and new applications of sapphires," *J. Cryst. Growth* **360**, 134–145 (2012).
- ²⁷⁴M. Ritala, M. Leskelä, J.-P. Dekker, C. Mutsaers, P. J. Soininen, and J. Skarp, "Perfectly conformal TiN and Al₂O₃ films deposited by atomic layer deposition," *Chem. Vapor Deposition* **5**, 7–9 (1999).
- ²⁷⁵A. Abyzov, "Aluminum oxide and alumina ceramics (review). Part 1. Properties of Al₂O₃ and commercial production of dispersed Al₂O₃," *Refractories Ind. Ceram.* **60**, 24–32 (2019).
- ²⁷⁶A. Bourdillon, S. El-Mashri, and A. Forty, "Application of TEM extended electron energy loss fine structure to the study of aluminium oxide films," *Philos. Mag. A* **49**, 341–352 (1984).
- ²⁷⁷R. W. G. Wyckoff, *Crystal Structures*, 2nd ed. (Wiley, 1964).

- ²⁷⁸Y. Repelin and E. Husson, "Etudes structurales d'alumines de transition. I—alumines gamma et delta," *Mater. Res. Bull.* **25**, 611–621 (1990).
- ²⁷⁹V. Jayaram and C. Levi, "The structure of δ -alumina evolved from the melt and the γ δ transformation," *Acta Metall.* **37**, 569–578 (1989).
- ²⁸⁰H. C. Stumpf, A. S. Russell, J. Newsome, and C. Tucker, "Thermal transformations of aluminas and alumina hydrates-reaction with 44% technical acid," *Indus. Eng. Chem.* **42**, 1398–1403 (1950).
- ²⁸¹P. Liu and J. Skogsmo, "Space-group determination and structure model for κ - Al_2O_3 by convergent-beam electron diffraction (CBED)," *Acta Crystallogr. Sect. B* **47**, 425–433 (1991).
- ²⁸²G. Brindley and J. Choe, "The reaction series, gibbsite \rightarrow chi alumina \rightarrow kappa alumina \rightarrow corundum," *Am. Miner.* **46**, 771–785 (1961).
- ²⁸³G. Yamaguchi, I. Yasui, and W.-C. Chiu, "A new method of preparing θ -alumina and the interpretation of its x-ray-powder diffraction pattern and electron diffraction pattern," *Bull. Chem. Soc. Jpn.* **43**, 2487–2491 (1970).
- ²⁸⁴W. Ching and Y.-N. Xu, "First-principles calculation of electronic, optical, and structural properties of α - Al_2O_3 ," *J. Am. Ceram. Soc.* **77**, 404–411 (1994).
- ²⁸⁵I. P. Batra, "Electronic structure of α - Al_2O_3 ," *J. Phys. C* **15**, 5399 (1982).
- ²⁸⁶P. Aldebert and J. Traverse, "Neutron diffraction study of structural characteristics and ionic mobility of a- Al_2O_3 at high temperatures," *J. Am. Ceram. Soc.* **65**, 460–464 (1982).
- ²⁸⁷T. Shirai, H. Watanabe, M. Fuji, and M. Takahashi, "Structural properties and surface characteristics on aluminum oxide powders," in Annual Report of the Ceramics Research Laboratory Nagoya Institute of Technology (2010).
- ²⁸⁸H. P. Rooksby and C. J. M. Rooymans, "The formation and structure of delta alumina," *Clay Miner. Bull.* **4**, 234–238 (1961).
- ²⁸⁹I. Levin, L. Bendersky, D. Brandon, and M. Rühle, "Cubic to monoclinic phase transformations in alumina," *Acta Mater.* **45**, 3659–3669 (1997).
- ²⁹⁰G. Paglia, C. Buckley, A. Rohl, B. Hunter, R. Hart, J. Hanna, and L. Byrne, "Tetragonal structure model for boehmite-derived γ -alumina," *Phys. Rev. B* **68**, 144110 (2003).
- ²⁹¹L. Samain, A. Jaworski, M. Edén, D. M. Ladd, D.-K. Seo, F. J. Garcia-Garcia, and U. Häussermann, "Structural analysis of highly porous γ - Al_2O_3 ," *J. Solid State Chem.* **217**, 1–8 (2014).
- ²⁹²F. Ohuchi and R. French, "Effect of oxygen incorporation in AlN thin films," Ph.D. thesis (American Vacuum Society, 1988).
- ²⁹³I. Costina and R. Franchy, "Band gap of amorphous and well-ordered Al_2O_3 on Ni₃Al," *Appl. Phys. Lett.* **78**(100), 4139–4141 (2001).
- ²⁹⁴B. Elet, M. Elyakhloouf, E. Gillet, and M. Ricci, "Electronic and crystallographic structure of γ -alumina thin films," *Thin Solid Films* **250**, 92–100 (1994).
- ²⁹⁵M. Okumiya, G. Yamaguchi, O. Yamada, and S. Ono, "The formation of κ and κ - Al_2O_3 from the dehydration of tohrite 5 $\text{Al}_2\text{O}_3 \cdot \text{H}_2\text{O}$," *Bull. Chem. Soc. Jpn.* **44**, 418–423 (1971).
- ²⁹⁶A. Borosy, B. Silvi, M. Allavena, and P. Nortier, "Structure and bonding of bulk and surface θ -alumina from periodic Hartree-Fock calculations," *J. Phys. Chem.* **98**, 13189–13194 (1994).
- ²⁹⁷K. Nassau, "Dr. A. V. L. Verneuil: The man and the method," *J. Cryst. Growth* **13**, 12–18 (1972).
- ²⁹⁸K. Pande, V. Nair, and D. Gutierrez, "Plasma enhanced metal-organic chemical vapor deposition of aluminum oxide dielectric film for device applications," *J. Appl. Phys.* **54**, 5436–5440 (1983).
- ²⁹⁹T. Kobayashi, M. Okamura, E. Yamaguchi, Y. Shinoda, and Y. Hirota, "Effect of pyrolytic Al_2O_3 deposition temperature on inversion-mode InP metal-insulator-semiconductor field-effect transistor," *J. Appl. Phys.* **52**, 6434–6436 (1981).
- ³⁰⁰T. Maruyama and S. Arai, "Aluminum oxide thin films prepared by chemical vapor deposition from aluminum acetylacetone," *Appl. Phys. Lett.* **60**, 322–323 (1992).
- ³⁰¹J. Kim, H. Marzouk, P. Reucroft, J. Robertson, and C. Hamrin, Jr., "Fabrication of aluminum oxide thin films by a low-pressure metalorganic chemical vapor deposition technique," *Appl. Phys. Lett.* **62**, 681–683 (1993).
- ³⁰²A. Ott, J. Klaus, J. Johnson, and S. George, " Al_3O_3 thin film growth on Si (100) using binary reaction sequence chemistry," *Thin Solid Films* **292**, 135–144 (1997).
- ³⁰³A. Dillon, A. Ott, J. Way, and S. George, "Surface chemistry of Al_2O_3 deposition using $\text{Al}(\text{CH}_3)_3$ and H_2O in a binary reaction sequence," *Surf. Sci.* **322**, 230–242 (1995).
- ³⁰⁴M. Groner, J. Elam, F. Fabreguette, and S. M. George, "Electrical characterization of thin Al_2O_3 films grown by atomic layer deposition on silicon and various metal substrates," *Thin Solid Films* **413**, 186–197 (2002).
- ³⁰⁵S. J. Yun, K.-H. Lee, J. Skarp, H.-R. Kim, and K.-S. Nam, "Dependence of atomic layer-deposited Al_2O_3 films characteristics on growth temperature and al precursors of $\text{Al}(\text{CH}_3)_3$ and AlCl_3 ," *J. Vac. Sci. Technol. A* **15**, 2993–2997 (1997).
- ³⁰⁶N. V. Nguyen, O. A. Kirillov, W. Jiang, W. Wang, J. S. Suehle, P. Ye, Y. Xuan, N. Goel, K.-W. Choi, W. Tsai, and S. Sayan, "Band offsets of atomic-layer-deposited Al_2O_3 on GaAs and the effects of surface treatment," *Appl. Phys. Lett.* **93**, 082105 (2008).
- ³⁰⁷T. Kamimura, K. Sasaki, M. Hoi Wong, D. Krishnamurthy, A. Kuramata, T. Masui, S. Yamakoshi, and M. Higashiwaki, "Band alignment and electrical properties of $\text{Al}_2\text{O}_3/\beta\text{-Ga}_2\text{O}_3$ heterojunctions," *Appl. Phys. Lett.* **104**, 192104 (2014).
- ³⁰⁸M. J. Tadjer, F. Alema, A. Osinsky, M. A. Mastro, N. Nepal, J. M. Woodward, R. L. Myers-Ward, E. R. Glaser, J. A. Freitas, A. G. Jacobs *et al.*, "Characterization of $\beta\text{-Ga}_2\text{O}_3$ homoepitaxial films and MOSFETs grown by MOCVD at high growth rates," *J. Phys. D: Appl. Phys.* **54**, 034005 (2020).
- ³⁰⁹C. M. Tanner, Y.-C. Perng, C. Frewin, S. E. Saddow, and J. P. Chang, "Electrical performance of Al_2O_3 gate dielectric films deposited by atomic layer deposition on 4H-SiC," *Appl. Phys. Lett.* **91**, 203510 (2007).
- ³¹⁰M. J. Tadjer, T. J. Anderson, T. I. Feygelson, K. D. Hobart, J. K. Hite, A. D. Koehler, V. D. Wheeler, B. B. Pate, C. R. Eddy, Jr., and F. J. Kub, "Nanocrystalline diamond capped AlGaN/GaN high electron mobility transistors via a sacrificial gate process," *Phys. Status Solidi (a)* **213**, 893–897 (2016).
- ³¹¹M. Groner, F. Fabreguette, J. Elam, and S. George, "Low-temperature Al_2O_3 atomic layer deposition," *Chem. Mater.* **16**, 639–645 (2004).
- ³¹²X.-H. Zhang, B. Domercq, X. Wang, S. Yoo, T. Kondo, Z. L. Wang, and B. Kippelen, "High-performance pentacene field-effect transistors using Al_2O_3 gate dielectrics prepared by atomic layer deposition (ALD)," *Org. Electron.* **8**, 718–726 (2007).
- ³¹³P. Ma, L. Du, Y. Wang, R. Jiang, Q. Xin, Y. Li, and A. Song, "Low voltage operation of igzo thin film transistors enabled by ultrathin Al_2O_3 gate dielectric," *Appl. Phys. Lett.* **112**, 023501 (2018).
- ³¹⁴C. Park, U. Kim, C. J. Ju, J. S. Park, Y. M. Kim, and K. Char, "High mobility field effect transistor based on BaSnO₃ with Al_2O_3 gate oxide," *Appl. Phys. Lett.* **105**, 203503 (2014).
- ³¹⁵T. Marron, S. Takashima, Z. Li, and T. P. Chow, "Impact annealing ald Al_2O_3 gate dielectric GaN mos devices," *Phys. Status Solidi (c)* **9**, 907–910 (2012).
- ³¹⁶R. Santos, E. Longhinotti, V. Freire, R. Reinberg, and E. Caetano, "Elucidating the high-k insulator α - Al_2O_3 direct/indirect energy band gap type through density functional theory computations," *Chem. Phys. Lett.* **637**, 172–176 (2015).
- ³¹⁷T. Godin and J. P. LaFemina, "Atomic and electronic structure of the corundum (α -alumina)(0001) surface," *Phys. Rev. B* **49**, 7691 (1994).
- ³¹⁸Y.-N. Xu and W. Ching, "Self-consistent band structures, charge distributions, and optical-absorption spectra in MgO, α - Al_2O_3 , and MgAl₂O₄," *Phys. Rev. B* **43**, 4461 (1991).
- ³¹⁹E. Arakawa and M. Williams, "Optical properties of aluminum oxide in the vacuum ultraviolet," *J. Phys. Chem. Solids* **29**, 735–744 (1968).
- ³²⁰V. Afanas'eV, M. Houssa, A. Stesmans, and M. Heyns, "Band alignments in metal-oxide-silicon structures with atomic-layer deposited Al_2O_3 and ZrO_2 ," *J. Appl. Phys.* **91**, 3079–3084 (2002).
- ³²¹H. Yu, M. Li, B. J. Cho, C. Yeo, M. Joo, D.-L. Kwong, J. Pan, C. Ang, J. Zheng, and S. Ramanathan, "Energy gap and band alignment for $(\text{HfO}_2)_x(\text{Al}_2\text{O}_3)_{1-x}$ on (100) Si," *Appl. Phys. Lett.* **81**, 376–378 (2002).
- ³²²H. Nohira, W. Tsai, W. Besling, E. Young, J. Pétry, T. Conard, W. Vandervorst, S. De Gendt, M. Heyns, J. Maes, and M. Tuominen, "Characterization of ALCVD- Al_2O_3 and ZrO_2 layer using x-ray photoelectron spectroscopy," *J. Non-Cryst. Solids* **303**, 83–87 (2002).
- ³²³S. Andersson, P. A. Brühwiler, A. Sandell, M. Frank, J. Libuda, A. Giertz, B. Brena, A. Maxwell, M. Bäumer, H.-J. Freund, and N. Martensson,

- ³²¹ "Metal–oxide interaction for metal clusters on a metal-supported thin alumina film," *Surf. Sci.* **442**, L964–L970 (1999).
- ³²² M. Schmid, M. Shishkin, G. Kresse, E. Napetschnig, P. Varga, M. Kulawik, N. Nilius, H.-P. Rust, and H.-J. Freund, "Oxygen-deficient line defects in an ultrathin aluminum oxide film," *Phys. Rev. Lett.* **97**, 046101 (2006).
- ³²³ T. Tomiki, Y. Ganaha, T. Futemma, T. Shikenbaru, Y. Aiura, M. Yuri, S. Sato, H. Fukutani, H. Kato, T. Miyahara, J. Tamashiro, and A. Yonesu, "Anisotropic optical spectra of α -Al₂O₃ single crystals in the vacuum ultraviolet region. II. Spectra of optical constants," *J. Phys. Soc. Jpn.* **62**, 1372–1387 (1993).
- ³²⁴ A. K. Harman, S. Ninomiya, and S. Adachi, "Optical constants of sapphire (α -Al₂O₃) single crystals," *J. Appl. Phys.* **76**, 8032–8036 (1994).
- ³²⁵ S. Miyazaki, "Photoemission study of energy-band alignments and gap-state density distributions for high-k gate dielectrics," *J. Vac. Sci. Technol. B* **19**, 2212–2216 (2001).
- ³²⁶ M. Huang, Y. Chang, C. Chang, T. Lin, J. Kwo, T. Wu, and M. Hong, "Energy-band parameters atomic-layer-deposition Al₂O₃/InGaAs heterostructure," *Appl. Phys. Lett.* **89**, 012903 (2006).
- ³²⁷ P. Allen and M. Cardona, "Temperature dependence of the direct gap of Si and Ge," *Phys. Rev. B* **27**, 4760 (1983).
- ³²⁸ R. French, R. Coble, R. Kasowski, and F. Ohuchi, "Vacuum ultraviolet, photoemission and theoretical studies of the electronic structure of Al₂O₃ up to 1000°C," *Physica B* **150**, 47–49 (1988).
- ³²⁹ M. L. Cohen and D. Chadi, "Temperature dependence of semiconductor band states," *Handb. Semicond.* **2**, 155–180 (1980).
- ³³⁰ P. Auerkari, *Mechanical and Physical Properties of Engineering Alumina Ceramics* (Technical Research Centre of Finland Espoo, 1996), Vol. 23.
- ³³¹ E. Dorre and H. Hubner, *Alumina: Processing, Properties and Applications* (Springer-Verlag, 1984), p. 329.
- ³³² M. Munro, "Evaluated material properties for a sintered alpha-alumina," *J. Am. Ceram. Soc.* **80**, 1919–1928 (1997).
- ³³³ G. A. Slack, "The thermal conductivity of nonmetallic crystals," in *Solid State Physics* (Elsevier, 1979), Vol. 34, pp. 1–71.
- ³³⁴ D.-M. Liu, W. Tuan, and C.-C. Chiu, "Thermal diffusivity, heat capacity and thermal conductivity in Al₂O₃–Ni composite," *Mater. Sci. Eng.: B* **31**, 287–291 (1995).
- ³³⁵ C. J. Engberg and E. H. Zehms, "Thermal expansion of Al₂O₃, BeO, MgO, Ba₂C, SiC, and TiC above 1000°C," *J. Am. Ceram. Soc.* **42**, 300–305 (1959).
- ³³⁶ D. J. Klein, "Measurement on the crystallographic thermal expansion of alpha-alumina and beryllia to elevated temperatures emphasizing anisotropic effects," Technical Report No. NAA-SR-2542 (Atomics International Div., North American Aviation, Inc., Canoga Park, CA, 1958).
- ³³⁷ J. Wachtman, Jr., W. Tefft, D. Lam, Jr., and C. Apstein, "Exponential temperature dependence of Young's modulus for several oxides," *Phys. Rev.* **122**, 1754 (1961).
- ³³⁸ A. Amatuni, T. Malyutina, V. Y. Chekhovskoi, and V. Petukhov, "Standard samples for dilatometry," *High Temperatures-High Pressures* **8**, 565–570 (1976).
- ³³⁹ D. Chung and G. Simmons, "Pressure and temperature dependences of the isotropic elastic moduli of polycrystalline alumina," *J. Appl. Phys.* **39**, 5316–5326 (1968).
- ³⁴⁰ I. Stark, M. Stordeur, and F. Syrowatka, "Thermal conductivity of thin amorphous alumina films," *Thin Solid Films* **226**, 185–190 (1993).
- ³⁴¹ D. Ristau and J. Ebert, "Development of a thermographic laser calorimeter," *Appl. Opt.* **25**, 4571–4578 (1986).
- ³⁴² D. Ristau, S. M. J. Akhtar, and J. Ebert, NJST Spec. **752**, 300 (1988).
- ³⁴³ R. Zeller and R. Pohl, "Thermal conductivity and specific heat of noncrystalline solids," *Phys. Rev. B* **4**, 2029 (1971).
- ³⁴⁴ J. F. Schatz and G. Simmons, "Method of simultaneous measurement of radiative and lattice thermal conductivity," *J. Appl. Phys.* **43**, 2586–2594 (1972).
- ³⁴⁵ M. Ogawa, K. Mukai, T. Fukui, and T. Baba, "The development of a thermal diffusivity reference material using alumina," *Meas. Sci. Technol.* **12**, 2058 (2001).
- ³⁴⁶ S. Griffin, S. Knapen, T. Lin, and K. M. Zurek, "Directional detection of light dark matter with polar materials," *Phys. Rev. D* **98**, 115034 (2018).
- ³⁴⁷ M. C. Munisso, W. Zhu, and A. G. Pezzotti, "Raman tensor analysis of sapphire single crystal and its application to define crystallographic orientation in polycrystalline alumina," *Phys. Status Solidi (b)* **246**, 1893–1900 (2009).
- ³⁴⁸ G. Watson, Jr., W. Daniels, and C. Wang, "Measurements of raman intensities and pressure dependence of phonon frequencies in sapphire," *J. Appl. Phys.* **52**, 956–958 (1981).
- ³⁴⁹ M. Schubert, T. Tiwald, and C. Herzinger, "Infrared dielectric anisotropy and phonon modes of sapphire," *Phys. Rev. B* **61**, 8187 (2000).
- ³⁵⁰ A. Barker, Jr., "Infrared lattice vibrations and dielectric dispersion in corundum," *Phys. Review* **132**, 1474 (1963).
- ³⁵¹ F. Gervais and B. Piriou, "Anharmonicity in several-polar-mode crystals: adjusting phonon self-energy of LO and TO modes in Al₂O₃ and TiO₂ to fit infrared reflectivity," *J. Phys. C: Solid State Phys.* **7**, 2374 (1974).
- ³⁵² F. Gervais, D. Billard, and B. Piriou, "High-temperature phonon self energy—An application to infrared-spectra of corundum Al₂O₃," *Rev. Int. Hautes Temp. Refract.* **12**, 58–62 (1975).
- ³⁵³ W. Zhu and G. Pezzotti, "Phonon deformation potentials for the corundum structure of sapphire," *J. Raman Spectrosc.* **42**, 2015–2025 (2011).
- ³⁵⁴ R. Lyddane, R. Sachs, and E. Teller, "On the polar vibrations of alkali halides," *Phys. Rev.* **59**, 673 (1941).
- ³⁵⁵ J. Fontanella, C. Andeen, and D. Schuele, "Low-frequency dielectric constants of α -quartz, sapphire, MgF₂, and MgO," *J. Appl. Phys.* **45**, 2852–2854 (1974).
- ³⁵⁶ S. Pollack and C. Morris, "Electron tunneling through asymmetric films of thermally grown Al₂O₃," *J. Appl. Phys.* **35**, 1503–1512 (1964).
- ³⁵⁷ O. Nelson and D. Anderson, "Potential barrier parameters in thin-film Al-Al₂O₃-metal diodes," *J. Appl. Phys.* **37**, 77–82 (1966).
- ³⁵⁸ W. Pong, "Photoemission from Al-Al₂O₃ films in the vacuum ultraviolet region," *J. Appl. Phys.* **40**, 1733–1739 (1969).
- ³⁵⁹ G. Higashi and C. Fleming, "Sequential surface chemical reaction limited growth of high quality Al₂O₃ dielectrics," *Appl. Phys. Lett.* **55**, 1963–1965 (1989).
- ³⁶⁰ J.-F. Fan, K. Sugioka, and K. Toyoda, "Low-temperature growth of thin films of Al₂O₃ by sequential surface chemical reaction of trimethylaluminum and H₂O₂," *Jpn. J. Appl. Phys., Part 2* **30**, L1139 (1991).
- ³⁶¹ T. V. Perevalov, A. Shaposhnikov, V. A. Gritsenko, H. Wong, J. Han, and C. Kim, "Electronic structure of α -Al₂O₃: *Ab initio* simulations and comparison with experiment," *JETP Lett.* **85**, 165–168 (2007).
- ³⁶² Z. Burshtein and J. Levinson, "Photo-induced tunnel currents in Al-Al₂O₃-Au structures," *Phys. Rev. B* **12**, 3453 (1975).
- ³⁶³ Y.-C. Yeo, T.-J. King, and C. Hu, "MOSFET gate leakage modeling and selection guide for alternative gate dielectrics based on leakage considerations," *IEEE Trans. Electron Devices* **50**, 1027–1035 (2003).
- ³⁶⁴ A. Kerber, E. Cartier, R. Degraeve, P. J. Roussel, L. Pantisano, T. Kauerauf, G. Groeseneken, H. E. Maes, and U. Schwelke, "Charge trapping and dielectric reliability of SiO₂/Al₂O₃/gate stacks with TiN electrodes," *IEEE Trans. Electron Devices* **50**, 1261–1269 (2003).
- ³⁶⁵ F. G. Will, H. G. DeLorenzi, and K. H. Janora, "Effect of crystal orientation on conductivity and electron mobility in single-crystal alumina," *J. Am. Ceram. Soc.* **75**, 2790–2794 (1992).
- ³⁶⁶ P. Pickard, G. Myers, and M. Davis, "Electron trapping in metal oxides caused by high radiation fields," *Trans. Amer. Nucl. Soc.* **14**(2), 574–575 (1971).
- ³⁶⁷ B. Green and M. Davis, "Temperature-dependent Hall effect measurements in alumina," *Trans. Am. Nucl. Soc.* **16**, 75 (1973).
- ³⁶⁸ S. Dasgupta, "The Hall effect and magnetoresistance of alumina single crystals," *J. Phys. D: Appl. Phys.* **8**, 1822 (1975).
- ³⁶⁹ S. Mohapatra and F. Kröger, "Defect structure of α -Al₂O₃ doped with titanium," *J. Am. Ceram. Soc.* **60**, 381–387 (1977).
- ³⁷⁰ R. D. Bagley, I. B. Cutler, and D. L. Johnson, "Effect of TiO₂ on initial sintering of Al₂O₃," *J. Am. Ceram. Soc.* **53**, 136–141 (1970).
- ³⁷¹ W. Dean McKee, Jr. and E. Aleshin, "Aluminum oxide-titanium oxide solid solution," *J. Am. Ceram. Soc.* **46**, 54–58 (1963).
- ³⁷² S. K. Roy and R. L. Coble, "Solubilities of magnesia, titania, and magnesium titanate in aluminum oxide," *J. Am. Ceram. Soc.* **51**, 1–6 (1968).
- ³⁷³ R. Brook, J. Yee, and F. Kröger, "Electrochemical cells and electrical conduction of pure and doped Al₂O₃," *J. Am. Ceram. Soc.* **54**, 444–451 (1971).
- ³⁷⁴ B. Dutt, J. Hurrell, and F. Kröger, "High-temperature defect structure of cobalt-doped α -alumina," *J. Am. Ceram. Soc.* **58**, 420–427 (1975).
- ³⁷⁵ B. Dutt and F. Kröger, "High-temperature defect structure of iron-doped α -alumina," *J. Am. Ceram. Soc.* **58**, 474–476 (1975).

- ³⁷⁸Z. K. Heiba, M. B. Mohamed, A. M. Wahba, and N. Imam, "Structural, optical, and electronic characterization of Fe-doped alumina nanoparticles," *J. Electron. Mater.* **47**, 711–720 (2018).
- ³⁷⁹S. Mohapatra and F. Kröger, "Defect structure of α -Al₂O₃ doped with magnesium," *J. Am. Ceram. Soc.* **60**, 141–148 (1977b).
- ³⁸⁰T. Nakagawa, I. Sakaguchi, N. Shibata, K. Matsunaga, T. Mizoguchi, T. Yamamoto, H. Haneda, and Y. Ikuhara, "Yttrium doping effect on oxygen grain boundary diffusion in α -Al₂O₃," *Acta Mater.* **55**, 6627–6633 (2007).
- ³⁸¹J. Rasmussen and W. Kingery, "Effect of dopants on the defect structure of single-crystal aluminum oxide," *J. Am. Ceram. Soc.* **53**, 436–440 (1970).
- ³⁸²E. Winkler, J. Sarver, and I. B. Cutler, "Solid solution of titanium dioxide in aluminum oxide," *J. Am. Ceram. Soc.* **49**, 634–637 (1966).
- ³⁸³A. A. Sokol, A. Walsh, and C. R. A. Catlow, "Oxygen interstitial structures in close-packed metal oxides," *Chem. Phys. Lett.* **492**, 44–48 (2010).
- ³⁸⁴M. Choi, A. Janotti, and C. G. Van de Walle, "Native point defects and dangling bonds in α -Al₂O₃," *J. Appl. Phys.* **113**, 044501 (2013).
- ³⁸⁵E. Wahlström, N. Lopez, R. Schaub, P. Thostrup, A. Rønnaug, C. Africh, E. Lægsgaard, J. Nørskov, and F. Besenbacher, "Bonding of gold nanoclusters to oxygen vacancies on rutile TiO₂," *Phys. Rev. Lett.* **90**(110), 026101 (2003).
- ³⁸⁶M. Bäumer and H.-J. Freund, "Metal deposits on well-ordered oxide films," *Prog. Surf. Sci.* **61**, 127–198 (1999).
- ³⁸⁷S. M. Sze and K. K. Ng, *Physics of Semiconductor Devices* (John Wiley & Sons, 2006).
- ³⁸⁸D. Liu, S. Clark, and J. Robertson, "Oxygen vacancy levels and electron transport in Al₂O₃," *Appl. Phys. Lett.* **96**, 032905 (2010).
- ³⁸⁹B. H. Lee, L. Kang, R. Nieh, W.-J. Qi, and J. C. Lee, "Thermal stability and electrical characteristics of ultrathin hafnium oxide gate dielectric reoxidized with rapid thermal annealing," *Appl. Phys. Lett.* **76**, 1926–1928 (2000).
- ³⁹⁰S. Jachalke, T. Schenk, M. H. Park, U. Schroeder, T. Mikolajick, H. Stöcker, E. Mehner, and D. C. Meyer, "Pyroelectricity of silicon-doped hafnium oxide thin films," *Appl. Phys. Lett.* **112**, 142901 (2018).
- ³⁹¹J. Yan, Y. Kuo, and J. Lu, "Zirconium-doped hafnium oxide high-k dielectrics with subnanometer equivalent oxide thickness by reactive sputtering," *Electrochem. Solid State Lett.* **10**, H199 (2007).
- ³⁹²M. Esro, G. Vourlias, C. Somerton, W. I. Milne, and G. Adamopoulos, "High-mobility ZnO thin film transistors based on solution-processed hafnium oxide gate dielectrics," *Adv. Funct. Mater.* **25**, 134–141 (2015).
- ³⁹³T. Jones, R. Coble, and C. Mogab, "Defect diffusion in single crystal aluminum oxide," *J. Am. Ceram. Soc.* **52**, 331–334 (1969).
- ³⁹⁴N. Nilius, M. Kulawik, H.-P. Rust, and H.-J. Freund, "Defect-induced gap states in Al₂O₃ thin films on NiAl," *Phys. Rev. B* **69**(110), 121401 (2004).
- ³⁹⁵A. Janotti and C. G. Van de Walle, "Oxygen vacancies in ZnO," *Appl. Phys. Lett.* **87**, 122102 (2005).
- ³⁹⁶A. Kerber, E. Cartier, L. Pantisano, R. Degraeve, T. Kauerauf, Y. Kim, A. Hou, G. Groeseneken, H. Maes, and U. Schwalke, "Origin of the threshold voltage instability in SiO₂/HfO₂ dual layer gate dielectrics," *IEEE Electron Device Lett.* **24**, 87–89 (2003).
- ³⁹⁷Y. Sato and S-I. Akimoto, "Hydrostatic compression of four corundum-type compounds: α -Al₂O₃, V₂O₃, Cr₂O₃, and α -Fe₂O₃," *J. Appl. Phys.* **50**, 5285–5291 (1979).
- ³⁹⁸J. Leger, J. Haines, M. Schmidt, J. Petitet, A. Pereira, and J. Da Jornada, "Discovery of hardest known oxide," *Nature* **383**, 401–401 (1996).
- ³⁹⁹C.-M. Sung and M. Sung, "Carbon nitride and other speculative superhard materials," *Mater. Chem. Phys.* **43**, 1–18 (1996).
- ⁴⁰⁰W. Martienssen and H. Warlimont, *Springer Handbook of Condensed Matter and Materials Data* (Springer Science & Business Media, 2006).
- ⁴⁰¹J. Robertson and B. Falabretti, "Band offsets of high k gate oxides on III-V semiconductors," *J. Appl. Phys.* **100**, 014111 (2006).
- ⁴⁰²A. Jimenez-Gonzalez and D. Schmeisser, "Preparation and spectroscopic characterization of γ -Al₂O₃ thin films," *Surf. Sci.* **250**, 59–70 (1991).
- ⁴⁰³J. Manifacier and L. Szepessy, "Efficient sprayed In₂O₃:Sn n-type silicon heterojunction solar cell," *Appl. Phys. Lett.* **31**, 459–462 (1977).
- ⁴⁰⁴T. Koida, H. Fujiwara, and M. Kondo, "High-mobility hydrogen-doped In₂O₃ transparent conductive oxide for a-Si:H/c-Si heterojunction solar cells," *Sol. Energy Mater. Sol. Cells* **93**, 851–854 (2009).
- ⁴⁰⁵R. Sharma, R. S. Mane, S.-K. Min, and S.-H. Han, "Optimization of growth of In₂O₃ nano-spheres thin films by electrodeposition for dye-sensitized solar cells," *J. Alloys Compd.* **479**, 840–843 (2009).
- ⁴⁰⁶I. Hamberg and C. G. Granqvist, "Evaporated Sn-doped In₂O₃ films: Basic optical properties and applications to energy-efficient windows," *J. Appl. Phys.* **60**, R123–R160 (1986).
- ⁴⁰⁷Y. Meng, X-l Yang, H-x Chen, J. Shen, Y-m Jiang, Z-j Zhang, and Z-y Hua, "A new transparent conductive thin film In₂O₃: Mo," *Thin Solid Films* **394**, 218–222 (2001).
- ⁴⁰⁸J. S. Lee, Y.-J. Kwack, and W.-S. Choi, "Inkjet-printed In₂O₃ thin-film transistor below 200°C," *ACS Appl. Mater. Interfaces* **5**, 11578–11583 (2013).
- ⁴⁰⁹Z. Yuan, X. Zhu, X. Wang, X. Cai, B. Zhang, D. Qiu, and H. Wu, "Annealing effects of In₂O₃ thin films on electrical properties and application in thin film transistors," *Thin Solid Films* **519**, 3254–3258 (2011).
- ⁴¹⁰P. K. Nayak, M. N. Hedhili, D. Cha, and H. N. Alshareef, "High performance In₂O₃ thin film transistors using chemically derived aluminum oxide dielectric," *Appl. Phys. Lett.* **103**, 0 33518 (2013).
- ⁴¹¹R. Gupta and F. Yakuphanoglu, "Analysis of device parameters of Al/In₂O₃/p-Si schottky diode," *Microelectron. Eng.* **105**, 13–17 (2013).
- ⁴¹²J. Michel, D. Splith, J. Rombach, A. Papadogianni, T. Berthold, S. Krischok, M. Grundmann, O. Bierwagen, H. von Wenckstern, and M. Himmerlich, "Processing strategies for high-performance schottky contacts on n-type oxide semiconductors: Insights from In₂O₃," *ACS Appl. Mater. Interfaces* **11**, 27073–27087 (2019).
- ⁴¹³H. von Wenckstern, D. Splith, F. Schmidt, M. Grundmann, O. Bierwagen, and J. S. Speck, "Schottky contacts to In₂O₃," *APL Mater.* **2**, 046104 (2014).
- ⁴¹⁴P. Guo and H. Pan, "Selectivity of Ti-doped In₂O₃ ceramics as an ammonia sensor," *Sens. Actuators B* **114**, 762–767 (2006).
- ⁴¹⁵D.-H. Park, K.-Y. Son, J.-H. Lee, J.-J. Kim, and J.-S. Lee, "Effect of ZnO addition in In₂O₃ ceramics: Defect chemistry and sintering behavior," *Solid State Ionics* **172**, 431–434 (2004).
- ⁴¹⁶Y. Liu, Y.-H. Lin, J. Lan, W. Xu, B.-P. Zhang, C.-W. Nan, and H. Zhu, "Effect of transition-metal cobalt doping on the thermoelectric performance of In₂O₃ ceramics," *J. Am. Ceram. Soc.* **93**, 2938–2941 (2010a).
- ⁴¹⁷O. Myrasov and A. J. Freeman, "Electronic band structure of indium tin oxide and criteria for transparent conducting behavior," *Phys. Rev. B* **64**, 233111 (2001).
- ⁴¹⁸E. B. Aydin and M. K. Sezginer, "Indium tin oxide (ITO): A promising material in biosensing technology," *TrAC Trends Anal. Chem.* **97**, 309–315 (2017).
- ⁴¹⁹M. Mizuhashi, "Electrical properties of vacuum-deposited indium oxide and indium tin oxide films," *Thin Solid Films* **70**, 91–100 (1980).
- ⁴²⁰C. Y. Wang, Y. Dai, J. Pezoldt, B. Lu, T. Kups, V. Cimalla, and O. Ambacher, "Phase stabilization and phonon properties of single crystalline rhombohedral indium oxide," *Cryst. Growth Design* **8**, 1257–1260 (2008).
- ⁴²¹D. R. Hagleitner, M. Menhart, P. Jacobson, S. Blomberg, K. Schulte, E. Lundgren, M. Kubicek, J. Fleig, F. Kubel, C. Puls, A. Limbeck, H. Hutter, L. A. Boatner, M. Schmid, and U. Diebold, "Bulk and surface characterization of In₂O₃ (001) single crystals," *Phys. Rev. B* **85**, 115441 (2012).
- ⁴²²K. Zhang, V. Lazarov, P. Galindo, F. Oropeza, D. Payne, H.-C. Lai, and R. Egdel, "Domain matching epitaxial growth of In₂O₃ thin films on α -Al₂O₃ (001)," *Cryst. Growth Design* **12**, 1000–1007 (2012).
- ⁴²³R. S. Roth, "Classification of perovskite and other ABOS-type compounds," *J. Res. Natl. Bureau Standards* **58**, 75–88 (1957).
- ⁴²⁴M. Marezio, "Refinement of the crystal structure of In₂O₃ at two wavelengths," *Acta Crystallogr.* **20**, 723–728 (1966).
- ⁴²⁵J. De Wit, "Structural aspects and defect chemistry in In₂O₃," *J. Solid State Chem.* **20**, 143–148 (1977).
- ⁴²⁶I. Tanaka, M. Mizuno, and H. Adachi, "Electronic structure of indium oxide using cluster calculations," *Phys. Rev. B* **56**, 3536 (1997).
- ⁴²⁷S. Z. Karazhanov, P. Ravindran, P. Vajeeston, A. Ulyashin, T. Finstad, and H. Fjellvåg, "Phase stability, electronic structure, and optical properties of indium oxide polytypes," *Phys. Rev. B* **76**, 075129 (2007).
- ⁴²⁸F. Fuchs and F. Bechstedt, "Indium-oxide polymorphs from first principles: Quasiparticle electronic states," *Phys. Rev. B* **77**, 155107 (2008).
- ⁴²⁹C. Y. Wang, V. Cimalla, H. Romanus, T. Kups, G. Ecke, T. Stauden, M. Ali, V. Lebedev, J. Pezoldt, and O. Ambacher, "Phase selective growth and properties of rhombohedral and cubic indium oxide," *Appl. Phys. Lett.* **89**, 011904 (2006).

- ⁴³⁰M. F. Bekheet, M. R. Schwarz, S. Lauterbach, H.-J. Kleebe, P. Kroll, R. Riedel, and A. Gurlo, "Orthorhombic In_2O_3 : A metastable polymorph of indium sesquioxide," *Angew. Chem. Int. Ed.* **52**, 6531–6535 (2013).
- ⁴³¹H. Yusa, T. Tsuchiya, J. Tsuchiya, N. Sata, and Y. Ohishi, " α - Gd_2S_3 -type structure in In_2O_3 : Experiments and theoretical confirmation of a high-pressure polymorph in sesquioxide," *Phys. Rev. B* **78**, 092107 (2008).
- ⁴³²H. Yusa, T. Tsuchiya, N. Sata, and Y. Ohishi, "High-pressure phase transition to the Gd_2S_3 structure in Sc_2O_3 : A new trend in dense structures in sesquioxides," *Inorg. Chem.* **48**, 7537–7543 (2009).
- ⁴³³ICDD PDF-2 Database, JCPDS-Int., Center for Diffraction Data, Pennsylvania, 1994.
- ⁴³⁴R. Weiher, "Electrical properties of single crystals of indium oxide," *J. Appl. Phys.* **33**, 2834–2839 (1962).
- ⁴³⁵R. Roy and M. Shafer, "Phases present and phase equilibrium in the system In_2O_3 – H_2O ," *J. Phys. Chem.* **58**, 372–375 (1954).
- ⁴³⁶Z. Galazka, *Transparent Semiconducting Oxides: Bulk Crystal Growth and Fundamental Properties* (CRC Press, 2020).
- ⁴³⁷J. Remeika and E. Spencer, "Electrical conductivity and growth of single-crystal indium sesquioxide," *J. Appl. Phys.* **35**, 2803–2803 (1964).
- ⁴³⁸J. De Wit, "Electrical properties of In_2O_3 ," *J. Solid State Chem.* **8**, 142–149 (1973).
- ⁴³⁹Z. Galazka, R. Uecker, K. Irmscher, D. Schulz, D. Klimm, M. Albrecht, M. Pietsch, S. Ganschow, A. Kwasnewski, and R. Fornari, "Melt growth, characterization and properties of bulk In_2O_3 single crystals," *J. Cryst. Growth* **362**, 349–352 (2013).
- ⁴⁴⁰Z. Galazka, R. Uecker, and R. Fornari, "A novel crystal growth technique from the melt: Levitation-assisted self-seeding crystal growth method," *J. Cryst. Growth* **388**, 61–69 (2014).
- ⁴⁴¹D.-J. Lee, J.-Y. Kwon, J. I. Lee, and K.-B. Kim, "Self-limiting film growth of transparent conducting In_2O_3 by atomic layer deposition using trimethylindium and water vapor," *J. Phys. Chem. C* **115**, 15384–15389 (2011a).
- ⁴⁴²O. Nilsen, R. Balasundaraprabhu, E. Monakhov, N. Muthukumarasamy, H. Fjellvåg, and B. Svensson, "Thin films of In_2O_3 by atomic layer deposition using In(acac)(3)," *Thin Solid Films* **517**, 6320–6322 (2009).
- ⁴⁴³R. K. Ramachandran, J. Dendooven, H. Poelman, and C. Detavernier, "Low temperature atomic layer deposition of crystalline In_2O_3 films," *J. Phys. Chem. C* **119**, 11786–11791 (2015).
- ⁴⁴⁴W.-Y. Chung, G. Sakai, K. Shimano, N. Miura, D.-D. Lee, and N. Yamazoe, "Spin-coated indium oxide thin film on alumina and silicon substrates and their gas sensing properties," *Sens. Actuators B* **65**, 312–315 (2000).
- ⁴⁴⁵E. Tarsa, J. English, and J. Speck, "Pulsed laser deposition of oriented In_2O_3 on (001) InAs, MgO, and yttria-stabilized zirconia," *Appl. Phys. Lett.* **62**, 2332–2334 (1993).
- ⁴⁴⁶R. Gupta, K. Ghosh, S. Mishra, and P. Kahol, "Opto-electrical properties of Ti-doped In_2O_3 thin films grown by pulsed laser deposition," *Appl. Surf. Sci.* **253**, 9422–9425 (2007).
- ⁴⁴⁷N. Taga, M. Maekawa, Y. Shigesato, I. Yasui, M. Kakei, and T. Haynes, "Deposition of heteroepitaxial In_2O_3 thin films by molecular beam epitaxy," *Jpn. J. Appl. Phys., Part 1* **37**, 6524–6529 (1998).
- ⁴⁴⁸L. Kong, J. Ma, F. Yang, Z. Zhu, C. Luan, and H. Xiao, "Characterization of single-crystalline In_2O_3 films deposited on y -stabilized ZrO_2 (1 0 0) substrates by MOCVD," *Appl. Surf. Sci.* **257**, 518–522 (2010).
- ⁴⁴⁹X. Du, J. Yu, X. Xiu, Q. Sun, W. Tang, and B. Man, "Epitaxial growth and characterization of high quality In_2O_3 films on a-plane sapphire substrates by MOCVD," *Vacuum* **167**, 1–5 (2019).
- ⁴⁵⁰J. J. Prince, S. Ramamurthy, B. Subramanian, C. Sanjeeviraja, and M. Jayachandran, "Spray pyrolysis growth and material properties of In_2O_3 films," *J. Cryst. Growth* **240**, 142–151 (2002).
- ⁴⁵¹Z. Qiao, R. Latz, and D. Mergel, "Thickness dependence of In_2O_3 :Sn film growth," *Thin Solid Films* **466**, 250–258 (2004).
- ⁴⁵²H. Peelaers, E. Kioupakis, and C. Van de Walle, "Limitations of In_2O_3 as a transparent conducting oxide," *Appl. Phys. Lett.* **115**, 0 82105 (2019).
- ⁴⁵³J. Furthmüller, P. Hahn, F. Fuchs, and F. Bechstedt, "Band structures and optical spectra of inn polymorphs: Influence of quasiparticle and excitonic effects," *Phys. Rev. B* **72**, 205106 (2005).
- ⁴⁵⁴P. Erhart, A. Klein, R. G. Egdel, and K. Albe, "Band structure of indium oxide: Indirect versus direct band gap," *Phys. Rev. B* **75**, 153205 (2007).
- ⁴⁵⁵P. King, T. D. Veal, F. Fuchs, C. Y. Wang, D. Payne, A. Bourlange, H. Zhang, G. R. Bell, V. Cimalla, O. Ambacher, R. Egdel, F. Bechstedt, and C. McConville, "Band gap, electronic structure, and surface electron accumulation of cubic and rhombohedral In_2O_3 ," *Phys. Rev. B* **79**, 205211 (2009).
- ⁴⁵⁶M. Bender, N. Katsarakis, E. Gagouadakis, E. Hourdakis, E. Douloufakis, V. Cimalla, and G. Kiriakidis, "Dependence of the photoreduction and oxidation behavior of indium oxide films on substrate temperature and film thickness," *J. Appl. Phys.* **90**, 5382–5387 (2001).
- ⁴⁵⁷K. Zhang, V. Lazarov, T. Veal, F. Oropeza, C. McConville, R. Egdel, and A. Walsh, "Thickness dependence of the strain, band gap and transport properties of epitaxial In_2O_3 thin films grown on y -stabilised ZrO_2 ," *J. Phys.: Condens. Matter* **23**(111), 334211 (2011).
- ⁴⁵⁸K. Irmscher, M. Naumann, M. Pietsch, Z. Galazka, R. Uecker, T. Schulz, R. Schewski, M. Albrecht, and R. Fornari, "On the nature and temperature dependence of the fundamental band gap of In_2O_3 ," *Phys. Status Solidi (a)* **211**, 54–58 (2014).
- ⁴⁵⁹M. Ramzan, Y. Li, and R. Ahuja, "Electronic structure, mechanical and optical properties of In_2O_3 with hybrid density functional (HSe06)," *Solid State Commun.* **172**, 37–40 (2013).
- ⁴⁶⁰R. Schmidt-Grund, H. Krauß, C. Kranert, M. Bonholzer, and M. Grundmann, "Temperature dependence of the dielectric function in the spectral range (0.5–8.5) eV of an In_2O_3 thin film," *Appl. Phys. Lett.* **105**, 111906 (2014).
- ⁴⁶¹M. Wheeler, "Thermal diffusivity at incandescent temperatures by a modulated electron beam technique," *Br. J. Appl. Phys.* **16**, 365 (1965).
- ⁴⁶²D. Liu, W. Lei, B. Zou, S. Yu, J. Hao, K. Wang, B. Liu, Q. Cui, and G. Zou, "High-pressure x-ray diffraction and Raman spectra study of indium oxide," *J. Appl. Phys.* **104**, 083506 (2008).
- ⁴⁶³A. Walsh, C. R. A. Catlow, A. A. Sokol, and S. M. Woodley, "Physical properties, intrinsic defects, and phase stability of indium sesquioxide," *Chem. Mater.* **21**, 4962–4969 (2009).
- ⁴⁶⁴Z. Galazka, K. Irmscher, M. Pietsch, T. Schulz, R. Uecker, D. Klimm, and R. Fornari, "Effect of heat treatment on properties of melt-grown bulk In_2O_3 single crystals," *CryEngComm* **15**, 2220–2226 (2013b).
- ⁴⁶⁵L. Xu, B. Fauqué, Z. Zhu, Z. Galazka, K. Irmscher, and K. Behnia, "Thermal conductivity of bulk In_2O_3 single crystals," *arXiv:2008.13519* (2020).
- ⁴⁶⁶K. Kundra and S. Ali, "Thermal expansion of In_2O_3 ," *J. Appl. Crystallogr.* **3**, 543–545 (1970).
- ⁴⁶⁷R. Weiher and R. Ley, "Thermal expansion of indium oxide," *J. Appl. Phys.* **34**, 1833–1834 (1963).
- ⁴⁶⁸D. Bhattacharyya and M. Carter, "Effect of substrate on the structural and optical properties of chemical-bath-deposited CDS films," *Thin Solid Films* **288**, 176–181 (1996).
- ⁴⁶⁹K. Bachmann, F. Hsu, and J. Remeika, "The low temperature heat capacities of SnO_2 and In_2O_3 ," *Phys. Status Solidi A* **67**, K39–K42 (1981).
- ⁴⁷⁰N. Preissler, O. Bierwagen, A. T. Ramu, and J. S. Speck, "Electrical transport, electrothermal transport, and effective electron mass in single-crystalline In_2O_3 films," *Phys. Rev. B* **88**, 085305 (2013).
- ⁴⁷¹E. H. P. Cordfunke and E. F. Westrum, Jr., "The heat capacity and derived thermophysical properties of In_2O_3 from 0 to 1000 k," *J. Phys. Chem. Solids* **53**, 361–365 (1992).
- ⁴⁷²T. Yagi, K. Tamano, Y. Sato, N. Taketoshi, T. Baba, and Y. Shigesato, "Analysis on thermal properties of TiN doped indium oxide films by picosecond thermoreflectance measurement," *J. Vac. Sci. Technol. A* **23**, 1180–1186 (2005).
- ⁴⁷³M. Jothibas, C. Manoharan, S. Ramalingam, S. Dhanapandian, S. J. Jeyakumar, and M. Bououdina, "Preparation, characterization, spectroscopic (FT-IR, FT-raman, UV and visible) studies, optical properties and Kubo gap analysis of In_2O_3 thin films," *J. Mol. Struct.* **1049**, 239–249 (2013).
- ⁴⁷⁴T. Ashida, A. Miyamura, N. Oka, Y. Sato, T. Yagi, N. Taketoshi, T. Baba, and Y. Shigesato, "Thermal transport properties of polycrystalline TiN-doped indium oxide films," *J. Appl. Phys.* **105**, 073709 (2009).
- ⁴⁷⁵T. Ashida, A. Miyamura, Y. Sato, T. Yagi, N. Taketoshi, T. Baba, and Y. Shigesato, "Effect of electrical properties on thermal diffusivity of amorphous indium zinc oxide films," *J. Vac. Sci. Technol. A* **25**, 1178–1183 (2007).
- ⁴⁷⁶V. Martelli, J. L. Jiménez, M. Continentino, E. Baggio-Saitovitch, and K. Behnia, "Thermal transport and phonon hydrodynamics in strontium titanate," *Phys. Rev. Lett.* **120**, 125901 (2018).

- ⁴⁷⁷A. Inyushkin, A. Taldenkov, V. Ralchenko, A. Bolshakov, A. Koliadin, and A. Katrusha, "Thermal conductivity of high purity synthetic single crystal diamonds," *Phys. Rev. B* **97**, 144305 (2018).
- ⁴⁷⁸C. J. Glassbrenner and G. A. Slack, "Thermal conductivity of silicon and germanium from 3 K to the melting point," *Phys. Rev. A* **134**, 1058 (1964).
- ⁴⁷⁹D. G. Cahill and R. O. Pohl, "Lattice vibrations and heat transport in crystals and glasses," *Annu. Rev. Phys. chem.* **39**, 93–121 (1988).
- ⁴⁸⁰W. Xu, Y. Liu, B. Chen, D.-B. Liu, Y.-H. Lin, and A. Marcelli, "Nano-inclusions: A novel approach to tune the thermal conductivity of In_2O_3 ," *Phys. Chem. Chem. Phys.* **15**, 17595–17600 (2013).
- ⁴⁸¹T. Miyasako, M. Senoo, and E. Tokumitsu, "Ferroelectric-gate thin-film transistors using indium-tin-oxide channel with large charge controllability," *Appl. Phys. Lett.* **86**, 162902 (2005).
- ⁴⁸²M. Grover, P. Hersh, H. Chiang, E. Kettenring, J. Wager, and D. Keszler, "Thin-film transistors with transparent amorphous zinc indium tin oxide channel layer," *J. Phys. D: Appl. Phys.* **40**, 1335 (2007).
- ⁴⁸³D. Béardin, E. Guillemeau, A. Maignan, and B. Raveau, " $\text{In}_2\text{O}_3:\text{Ge}$, a promising n-type thermoelectric oxide composite," *Solid State Commun.* **146**, 97–101 (2008).
- ⁴⁸⁴M. Stoekey, R. Korlacki, S. Knight, A. Ruder, M. Hilfiker, Z. Galazka, K. Irmscher, Y. Zhang, H. Zhao, V. Darakchieva, and M. Schubert, "Optical phonon modes, static and high frequency dielectric constants, and effective electron mass parameter in cubic In_2O_3 ," *J. Appl. Phys.* **129**, 225102 (2021).
- ⁴⁸⁵C. Kranert, R. Schmidt-Grund, and M. Grundmann, "Raman active phonon modes of cubic In_2O_3 ," *Phys. Status Solidi RRL* **8**, 554–559 (2014).
- ⁴⁸⁶H. Sobotta, H. Neumann, G. Kühn, and V. Riede, "Infrared lattice vibrations of In_2O_3 ," *Cryst. Res. Technol.* **25**, 61–64 (1990).
- ⁴⁸⁷M. Feneberg, J. Nixdorf, C. Lidig, R. Goldhahn, Z. Galazka, O. Bierwagen, and J. S. Speck, "Many-electron effects on the dielectric function of cubic In_2O_3 : Effective electron mass, band nonparabolicity, band gap renormalization, and burstein-moss shift," *Phys. Rev. B* **93**, 045203 (2016).
- ⁴⁸⁸B. García-Domene, H. Ortiz, O. Gomis, J. Sans, F. Manjón, A. Muñoz, P. Rodríguez-Hernández, S. Achary, D. Errandonea, D. Martínez-García, A. Romero, A. Singhal, and A. Tyagi, "High-pressure lattice dynamical study of bulk and nanocrystalline In_2O_3 ," *J. Appl. Phys.* **112**, 123511 (2012).
- ⁴⁸⁹H. Ehrenreich, "Band structure and electron transport of GaAs," *Phys. Rev.* **120**, 1951 (1960).
- ⁴⁹⁰J. Singh, *Physics of Semiconductors and their Heterostructures* (McGraw-Hill, New York, 1993), Vol. 84.
- ⁴⁹¹W. Jia and W. Yen, "Raman scattering from sapphire fibers," *J. Raman Spectrosc.* **20**, 785–788 (1989).
- ⁴⁹²J. Shewchun, J. Dubow, A. Myszkowski, and R. Singh, "The operation of the semiconductor-insulator-semiconductor (SIS) solar cell: Theory," *J. Appl. Phys.* **49**, 855–864 (1978).
- ⁴⁹³W. Thompson and R. Anderson, "Electrical and photovoltaic characteristics of indium-tin oxide/silicon heterojunctions," *Solid-State Electron.* **21**, 603–608 (1978).
- ⁴⁹⁴R. Singh and J. Shewchun, "The importance of the electron affinity of oxide-semiconductors as used in solar cells," *Appl. Phys. Lett.* **33**, 601–603 (1978).
- ⁴⁹⁵E. Y. Wang and L. Hsu, "Determination of electron affinity of In_2O_3 from its heterojunction photovoltaic properties," *J. Electrochem. Soc.* **125**, 1328 (1978).
- ⁴⁹⁶O. Lang, C. Pettenkofer, J. F. Sánchez-Royo, A. Segura, A. Klein, and W. Jaegermann, "Thin film growth and band lineup of In_2O_3 on the layered semiconductor ince," *J. Appl. Phys.* **86**, 5687–5691 (1999).
- ⁴⁹⁷A. Myszkowski, L. Sansores, and J. Tagüeña-Martínez, "Tunneling solar cell under concentrated light illumination," *J. Appl. Phys.* **52**, 4288–4296 (1981).
- ⁴⁹⁸J. Szczyrbowski, A. Dietrich, and H. Hoffmann, "Optical and electrical properties of rf-sputtered indium-tin oxide films," *Phys. Status Solidi (a)* **78**, 243–252 (1983).
- ⁴⁹⁹G. Frank, E. Kauer, H. Koestlin, and F. Schmitte, "Optical coatings for energy efficiency and solar applications," *Proc. SPIE* **324**, 58 (1982).
- ⁵⁰⁰J. De Wit, J. Van Der Bom, and J. De Groot, "The thermoelectric power in In_2O_3 ," *J. Solid State Chem.* **25**, 101–105 (1978).
- ⁵⁰¹O. Bierwagen and J. S. Speck, "High electron mobility In_2O_3 (001) and (111) thin films with nondegenerate electron concentration," *Appl. Phys. Lett.* **97**, 072103 (2010).
- ⁵⁰²P. Thilakan and J. Kumar, "Reactive thermal deposition of indium oxide and tin-doped indium oxide thin films on inp substrates," *Thin Solid Films* **292**, 50–54 (1997).
- ⁵⁰³T. Koida and M. Kondo, "High electron mobility of indium oxide grown on yttria-stabilized zirconia," *J. Appl. Phys.* **99**, 123703 (2006).
- ⁵⁰⁴H. Ohta, M. Orita, M. Hirano, H. Tanji, H. Kawazoe, and H. Hosono, "Highly electrically conductive indium–tin–oxide thin films epitaxially grown on yttria-stabilized zirconia (100) by pulsed-laser deposition," *Appl. Phys. Lett.* **76**, 2740–2742 (2000).
- ⁵⁰⁵P. Thilakan and J. Kumar, "Studies on the preferred orientation changes and its influenced properties on ito thin films," *Vacuum* **48**, 463–466 (1997).
- ⁵⁰⁶E. Korhonen, F. Tuomisto, O. Bierwagen, J. Speck, and Z. Galazka, "Compensating vacancy defects in Sn-and Mg-doped In_2O_3 ," *Phys. Rev. B* **90**, 245307 (2014).
- ⁵⁰⁷Y. W. Kim, J. S. Goo, T. H. Lee, B. R. Lee, S.-C. Shin, H. Kim, J. W. Shim, and T. G. Kim, "Tailoring opto-electrical properties of ultra-thin indium tin oxide films via filament doping: Application as a transparent cathode for indoor organic photovoltaics," *J. Power Sources* **424**, 165–175 (2019).
- ⁵⁰⁸V. Vaishnav, P. Patel, and N. Patel, "Preparation and characterization of indium tin oxide thin films for their application as gas sensors," *Thin Solid Films* **487**, 277–282 (2005).
- ⁵⁰⁹R. Bel Hadj Tahar, T. Ban, Y. Ohya, and Y. Takahashi, "Tin doped indium oxide thin films: Electrical properties," *J. Appl. Phys.* **83**, 2631–2645 (1998).
- ⁵¹⁰Y. Shigesato and D. C. Paine, "Study of the effect of Sn doping on the electronic transport properties of thin film indium oxide," *Appl. Phys. Lett.* **62**, 1268–1270 (1993).
- ⁵¹¹R. Gupta, K. Ghosh, S. Mishra, and P. Kahol, "High mobility Ti-doped In_2O_3 transparent conductive thin films," *Mater. Lett.* **62**, 1033–1035 (2008).
- ⁵¹²Z. Dong, D. Ding, T. Li, and C. Ning, "High-efficiency photoelectrochemical water splitting with heterojunction photoanode of In_2O_3 -x nanorods/black ti-Si o nanotubes," *Int. J. Hydrogen Energy* **44**, 17611–17621 (2019b).
- ⁵¹³D.-J. Kim, B.-S. Kim, and H.-K. Kim, "Effect of thickness and substrate temperature on the properties of transparent ti-doped In_2O_3 films grown by direct current magnetron sputtering," *Thin Solid Films* **547**, 225–229 (2013).
- ⁵¹⁴Y. Ohhata, F. Shinoki, and S. Yoshida, "Optical properties of rf reactive sputtered tin-doped In_2O_3 films," *Thin Solid Films* **59**, 255–261 (1979).
- ⁵¹⁵L. G. Bloor, J. Manzi, R. Binions, I. P. Parkin, D. Pugh, A. Afonja, C. S. Blackman, S. Sathasivam, and C. J. Carmalt, "Tantalum and titanium doped In_2O_3 thin films by aerosol-assisted chemical vapor deposition and their gas sensing properties," *Chem. Mater.* **24**, 2864–2871 (2012).
- ⁵¹⁶W. J. Lee, Y.-K. Fang, J.-J. Ho, C.-Y. Chen, L.-H. Chiou, S.-J. Wang, F. Dai, T. Hsieh, R.-Y. Tsai, D. Huang, and F. Ho, "Organic light-emitting diode on indium zinc oxide film prepared by ion assisted deposition dc sputtering system," *Solid-State Electron.* **46**, 477–480 (2002).
- ⁵¹⁷M. Van Hest, M. Dabney, J. Perkins, and D. Ginley, "High-mobility molybdenum doped indium oxide," *Thin Solid Films* **496**, 70–74 (2006).
- ⁵¹⁸D. S. Bhachu, D. O. Scanlon, G. Sankar, T. Veal, R. G. Egdell, G. Cibin, A. J. Dent, C. E. Knapp, C. J. Carmalt, and I. P. Parkin, "Origin of high mobility in molybdenum-doped indium oxide," *Chem. Mater.* **27**, 2788–2796 (2015).
- ⁵¹⁹S.-Y. Sun, J.-L. Huang, and D.-F. Lii, "Effects of oxygen contents on the electrical and optical properties of indium molybdenum oxide films fabricated by high density plasma evaporation," *J. Vac. Sci. Technol. A* **22**, 1235–1241 (2004).
- ⁵²⁰T. Koida, H. Fujiwara, and M. Kondo, "Hydrogen-doped In_2O_3 as high-mobility transparent conductive oxide," *Jpn. J. Appl. Phys., Part 2* **46**, L685 (2007).
- ⁵²¹F. Meng, J. Shi, Z. Liu, Y. Cui, Z. Lu, and Z. Feng, "High mobility transparent conductive W-doped In_2O_3 thin films prepared at low substrate temperature and its application to solar cells," *Sol. Energy Mater. Solar Cells* **122**, 70–74 (2014).
- ⁵²²H. Kim, M. Osofsky, M. Miller, S. Qadri, R. Auyeung, and A. Pique, "Room temperature ferromagnetism in transparent Fe-doped In_2O_3 films," *Appl. Phys. Lett.* **100**, 032404 (2012).
- ⁵²³X. Luo, L.-T. Tseng, Y. Wang, N. Bao, Z. Lu, X. Ding, R. Zheng, Y. Du, K. Huang, L. Shu, A. Suter, W. T. Lee, R. Liu, J. Ding, K. Suzuki, T. Prokscha, E. Morenzoni, and J. B. Yi, "Intrinsic or interface clustering-induced

- ferromagnetism in Fe-doped In_2O_3 -diluted magnetic semiconductors," *ACS Appl. Mater. Interfaces* **10**, 22372–22380 (2018).
- ⁵²⁴M. Jothibas, C. Manoharan, S. Ramalingam, S. Dhanapandian, and M. Bououdina, "Spectroscopic analysis, structural, microstructural, optical and electrical properties of Zn-doped In_2O_3 thin films," *Spectrochim. Acta, Part A* **122**, 171–178 (2014).
- ⁵²⁵S. Li, Z. Shi, Z. Tang, and X. Li, "Comparison of ITO, $\text{In}_2\text{O}_3:\text{Zn}$ and $\text{In}_2\text{O}_3:\text{H}$ transparent conductive oxides as front electrodes for silicon heterojunction solar cell applications," *Vacuum* **145**, 262–267 (2017).
- ⁵²⁶S. Lany and A. Zunger, "Dopability, intrinsic conductivity, and nonstoichiometry of transparent conducting oxides," *Phys. Rev. Lett.* **98**, 045501 (2007).
- ⁵²⁷P. Agoston, P. Erhart, A. Klein, and K. Albe, "Geometry, electronic structure and thermodynamic stability of intrinsic point defects in indium oxide," *J. Phys.: Condens. Matter* **21**, 455801 (2009).
- ⁵²⁸P. Reunchan, X. Zhou, S. Limpijumnong, A. Janotti, and C. G. Van de Walle, "Vacancy defects in indium oxide: An ab-initio study," *Curr. Appl. Phys.* **11**, S296–S300 (2011).
- ⁵²⁹O. Bierwagen and J. S. Speck, "Mg acceptor doping of In_2O_3 and overcompensation by oxygen vacancies," *Appl. Phys. Lett.* **101**, 102107 (2012).
- ⁵³⁰I. Makkonen, E. Korhonen, V. Prozheeva, and F. Tuomisto, "Identification of vacancy defect complexes in transparent semiconducting oxides ZnO , In_2O_3 and SnO_2 ," *J. Phys.: Condens. Matter* **28**, 224002 (2016).
- ⁵³¹V. Scherer, C. Janowitz, A. Krapf, H. Dwelk, D. Braun, and R. Manzke, "Transport and angular resolved photoemission measurements of the electronic properties of In_2O_3 bulk single crystals," *Appl. Phys. Lett.* **100**, 212108 (2012).
- ⁵³²W. B. White and V. G. Keramidas, "Vibrational spectra of oxides with the c-type rare earth oxide structure," *Spectrochim. Acta Part A* **28**, 501–509 (1972).
- ⁵³³V. Karpina, V. Lazorenko, C. Lashkarev, V. Dobrowski, L. Kopylova, V. Baturin, S. Pustovoytov, A. J. Karpenko, S. Eremin, P. Lytvyn, P. Ovsyannikov, and E. Mazurenko, "Zinc oxide-Analogue of GaN with new perspective possibilities," *Cryst. Res. Technol.* **39**, 980–992 (2004).
- ⁵³⁴E. Muchuweni, T. Sathiaraj, and H. Nyakoto, "Synthesis and characterization of zinc oxide thin films for optoelectronic applications," *Helion* **3**, e00285 (2017).
- ⁵³⁵S. Roy and S. Basu, "Improved zinc oxide film for gas sensor applications," *Bull. Mater. Sci.* **25**, 513–515 (2002).
- ⁵³⁶A. M. Ma, M. Gupta, F. R. Chowdhury, M. Shen, K. Bothe, K. Shankar, Y. Tsui, and D. W. Barlage, "Zinc oxide thin film transistors with schottky source barriers," *Solid-State Electron.* **76**, 104–108 (2012).
- ⁵³⁷K. S. Leschkies, A. G. Jacobs, D. J. Norris, and E. S. Aydin, "Nanowire-quantum-dot solar cells and the influence of nanowire length on the charge collection efficiency," *Appl. Phys. Lett.* **95**, 193103 (2009).
- ⁵³⁸K. Ellmer, A. Klein, and B. Rech, *Transparent Conductive Zinc Oxide: Basics and Applications in Thin Film Solar Cells* (Springer Science & Business Media, 2007), Vol. 104.
- ⁵³⁹K. Ellmer and A. Klein, "ZnO and its applications," in *Transparent Conductive Zinc Oxide* (Springer, 2008), pp. 1–33.
- ⁵⁴⁰A. Kolodziejczak-Radzimska and T. Jasionowski, "Zinc oxide—from synthesis to application: A review," *Mater.* **7**, 2833–2881 (2014).
- ⁵⁴¹C. Jagadish and S. J. Pearton, *Zinc Oxide Bulk, Thin Films and Nanostructures: Processing, Properties, and Applications* (Elsevier, 2011).
- ⁵⁴²Ü. Özgür, Y. I. Alivov, C. Liu, A. Teke, M. Reshchikov, S. Dogan, V. Avrutin, S.-J. Cho, and H. Morkoç, "A comprehensive review of ZnO materials and devices," *J. Appl. Phys.* **98**, 041301 (2005).
- ⁵⁴³E. H. Kisi and M. M. Elcombe, " u parameters for the wurtzite structure of zns and ZnO using powder neutron diffraction," *Acta Crystallogr. Sect. C* **45**, 1867–1870 (1989).
- ⁵⁴⁴L. Gerward and J. S. Olsen, "The high-pressure phase of zincite," *J. Synchrotron Radiat.* **2**, 233–235 (1995).
- ⁵⁴⁵M. Catti, Y. Noel, and R. Dovesi, "Full piezoelectric tensors of wurtzite and zinc blende ZnO and ZnS by first-principles calculations," *J. Phys. Chem. Solids* **64**, 2183–2190 (2003).
- ⁵⁴⁶A. A. Ashrafi, A. Ueta, A. Avramescu, H. Kumano, I. Suemune, Y.-W. Ok, and T.-Y. Seong, "Growth and characterization of hypothetical zinc-blende ZnO films on GaAs (001) substrates with ZnS buffer layers," *Appl. Phys. Lett.* **76**, 550–552 (2000).
- ⁵⁴⁷J. Jaffe and A. Hess, "Hartree-Fock study of phase changes in ZnO at high pressure," *Phys. Rev. B* **48**, 7903 (1993).
- ⁵⁴⁸H. Karzel, W. Potzel, M. Köfferlein, W. Schiessl, M. Steiner, U. Hiller, G. Kalvius, D. Mitchell, T. Das, P. Blaha, K. Schwarz, and M. Pasternak, "Lattice dynamics and hyperfine interactions in ZnO and znse at high external pressures," *Phys. Rev. B* **53**, 11425 (1996).
- ⁵⁴⁹D. R. Lide, *Handbook of Chemistry and Physics*, 73rd ed. (CRC, 1992), Vol. 73.
- ⁵⁵⁰T. Sekiguchi, S. Miyashita, K. Obara, T. Shishido, and N. Sakagami, "Hydrothermal growth of ZnO single crystals and their optical characterization," *J. Cryst. Growth* **214**, 72–76 (2000).
- ⁵⁵¹N. Sakagami, M. Yamashita, T. Sekiguchi, S. Miyashita, K. Obara, and T. Shishido, "Variation of electrical properties on growth sectors of ZnO single crystals," *J. Cryst. Growth* **229**, 98–103 (2001).
- ⁵⁵²M. Suscavage, M. Harris, D. Bliss, P. Yip, S.-Q. Wang, D. Schwall, L. Bouthillette, J. Bailey, M. Callahan, D. C. Look, D. Reynolds, R. Jones, and C. Litton, "High quality hydrothermal ZnO crystals," *Mater. Res. Soc. Internet J. Nitride Semicond. Res.* **4**, 287–292 (1999).
- ⁵⁵³O. Fritsch, "Electrical and optical behavior of semiconductors. X. Electrical measurements on zinc oxide," *Ann. Phys.* **414**, 375–401 (1935).
- ⁵⁵⁴A. Walker, "Hydrothermal synthesis of quartz crystals," *J. Am. Ceram. Soc.* **36**, 250–256 (1953).
- ⁵⁵⁵D. Ehrentraut, H. Sato, Y. Kagamitani, H. Sato, A. Yoshikawa, and T. Fukuda, "Solvothermal growth of ZnO," *Prog. Cryst. Growth Charact. Mater.* **52**, 280–335 (2006).
- ⁵⁵⁶I. Kubo, *Jpn. J. Cryst. Growth* **4**, 225–226 (1965).
- ⁵⁵⁷D. C. Look, D. C. Reynolds, J. Sizelove, R. Jones, C. W. Litton, G. Cantwell, and W. Harsch, "Electrical properties of bulk ZnO," *Solid State Commun.* **105**, 399–401 (1998).
- ⁵⁵⁸A. Hachigo, H. Nakahata, K. Higaki, S. Fujii, and S.-I. Shikata, "Heteroepitaxial growth of ZnO films on diamond (111) plane by magnetron sputtering," *Appl. Phys. Lett.* **65**, 2556–2558 (1994).
- ⁵⁵⁹M. Purica, E. Budianu, E. Rusu, M. Danila, and R. Gavrila, "Optical and structural investigation of ZnO thin films prepared by chemical vapor deposition (CVD)," *Thin Solid Films* **403**, 485–488 (2002).
- ⁵⁶⁰S. Tiku, C. Lau, and K. Lakin, "Chemical vapor deposition of ZnO epitaxial films on sapphire," *Appl. Phys. Lett.* **36**, 318–320 (1980).
- ⁵⁶¹Y. Chen, D. Bagnall, H.-J. Koh, K.-T. Park, K. Hiraga, Z. Zhu, and T. Yao, "Plasma assisted molecular beam epitaxy of ZnO on c-plane sapphire: Growth and characterization," *J. Appl. Phys.* **84**, 3912–3918 (1998).
- ⁵⁶²K. Iwata, P. Fons, S. Niki, A. Yamada, K. Matsubara, K. Nakahara, and H. Takasu, "Improvement of electrical properties in ZnO thin films grown by radical source (RS)-MBE," *Phys. Status Solidi (a)* **180**, 287–292 (2000).
- ⁵⁶³A. Ohtomo and A. Tsukazaki, "Pulsed laser deposition of thin films and superlattices based on ZnO," *Semicond. Sci. Technol.* **20**, S1 (2005).
- ⁵⁶⁴Y. Liu, C. Gorla, S. Liang, N. Emanetoglu, Y. Lu, H. Shen, and M. Wraback, "Ultraviolet detectors based on epitaxial ZnO films grown by MOCVD," *J. Electron. Mater.* **29**, 69–74 (2000).
- ⁵⁶⁵M. Wei, "Growth and characterization of ZnO based semiconductor materials and devices," Doctoral dissertation (University of Central Florida, 2013).
- ⁵⁶⁶J. Zhu, B. Lin, X. Sun, R. Yao, C. Shi, and Z. Fu, "Heteroepitaxy of ZnO film on Si (111) substrate using a 3c-SiC buffer layer," *Thin Solid Films* **478**, 218–222 (2005).
- ⁵⁶⁷D. Vogel, P. Krüger, and J. Pollmann, "*Ab initio* electronic-structure calculations for II-VI semiconductors using self-interaction-corrected pseudopotentials," *Phys. Rev. B* **52**, R14316 (1995).
- ⁵⁶⁸J. R. Chelikowsky, "An oxygen pseudopotential: Application to the electronic structure of ZnO," *Solid State Commun.* **22**, 351–354 (1977).
- ⁵⁶⁹U. Rössler, "Energy bands of hexagonal II-VI semiconductors," *Phys. Rev.* **184**, 733 (1969).
- ⁵⁷⁰D. Langer and C. Vesely, "Electronic core levels of zinc chalcogenides," *Phys. Rev. B* **2**, 4885 (1970).
- ⁵⁷¹R. Powell, W. Spicer, and J. McMenamin, "Location of the Zn 3D states in ZnO," *Phys. Rev. Lett.* **27**, 97 (1971).

- ⁵⁷²R. Powell, W. Spicer, and J. McMenamin, "Photoemission studies of wurtzite zinc oxide," *Phys. Rev. B* **6**, 3056 (1972).
- ⁵⁷³C. Vesely, R. Hengehold, and D. Langer, "UV photoemission measurements of the upper *d* levels in the IIB-VIA compounds," *Phys. Rev. B* **5**, 2296 (1972).
- ⁵⁷⁴L. Ley, R. Pollak, F. McFeely, S. P. Kowalczyk, and D. Shirley, "Total valence-band densities of states of III-V and II-VI compounds from x-ray photoemission spectroscopy," *Phys. Rev. B* **9**, 600 (1974).
- ⁵⁷⁵I. Ivanov and J. Pollmann, "Electronic structure of ideal and relaxed surfaces of ZnO: A prototype ionic wurtzite semiconductor and its surface properties," *Phys. Rev. B* **24**, 7275 (1981).
- ⁵⁷⁶C. Bundesmann, R. Schmidt-Grund, and M. Schubert, "Optical properties of ZnO and related compounds," in *Transparent Conductive Zinc Oxide* (Springer, 2008), pp. 79–124.
- ⁵⁷⁷D. Reynolds, D. C. Look, B. Jogai, C. Litton, T. Collins, M. Harris, M. Callahan, and J. Bailey, "Strain splitting of the Γ_5 and Γ_6 free excitons in ZnO," *J. Appl. Phys.* **86**, 5598–5600 (1999).
- ⁵⁷⁸B. Gil, "Oscillator strengths of A, B, and C excitons in ZnO films," *Phys. Rev. B* **64**, 201310 (2001).
- ⁵⁷⁹P. Schröer, P. Krüger, and J. Pollmann, "First-principles calculation of the electronic structure of the wurtzite semiconductors ZnO and ZnS," *Phys. Rev. B* **47**, 6971 (1993).
- ⁵⁸⁰F. Fuchs, J. Furthmüller, F. Bechstedt, M. Shishkin, and G. Kresse, "Quasiparticle band structure based on a generalized Kohn-Sham scheme," *Phys. Rev. B* **76**, 115109 (2007).
- ⁵⁸¹C. Friedrich, M. C. Müller, and S. Blügel, "Band convergence and linearization error correction of all-electron GW calculations: The extreme case of zinc oxide," *Phys. Rev. B* **83**, 081101 (2011).
- ⁵⁸²M. Shishkin and G. Kresse, "Self-consistent GW calculations for semiconductors and insulators," *Phys. Rev. B* **75**, 235102 (2007).
- ⁵⁸³M. Usuda, N. Hamada, T. Kotani, and M. van Schilfgaarde, "All-electron GW calculation based on the LAPW method: Application to wurtzite ZnO," *Phys. Rev. B* **66**, 125101 (2002).
- ⁵⁸⁴G. Jellison and L. Boatner, "Optical functions of uniaxial ZnO determined by generalized ellipsometry," *Phys. Rev. B* **58**, 3586 (1998).
- ⁵⁸⁵T. Kang, H. Lee, W.-I. Park, and G.-C. Yi, "Ellipsometry on uniaxial ZnO and $Zn_{1-x}Mg_xO$ thin films grown on (0001) sapphire substrate," *Thin Solid Films* **455**, 609–614 (2004).
- ⁵⁸⁶A. Djurišić, Y. Chan, and E. Li, "The optical dielectric function of ZnO," *Appl. Phys. A* **76**, 37–43 (2003).
- ⁵⁸⁷W. Liang and A. Yoffe, "Transmission spectra of ZnO single crystals," *Phys. Rev. Lett.* **20**, 59 (1968).
- ⁵⁸⁸H. Yoshikawa and S. Adachi, "Optical constants of ZnO," *Jpn. J. Appl. Phys., Part 1* **36**, 6237 (1997).
- ⁵⁸⁹V. Srikanth and D. R. Clarke, "On the optical band gap of zinc oxide," *J. Appl. Phys.* **83**, 5447–5451 (1998).
- ⁵⁹⁰R. Schmidt, B. Rheinländer, M. Schubert, D. Spemann, T. Butz, J. Lenzner, E. Kaidashev, M. Lorenz, A. Rahm, H. Semmelhack, and Grundmann, "Dielectric functions (1 to 5 eV) of wurtzite $Mg_xZn_{1-x}O$ ($x \leq 0.29$) thin films," *Appl. Phys. Lett.* **82**, 2260–2262 (2003).
- ⁵⁹¹S. Benramache, O. Belahssen, A. Guettaf, and A. Arif, "Correlation between electrical conductivity-optical band gap energy and precursor molarities ultrasonic spray deposition of ZnO thin films," *J. Semicond.* **34**, 113001 (2013).
- ⁵⁹²B. Zhu, X. Sun, X. Zhao, F. Su, G. Li, X. Wu, J. Wu, R. Wu, and J. Liu, "The effects of substrate temperature on the structure and properties of ZnO films prepared by pulsed laser deposition," *Vacuum* **82**, 495–500 (2008).
- ⁵⁹³S.-S. Lin and J.-L. Huang, "Effect of thickness on the structural and optical properties of ZnO films by rf magnetron sputtering," *Surf. Coat. Technol.* **185**, 222–227 (2004).
- ⁵⁹⁴S. Ilican, Y. Caglar, and M. Caglar, "Preparation and characterization of ZnO thin films deposited by sol-gel spin coating method," *J. Optoelectron. Adv. Mater.* **10**, 2578–2583 (2008).
- ⁵⁹⁵M. Izaki and T. Omi, "Transparent zinc oxide films prepared by electrochemical reaction," *Appl. Phys. Lett.* **68**, 2439–2440 (1996).
- ⁵⁹⁶B.-C. Shih, Y. Xue, P. Zhang, M. L. Cohen, and S. G. Louie, "Quasiparticle band gap of ZnO: High accuracy from the conventional G0W0 approach," *Phys. Rev. Lett.* **105**, 146401 (2010).
- ⁵⁹⁷L. Wang and N. Giles, "Temperature dependence of the free-exciton transition energy in zinc oxide by photoluminescence excitation spectroscopy," *J. Appl. Phys.* **94**, 973–978 (2003).
- ⁵⁹⁸N. Ohashi, T. Sekiguchi, K. Aoyama, T. Ohgaki, Y. Terada, I. Sakaguchi, T. Tsurumi, and H. Haneda, "Band-edge emission of undoped and doped ZnO single crystals at room temperature," *J. Appl. Phys.* **91**, 3658–3663 (2002).
- ⁵⁹⁹J. E. Jaffe, J. A. Snyder, Z. Lin, and A. C. Hess, "Lda and gga calculations for high-pressure phase transitions in ZnO and mgo," *Phys. Rev. B* **62**, 1660 (2000).
- ⁶⁰⁰J. Majewski and P. Vogl, "Simple model for structural properties and crystal stability of sp-bonded solids," *Phys. Rev. B* **35**, 9666 (1987).
- ⁶⁰¹S. Desgreniers, "High-density phases of ZnO: Structural and compressive parameters," *Phys. Rev. B* **58**, 14102 (1998).
- ⁶⁰²S. Abrahams and J. Bernstein, "Remeasurement of the structure of hexagonal ZnO," *Acta Crystallogr. Sect. B* **25**, 1233–1236 (1969).
- ⁶⁰³C. Boemare, T. Monteiro, M. Soares, J. Guilherme, and E. Alves, "Photoluminescence studies in ZnO samples," *Physica B* **308**, 985–988 (2001).
- ⁶⁰⁴R. Pässler, E. Griebl, H. Riepl, G. Lautner, S. Bauer, H. Preis, W. Gebhardt, B. Budra, D. As, D. Schikora *et al.*, "Temperature dependence of exciton peak energies in ZnS, ZnSe, and ZnTe epitaxial films," *J. Appl. Phys.* **86**, 4403–4411 (1999).
- ⁶⁰⁵C. Ehrhardt and K. Lark-Horovitz, "Intensity distribution in x-ray and electron diffraction patterns. X-ray atom factors of zinc in zinc oxide and chemical binding," *Phys. Rev.* **57**, 603 (1940).
- ⁶⁰⁶W. N. Lawless and T. K. Gupta, "Thermal properties of pure and varistor ZnO at low temperatures," *J. Appl. Phys.* **60**, 607–611 (1986).
- ⁶⁰⁷L. Tröger, T. Yokoyama, D. Arvanitis, T. Lederer, M. Tischer, and K. Baberschke, "Determination of bond lengths, atomic mean-square relative displacements, and local thermal expansion by means of soft-x-ray photoabsorption," *Phys. Rev. B* **49**, 888 (1994).
- ⁶⁰⁸S. Adachi, *Properties of Group-IV, III-V and II-VI Semiconductors* (John Wiley & Sons, 2005), Vol. 16.
- ⁶⁰⁹R. R. Reeber, "Lattice parameters of ZnO from 4.2 to 296 K," *J. Appl. Phys.* **41**, 5063–5066 (1970).
- ⁶¹⁰D. Klimm, D. Schulz, and S. Ganschow, in *Comprehensive Semiconductor Science and Technology*, edited by P. Bhattacharya, R. Fornari, and H. Kamimura (Elsevier Science, 2011), Vol. 3.
- ⁶¹¹Ü. Özgür, X. Gu, S. Chevchenko, J. Spradlin, S.-J. Cho, H. Morkoç, F. Pollak, H. Everitt, B. Nemeth, and J. Nause, "Thermal conductivity of bulk ZnO after different thermal treatments," *J. Electron. Mater.* **35**, 550–555 (2006).
- ⁶¹²D. I. Florescu, L. Mouroukh, F. H. Pollak, D. C. Look, G. Cantwell, and X. Li, "High spatial resolution thermal conductivity of bulk ZnO (0001)," *J. Appl. Phys.* **91**, 890–892 (2002).
- ⁶¹³A. Calzolari and M. B. Nardelli, "Dielectric properties and raman spectra of ZnO from a first principles finite-differences/finite-fields approach," *Sci. Rep.* **3**, 2999 (2013).
- ⁶¹⁴C. A. Arguello, D. L. Rousseau, and S. D. S. Porto, "First-order Raman effect in wurtzite-type crystals," *Phys. Rev.* **181**, 1351 (1969).
- ⁶¹⁵B. Bairamov, A. Heinrich, G. Irmer, V. Toporov, and E. Ziegler, "Raman study of the phonon halfwidths and the phonon-plasmon coupling in ZnO," *Phys. Status Solidi (b)* **119**, 227–234 (1983).
- ⁶¹⁶E. Venger, A. Melnichuk, L. Y. Melnichuk, and Y. A. Pasechnik, "Anisotropy ZnO single crystal reflectivity region residual rays," *Phys. Status Solidi (b)* **188**, 823–831 (1995).
- ⁶¹⁷N. Ashkenov, B. Mbenkum, C. Bundesmann, V. Riede, M. Lorenz, D. Spemann, E. Kaidashev, A. Kasic, M. Schubert, M. Grundmann, G. Wagner, H. Neumann, V. Darakchieva, H. Arwin, and B. Monemar, "Infrared dielectric functions and phonon modes of high-quality ZnO films," *J. Appl. Phys.* **93**, 126–133 (2003).
- ⁶¹⁸A. Zaoui and W. Sekkal, "Pressure-induced softening of shear modes in wurtzite ZnO: A theoretical study," *Phys. Rev. B* **66**, 174106 (2002).
- ⁶¹⁹M. Tsuboi and A. Wada, "Optically active lattice vibrations in wurtzite-type crystals of zinc oxide and cadmium sulfide," *J. Chem. Phys.* **48**, 2615–2618 (1968).
- ⁶²⁰T. C. Damen, S. Porto, and B. Tell, "Raman effect in zinc oxide," *Phys. Rev.* **142**, 570 (1966).

- ⁶²¹M. Koyano, P. QuocBao, L. T. ThanhBinh, L. HongHa, N. NgocLong, and S. Katayama, "Photoluminescence and raman spectra of ZnO thin films by charged liquid cluster beam technique," *Phys. Status Solidi (a)* **193**, 125–131 (2002).
- ⁶²²K. Sundaram and A. Khan, "Work function determination of zinc oxide films," *J. Vac. Sci. Technol. A* **15**, 428–430 (1997).
- ⁶²³C. Teng, J. Muth, Ü. Özgür, M. Bergmann, H. Everitt, A. Sharma, C. Jin, and J. Narayan, "Refractive indices and absorption coefficients of Mg_xZn_{1-x}O alloys," *Appl. Phys. Lett.* **76**, 979–981 (2000).
- ⁶²⁴W. Bond, "Measurement of the refractive indices of several crystals," *J. Appl. Phys.* **36**, 1674–1677 (1965).
- ⁶²⁵Y. Imanaka, M. Oshikiri, K. Takehana, T. Takamasu, and G. Kido, "Cyclotron resonance in n-type ZnO," *Physica B* **298**, 211–215 (2001).
- ⁶²⁶W. Baer, "Faraday rotation in ZnO: Determination of the electron effective mass," *Phys. Rev.* **154**, 785 (1967).
- ⁶²⁷R. Weiher, "Optical properties of free electrons in ZnO," *Phys. Rev.* **152**, 736 (1966).
- ⁶²⁸K. J. Button, D. R. Cohn, M. von Ortenbert, B. Lax, E. Mollwo, and R. Helbig, "Zeeman splitting of anomalous shallow bound states in ZnO," *Phys. Rev. Lett.* **28**, 1637 (1972).
- ⁶²⁹S. Pearton, D. Norton, K. Ip, Y. Heo, and T. Steiner, "Recent advances in processing of ZnO," *J. Vac. Sci. Technol. B* **22**, 932–948 (2004).
- ⁶³⁰G. Beni and T. Rice, "Theory of electron-hole liquid in semiconductors," *Phys. Rev. B* **18**, 768 (1978).
- ⁶³¹J. Albrecht, P. Ruden, S. Limpijumnong, W. Lambrecht, and K. Brennan, "High field electron transport properties of bulk ZnO," *J. Appl. Phys.* **86**, 6864–6867 (1999).
- ⁶³²D. S. Ginley and C. Bright, "Transparent conducting oxides," *MRS Bull.* **25**, 15–18 (2000).
- ⁶³³H. Kato, M. Sano, K. Miyamoto, and T. Yao, "Effect of O/Zn flux ratio on crystalline quality of ZnO films grown by plasma-assisted molecular beam epitaxy," *Jpn. J. Appl. Phys., Part 1* **42**, 2241 (2003).
- ⁶³⁴E. Kaidashev, M. v Lorenz, H. Von Wenckstern, A. Rahm, H.-C. Semmelhack, K.-H. Han, G. Benndorf, C. Bundesmann, H. Hochmuth, and M. Grundmann, "High electron mobility of epitaxial ZnO thin films on c-plane sapphire grown by multistep pulsed-laser deposition," *Appl. Phys. Lett.* **82**, 3901–3903 (2003).
- ⁶³⁵M. Allen, P. Miller, R. Reeves, and S. Durbin, "Influence of spontaneous polarization on the electrical and optical properties of bulk, single crystal ZnO," *Appl. Phys. Lett.* **90**, 062104 (2007).
- ⁶³⁶K. Maeda, M. Sato, I. Niikura, and T. Fukuda, "Growth of 2 inch ZnO bulk single crystal by the hydrothermal method," *Semicond. Sci. Technol.* **20**, S49 (2005).
- ⁶³⁷T. M. Barnes, K. Olson, and C. A. Wolden, "On the formation and stability of p-type conductivity in nitrogen-doped zinc oxide," *Appl. Phys. Lett.* **86**, 112112 (2005).
- ⁶³⁸J. Lu, Y. Zhang, Z. Ye, L. Wang, B. Zhao, and J. Huang, "p-type ZnO films deposited by dc reactive magnetron sputtering at different ammonia concentrations," *Mater. Lett.* **57**, 3311–3314 (2003).
- ⁶³⁹A. Malashovich and D. Vanderbilt, "First-principles study of polarization in Zn_{1-x}Mg_xO," *Phys. Rev. B* **75**, 045106 (2007).
- ⁶⁴⁰A. Dal Corso, M. Posternak, R. Resta, and A. Baldereschi, "Ab initio study of piezoelectricity and spontaneous polarization in ZnO," *Phys. Rev. B* **50**, 10715 (1994).
- ⁶⁴¹Y. Noel, C. Zicovich-Wilson, B. Civalleri, P. D'arco, and R. Dovesi, "Polarization properties of ZnO and BEO: An ab initio study through the berry phase and wannier functions approaches," *Phys. Rev. B* **65**, 014111 (2001).
- ⁶⁴²J. Jerphagnon and H. Newkirk, "Optical nonlinear susceptibilities of beryllium oxide," *Appl. Phys. Lett.* **18**, 245–247 (1971).
- ⁶⁴³H. Matsui, H. Saeki, T. Kawai, H. Tabata, and B. Mizobuchi, "N doping using N₂O and NO sources: From the viewpoint of ZnO," *J. Appl. Phys.* **95**, 5882–5888 (2004).
- ⁶⁴⁴Y. Ryu, S. Zhu, D. C. Look, J. Wrobel, H. Jeong, and H. White, "Synthesis of p-type ZnO films," *J. Cryst. Growth* **216**, 330–334 (2000).
- ⁶⁴⁵Y. Heo, S. Park, K. Ip, S. Pearton, and D. Norton, "Transport properties of phosphorus-doped ZnO thin films," *Appl. Phys. Lett.* **83**, 1128–1130 (2003).
- ⁶⁴⁶M. Joseph, H. Tabata, and T. Kawai, "p-type electrical conduction in ZnO thin films by Ga and N codoping," *Jpn. J. Appl. Phys., Part 1* **38**, L1205 (1999).
- ⁶⁴⁷K. Abe, Y. Banno, T. Sasayama, and K. Koizumi, "Growth of ZnO by cold-wall chemical vapor transport," *J. Vac. Sci. Technol. B* **27**, 1652–1654 (2009).
- ⁶⁴⁸B. Wang, M. Callahan, C. Xu, L. Bouthillette, N. Giles, and D. Bliss, "Hydrothermal growth and characterization of indium-doped-conducting ZnO crystals," *J. Cryst. Growth* **304**, 73–79 (2007).
- ⁶⁴⁹D. C. Look, J. W. Hemsky, and J. Sizelove, "Residual native shallow donor in ZnO," *Phys. Rev. Lett.* **82**, 2552 (1999).
- ⁶⁵⁰C. G. Van de Walle, "Hydrogen as a cause of doping in zinc oxide," *Phys. Rev. Lett.* **85**, 1012 (2000).
- ⁶⁵¹H. Von Wenckstern, H. Schmidt, M. Brandt, A. Lajn, R. Pickenhain, M. Lorenz, M. Grundmann, D. Hofmann, A. Polity, B. Meyer, H. Saal, M. Binnewies, A. Börger, K. Becker, V. Tikhomirov, and K. Jug, "Anionic and cationic substitution in ZnO," *Prog. Solid State Chem.* **37**, 153–172 (2009).
- ⁶⁵²J. G. Reynolds and C. L. Reynolds, "Progress in ZnO acceptor doping: What is the best strategy?" *Adv. Condens. Matter Phys.* **2014**, 457058.
- ⁶⁵³P. Erhart, A. Klein, and K. Albe, "First-principles study of the structure and stability of oxygen defects in zinc oxide," *Phys. Rev. B* **72**, 085213 (2005).
- ⁶⁵⁴P. Erhart and K. Albe, "Diffusion of zinc vacancies and interstitials in zinc oxide," *Appl. Phys. Lett.* **88**, 201918 (2006).
- ⁶⁵⁵H. Dixit, R. Saniz, D. Lamoen, and B. Partoens, "The quasiparticle band structure of zincblende and rocksalt ZnO," *J. Phys.: Condens. Matter* **22**, 125505 (2010).
- ⁶⁵⁶P. Rinke, A. Qteish, J. Neugebauer, C. Freysoldt, and M. Scheffler, "Combining GW calculations with exact-exchange density-functional theory: An analysis of valence-band photoemission for compound semiconductors," *New J. Phys.* **7**, 126 (2005).
- ⁶⁵⁷H. Ni, Y. Lu, and Z. Ren, "Quasiparticle band structures of wurtzite and rock-salt ZnO," *J. Appl. Phys.* **91**, 1339–1343 (2002).
- ⁶⁵⁸J. Jaffe, R. Pandey, and A. Kunz, "Electronic structure of the rocksalt-structure semiconductors ZnO and CdO," *Phys. Rev. B* **43**, 14030 (1991).
- ⁶⁵⁹J. A. Sans, A. Segura, F. J. Manjón, B. Mari, A. Muñoz, and M. Herrera-Cabrera, "Optical properties of wurtzite and rock-salt ZnO under pressure," *Microelectron. J.* **36**, 928–932 (2005).
- ⁶⁶⁰A. Segura, J. Sans, F. Manjón, A. Munoz, and M. Herrera-Cabrera, "Optical properties and electronic structure of rock-salt ZnO under pressure," *Appl. Phys. Lett.* **83**, 278–280 (2003).
- ⁶⁶¹A. Ohtomo, M. Kawasaki, T. Koida, K. Masubuchi, H. Koinuma, Y. Sakurai, Y. Yoshida, T. Yasuda, and Y. Segawa, " $Mg_xZn_{1-x}O$ as a II–VI widegap semiconductor alloy," *Appl. Phys. Lett.* **72**, 2466–2468 (1998).
- ⁶⁶²R. Schmidt-Grund, M. Schubert, B. Rheinländer, D. Fritsch, H. Schmidt, E. Kaidashev, M. Lorenz, C. Herzinger, and M. Grundmann, "UV–VUV spectroscopic ellipsometry of ternary $Mg_xZn_{1-x}O$ ($0 \leq x \leq 0.53$) thin films," *Thin Solid Films* **455**, 500–504 (2004).
- ⁶⁶³R. Schmidt-Grund, A. Carstens, B. Rheinländer, D. Spemann, H. Hochmut, G. Zimmermann, M. Lorenz, M. Grundmann, C. M. Herzinger, and M. Schubert, "Refractive indices and band-gap properties of rocksalt $Mg_xZn_{1-x}O$ (0.68×1)," *J. Appl. Phys.* **99**, 123701 (2006).
- ⁶⁶⁴D. Roessler and W. Walker, "Electronic spectrum and ultraviolet optical properties of crystalline mgo," *Phys. Rev.* **159**, 733 (1967).
- ⁶⁶⁵R. Synowicki and T. E. Tiwald, "Optical properties of bulk c-ZrO₂, c-MgO and a-As₂S₃ determined by variable angle spectroscopic ellipsometry," *Thin Solid Films* **455**, 248–255 (2004).
- ⁶⁶⁶I. Takeuchi, W. Yang, K.-S. Chang, M. Aronova, T. Venkatesan, R. Vispute, and L. Bendersky, "Monolithic multichannel ultraviolet detector arrays and continuous phase evolution in $MgxZn_{1-x}O$ composition spreads," *J. Appl. Phys.* **94**, 7336–7340 (2003).
- ⁶⁶⁷J. Chen, W. Shen, N. Chen, D. Qiu, and H. Wu, "The study of composition non-uniformity in ternary $Mg_xZn_{1-x}O$ thin films," *J. Phys.: Condens. Matter* **15**, L475 (2003).
- ⁶⁶⁸T. Takagi, H. Tanaka, S. Fujita, and S. Fujita, "Molecular beam epitaxy of high magnesium content single-phase wurzite $Mg_xZn_{1-x}O$ alloys ($x \approx 0.5$) and their application to solar-blind region photodetectors," *Jpn. J. Appl. Phys., Part 2* **42**, L401 (2003).

- ⁶⁶⁹C. Bundesmann, A. Rahm, M. Lorenz, M. Grundmann, and M. Schubert, "Infrared optical properties of $Mg_xZn_{1-x}O$ thin films ($0 \leq x \leq 1$): Long-wavelength optical phonons and dielectric constants," *J. Appl. Phys.* **99**, 113504 (2006).
- ⁶⁷⁰W. E. Mahmoud and A. Al-Ghamdi, "Synthesis of CdZnO thin film as a potential candidate for optical switches," *Opt. Laser Technol.* **42**, 1134–1138 (2010).
- ⁶⁷¹V. Venkatachalamapathy, A. Galeckas, R. Sellappan, D. Chakarov, and A. Y. Kuznetsov, "Tuning light absorption by band gap engineering in ZnCdO as a function of movpe-synthesis conditions and annealing," *J. Cryst. Growth* **315**, 301–304 (2011).
- ⁶⁷²A. Zaoui, M. Zaoui, S. Kacimi, A. Boukortt, and B. Bouhafs, "Stability and electronic properties of $Zn_xCd_{1-x}O$ alloys," *Mater. Chem. Phys.* **120**, 98–103 (2010).
- ⁶⁷³Y. Caglar, M. Caglar, S. Ilican, and A. Ates, "Morphological, optical and electrical properties of CdZnO films prepared by sol-gel method," *J. Phys. D: Appl. Phys.* **42**, 065421 (2009).
- ⁶⁷⁴X. Ma, P. Chen, R. Zhang, and D. Yang, "Optical properties of sputtered hexagonal CdZnO films with band gap energies from 1.8 to 3.3 eV," *J. Alloys Compd.* **509**, 6599–6602 (2011).
- ⁶⁷⁵J. Watson, "The tin oxide gas sensor and its applications," *Sens. Actuators* **5**, 29–42 (1984).
- ⁶⁷⁶S.-C. Lee, J.-H. Lee, T.-S. Oh, and Y.-H. Kim, "Fabrication of tin oxide film by sol-gel method for photovoltaic solar cell system," *Sol. Energy Mater. Solar Cells* **75**, 481–487 (2003).
- ⁶⁷⁷H. De Waal and F. Simons, "Tin oxide coatings: Physical properties and applications," *Thin Solid Films* **77**, 253–258 (1981).
- ⁶⁷⁸R. Presley, C. Munsee, C. Park, D. Hong, J. Wager, and D. Keszler, "Tin oxide transparent thin-film transistors," *J. Phys. D: Appl. Phys.* **37**, 2810 (2004).
- ⁶⁷⁹L.-L. Chi, J.-C. Chou, W.-Y. Chung, T.-P. Sun, and S.-K. Hsiung, "Study on extended gate field effect transistor with tin oxide sensing membrane," *Mater. Chem. Phys.* **63**, 19–23 (2000).
- ⁶⁸⁰J. Jacquemin and G. Bordure, "Band structure and optical properties of intrinsic tetragonal dioxides of groups-IV elements," *J. Phys. Chem. Solids* **36**, 1081–1087 (1975).
- ⁶⁸¹J. Robertson and B. Falabretti, "Electronic structure of transparent conducting oxides," in *Handbook of Transparent Conductors* (Springer, 2011), pp. 27–50.
- ⁶⁸²B. Hamad, "First-principle calculations of structural and electronic properties of rutile-phase dioxides (MO_2), $M = Ti, V, Ru, Ir$ and Sn ," *Eur. Phys. J. B* **70**, 163–169 (2009).
- ⁶⁸³M. Batzill and U. Diebold, "The surface and materials science of tin oxide," *Prog. Surf. Sci.* **79**, 47–154 (2005).
- ⁶⁸⁴K. Ellmer, "Resistivity of polycrystalline zinc oxide films: Current status and physical limit," *J. Phys. D: Appl. Phys.* **34**, 3097 (2001).
- ⁶⁸⁵Y. Li, W. Fan, H. Sun, X. Cheng, P. Li, X. Zhao, J. Hao, and M. Jiang, "Optical properties of the high-pressure phases of SnO_2 : First-principles calculation," *J. Phys. Chem. A* **114**, 1052–1059 (2010).
- ⁶⁸⁶L. Gracia, A. Beltrán, and J. Andrés, "Characterization of the high-pressure structures and phase transformations in SnO_2 . A density functional theory study," *J. Phys. Chem. B* **111**, 6479–6485 (2007).
- ⁶⁸⁷F. E. H. Hassan, S. Moussawi, W. Noun, C. Salameh, and A. Postnikov, "Theoretical calculations of the high-pressure phases of SnO_2 ," *Comput. Mater. Sci.* **72**, 86–92 (2013).
- ⁶⁸⁸J. Haines and J. Léger, "X-ray diffraction study of the phase transitions and structural evolution of tin dioxide at high pressure: Relationships between structure types and implications for other rutile-type dioxides," *Phys. Rev. B* **55**, 11144 (1997).
- ⁶⁸⁹S. Das and V. Jayaraman, " SnO_2 : A comprehensive review on structures and gas sensors," *Prog. Mater. Sci.* **66**, 112–255 (2014).
- ⁶⁹⁰S. R. Shieh, A. Kubo, T. S. Duffy, V. B. Prakapenka, and G. Shen, "High-pressure phases in SnO_2 to 117 GPa," *Phys. Rev. B* **73**, 014105 (2006).
- ⁶⁹¹J. Marley and T. MacAvoy, "Growth of stannic oxide crystals from the vapor phase," *J. Appl. Phys.* **32**, 2504–2505 (1961).
- ⁶⁹²J. Marley and R. Dockerty, "Electrical properties of stannic oxide single crystals," *Phys. Rev. A* **140**, 304 (1965).
- ⁶⁹³M. Nagasawa, S. Shionoya, and S. Makishima, "Vapor reaction growth of SnO_2 single crystals and their properties," *Jpn. J. Appl. Phys., Part 1* **4**, 195 (1965).
- ⁶⁹⁴I. Kuzmina and B. Litvin, "Crystallization of cassiterite (SnO_2) in hydrothermal condition," *Krystallografiya* **8**, 478–480 (1963).
- ⁶⁹⁵M. Harvill and R. Roy, "Hydrothermal growth of GeO_2 and SnO_2 single crystals," *Am. Ceram. Soc. Bull.* **44**, 297 (1965).
- ⁶⁹⁶S. Shimada, K. Kodaira, and T. Matsushita, "Crystal growth of SnO_2 and Me_2SnO_4 ($Me = Mg, Zn, Co$) by flux method," *J. Cryst. Growth* **59**, 662–664 (1982).
- ⁶⁹⁷H. Kunkle and E. Kohnke, "Flux growth of stannic oxide crystals," *J. Appl. Phys.* **36**, 1489–1489 (1965).
- ⁶⁹⁸R. Khandelwal, A. P. Singh, A. Kapoor, S. Grigorescu, P. Miglietta, N. E. Stankova, and A. Perrone, "Effects of deposition temperature on the structural and morphological properties of SnO_2 films fabricated by pulsed laser deposition," *Opt. Laser Technol.* **41**, 89–93 (2009).
- ⁶⁹⁹S. Yu, L. Ding, C. Xue, L. Chen, and W. Zhang, "Transparent conducting Sb-doped SnO_2 thin films grown by pulsed laser deposition," *J. Non-Crystall. Solids* **358**, 3137–3140 (2012a).
- ⁷⁰⁰H. Enoki, T. Nakayama, and J. Echigoya, "The electrical and optical properties of the $ZnO-SnO_2$ thin films prepared by rf magnetron sputtering," *Phys. Status Solidi (a)* **129**, 181–191 (1992).
- ⁷⁰¹A. Alhuthali, M. El-Nahass, A. Atta, M. Abd El-Raheem, K. M. Elsabawy, and A. Hassani, "Study of topological morphology and optical properties of SnO_2 thin films deposited by rf sputtering technique," *J. Lumin.* **158**, 165–171 (2015).
- ⁷⁰²S. Hamzaoui and M. Adnane, "Effects of temperature and rf power sputtering on electrical and optical properties of SnO_2 ," *Appl. Energy* **65**, 19–28 (2000).
- ⁷⁰³M. Batzill, J. M. Burst, and U. Diebold, "Pure and cobalt-doped SnO_2 (101) films grown by molecular beam epitaxy on Al_2O_3 ," *Thin Solid Films* **484**, 132–139 (2005).
- ⁷⁰⁴M. Tsai, M. White, and J. Speck, "Plasma-assisted molecular beam epitaxy of SnO_2 on TiO_2 ," *J. Cryst. Growth* **310**, 4256–4261 (2008).
- ⁷⁰⁵T. Wang, A. Prakash, E. Warner, W. L. Gladfelter, and B. Jalan, "Molecular beam epitaxy growth of SnO_2 using a tin chemical precursor," *J. Vac. Sci. Technol. A* **33**, 020606 (2015).
- ⁷⁰⁶R. Drevet, C. Legros, D. Bérardan, P. Ribot, D. Dragoé, C. Cannizzo, M. Barthès-Labrousse, A. Chaussé, and M. Andrieux, "Metal organic precursor effect on the properties of SnO_2 thin films deposited by MOCVD technique for electrochemical applications," *Surf. Coat. Technol.* **271**, 234–241 (2015).
- ⁷⁰⁷Z. Zhu, J. Ma, C. Luan, L. Kong, and Q. Yu, "Structure and photoluminescence properties of epitaxial SnO_2 films grown on $\alpha-Al_2O_3$ (0 1 2) by MOCVD," *J. Lumin.* **131**, 88–91 (2011a).
- ⁷⁰⁸V. Aravindan, K. Jinesh, R. R. Prabhakar, V. S. Kale, and S. Madhavi, "Atomic layer deposited (ALD) SnO_2 anodes with exceptional cycleability for Li-ion batteries," *Nano Energy* **2**, 720–725 (2013).
- ⁷⁰⁹F. Gu, S. F. Wang, M. K. Lü, X. F. Cheng, S. W. Liu, G. J. Zhou, D. Xu, and D. R. Yuan, "Luminescence of SnO_2 thin films prepared by spin-coating method," *J. Cryst. Growth* **262**, 182–185 (2004).
- ⁷¹⁰X. Zhang, X. Liu, H. Ning, W. Yuan, Y. Deng, X. Zhang, S. Wang, J. Wang, R. Yao, and J. Peng, "Characterization studies of the structure and properties of Zr-doped SnO_2 thin films by spin-coating technique," *Superlattices Microstruct.* **123**, 330–337 (2018b).
- ⁷¹¹T. Serin, N. Serin, S. Karadeniz, H. Sarı, N. Tuğluoğlu, and O. Pakma, "Electrical, structural and optical properties of SnO_2 thin films prepared by spray pyrolysis," *J. Non-Cryst. Solids* **352**, 209–215 (2006).
- ⁷¹²G. Gordillo, L. Moreno, W. De la Cruz, and P. Teheran, "Preparation and characterization of SnO_2 thin films deposited by spray pyrolysis from $SnCl_2$ and $SnCl_4$ precursors," *Thin Solid Films* **252**, 61–66 (1994).
- ⁷¹³A. Svane and E. Antoncik, "Electronic structure of rutile SnO_2 , GeO_2 and TeO_2 ," *J. Phys. Chem. Solids* **48**, 171–180 (1987).
- ⁷¹⁴F. Arlinghaus, "Energy bands in stannic oxide (SnO_2)," *J. Phys. Chem. Solids* **35**, 931–935 (1974).
- ⁷¹⁵A. Schleife, J. Varley, F. Fuchs, C. Rödl, F. Bechstedt, P. Rinke, A. Janotti, and C. Van de Walle, "Tin dioxide from first principles: Quasiparticle electronic states and optical properties," *Phys. Rev. B* **83**, 035116 (2011).
- ⁷¹⁶K. Reimann and M. Steube, "Experimental determination of the electronic band structure of SnO_2 ," *Solid State Commun.* **105**, 649–652 (1998).
- ⁷¹⁷J. Berger, L. Reining, and F. Sottile, "Efficient GW calculations for SnO_2 , ZnO , and rubrene: The effective-energy technique," *Phys. Rev. B* **85**, 085126 (2012).

- ⁷¹⁸K. Mishra, K. Johnson, and P. Schmidt, "Electronic structure of antimony-doped tin oxide," *Phys. Rev. B* **51**, 013972 (1995).
- ⁷¹⁹E. Kohnke, "Electrical and optical properties of natural stannic oxide crystals," *J. Phys. Chem. Solids* **23**, 1557–1562 (1962).
- ⁷²⁰J. E. Houston and E. Kohnke, "Photoelectronic analysis of imperfections in grown stannic oxide single crystals," *J. Appl. Phys.* **36**, 3931–3938 (1965).
- ⁷²¹T. Arai, "The study of the optical properties of conducting tin oxide films and their interpretation in terms of a tentative band scheme," *J. Phys. Soc. Jpn.* **15**, 916–927 (1960).
- ⁷²²W. Spence, "The UV absorption edge of tin oxide thin films," *J. Appl. Phys.* **38**, 3767–3770 (1967).
- ⁷²³M. Nagasawa and S. Shionoya, "Properties of oxidized SnO_2 single crystals," *Jpn. J. Appl. Phys., Part 1* **10**, 727 (1971).
- ⁷²⁴R. Summitt, J. A. Marley, and N. F. Borrelli, "The ultraviolet absorption edge of stannic oxide (SnO_2)," *J. Phys. Chem. Solids* **25**, 1465–1469 (1964).
- ⁷²⁵A. Abdelkrim, S. Rahmene, O. Abdelouahab, A. Hafida, and K. Nabila, "Optoelectronic properties of SnO_2 thin films sprayed at different deposition times," *Chin. Phys. B* **25**, 046801 (2016).
- ⁷²⁶M. Feneberg, C. Lidig, K. Lange, R. Goldhahn, M. D. Neumann, N. Esser, O. Bierwagen, M. E. White, M. Y. Tsai, and J. S. Speck, "Ordinary and extraordinary dielectric functions of rutile SnO_2 up to 20 eV," *Appl. Phys. Lett.* **104**, 231106 (2014b).
- ⁷²⁷D. Fröhlich, R. Kenkles, and R. Helbig, "Band-gap assignment in SnO_2 by two-photon spectroscopy," *Phys. Rev. Lett.* **41**, 1750 (1978).
- ⁷²⁸V. Agekyan, "Spectroscopic properties of semiconductor crystals with direct forbidden energy gap," *Phys. Status Solidi (a)* **43**, 11–42 (1977).
- ⁷²⁹M. Nagasawa and S. Shionoya, "Exciton structure in optical absorption of SnO_2 crystals," *Phys. Lett.* **22**, 409–410 (1966).
- ⁷³⁰E. Shanthi, V. Dutta, A. Banerjee, and K. Chopra, "Electrical and optical properties of undoped and antimony-doped tin oxide films," *J. Appl. Phys.* **51**, 6243–6251 (1980).
- ⁷³¹M. Dou and C. Persson, "Comparative study of rutile and anatase SnO_2 and TiO_2 : Band-edge structures, dielectric functions, and polaron effects," *J. Appl. Phys.* **113**, 083703 (2013).
- ⁷³²P. D. Borges, L. M. Scolfaro, H. W. L. Alves, and E. F. da Silva, "DFT study of the electronic, vibrational, and optical properties of SnO_2 ," *Theor. Chem. Acc.* **126**, 39–44 (2010).
- ⁷³³Q.-J. Liu, Z.-T. Liu, and L.-P. Feng, "First-principles calculations of structural, electronic and optical properties of tetragonal SnO_2 and SnO ," *Comput. Mater. Sci.* **47**, 1016–1022 (2010).
- ⁷³⁴R. Saniz, H. Dixit, D. Lamoen, and B. Partoens, "Quasiparticle energies and uniaxial pressure effects on the properties of SnO_2 ," *Appl. Phys. Lett.* **97**, 261901 (2010).
- ⁷³⁵L. A. Errico, "Ab initio FP-LAPW study of the semiconductors SnO and SnO_2 ," *Physica B* **389**, 140–144 (2007).
- ⁷³⁶G. Sanon, R. Rup, and A. Mansingh, "Band-gap narrowing and band structure in degenerate tin oxide (SnO_2) films," *Phys. Rev. B* **44**, 5672 (1991).
- ⁷³⁷P. Turkes, C. Pluntke, and R. Helbig, "Thermal conductivity of SnO_2 single crystals," *J. Phys. C: Solid State Phys.* **13**, 4941 (1980).
- ⁷³⁸E. Chang and E. Graham, "The elastic constants of cassiterite SnO_2 and their pressure and temperature dependence," *J. Geophys. Res.* **80**, 2595–2599, <https://doi.org/10.1029/JB080i017p02595> (1975).
- ⁷³⁹B. Zhu, C.-M. Liu, M.-B. Lv, X.-R. Chen, J. Zhu, and G.-F. Ji, "Structures, phase transition, elastic properties of SnO_2 from first-principles analysis," *Physica B* **406**, 3508–3513 (2011b).
- ⁷⁴⁰R. G. Gordon, "Criteria for choosing transparent conductors," *MRS Bull.* **25**, 52–57 (2000).
- ⁷⁴¹S. Aukkaravittayapun, N. Wongtida, T. Kasewatin, S. Charojrochkul, K. Unnanon, and P. Chindaoudom, "Large scale f-doped SnO_2 coating on glass by spray pyrolysis," *Thin Solid Films* **496**, 117–120 (2006).
- ⁷⁴²V. Zhitomirsky, T. David, R. Boxman, S. Goldsmith, A. Verdyan, Y. M. Soifer, and L. Rapoport, "Properties of SnO_2 coatings fabricated on polymer substrates using filtered vacuum arc deposition," *Thin Solid Films* **492**, 187–194 (2005).
- ⁷⁴³G. Bräuer, J. Szczyrkowski, and G. Teschner, "Mid frequency sputtering—A novel tool for large area coating," *Surf. Coat. Technol.* **94**, 658–662 (1997).
- ⁷⁴⁴H. Li and R. C. Bradt, "Knoop microhardness anisotropy of single-crystal cassiterite (SnO_2)," *J. Am. Ceram. Soc.* **74**, 1053–1060 (1991).
- ⁷⁴⁵Z. Galazka, R. Uecker, D. Klimm, K. Irmscher, M. Pietsch, R. Schewski, M. Albrecht, A. Kwasniewski, S. Ganschow, D. Schulz, C. Guguschev, R. Bertram, M. Bickermann, and R. Fornari, "Growth, characterization, and properties of bulk SnO_2 single crystals," *Physica Status Solidi (a)* **211**, 66–73 (2014).
- ⁷⁴⁶P. Peercy and B. Morosin, "Pressure and temperature dependences of the Raman-active phonons in SnO_2 ," *Phys. Rev. B* **7**, 2779 (1973).
- ⁷⁴⁷V. Polyakov, S. Mineev, R. Clayton, G. Hu, V. Gurevich, D. Khramov, K. Gavrichev, V. Gorbunov, and L. Golushina, "Oxygen isotope fractionation factors involving cassiterite (SnO_2): I. Calculation of reduced partition function ratios from heat capacity and x-ray resonant studies," *Geochim. Cosmochim. Acta* **69**, 1287–1300 (2005).
- ⁷⁴⁸D. Kohl, "Surface processes in the detection of reducing gases with SnO_2 -based devices," *Sens. Actuators* **18**, 71–113 (1989).
- ⁷⁴⁹F. Yang and S. R. Forrest, "Organic solar cells using transparent SnO_2 -F anodes," *Adv. Mater.* **18**, 2018–2022 (2006).
- ⁷⁵⁰S. Altindal, S. Karadeniz, N. Tuğluoğlu, and A. Tataroğlu, "The role of interface states and series resistance on the I-V and C-V characteristics in $\text{Al/SnO}_2/\text{p-Si}$ schottky diodes," *Solid-State Electron.* **47**, 1847–1854 (2003).
- ⁷⁵¹S. Fayette, D. S. Smith, A. Smith, and C. Martin, "Influence of grain size on the thermal conductivity of tin oxide ceramics," *J. Eur. Ceram. Soc.* **20**, 297–302 (2000).
- ⁷⁵²A. Dieguez, A. Romano-Rodriguez, A. Vila, and J. Morante, "The complete raman spectrum of nanometric SnO_2 particles," *J. Appl. Phys.* **90**, 1550–1557 (2001).
- ⁷⁵³R. Katiyar, P. Dawson, M. Hargreave, and G. Wilkinson, "Dynamics of the rutile structure. III. Lattice dynamics, infrared and Raman spectra of SnO_2 ," *J. Phys. C: Solid State Phys.* **4**, 2421 (1971).
- ⁷⁵⁴A. K. Ghosh, C. Fishman, and T. Feng, " SnO_2/Si solar cells-heterostructure or schottky-barrier or MIS-type device," *J. Appl. Phys.* **49**, 3490–3498 (1978).
- ⁷⁵⁵M. Butler and D. Ginley, "Prediction of flatband potentials at semiconductor-electrolyte interfaces from atomic electronegativities," *J. Electrochem. Soc.* **125**, 228 (1978).
- ⁷⁵⁶H. Van Daal, "The static dielectric constant of SnO_2 ," *J. Appl. Phys.* **39**, 4467–4469 (1968).
- ⁷⁵⁷D. Crabtree, R. Mehdi, and D. Wright, "Electron mobility and infra-red absorption in reduced tin oxide crystals," *J. Phys. D: Appl. Phys.* **2**, 1503 (1969).
- ⁷⁵⁸D. Morgan and D. Wright, "Electrical properties of single crystals of antimony-doped stannic oxide," *Br. J. Appl. Phys.* **17**, 337 (1966).
- ⁷⁵⁹K. J. Button, C. G. Fonstad, and W. Dreybrodt, "Determination of the electron masses in stannic oxide by submillimeter cyclotron resonance," *Phys. Rev. B* **4**, 4539 (1971).
- ⁷⁶⁰A. Kasic, M. Schubert, S. Einfeldt, D. Hommel, and T. Tiwald, "Free-carrier and phonon properties of n-and p-type hexagonal GaN films measured by infrared ellipsometry," *Phys. Rev. B* **62**, 7365 (2000).
- ⁷⁶¹C. Fonstad and R. Rediker, "Electrical properties of high-quality stannic oxide crystals," *J. Appl. Phys.* **42**, 2911–2918 (1971).
- ⁷⁶²W. Liu, X. Cao, Y. Zhu, and L. Cao, "The effect of dopants on the electronic structure of SnO_2 thin film," *Sens. Actuators, B* **66**, 219–221 (2000b).
- ⁷⁶³D. Boukhvalov, D. Manikandan, I. Zhidkov, A. Kukharenko, S. Cholakh, E. Kurmaev, and R. Murugan, "Effect of doping and annealing on the electronic structure and magnetic properties of nanoscale Co and Zn co-doped SnO_2 : An experimental study and first-principles modeling," *J. Alloys Compd.* **799**, 433–441 (2019).
- ⁷⁶⁴D. Manikandan and R. Murugan, "Room temperature dilute magnetism in nanoscale Co and Zn co-doped SnO_2 ," *Superlattices Microstruct.* **89**, 7–14 (2016).
- ⁷⁶⁵A. El Sayed, S. Taha, M. Shaban, and G. Said, "Tuning the structural, electrical and optical properties of tin oxide thin films via cobalt doping and annealing," *Superlattices Microstruct.* **95**, 1–13 (2016).
- ⁷⁶⁶G. Zhang and M. Liu, "Effect of particle size and dopant on properties of SnO_2 -based gas sensors," *Sens. Actuators B* **69**, 144–152 (2000).
- ⁷⁶⁷K. Jain, R. Pant, and S. Lakshminarayanan, "Effect of Ni doping on thick film SnO_2 gas sensor," *Sens. Actuators, B* **113**, 823–829 (2006).

- ⁷⁶⁸Y. Wang, T. Brezesinski, M. Antonietti, and B. Smarsly, "Ordered mesoporous Sb-, Nb-, and Ta-doped SnO₂ thin films with adjustable doping levels and high electrical conductivity," *Acs Nano* **3**, 1373–1378 (2009a).
- ⁷⁶⁹A. M. Ganose and D. O. Scanlon, "Band gap and work function tailoring of SnO₂ for improved transparent conducting ability in photovoltaics," *J. Mater. Chem. C* **4**, 1467–1475 (2016).
- ⁷⁷⁰K. G. Godinho, A. Walsh, and G. W. Watson, "Energetic and electronic structure analysis of intrinsic defects in SnO₂," *J. Phys. Chem. C* **113**, 439–448 (2009).
- ⁷⁷¹J. Jiang, L. Gerward, and J. S. Olsen, "Pressure induced phase transformation in nanocrystal SnO₂," *Scr. Mater.* **44**, 1983–1986 (2001).
- ⁷⁷²A. M. Mas'ut, Z. A. Wahab, W. Yunus, and N. H. Edros, "Thermal diffusivity measurement of SnO₂-CuO ceramic at room temperature," *J. Sci. Technol.* **16**(2), 265–273 (2008).
- ⁷⁷³R. G. Drabeski, J. V. Gunha, A. Novatski, G. B. de Souza, S. M. Tebcherani, E. T. Kubaski, and D. T. Dias, "Raman and photoacoustic spectroscopies of SnO₂ thin films deposited by spin coating technique," *Vib. Spectrosc.* **109**, 103094 (2020).
- ⁷⁷⁴R. Summitt, "Infrared absorption in single-crystal stannic oxide: Optical lattice-vibration modes," *J. Appl. Phys.* **39**, 3762–3767 (1968).
- ⁷⁷⁵K. Tanaka, A. Kunioka, and Y. Sakai, "Electrical and optical properties of sputtered cdo films," *Jpn. J. Appl. Phys., Part 1* **8**, 681 (1969).
- ⁷⁷⁶L. Li, S. Liang, S. Li, J. Wang, S. Wang, G. Dong, and G. Fu, "Enhanced thermoelectric performance in CdO by nano-SiO₂ inclusions," *Nanotechnology* **25**, 425402 (2014).
- ⁷⁷⁷Q. Lü, S. Wang, L. Li, J. Wang, S. Dai, W. Yu, and G. Fu, "Electrical and thermal transport properties of CdO ceramics," *Sci. China Phys.* **57**, 1644–1648 (2014).
- ⁷⁷⁸K. M. Yu, M. A. Mayer, D. T. Speaks, H. He, R. Zhao, L. Hsu, S. S. Mao, E. Haller, and W. Walukiewicz, "Ideal transparent conductors for full spectrum photovoltaics," *J. Appl. Phys.* **111**, 123505 (2012b).
- ⁷⁷⁹E. Sachet, C. T. Shelton, J. S. Harris, B. E. Gaddy, D. L. Irving, S. Curtarolo, B. F. Donovan, P. E. Hopkins, P. A. Sharma, A. L. Sharma, J. Ihefeld, S. Franzen, and J.-P. Maria, "Dysprosium-doped cadmium oxide as a gateway material for mid-infrared plasmonics," *Nat. Mater.* **14**, 414–420 (2015).
- ⁷⁸⁰Y. Yang, S. Jin, J. E. Medvedeva, J. R. Ireland, A. W. Metz, J. Ni, M. C. Hersam, A. J. Freeman, and T. J. Marks, "CdO as the archetypical transparent conducting oxide. systematics of dopant ionic radius and electronic structure effects on charge transport and band structure," *J. Am. Chem. Soc.* **127**, 8796–8804 (2005).
- ⁷⁸¹A. Breeze and P. Perkins, "An LCAO calculation of the band structure of cadmium oxide," *Solid State Commun.* **13**, 1031–1033 (1973).
- ⁷⁸²A. Schleife, F. Fuchs, J. Furthmüller, and F. Bechstedt, "First-principles study of ground-and excited-state properties of MgO, ZnO, and CdO polymorphs," *Phys. Rev. B* **73**, 245212 (2006).
- ⁷⁸³J. C. Boettger, "First principles electronic structure and band gap pressure coefficient for cadmium-oxide," *Int. J. Quantum Chem.* **107**, 2988–2994 (2007).
- ⁷⁸⁴H. Singh and B. Dayal, "Lattice parameters of cadmium oxide at elevated temperatures," *Solid State Commun.* **7**, 725–726 (1969).
- ⁷⁸⁵R. J. Guerrero-Moreno and N. Takeuchi, "First principles calculations of the ground-state properties and structural phase transformation in CdO," *Phys. Rev. B* **66**, 205205 (2002).
- ⁷⁸⁶K. Gurumurugan, D. Mangalaraj, and S. K. Narayandass, "Structural characterization of cadmium oxide thin films deposited by spray pyrolysis," *J. Cryst. Growth* **147**, 355–360 (1995).
- ⁷⁸⁷A. Dakhel, "Influence of dysprosium doping on the electrical and optical properties of CdO thin films," *Sol. Energy* **83**, 934–939 (2009).
- ⁷⁸⁸B. Lokhande, P. Patil, and M. Upalane, "Studies on cadmium oxide sprayed thin films deposited through non-aqueous medium," *Mater. Chem. Phys.* **84**, 238–242 (2004).
- ⁷⁸⁹C. Sravani, P. S. Reddy, and P. J. Reddy, "Preparation and properties of sprayed transparent conducting CdO films," *Mater. Lett.* **12**, 406–408 (1992).
- ⁷⁹⁰P. Jefferson, S. Hatfield, T. Veal, P. King, C. McConville, J. Zúñiga-Pérez, and V. Muñoz-Sanjosé, "Bandgap and effective mass of epitaxial cadmium oxide," *Appl. Phys. Lett.* **92**, 022101 (2008).
- ⁷⁹¹J. Zúñiga-Pérez, C. Munuera, C. Ocal, and V. Muñoz-Sanjosé, "Structural analysis of CdO layers grown on r-plane sapphire (011̄2) by metalorganic vapor-phase epitaxy," *J. Cryst. Growth* **271**, 223–228 (2004).
- ⁷⁹²N. Ueda, H. Maeda, H. Hosono, and H. Kawazoe, "Band-gap widening of CdO thin films," *J. Appl. Phys.* **84**, 6174–6177 (1998).
- ⁷⁹³M. Yan, M. Lane, C. Kannewurf, and R. P. Chang, "Highly conductive epitaxial CdO thin films prepared by pulsed laser deposition," *Appl. Phys. Lett.* **78**, 2342–2344 (2001).
- ⁷⁹⁴D. Speaks, M. Mayer, K. Yu, S. Mao, E. Haller, and W. Walukiewicz, "Fermi level stabilization energy in cadmium oxide," *J. Appl. Phys.* **107**, 113706 (2010).
- ⁷⁹⁵I. Demchenko, J. Denlinger, M. Chernyshova, K. Yu, D. Speaks, P. Olalde-Velasco, O. Hemmers, W. Walukiewicz, A. Derkachova, and K. Lawniczak-Jablonska, "Full multiple scattering analysis of xanes at the CdL₃ and OK edges in CdO films combined with a soft-x-ray emission investigation," *Phys. Rev. B* **82**, 075107 (2010).
- ⁷⁹⁶R. A. Ismail, B. G. Rasheed, E. T. Salm, and M. Al-Hadethy, "High transmittance-low resistivity cadmium oxide films grown by reactive pulsed laser deposition," *J. Mater. Sci.: Mater. Electron.* **18**, 1027–1030 (2007).
- ⁷⁹⁷A. J. Varkey and A. Fort, "Transparent conducting cadmium oxide thin films prepared by a solution growth technique," *Thin Solid Films* **239**, 211–213 (1994).
- ⁷⁹⁸S. Vasheghani Farahani, V. Muñoz-Sanjosé, J. Zúñiga-Pérez, C. McConville, and T. Veal, "Temperature dependence of the direct bandgap and transport properties of CdO," *Appl. Phys. Lett.* **102**, 022102 (2013).
- ⁷⁹⁹F. Koffyberg, "Thermoreflectance spectra of CdO: Band gaps and band-population effects," *Phys. Rev. B* **13**, 4470 (1976).
- ⁸⁰⁰H. Finkenrath and M. Von Ortenberg, "The influence of own absorption and line electrons on the reflection spectrum of cadmiumoxide," *Mag. Appl. Phys.* **23**, 323 (1967).
- ⁸⁰¹K. Maschke and U. Rössler, "The electronic structure of CdO. I. The energy-band structure (APW method)," *Phys. Status Solidi (b)* **28**, 577–581 (1968).
- ⁸⁰²L. Lindsay and D. S. Parker, "Calculated transport properties of CdO: Thermal conductivity and thermoelectric power factor," *Phys. Rev. B* **92**, 144301 (2015).
- ⁸⁰³Y. Dou, R. Egdell, D. Law, N. Harrison, and B. Searle, "An experimental and theoretical investigation of the electronic structure of CdO," *J. Phys.: Condens. Matter* **10**, 8447 (1998).
- ⁸⁰⁴L. Piper, A. DeMasi, K. E. Smith, A. Schleife, F. Fuchs, F. Bechstedt, J. Zuniga-Pérez, and V. Munoz-Sanjosé, "Electronic structure of single-crystal rocksalt CdO studied by soft x-ray spectroscopies and *ab initio* calculations," *Phys. Rev. B* **77**, 125204 (2008).
- ⁸⁰⁵S. Tewari, "The electronic bandstructure of CdO by the augmented plane wave method," *Solid State Commun.* **12**, 437–441 (1973).
- ⁸⁰⁶H. Köhler, "Optical properties and energy-band structure of CdO," *Solid State Commun.* **11**, 1687–1690 (1972).
- ⁸⁰⁷J. Kocka and C. Konak, "The structure of the indirect absorption edge of CdO," *Phys. Status Solidi (b)* **43**, 731–738 (1971).
- ⁸⁰⁸M. Altwein, H. Finkenrath, Č. Koňák, J. Stuke, and G. Zimmerer, "The electronic structure of CdO. II. Spectral distribution of optical constants," *Phys. Status Solidi (b)* **29**, 203–209 (1968).
- ⁸⁰⁹M. Burbano, D. O. Scanlon, and G. W. Watson, "Sources of conductivity and doping limits in CdO from hybrid density functional theory," *J. Am. Chem. Soc.* **133**, 15065–15072 (2011).
- ⁸¹⁰A. Janotti, D. Segev, and C. G. Van de Walle, "Effects of cation d states on the structural and electronic properties of III-nitride and II-oxide wide-band-gap semiconductors," *Phys. Rev. B* **74**, 045202 (2006).
- ⁸¹¹S. Vasheghani Farahani, T. Veal, P. King, J. Zúñiga-Pérez, V. Muñoz-Sanjosé, and C. McConville, "Electron mobility in CdO films," *J. Appl. Phys.* **109**, 073712 (2011).
- ⁸¹²J. R. Nolen, E. L. Runnerstrom, K. P. Kelley, T. S. Luk, T. G. Folland, A. Cleri, J.-P. Maria, and J. D. Caldwell, "Ultraviolet to far-infrared dielectric function of n-doped cadmium oxide thin films," *Phys. Rev. Mater.* **4**, 025202 (2020).
- ⁸¹³A. Cleri, J. Tomko, K. Quiambao-Tomko, M. V. Imperatore, Y. Zhu, J. R. Nolen, J. Nordlander, J. D. Caldwell, Z. Mao, N. C. Giebink, K. P. Kelley, E. L. Runnerstrom, P. E. Hopkins, and J.-P. Maria, "Mid-wave to near-IR

- optoelectronic properties and epsilon-near-zero behavior in indium-doped cadmium oxide," *Phys. Rev. Mater.* **5**, 035202 (2021).
- ⁸¹⁴T. Chu and S. S. Chu, "Degenerate cadmium oxide films for electronic devices," *J. Electron. Mater.* **19**, 1003–1005 (1990).
- ⁸¹⁵H. Finkenrath and H. Kohler, "Temperature dependency of the optical constants of the cadmium oxide layers," *Mag. Nat. Res. A* **19**, 1236–1237 (1964).
- ⁸¹⁶J. S. Choi, Y. H. Kang, and K. H. Kim, "Electrical conductivity of cadmium oxide," *J. Phys. Chem.* **81**, 2208–2211 (1977).
- ⁸¹⁷H.-Y. He and J. Lu, "Band gap narrowing of cadmium oxide powder by rare earth praseodymium doping," *MRS Commun.* **3**, 47–50 (2013).
- ⁸¹⁸J. Zhang, "Room-temperature compressibilities of MnO and CdO: Further examination of the role of cation type in bulk modulus systematics," *Phys. Chem. Miner.* **26**, 644–648 (1999).
- ⁸¹⁹H. Drickamer, R. Lynch, R. Clendenen, and E. Perez-Albueene, "X-ray diffraction studies of the lattice parameters of solids under very high pressure," *Solid State Phys.* **19**, 135–228 (1967).
- ⁸²⁰H. Lu, L. Liao, H. Li, Y. Tian, D. Wang, J. Li, Q. Fu, B. Zhu, and Y. Wu, "Fabrication of CdO nanotubes via simple thermal evaporation," *Mater. Lett.* **62**, 3928–3930 (2008).
- ⁸²¹M. Roufosse and P. Klemens, "Thermal conductivity of complex dielectric crystals," *Phys. Rev. B* **7**, 5379 (1973).
- ⁸²²W. M. Haynes, *CRC Handbook of Chemistry and Physics* (CRC Press, 2014).
- ⁸²³R. Oliva, J. Ibanez, L. Artús, R. Cuscó, J. Zuniga-Perez, and V. Munoz-Sanjose, "High-pressure raman scattering of CdO thin films grown by metal-organic vapor phase epitaxy," *J. Appl. Phys.* **113**, 053514 (2013).
- ⁸²⁴H. Finkenrath, N. Uhle, and W. Waidelich, "The influence of phonons and polarons on the infrared absorption of cadmium oxide," *Solid State Commun.* **7**, 11–14 (1969).
- ⁸²⁵G. Schaack and N. Uhle, "Raman spectra in doped cadmium oxide," *Solid State Commun.* **19**, 315–318 (1976).
- ⁸²⁶R. Ferro and J. Rodriguez, "Influence of f-doping on the transmittance and electron affinity of CdO thin films suitable for solar cells technology," *Sol. Energy Mater. Sol. Cells* **64**, 363–370 (2000).
- ⁸²⁷H. Finkenrath and N. Uhle, "Der einfluss der gitterschwingungen auf die ultrarot-reflexion von CdO," *Solid State Commun.* **5**, 875–877 (1967).
- ⁸²⁸I. Broser, R. Broser, H. Finkenrath, R. Galazka, H. Gumlich, A. Hoffmann, J. Kossut, E. Mollwo, H. Nelkowski, G. Nimtz, W. V. D. Osten, M. Rosenzweig, H. Schulz, D. Theis, and D. Tschierse, *Physics of II-VI and I-VII Compounds, Semimagnetic Semiconductors/Physik Der II-VI und I-VII-Verbindungen, Semimagnetische Halbleiter Elemente* (Springer, 1982), Vol. 17.
- ⁸²⁹C. P. Liu, Y. Foo, M. Kamruzzaman, C. Y. Ho, J. Zapien, W. Zhu, Y. Li, W. Walukiewicz, and K. M. Yu, "Effects of free carriers on the optical properties of doped CdO for full-spectrum photovoltaics," *Phys. Rev. Appl.* **6**, 064018 (2016).
- ⁸³⁰F. Koffyberg, "Electron concentration and mobility in semimetallic CdO," *Can. J. Phys.* **49**, 435–440 (1971).
- ⁸³¹C. Rödl and A. Schleife, "Photoemission spectra and effective masses of n-and p-type oxide semiconductors from first principles: ZnO, CdO, SnO₂, MnO, NiO," *Phys. Status Solidi (a)* **211**, 74–81 (2014).
- ⁸³²S. V. Farahani, C. McConville, T. Veal, and A. Schleife, "Impact of degenerate n-doping on the optical absorption edge in transparent conducting cadmium oxide," *Proc. SPIE* **8626**, 862604 (2013).
- ⁸³³P. King, T. Veal, P. Jefferson, J. Zúñiga-Pérez, V. Muñoz-Sanjosé, and C. McConville, "Unification of the electrical behavior of defects, impurities, and surface states in semiconductors: Virtual gap states in CdO," *Phys. Rev. B* **79**, 035203 (2009b).
- ⁸³⁴A. Cimino and M. Marezio, "Lattice parameter and defect structure of cadmium oxide containing foreign atoms," *J. Phys. Chem. Solids* **17**, 57–64 (1960).
- ⁸³⁵R. Haul and D. Just, "Disorder and oxygen transport in cadmium oxide," *J. Appl. Phys.* **33**, 487–493 (1962).
- ⁸³⁶B. Ingram, G. Gonzalez, D. Kammler, M. Bertoni, and T. O. Mason, "Chemical and structural factors governing transparent conductivity in oxides," *J. Electroceram.* **13**, 167–175 (2004).
- ⁸³⁷S. Cox, J. Lord, S. Cottrell, J. Gil, H. Alberto, A. Keren, D. Prabhakaran, R. Scheuermann, and A. Stoykov, "Oxide muonics: I. Modelling the electrical activity of hydrogen in semiconducting oxides," *J. Phys.: Condens. Matter* **18**, 1061 (2006).
- ⁸³⁸Ç. Kılıç and A. Zunger, "n-type doping of oxides by hydrogen," *Appl. Phys. Lett.* **81**, 73–75 (2002).
- ⁸³⁹K. M. Yu, D. Detert, G. Chen, W. Zhu, C. Liu, S. Grankowska, L. Hsu, O. Dubon, and W. Walukiewicz, "Defects and properties of cadmium oxide based transparent conductors," *J. Appl. Phys.* **119**, 181501 (2016).
- ⁸⁴⁰H. Sato, T. Minami, S. Takata, and T. Yamada, "Transparent conducting p-type nio thin films prepared by magnetron sputtering," *Thin Solid Films* **236**, 27–31 (1993).
- ⁸⁴¹E. Fujii, A. Tomozawa, H. Torii, and R. Takayama, "Preferred orientations of NiO films prepared by plasma-enhanced metalorganic chemical vapor deposition," *Jpn. J. Appl. Phys., Part 2* **35**, L328 (1996).
- ⁸⁴²M. Kitao, K. Izawa, K. Urabe, T. Komatsu, S. Kuwano, and S. Yamada, "Preparation and electrochromic properties of rf-sputtered NiO_x films prepared in Ar/O₂/H₂ atmosphere," *Jpn. J. Appl. Phys., Part 1* **33**, 6656 (1994).
- ⁸⁴³M. Tyagi, M. Tomar, and V. Gupta, "Influence of hole mobility on the response characteristics of p-type nickel oxide thin film based glucose bio-sensor," *Anal. Chim. Acta* **726**, 93–101 (2012).
- ⁸⁴⁴N. Kaneko, O. Machida, M. Yanagihara, S. Iwakami, R. Baba, H. Goto, and A. Iwabuchi, "Normally-off AlGaN/GaN HFETs using NiO_x gate with recess," in *2009 21st International Symposium on Power Semiconductor Devices and IC's* (IEEE, 2009), pp. 25–28.
- ⁸⁴⁵Y. Ma, M. Xiao, Z. Du, X. Yan, K. Cheng, M. Clavel, M. K. Hudait, I. Kravchenko, H. Wang, and Y. Zhang, "Tri-gate GaN junction hemt," *Appl. Phys. Lett.* **117**, 143506 (2020).
- ⁸⁴⁶J.-L. Yang, Y.-S. Lai, and J.-S. Chen, "Effect of heat treatment on the properties of non-stoichiometric p-type nickel oxide films deposited by reactive sputtering," *Thin Solid Films* **488**, 242–246 (2005).
- ⁸⁴⁷H.-L. Chen, Y.-M. Lu, and W.-S. Hwang, "Characterization of sputtered NiO thin films," *Surf. Coat. Technol.* **198**, 138–142 (2005).
- ⁸⁴⁸C. M. Lin and C. C. Wu, "Effect of the Ni²⁺/Ni³⁺ concentration on the optoelectronic properties of lithium-doped nickel oxide films," *ACS Appl. Electron. Mater.* **3**, 1050–1057 (2020).
- ⁸⁴⁹M. Ono, K. Sasaki, H. Nagai, T. Yamaguchi, M. Higashiwaki, A. Kuramata, S. Yamakoshi, M. Sato, T. Honda, and T. Onuma, "Relation between electrical and optical properties of p-type NiO films," *Phys. Status Solidi (b)* **255**, 1700311 (2018).
- ⁸⁵⁰M. Guziewicz, J. Grochowski, M. Borysiewicz, E. Kaminska, J. Z. Domagala, W. Rzodkiewicz, B. S. Witkowski, K. Golaszewska, R. Kruszka, M. Ekielski et al., "Electrical and optical properties of NiO films deposited by magnetron sputtering," *Opt. Appl.* **41**, 431 (2011).
- ⁸⁵¹M. Predanoc, I. Hotový, and M. Čaplovicová, "Structural, optical and electrical properties of sputtered NiO thin films for gas detection," *Appl. Surf. Sci.* **395**, 208–213 (2017).
- ⁸⁵²J. Bachmann, A. Zolotaryov, O. Albrecht, S. Goetze, A. Berger, D. Hesse, D. Novikov, and K. Nielsch, "Stoichiometry of nickel oxide films prepared by ALD," *Chem. Vapor Deposition* **17**, 177–180 (2011).
- ⁸⁵³F. Morin, "Electrical properties of NiO," *Phys. Rev.* **93**, 1199 (1954).
- ⁸⁵⁴J. Hwang and T. Ho, "Effects of oxygen content on the structural, optical, and electrical properties of NiO films fabricated by radio-frequency magnetron sputtering," *Mater. Sci. Semicond. Process.* **71**, 396–400 (2017).
- ⁸⁵⁵R. Newman and R. Chrenko, "Optical properties of nickel oxide," *Phys. Rev.* **114**, 1507 (1959).
- ⁸⁵⁶N. Mironova-Ulmane, A. Kuzmin, I. Sildos, and M. Pärs, "Polarisation dependent Raman study of single-crystal nickel oxide," *Open Phys.* **9**, 1096–1099 (2011).
- ⁸⁵⁷W. Roth, "Magnetic structures of MnO, FeO, CoO, and NiO," *Phys. Rev.* **110**, 1333 (1958).
- ⁸⁵⁸C. Toussaint, "A high-temperature x-ray diffraction study of the NiO-Li₂O system," *J. Appl. Crystallogr.* **4**, 293–297 (1971).
- ⁸⁵⁹H. Rooksby, "Structure of nickel oxide," *Nature* **152**, 304–304 (1943).
- ⁸⁶⁰R. Cairns and E. Ott, "X-ray studies of the system nickel-oxygen-water. I. Nickelous oxide and hydroxide I," *J. Am. Chem. Soc.* **55**, 527–533 (1933).
- ⁸⁶¹S. Dudarev, G. Botton, S. Savrasov, C. Humphreys, and A. Sutton, "Electron-energy-loss spectra and the structural stability of nickel oxide: An LSDA+U study," *Phys. Rev. B* **57**, 1505 (1998).

- ⁸⁶²F. Fievet, P. Germi, F. De Bergevin, and M. Figlarz, "Lattice parameter, micro-strains and non-stoichiometry in NiO. comparison between mosaic micro-crystals and quasi-perfect single microcrystals," *J. Appl. Crystallogr.* **12**, 387–394 (1979).
- ⁸⁶³S. P. Srivastava, R. C. Srivastava, I. D. Singh, S. D. Pandey, and P. L. Gupta, "Temperature dependence of thermal expansion and infrared lattice vibrational mode of nickel oxide," *J. Phys. Soc. Jpn.* **43**, 885–890 (1977).
- ⁸⁶⁴P. d V. Du Plessis, S. Van Tonder, and L. Alberts, "Elastic constants of a NiO single crystal: I (magnetic transitions)," *J. Phys. C: Solid State Phys.* **4**, 1983 (1971).
- ⁸⁶⁵R. Nesbet, "Antiferromagnetic superexchange effect," *Phys. Rev.* **119**, 658 (1960).
- ⁸⁶⁶A. B. Kunz, "Electronic structure of NiO," *J. Phys. C: Solid State Phys.* **14**, L455 (1981).
- ⁸⁶⁷M. O'Keeffe and W. J. Moore, "Diffusion of oxygen in single crystals of nickel oxide," *J. Phys. Chem.* **65**, 1438–1439 (1961).
- ⁸⁶⁸S. C. Choi, K. Koumoto, and H. Yanagida, "Electrical conduction and effective mass of a hole in single-crystal NiO," *J. Mater. Sci.* **21**, 1947–1950 (1986).
- ⁸⁶⁹G. J. Hill and B. M. Wanklyn, "Fluxed-melt growth of nickel oxide crystals and their electrical properties," *J. Cryst. Growth* **3**, 475–479 (1968).
- ⁸⁷⁰J. Aiken and A. Jordan, "Electrical transport properties of single crystal nickel oxide," *J. Phys. Chem. Solids* **29**, 2153–2167 (1968).
- ⁸⁷¹P. Gielisse, J. Plendl, L. Mansur, R. Marshall, S. Mitra, R. Mykolajewycz, and A. Smakula, "Infrared properties of NiO and CoO and their mixed crystals," *J. Appl. Phys.* **36**, 2446–2450 (1965).
- ⁸⁷²K. N. Manjunatha and S. Paul, "Investigation of optical properties of nickel oxide thin films deposited on different substrates," *Appl. Surf. Sci.* **352**, 10–15 (2015).
- ⁸⁷³P. Patil and L. Kadam, "Preparation and characterization of spray pyrolyzed nickel oxide (NiO) thin films," *Appl. Surf. Sci.* **199**, 211–221 (2002).
- ⁸⁷⁴M. Tanaka, M. Mukai, Y. Fujimori, M. Kondoh, Y. Tasaka, H. Baba, and S. Usami, "Transition metal oxide films prepared by pulsed laser deposition for atomic beam detection," *Thin Solid Films* **281**, 453–456 (1996).
- ⁸⁷⁵T. Seike and J. Nagai, "Electrochromism of 3d transition metal oxides," *Sol. Energy Mater.* **22**, 107–117 (1991).
- ⁸⁷⁶C. Lampert, T. Omstead, and P. Yu, "Chemical and optical properties of electrochromic nickel oxide films," *Sol. Energy Mater.* **14**, 161–174 (1986).
- ⁸⁷⁷X. Xia, J. Tu, J. Zhang, X. Wang, W. Zhang, and H. Huang, "Electrochromic properties of porous NiO thin films prepared by a chemical bath deposition," *Sol. Energy Mater. Sol. Cells* **92**, 628–633 (2008).
- ⁸⁷⁸G. A. Slack, "Crystallography and domain walls in antiferromagnetic NiO crystals," *J. Appl. Phys.* **31**, 1571–1582 (1960).
- ⁸⁷⁹M. Dare-Edwards, J. Goodenough, A. Hamnett, and N. Nicholson, "Photoelectrochemistry of nickel (ii) oxide," *J. Chem. Soc., Faraday Trans. 2* **77**, 643–661 (1981).
- ⁸⁸⁰R. Powell and W. Spicer, "Optical properties of NiO and CoO," *Phys. Rev. B* **2**, 2182 (1970).
- ⁸⁸¹D. Adler and J. Feinleib, "Electrical and optical properties of narrow-band materials," *Phys. Rev. B* **2**, 3112 (1970).
- ⁸⁸²L. Mattheiss, "Electronic structure of the 3D transition-metal monoxides. I. Energy-band results," *Phys. Rev. B* **5**, 290 (1972).
- ⁸⁸³L. A. Agapito, S. Curtarolo, and M. B. Nardelli, "Reformulation of DFT+U as a pseudohybrid hubbard density functional for accelerated materials discovery," *Phys. Rev. X* **5**, 011006 (2015).
- ⁸⁸⁴J. Choisnet, R. Evarestov, I. Tupitsyn, and V. Veryazov, "Investigation of the chemical bonding in nickel mixed oxides from electronic structure calculations," *J. Phys. Chem. Solids* **57**, 1839–1850 (1996).
- ⁸⁸⁵L. D'Amario, J. Föhlinger, G. Boschloo, and L. Hammarström, "Unveiling hole trapping and surface dynamics of NiO nanoparticles," *Chem. Sci.* **9**, 223–230 (2018).
- ⁸⁸⁶V. I. Anisimov, J. Zaanen, and O. K. Andersen, "Band theory and Mott insulators: Hubbard U instead of Stoner I ," *Phys. Rev. B* **44**, 943 (1991).
- ⁸⁸⁷A. Svane and O. Gunnarsson, "Transition-metal oxides in the self-interaction-corrected density-functional formalism," *Phys. Rev. Lett.* **65**, 1148 (1990).
- ⁸⁸⁸A. Varkey and A. Fort, "Solution growth technique for deposition of nickel oxide thin films," *Thin Solid Films* **235**, 47–50 (1993).
- ⁸⁸⁹G. Sawatzky and J. Allen, "Magnitude and origin of the band gap in NiO," *Phys. Rev. Lett.* **53**, 2339 (1984).
- ⁸⁹⁰R. S. Conell, D. A. Corrigan, and B. R. Powell, "The electrochromic properties of sputtered nickel oxide films," *Sol. Energy Mater. Sol. Cells* **25**, 301–313 (1992).
- ⁸⁹¹F. Koffyberg and F. Benko, "p-type NiO as a photoelectrolysis cathode," *J. Electrochem. Soc.* **128**, 2476 (1981).
- ⁸⁹²G. Boschloo and A. Hagfeldt, "Spectroelectrochemistry of nanostructured NiO," *J. Phys. Chem. B* **105**, 3039–3044 (2001).
- ⁸⁹³M. D. Irwin, D. B. Buchholz, A. W. Hains, R. P. Chang, and T. J. Marks, "p-type semiconducting nickel oxide as an efficiency-enhancing anode interfacial layer in polymer bulk-heterojunction solar cells," in *Proc. Natl. Acad. Sci.* **105**, 2783–2787 (2008).
- ⁸⁹⁴I. Valyukh, S. Green, H. Arwin, G. A. Niklasson, E. Wäckelgård, and C.-G. Granqvist, "Spectroscopic ellipsometry characterization of electrochromic tungsten oxide and nickel oxide thin films made by sputter deposition," *Sol. Energy Mater. Sol. Cells* **94**, 724–732 (2010).
- ⁸⁹⁵P. Godse, R. Sakhare, S. Pawar, M. Chougule, S. Sen, P. Joshi, and V. P. Patil, "Effect of annealing on structural, morphological, electrical and optical studies of nickel oxide thin films," *J. Surf. Eng. Mater. Adv. Technol.* **1**, 35 (2011).
- ⁸⁹⁶S. Hüfner, J. Osterwalder, T. Riesterer, and F. Hulliger, "Photoemission and inverse photoemission spectroscopy of NiO," *Solid State Commun.* **52**, 793–796 (1984).
- ⁸⁹⁷S. G. Danjumma, Y. Abubakar, and S. Suleiman, "Nickel oxide (NiO) devices and applications: A review," *Int. J. Eng. Res. Technol.* **8**, 12–21 (2019).
- ⁸⁹⁸H. Watanabe, "Thermal constants for Ni, NiO, MgO, MnO and CoO at low temperatures," *Thermochim. Acta* **218**, 365–372 (1993).
- ⁸⁹⁹W. Jifang, E. Fisher, and M. Manghnani, "Elastic constants of nickel oxide," *Chin. Phys. Lett.* **8**, 153 (1991).
- ⁹⁰⁰R. Clendenen and H. Drickamer, "Lattice parameters of nine oxides and sulfides as a function of pressure," *J. Chem. Phys.* **44**, 4223–4228 (1966).
- ⁹⁰¹M. Notis, R. Spriggs, and W. Hahn, Jr., "Elastic moduli of pressure-sintered nickel oxide," *J. Geophys. Res.* **76**, 7052–7061, <https://doi.org/10.1029/JB076i029p07052> (1971).
- ⁹⁰²G. Wood and T. Hodgkiess, "The hardness of oxides at ambient temperatures," *Mater. Corrosion* **23**, 766–773 (1972).
- ⁹⁰³P. Oliver, G. Watson, and S. Parker, "Molecular-dynamics simulations of nickel oxide surfaces," *Phys. Rev. B* **52**, 5323 (1995).
- ⁹⁰⁴R. Allen, T. Stephenson, C. Stanford, and S. Bernstein, "Slow neutron cross sections of gold, silver, indium, nickel, and nickel oxide," *Phys. Rev.* **96**, 1297 (1954).
- ⁹⁰⁵J. Keem and J. Honig, "Selected electrical and thermal properties of undoped nickel oxide," Technical Report No. ADA128940 (Thermophysical and Electronic Properties Information Analysis Center, 1978).
- ⁹⁰⁶H. White, "Specific heat of single crystal NiO from 3.2 to 18.75 K," *J. Chem. Phys.* **61**, 4907–4909 (1974).
- ⁹⁰⁷J. DuBose and D. Naugle, "Specific heat of bulklike NiO powder from 14 to 280 K," *J. Chem. Phys.* **70**, 4232–4237 (1979).
- ⁹⁰⁸P. Sahoo, D. K. Misra, J. Salvador, J. P. Makongo, G. S. Chaubey, N. J. Takas, J. B. Wiley, and P. F. Poudeu, "Microstructure and thermal conductivity of surfactant-free NiO nanostructures," *J. Solid State Chem.* **190**, 29–35 (2012).
- ⁹⁰⁹F. Lewis and N. Saunders, "The thermal conductivity of NiO and CoO at the neel temperature," *J. Phys. C: Solid State Phys.* **6**, 2525 (1973).
- ⁹¹⁰E. Aytan, B. Debnath, F. Kargar, Y. Barlas, M. Lacerda, J. Li, R. Lake, J. Shi, and A. Balandin, "Spin-phonon coupling in antiferromagnetic nickel oxide," *Appl. Phys. Lett.* **111**, 252402 (2017).
- ⁹¹¹W. Hayes and R. Loudon, *Scattering of Light by Crystals* (John Wiley & Sons Ltd, 1978).
- ⁹¹²T. I. Willett-Gies, C. M. Nelson, L. S. Abdallah, and S. Zollner, "Two-phonon absorption in LiF and NiO from infrared ellipsometry," *J. Vac. Sci. Technol. A* **33**, 061202 (2015).
- ⁹¹³R. Dietz, G. Parisot, and A. Meixner, "Infrared absorption and Raman scattering by two-magnon processes in NiO," *Phys. Rev. B* **4**, 2302 (1971).
- ⁹¹⁴M. Lacerda, F. Kargar, E. Aytan, R. Samnakay, B. Debnath, J. Li, A. Khitun, R. Lake, J. Shi, and A. Balandin, "Variable-temperature inelastic light scattering spectroscopy of nickel oxide: Disentangling phonons and magnons," *Appl. Phys. Lett.* **110**, 202406 (2017).

- ⁹¹⁵H. Wu and L.-S. Wang, "A study of nickel monoxide (NiO), nickel dioxide (ONiO), and Ni(O₂) complex by anion photoelectron spectroscopy," *J. Chem. Phys.* **107**, 16–21 (1997).
- ⁹¹⁶V. D. Moravec and C. C. Jarrold, "Study of the low-lying states of NiO- and NiO using anion photoelectron spectroscopy," *J. Chem. Phys.* **108**, 1804–1810 (1998).
- ⁹¹⁷K. Rao and A. Smakula, "Dielectric properties of cobalt oxide, nickel oxide, and their mixed crystals," *J. Appl. Phys.* **36**, 2031–2038 (1965).
- ⁹¹⁸V. Makarov, Y. M. Ksendzov, and V. Kruglov, "Drift mobility of carriers in nickel oxide," *Fizika* **9**, 512 (1967).
- ⁹¹⁹J. B. Goodenough, "Metallic oxides," *Prog. Solid State Chem.* **5**, 145–399 (1971).
- ⁹²⁰K. Koumoto, Z.-T. Zhang, and H. Yanahida, "High-temperature defect structure and electrical conduction in undoped and Li-or Al-doped NiO," *J. Ceram. Assoc. Jpn.* **92**, 83–89 (1984).
- ⁹²¹S. Handley and G. Bradberry, "Estimates of charge carrier mobility and lifetime in nickel oxide," *Phys. Lett. A* **40**, 277–278 (1972).
- ⁹²²C. Osburn and R. Vest, "Defect structure and electrical properties of NiO-I. High temperature," *J. Phys. Chem. Solids* **32**, 1331–1342 (1971).
- ⁹²³L. Li, X. Wang, Y. Liu, and J.-P. Ao, "NiO/GaN heterojunction diode deposited through magnetron reactive sputtering," *J. Vac. Sci. Technol. A* **34**, 02D104 (2016).
- ⁹²⁴H. Ohta, M. Kamiya, T. Kamiya, M. Hirano, and H. Hosono, "UV-detector based on pn-heterojunction diode composed of transparent oxide semiconductors, p-NiO/n-ZnO," *Thin Solid Films* **445**, 317–321 (2003).
- ⁹²⁵D. Snowden and H. Saltsburg, "Hopping conduction in NiO," *Phys. Rev. Lett.* **14**, 497 (1965).
- ⁹²⁶K. H. Kim, C. Takahashi, Y. Abe, and M. Kawamura, "Effects of Cu doping on nickel oxide thin film prepared by sol-gel solution process," *Optik* **125**, 2899–2901 (2014).
- ⁹²⁷G. Niu, S. Wang, J. Li, W. Li, and L. Wang, "Oxygen doping in nickel oxide for highly efficient planar perovskite solar cells," *J. Mater. Chem. A* **6**, 4721–4728 (2018).
- ⁹²⁸E. L. Miller and R. E. Rocheleau, "Electrochemical behavior of reactively sputtered iron-doped nickel oxide," *J. Electrochem. Soc.* **144**, 3072 (1997).
- ⁹²⁹R. Sharma, A. Acharya, S. Moghe, S. Shrivastava, M. Gangrade, T. Shripathi, and V. Ganeshan, "Effect of cobalt doping on microstructural and optical properties of nickel oxide thin films," *Mater. Sci. Semicond. Process.* **23**, 42–49 (2014).
- ⁹³⁰B. Meyer, A. Polity, D. Reppin, M. Becker, P. Hering, P. Klar, T. Sander, C. Reindl, J. Benz, M. Eickhoff, C. Heiliger, M. Heinemann, J. Bläsing, A. Krost, S. Shokovets, C. Müller, and C. Ronning, "Binary copper oxide semiconductors: From materials towards devices," *Phys. Status Solidi (b)* **249**, 1487–1509 (2012).
- ⁹³¹M. Heinemann, B. Eifert, and C. Heiliger, "Band structure and phase stability of the copper oxides Cu₂O, CuO, and Cu₄O₃," *Phys. Rev. B* **87**, 115111 (2013).
- ⁹³²W. Shockley and H. J. Queisser, "Detailed balance limit of efficiency of p-n junction solar cells," *J. Appl. Phys.* **32**, 510–519 (1961).
- ⁹³³A. Bhaumik, A. Haque, P. Karnati, M. Taufique, R. Patel, and K. Ghosh, "Copper oxide based nanostructures for improved solar cell efficiency," *Thin Solid Films* **572**, 126–133 (2014).
- ⁹³⁴M. I. Hossain, F. H. Alharbi, and N. Tabet, "Copper oxide as inorganic hole transport material for lead halide perovskite based solar cells," *Sol. Energy* **120**, 370–380 (2015).
- ⁹³⁵Z. Starowicz, K. Gawlińska-Nęcek, M. Bartmański, M. Wlazlo, T. Płociński, B. Adamczyk-Cieślak, G. Putynkowski, and P. Panek, "Investigation of the Zn and Cu oxides for heterojunction thin film solar cell application," *Microelectron. Eng.* **221**, 111196 (2020).
- ⁹³⁶M. Kastner, R. Birgeneau, G. Shirane, and Y. Endoh, "Magnetic, transport, and optical properties of monolayer copper oxides," *Rev. Mod. Phys.* **70**, 897 (1998).
- ⁹³⁷F. Koffyberg and F. Benko, "A photoelectrochemical determination of the position of the conduction and valence band edges of p-type CuO," *J. Appl. Phys.* **53**, 1173–1177 (1982).
- ⁹³⁸F. Brown, R. E. Menzel, M. M. Stewart, and P. A. Lefrancois, "Cuprous oxide as a catalyst. I. Preparation and promotion by metallic oxides," *J. Am. Chem. Soc.* **72**, 5602–5605 (1950).
- ⁹³⁹A. Junod, D. Eckert, G. Triscone, J. Müller, and W. Reichardt, "A study of the magnetic transitions in CuO: Specific heat (1–330 K), magnetic susceptibility and phonon density of states," *J. Phys.: Condens. Matter* **1**, 8021 (1989).
- ⁹⁴⁰D. H. Yoon, J. H. Yu, and G. M. Choi, "Co gas sensing properties of ZnO–CuO composite," *Sens. Actuators B* **46**, 15–23 (1998).
- ⁹⁴¹V. Malyshev and A. Pislyakov, "SnO₂-based thick-film-resistive sensor for H₂S detection in the concentration range of 1–10 mg m^{−3}," *Sens. Actuators B* **47**(1–3), 181–188 (1998).
- ⁹⁴²K. Muthe, J. Vyas, S. N. Narang, D. Aswal, S. Gupta, D. Bhattacharya, R. Pinto, G. Kothiyal, and S. Sabharwal, "A study of the CuO phase formation during thin film deposition by molecular beam epitaxy," *Thin Solid Films* **324**, 37–43 (1998).
- ⁹⁴³A. Ogwu, T. Darma, and E. Bouquerel, "Electrical resistivity of copper oxide thin films prepared by reactive magnetron sputtering," *J. Achiev. Mater. Manuf. Eng.* **24**, 172–177 (2007).
- ⁹⁴⁴S. Rehman, J.-H. Hur, and D.-k Kim, "Resistive switching in solution-processed copper oxide (Cu_xO) by stoichiometry tuning," *J. Phys. Chem. C* **122**, 11076–11085 (2018).
- ⁹⁴⁵S. Åsbrink and L.-J. Norrby, "A refinement of the crystal structure of copper (II) oxide with a discussion of some exceptional e.s.d.'s," *Acta Crystallogr. Sect. B* **26**, 8–15 (1970).
- ⁹⁴⁶J. Forsyth, P. Brown, and B. Wanklyn, "Magnetism in cupric oxide," *J. Phys. C: Solid State Phys.* **21**, 2917 (1988).
- ⁹⁴⁷G. Tunell, E. Posnjak, and C. Ksanda, "The crystal structure of tenorite (cupric oxide)," *J. Washington Acad. Sci.* **23**, 195–198 (1933), <https://www.jstor.org/stable/24532884>.
- ⁹⁴⁸A. Kirfel and K. Eichhorn, "Accurate structure analysis with synchrotron radiation. the electron density in Al₂O₃ and Cu₂O," *Acta Crystallogr. Sect. A* **46**, 271–284 (1990).
- ⁹⁴⁹J.-M. Zuo, M. Kim, M. O'keeffe, and J. Spence, "Direct observation of d-orbital holes and Cu–Cu bonding in Cu₂O," *Nature* **401**, 49–52 (1999).
- ⁹⁵⁰T. Lippmann and J. R. Schneider, "Accurate structure-factor measurements using high-energy synchrotron radiation: A test on cuprite, Cu₂O," *J. Appl. Crystallogr.* **33**, 156–167 (2000).
- ⁹⁵¹M. O'keeffe and J. Bovin, "The crystal structure of paramelaconite, Cu₄O₃," *Am. Miner.* **63**, 180–185 (1978).
- ⁹⁵²C. Frondel, "Paramelaconite. A tetragonal oxide of copper," *Am. Miner.: J. Earth Planet. Mater.* **26**, 657–672 (1941).
- ⁹⁵³L. Debbichi, M. C. M. de Lucas, and P. Krüger, "Electronic structure, lattice dynamics and thermodynamic stability of paramelaconite Cu₄O₃," *Mater. Chem. Phys.* **148**, 293–298 (2014).
- ⁹⁵⁴J. Medina-Valtierra, C. Frausto-Reyes, G. Camarillo-Martínez, and J. A. Ramírez-Ortiz, "Complete oxidation of isopropanol over Cu₄O₃ (paramelaconite) coating deposited on fiberglass by CVD," *Appl. Catal. A* **356**, 36–42 (2009).
- ⁹⁵⁵L. Pinsard-Gaudart, J. Rodriguez-Carvajal, A. Gukasov, and P. Monod, "Magnetic properties of paramelaconite (Cu₄O₃): A pyrochlore lattice with S=½," *Phys. Rev. B* **69**, 104408 (2004).
- ⁹⁵⁶A. Sanson, F. Rocca, G. Dalba, P. Fornasini, R. Grisenti, M. Dapiaggi, and G. Artioli, "Negative thermal expansion and local dynamics in Cu₂O and Ag₂O," *Phys. Rev. B* **73**, 214305 (2006).
- ⁹⁵⁷N. Datta and J. Jeffery, "The crystal structure of paramelaconite, Cu₁₂⁺ Cu₄⁺ O₁₄," *Acta Crystallogr. Sect. B* **34**, 22–26 (1978).
- ⁹⁵⁸R. Schmidt-Whitley, M. Martinez-Clemente, and A. Revcolevschi, "Growth and microstructural control of single crystal cuprous oxide Cu₂O," *J. Cryst. Growth* **23**, 113–120 (1974).
- ⁹⁵⁹T. Ito, H. Yamaguchi, K. Okabe, and T. Masumi, "Single-crystal growth and characterization of Cu₂O and CuO," *J. Mater. Sci.* **33**, 3555–3566 (1998a).
- ⁹⁶⁰D. Prabhakaran and A. Boothroyd, "Single crystal growth of Zn-doped CuO by the floating-zone method," *J. Cryst. Growth* **250**, 77–82 (2003).
- ⁹⁶¹B. Wanklyn and B. Garrard, "The flux growth of some simple and complex oxides," *J. Mater. Sci. Lett.* **2**, 285–290 (1983).
- ⁹⁶²T. W. Pieters and J. Nedermeyer, "Single crystal preparation of CuO," *J. Cryst. Growth* **15**, 299–300 (1972).
- ⁹⁶³N. Yamamoto, Y. Bando, and T. Takada, "Single crystal growth of CuO by chemical transport method," *Jpn. J. Appl. Phys., Part 1* **12**, 1115 (1973).

- ⁹⁶⁴E. C. Milliken and J. F. Cordaro, "Influence of oxygen atmosphere on the crystal growth of copper (II) oxide," *J. Mater. Res.* **5**, 53–56 (1990).
- ⁹⁶⁵X. Zheng, M. Suzuki, and C. Xu, "A new approach to single crystal growth of cuo," *Mater. Res. Bull.* **33**, 605–610 (1998).
- ⁹⁶⁶A. Chen, H. Long, X. Li, Y. Li, G. Yang, and P. Lu, "Controlled growth and characteristics of single-phase Cu₂O and CuO films by pulsed laser deposition," *Vacuum* **83**, 927–930 (2009).
- ⁹⁶⁷J. Pierson, A. Thobor-Keck, and A. Billard, "Cuprite, paramelaconite and tenorite films deposited by reactive magnetron sputtering," *Appl. Surf. Sci.* **210**, 359–367 (2003).
- ⁹⁶⁸S. Cho, "Optical and electrical properties of CuO thin films deposited at several growth temperatures by reactive rf magnetron sputtering," *Met. Mater. Int.* **19**, 1327–1331 (2013).
- ⁹⁶⁹K. Kawaguchi, R. Kita, M. Nishiyama, and T. Morishita, "Molecular beam epitaxy growth of CuO and Cu₂O films with controlling the oxygen content by the flux ratio of Cu/O," *J. Cryst. Growth* **143**, 221–226 (1994).
- ⁹⁷⁰Y. Akaltun, "Effect of thickness on the structural and optical properties of CuO thin films grown by successive ionic layer adsorption and reaction," *Thin Solid Films* **594**, 30–34 (2015).
- ⁹⁷¹J. Ghijssen, L.-H. Tjeng, J. van Elp, H. Eskes, J. Westerink, G. A. Sawatzky, and M. T. Czyzyk, "Electronic structure of Cu₂O and CuO," *Phys. Rev. B* **38**, 11322 (1988).
- ⁹⁷²H. P. Maruska and A. K. Ghosh, "A study of oxide-based heterostructure photoelectrodes," *Sol. Energy Mater.* **1**, 411–429 (1979).
- ⁹⁷³S. Hüfner and G. Wertheim, "X-ray photoelectron band structure of some transition-metal compounds," *Phys. Rev. B* **8**, 4857 (1973).
- ⁹⁷⁴T. Ito, H. Yamaguchi, T. Masumi, and S. Adachi, "Optical properties of CuO studied by spectroscopic ellipsometry," *J. Phys. Soc. Jpn.* **67**, 3304–3309 (1998b).
- ⁹⁷⁵F. Tran and P. Blaha, "Implementation of screened hybrid functionals based on the yukawa potential within the lapw basis set," *Phys. Rev. B* **83**, 235118 (2011).
- ⁹⁷⁶E. Ruiz, S. Alvarez, P. Alemany, and R. A. Evarestov, "Electronic structure and properties of Cu₂O," *Phys. Rev. B* **56**, 7189 (1997).
- ⁹⁷⁷W. Ching, Y.-N. Xu, and K. Wong, "Ground-state and optical properties of Cu₂O and CuO crystals," *Phys. Rev. B* **40**, 7684 (1989).
- ⁹⁷⁸J. Dahl and A. Switendick, "Energy bands in cuprous oxide," *J. Phys. Chem. Solids* **27**, 931–942 (1966).
- ⁹⁷⁹L. Kleinman and K. Mednick, "Self-consistent energy bands of Cu₂O," *Phys. Rev. B* **21**, 1549 (1980).
- ⁹⁸⁰Z. Szotek, W. Temmerman, and H. Winter, "Application of the self-interaction correction to transition-metal oxides," *Phys. Rev. B* **47**, 4029 (1993).
- ⁹⁸¹M. Nolan and S. D. Elliott, "The p-type conduction mechanism in Cu₂O: A first principles study," *Phys. Chem. Chem. Phys.* **8**, 5350–5358 (2006).
- ⁹⁸²K. L. Hardee and A. J. Bard, "Semiconductor electrodes: X. photoelectrochemical behavior of several polycrystalline metal oxide electrodes in aqueous solutions," *J. Electrochem. Soc.* **124**, 215 (1977).
- ⁹⁸³Y. P. Sukhorukov, N. Loshkareva, A. Samokhvalov, and A. Moskvin, "Absorption spectra of CuO single crystals near the absorption edge and the nature of the optical gap in copper oxides," *J. Exp. Theor. Phys.* **81**, 998–1002 (1995).
- ⁹⁸⁴Y. S. Chaudhary, A. Agrawal, R. Shrivastav, V. R. Satsangi, and S. Dass, "A study on the photoelectrochemical properties of copper oxide thin films," *Int. J. Hydrogen Energy* **29**, 131–134 (2004).
- ⁹⁸⁵D. Wu, Q. Zhang, and M. Tao, "LSDA+U study of cupric oxide: Electronic structure and native point defects," *Phys. Rev. B* **73**, 235206 (2006).
- ⁹⁸⁶Y. Wang, S. Lany, J. Ghanbaja, Y. Fagot-Revrat, Y. Chen, F. Soldera, D. Horwat, F. Mücklich, and J. Pierson, "Electronic structures of Cu₂O, Cu₄O₃, and CuO: A joint experimental and theoretical study," *Phys. Rev. B* **94**, 245418 (2016).
- ⁹⁸⁷A. Filippetti and V. Fiorentini, "Magnetic ordering in CuO from first principles: A cuprate antiferromagnet with fully three-dimensional exchange interactions," *Phys. Rev. Lett.* **95**, 086405 (2005).
- ⁹⁸⁸F. Brunoval, N. Vast, L. Reining, M. Izquierdo, F. Sirotti, and N. Barrett, "Exchange and correlation effects in electronic excitations of Cu₂O," *Phys. Rev. Lett.* **97**, 267601 (2006).
- ⁹⁸⁹D. O. Scanlon, B. J. Morgan, G. W. Watson, and A. Walsh, "Acceptor levels in p-type Cu₂O: Rationalizing theory and experiment," *Phys. Rev. Lett.* **103**, 096405 (2009).
- ⁹⁹⁰P. Marksteiner, P. Blaha, and K. Schwarz, "Electronic structure and binding mechanism of Cu₂O," *Z. Phys. B* **64**, 119–127 (1986).
- ⁹⁹¹T. Kotani, M. van Schilfgaarde, and S. V. Faleev, "Quasiparticle self-consistent GW method: A basis for the independent-particle approximation," *Phys. Rev. B* **76**, 165106 (2007).
- ⁹⁹²S. Lany, "Band-structure calculations for the 3d transition metal oxides in GW," *Phys. Rev. B* **87**, 085112 (2013).
- ⁹⁹³S. Nikitine, *Optical Properties of Solids* (Springer, 1969).
- ⁹⁹⁴Y. Wang, P. Miska, D. Pilloud, D. Horwat, F. Mücklich, and J.-F. Pierson, "Transmittance enhancement and optical band gap widening of Cu₂O thin films after air annealing," *J. Appl. Phys.* **115**, 073505 (2014).
- ⁹⁹⁵A. Daunois, J. Deiss, and B. Meyer, "Étude spectrophotométrique de l'absorption bleue et violette de Cu₂O," *J. Phys.* **27**, 142–146 (1966).
- ⁹⁹⁶A. Živković, A. Roldan, and N. H. De Leeuw, "Density functional theory study explaining the underperformance of copper oxides as photovoltaic absorbers," *Phys. Rev. B* **99**, 035154 (2019).
- ⁹⁹⁷M. Beg and S. Shapiro, "Study of phonon dispersion relations in cuprous oxide by inelastic neutron scattering," *Phys. Rev. B* **13**, 1728 (1976).
- ⁹⁹⁸P. Cortona and M. Mebarki, "Cu₂O behavior under pressure: An ab initio study," *J. Phys.: Condens. Matter* **23**, 045502 (2011).
- ⁹⁹⁹J. Loram, K. Mirza, C. Joyce, and A. Osborne, "Specific-heat evidence for quasi-1d magnetic order in CuO," *Europhys. Lett.* **8**, 263 (1989).
- ¹⁰⁰⁰I. Krynetskii, A. Moskvin, S. Naumov, A. Samokhvalov, and D. Parsons, "The CuO single crystal anomalies in the thermal expansion and the magnetostriction," *JETP Lett.* **56**, 566–566 (1992).
- ¹⁰⁰¹J.-H. Hu and H. L. Johnston, "Low temperature heat capacities of inorganic solids. XVI. Heat capacity of cupric oxide from 15 to 300 K," *J. Am. Chem. Soc.* **75**, 2471–2473 (1953).
- ¹⁰⁰²J. A. Eastman, U. Choi, S. Li, L. Thompson, and S. Lee, "Enhanced thermal conductivity through the development of nanofluids," *MRS Online Proc. Library* **457**, 3–11 (1996).
- ¹⁰⁰³S. Nallusamy, "Thermal conductivity analysis and characterization of copper oxide nanofluids through different techniques," *J. Nano Res.* **40**, 105–112 (2016).
- ¹⁰⁰⁴S. Lee, S.-S. Choi, S. Li, and J. Eastman, "Measuring thermal conductivity of fluids containing oxide nanoparticles," *J. Heat Transfer* **121**(2), 280–289 (1999).
- ¹⁰⁰⁵Y. Hwang, Y. Ahn, H. Shin, C. Lee, G. Kim, H. Park, and J. Lee, "Investigation on characteristics of thermal conductivity enhancement of nanofluids," *Curr. Appl. Phys.* **6**, 1068–1071 (2006).
- ¹⁰⁰⁶M. Liu, M. C. Lin, and C. Wang, "Enhancements of thermal conductivities with Cu, CuO, and carbon nanotube nanofluids and application of mwnt/water nanofluid on a water chiller system," *Nanoscale Res. Lett.* **6**, 297 (2011).
- ¹⁰⁰⁷J. Chrzanowski and J. Irwin, "Raman scattering from cupric oxide," *Solid State Commun.* **70**, 11–14 (1989).
- ¹⁰⁰⁸H. Goldstein, D.-S. Kim, Y. Y. Peter, L. Bourne, J. Chaminade, and L. Nganga, "Raman study of CuO single crystals," *Phys. Rev. B* **41**, 7192 (1990).
- ¹⁰⁰⁹L. Debbichi, M. Marco de Lucas, J. Pierson, and P. Kruger, "Vibrational properties of CuO and Cu₄O₃ from first-principles calculations, and Raman and infrared spectroscopy," *J. Phys. Chem. C* **116**, 10232–10237 (2012).
- ¹⁰¹⁰A. Kuž'menko, D. Van der Marel, P. Van Bentum, E. Tishchenko, C. Presura, and A. Bush, "Infrared spectroscopic study of CuO: Signatures of strong spin-phonon interaction and structural distortion," *Phys. Rev. B* **63**, 094303 (2001).
- ¹⁰¹¹G. Kliche and Z. Popovic, "Far-infrared spectroscopic investigations on CuO," *Phys. Rev. B* **42**, 10060 (1990).
- ¹⁰¹²X. Chen, J. Irwin, and J. Franck, "Evidence for a strong spin-phonon interaction in cupric oxide," *Phys. Rev. B* **52**, R13130 (1995).
- ¹⁰¹³W. Reichardt, F. Gompf, M. Ain, and B. Wanklyn, "Lattice dynamics of cupric oxide," *Z. Phys. B* **81**, 19–24 (1990).
- ¹⁰¹⁴E. Kroumova, M. Aroyo, J. Perez-Mato, A. Kirov, C. Capillas, S. Ivantchev, and H. Wondratschek, "Bilbao crystallographic server: Useful databases and tools for phase-transition studies," *Phase Transitions* **76**, 155–170 (2003).

- ¹⁰¹⁵M. L. Polak, M. K. Gilles, J. Ho, and W. Lineberger, "Photoelectron spectroscopy of copper oxide (CuO')," *J. Phys. Chem.* **95**, 3460–3463 (1991).
- ¹⁰¹⁶R. Kužel and F. Weichman, "Hole mobility in Cu_2O . I. Scattering by lattice vibrations," *Can. J. Phys.* **48**, 2643–2656 (1970).
- ¹⁰¹⁷S. Knight, D. Prabhakaran, C. Binek, and M. Schubert, "Electromagnon excitation in cupric oxide measured by Fabry-Pérot enhanced terahertz mueller matrix ellipsometry," *Sci. Rep.* **9**, 1353 (2019).
- ¹⁰¹⁸X. Nie, S.-H. Wei, and S. Zhang, "First-principles study of transparent p-type conductive SrCu_2O_2 and related compounds," *Phys. Rev. B* **65**, 075111 (2002).
- ¹⁰¹⁹J. Hodby, T. Jenkins, C. Schwab, H. Tamura, and D. Trivich, "Cyclotron resonance of electrons and of holes in cuprous oxide, Cu_2O ," *J. Phys. C: Solid State Phys.* **9**, 1429 (1976).
- ¹⁰²⁰Y. S. Lee, M. T. Winkler, S. C. Siah, R. Brandt, and T. Buonassisi, "Hall mobility of cuprous oxide thin films deposited by reactive direct-current magnetron sputtering," *Appl. Phys. Lett.* **98**, 192115 (2011b).
- ¹⁰²¹B. Li, K. Akimoto, and A. Shen, "Growth of Cu_2O thin films with high hole mobility by introducing a low-temperature buffer layer," *J. Cryst. Growth* **311**, 1102–1105 (2009).
- ¹⁰²²D. S. Murali and A. Subrahmanyam, "Synthesis of low resistive p type Cu_4O_3 thin films by dc reactive magnetron sputtering and conversion of Cu_4O_3 into CuO by laser irradiation," *J. Phys. D: Appl. Phys.* **49**, 375102 (2016).
- ¹⁰²³Z.-X. Shen, J. Allen, J. Yeh, J.-S. Kang, W. Ellis, W. Spicer, I. Lindau, M. Maple, Y. Dalichaouch, M. Torikachvili, J. Sun, and T. Geballe, "Anderson hamiltonian description of the experimental electronic structure and magnetic interactions of copper oxide superconductors," *Phys. Rev. B* **36**, 8414 (1987).
- ¹⁰²⁴Y. Peng, Z. Zhang, T. Viet Pham, Y. Zhao, P. Wu, and J. Wang, "Density functional theory analysis of dopants in cupric oxide," *J. Appl. Phys.* **111**, 103708 (2012).
- ¹⁰²⁵A. Živković and N. H. de Leeuw, "Exploring the formation of intrinsic p-type and n-type defects in CuO ," *Phys. Rev. Mater.* **4**, 074606 (2020).
- ¹⁰²⁶Y. Du, X. Gao, and X. Meng, "Preparation and characterization of single-phased n-type CuO film by dc magnetron sputtering," *Phys. B: Condens. Matter* **560**, 37–40 (2019).
- ¹⁰²⁷R. Singh, L. Yadav, Shrey, and T. Shweta, "Effect of annealing time on the structural and optical properties of n-cuo thin films deposited by sol-gel spin coating technique and its application in n-cuo/p-Si heterojunction diode," *Thin Solid Films* **685**, 195–203 (2019).
- ¹⁰²⁸S. Baturay, A. Tombak, D. Batibay, and Y. S. Ocak, "n-type conductivity of CuO thin films by metal doping," *Appl. Surf. Sci.* **477**, 91–95 (2019).
- ¹⁰²⁹W. Heitmann, "Reactively evaporated films of scandia and yttria," *Appl. Opt.* **12**, 394–397 (1973).
- ¹⁰³⁰G. Liu, Y. Jin, H. He, and Z. Fan, "Effect of substrate temperatures on the optical properties of evaporated Sc_2O_3 thin films," *Thin Solid Films* **518**, 2920–2923 (2010b).
- ¹⁰³¹I. Ladany, P. Zanzucchi, J. Andrews, J. Kane, and E. DePiano, "Scandium oxide antireflection coatings for superluminescent LEDs," *Appl. Opt.* **25**, 472–473 (1986).
- ¹⁰³²A. Herrero, B. Gila, C. Abernathy, S. Pearton, V. Craciun, K. Siebein, and F. Ren, "Epitaxial growth of Sc_2O_3 films on GaN," *Appl. Phys. Lett.* **89**, 092117 (2006).
- ¹⁰³³A. Liu, G. Liu, H. Zhu, H. Song, B. Shin, E. Fortunato, R. Martins, and F. Shan, "Water-induced scandium oxide dielectric for low-operating voltage n- and p-type metal-oxide thin-film transistors," *Adv. Funct. Mater.* **25**, 7180–7188 (2015).
- ¹⁰³⁴R. Mehandru, B. Luo, J. Kim, F. Ren, B. Gila, A. Onstine, C. Abernathy, S. Pearton, D. Gotthold, R. Birkhahn, B. Peres, R. Fitch, J. Gillespie, T. Jenkins, J. Sewell, D. Via, and A. Crespo, "AlGaN/GaN metal-oxide-semiconductor high electron mobility transistors using Sc_2O_3 as the gate oxide and surface passivation," *Appl. Phys. Lett.* **82**, 2530–2532 (2003).
- ¹⁰³⁵P. Langston, E. Krous, D. Schultz, D. Patel, L. Emmert, A. Markosyan, B. Reagan, K. Wernsing, Y. Xu, Z. Sun, R. Route, M. Fejer, J. Rocca, W. Rudolph, and C. Menoni, "Point defects in Sc_2O_3 thin films by ion beam sputtering," *Appl. Opt.* **53**, A276–A280 (2014).
- ¹⁰³⁶D. O. Klenov, L. F. Edge, D. G. Schlom, and S. Stemmer, "Extended defects in epitaxial Sc_2O_3 films grown on (111) Si," *Appl. Phys. Lett.* **86**, 051901 (2005).
- ¹⁰³⁷Z. Xu, A. Daga, and H. Chen, "Microstructure and optical properties of scandium oxide thin films prepared by metalorganic chemical-vapor deposition," *Appl. Phys. Lett.* **79**, 3782–3784 (2001).
- ¹⁰³⁸C. Adelmann, P. Lehnert, S. Van Elshocht, C. Zhao, B. Brijs, A. Franquet, T. Conard, M. Roeckerath, J. Schubert, O. Boissiere, C. Lohe, and S. De Gendt, "Growth of dysprosium-, scandium-, and hafnium-based third generation high- κ dielectrics by atomic vapor deposition," *Chem. Vap. Deposition* **13**, 567–573 (2007).
- ¹⁰³⁹A. Markosyan, R. Route, M. Fejer, D. Patel, and C. Menoni, "Study of spontaneous and induced absorption in amorphous Ta_2O_5 and SiO_2 dielectric thin films," *J. Appl. Phys.* **113**, 133104 (2013).
- ¹⁰⁴⁰A. S. Foster, V. Sulimov, F. L. Gejo, A. Shluger, and R. M. Nieminen, "Structure and electrical levels of point defects in monoclinic zirconia," *Phys. Rev. B* **64**, 224108 (2001).
- ¹⁰⁴¹A. S. Foster, F. L. Gejo, A. Shluger, and R. M. Nieminen, "Vacancy and interstitial defects in hafnia," *Phys. Rev. B* **65**, 174117 (2002).
- ¹⁰⁴²C. S. Menoni, E. M. Krous, D. Patel, P. Langston, J. Tollerud, D. N. Nguyen, L. A. Emmert, A. Markosyan, R. Route, M. Fejer, and W. Rudolph, "Advances in ion beam sputtered Sc_2O_3 for optical interference coatings," *Proc. SPIE* **7842**, 784202 (2010).
- ¹⁰⁴³O. Belosludtsev, K. Juškevičius, L. Ceizaris, R. Samuilovas, S. Stanionytė, V. Jasulaitienė, and S. Kičas, "Correlation between stoichiometry and properties of scandium oxide films prepared by reactive magnetron sputtering," *Appl. Surf. Sci.* **427**, 312–318 (2018).
- ¹⁰⁴⁴D. Richard, E. Munoz, T. Butz, L. Errico, and M. Rentería, "Electronic and structural properties, and hyperfine interactions at sc sites in the semiconductor Sc_2O_3 : TDPAc and ab initio study," *Phys. Rev. B* **82**, 035206 (2010).
- ¹⁰⁴⁵O. Knop and J. M. Hartley, "Refinement of the crystal structure of scandium oxide," *Can. J. Chem.* **46**, 1446–1450 (1968).
- ¹⁰⁴⁶S. Geller, P. Romo, and J. Remeika, "Refinement of the structure of scandium sesquioxide," *Z. Kristallogr.-Cryst. Mater.* **124**, 136–142 (1967).
- ¹⁰⁴⁷C. T. Horowitz, *Scandium its Occurrence, Chemistry Physics, Metallurgy, Biology and Technology* (Elsevier, 2012).
- ¹⁰⁴⁸A. Ubaldini and M. M. Carnasciali, "Raman characterisation of powder of cubic Re_2O_3 ($\text{Re}=\text{Nd}, \text{Gd}, \text{Dy}, \text{Tm}, \text{and Lu}$), Sc_2O_3 and Y_2O_3 ," *J. Alloys Compd.* **454**, 374–378 (2008).
- ¹⁰⁴⁹T. Masui, Y. W. Kim, N. Imanaka, and G.-Y. Adachi, "Electrochemical Sc_2O_3 single crystal growth," *J. Alloys Compd.* **374**, 97–100 (2004).
- ¹⁰⁵⁰D. Gross and P. Sermon, "Scandia optical coatings for application at 351 nm," *Thin Solid Films* **368**, 116–124 (2000).
- ¹⁰⁵¹A. Reid and A. Ringwood, "High-pressure scandium oxide and its place in the molar volume relationships of dense structures of M_2X_3 and ABX_3 type," *J. Geophys. Res.* **74**, 3238–3252, <https://doi.org/10.1029/JB074i012p03238> (1969).
- ¹⁰⁵²H. H. Tippins, "Absorption edge spectrum of scandium oxide," *J. Phys. Chem. Solids* **27**, 1069–1071 (1966).
- ¹⁰⁵³L. Pauling and M. Shappell, "The crystal structure of bixbyite and the c-modification of the sesquioxides," *Z. Kristallogr.-Cryst. Mater.* **75**, 128–142 (1930).
- ¹⁰⁵⁴W. Hu, B. Frost, and R. L. Peterson, "Thermally stable yttrium-scandium oxide high-dielectrics deposited by a solution process," *J. Phys. D: Appl. Phys.* **49**, 115109 (2016).
- ¹⁰⁵⁵P. de Rouffignac, A. P. Yousef, K. H. Kim, and R. G. Gordon, "ALD of scandium oxide from scandium tris (n, n-diisopropylacetamidinate) and water," *Electrochem. Solid State Lett.* **9**, F45 (2006).
- ¹⁰⁵⁶M. Al-Kuhaili, "Optical properties of scandium oxide films prepared by electron beam evaporation," *Thin Solid Films* **426**, 178–185 (2003).
- ¹⁰⁵⁷A. Companion, "The optical energy gap of scandium oxide," *Phys. Chem. Solids* **25**, 357–358 (1964).
- ¹⁰⁵⁸A. L. Companion and R. E. Wyatt, "The diffuse reflectance spectra of some titanium oxides," *J. Phys. Chem. Solids* **24**, 1025–1028 (1963).
- ¹⁰⁵⁹B. Angelov, "Covalency in cubic lanthanide sesquioxides," *J. Phys. C: Solid State Phys.* **10**, L505 (1977).
- ¹⁰⁶⁰B. Angelov, "Lattice and binding energies of cubic lanthanide sesquioxides," *J. Phys. C: Solid State Phys.* **15**, L239 (1982).
- ¹⁰⁶¹P. Herve and L. Vandamme, "Empirical temperature dependence of the refractive index of semiconductors," *J. Appl. Phys.* **77**, 5476–5477 (1995).

- ¹⁰⁶²C. Larez and C. Rincon, "Temperature dependence of the fundamental energy gap in InSb," *Mater. Lett.* **24**, 211–213 (1995).
- ¹⁰⁶³A. Polimeni, M. Capizzi, Y. Nabetani, Y. Ito, T. Okuno, T. Kato, T. Matsumoto, and T. Hirai, "Temperature dependence and bowing of the bandgap in ZnSe_{1-x}O_x," *Appl. Phys. Lett.* **84**, 3304–3306 (2004).
- ¹⁰⁶⁴G. Gogotsi, "Thermal stress behaviour of yttria, scandia and AlN ceramics," *Ceram. Int.* **6**, 31–35 (1980).
- ¹⁰⁶⁵M. Berard, C. Wirkus, and D. Wilder, "Diffusion of oxygen in selected monocrystalline rare earth oxides," *J. Am. Ceram. Soc.* **51**, 643–647 (1968).
- ¹⁰⁶⁶S. Dole, O. Hunter, Jr., and F. Calderwood, "Elastic properties of polycrystalline scandium and thulium sesquioxides," *J. Am. Ceram. Soc.* **60**, 167–168 (1977).
- ¹⁰⁶⁷The Materials Project, *Materials Data on Sc₂O₃ by Materials Project* (The Materials Project, 2020).
- ¹⁰⁶⁸Y. Repelin, C. Proust, E. Husson, and J. Beny, "Vibrational spectroscopy of the c-form of yttrium sesquioxide," *J. Solid State Chem.* **118**, 163–169 (1995).
- ¹⁰⁶⁹S. J. Pearton, C. R. Abernathy, and F. Ren, *Gallium Nitride Processing for Electronics, Sensors and Spintronics* (Springer Science & Business Media, 2006).
- ¹⁰⁷⁰M. Pachecka, C. J. Lee, J. Sturm, and F. Bijkerk, "Metal diffusion properties of ultra-thin high-k Sc₂O₃ films," *AIP Adv.* **7**, 105324 (2017).
- ¹⁰⁷¹J. Wang, Y. Wang, S. Tao, H. Li, J. Yang, and M. Zhou, "Scandia-doped tungsten bodies for Sc-type cathodes," *Appl. Surf. Sci.* **215**, 38–48 (2003).
- ¹⁰⁷²J. Wang, W. Liu, L. Li, Y. Wang, Y. Wang, and M. Zhou, "A study of scandia-doped pressed cathodes," *IEEE Trans. Electron Devices* **56**, 799–804 (2009b).
- ¹⁰⁷³M. Hirano and K. Date, "Scandium-doped anatase (TiO₂) nanoparticles directly formed by hydrothermal crystallization," *J. Am. Ceram. Soc.* **88**, 2604–2607 (2005).
- ¹⁰⁷⁴D. Agarkov, M. Borik, S. Bredikhin, A. Kulebyakin, I. Kuritsyna, E. Lomonova, F. Milovich, V. Myzina, V. Osiko, E. Agarkova, and N. Tabachkova, "Structure and transport properties of zirconia-based solid solution crystals co-doped with scandium and cerium oxides," *Russ. J. Electrochim.* **54**, 459–463 (2018).
- ¹⁰⁷⁵X. Li, X. Jiang, H. Xu, Q. Xu, L. Jiang, Y. Shi, and Q. Zhang, "Scandium-doped PrBaCo_{2-x}Sc_xO_{6-δ} oxides as cathode material for intermediate-temperature solid oxide fuel cells," *Int. J. Hydrogen Energy* **38**, 12035–12042 (2013).
- ¹⁰⁷⁶P. Kong, Y. Pu, P. Ma, and J. Zhu, "Relationship between oxygen defects and properties of scandium oxide films prepared by ion-beam sputtering," *Coating* **9**, 517 (2019).
- ¹⁰⁷⁷G. Kuz'micheva, V. Rybakov, and S. Kutovoi, "Preparation and structure of Ga_{2-x}Sc_xO₃ (0.42 × 0.52)," *Inorg. Mater.* **40**, 1066–1069 (2004).
- ¹⁰⁷⁸N. Zhu, B. Wang, K. Ma, X. Xue, and J. Su, "Structural characters and band offset of Ga₂O₃–Sc₂O₃ alloys," *Appl. Phys. Lett.* **120**(5), 053503 (2022).
- ¹⁰⁷⁹Y. Kakehi, S. Nakao, K. Satoh, and T. Yotsuya, "Properties of copper-scandium oxide thin films prepared by pulsed laser deposition," *Thin Solid Films* **445**, 294–298 (2003).
- ¹⁰⁸⁰G. Li, W. Chen, Y. Wang, and B. Duhan, "Electronic structure, photoluminescence and phosphorescence properties in Sr₂ScGaO₅:Sm₃," *Dyes Pigments* **157**, 259–266 (2018).
- ¹⁰⁸¹S. V. Chernov, Y. A. Dobrovolsky, S. Y. Istomin, E. V. Antipov, J. Grins, G. Svensson, N. V. Tarakina, A. M. Abakumov, G. Van Tendeloo, S. G. Eriksson, and S. M. Rahman, "Sr₂GaScO₅, Sr₁₀Ga₆Sc₄O₂₅, and SrGa_{0.75}Sc_{0.25}O_{2.5}: A play in the octahedra to tetrahedra ratio in oxygen-deficient perovskites," *Inorg. Chem.* **51**, 1094–1103 (2012).
- ¹⁰⁸²M. Akiyama, T. Kamohara, K. Kano, A. Teshigahara, Y. Takeuchi, and N. Kawahara, "Enhancement of piezoelectric response in scandium aluminum nitride alloy thin films prepared by dual reactive cosputtering," *Adv. Mater.* **21**, 593–596 (2009).
- ¹⁰⁸³M. Akiyama, K. Kano, and A. Teshigahara, "Influence of growth temperature and scandium concentration on piezoelectric response of scandium aluminum nitride alloy thin films," *Appl. Phys. Lett.* **95**, 162107 (2009).
- ¹⁰⁸⁴M. Akiyama, K. Umeda, A. Honda, and T. Nagase, "Influence of scandium concentration on power generation figure of merit of scandium aluminum nitride thin films," *Appl. Phys. Lett.* **102**, 021915 (2013).
- ¹⁰⁸⁵Q. Wang, Y. Lu, S. Mishin, Y. Oshmyansky, and D. A. Horsley, "Design, fabrication, and characterization of scandium aluminum nitride-based piezoelectric micromachined ultrasonic transducers," *J. Microelectromech. Syst.* **26**, 1132–1139 (2017).
- ¹⁰⁸⁶M. Passlack, E. Schubert, W. Hobson, M. Hong, N. Moriya, S. Chu, K. Konstadinidis, J. Mannaerts, M. Schnoes, and G. Zydzik, "Ga₂O₃ films for electronic and optoelectronic applications," *J. Appl. Phys.* **77**, 686–693 (1995).
- ¹⁰⁸⁷A. A. Malygin, V. E. Drozd, A. A. Malkov, and V. M. Smirnov, "From VB Aleskovskii's 'Framework' hypothesis to the method of molecular layering/atomic layer deposition," *Chem. Vapor Deposition* **21**, 216–240 (2015).
- ¹⁰⁸⁸R. L. Puurunen, "A short history of atomic layer deposition: Tuomo sunta's atomic layer epitaxy," *Chem. Vapor Deposition* **20**, 332–344 (2014).
- ¹⁰⁸⁹N. Parsons, J. W. Elam, S. M. George, S. Haukka, H. Jeon, W. Kessels, M. Leskelä, P. Poodt, M. Ritala, and S. M. Rossnagel, "History of atomic layer deposition and its relationship with the American Vacuum Society," *J. Vac. Sci. Technol. A* **31**, 050818 (2013).
- ¹⁰⁹⁰R. L. Puurunen, "Surface chemistry of atomic layer deposition: A case study for the trimethylaluminum/water process," *J. Appl. Phys.* **97**, 121301 (2005).
- ¹⁰⁹¹H. Schäfer, *Chemical Transport Reactions* (Elsevier, 2016).
- ¹⁰⁹²P. E. Tomaszewski, "Jan Czochralski—Father of the Czochralski method," *J. Cryst. Growth* **236**, 1–4 (2002).
- ¹⁰⁹³D. C. Harris, "A century of sapphire crystal growth: Origin of the EFG method," *Proc. SPIE* **7425**, 74250P (2009).
- ¹⁰⁹⁴S. Millman, *A History of Engineering and Science in the Bell System: Physical Sciences (1925–1980)* (AT&T Bell Laboratories Short Hills, NJ, 1983).
- ¹⁰⁹⁵H. Theurer, "Method of processing semiconductor materials" U.S. patent 3060123A (23 October 1962).
- ¹⁰⁹⁶H. Theurer, "Purification of silicon," *Bell Lab. Rec.* **3**, 327–330 (1955).
- ¹⁰⁹⁷D. Elwell, "Fundamentals of flux growth," in *Crystal Growth in Science and Technology* (Springer, 1989), pp. 133–142.
- ¹⁰⁹⁸I. V. Tudose, F. Comanescu, P. Pascaiu, S. Bucur, L. Rusen, F. Iacomi, E. Koudoumas, and M. P. Suciu, "Chemical and physical methods for multifunctional nanostructured interface fabrication," in *Functional Nanostructured Interfaces for Environmental and Biomedical Applications* (Elsevier, 2019), pp. 15–26.
- ¹⁰⁹⁹H. M. Manasevit, "Single-crystal gallium arsenide on insulating substrates," *Appl. Phys. Lett.* **12**, 156–159 (1968).
- ¹¹⁰⁰H. Manasevit and W. I. Simpson, "The use of metal-organics in the preparation of semiconductor materials: I. epitaxial gallium-v compounds," *J. Electrochem. Soc.* **116**, 1725 (1969).
- ¹¹⁰¹K. Günther, "Aufdampfschichten aus halbleitenden III-V-verbindungen," *Z. Naturforsch. A* **13**, 1081–1089 (1958).
- ¹¹⁰²J. E. Davey and T. Pankey, "Epitaxial GaAs films deposited by vacuum evaporation," *J. Appl. Phys.* **39**, 1941–1948 (1968).
- ¹¹⁰³A. Y. Cho and J. Arthur, "Molecular beam epitaxy," *Prog. Solid State Chemistry* **10**, 157–191 (1975).
- ¹¹⁰⁴H. A. Dabkowska and A. B. Dabkowski, "Crystal growth of oxides by optical floating zone technique," in *Springer Handbook of Crystal Growth* (Springer, 2010), pp. 367–391.
- ¹¹⁰⁵I. N. Mihailescu and E. György, "Pulsed laser deposition: An overview," in *International Trends in Optics and Photonics* (Springer, 1999), pp. 201–214.
- ¹¹⁰⁶H. M. Smith and A. Turner, "Vacuum deposited thin films using a ruby laser," *Appl. Opt.* **4**, 147–148 (1965).
- ¹¹⁰⁷J. B. Mooney and S. B. Radding, "Spray pyrolysis processing," *Annu. Rev. Mater. Sci.* **12**, 81–101 (1982).
- ¹¹⁰⁸R. Chamberlin and J. Skarman, "Chemical spray deposition process for inorganic films," *J. Electrochem. Soc.* **113**, 86 (1966a).
- ¹¹⁰⁹R. Chamberlin and J. Skarman, "Chemically sprayed thin film photovoltaic converters," *Solid-State Electron.* **9**, 819–823 (1966b).
- ¹¹¹⁰V. Vasu and A. Subrahmanyam, "Reaction kinetics of the formation of indium tin oxide films grown by spray pyrolysis," *Thin Solid Films* **193**, 696–703 (1990).
- ¹¹¹¹M. Ueltzen, "The Verneuil flame fusion process: Substances," *J. Cryst. Growth* **132**, 315–328 (1993).